

**New engineered FcRn-targeting  
nanoplatfoms for oral delivery of  
biopharmaceuticals**

Cláudia Azevedo

**D**  
2021



**Cláudia Azevedo:** New engineered  
FcRn-targeting nanoplatfoms for oral  
delivery of biopharmaceuticals



**D.ICBAS 2021**

**New engineered FcRn-targeting nanoplatfoms  
for oral delivery of biopharmaceuticals**  
Cláudia Azevedo



Cláudia Azevedo

## **NEW ENGINEERED FcRn-TARGETING NANOPLATFOMS FOR ORAL DELIVERY OF BIOPHARMACEUTICALS**

Tese de Candidatura ao grau de Doutor em Ciências  
Biomédicas submetida ao Instituto de Ciências  
Biomédicas Abel Salazar da Universidade do Porto

Orientador:

Doutor Bruno Filipe Carmelino Cardoso Sarmiento  
Categoria – Investigador Principal/Professor Auxiliar  
Afiliação – i3S – Instituto de Investigação e Inovação em  
Saúde & INEB - Instituto Nacional de Engenharia  
Biomédica, Universidade do Porto / IUCS – Instituto  
Universitário de Ciências da Saúde

Co-Orientador:

Doutor Jan Terje Andersen  
Categoria – Investigador Principal  
Afiliação – Oslo University Hospital - Department of  
Biosciences, University of Oslo, Norway

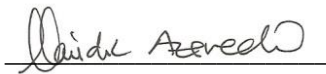


# DECLARAÇÃO DE HONRA

---

Eu, Cláudia Filipa Maia Azevedo, declaro que a presente tese é de minha autoria e não foi utilizada previamente noutro curso ou unidade curricular, desta ou de outra instituição. As referências a outros autores (afirmações, ideias, pensamentos) respeitam escrupulosamente as regras da atribuição, e encontram-se devidamente indicadas no texto e nas referências bibliográficas, de acordo com as normas de referenciação. Tenho consciência de que a prática de plágio e auto-plágio constitui um ilícito académico.

Porto, 15 de Janeiro de 2021



Cláudia Azevedo



The work presented in this thesis was developed at:

Nanomedicines & Translational Drug Delivery Group  
i3S - Instituto de Investigação e Inovação em Saúde and  
INEB - Instituto Nacional de Engenharia Biomédica  
Universidade do Porto, Porto, Portugal  
Rua Alfredo Allen, 208  
4200-135 Porto, Portugal  
<https://www.i3s.up.pt/> | [www.ineb.up.pt](http://www.ineb.up.pt)



And

Oslo University Hospital and University of Oslo  
Department of Immunology and department of Pharmacology  
Centre for Immune Regulation  
UiO FOCIS Center of Excellence  
Sognsvannsveien 20, 0372 Oslo, Norway  
<https://www.ous-research.no/andersen/>



And

Massachusetts Institute of Technology  
Department of Mechanical Engineering and The Langer Lab  
77 Massachusetts Ave., Room 76-661c, Cambridge, MA 02139  
<https://meche.mit.edu/> | <https://langer-lab.mit.edu/>



**Massachusetts  
Institute of  
Technology**



**KOCH INSTITUTE**  
for Integrative Cancer Research at MIT

And

European Space Agency  
European Space Research and Technology Centre  
Keplerlaan 1, 2201 AZ Noordwijk, Netherlands  
[https://www.esa.int/About\\_Us/ESTEC](https://www.esa.int/About_Us/ESTEC)



**esa**

European Space Agency



**spin your  
thesis!**

## FINANCIAL SUPPORT

---

Cláudia Azevedo was supported by a national PhD grant (SFRH/BD/117598/2016) from Fundação para a Ciência e Tecnologia (FCT), Portugal. Cláudia Azevedo was also supported by a Fulbright (PS00293218) and FLAD (137/2019) grants during 6 months in 2019/2020. This work is a result of the project NORTE-01-0145-FEDER-000012, supported by Norte Portugal Regional Operational Programme (NORTE 2020), under the PORTUGAL 2020 Partnership Agreement, through the Europe and Regional Development Fund (ERDF). This work was financed by FEDER - Fundo Europeu de Desenvolvimento Regional funds through the COMPETE 2020 - Operacional Programme for Competitiveness and Internationalisation (POCI), Portugal 2020, and by Portuguese funds through FCT- Fundação para a Ciência e a Tecnologia/Ministério da Ciência, Tecnologia e Ensino Superior in the framework of the project "Institute for Research and Innovation in Health Sciences" (UID/BIM/04293/2019), and also Partnership Agreement PT2020 UID/QUI/50006/2013 -POCI/01/0145/FEDER/007265. This work was also supported by the Research Council of Norway (Grant no. 274993), the Koch Institute/MIT, Merck, the Spin Your Thesis! 2020 program organized by the European Space Agency (ESA) Education Office, Abbott, COST and by Instituto Ciências Biomédicas de Abel Salazar (ICBAS).







## PUBLICATIONS

---

Ao abrigo do disposto do nº 2, alínea a) do artigo 31º do Decreto-Lei n.º 115/2013 de 7 de Agosto, fazem parte integrante desta tese de doutoramento os seguintes trabalhos já publicados ou submetidos para publicação:

- **Azevedo C.**, Andersen J.T., Sarmento B., Traverso G., The potential of porcine *ex vivo* platform for intestinal permeability screening of FcRn-targeted drugs, *European Journal of Pharmaceutics and Biopharmaceutics* 2021, 162: 99-104.
- **Azevedo C.\***, Almeida A.\*, Macedo M.H.\*, Pinto S.\*, van Loon J., Sarmento B, The effect of hypergravity in intestinal permeability of nanoformulations and molecules, *European Journal of Pharmaceutics and Biopharmaceutics* 2021, 163: 38-48. (\*equal contribution)
- **Azevedo C.\***, Pinto S.\*, Benjakul S., Santos H.A., Andersen J.T., Traverso G., Sarmento S., Prevention of diabetes-associated fibrosis: Strategies to orally treat diabetes with FcRn-targeted nanosystems, *Advanced Drug Delivery Reviews* 2021. (\*equal contribution)
- **Azevedo C.**, Nilsen J., Grevys A., Nunes R., Andersen J.T., Sarmento B., Engineered albumin-functionalized nanoparticles for improved FcRn binding enhances oral delivery of insulin, *Journal of Controlled Release* 2020, 327: 161-173.
  - Outside Front Cover Page, *Journal of Controlled Release* 2020, Volume 327, ISSN:0168-3659.
- Almeida A\*, **Azevedo C\***, Macedo MH\*, Sarmento B, 3D intestinal models towards a more realistic permeability screening, in Santos H. and Martins J.P., *Nanotechnology for Oral Drug Delivery*, Elsevier 2020, ISBN 9780128180389. (\*equal contribution)
- **Azevedo C.**, Pereira I., Sarmento B., Intestinal mucosal tissue models to validate functionalized nanosystems, in Fahr A., *et al.*, *Characterization of Pharmaceutical Nano- and Microsystems*, Wiley 2020, ISBN: 978-1-119-41404-9.
- **Azevedo C.**, Macedo M. H., Sarmento B., Strategies for enhanced intracellular delivery of nanomaterials, *Drug Discovery Today* 2018, 23:944-959, DOI: 10.1016/j.drudis.2017.08.011.



# ACKNOWLEDGEMENTS

---

## **Addressee unknown - retour à l'expéditeur**

Many thanks for the clouds.

Many thanks for the well-tempered Clavier  
and, why not, for the warm winter boots.

Many thanks for my strange brain  
and for all manner of other hidden organs,  
for the air, and, of course, for the claret.

Heartfelt thanks for my lighter  
and my desire not running out of fuel,  
as well as my regret, my deep regret.

Many thanks for the four seasons,  
for the number  $e$ , for my dose of caffeine,  
and, of course, for the strawberry dish  
painted by Chardin, as well as for sleep,  
for sleep quite especially,  
and, last not least, for the beginning  
and the end and the few minutes in between  
fervent thanks, even, if you like,  
the voles out there in the garden.

(Hans Magnus Enzensberger)

My PhD was *painted*, throughout four years, with the motivation and orientation of many people. This *canvas* was a roller coaster of emotions, which sometimes was a bit hard to manage. Fortunately, I have a lot of *painters* in my life that *draw good lines* on their unique style and helped me to achieve one more goal. To all of them, I express my sincere appreciation for their support on getting a great work and helping me to grow personally and professionally. All these people and experiences will be with me for a lifetime and I am very grateful for that! Particularly:

And first of all, to my supervisor, Professor **Bruno Sarmiento**, for believing in my potential, being always present and careful, the daily effort to provide *easel, brushes* and the *canvas*, to take this painting to a good *atelier*. I am very thankful for his trust, guidance, encouragement and friendship. For sure, he is an example of leader and mentor, who taught me to be more assertive and confident, motivated me in more frustrated moments, challenged me and supported my projects “outside the box”. You have my acknowledgement and respect!

To my co-supervisor, **Jan Terje Andersen**, for the warm welcome in his lab, at Norway. The experience in Oslo was so productive and I feel so grateful for have learned so much. Jan is a very dynamic and positive person, supports young generations and eagers for innovation. Characteristics that inspire and motivate me. I am very thankful for the constructive discussions, attentive readings and the feeling of “family” that I found in his group. It’s good to be an “Albumin Girl”!

To **Jeannette Nilsen**, the best lab partner that I could have. Thank you very much for all the scientific sharing about albumin and FcRn, smiles, adventures in and outside the lab and friendship. I will never forget my norwegian sister and *The scream (Edvard Munch)*! Also, to **Julia Alopaeus**, for helping me with some logistics and social meetings in Norway.

To **Giovanni Traverso**, for accepting me at MIT, Boston. It was both a blast and a challenging experience. This was for sure the experience that I grew the most. Thank you for allowing me to be in an environment full of opportunities, conducive to innovation, networking and entrepreneurship. It was great to experience a bit of the american dream and know the *Nighthawks (Edward Hopper)* style!

To **Raquel Almeida**, for giving me incentive to try new *colors*. To **Jack van Loon, Alan Downson** and **Nigel Savage**, for warmly receiving and helping the team ARTEMIS at ESA, The Netherlands. It was refreshing to see a *Starry Night (Van Gogh)* and the immensity that is beyond our eyes! “The only limit is the one that you set yourself” and we raised the spark!

To Professor **Vítor Seabra**, for giving me access to CESPÚ - Instituto de Investigaç o e Forma o Avançada em Ci ncias e Tecnologias da Sa de, and to adequate equipment to perform some assays of this work. And to **Virg nia Gonalves** for helping me to solve some troubleshooting with HPLC.

To the “**Quarteto Fant stico**”, the marvelous group that was born alongside with this project. I am grateful for the surprise of our friendship, shared trips and craziness. To **Fl via Sousa**, my trip partner, for sharing experiences, advices and motivation to be and do more and better; to **Andreia Almeida** for having a relaxed way of being and a positive vibe and for sharing adrenalin with me; and **Helena Macedo**, for being a conscious, critical and just person. This group is always ready for a great adventure! Many thanks for supporting me throughout my path. Following *Afremov*, you gave a bunch of *colors* to my PhD!

To **all team members** of different groups that I was in, especially from **NTDD group**, for all the sharing of knowledge, fellowship, help and sweeties. I would like to highlight the important role of **Jos  das Neves** (general, sincere and critical input), **Rute Nunes** (animal assays), **Algirdas Grevys** (transcytosis and recycling assays) and **Ming Zhao** (help in Boston) for their motivation, wise advices through different moments of the *painting*.

To all the Portuguese that I met in Boston, specially to **Ana Cadete** and ** ngelo Crespo** for helping me throughout this process and giving me a bit of familiar *lines*. Also, to **Abhisheck** and **Samip**, my indian friends, for adding some joy, kindness and company during my stay. They are all friends for life that were met in an unexpected way!

The last but not the least, to my **Family**:

Aos **meus Pais**, Paula e Ant nio, e aos **meus Irm os**, Marco e Sim o, pelo apoio incondicional, por ficarem genuinamente felizes com as minhas conquistas, apesar de  s vezes n o perceberem muito bem em que se traduzem. Aos **meus Padrinhos**, Olinda e Joaquim, por se orgulharem de mim e darem sempre uma palavra de apreo e motiva o.   **minha Av ** por rezar por mim! Ao **meu Namorado**, melhor amigo e companheiro, Jo o, por me confortar, por me fazer sentir especial todos os dias, por me aceitar tal como sou, por ter paci ncia para as minhas ansiedades, por o ter sentido perto apesar de estar 6 meses longe. Com ele aprendi a redefinir prioridades e a tornar-me na minha melhor vers o. Agradeo profundamente a todos pela intimidade, confiana, apoio e *cores cintilantes*, bem ao jeito d’ *O Beijo (Gustav Klimt)*, que deram vida   minha *tela*!

“Questions you cannot answer are usually far better for you than  
answers you cannot question.”  
(Yuval Noah Harari)

# TABLE OF CONTENTS

---

ABSTRACT .....	i
RESUMO .....	iii
GRAPHICAL ABSTRACT.....	v
LIST OF FIGURES .....	vii
LIST OF TABLES .....	xv
ACRONYMS AND ABBREVIATIONS LIST .....	xvii
<b>CHAPTER I: LITERATURE REVIEW</b> .....	1
1. Introduction.....	5
1.1. Epidemiology and the biology behind the disease .....	5
1.2. Oral insulin delivery for T1DM .....	5
1.3. Biologic barriers of oral delivery drugs.....	7
2. Nanoparticles as a strategy for drug delivery .....	7
2.1. The evolution of Nanomedicine .....	7
2.2. Nanoparticles characteristics and their influence .....	8
3. Functionalized nanoparticles for an enhanced bioavailability .....	11
3.1. Albumin as a ligand .....	11
3.2. FcRn as a receptor .....	12
3.2.1. <i>FcRn structure and interaction with albumin</i> .....	12
3.2.2. <i>Biologic mechanisms mediated by FcRn</i> .....	14
3.3. Albumin- based drug delivery of insulin .....	16
3.4. Albumin-targeted nanosystems for oral delivery of insulin .....	17
4. Intestinal models for preclinical validation .....	18
4.1. Intestinal morphology.....	18
4.2. <i>In vitro</i> models.....	21
4.2.1. <i>Monoculture model</i> .....	22
4.2.2. <i>Co-culture model</i> .....	23
4.2.3. <i>3D co-culture model</i> .....	25
4.2.4. <i>Gut-on-a-chip model</i> .....	26
4.3. <i>Ex vivo</i> models.....	31
4.3.1. <i>FcRn tissue expression and cross-species differences</i> .....	32
4.3.1.1. <i>Human</i> .....	32
4.3.1.2. <i>Mouse</i> .....	32
4.3.1.3. <i>Porcine</i> .....	33
4.3.2. <i>Standard models</i> .....	35
4.3.2.1. <i>Diffusion chambers</i> .....	35
4.3.2.2. <i>Everted intestinal sac model</i> .....	36
4.3.2.3. <i>Non-everted intestinal sac model</i> .....	36
4.3.2.4. <i>Everted intestinal ring</i> .....	37
4.4. <i>In vivo</i> FcRn model systems.....	37
<b>CHAPTER II: OVERVIEW AND AIMS</b> .....	41
1. Overview.....	43



2. Aims.....	44
<b>CHAPTER III: MATERIALS AND METHODS</b> .....	<b>45</b>
1. Cell culture.....	47
2. Protein production .....	47
3. Polymeric nanoparticles production .....	47
4. Physical chemical characterization .....	48
4.1. Particle size and zeta potential analysis .....	48
4.2. Morphological characterization and elementary analysis .....	48
4.3. Insulin association efficiency and drug loading .....	49
4.4. Insulin release .....	49
4.5. Albumin conjugation efficiency .....	50
5. Protein structure .....	50
5.1. Determination of secondary structure.....	50
5.2. Confirmation of the conjugation .....	51
6. Binding to human FcRn .....	51
7. <i>In vitro</i> experiments .....	52
7.1. Transcytosis assay .....	52
7.2. Uptake and recycling assays .....	52
8. <i>Ex vivo</i> experiments .....	53
8.1. Tissue dissection and cultivation .....	53
8.2. Immunohistochemistry and hematoxylin and eosin staining .....	54
8.3. RT-PCR analysis .....	54
8.4. Transport experiments using the <i>ex vivo</i> platform.....	55
9. <i>In vivo</i> experiments.....	55
9.1. Induction of T1DM.....	55
9.2. Pharmacodynamics .....	56
10. Statistical analysis .....	57
<b>CHAPTER IV: RESULTS AND DISCUSSION</b> .....	<b>59</b>
1. Rationale for the design of albumin decorated nanoparticles .....	63
2. Characterization of the produced nanoparticles.....	64
2.1. Physical-chemical properties of albumin-decorated PLGA-PEG NPs.....	64
2.2. Albumin conjugation to NPs.....	64
2.3. Functional encapsulation of insulin in NPs .....	67
2.4. Albumin decorated NPs bind FcRn in a pH dependent manner .....	70
3. <i>In vitro</i> validation.....	71
3.1. Produced NPs show enhanced <i>in vitro</i> transcytosis in epithelial cells .....	71
3.2. Produced NPs show enhanced <i>in vitro</i> uptake and recycling in endothelial cells.....	73
4. <i>Ex vivo</i> validation .....	76
4.1. The tissue integrity is maintained in the porcine <i>ex vivo</i> model .....	76
4.2. FcRn is expressed across the gastrointestinal tract .....	78
4.3. Engineered albumin variant shows enhanced transcytosis in the porcine <i>ex vivo</i> platform.....	80
5. <i>In vivo</i> validation .....	83
<b>CHAPTER V: CONCLUSIONS AND FUTURE PERSPECTIVES</b> .....	<b>89</b>

1. Conclusions .....	91
2. Future Perspectives.....	93
<b>CHAPTER VI: REFERENCES</b> .....	<b>95</b>
<b>APPENDIX</b> .....	<b>109</b>
<b>NMR RESULTS</b> .....	<b>111</b>
<b>THE EFFECT OF HYPERGRAVITY IN INTESTINAL PERMEABILITY</b> .....	<b>117</b>
1. Introduction .....	121
2. Materials and Methods .....	122
2.1. Metabolic activity studies .....	122
2.2. Expression of cellular components by immunocytochemistry .....	123
2.3. Cell culture .....	124
2.4. Hypergravity exposure .....	125
2.5. Cellular integrity by hematoxylin and eosin staining.....	125
2.6. Intestinal permeability study .....	125
3. Results and Discussion .....	127
3.1. No influence of hypergravity in cellular metabolic activity .....	127
3.2. Hypergravity effect might induce a tipping point on the expression of cellular components....	128
3.3. Barrier integrity is maintained after hypergravity exposure .....	132
3.4. Hypergravity interfered differently among transport mechanisms .....	133
4. References .....	135
<b>THE ALBUMIN TRIPLE MUTANT</b> .....	<b>137</b>
1. Overview.....	139
2. Materials and Methods .....	139
2.1. Binding affinity to human FcRn.....	139
2.2. Assessment of FcRn expression in Caco-2 cells .....	139
2.3. <i>In vivo</i> studies .....	140
2.3.1. <i>Biodistribution</i> .....	140
2.3.1.1. <i>Production of fluorescent nanoparticles</i> .....	140
2.3.1.2. <i>Imaging</i> .....	140
2.3.2. <i>Pharmacokinetic</i> .....	141
3. Results and discussion.....	141
3.1. Physical-chemical characterization.....	141
3.2. Binding affinity to human FcRn.....	141
3.3. FcRn expression in Caco-2 cells .....	143
3.4. <i>In vitro</i> experiments.....	144
3.5. NPs are widely maintained in the gut .....	145
3.6. The hypoglycemic effect .....	147
4. References .....	148
<b>PUBLISHED AND SUBMITTED PAPERS</b> .....	<b>149</b>
Prevention of diabetes-associated fibrosis: Strategies in FcRn-targeted nanosystems for oral drug delivery .....	151
Strategies for enhanced intracellular delivery of nanomaterials .....	199

Engineered albumin-functionalized nanoparticles for improved FcRn binding enhance oral delivery of insulin.....	241
The potential of porcine ex vivo platform for intestinal permeability screening of FcRn-targeted drugs .....	277
The effect of hypergravity on intestinal permeability of nanoformulations and molecules.....	297
<b>BIBLIOGRAPHIC NOTE</b> .....	333

## ABSTRACT

---

Diabetes *mellitus* (DM) is a widespread metabolic and chronic disease. Current management of type 1 DM (T1DM) is based on exogenous subcutaneous administration of peptide drugs, as insulin. However, the invasive and painful routes associated to their administration frequently dictate poor patient compliance, contributing to a leading cause of mortality and morbidity. To secure patients' convenience and compliance, oral administration is the preferred route for drug delivery. Though, the harsh condition of the gastrointestinal tract (GIT) and selective epithelial barrier compromise efficient delivery of peptide drugs. The developments in nanomedicine drug delivery have opened new perspectives to design and synthesize efficient nanocarriers and multifunctional nanomaterials. Indeed, the potential of nanomaterials to overwhelm the biologic barriers have led to the development of platforms capable of improving the oral bioavailability of drugs. A strategy to overcome the intestinal barrier is the modulation of nanomaterials size, charge and surface composition, in order to dictate the internalization pathway, escape lysosomes and interact with the target. Particularly, targeting of drugs to receptors expressed at the epithelial cell layers may enhance uptake and transport across the mucosal barriers. One such receptor is the neonatal Fc receptor (FcRn), which naturally transports immunoglobulin G and albumin bidirectionally across polarized epithelial cells. Comparing the endogenous FcRn-targeted ligands, albumin is reported to be more efficiently transported through FcRn-expressing epithelial cells and produced in a cost-effective manner, compared with IgG.

The main aim of this thesis was to develop biodegradable poly(lactic-co-glycolic)-poly(ethylene glycol) (PLGA-PEG) mucodiffusive nanoparticles (NPs), surface-functionalized with albumin as FcRn-targeting moieties, to increase the oral bioavailability of biopharmaceuticals, using insulin as model drug. Initially, the focus was on the optimization of the physical-chemical characteristics of NPs regarding particle size and surface charge, insulin association efficiency (AE), albumin conjugation efficiency (CE), protein structure and insulin release. Specifically, NPs were decorated with site-specific conjugated human albumin, engineered for improved pH dependent binding to FcRn. The designed NPs of monodisperse 150 nm in size, had -9 mV of zeta potential, were 10% (w/w) loaded with insulin and their surface was further functionalized in theoretical surface of 0.5% with engineered human albumin. Insulin structure showed to be affected by the encapsulation method, while albumin structure was maintained after conjugation. Furthermore, the developed nanosystem revealed a prolonged release, of insulin, with only 2.5% being released within 8 hours. Importantly, the engineered albumin-functionalized NPs bound human FcRn (hFcRn) favorably and showed enhanced transport across epithelial polarized MDCK-hFcRn cell layers. After epithelial transcytosis, it was demonstrated that NPs can be taken up and recycled by endothelial HMEC1-hFcRn cells, with the same binding pattern.

After exploring the biologic mechanisms related to FcRn, it was investigated the potential of simulated hypergravity to be used in oral delivery of biopharmaceuticals. Thus, it was explored the effect of hypergravity in *in vitro* intestinal permeability of NPs, using Caco-2 cells. It was shown that the cellular metabolic activity and integrity were maintained after exposure to different gravity levels (g-levels), compared to reference conditions. The application of different g-levels can lead to changes in the expression of different proteins on intestinal cells. However, the FcRn-mediated transport of the produced nanoparticles showed no significant changes, when increasing the g-levels.

Next, a porcine *ex vivo* model was used as a more realistic validation of the intestinal permeability, due to its physiological and anatomical similarities, which allow the reduced animal usage in preclinical validation. After analyzing the integrity and morphology of the porcine tissue, the FcRn expression across the GIT was verified. Studying the stomach, duodenum and jejunum, it was demonstrated that FcRn-expression was maintained for up 7 days, especially in duodenum. When evaluating the duodenal permeability, the engineered human albumin variant with higher affinity to FcRn, showed to be more efficiently transported, as demonstrated *in vitro*.

Finally, the conjugated NPs to engineered albumin variant with high binding affinity to FcRn, were orally administered to hFcRn expressing mice induced with diabetes. In pharmacodynamic *in vivo* studies, a reduction of glycemia was measured as a function of receptor targeting, with up to around 40% reduction after 1 hour post-delivery.

Overall, a FcRn-targeted nanoplatform was developed for oral delivery of insulin, which was validated in *in vitro*, *ex vivo* and *in vivo* models. These PLGA-PEG NPs decorated with human engineered albumin for improved FcRn-dependent transport showed to offer a novel attractive strategy in overcoming the barriers along the GIT, delivering encapsulated insulin and increasing its oral bioavailability. Thus, shows clinical potential as an oral insulin delivery system for T1DM therapy, and, potentially, for other biopharmaceutical-based therapies, since FcRn is broadly expressed in humans.

## RESUMO

---

Diabetes *mellitus* (DM) é uma doença metabólica e crônica prevalente. O tratamento atual da DM tipo 1 (T1DM) é baseado na administração exógena subcutânea de fármacos peptídicos, como a insulina. No entanto, a administração está associada a vias invasivas e dolorosas, o que frequentemente ditam a baixa adesão do paciente, contribuindo para uma das principais causas de mortalidade e morbidade. Para garantir a conveniência e conformidade dos pacientes, a administração oral é a via preferida para a administração do medicamento. Contudo, as condições adversas do trato gastrointestinal (GIT) e a barreira epitelial seletiva comprometem a administração eficiente de fármacos peptídicos. Os desenvolvimentos da nanomedicina, para a administração oral de fármacos, abriram novas perspectivas para desenhar e sintetizar nanotransportadores eficientes e nanomateriais multifuncionais. Na verdade, o potencial dos nanomateriais para ultrapassar as barreiras biológicas levou ao desenvolvimento de plataformas capazes de melhorar a biodisponibilidade oral dos fármacos. Uma estratégia para superar a barreira intestinal é a modulação das características físico-químicas dos nanossistemas, como tamanho, carga e composição da superfície, a fim de ditar a via de internalização, escapar aos lisossomas e interagir com o alvo. Particularmente, o direcionamento de fármacos para recetores expressos nas células epiteliais, pode aumentar a absorção e o transporte através das barreiras mucosas. Um desses recetores é o recetor Fc neonatal (FcRn), que transporta naturalmente imunoglobulina G e albumina bidirecionalmente através de células epiteliais polarizadas. Comparando os ligandos endógenos direcionados ao FcRn, a albumina é descrita como sendo mais eficientemente transportada através de células epiteliais que expressam FcRn e produzida de uma maneira mais econômica, em comparação com a IgG.

O objetivo principal desta tese foi desenvolver nanopartículas (NPs) biodegradáveis e mucodifusivas de poli(láctico-co-glicólico)-poli(etilenoglicol) (PLGA-PEG), funcionalizadas com albumina como ligando do FcRn, para aumentar a biodisponibilidade oral de fármacos, usando a insulina como fármaco modelo. Inicialmente, foi focada a otimização das características físico-químicas dos NPs, em termos de tamanho de partícula e carga superficial, eficiência de associação de insulina (EA), eficiência de conjugação de albumina (CE), estrutura das proteínas e liberação do fármaco. Especificamente, as NPs foram funcionalizadas com albumina humana, desenhada para melhorar a ligação dependente do pH ao FcRn. As NPs produzidas tinham 150 nm de tamanho, eram monodispersas, tinham -9 mV de zeta potencial, eram 10% (w/w) carregadas com insulina e a sua superfície teórica foi 0.5% funcionalizada, com albumina humana. A estrutura da insulina foi afetada pelo método de encapsulação, enquanto que a estrutura da albumina foi mantida após a conjugação. Além disso, o nanossistema desenvolvido revelou uma liberação controlada e prolongada, de insulina, com apenas 2.5% de liberação durante 8 horas. É importante ressaltar que as NPs funcionalizadas com albumina ligaram-se favoravelmente ao hFcRn e

mostraram um transporte aprimorado através das células epiteliais MCDK-hFcRn polarizadas. Após a transcitose epitelial, foi demonstrado que as NPs podem ser absorvidas e recicladas pelas células endoteliais HMEC1-hFcRn, com o mesmo padrão de ligação.

Após explorar os mecanismos biológicos relacionados com o FcRn, foi investigado o potencial da hipergravidade simulada para ser utilizada na administração oral de fármacos. Assim, foi explorado o efeito da hipergravidade na permeabilidade *in vitro* intestinal de NPs, usando as células Caco-2. Foi demonstrado que a atividade metabólica e integridade celular foram mantidas após exposição a diferentes níveis de gravidade (níveis de g), em comparação com as condições de referência. A aplicação de diferentes níveis de g pode levar a alterações de expressão de diferentes proteínas das células intestinais. Contudo, o transporte mediado por FcRn das NPs produzidas, não apresentou alterações significativas, com o aumento dos níveis de g.

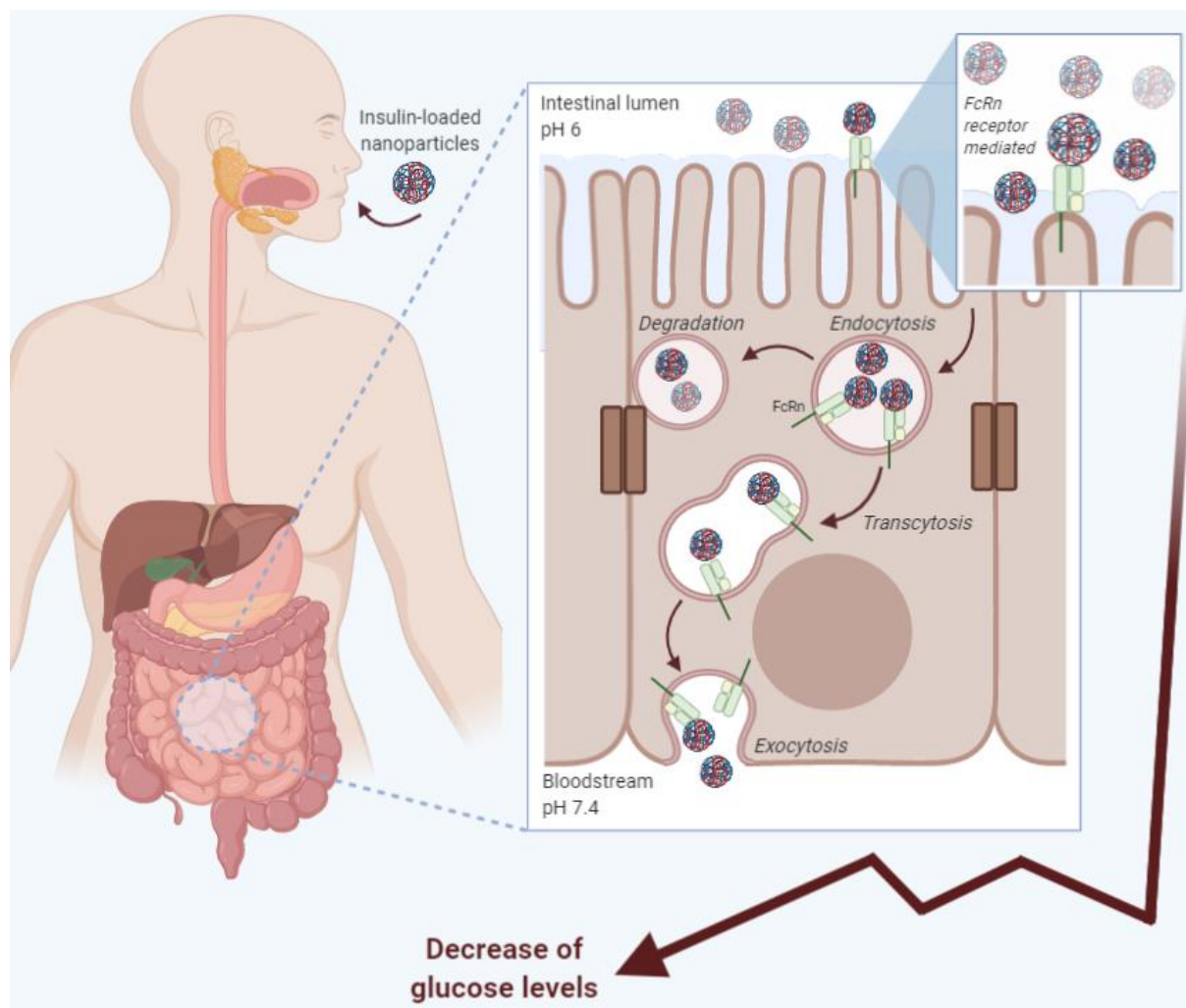
Em seguida, um modelo *ex vivo* de porco foi utilizado como validação mais realista da permeabilidade intestinal, devido às suas semelhanças fisiológicas e anatômicas, o que permite diminuir o uso de animais na validação pré-clínica. Após análise da integridade e morfologia do tecido suíno, foi verificada a expressão do FcRn no GIT. Estudando o estômago, duodeno e jejuno, foi demonstrado que a expressão do FcRn foi mantida durante 7 dias, principalmente no duodeno. Ao avaliar a permeabilidade duodenal, a variante de albumina humana com maior afinidade para FcRn, mostrou ser transportada de forma mais eficiente, conforme demonstrado *in vitro*.

Finalmente, as NPs conjugadas à variante de albumina com maior afinidade para o FcRn, foram administradas por via oral a ratinhos, induzidos com diabetes, que expressam hFcRn. Em estudos de farmacodinâmica *in vivo*, uma redução da glicemia foi medida em função da ligação ao receptor, com cerca de 40% de redução após 1 hora de administração.

De uma forma geral, uma nanoplataforma direcionada ao FcRn foi desenvolvida para a administração oral de insulina, que foi validada em modelos *in vitro*, *ex vivo* e *in vivo*. Estas NPs de PLGA-PEG decoradas com albumina humana modificada, para melhor transporte dependente de FcRn, mostraram oferecer uma estratégia nova e atrativa para ultrapassar as barreiras ao longo do GIT, entregando a insulina encapsulada e aumentando a sua biodisponibilidade oral. Assim, o sistema de entrega de insulina oral mostra potencial clínico, para terapia de DMT1 e potencialmente, para outras terapias, uma vez que FcRn é amplamente expresso em humanos.

## GRAPHICAL ABSTRACT

Outside Front Cover Page, Journal of Controlled Release 2020, Volume 327, ISSN:0168-3659.



This graphical abstract was entirely made by me, using the Biorender.





## LIST OF FIGURES

---

**Figure 1 | Schematic representation of human insulin.** It is formed by chain A with 21 a.a., chain B with 30 a.a., two disulfide bonds connecting the two chains and one disulfide linkage within chain A.

**Figure 2 | Crystallographic illustration of the ternary complex of hFcRn bound to hlgG and HSA.** The three domains of the hFcRn heavy chain (denoted  $\alpha 1$ ,  $\alpha 2$ , and  $\alpha 3$ ) are shown in green, and the  $\beta 2m$  subunit in gray. The hlgG1 Fc fragment is shown in brown. The subdomains DI, DII, DIIIa and DIIIb of HSA are colored in orange, wheat, light cyan and light blue, respectively. **(A)** Close-ups showing key amino acid residues involved in the interaction between hlgG1 (H310, I253, H435, N434) and hFcRn (E115, W131, D130). **(B and C)** Close-ups of the interactions between two loops in DI of albumin (loop I; R81, D89, and loop II; N109, N111) and hFcRn (T153, K63, S58). **(D)** Close-ups of the intramolecular interactions between H166 of the  $\alpha 2$  domain and E54 and Y60 of the  $\alpha 1$  domain in hFcRn, which form at acidic pH and in turn stabilize the loop containing W51, W53, W59 and W61. **(E and F)** Close-ups showing W59 and W53 of hFcRn inserted into hydrophobic pockets in DIIIa (T422, V426, L460, L463, H464 and T467) and DIIIb (F502, F507, F509, T527 and F551) of HSA, respectively. The figure was made using PyMol and the crystal structure data of hFcRn in complex with hlgG1 Fc and HSA (4N0U).

**Figure 3 | Schematic representation of FcRn transcytosis and recycling pathways in intestinal epithelial cells and endothelial cells, respectively.** **(A) Transcytosis:** In the polarized epithelial cell monolayer of the intestine, the acidic conditions of intestinal lumen (apical side) favor the binding of endogenous ligands (IgG and albumin) to FcRn located on the cell surface. (1) The receptor-ligand complex is internalized by receptor-mediated endocytosis, and subsequently (2) transported across the intestinal epithelium, within acidic endosomes ( $\text{pH} \leq 6$ ), to the other side of the cells (basolateral side) by transcytosis. (3) Upon exposure to neutral pH, the endosomes fuse with the basolateral membrane. This neutral pH condition allows the release of ligands to the lamina propria. **(B) Recycling:** (1) IgG and albumin present in the systemic circulation are internalized into the endothelial cells by fluid-phase pinocytosis, and subsequently (2) bind to the FcRn located within the acidic endosomes. (3) The receptor-ligand complex is trafficked through the endothelial cells and recycled back to the cell surface, (4) where the endosome fuses with the cellular membrane by exocytosis and releases the ligands into the blood under neutral pH condition. (5) The ligands that do not bind to the receptor are degraded by intracellular catabolism.

**Figure 4 | Schematic representation of the intestinal barrier.** The intestinal mucosa is a biologic barrier responsible for the absorption, composed by mucosa (epithelium, lamina

propria and muscularis mucosae), sub mucosa (lymph nodes, glands and blood vessels), muscularis externa (smooth muscle) and serosa (mesothelium).

**Figure 5 | Schematic illustration of *in vitro* models: (A)** Caco-2 mono-culture model, **(B)** Caco-2/HT29-MTX co-culture model, **(C)** Caco-2/ Raji B co-culture model, **(D)** Caco-2/HT29-MTX/ Raji B co-culture model and **(E)** 3D co-culture model.

**Figure 6 | The mechanically active human Gut Chip. (A)** Human villus intestinal epithelium and vascular endothelium are lined on opposite sides of a flexible porous membrane under fluid flow and peristalsis-like strains. A zoom-in schematic shows the intestinal microenvironment undergoing complex crosstalk between commensal gut microbiome, bacterial pathogens, and immune cells in parenchymal and vascular channels, respectively. **(B)** Villus morphogenesis of human Caco-2 intestinal epithelium in the Gut Chip under physiologically controlled motions and flow. **(C)** An overlaid image of the coculture of green fluorescent protein–labeled *Escherichia coli* and microengineered villi in the Gut Chip. Bars = 50  $\mu$ m. Reprinted with permission from <sup>137</sup>.

**Figure 7 | Schematic representations of the four of the organ systems used for functional coupling. (A)** The intestinal module is constructed in Transwell<sup>®</sup> from primary jejunum enteroids. Test agents are applied in the apical compartment (1). The media collected in the basolateral compartment (2) is used to add to the liver. **(B)** Media from the jejunum intestine basolateral compartment (2) is perfused as a 1:3 jejunum/naïve liver media into the influx port of the SQL SAL liver model (3). Efflux media is collected (4) and used to add to two downstream organ models. **(C)** The vascularized kidney proximal tubule module is a two lumen, dual perfusion system. For the vascular compartment, jejunum/liver-conditioned media (4) is diluted 1:2 or 1:4 with naïve EGM-2 media and then perfused into the influx port (5) to collect effluent from the proximal tubule at (6). In parallel with perfusion through the vascular compartment, the proximal tubule compartment is perfused with naïve DMEM/F12 PTEC media (6) for effluent collection. **(D)** The blood-brain barrier with NVU is constructed in a membrane-separated, two-chambered microfluidic device. The brain-derived endothelial vascular compartment is perfused at the influx port (7) with jejunum/liver-conditioned media (4) diluted 1:4 with naïve EGM-2 media. The effluent is collected at the efflux port (7). In parallel with perfusion through the vascular compartment, the neuronal cell compartment is perfused with naïve EBM-2 media at the influx port < 8 > for effluent collection at (8). Reprinted with permission from <sup>152</sup>.

**Figure 8 | Alignment of predicted porcine FcRn amino acid sequence (*Sus scrofa*, NP\_999362.2) with other species.** The degree of homology is indicated by darker shading.

Protein sequences are from GenBank (locus numbers: Human (*Homo sapiens*, NP\_001129491.1), Mouse (*Mus musculus*, NP\_034319.2). Reprinted with permission from <sup>171</sup>.

**Figure 9 | Human FcRn transgenic mouse models for evaluation of IgG and albumin-based therapeutics.** Conventional C57BL/6J mice have been used to generate humanized mouse strains that are transgenic for hFcRn. While **(A)** the Tg32 and Tg276 strains express mIgG, **(B)** the Tg32-hFc strain expresses chimeric hIgG1 (chIgG1). In comparison to these mouse strains, **(C)** Tg32 albumin knockout mice do not express MSA, while **(D)** the double transgenic mouse model (Albumus™) have both hFcRn and HSA. The figure was created with BioRender.

**Figure 10 | Representation of the rationale of this study: (A)** Illustration of the crystal structure of human albumin where targeted residues are shown as spheres: the free cys34 (black) in the N-terminal domain I and K500 (orange), H510 (orange) and K573 (blue) in the C-terminal domain III. The figure was made using Pymol and the crystal structure data of human albumin (PDB 1AO6); **(B)** Schematic illustration of the designed NPs build up of PLGA and PLGA-PEG-MAL with encapsulated soluble recombinant insulin and recombinant human albumin on the NPs' surface. Albumin was conjugated to the NP using maleimide chemistry, which resulted in a thioether bond formed between the Cys34 of albumin and the maleimide group of PLGA-PEG-MAL.

**Figure 11 | Site-specific conjugation of albumin to NPs: (A)** ELISA quantification of free WT albumin detected after the washing step with Amicon® filter of 100 KDa; **(B)** Conjugation efficiency (CE) with or without the presence of maleimide (MAL) after conjugation of 1 h or overnight (ON) with WT albumin; **(C)** Conjugation efficiency (CE) of NPs conjugated with reduced WT albumin (NP-WT) and non-reduced WT albumin (NP-WT without TCEP); **(D)** Elementary analysis of native albumin, non-functionalized empty NPs (NPs-NF) and WT albumin-conjugated empty NPs (NPs-WT); **(E)** Qualitative and **(F)** quantitative analysis showing the similarity of the FTIR spectra between WT albumin and NPs-WT, using the area overlap (AO) and spectral correlation coefficient (SCC) algorithms. Shown are the arithmetic means ± SD. \*P < 0.05, comparing with native albumin by Student's t-test.

**Figure 12 | Insulin NPs characterization: (A)** Representative TEM microphotograph of WT albumin decorated PLGA-PEG NPs encapsulated with insulin, lyophilized 25000x. Scale bar: 500 nm. **(B)** Insulin release profile of functionalized and non-functionalized NPs under SGF (2 h) and SIF (from 2 h to 6 h). **(C)** The qualitative and **(D)** quantitative effect of NPs encapsulation on protein structure. Analysis showing area-normalized second-derivative amide I spectra of native insulin vs insulin-encapsulated NPs using the area overlap (AO) and spectral correlation

coefficient (SCC) algorithms. Shown are the arithmetic means  $\pm$  SD. \*\*P<0.001, \*\*\*P<0.0001 comparing with native insulin by Student's t-test.

**Figure 13 | Albumin decorated NPs bind human FcRn. (A)** A schematic illustration of the ELISA set-up for measuring functional binding to human FcRn at pH 5.5. An engineered IgG1 antibody (MST/HN) was coated in wells, to which recombinant soluble human FcRn was captured, before adding naked albumin or albumin-decorated NPs. Bound albumin and albumin-decorated NPs were detected using ALP-conjugated polyclonal anti-human albumin antibodies. **(B)** Binding of naked human albumin variants (WT, KAHQ or KP) to human FcRn at pH 5.5. **(C)** Binding of NPs decorated with human albumin variants (WT, KAHQ or KP) to human FcRn at pH 5.5.

**Figure 14 | Albumin-decorated NPs showed enhanced transcytosis capacity.** Relative amounts of **(A)** naked albumin variants (WT, KAHQ and KP) and **(B)** albumin-decorated NPs detected in media collected at the basolateral side of polarized epithelial MDCK-hFcRn cells 4 h after adding the variants to the apical side in the Transwell® system (n=5-9). The amounts were quantified by two-way anti-albumin ELISA, where WT albumin or NPs decorated with WT albumin were set to 1, as a control. Shown are the arithmetic means  $\pm$  SD. \*\*P<0.001, \*\*\*P<0.0001 comparing with WT or NPs-WT by one-way ANOVA Dunnett's multiple comparison test; n.a.: non applicable; ns: non-significant.

**Figure 15 | HERA screening of engineered albumin variants and albumin-conjugated NPs: (A)** Relative uptake of naked albumin and albumin-conjugated NPs and **(B)** their correspondent amount quantified by ELISA. **(C)** Relative recycling of naked albumin and albumin-conjugated NPs and **(D)** their correspondent amount quantified by ELISA (n=9-11) in HMEC1-hFcRn cells. Shown are the arithmetic means  $\pm$  SD. \*P<0.05, \*\*P<0.005, \*\*\*P<0.0005, \*\*\*\* P< 0.0001 comparing with WT or NPs-WT, n.a.: non applicable, by one-way ANOVA Dunnett's multiple comparison test.

**Figure 16 | Mean HERA score for naked albumin variants or conjugated to NPs.** These were calculated from the data shown in Figure 4.2 B and D.

**Figure 17 | H&E stained sections of porcine GI tract. (A)** Morphologic differences between esophagus, stomach, duodenum, jejunum, ileum, caecum, colon and rectum (10X); **(B)** Identification of duodenum sections, as mucosa, sub mucosa, muscularis externa and serosa (20X); **(C)** Schematic representation of intestinal morphology and sections division (mucosa, sub mucosa and muscularis externa).

**Figure 18 | Confirmation of FcRn gene expression across GI tract.** Before performing the RT-PCR, RNA was extracted from fresh tissue of different sections of GI tract and cDNA was amplified. Results shown were performed with one tissue batch. Water and porcine blood were included as negative and positive controls, respectively. Results shown were performed with one tissue batch.

**Figure 19 | Evaluation of FcRn expression over time, of stomach, duodenum and jejunum. (A)** Evaluation of FcRn expression by IHC of fresh porcine tissue. Control samples were only treated with the secondary antibody, to check non-specific binding. **Brown** indicates the antibody signal, while **blue** is the counterstain. **(B)** FcRn expression after 7 days of porcine *ex vivo* incubation or freshly isolated at day zero. Before the RT-PCR, RNA was extracted from fresh tissue and cDNA was amplified. Water and porcine blood were included as negative and positive controls, respectively. Results shown were performed with one tissue batch.

**Figure 20 | Engineered albumin showed enhanced transcytosis capacity in the porcine *ex vivo* platform. (A)** Representation showing porcine duodenum, as the tissue used to study the intestinal permeability, using the porcine *ex vivo* platform. **(B)** Schematic illustration of the cross-section of the interface design in a 96-well plate format. 100  $\mu$ L of HBSS pH 7.4 was added to the plate from the bottom, mimicking the basolateral side. Next, the tissue was put on the plate, facing the apical side upwards. Finally, the magnetic plate from the top was added, pressing the tissue to avoid leakage, and samples prepared in HBSS pH 6 were added. **(C)** Relative amounts of naked albumin variants (WT, KAHQ, KP and PSA) detected in media collected at the basolateral side, 4 h after adding the variants to the apical side in the porcine *ex vivo* platform (n=6-10); **(D)** Relative amounts of NPs functionalized with albumin variants (n=4-10). The amounts were quantified by two-way anti-albumin ELISA, where WT albumin and NPs-WT were set to 1, as a control. These results were obtained from 3 different pigs. Shown are the arithmetic means  $\pm$  SD. \*P < 0.05, \*\*P < 0.005, and #P < 0.0001, comparing with WT by one-way ANOVA Dunnett's multiple comparison test.

**Figure 21 | Glycemia in human FcRn expressing mice induced with diabetes. (A)** T1DM-induced Tg32 mice were i.p. administered with STZ (150 mg kg<sup>-1</sup>) to induce diabetes. Body weight and glucose levels were followed up every 2 days, during 7 days. **(B)** At day 7, formulations were administered and plasma glucose levels were analyzed at different time points, during 8 h: PBS, oral insulin 50 IU/Kg, s.c. insulin 2.5 IU/Kg, oral insulin 50 IU/Kg loaded and non-functionalized NPs (NP-NF) and oral insulin 50 IU/Kg loaded and albumin-functionalized WT albumin and KP NPs (n = 3-6/ group). Shown are the arithmetic means  $\pm$  SEM. \*P<0.05, \*\* P< 0.001 comparing with oral insulin by one-way ANOVA.

**Figure A1 | NMR analysis of all constituents from albumin-conjugated NPs loaded with insulin: (A) HSA, (B) PLGA, (C) PLGA-PEG, (D) PLGA-PEG-MAL, (E) TCEP, (F) non-functionalized NPs without maleimide, (G) non-functionalized NPs, (H) NPs functionalized with non-reduced albumin, (I) albumin-functionalized NPs without maleimide and (J) albumin-functionalized NPs.**

**Figure A2.1 | Experimental procedure of the intestinal permeability under different g-levels; (A) Schematic illustration of cell culture and HG exposure process: Caco-2 cells were cultured for 21 days, to allow their differentiation into enterocyte-like cells. After this, Ins-NPs-Alb were incubated for 4 h, at different g-levels; (B) Schematic diagram for an example of HG exposure at different time points (0.5, 1, 2, 3 and 4 h). During this rest period at 1 g, TEER was measured and samples were removed from the basolateral side, for further quantification. This set up was performed for 2.5 g, 5.0 g and 7.5 g using the LDC and 1.0 g using an orbital-shaker, as control.**

**Figure A2.2 | Evaluation of metabolic activity of Caco-2 clone cells after HG exposure. (A) Evaluation of cellular viability through resazurin assays; (B) Evaluation of cellular toxicity through LDH assay. Shown are the arithmetic means  $\pm$  SD. \* $P < 0.05$  comparing with 1 g, by one-way analysis of variance (ANOVA) Dunnett's multiple comparison test. N=6.**

**Figure A2.3 | Assessment and comparison of cellular integrity at different g-levels. (A) Schematic illustration of the studied cellular components involved in different transport vias. Visualization of (B) claudin-1 and MUC2; (C) ZO-1 and PEPT1, (D) actin and FcRn. Claudin-1, ZO-1 and actin are presented in **green**. MUC2, PEPT1 and FcRn are presented in **red**. Nuclei are **blue**.**

**Figure A2.4 | Overview sketch of the quantitative expression. Analysis of the expression percentage of (A) transporters of influx and efflux; (B) components of tight junctions; (C) cytoskeleton and (D) mucus production, after exposure to different g-levels. The quantitative data are related to images presented at Figure 3. Quantification was done using ImageJ and each sample was normalized to the reference condition.**

**Figure A2.5 | ORTO visualization of cellular components at different g-levels. Claudin-1, ZO-1 and actin are presented in **green**. MUC2, PEPT1 and FcRn are presented in **red**. Nuclei are **blue**.**

**Figure A2.6 | H&E staining to address the cellular integrity when exposing to different g-levels. Ins-NPs-Alb were exposed to different g-levels (2.5 g, 5.0 g and 7.5 g) for 4 h. Cells**

with no treatment and shaking at 1.0 g were included as controls. Cytoplasm stained with **pink** and nucleus with **purple**. The Transwell<sup>®</sup> membrane is transparent and is right below the cellular monolayer. Scale bar = 100  $\mu$ m.

**Figure A2.7 | Evaluation of the safety of Ins-NPs-Alb in Caco-2 clone cells. (A)** Cellular viability, assessed by the MTT assays and **(B)** cellular cytotoxicity assessed by the LDH assay, of NPs loaded or not with insulin and conjugated or not with WT albumin. Free insulin was included as a control.

**Figure A2.8 | Intestinal permeability and respective TEER values of Ins-NPs-Alb after HG exposure. (A)** Schematic representation of FcRn-mediated transcytosis used by Ins-NPs-Alb through intestinal epithelial cells; **(B)** Permeability percentage of Ins-NPs-Alb, quantified by ELISA, and **(C)** respective TEER values during 4 h of incubation at different g-levels. Shown are the arithmetic means  $\pm$  SD. \* $P < 0.05$  comparing with 1.0 g, by two-way analysis of variance (ANOVA) Dunnett's multiple comparison test. N=6 for all groups.

**Figure A3.1 | Analysis of protein interaction using Bio-layer interferometry (BLI): (A)** screening of NPs concentrations; **(B)** regeneration test, **(C)** kinetic test of the three formulations, against different FcRn concentrations, and **(D)** differences between shape and intensity of the FcRn binding affinity with engineered albumin conjugated NPs. Relative binding of **(E)** naked human albumin variants and **(F)** NPs decorated with human albumin variants to human FcRn at pH 5.5.

**Figure A3.2 | The relative transport of: (A)** naked albumin variants (WT, KAHQ and TNNEKP), and **(B)** albumin-decorated NPs detected in media collected at the basolateral side of polarized epithelial MDCK-hFcRn cells 4 h after adding the variants to the apical side in the Transwell<sup>®</sup> system (n=5-12). The amounts were quantified by ELISA, where WT albumin or NPs decorated with WT albumin were set to 1, as a control. Shown are the arithmetic means  $\pm$  SD. \*\* $P < 0.005$ , \*\*\* $P < 0.0001$  comparing with WT or NPs-WT by one-way ANOVA Dunnett's multiple comparison test.

**Figure A3.3 | The relative uptake and recycling of: (A)** naked albumin variants (WT, KAHQ and TNNEKP), and **(B)** albumin-decorated NPs, and their correspondent amount quantified by ELISA (n=9-15) in HMEC1-hFcRn cells. Shown are the arithmetic means  $\pm$  SD. \*\*\* $P < 0.0005$ , \*\*\*\*  $P < 0.0001$  comparing with WT or NPs-WT, by one-way ANOVA Dunnett's multiple comparison test.

**Figure A3.4 | Biodistribution *in vivo* detection. (A)** Qualitative analysis of the fluorescence,



after 30 min of administration of NPs with cy7.5 and respective blanks without cy7.5; and **(B)** quantitative of the fluorescence present in mice, at different time points during 8 h. **(C)** Qualitative and **(D)** quantitative analysis of the GIT after 2 h of administration. NPs without cy7.5 were included as controls. All images were normalized by the control (same scale and ROI window).

**Figure A3.5 | Hypoglycemic effect of T1DM-induced mice following i.p. administration of STZ (150 mg kg<sup>-1</sup>). (A) Plasma glucose levels and (B) Plasma insulin level following PBS, oral insulin 50 IU/Kg, s.c. insulin 2.5 IU/Kg, non-functionalized NPs (NPs-NF) and functionalized with KAHQ and TNNEKP (n = 5-6 animals).**

## LIST OF TABLES

---

**Table 1** | Oral insulin formulations for T1DM under clinical trials.

**Table 2** | The influence of NPs characteristics on cellular uptake, internalization pathway and their strategies.

**Table 3** | Physical-chemical properties of developed PLGA-NPs.

**Table 4** | Permeability percentage and apparent permeability coefficient calculated after 4 h of incubation in MDCK-hFcRn cells.

**Table 5** | Apparent permeability coefficient calculated after 4 h of incubation in *ex vivo* porcine, based on the albumin amount quantified by ELISA. These results were obtained from 3 different pigs.

**Table 6** | Pharmacodynamic parameters of formulations at different time points after administration.

**Table 7** | Pharmacodynamic parameters.

**Table A3.1** | The pharmacokinetic parameters.



## ACRONYMS AND ABBREVIATIONS LIST

---

<sup>1</sup> H NMR	Proton nuclear magnetic resonance
a.a.	Amino acid
AAC	Area above the curve
ADMET	Administration, distribution, metabolism, excretion and toxicity
AE	Association efficiency
AO	Area overlap
AUC	Area under the curve
CE	Conjugation efficiency
Cys	Cystein
DAPI	4', 6-diamidino-2-phenylindole, dihydrochloride
DL	Drug loading
DLS	Dynamic light scattering
DM	Diabetes <i>mellitus</i>
DMEM	Dulbecco's Modified Eagle's Medium
EDS	Elementary dispersive scanning
ELISA	Enzyme-linked immunosorbent assay
ESA	European Space Agency
ESTEC	European Space Research and Technology Centre
FcRn	Neonatal Fc receptor
FDA	Food and Drug Administration
FITC	Fluorescein isothiocyanate
FTIR	Fourier Transform Infrared Spectroscopy
GIT	Gastrointestinal tract
HSA	Human serum albumin
HBSS	Hank's balanced salt solution
HD	Hypoglycemic decrease
H&E	Hematoxylin and eosin
HG	Hypergravity
hFcRn	Human FcRn
HPLC	High performance liquid chromatography
i.p.	Intraperitoneal
KAHQ	K500A/H464Q
kDa	kilodalton
KP	K573P
LDC	Large diameter centrifuge

LDH	Lactate dehydrogenase
MAL	Maleimide
MDCK-hFcRn	Madin-Darby Canine Kidney cell line over-expressing human FcRn
MES	2-(N-morpholino) ethanesulfonic acid
mFcRn	Mouse FcRn
MTT	Triazolyl blue tetrazolium bromide
NMR	Nuclear magnetic resonance
NPs	Nanoparticles
PA	Pharmacologic availability
<i>Papp</i>	Apparent permeability
PB	Phosphate buffer
PBSTM	PB saline with 0.05% (v/v) of Tween 20 and 4% skimmed milk
PD	Pharmacodynamics
PdI	Polydispersity index
PEG	Polyethylene glycol
PEPT-1	Peptide transporter 1
pFcRn	Porcine FcRn
PK	Pharmacokinetics
PLGA	Poly(lactic-co-glycolic acid)
PSA	Porcine serum albumin
RT	Room temperature
RT-PCR	Reverse transcription polymerase chain reaction
s.c.	Subcutaneous
SCC	Spectral correlation coefficient
SGF	Simulated gastric fluid
SIF	Simulated intestinal fluid
SD	Standard deviation
TCEP	Tris(2-carboxyethyl)phosphine hydrochloride
TEER	Transepithelial electrical resistance
TEM	Transmission electron microscopy
TJ	Tight junction
T1DM	Type 1 diabetes <i>mellitus</i>
STZ	Streptozotocin
WT	Wild type
ZO-1	Zona occludens 1
ZP	Zeta potential

## Chapter I

---

# LITERATURE REVIEW

---



This chapter was based in the following publications:

- **Azevedo C.\***, Pinto S.\*, Benjakul S.\*, Santos H.A., Andersen J.T., Traverso G., Sarmiento S., Prevention of diabetes-associated fibrosis: Strategies to orally treat diabetes with FcRn-targeted nanosystems, *Advanced Drug Delivery Reviews* 2021. (\*equal contribution)

In this review paper, I was responsible for the conception and execution of half of the contained information. The other half was complemented by Soraia Pinto. Sopisa Benjakul was responsible for reorganizing the topics and improve the discussion and images. The supervisors were responsible for reviewing and submit the manuscript. This review was not previously included in other thesis and it is partially reproduced in this section. The integral version of the review paper was included at the end of the thesis, at **Appendix IV**.

- Almeida A.\*, **Azevedo C.\***, Macedo M.H.\*, Sarmiento B., 3D intestinal models towards a more realistic permeability screening, in Santos H. and Martins J.P., *Nanotechnology for Oral Drug Delivery*, 2020, Elsevier, ISBN 9780128180389. (\*equal contribution)

In this book chapter, I was responsible for the conception and execution of the gut-on-a-chip's section. Andreia Almeida was responsible for the organoids' section and Helena Macedo for the multilayered models' section. The rest of the book chapter was written and revised by all of us. The supervisor was responsible for reviewing and submit the manuscript. This review was not previously included in other thesis and it is partially reproduced in this section.

- **Azevedo C.**, Pereira I., Sarmiento B., Intestinal mucosal tissue models to validate functionalized nanosystems, in Fahr A., et al., *Characterization of Pharmaceutical Nano- and Microsystems*, Wiley 2020, ISBN: 978-1-119-41404-9.

In this book chapter, I was responsible for the conception, execution and revision of the manuscript. Inês Pereira helped writing the *ex vivo*'s section and the supervisor was



responsible for reviewing and submit the manuscript. This review was not previously included in other thesis and it is partially reproduced in this section.

- **Azevedo C.**, Macedo M. H., Sarmiento B., Strategies for enhanced intracellular delivery of nanomaterials, *Drug Discovery Today* 2018, 23(5):944-959, DOI: 10.1016/j.drudis.2017.08.011.

In this review paper, I was responsible for the conception, execution and revision of the manuscript. Helena Macedo revised the manuscript and the supervisor was responsible for reviewing and submit the manuscript. This review was not previously included in other thesis and it is partially reproduced in this section. The integral version of the review paper was included at the end of the thesis, at **Appendix IV**.

## 1. Introduction

### 1.1. Epidemiology and the biology behind the disease

Diabetes *mellitus* (DM) is a major worldwide health burden. Around 463 million people were living with diabetes worldwide by 2019, and this number will rise to 700 million by 2045 if current trends are maintained <sup>1</sup>. In addition, it is estimated that the full global costs of diabetes in adults will increase from U.S. \$1.3 trillion in 2015 to \$2.1 trillion by 2030 <sup>2</sup>. There are three main types of DM: type I diabetes *mellitus* (T1DM), type II diabetes *mellitus* (T2DM) and gestational diabetes. Also, intermediate conditions, such as impaired glucose tolerance and impaired fasting glycemia can be considered, since they can progress into diabetes <sup>3</sup>. T1DM is caused by an autoimmune reaction, characterized by the attack of the immune system to the pancreatic insulin-producing beta cells. Commonly, it is a childhood-onset disease and patients are insulin dependent. In this case, patients have to chronically administer multiple daily injections, which is painful, invasive and reduces patient's compliance <sup>4</sup>. In T2DM, hyperglycemia is initially the result of the inability of cells to fully respond to insulin and, over time, to inadequate production of insulin as a result of failure of the pancreatic beta cells. T2DM, predominant in adults, also implies recurrent administration of GLP-1 incretin analogs by invasive routes <sup>5</sup>.

### 1.2. Oral insulin delivery for T1DM

Insulin, with 5.8 KDa of molecular weight, is composed by 51 aminoacids (a.a.), which are divided into two chains: chain A with 21 a.a. and chain B with 30 a.a. As shown in **Figure 1**, these two chains are connected by two disulfide bonds (A7–B7 and A20–B19) and the chain A also presents one disulfide linkage (A6–A11). Typically, the basal insulin correspond to 5-15 U/mL and the response to meal intake is 60-80 U/mL <sup>3</sup>.

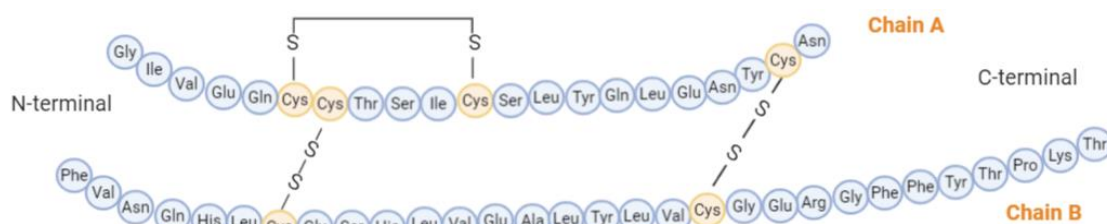


**Figure 1 | Schematic representation of human insulin.** It is formed by chain A with 21 a.a., chain B with 30 a.a., two disulfide bonds connecting the two chains and one disulfide linkage within chain A.

Doubtless, insulin is considered the main candidate to treat the symptomatology of T1DM. Some user-friendly products have been slowly reaching the market, as insulin

patch-pumps systems as well as inhaled and buccal insulin. However, these are currently used for T2DM or do not have an advantageous bioavailability, compared to the current subcutaneous (s.c.) administration. Lately, a lot of investigation has been focused on oral delivery of insulin for T1DM, as the most preferable route of administration. In fact, the s.c. insulin do not mimic a physiologic situation, since insulin is delivered to peripheral circulation. In an oral delivery situation, insulin is absorbed in the intestinal lumen and transported to the liver via portal circulation, where can avoid the hepatic glucose production. This biodistribution was already studied elsewhere <sup>6</sup>. The liver is the primary site to regulate glucose homeostasis and it is known that 80% of the oral insulin is retained in it and the rest reaches systemic circulation, creating a 3-fold higher insulin concentration in portal vein than in systemic circulation. However, in case of s.c., insulin is obviously more concentrated in peripheral circulation, which disrupt the liver's balance between glycogen storage and glucose output. This unbalanced state drives to hiperglycemia, which can easily lead to hypoglycemia when treated with high insulin doses <sup>7</sup>. Insulin has a hydrophilic nature, so the paracellular route is the main way to surpass the intestinal epithelium. However, as happens with other proteins, insulin can be degraded throughout the gastrointestinal tract (GIT), reducing the oral bioavailability. In this sense, absorption enhancers and protease inhibitors are currently used as strategies to enhance insulin bioavailability. However, these can be a concern regarding the long-term toxicity. **Table 1** presents some examples of oral insulin formulations that are currently in clinical trials. From these, the system developed by Diasome seems to be the most promising strategy. The technology contains proteolytic enzymes and mimics endogenous insulin via HTM guidance towards hepatocytes. Besides, it uses low insulin doses, reducing the risk of hypoglycemia <sup>8</sup>.

**Table 1 | Oral insulin formulations for T1DM under clinical trials.**

Name	Technology	Clinical trial	Company	Ref
ORMD-0801	Protein Oral Delivery™ (POD) technology comprises an enteric-coated capsule that incorporates insulin, protease inhibitors and absorption enhancers.	IIa	Oramed Pharmaceuticals	9
Oshadi Icp	Silica nanoparticles with a combination of insulin, proinsulin, and C-peptide.	II	Oshadi Drug Administration	10
HDV	Oral hepatocyte-directed vesicle insulin gel capsule.	II	Diasome Pharmaceuticals	8
IN-105	Insulin analog: Lys-β29 bond to PEG.	I	Biocon	11

### **1.3. Biologic barriers of oral delivery drugs**

During drug design for drug delivery, some details should be taken into account: (1) drugs must be able to surpass the harsh conditions of GIT; (2) once internalized, they must reach the target; and (3) guarantee that pharmacokinetics is maintained.

Drugs can be administered by ocular, buccal, sublingual, oral, intravenous, intramuscular, subcutaneous, transdermal, pulmonary/nasal or vaginal/rectal routes, being the oral the most convenient <sup>12</sup>. However, for orally delivering, the preferred route, they have to pass through: the oral cavity coated by proteins, mucosal compounds and bacterial flora; the stomach, and be attacked by acid bath; and the intestine and contact with the alkaline environment, being subjected to the activity of different digestive enzymes, the presence of a mucus layer (glycoprotein mucin) and tight junctions. After being absorbed, drugs pass through endothelial cells, and reach the blood, where can be taken up by a monocyte. Meanwhile, and in case of intracellular delivery, drugs travel through endosomal and lysosomal environments, which might contribute for drug degradation, until reach the target <sup>13</sup>.

Taking all this in mind, it is mandatory that nanomaterials surpass the mononuclear phagocyte system (MPS), avoid nonspecific distribution, drug resistance, escape to lysosomes and reach the target with the original bioavailability <sup>14</sup>.

## **2. Nanoparticles as a strategy for drug delivery**

Nanoparticles (NPs) are seen as carriers that protect peptides from degradation and deliver active payloads more efficiently to the intended sites within the GIT, ultimately potentiating the oral bioavailability.

### **2.1. The evolution of Nanomedicine**

The developments in nanomedicine drug delivery have opened new perspectives to design and synthesize efficient nanocarriers and multifunctional nanomaterials. At the beginning, the production was focused on biocompatibility and toxicity. The second-generation of nanomaterials aimed for having an optimized surface, to give more stability, stealth, and targeting capabilities. The most recent model support the “smart nanomedicine” idea, improving targeting mechanisms and theranostic abilities <sup>15</sup>. In fact, nanomaterials provide a stable biocompatible environment to encapsulate drugs, promote a controlled release and an efficient absorption <sup>16, 17</sup>. It is also noted that they

improve the therapeutic effects duration and minimize unwanted effects by driving drugs and increasing their concentration in the site of action <sup>18, 19</sup>. Depending on the accumulation of the delivery system in the tissue, cell or in a specific subcellular compartment of interest, targeting approaches can be primary, secondary or tertiary, respectively <sup>20</sup>. This nanotechnological advance became very important since it allows drugs to cross physiological barriers to reach target sites, safely and sustainably <sup>21</sup>.

## **2.2. Nanoparticles characteristics and their influence**

Internalization and intracellular transport mechanisms are affected by nanomaterials properties. Different characteristics (size, charge, shape, elasticity) contribute to a different interaction between the nanomaterial and the cell membrane, causing altered signaling events and activation of different pathways of adhesion and internalization. Thus, the desired result, for more effective and distinctly targeted delivery, can be obtained controlling these parameters, which are important to attain the target and specific activity at a predetermined rate and time <sup>12, 15</sup>.

### *Size*

Size is the priority parameter because it determines the endocytosis pathway and also states which cells uptake the particle. Particles smaller than 10 nm are mainly removed by renal clearance <sup>22</sup>. Particles, when orally administered, with a size between 10-100 nm have higher cellular uptake efficiency, since they are taken up in Peyer's patches, and then absorbed into systemic circulation, avoiding rapid renal clearance. On the other hand, larger particles are removed by MPS, and those within 200–300 nm cannot even pass, being concentrated in the spleen <sup>23, 24</sup>. In internalization, larger particles (>1 $\mu$ m) enter the cell by macropinocytosis; with 120 nm by clathrin-dependent pathway; those with 50–100 nm by caveolae-dependent pathway and finally smaller particles (<50 nm) can be internalized through clathrin- and caveolae-independent pathway. So the internalized nanomaterials are intimately connected with the size of vacuole formed <sup>25</sup>.

### *Surface composition*

Nanomaterials surface is also an important aspect, since its composition is in contact with the cell, which can be affected by hydrophobicity or hydrophilicity. So, this parameter determines the cellular internalization and intracellular transport and influences the circulation time and nanocarrier association with cells and their recognition. Hydrophobic particles can be delivered to immune cells and penetrate into the bilayer membrane,

being easily internalized <sup>26, 27</sup>. Normally, polymers are added to nanomaterials to turn their surface more inert, hydrophilic, avoid immune clearance and increase the blood circulation time. PEGylation is a strategy to make nanomaterials invisible to macrophages or phagocytes and to prolong half-life <sup>28</sup>. In this case, polyethylene glycol (PEG) chains are covalently conjugated to nanomaterials, conferring a hydrophilic nature <sup>29</sup>. PEG can capture water molecules and form a natural barrier around the nanomaterial hindering proteins from adsorption, usually known as the “stealth” effect <sup>30</sup>.

### *Charge*

Also surface charge can be manipulated. For example, intestinal cell membrane is negatively charged, as plasmatic membrane, due to phospholipids, so positively charged nanomaterials interact more strongly, enhancing internalization <sup>31</sup>. A typical example is polyethyleneimine (PEI), which is commonly used to permeate membranes and let nanomaterials enter <sup>32</sup>. In terms of transport, positively charged particles utilize clathrin and macropinocytosis <sup>33</sup> while negatively charged particles tend to utilize caveolae mediated pathway <sup>34, 35</sup>. Neutral or slightly negatively charged particles are considered the best for long circulation, since they are not susceptible to MPS. On the other hand, charges highly positive or negative are taken up by macrophages <sup>35-37</sup>.

### *Shape*

Shape can also dictate the path of the particle and, inclusively, can change over time or after receiving external stimuli for long circulation and surpass barriers. It is an important factor in flow margination, avoidance of immune system and tissue accumulation. Spherical particles are better internalized by macrophages, while asymmetrical nanomaterials are more advantageous for sensing, self-assembly, tissue engineering, immunoengineering, therapeutic and diagnostic delivery <sup>15, 26</sup>. One of the strategies is to create elliptical particles to escape macrophages and then, after a stimuli, change to a sphere form for a better internalization <sup>25, 38</sup>.

### *Elasticity and solubility*

Finally, increasing elasticity also increases blood residence time and avoids clearance by immune system. Soft nanomaterials use macropinocytosis while harder ones are internalized through clathrin-dependent mechanisms <sup>26, 39</sup>.

It is also popular chemically modify nanomaterials to change the fluidity and/or solubility of mucus, regarding oral administration. According to literature it is possible to add fatty

acids or to substitute a.a. to obtain an increased solubility. The fatty acids addition is proportional to the increased solubility, which may increase 16-fold with linoleic acid <sup>40</sup>. A similar effect was also observed with capric acid, lauric acid and oleic acid. These fatty acids increase the hydrophilic transport and reduce the transepithelial electrical resistance, which indicates the opening of tight junctions <sup>41</sup>. In fact, the paracellular transport has been related, in several papers, with the transport of poorly absorbed drugs. It was even studied the relation of that event with fatty acids and their effects on increased absorption of mannitol, a paracellular marker, and on morphology changes of tight junctions <sup>42</sup>. The a.a. substitution is demonstrated by a group of scientists that introduced 20 a.a. in ribonuclease (Rnase) Sa at position 76, confirming that asparagine, glutamine and threonine have more significant protein solubility <sup>43</sup>. In short, it is clear that these characteristics (**Table 2**) influence the uptake, renal clearance, drug stability, circulation time, drug release or even change NPs properties after internal (pH, redox, temperature, enzymes) or external stimuli (ultrasound, magnetic, light, electrical) <sup>12, 31</sup>.

**Table 2 |** The influence of NPs characteristics on cellular uptake, internalization pathway and their strategies.

Characteristic	Cellular uptake	Internalization pathway	Strategy	
<b>Size</b>	<10 nm	Renal clearance	---	
	10-100 nm	Peyer's patches	---	
	100-200 nm	Removed by MPS	<b>&lt;50 nm:</b> clathrin- and caveolae-independent <b>50-100 nm:</b> caveolae-dependent <b>120 nm:</b> clathrin-dependent	Add a penetration enhancer (PPS, polyacrylate, chitosan, phytic acid, self-assembling lipid-like peptides, thiomers and lectins) to macromolecules to open tight junctions
	200-300 nm	Spleen	Macropinocytosis	Avoid phagocytic clearance, prolong drug circulation and improve their biocompatibility: -Add hydrophilic polymers (PEGylation) -Biomimetic surfaces (CD47, leukocytes)
<b>Surface composition</b>	Hydrophobic	Immune cells	---	
	Positive	Highly positive: taken up by macrophages	Clathrin and macropinocytosis	
	Neutral	The best for long circulation	---	
<b>Charge</b>	Negative	-Highly negative: taken up by macrophages - Slightly negative: the best for long circulation	Caveolae mediated	
				Positively charged nanomaterials interact more strongly with the negatively intestinal cell membrane
<b>Shape</b>	Spherical	Macrophages	---	
	Asymmetrical	---	---	Elliptical particles to escape macrophages and

				after a stimulus change to a sphere form for a better internalization
<b>Elasticity and Solubility</b>	Soft Harder	Avoid immune system ---	Macropinocytosis Clathrin-dependent mechanisms	-Add fatty acids -Substitute amino acids

### 3. Functionalized nanoparticles for an enhanced bioavailability

Functionalized nanomaterials are guided to a specific target, improving drug effect and minimizing unwanted effects by driving drugs towards the exact site of action. Inclusively, the upgrading of their ADME (absorption, distribution, metabolism, and excretion), enhance the therapeutic efficiency <sup>13, 25</sup>.

Active targeting of NPs is commonly referred when drugs reach the right target through the site-specific targeting. This means that there is an interaction between the targeting ligands on nanocarriers and the receptors on cell membranes. The recognition performed during the interaction is specific, promoting particles internalization <sup>44, 45</sup>. So, modifying nanomaterials surface with certain ligands is an option to improve cell uptake and endosomal escape <sup>46</sup>.

#### 3.1. Albumin as a ligand

Albumin is an endogenous protein with nontoxic and nonimmunogenic properties, and biodegradable and biocompatible in nature, being a desirable carrier for drugs. In addition, albumin is one of the most abundant protein in blood (40 mg/mL in mouse and humans) <sup>47</sup>, possessing high binding capacity and good water solubility, which promotes the transport of poorly soluble drugs <sup>48</sup>. Through the 3D crystalline structure of albumin, it is known that is made up by 585 a.a. in a heart shape, contains three domains (I, II and III), each of them divided into two subdomains (A and B) and stabilized by 17 disulfide bridges. Moreover, albumin has binding sites within hydrophobic cavities in subdomains IIA (site I) and IIIA (site II). The subdomain IIA has one Trp residue (Trp214) and is the binding site for several drugs. Furthermore, albumin structure also contains seven binding sites for fatty acids in IB, IIIA and IIIB subdomains, and a high affinity metal binding at the N-terminus <sup>49</sup>.

The C-terminal DIII of albumin contains the principal binding sites for FcRn, while the N-terminal DI modulates the binding <sup>50, 51</sup>. Mutations within DIII can therefore alter the binding affinity of albumin for FcRn <sup>52</sup>. The albumin residues Lys500 and His510 are



considered to be crucial for the receptor binding, in which the two-point mutation of lysine with proline (K500A) and histidine with glutamine (H510Q) results in a 14-fold reduction in FcRn binding (KAHQ) compared to the WT albumin<sup>50</sup>. Individual mutations at these positions have been shown to decrease the binding affinity to the receptor by 30-fold (KA) and 14-fold (HQ). Conversely, a single-point mutation at position 573 with any a.a. improves ligand binding to FcRn. In particular, K573P (KP), where Lys573 is substituted by proline, increases the binding affinity by 12-fold and extends 1.4- and 1.6-fold the serum half-life in human transgenic mice and cynomolgus monkeys, respectively<sup>51</sup>.

### 3.2. FcRn as a receptor

#### 3.2.1. FcRn structure and interaction with albumin

FcRn is a transmembrane heterodimeric glycoprotein structurally similar to major histocompatibility complex class I (MHC-I) molecules with an alpha ( $\alpha$ ) heavy chain (40-46 kDa), composed of three extracellular domains ( $\alpha$ 1,  $\alpha$ 2 and  $\alpha$ 3), and a beta-2-microglobulin ( $\beta$ <sub>2m</sub>) light chain (12 kDa)<sup>53, 54</sup>. The  $\alpha$ 1 and  $\alpha$ 2 domains assemble a platform of eight antiparallel  $\beta$ -strands topped by two  $\alpha$ -helices, while the  $\alpha$ 3 domain, located below the  $\alpha$ 1-  $\alpha$ 2 platform, is non-covalently associated with the  $\beta$ <sub>2m</sub> light chain<sup>55, 56</sup>. Unlike MHC-I, the peptide binding groove of FcRn is occluded. Instead, FcRn exhibits high binding affinity to IgG and albumin at an acidic pH of 5.0-6.5 and no binding at physiological pH (7.4), except some IgG2 and IgG3 allotypes<sup>50, 57-60</sup>. This pH-dependent behavior can be attributed to the pH-sensitive histidines (His) residues, located in the domain III (DIII) of albumin and in FcRn. According to the literature, His is the only amino acid that changes its charge between pH 5.5 to 7.4, which is due to the presence of an imidazole group. At acidic conditions, the imidazole group becomes positively charged and binds to a.a. that are negatively charged. However, at physiological pH (7.4), His residues lose their protonation and, consequently, are unable to interact with oppositely charged aminoacids. As result, FcRn releases their ligands, IgG and albumin, and does not interact with them at physiological pH<sup>50, 61, 62</sup>. FcRn can simultaneously bind both IgG and albumin as a ternary complex (**Figure 2**) with a stoichiometry of 1:1 for albumin:FcRn<sup>61</sup> and 1:2 for IgG:FcRn<sup>55, 63</sup>. This simultaneous binding occurs in a non-cooperative manner without undergoing major conformational changes<sup>50, 61, 64, 65</sup>.

Compared to IgG, albumin is more hydrophobic in nature and hence involves a larger FcRn binding region located at the opposite binding site for IgG. Both DI and DIII of

albumin play a critical role in the FcRn-albumin interaction. While DIII is the core binding site of FcRn, DI modulates the binding of albumin to the receptor<sup>50, 51</sup>. The hydrophobic pockets DIIIA and DIIIB interact with the FcRn residues Trp59 and Trp53 located within a pH-sensitive  $\alpha$ 1-domain loop. This loop regulates interaction of the receptor with albumin<sup>62, 66</sup>. At acidic pH, the histidine residue, His166 residing within the FcRn  $\alpha$ 2-domain, is protonated and interacts with Glu54 and Tyr60 found on the loop via hydrogen bonding, resulting in loop stabilization, and an ordered FcRn structure required for efficient albumin binding. The mutations of His166 have shown to diminish or considerably reduce the binding affinity of FcRn to albumin<sup>50</sup>. Several other DIII residues of albumin essential for binding include histidine residues (His464, His510 and His535), as well as Lys500<sup>50, 62</sup>. In addition to DIII, DI of albumin contributes to FcRn binding by interacting with residues of the FcRn  $\alpha$ 1- $\alpha$ 2 platform. Asn109, Asn111, and Asp89-Arg81 of albumin form contacts with Lys63, Ser58, and Thr153 of FcRn, respectively<sup>57, 66</sup>.

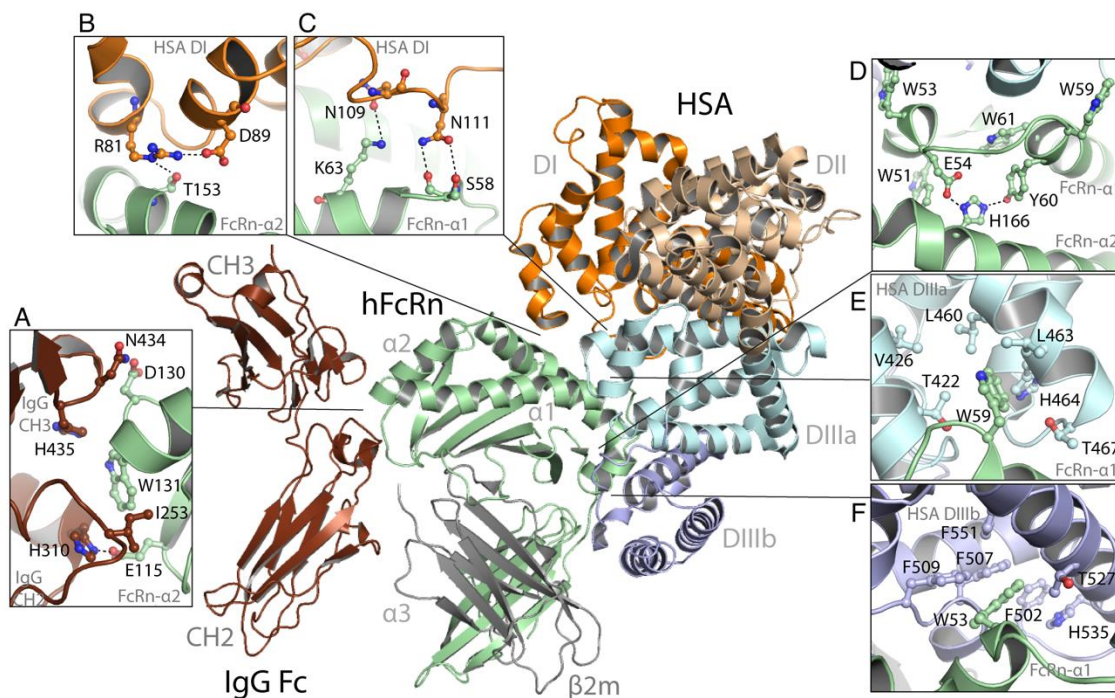


**Figure 2 | Crystallographic illustration of the ternary complex of hFcRn bound to hIgG and HSA.** The three domains of the hFcRn heavy chain (denoted  $\alpha$ 1,  $\alpha$ 2, and  $\alpha$ 3) are shown in green, and the  $\beta$ 2m subunit in gray. The hIgG1 Fc fragment is shown in brown. The subdomains DI, DII, DIIIA and DIIIB of HSA are colored in orange, wheat, light cyan and light blue, respectively. (A) Close-ups showing key amino acid residues involved in the interaction between hIgG1 (H310, I253, H435, N434) and hFcRn (E115, W131, D130). (B and C) Close-ups of the interactions between two loops in DI of albumin (loop I; R81, D89, and loop II; N109, N111) and hFcRn (T153,

K63, S58). **(D)** Close-ups of the intramolecular interactions between H166 of the  $\alpha 2$  domain and E54 and Y60 of the  $\alpha 1$  domain in hFcRn, which form at acidic pH and in turn stabilize the loop containing W51, W53, W59 and W61. **(E and F)** Close-ups showing W59 and W53 of hFcRn inserted into hydrophobic pockets in DIIIa (T422, V426, L460, L463, H464 and T467) and DIIIb (F502, F507, F509, T527 and F551) of HSA, respectively. The figure was made using PyMol and the crystal structure data of hFcRn in complex with hIgG1 Fc and HSA (4N0U).

### 3.2.2. *Biologic mechanisms mediated by FcRn*

FcRn has a key role in bidirectional transporting and prolonging half-life of IgG and albumin at mucosal and systemic sites, respectively. The receptor is predominantly expressed within acidified endosomes of endothelial cells lining the inner surface of blood vessels and lymphatic vessels, which is associated to the long half-life of both IgG and albumin in the systemic circulation<sup>67, 68</sup>. However, FcRn can also be found on the outer surface of plasma membrane of polarized epithelial cells<sup>69</sup>. At both cell types, the interaction of IgG and albumin to FcRn befalls simultaneously in a strict pH-dependent manner, with binding at acidic pH (5.0-6.5) and release at neutral pH. Due to lysosomal escape and recycling pathway, the FcRn ligands are the most abundant blood proteins in humans with half-lives around 3 weeks, which is much higher than most other proteins in the human body<sup>68</sup>.

Regarding the transcytosis mechanism, it can occur in polarized epithelial cells of intestinal epithelium of the GIT, where the mildly acidic conditions of the intestinal lumen promotes the binding of IgG and albumin to FcRn and their trafficking through the enterocytes. Briefly, at the apical surface of the mucosal membranes, IgG and albumin bind to FcRn and form FcRn-ligand complexes, which are then transcytosed through the polarized epithelial cells from the intestinal lumen to the basolateral side of the epithelium (lamina propria) **(Figure 3 A)**. Upon the pH change to neutral on the basolateral side, the ligands are dissociated from FcRn and released into the lymphatic system, entering the systemic circulation via the thoracic lymph nodes. The ligands that do not bind to FcRn are degraded by lysosomes<sup>61, 64</sup>. The amount of endogeneous ligands transcytosed can be quantified through the traditional Transwell<sup>®</sup> assay<sup>70</sup>. For this assay it is normally used human colonic adenocarcinoma-derived Caco-2 and T84 epithelial cell lines or Madin-Darby Canine Kidney (MDCK) cells, among others, since endogenously express FcRn.

In comparison to epithelial cells, endothelial cells take up surrounding IgG and albumin

by fluid-phase pinocytosis due to the neutral pH of the blood and form intracellular vesicles. The low pH into the acidified endosomes (pH 5.0-6.0) allows ligands to bind FcRn. FcRn-ligand complexes are subsequently recycled back to the cell surface and dissociated from FcRn under neutral conditions of the bloodstream, while unbound ligands are broken down by lysosomes (**Figure 3 B**). FcRn recycling can be a strategy to prolong drug circulation and enhance the therapeutic drug profile, when it comes to drug degradation, rapid renal clearance and non-specific accumulation. The recycling can be quantified through the human endothelial cell-based recycling assay (HERA) <sup>71</sup>. In addition, through this assay it is possible to estimate the extended half-life in human FcRn (hFcRn), transgenic mice and cynomolgus monkeys. In this assay is normally used a modified human dermal microvascular endothelial (HMEC1) cell line to express human  $\beta$ 2-microglobulin and the hFcRn HC with an N-terminal HA-tag and EGFP-fused C-terminally (HMEC1-hFcRn) <sup>72</sup>.

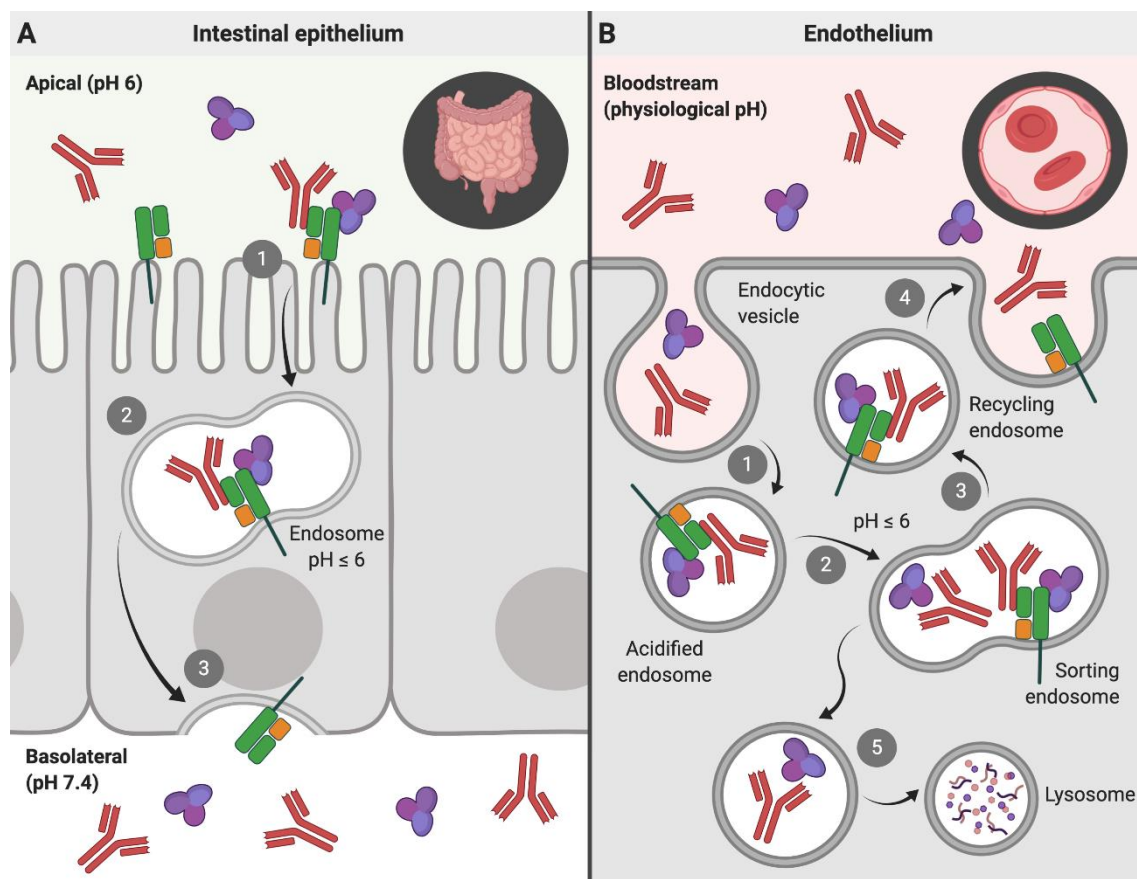


**Figure 3 | Schematic representation of FcRn transcytosis and recycling pathways in intestinal epithelial cells and endothelial cells, respectively. (A) Transcytosis:** In the polarized epithelial cell monolayer of the intestine, the acidic conditions of intestinal lumen (apical

side) favor the binding of endogenous ligands (IgG and albumin) to FcRn located on the cell surface. **(1)** The receptor-ligand complex is internalized by receptor-mediated endocytosis, and subsequently **(2)** transported across the intestinal epithelium, within acidic endosomes (pH ≤ 6), to the other side of the cells (basolateral side) by transcytosis. **(3)** Upon exposure to neutral pH, the endosomes fuse with the basolateral membrane. This neutral pH condition allows the release of ligands to the lamina propria. **(B) Recycling:** **(1)** IgG and albumin present in the systemic circulation are internalized into the endothelial cells by fluid-phase pinocytosis, and subsequently **(2)** bind to the FcRn located within the acidic endosomes. **(3)** The receptor-ligand complex is trafficked through the endothelial cells and recycled back to the cell surface, **(4)** where the endosome fuses with the cellular membrane by exocytosis and releases the ligands into the blood under neutral pH condition. **(5)** The ligands that do not bind to the receptor are degraded by intracellular catabolism.

### 3.3. Albumin- based drug delivery of insulin

By harvesting recent knowledge about FcRn biology, it was possible to fuse receptor-targeting molecules to the peptides, to provide a favorable binding and transport properties. For the treatment of both T1DM and T2DM, fatty acid-based strategies have been developed for insulin. One is insulin detemir (Levemir<sup>®</sup>)<sup>73, 74</sup> and another is insulin degludec (Tresiba<sup>®</sup>)<sup>75, 76</sup>. Both are recombinant human insulin analogs with a fatty acid linked to a lysine residue, while insulin degludec also lacks a threonine residue. They have distinct half-lives of 18-26 hours and 42 hours for insulin detemir and insulin degludec, respectively<sup>73-78</sup>. An insulin analog with an activity profile close to that of insulin detemir is insulin glargine (Lantus<sup>®</sup>) with a half-life of about 24 hours<sup>79</sup>. Instead of modification of the fatty acid side chains, insulin glargine includes two additional arginine residues in the beta chain and an amino acid replacement of asparagine at position 21 with glycine. Nevertheless, these products have gained market approval for once-daily dosing. To further extend half-lives of insulin analogs, insulin icodec (LAI-287) has been developed as a once-weekly insulin that is currently in phase I and phase III clinical trials in patients with T1DM and T2DM, respectively<sup>80, 81</sup>. As a result of three amino acid substitutions and the addition of an icosane fatty diacid to this insulin analog, it shows an extended half-life of 8 days in humans and improved stability and solubility.

Despite that these strategies secure prolonged blood persistence compared with native peptides, treatment relies on s.c. injections. Currently, there are no oral insulin (OI)-based drugs available for DM treatment. However, very recently, the first clinically tested once-weekly OI analog, named OI338, demonstrated efficacy near subcutaneously injected insulin glargine<sup>82</sup>, which has led to the development of long-acting OI

formulations<sup>83</sup>. Commonly, a tyrosine at position 14 and a phenylalanine at position 25 are replaced by glycine and histidine, respectively, in addition of a deletion of threonine at position 30<sup>83</sup>. These amino acid modifications make OI less susceptible to degradation in the GIT upon oral administration<sup>82, 83</sup>, in combination with the use of an absorption enhancer, such as Gastro Intestinal Permeation Enhancer Tablet I (GIPET®1) based on sodium caprate<sup>84</sup>. To gain improved HSA binding, the lysine residue at position 29 of the OI is coupled to a strong albumin binding molecule (C18 fatty diacid) via a hydrophilic linker. Moreover, OI molecules can be designed for prolonged half-life by engineering for decreased insulin receptor affinity. This design resulted in OI338 with a half-life of 70 hours in T2DM patients<sup>82</sup>. In the context of FcRn, it has been demonstrated that binding of fatty acids to the hydrophobic pockets of HSA is, in fact, negatively affecting receptor binding, in which the effect depends on the length of the fatty acid<sup>66</sup>. As such, half-life extension upon conjugation to fatty acids will have limitations. Regarding oral delivery, this means that fatty acid-based strategies may not benefit from albumin binding to FcRn expressed at epithelial cell barriers. This is a highly interesting topic that should be addressed in future studies.

Antidiabetic peptide strategies may be combined with nanosystems tailored for oral administration to achieve more efficient delivery across the selective mucosal barriers. Although, this requires a sophisticated design that allows the nanosystems to be taken up and delivered to the circulatory system more efficiently than what has been demonstrated to date. Receptor-targeting molecules may also be used to decorate nanosystems, as will be discussed below.

### **3.4. Albumin-targeted nanosystems for oral delivery of insulin**

Although IgG Fc have been explored as FcRn-targeting moieties, their use is impeded due to the need for chemical modification for conjugation. As such, HSA may be used for decoration of NPs owing to low immunogenicity and ease of production<sup>85, 86</sup>. Furthermore, it was very recently shown that HSA is transported more efficiently than hIgG across mucosal lung barriers *in vivo* in hFcRn transgenic mice<sup>87</sup>. On this basis, HSA may be an attractive targeting molecule for favorable FcRn-mediated transepithelial delivery of nanosystems for oral administration of antidiabetic peptides<sup>88-90</sup>.

An example of nanosystems that have been combined with albumin is polymeric alginate-dextran sulfate-based (ADS) NPs with an average hydrodynamic diameter of 233 nm, that were coated with chitosan<sup>89</sup>. In contrast to synthetic PLA and PLGA, the polymers alginate, dextran and chitosan used to synthesize NPs are natural product-

derived compounds that provide nanosystems with mucoadhesive characteristics <sup>86</sup>. In this study, bovine serum albumin (BSA) was non-specifically adsorbed onto the surface of ADS NPs <sup>89</sup>, in contrary to site-directed chemical coupling of Fc-decorated NPs <sup>91-93</sup>. In an *in vitro* model of polarized epithelial cells expressing hFcRn combined with mucus-producing goblet cells, BSA-decorated NPs loaded with insulin showed an improved permeability profile of the peptides compared to free insulin <sup>89</sup>. However, cautious should be taken when interpreting the result since the binding kinetics of BSA for hFcRn is not identical to that of HSA <sup>64</sup>. Aside from that, strategies for surface modification of NPs and pH-dependent functionality of ligands are two other important parameters to address. An attempt was made to decorate the surface of HPMC-treated undecylenic acid-coated SiNPs with HSA via EDC/NHS reaction <sup>90</sup>. The chemical surface modification of NPs with HSA showed an increase in particle size from 162 nm to 238 nm after conjugation, with high monodispersity. Interestingly, HSA-conjugated NPs (HSA-NPs) exhibited improved cytocompatibility in human epithelial cell lines relative to non-conjugated NPs, which suggests that decorating nanosystems with biocompatible compounds, such as HSA, may reduce the toxicity of inorganic nanomaterials. Furthermore, the presence of HSA on the NP surface demonstrated enhanced cellular uptake and internalization of nanosystems *in vitro* with the aid of hFcRn expressed on the cell surface <sup>90</sup>. Done in this fashion, HSA-NPs encapsulating insulin showed enhanced transport of loaded peptides across polarized epithelial cell monolayers in an *in vitro* transcytosis assays. The data also suggested an improvement in the transepithelial delivery of encapsulated antidiabetic peptides when comparing HSA-NPs with IgG Fc-NPs <sup>91</sup>, which encourages research on the use of engineered HSA variants tailored for improved FcRn binding and transport properties as targeting ligands <sup>87</sup>.

#### **4. Intestinal models for preclinical validation**

The intestinal epithelium is responsible for the control of drugs passage, namely digestion, absorption of nutrients and water homeostasis. The intestine is thus important for the permeability of NPs, which depends on intestinal morphology, biochemical factors and dosage <sup>94</sup>.

##### **4.1. Intestinal morphology**

Morphologically, the small intestine is divided into mucosa, sub mucosa, muscularis

propria and serosa <sup>95</sup>. The mucosa is 90% covered by enterocytes and consequently by microvilli, having an important impact on absorption <sup>36</sup>. This area is composed by epithelium, lamina propria and muscularis mucosae. In more detail, epithelium, the layer in contact with lumen, is where cell proliferation, differentiation and apoptosis may occur, due to the presence of proliferative crypts. These differentiated cells can be absorptive enterocytes or secretory cells (goblet cells, enteroendocrine cells and Paneth cells). In terms of function, enterocytes present the most important one, the absorption of nutrients, since they are highly polarized cells and can transport them from the apical, through the epithelium, to basolateral side. Other than those, goblet cells are responsible for lubricate and protect the gut by secreting mucins, which produce mucus; enteroendocrine cells can secrete hormones and coordinate the intestinal functioning; finally, Paneth cells secrete proteins responsible for innate immunity <sup>96</sup>. Away from intestinal crypts there are isolated lymphoid follicles, Peyer's patches, which contain the specialized microfold cells (M cells). M cells are essential for the transepithelial transport of macromolecules or particles and microorganisms. In addition, M cells have the particularity of possessing sparse microvilli on their apical side, not possessing a glycocalix layer and forming a pocket with lymphocytes or macrophages at the basolateral side. These specific characteristics make these cells an ideal place for antigen sampling, which facilitates the contact with the immune system <sup>16,97</sup>. The second layer, lamina propria works as a connective tissue presenting a set of cells (macrophages, dendritic cells, B and T cells and blood capillaries), while the third layer is composed by a smooth muscle <sup>96</sup>.

The sub mucosa is formed by a connective tissue with lymphatic and blood vessels, ganglion and nerve cells. The muscularis propria layer is made by smooth muscles and finally, the serosa layer by mesothelium, a continuous connective tissue with the abdominal peritoneum <sup>95</sup> (**Figure 4**).



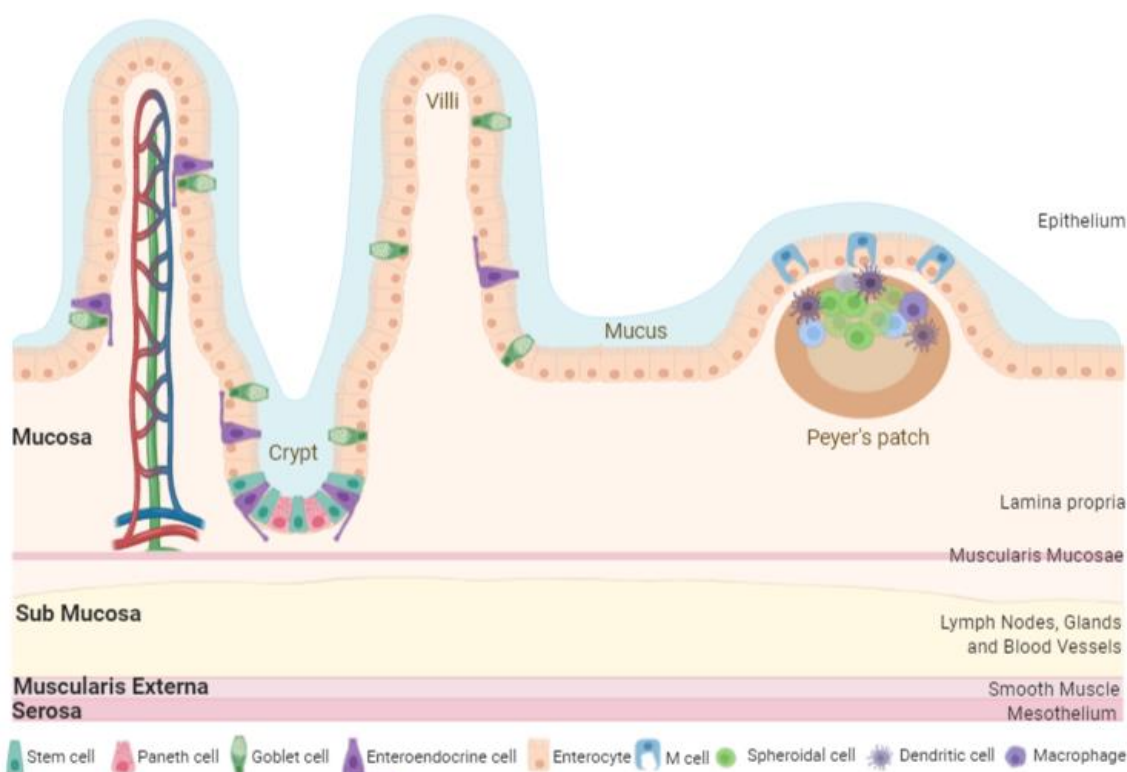


**Figure 4 | Schematic representation of the intestinal barrier.** The intestinal mucosa is a biologic barrier responsible for the absorption, composed by mucosa (epithelium, lamina propria and muscularis mucosae), sub mucosa (lymph nodes, glands and blood vessels), muscularis externa (smooth muscle) and serosa (mesothelium).

The intestine is a biologic barrier that significantly reduces the bioavailability of drug-loaded NPs. This can occur due to enzymes such as proteolytic enzymes present in lysosomes, brush-border peptidases in the villi and pancreatic proteases in the duodenal region as well as bacterial flora from the complex hydrogel containing mucin, known as mucus of the intestine. All these factors can modulate the solubility at gastrointestinal pH, lipophilicity, pKa and molecular weight of NPs and consequently their permeability<sup>98</sup>. Also epithelial cells, bond by tight junctions, plus the transit time, fluid dynamics, physiological response, gut mucosa, transporters and receptors may contribute as physiological and anatomical barriers<sup>99</sup>. As previously mentioned, NPs can suffer physicochemical modifications originated by low pH, high temperature, reactions with surrounding molecules, besides NPs weight, shape and charge which also influence absorption and degradation<sup>35, 100</sup>. Finally, factors regarding luminal complexation, drug metabolism, liver uptake and bile excretion are related with permeability efficiency<sup>101</sup>. A strategy to mimic the intestinal morphology, transport mechanisms and to study the

permeability of NPs is using *in vitro*, *ex vivo* or *in vivo* models, which will be focused on the following sections.

#### **4.2. *In vitro* models**

Despite the fact that *in vitro* models do not mimic a real *in vivo* situation, they can easily simulate a multiple transport system and be reproduced in laboratory. Besides, this type of studies are becoming more important to the pharmaceutical industry, since the obtained results can influence the initial steps of drugs developing. This method is characterized for being less labor-intensive and cost-intensive, and raise less ethical considerations compared to *in vivo* studies. Plus, the use of *in vitro* models allows an early evaluation of drugs, without using *in vivo* models and large amounts of drug to analyze its ADMET<sup>96</sup>. In this sense, it is possible to have *in vitro* models where gastric and intestinal fluid can be simulated, and dialysis membrane system and Transwell® to test the permeability of compounds.

The simulated gastric and intestinal fluid model can be used as a preliminary study to analyse the reaction of the NPs to the GIT environment. The used medium has to be representative of the stomach and intestine fluid, presenting characteristics as enzymes and ionic strength, which influences the interaction and stability of NPs. According with the United States Pharmacopeia (USP) the simulated gastric fluid (SGF) medium should be at pH 1.2 and the simulated intestinal fluid (SIF) medium at pH 6.8. These mediums are easily prepared and normally experiences are performed at 37 °C with agitation (100 rpm). At different time points the supernatant can be removed by centrifugation and quantified. It is known that these conditions reduce the number of NPs, besides changing size and morphology and consequently bioavailability<sup>102</sup>. On the other hand, the dialysis membrane system test the transport of the nanosystems across the barriers of the gut. In this method, nanosystems are added to a dialysis membrane with the same conditions as the last technique, in order to represent the GIT characteristics and movements. These two models can be done without using human cell lines, which can be a drawback since do not represent the epithelial behaviour<sup>103</sup>. Lastly, the Transwell® system is the most used model to evaluate the permeability of drugs from lumen to blood circulation. Briefly, this system is composed by a membrane with pores that separate the apical from the basolateral side. The epithelial cells are seeded at the apical side and when confluent with an ideal transepithelial electrical resistance (TEER), the experience can be performed. Nowadays, this system can be performed with only one cell line (mono-culture) or combined with other cell lines (co-culture)<sup>96</sup>.

#### 4.2.1. Monoculture model

In this type of model a single cell line is seeded forming a monolayer. There are several cell lines being used in *in vitro* models of the intestine, but the most widely used to recreate the human environment is the Caco-2 cell line. According to the Food and Drug Administration (FDA), Caco-2 cell line integrates the Biopharmaceutics Classification System (BCS), since it has the advantageous ability to screen and predict NPs solubility and bioavailability, as well as their interaction with the gut<sup>104</sup>. Caco-2 is a high-resistance cell line from a human colorectal carcinoma and is considered the gold standard permeability screen for compounds in drug discovery, due to its morphological and functional characteristics as well as the presence of cytochrome P450 3A4 (CYP3A4) enzymes, sucrase-isomaltase, mature enterocyte alkaline phosphatase, drug transporters and efflux proteins. It was also previously confirmed the presence of FcRn expression in Caco-2 cells. In addition, the albumin transport through Caco-2 monolayer was considered a saturable process, above 40 µg/mL, indicating a receptor-mediated uptake<sup>105, 106</sup>. After culturing (3-4 days), cells are undifferentiated and do not present microvilli, neither their indicator (sucrase immunoreactivity). When confluent, they form a polarized monolayer with microvilli and connected by tight junctions (**Figure 5 A**). The strength and tightness of the monolayer, meaning confluence and viability, can be identified by measuring the TEER. Higher TEER values indicate tighter membranes and consequently the modulation of the paracellular transport. Also, an indicative of the membrane integrity is the paracellular transport of small molecules like lucifer yellow, FITC-dextran or mannitol<sup>96</sup>. Although, Caco-2 cells present some drawbacks, namely the low expression of the CYP3A4 metabolizing enzyme, high and variable expression of P-glycoprotein (P-gp) and low paracellular transport of hydrophilic compounds, because of the tighter junctions<sup>107</sup>. Also, the permeability of drugs with slow absorption is poor in this model, comparing with rates in humans, and may be due to the lack of a 3D architecture. Plus, this model lacks the presence of mucus production, which excludes the main barrier of NPs absorption.

Furthermore, there have been suggested some alternative cell lines to find a model that better mimics the human system, being inclusively some of them used to analyze NPs permeability. In this line of thought, human colonic adenocarcinoma cell line (T84) is a possibility for permeability studies, specially regarding the transport of IgG and albumin in a FcRn-dependent manner<sup>70</sup>. Studies show that T84 cell line produces mucin in culture and releases it in response to various secretagogues<sup>108</sup>. It is known that the

absorption mainly occurs at the small intestine, so cells from colon have, *per se*, the drawback of differing in the paracellular permeability since, they present a tighter conformation and the absorption of compounds paracellularly is lower.

Despite having a nonintestinal origin, the Madin-Darby canine kidney (MDCK), from the distal tubule and collecting duct, is highly correlated with Caco-2 cells, working as a strong alternative to study drugs that are absorbed passively <sup>109</sup>. Authors showed the utility of MDCK cells in probing interactions between P-gp and their substrates. Comparing the permeability of anti-malaria compounds in Caco-2 and MDCK cells, they verified the overexpression of P-gp in MDCK-MDR1 cells, which allows high permeability <sup>110</sup>. It was analysed the mechanisms of transport of Deoxynivalenol (DON), using inhibitors, verifying the presence of organic anion and cation transporters. P-gp was also identified as the major efflux protein, due to the higher basolateral-to-apical observed transport <sup>111</sup>. Regarding NPs permeability, it was also proved the transport of nanoemulsions of self-nano-emulsifying drug delivery systems (SNEDDS) through MDCK cells <sup>112</sup>. Also, these cells only need 3-6 days to become confluent and form tight junctions <sup>109</sup>. Conversely, the fact that they are not intestinal neither human confer them different levels of transporters expression as well as different metabolic activity <sup>113</sup>.

#### *4.2.2. Co-culture model*

##### *Caco-2/HT29-MTX model*

HT29 cell line is originally from human colorectal adenocarcinoma and can mimic goblet cells. Though, HT29 cells need a different medium, comparing with Caco-2 cells, so they can differentiate and acquire a heterogeneous phenotype. To surpass this barrier, authors verified that by adding  $10^{-6}$  M methotrexate (MTX), HT29-MTX cell line is able to form a polarized monolayer with goblet cells and differentiate into mature goblet cells, able to produce mucus, after 21 days in culture <sup>114</sup>. The differentiation character can be approved by confirming MUC cell markers. Mucus is a viscoelastic gel produced by mucin glycoproteins and is responsible to prevent pathogens entrance, also acting as a barrier of NPs absorption, which affects the retention time <sup>95</sup>. In fact, authors already demonstrated that mucus clearly decreases the uptake and transport of NPs <sup>115</sup>. It is known that NPs (with positive charges) can interact with mucus (negatively charged) through electrostatic interactions, as well as hydrophobic or van der Waals interactions <sup>116</sup>. The role of mucus in cell-based models is already well described elsewhere <sup>117</sup>. So, this parameter must be taken into consideration when evaluating NPs permeability. When cultured with Caco-2 cells, there was the necessity to study different ratios to

prevent alterations in barrier properties caused by the overgrowth of HT29-MTX cells <sup>118</sup>. When  $10^5$  Caco-2 cells/cm<sup>2</sup> are combined with HT29-MTX in a 9:1 proportion, the model (**Figure 5 B**) gets closer to the human intestine characteristics, generating more predictable results <sup>119</sup>. Furthermore, HT29-MTX do not express P-gp and present tight junction less tight than Caco-2 (decreasing TEER values), which facilitate the passive permeability of nanosystems and represent a more physiological model <sup>120</sup>.

#### *Caco-2/Raji B model*

It is also described that Raji B cells, from a human Burkitt's lymphoma, when combined in a 1:2 proportion with  $10^5$  Caco-2 cells/cm<sup>2</sup> induce M cell phenotype (sparse microvilli and high transcytosis activity) (**Figure 5 C**). This happens due to the interaction between Caco-2 cells and lymphocytes and the presence of galectin-9 or SLAA, a signal of differentiation. In this model, Raji B lymphocytes cells are only added at the basolateral side after 14 days of seeding Caco-2 cells at the apical side. It was recently published a protocol suggesting an inverted *in vitro* M-cell model, where it is possible to do transport experiments every 10 h, after 3 weeks <sup>121</sup>. Despite not being in contact with Caco-2 cells, it is possible to observe cells with M cell characteristics. As mentioned before, M cells serve as antigen-sampling cells and unlike enterocytes, they can translocate particles without digesting them. Indeed, studies confirm that M cells play a major role in translocation and permeability of NPs, claiming that these parameters are higher in this type of co-culture comparing to Caco-2 mono-culture <sup>122</sup>. All in all, as a drawback, this model do not take into account the mucus, which is an important intestinal characteristic.

#### *Caco-2/HT29-MTX/Raji B model*

Taking all the above information into consideration, Sarmiento's group developed a triple co-culture model, with the three cell lines: Caco-2, HT29-MTX and Raji B cells (**Figure 5 D**). This group tested the model with normal and inverted orientation, verifying higher permeation with normal orientation <sup>123</sup>. This is actually a more accurate and realistic model due to its similarity with human intestine characteristics: enterocytes (Caco-2 cells), mucus production by goblet cells (HT29-MTX cells) and M-cells (Raji B cells). The proportions mentioned before were based on physiological ratios and previous works <sup>124</sup>. In addition, it was already shown that Caco-2/HT29-MTX co-culture and the triple Caco-2/HT29-MTX/Raji B co-culture models are useful to predict the intestinal transport of free drugs and NPs and to classify them, according to BCS, with low or high permeability. Furthermore, they have a good correlation with *ex vivo* models, which will be explained

later <sup>125</sup>.

#### 4.2.3. 3D co-culture model

All the models mentioned before are based on a 2D-surface which, once again, do not represent *in vivo* cells with a heterogenous environment containing several cellular events <sup>96</sup>. So, there was a necessity to create a 3D model with physiological structures to reproduce more accurately intestinal functions, namely growth, differentiation, interactions between cells themselves and with matrix and mechanical forces as well. In addition, cells in a 3D architecture are easily differentiated and polarized when on top, comparing with those that are near the villus base, which may be an advantage for NPs that remains longer in the lumen (slow absorption) <sup>126</sup>. Like atenolol, a hydrophilic and slow absorbed drug, certain NPs can migrate to the bottom of cells and be transported through cell-cell tight junctions <sup>127</sup>. Furthermore, 3D models have tight junctions less tight, comparing with Caco-2 monolayer, contributing for a better permeability which allies to less expression of P-gp and is consistent with *in vivo* observations <sup>128</sup>.

Some authors verified that MDCK cells in Matrigel can form a 3D architecture when the viscosity is low and the cellular contractile forces are strong. The 3D structure can then be changed in a viscosity-dependent manner. A way to play with it is to do a treatment with genipin (GP), since it allows the cross-link between amino groups of the matrigel peptide chains <sup>129</sup>. The 3D model can also include macrophages, increasing the uptake of particles, as well as other type of cells or even polymeric scaffolds to comprise the intestinal microvilli architecture. For instance, a recent model was proposed, where  $10^4$  cells/cm<sup>2</sup> of intestinal myofibroblasts (CCD18-Co cells) are entrapped in a thick layer of Matrigel and then  $10^5$  cells/cm<sup>2</sup> of Caco-2 cells are added over <sup>130</sup>. The differentiation of CCD18-Co cells can be confirmed by the observation of  $\alpha$ -SMA or CD90 through immunocytochemistry. It was verified that the matrix is important to maintain the architecture and support the model. On the other hand, fibroblasts contribute for epithelial cells growth (**Figure 5 E**) <sup>130</sup>. There is, inclusively, a model using Caco-2, HT-29 and T84 cell lines as well as proinflammatory stimuli, to mimic an inflamed intestinal mucosa <sup>131</sup>. Also, a model with the traditional Caco-2 cell line and human immune cell lines (Human macrophages (THP-1) and human dendritic cells (MUTZ-3)) was developed to evaluate the toxicity/safety of NPs <sup>132</sup>. The 3D co-culture model presents, in fact, additional complexity that may contribute for developing NPs to treat inflammatory diseases or even to study the interaction of the NPs with an inflamed intestine. Some authors already investigated the genetic and physiological properties of the 3D model,

verifying that knocking down MUC17 it is possible to reduce the protein expression of tight junctions (occludin) and increase the permeability. These authors inclusively created a 3D collagen scaffold enabling the exact geometry and density of the intestine in *in vivo* situation and more recently a synthetic and biodegradable hydrogel<sup>131, 133</sup>.

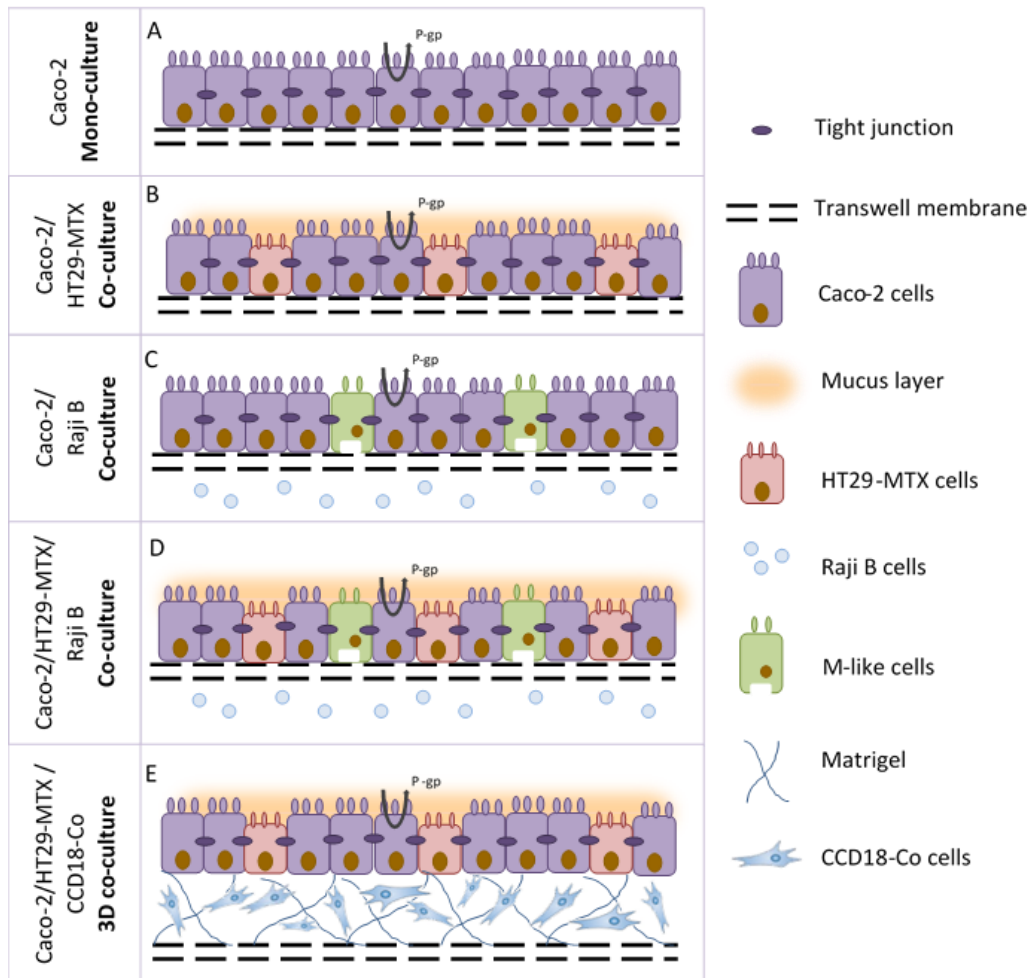


**Figure 5 | Schematic illustration of *in vitro* models: (A)** Caco-2 mono-culture model, **(B)** Caco-2/HT29-MTX co-culture model, **(C)** Caco-2/ Raji B co-culture model, **(D)** Caco-2/HT29-MTX/ Raji B co-culture model and **(E)** 3D co-culture model.

#### 4.2.4. Gut-on-a-chip model

Microfluidics has been revealing a very promising strategy to mimic the human intestine. In this way, human gut-on-a-chip has been developed as a more cost-effective, simple, fast and physiological relevant model. This model presents 3D architecture, constant flow and mimics the mechanically active microenvironment of living intestine, which facilitates cell-cell and cell-matrix interactions<sup>134</sup>. In fact, if a system is able to replicate external cellular conditions, more closely cells will replicate and behave as *in vivo*. For

instance, for clinical applications, flow is useful to study drug's dynamics, delivery of molecules, transport and absorption mechanisms that are not present in static models. Besides, with this type of systems, low volumes are required and so, can, for example, concentrate cell-derived factors. Plus, the user has easy access to cell-conditioned medium and can control the shape and interconnectivity of cell compartments <sup>134</sup>.

The chip can be produced by semiconductor industry, using computer microchip manufacturing, as lithography techniques. The mold is typically generated from silicon, glass or plastic and parameters such as mechanical compression or cyclic stress can be regulated and adjusted as desired in order to better mimic the intestinal environment <sup>135</sup>.

In general, gut-on-a-chip consists in 4 chambers (**Figure 6**): 2 central chambers where cells can be seeded and the culture medium circulate, and 2 vacuum chambers (one on each lateral side) responsible for controlling external factors, such as the membrane stretch and the peristaltic motion simulation <sup>136, 137</sup>.

Some devices are inclusively used to study the intestinal drug metabolism as well as interaction with NPs, nutrients or host-microbe. For instance, it was observed that 3D porous membrane in a gut-on-a-chip model potentiates the upregulation of villin and sucrase-isomaltase genes, responsible for intestinal cell differentiation, as well as CYP3A4 and CYP2C9, two cytochrome enzymes related to intestinal metabolism <sup>138, 139</sup>. Despite forming a planar epithelial monolayer, Caco-2 cells can form undulating structures when in a gut-on-a-chip after 2 days. In addition, it was found that gut-on-a-chip model promotes the Caco-2 cells' differentiation in the four main types (absorptive, mucus-secretory and enteroendocrine cells present in the villus regions and, Paneth cells present in the crypt region). These authors also showed that the mechanically active intestine stimulates CYP3A4 activity, glucose reuptake and mucus production, which is known to be absent in static Caco-2 models <sup>140</sup>. Here, once again it was shown the importance of external factors, like mechanical forces in getting closer to the *in vivo* human intestine. Also, it was reported that fluidic shear contributes for higher expression of tight junction Occludin and ZO-1 proteins in Caco-2 cells, which are responsible for forming tight junctions and, consequently, an increased TEER <sup>139</sup>. Plus, authors considered mechanical strain and created a biomimetic gut-on-a-chip that mimics the structure, physiology and microflora. Interestingly, under these conditions, the co-culture of Caco-2 cells with *Lactobacillus rhamnosus* GG (LGG) demonstrated high TEER values over time. It is also described that external factors accelerate cell differentiation within 3 days <sup>136</sup>. However, this can be a disadvantage since tighter tight junctions do not facilitate the transport of molecules and thus, do not mimic a real situation. On the other



hand, other authors verified that cyclic strain enhances the cell differentiation, formation of 3D villi-like structures and paracellular permeability, without changing TEER values in the monolayer, meaning that mechanical forces act directly in paracellular mechanisms<sup>136</sup>. All in all, the TEER values are not always concordant across literature and this might be due to the current TEER measure devices being designed to fit into conventional Transwell® culture plates and not into microfluidic device. As curiosity, embedding electrodes inside microfluidic organ chips have already been designed. The creators showed both in human lung airway chip and human gut chip the utility of this embedding electrodes to assess formation and disruption of barrier function. In this way, the users can have real-time results through a non-invasive approach<sup>141</sup>.

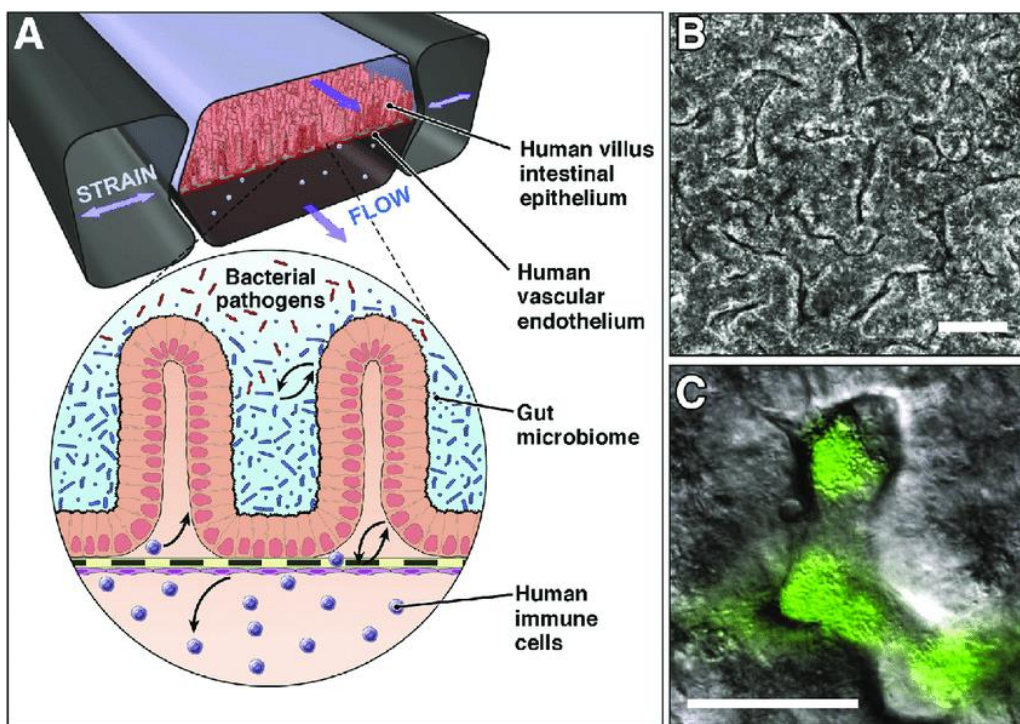


**Figure 6 | The mechanically active human Gut Chip.** (A) Human villus intestinal epithelium and vascular endothelium are lined on opposite sides of a flexible porous membrane under fluid flow and peristalsis-like strains. A zoom-in schematic shows the intestinal microenvironment undergoing complex crosstalk between commensal gut microbiome, bacterial pathogens, and immune cells in parenchymal and vascular channels, respectively. (B) Villus morphogenesis of human Caco-2 intestinal epithelium in the Gut Chip under physiologically controlled motions and flow. (C) An overlaid image of the coculture of green fluorescent protein-labeled *Escherichia coli* and microengineered villi in the Gut Chip. Bars = 50 mm. Reprinted with permission from<sup>137</sup>.

Alternatively, some authors choose to incorporate human intestinal organoids (HIO) through induced pluripotent stem cells (iPSCs) to an amenable model for study. To form

HIO, these authors supplemented iPSCs with Actividin A, CHIR99021, noggin, fibroblast growth factor 4 and epidermal growth factor to induce endoderm and hindgut formation, as to maintain the organoid formation <sup>142</sup>. Besides having the four intestinal cell types of differentiation and the characteristic crypt-villus 3D architecture, this model has the advantage of responding to exogenous stimuli <sup>142</sup>. More recently, the same authors aprimorated the intestine-on-a-chip to recapitulate the dynamic host-microbiota interface. In this sense, they recreated a system with hipoxia gradient across an endothelial-epithelial interface. The authors claim that the intestinal barrier integrity is actually better under these conditions. This system includes microscale oxygen sensors, Caco-2 cells or human organoid derived epithelial cells, housed in an anaerobic chamber, and enables to keep different commensal aerobic and anaerobic microorganisms in direct contact with patient-derived human intestinal epithelium for 5 days <sup>143</sup>. Donald Ingber and colleagues also fabricated a human small intestine-on-a-chip composed by 3D organoids of epithelial cells isolated from healthy regions of intestinal biopsies. According to their transcriptomic analysis, this intestine chip is closer to human duodenum than duodenal organoids <sup>144</sup>. This can be a personalized strategy for each individual, a way to understand specific mechanisms and therapies and get more reliable results. These organoids are dissociated and cultured on a porous membrane. This system is also characterized by having human intestinal microvascular endothelium cultured in a parallel microchannel under flow and cyclic deformation. Plus, as advantage, this intestine-on-a-chip is useful for metabolism, nutrition, infection and drug pharmacokinetics studies, considering the easiness to quantify nutrient digestion, mucus secretion and establish a intestinal barrier function <sup>144</sup>. Meanwhile, there is a commercial version available. Mimetas, the organ-on-a-chip company, created the Organoplate that combine microfluidics to a standard well plate. This allows the user the freedom to decide which extracellular matrix (ECM), cell types, co-culture and perfusion to use, according to each interest. In addition, this company recently developed a methodology to assess the barrier integrity using 40 leak-tight, polarized epithelial gut tubes, exposed to an ECM. The method was recreated in a microfluidic environment, expressing polarization and transporters. This can be a way to simulate a pathological situation like dysfunction of epithelial barriers, or drug-induced toxicity, which can reduce cellular life conditions and drug development. The epithelial barrier disruption condition is characterized for having an increased paracellular permeability. The authors claim to be a method of friendly-use, sensible, with real-time analysis <sup>145</sup>.

Basically, it is possible to combine different approaches and aprimorate the intestinal

models with p.e. immune cells, intestinal microbiota, organoids, mechanical forces, to approximate in the maximum possible way to an *in vivo* situation <sup>146</sup>. Although, further studies are developing systems encouraging the integration of liver, for instance, since it is important for reproducing the first-pass metabolism. In this sense, different organs-on-a-chip have been developed, in order to connect them and mimic the whole system present in the body and have more trustable results <sup>147</sup>. In addition, with a more complex system it is possible to have a broader perspective of drugs' effects, meaning it is possible to check possible side effects at different organs <sup>148, 149</sup>. The future goal is to include in the whole system and cells from patients like iPSCs. In this way, treatments can be uniquely designed for each patient <sup>150, 151</sup>. It was already reported a functional coupling between five microphysiological systems (MS) to validate the transport, metabolism, blood-brain barrier permeability, and toxicity of drugs. These MS represent the organs responsible for absorption, metabolism and clearance, as jejunum, liver and kidney, respectively, as well as skeletal muscle and neurovascular models. After testing terfenadine, trimethylamine (TMA) and vitamin D3, the authors obtained results showing an agreement between organ-on-a-chip and clinical data. Plus, it was discovered that trimethylamine-N-oxide (TMAO) was able to cross the blood-brain-barrier. Here, it is obvious the potential of these MS to use sequential fluid transport to study different organs' effects on downstream organs and to evaluate drug's toxicity and ADME (**Figure 7**) <sup>152</sup>. As future perspectives, some authors are considering to incorporate induced pluripotent stem cell-derived organoids in gut-on-a-chip models, which enhances the personalized therapeutics. Others are thinking in integrating important components such as intestinal fibroblasts, immune cells and the enteric nervous system. The value offer of this models is the possibility to mimic *in vivo* human intestine by integrating different cell types and external factors (shear stress, mechanical forces, flux) as well as the ability to analyze the complexity of the systems at different growth stages.

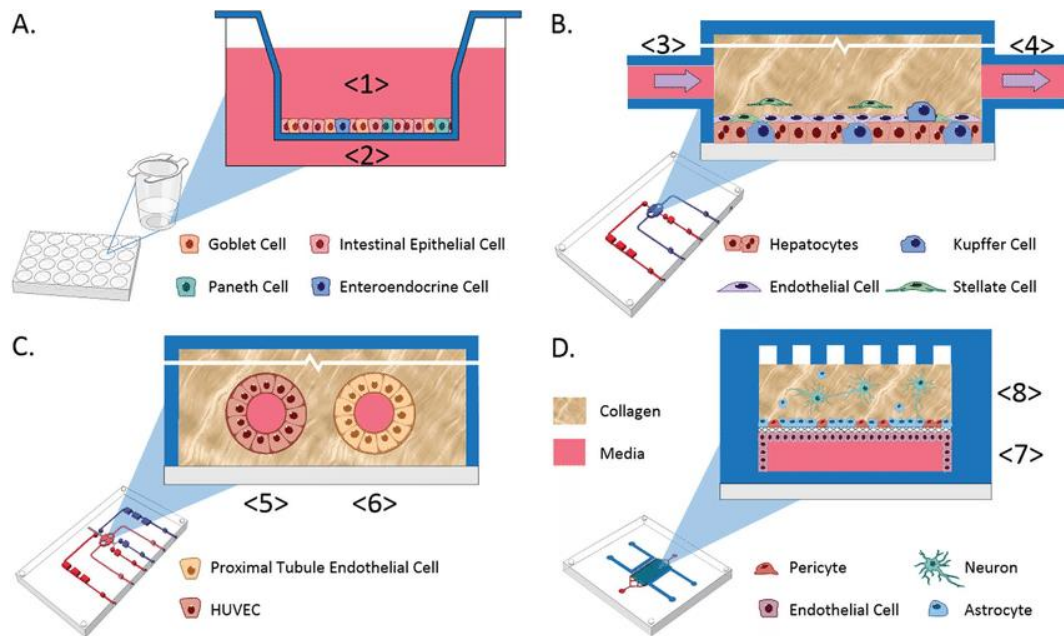


**Figure 7 | Schematic representations of the four of the organ systems used for functional coupling. (A)** The intestinal module is constructed in Transwell® from primary jejunum enteroids. Test agents are applied in the apical compartment (1). The media collected in the basolateral compartment (2) is used to add to the liver. **(B)** Media from the jejunum intestine basolateral compartment (2) is perfused as a 1:3 jejunum/naïve liver media into the influx port of the SQL SAL liver model (3). Efflux media is collected (4) and used to add to two downstream organ models. **(C)** The vascularized kidney proximal tubule module is a two lumen, dual perfusion system. For the vascular compartment, jejunum/liver-conditioned media (4) is diluted 1:2 or 1:4 with naïve EGM-2 media and then perfused into the influx port (5) to collect effluent from the proximal tubule at (6) . In parallel with perfusion through the vascular compartment, the proximal tubule compartment is perfused with naïve DMEM/F12 PTEC media (6) for effluent collection. **(D)** The blood-brain barrier with NVU is constructed in a membrane-separated, two-chambered microfluidic device. The brain-derived endothelial vascular compartment is perfused at the influx port (7) with jejunum/liver-conditioned media (4) diluted 1:4 with naïve EGM-2 media. The effluent is collected at the efflux port (7). In parallel with perfusion through the vascular compartment, the neuronal cell compartment is perfused with naïve EBM-2 media at the influx port < 8> for effluent collection at (8). Reprinted with permission from <sup>152</sup>.

### 4.3. Ex vivo models

*In vitro* tissue-based models, also called *ex vivo* are used in intestinal permeability studies in a way to move from *in vitro* to *in vivo* models. In this type of models, living functional tissues or organs are cultivated in a controlled environment after being isolated from organisms. These models present features that are normally not present in cell

models such as the adequate presence of mucus, paracellular permeability or the expression of transport proteins and drug metabolism. The main drawbacks of this and all *in vitro* models is the impossibility to recreate the gastric empty rate, GI pH or transit rate.

#### 4.3.1. *FcRn tissue expression and cross-species differences*

FcRn is expressed in nearly every organ in mammals, as blood-brain barrier, eye, lungs, breast, kidneys, intestine, skin, endothelial cells, antigen-presenting cells (e.g. macrophages, monocytes and dendritic cells), placenta, genitals and bone, which are described elsewhere<sup>153, 154</sup>. However, only intestine will be highlighted here, since this work focus oral delivery of FcRn-targeted NPs for an enhanced intestinal permeability with application in DM.

##### 4.3.1.1. *Human*

FcRn has a special role in early life stages for transporting IgG from mothers to neonates. However, the expression of FcRn is maintained along the adult stage in human intestine. Through immunohistochemical studies, it was possible to verify that FcRn is mostly located in the apical region of epithelial cells, in different sections of human intestine<sup>155</sup>. Moreover, FcRn is highly expressed in colon and ileum and less expressed in jejunum and duodenum<sup>93</sup>.

##### 4.3.1.2. *Mouse*

FcRn is also expressed in several tissues of mice and has the same importance when transporting the maternal IgG. It was previously reported that neonatal mice deficient in  $\beta_2m$  and FcRn HC were not able to absorb IgG from mother's milk, which demonstrated the highlight impact of FcRn in the IgG transport<sup>155</sup>. In adults, these mice had low levels of IgG in the bloodstream owing to the lysosomal degradation<sup>156-158</sup>. Thus, the expression of mFcRn is restricted to the suckling period, being down-regulated after weaning<sup>159</sup>. For this reason, it is recommended to use mice 6-16 weeks after weaning, since FcRn levels are stable. Besides, the homology to the rodent FcRn is around 70% compared to hFcRn, which is one more cause for the cross-species differences<sup>160</sup>. Thus, the transgenic mouse model mimics the tissue expression profile of hFcRn<sup>157</sup>. Overall, it is described that FcRn has higher expression in duodenum and jejunum in rat pup intestine, which is ~10-fold higher than human proximal colon<sup>106, 161</sup>.

Structurally, it was verified that some sequence variations may cause cross-species binding differences. Among these variations are the residues 132-147, the nonconserved residue 137 (Leu in hFcRn and Glu in mFcRn) <sup>162</sup> and residues 79-89, of which there is a two-residue deletion in hFcRn and a possible glycosylation site in mFcRn <sup>163</sup>. Regarding the FcRn-albumin interaction, HSA has a 5-fold lower affinity to hFcRn compared to mouse serum albumin (MSA) <sup>60, 164</sup>, while MSA has a 25-fold stronger affinity to mFcRn than HSA <sup>51, 165</sup>. These cross-species differences are related to nonconserved amino acid found in the conserved His166 within the  $\alpha 2$  domain of FcRn <sup>51, 60, 165</sup>, but also with different amino acid structure of DI and DIII from both species <sup>52, 165</sup>. The differences associated to DI are represented by four mutations in loop I and II of its domain. However, Arg114 (from loop II) as well as both loops of I are crucial role for the I-hFcRn interaction <sup>52</sup>. Regarding the DIII, the major difference is the amino acid at position 573, which is lysine in humans and proline in rodents <sup>51</sup>. The replacement of Lys573 for Pro573 increases 1.5-fold the half-life of HSA in mice and augment 12-fold and 15-fold the affinity for hFcRn and mFcRn, respectively <sup>51</sup>. Thereby, the interaction between mFcRn and MSA is stronger compared with the mFcRn interaction with HSA, which can contribute to rapid clearance and interfere with *in vivo* preclinical evaluation in mice. In this case, HSA competes with the higher amounts of endogenous MSA (40 mg/mL) for the binding to mFcRn, resulting in an augment in the half-life of endogenous MSA and no alteration in half-life of HSA <sup>165</sup>.

#### 4.3.1.3. Porcine

The pig has been confirmed as a non-primate model suitable for assessing PK of HSA, since porcine serum albumin (PSA) minimally competes for binding to FcRn <sup>160</sup>. In fact, pigs have gained importance as a large animal in pharmaceutical research due to its physiological and anatomical similarities to human. In addition, pigs are replacing dogs as the preferred non-human primate model in preclinical studies. Stirling *et al.* <sup>166</sup> characterized the porcine FcRn (pFcRn) and tested its utility as a potential model for transepithelial protein delivery <sup>166</sup>. The sequence of the pFcRn gene is 80% similar to the corresponding human gene and 69% similar to the rodent receptor gene (**Figure 8**). Structurally, the similarity between the pFcRn protein and the human version is based on the single N-linked glycosylation site (NVSV) in the  $\alpha$  domain, as well as both dileucine- and tryptophan-based endocytosis signals present in the cytoplasmic tail. In particular, the porcine receptor has a type 1 membrane protein with an N-terminal single peptide and a single transmembrane domain. However, it does not seem to be an

agreement about specific amino acid differences of the FcRn structure between the two species; this could be due to different polymorphisms, as described elsewhere <sup>166</sup>.

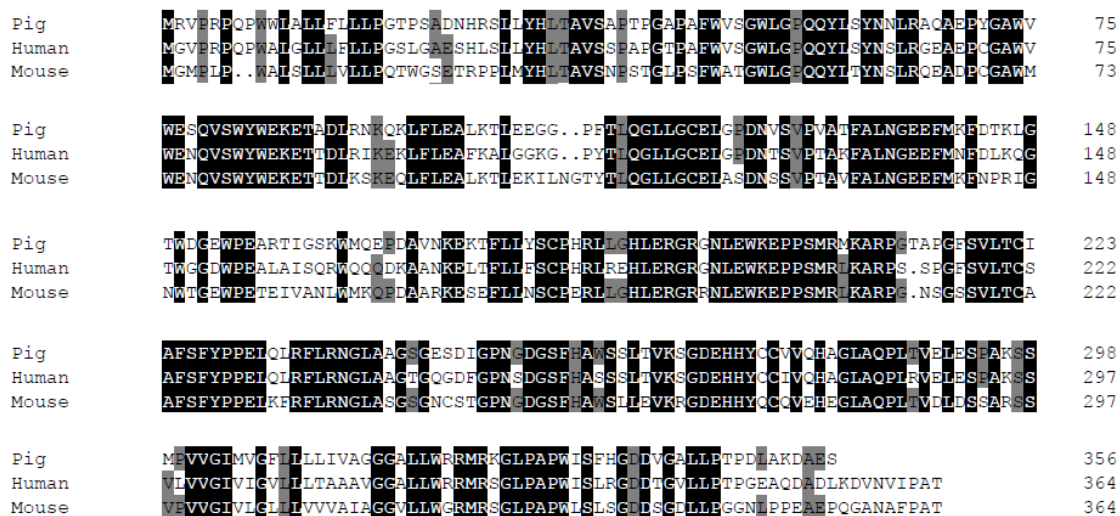


**Figure 8 | Alignment of predicted porcine FcRn amino acid sequence (Sus scrofa, NP\_999362.2) with other species.** The degree of homology is indicated by darker shading. Protein sequences are from GenBank (locus numbers: Human (Homo sapiens, NP\_001129491.1), Mouse (Mus musculus, NP\_034319.2). Reprinted with permission from <sup>167</sup>.

Porcine FcRn is expressed in endothelial cells and monocytes, as well as in cells in the heart, lung, kidney, intestine, muscle, and brain; it is also highly expressed in cells in the liver, spleen, thymus, and lymphoid. Also, porcine FcRn is maintained in the adult stage, as in humans <sup>166, 167</sup>. Despite PSA sequence being 75.1% similar to HSA, HSA has 2.9-fold higher affinity towards pFcRn, which does not cause competition <sup>160</sup>.

As for applicability, more and more devices and systems have used porcine tissues. As an example, Rani Therapeutics studied the pharmacokinetic/pharmacodynamic (PK/PD) of recombinant human insulin delivered by an ingestible device in the porcine jejunum <sup>168</sup>. Recently, a robotic system for the screening of oral drug formulations was developed using a porcine *ex vivo* intestine model. The tissue is placed between two magnetic plates. These researchers correlated *in vitro* data of the gold standard, Caco-2 cells, and the *ex vivo* porcine model, with drug permeability data in humans and verified that it was 0.3 and 0.9, respectively. The cultivation of intact tissue enabled the maintenance of the complex GI architecture, mucus layer and the expression of several drug transporters for 7 days. <sup>169</sup>

#### 4.3.2. Standard models

##### 4.3.2.1. Diffusion chambers

The most performed method using intestinal tissues is diffusing chambers, namely Ussing chamber or Franz cells. The main difference between these two is the direction of the flux. In the first, is horizontal, or side-by-side, and in the second is vertical <sup>170</sup>.

##### *Ussing chamber*

Ussing chamber was the first to be invented, in 1951, later using intestinal tissue in 1988 <sup>171, 172</sup>. The size, volume and area of exposed tissue are parameters that can vary. In this methodology, a section of intestinal tissue is excised, separated in small fragments and opened to form a flat surface. Then the tissue is placed in the chamber between two halves. The chamber is filled with physiological buffer, gassed with carbogen and warmed at 37°C. Two chambers, donor and receiver, are divided by the tissue, one of them representing the serosal side and the other the mucosal side. The drug or NPs to be tested in a permeability test can be placed in one of the chambers and samples should be removed from the other chamber, replacing the volume took with fresh buffer <sup>173, 174</sup>. The TEER is again one of the parameters that can be measured by placing the electrodes in each side of the membrane <sup>175</sup>. The main advantage of this model is the maintenance of the gut architecture, membrane transporters and enzymes when compared with cell-based models. It is also possible to study regional differences in the GIT by using different sections of it. Ussing chamber can also be used with human tissues instead of animal tissues. Since tissues can be easily obtained from tumor resections or gastric bypass surgeries, more recent studies have been using this type of tissue <sup>176</sup>. One disadvantage, though, is the fact that the experiments should be performed near a surgery clinic since the tissues can quickly deteriorate outside the body <sup>177</sup>.

##### *Franz cell*

On the other hand, Franz cell is mostly used for skin permeation studies than intestinal permeability, but used nevertheless. This model is not much different than Ussing chamber, since the tissue membrane is still placed between the donor and receptor chamber. The main significant difference, besides the direction of the flow, is the size of the chambers, since in the Ussing chamber the sizes are similar and in the Franz cell the donor compartment is smaller than the receptor <sup>178</sup>. This difference in volumes can induce discrepancies in the permeability when compared to the Ussing chamber, but can



be resolved by using a magnetic stirrer in the receptor chamber in order to reduce the unstirred water layer. It is important to use the tissue as soon as harvested and ensure sink conditions are maintained. Few work have been done using intestine tissue in Franz cells to evaluate nanoparticle permeability.

#### 4.3.2.2. *Everted intestinal sac model*

Another method used in *ex vivo* intestinal permeability studies is the everted intestinal sac. This model can be applied in the study of mechanisms and kinetics of drug absorption and metabolism including pro-drug conversion in the GIT, efflux transport, drug resistance and interactions<sup>179</sup>. A section of the intestine of the animal is removed, washed, inverted with a rod and one of the ends is tied. The inside of the sac is filled with oxygenated buffer and the other end closed after. Then it is placed in the container. This container has the sample to be tested, and its presence in the interior of the sac is then evaluated, within the determined time-points. There are two different techniques that can be applied in this method, one where both sides are closed, creating a closed sac and the other where the end of the tissue is cannulated in the tubes. The main advantages of this model is the low cost, quickness, the possibility of test several drugs, the presence of the mucus layer, large surface area and the possibility of study passive and active transport. The main disadvantages are the possibility of damaging the tissue, the release of proteins and/or enzymes as well as the muscularis mucosa that mislead the results, and the time which the tissue remains viable, that is only two hours<sup>180, 181</sup>. The everted sac is the main method used to test NPs permeability.

#### 4.3.2.3. *Non-everted intestinal sac model*

In order to avoid tissue damaging, this model does not evert the gut sac after excision. The intestinal sac is removed from the animal, washed properly and one of the ends of the sac is tied. The sample solution is placed inside the sac and the other end is closed. Afterwards, the sac is placed in the release medium. This release medium should be able to mimic the conditions existing in the GIT. This method is more limited than the everted sac in terms of information that can be accessed, but it is simple and rapid to perform, while still capable of test drug absorption. It is not only simpler but also requires low amounts of the drug tested and samples are easier to quantify and can be collected at various time points<sup>178, 182</sup>. In terms of disadvantages, this method is quite similar to the everted sac, where the viability of the tissue is the main issue to carefully handle.

#### 4.3.2.4. Everted intestinal ring

Similar to the everted intestinal sac, the everted intestinal ring is also used in *ex vivo* intestinal permeability studies. Most used to assess the uptake and metabolism of the tested compounds, in this model, the intestinal tissue is harvested, everted and cut into small rings. Then it is put in an incubator with proper incubation media and agitation. The simplicity is the main advantage of this method allied with the ability of testing several compounds<sup>183</sup>. However, this technique also presents disadvantages. Since both connective tissue and muscular layer are exposed in the media, the diffusion of the tested compounds could not occur on the mucosal side. Also, the time of incubation is quite reduced, around 10 min<sup>174, 183</sup>.

#### 4.4. *In vivo* FcRn model systems

Primates are considered the best animal model to mimic the human PK parameters<sup>184</sup>, but the high costs and ethical subjects make their use unapproachable<sup>164, 185</sup>. In this sense, rodents have been considered the preferred models to assess the bioavailability of biopharmaceuticals<sup>184</sup>, due to the convenience, cost-effective and defined genetic background<sup>164, 185</sup>. Nevertheless, the expression of FcRn and the affinity of its ligands differ between humans and rodents, which can interfere with the FcRn therapeutics. Taking into account all the differences reported between humans and rodents, as previously discussed, the conventional rodent models do not reflect an adequate PK profile of FcRn-targeted ligands. To solve this preclinical challenge, several genetically engineered mouse strains have been developed where the mFcRn heavy chain has been replaced with the human counterpart, either under the control of the mouse or human promoter elements<sup>64, 157, 186-192</sup>. These strains are the current gold standards for the evaluation of hFcRn-targeting strategies addressing PK/PD and delivery across selective mucosal barriers prior to studies in non-human primates.

The most commonly used hFcRn-expressing strains are generated from conventional C57BL/6J mice, named Tg32 and Tg276 (**Figure 9 A**), which are extensively used to assess the half-life of hIgG and HSA variants<sup>64, 157, 186, 189, 191, 192</sup>. Both strains have substituted the mouse heavy chain with that of the human form, which can pair non-covalently with the endogenous mouse  $\beta 2m$ <sup>64, 157, 186, 191, 192</sup>. A distinct difference between these strains is that the Tg32 mice express the heavy chain under the control of its human regulatory elements<sup>157, 186, 189, 191, 192</sup>, while the expression in Tg276 mice is regulated by a constitutive CAG promoter, a human cytomegalovirus enhancer fused to chicken  $\beta$ -actin/rabbit  $\beta$ -globin hybrid<sup>64, 186</sup>. This results in a much more widespread

expression profile of hFcRn in Tg276, whereas the FcRn expression profile in Tg32 mice has been mapped to be similar to that in humans<sup>193, 194</sup>. There is also a modified version of Tg32 that expresses human  $\beta$ 2m, but no difference in half-life of the ligands has been reported that can be related to whether the mice carry a mouse or human form of  $\beta$ 2m<sup>191</sup>. In general, the half-life of IgG is shorter in Tg276 homozygous mice relative to the Tg32 strain, and longer in the Tg32 hemizygous than the homozygous strain<sup>191</sup>. Since the expression profile of the Tg32 strains resembles more closely to that of humans, studies of FcRn in mucosal immunity and receptor targeting for delivery across the epithelial barriers have been mainly studied in these mice, as recently reviewed<sup>195</sup>. Therefore, the Tg32 strains should be used for studies addressing the mucosal delivery of FcRn-targeted molecules or nanosystems.

In humans, injected hIgG and HSA variants as well as fusions will compete for binding to FcRn in the presence of high concentrations of IgG (10 mg/mL) and albumin (40 mg/mL), produced by the plasma cells and liver, respectively. This is in stark contrast to what has been found in mice kept under pathogen-free housing, where the concentrations of endogenous mIgG are low (roughly 1.0-0.2 mg/mL) compared to those found in nature, while the concentrations of MSA are high due to constitutive production by the liver (20-50 mg/mL)<sup>64, 196</sup>. These conditions must be taken into consideration in the preclinical evaluation of FcRn-targeted strategies, since the outcome can be greatly affected by a lack of competition for receptor binding, as in the case of the IgG binding site, which is in contrast to strong competition for the albumin-binding site. To address how competition for the IgG binding site of FcRn affects targeting approaches, mice may be pre-loaded with excess amounts of hIgG prior to administration, which has been shown to modulate the half-life of injected IgG variants<sup>185, 186, 188</sup>. Interestingly, a modified version of the Tg32 strain was recently reported that is engineered to produce hIgG1 Fc combined with mIgG Fab arms, which is rescued by hFcRn (**Figure 9 B**)<sup>188</sup>. The levels of endogenous chimeric mouse-human IgG1 were shown to be greatly increased upon immunization, which modulated the half-life of injected hIgG. Thus, this Tg32-hFc mouse model may be attractive for studies addressing competition for the IgG binding sites. A similar mouse model that also expresses the human classical Fc $\gamma$  receptors have been reported<sup>197</sup>.

Regarding studies of HSA-based strategies, a version of Tg32 that lacks expression of MSA has been developed<sup>190</sup>. This model allows studies in the absence of competition, but also in the presence HSA following preloading (**Figure 9 C**). An alternative to this is a mouse strain, named Albumus<sup>TM</sup>, that has been genetically modified to express both

hFcRn and HSA<sup>187</sup>. However, the expression of the heavy chain of hFcRn is here not under control of the human promoter (**Figure 9 D**). Despite this, studies of engineered HSA variants in Tg32 with competition and in the double transgenic mouse model have revealed similar half-lives<sup>51, 187, 192</sup>. Due to differences in the construction of these strain, they may vary regarding the expression of the receptor in different mucosal tissues, which has not yet been studied in detail. Importantly, it has recently been shown that competition for the albumin-binding site strongly affects the half-life of injected HSA<sup>87, 190</sup>. While the half-life in Tg32 mice lacking expression of albumin was measured to be around 3 weeks for injected WT HSA, it was only a few days in the presence of competition<sup>87, 190</sup>. This demonstrates that the competitive pressure is high for the albumin-binding site of FcRn. As such, only minor alterations to the binding kinetics of WT HSA fusions may affect their half-life. To compensate for this, HSA engineered for improved hFcRn binding may be used.

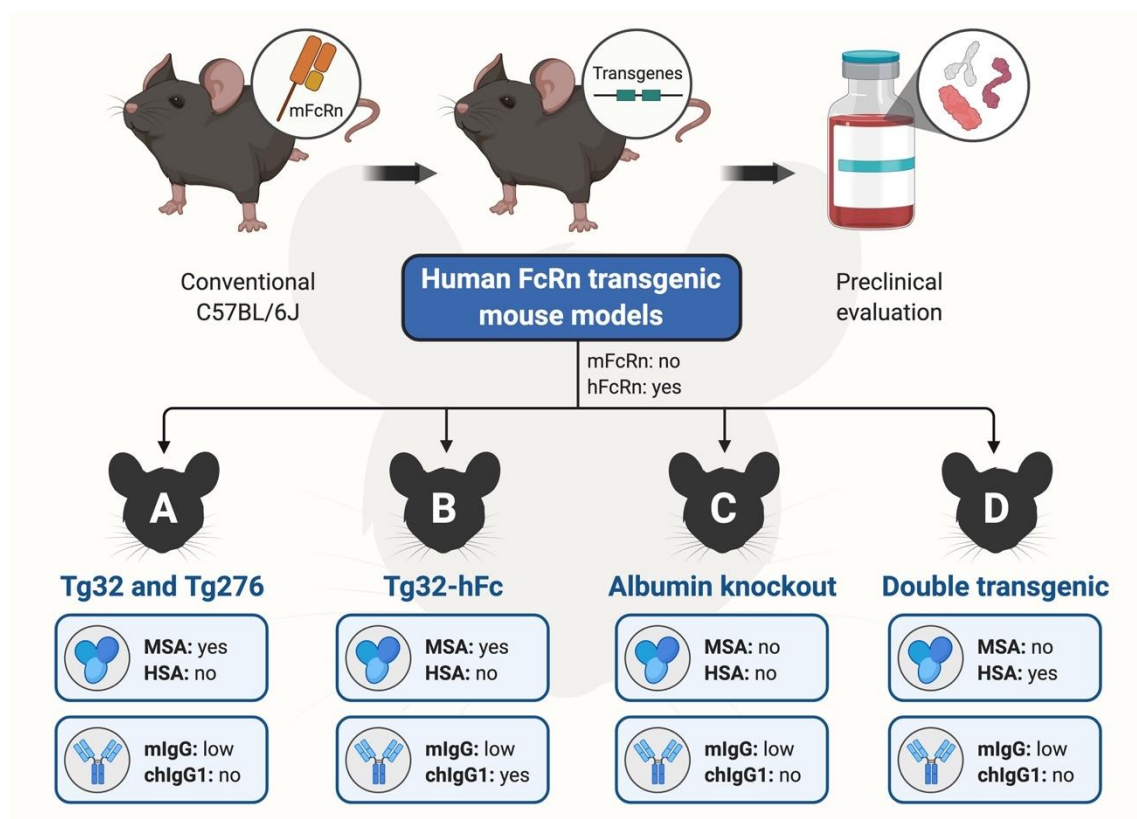


**Figure 9 | Human FcRn transgenic mouse models for evaluation of IgG and albumin-based therapeutics.** Conventional C57BL/6J mice have been used to generate humanized mouse strains that are transgenic for hFcRn. While (A) the Tg32 and Tg276 strains express mIgG, (B) the Tg32-hFc strain expresses chimeric hIgG1 (chIgG1). In comparison to these mouse strains,

(C) Tg32 albumin knockout mice do not express MSA, while (D) the double transgenic mouse model (Albumus™) have both hFcRn and HSA. The figure was created with BioRender.

## Chapter II

---

### OVERVIEW AND AIMS

---



## 1. Overview

Diabetes is a worldwide disease and its incidence is increasing over the years. The common treatment is based on daily injections of antidiabetic peptides, which is invasive and painful. Nanotechnology is revolutionizing drug delivery through multifunctionality and increased bioavailability. To maintain patient compliance, oral administration is the preferred drug delivery route. Nevertheless, biopharmaceuticals do not endure the harsh environment of GIT and poorly cross epithelial barriers. To surpassing inefficient delivery, the use of FcRn as a gateway for oral delivery of insulin encapsulated into polymeric mucopenetrating NPs is proposed as a novel strategy to control diabetes symptomatology.

In the framework of this thesis, a collaborative work between the Institute for Research and Innovation in Health (i3S) at the University of Porto (Portugal), Oslo University Hospital (Norway), European Space Agency (ESA) at Noordwijk (The Netherlands) and Massachusetts Institute of Technology (MIT) at Boston (USA) was established.

The expertise of Bruno Sarmiento's group, from i3S, is focused on developing functionalized nanomedicines and their application in pharmaceutical and biomedical fields. In particular, the group develop "smart" nanoformulations of peptides and proteins with interest in diabetes, able to overcome the physiological barriers, for mucosal delivery. Plus, the group is also specialized in mucosal engineering models to validate functionalized nanomedicines and *in vitro/in vivo* correlation. Jan Andersen's group, from Oslo University Hospital, is one of the few recognized worldwide experts on studies of interactions of IgG and albumin with FcRn, and the research center is aiming to unravel the basic structural and cellular mechanisms that govern functions of FcRn, with a particular focus on albumin as a multifunctional transporter. Furthermore, the group combines structural and biophysical approaches with cellular and *in vivo* studies, to design novel albumin and IgG molecules with improved binding properties and cellular functions. The TEC-MMG LIS Lab, from European Space Research and Technology Center (ESTEC) of ESA, supports work on life and physical sciences and experiments for micro and hypergravity research, as well as exploration related activities, as flight payloads and planetary exploration. Lastly, Dr. Traverso's research program, from MIT, is focused on developing novel technologies for drug delivery through the GIT. This group aims to enable a broader spectrum of therapeutics to be delivered through the GIT, to extend the duration of drug release after a single administration event, as well as to enhance precision in localization of drug delivery, to maximize drug delivery to areas of disease while minimizing side effects from drugs in non-diseased tissues.



These collaborations and combined expertise between groups allowed the performance of this thesis and benefit my personal and professional skills, throughout the development of FcRn-targeted nanoplatform for oral delivery of antidiabetic peptides.

## 2. Aims

The main aim of this thesis project was to develop nanoengineered platforms for delivery of biopharmaceuticals through the intestine, with impact on diabetes management. The main hypothesis is that surface-functionalized NPs with engineered albumin variants with improved pH dependent binding to FcRn will enhance transcellular transport across mucosal epithelial barriers and thus provide drug stability, controlled release and improve the PK/PD profile of insulin, as a biopharmaceutical model. The ultimate objective was to use the developed system as a therapy for T1DM.

The specific objectives of this thesis were:

- i. To produce and characterize the efficacy of engineered albumin variants conjugated to insulin-loaded NPs in a site-oriented manner (Chapter IV and Appendix I);
- ii. To analyze the FcRn binding and transport properties of the designed insulin encapsulated NPs using *in vitro* model systems (Chapter IV and Appendix III);
- iii. To explore the potential of simulated hypergravity in oral delivery of biopharmaceuticals (Appendix II);
- iv. To evaluate the intestinal permeability in a porcine *ex vivo* model, as a more realistic platform to screen oral FcRn-targeted drug formulations (Chapter IV);
- v. To assess *in vivo* the ability of the developed polymeric NPs to reduce glucose levels in a hFcRn transgenic mice model, induced with T1DM (Chapter IV).

## Chapter III

---

# MATERIALS AND METHODS

---



## 1. Cell culture

HEK293E (human embryonic kidney) cells were acquired from ATCC (Manassas, VA, USA) and maintained in RDMI 1640 (Sigma-Aldrich) with 10% heat-inactivated fetal calf serum (FCS) (Sigma-Aldrich). A MDCK (Madin-Darby Canine Kidney) cell line overexpressing human FcRn (MDCK-hFcRn) was generated by Drs. Alex Haas and Jens Fischer (Roche Pharma Research and Early Development, pRED, Roche Innovation Center Munich, Germany) and maintained until passage 20. MDCK-hFcRn cells were cultured in DMEM (Gibco) with 15% fetal calf serum (FCS) and 200 µg/mL of G418 (Sigma-Aldrich). The expression level of FcRn-Enhanced Green Fluorescent Protein (EGFP) was stably maintained by G418 and regularly checked by Thermofisher cell counter countless II equipped with EVOS Light Cubes for GFP detection, being always above 80%. Human microvascular endothelial cells (HMEC1) stably expressing HA-hFcRn-EGFP (HMEC1-hFcRn)<sup>198</sup> were grown in MCDB 131 (Gibco) supplemented with 10% FCS, 2 mM L-glutamine, 10 ng/mL mouse epidermal growth factor (PeproTech) and 1 µg/mL hydrocortisone (Sigma). Per flask was also added 5 µg/mL blasticidin S (InvivoGen) and 100 µg/mL G418 (Sigma) to maintain stable the expression of hFcRn. All the culture medium was supplied with 25 µg/mL streptomycin and 25 U/mL penicillin (BioWhittaker), and cells were incubated at 37°C in a humidified 5% CO<sub>2</sub>, 95% air incubator. All the cells were passaged twice per week.

## 2. Protein production

WT albumin and engineered albumin variants, namely K500A/K510Q (KAHQ) and K573P (KP), were produced by following the procedures previously described, using HEK293E cells<sup>199</sup>. Purification of albumin variants was performed using a Capture select albumin affinity column (GE Healthcare) and followed by gel filtration with a Superdex 200 increased column (GE Healthcare) connected to an Avant25 instrument (GE Healthcare). Human IgG1-MST/HN and recombinant soluble human FcRn were produced as previously described<sup>71</sup>.

## 3. Polymeric nanoparticles production

Engineered albumin-conjugated and insulin encapsulated poly(lactic-co-glycolic)-poly(ethylene glycol) (PLGA-PEG) NPs were prepared through a modified solvent emulsification-evaporation method based on a w/o/w double emulsion technique<sup>200, 201</sup>. Briefly, 100 mg of polymer, in which 95% was PLGA (PURASORB<sup>®</sup> PDLG 5004A, in a

50/50 molar ratio of DL-lactide and Glycolide, kindly provided by Corbion) and 5% PLGA-PEG-MAL (Akina, PolyScitech, AI110), was overnight dissolved in 2 mL of ethyl acetate. Then, 0.2 mL of 75 mg/mL insulin solution (Sigma-Aldrich) in 0.1 M of HCl was added to the polymeric solution and homogenized using a Bioblock vibracell 75186 sonicator (Fischer Bioblock Scientific), for 1 min with 70% of amplitude. This primary emulsion (w/o) was poured into 8 mL of 2% (w/v) Pluronic F-127 (Sigma) aqueous solution and homogenized for 1 min using the same equipment, forming the second emulsion (w/o/w). To this, it was added 15 mL of 2% Pluronic F-127 and the organic solvent was then removed by evaporation during 3 h under magnetic stirring (300 rpm). The NPs were washed twice with 0.25 mL of ultrapure water by centrifugation using Amicon® filters of 100 KDa (Millipore Corporation, Bedford, MA, USA) at 1000 x g for 40 min, and redisposed in 0.1 M phosphate buffer ( $\text{Na}_2\text{HPO}_4$ ,  $\text{NaH}_2\text{PO}_4$ ) at pH 6.

For conjugation, the amount of albumin was set to the molar ratio 1:0.1 of PLGA-PEG-MAL:Albumin. For each albumin variant, 500  $\mu\text{L}$  of NPs (20 mg/mL) were transferred to an eppendorf Amicon® filter of 100 KDa and centrifuged at 10,000 x g for 5 min at 4°C. The supernatant was discarded, and NPs were resuspended in 250  $\mu\text{L}$  of 0.1 M phosphate buffer. Thereafter, it was added 250  $\mu\text{L}$  of 5.71  $\mu\text{M}$  of albumin-TCEP solution. Each variant was diluted and incubated with 5.71  $\mu\text{M}$  tris(2-carboxyethyl)phosphine hydrochloride (TCEP) for 1 h at room temperature (RT), in order to have a 5.71  $\mu\text{M}$  of albumin-TCEP solution. The reaction was incubated overnight at 4°C. The following day, samples were washed three times with 0.1 M Phosphate Buffer at pH 7 by centrifugation using Amicon® filters of 100 KDa at 10,000 x g for 5 min at 4°C. The same procedure was followed to unloaded PLGA-PEG NPs.

#### **4. Physical chemical characterization**

##### **4.1. Particle size and zeta potential analysis**

Three  $\mu\text{L}$  of NPs were characterized for hydrodynamic diameter, polydispersity index (Pdl) and zeta potential (ZP) upon dispersion in 1 mL of 10 mM sodium chloride by dynamic light scattering (DLS) and laser Doppler electrophoresis (LDE) using a Zetasizer Nano ZS (Malvern Instruments, Malvern, UK).

##### **4.2. Morphological characterization and elementary analysis**

The morphology of NPs was measured by transmission electron microscopy (TEM) and the elementary analysis by elementary dispersive scanning (EDS). The samples were

placed on a grid and observed in a JEOL JEM-1400 electron microscope (JEOL Ltd, Tokyo, Japan). During the preparation, samples were mounted onto metal stubs and vacuum-coated with a layer of gold/palladium.

### 4.3. Insulin association efficiency and drug loading

The association efficiency (AE) and drug loading (DL) were determined using the following formulas:

$$\text{Equation (1)} \quad \text{AE (\%)} = \frac{\text{total amount of insulin-free insulin in supernatant}}{\text{total amount of insulin}} * 100$$

$$\text{Equation (2)} \quad \text{DL (\%)} = \frac{\text{total amount of insulin-free insulin in supernatant}}{\text{total amount of NPs}} * 100$$

The free insulin in supernatant was isolated during the first washing step by centrifugation with Amicon® filters at 1000 x g for 40 min at 4 °C. The insulin that did not associate to NPs and remained in the aqueous phase was then collected and quantified by a high-performance liquid chromatography (HPLC) method previously validated<sup>202</sup>. Briefly, insulin quantification was performed using a Merck-Hitachi LaChrom HPLC instrument (Merck, Whitehouse Station, NJ, U.S.A.) equipped with a XTerra RP 18 column, 5 µm particle size, 4.6 mm internal diameter, x250 mm length from Waters (Milford, MA, U.S.A.), and a LiChrospher 100 RP-18, 5 µm particle size guard column (Merk, Whitehouse Station, NJ, U.S.A.). Samples were run in triplicate.

### 4.4. Insulin release

Insulin-loaded NPs (1 mL) were dispersed in 10 mL of pH 1.2 buffer (50 mM KCl) to simulate the gastric fluid (SGF) and incubated at 37°C under magnetic stirring at 100 rpm. After 2 h, the 10 mL suspension was ultracentrifuged at 14,000 x g for 20 min to remove SGF and the NPs were then resuspended with 10 mL of pH 6.0 buffer (50 mM KH<sub>2</sub>PO<sub>4</sub>, 15 mM NaOH) to simulate the intestinal fluid (SIF) and incubated at 37°C under magnetic stirring at 100 rpm. Aliquots of 0.2 mL were taken at predetermined time points (15, 30, 45, 60, 120, 180, 240, 360 and 480 min) and the samples were replaced with a respective pre-heated fresh buffer, keeping the volume constant. With the purpose to calculate the released insulin, each aliquot was ultracentrifuged, and the supernatant was used for HPLC analysis in order to quantify the insulin released from the NPs over time. Samples were run in triplicate.

#### 4.5. Albumin conjugation efficiency

The conjugation efficiency (CE) of albumin was determined using the following formula:

$$\text{Equation (3)} \quad \text{CE (\%)} = \frac{\text{total amount of albumin-free albumin in supernatant}}{\text{total amount of albumin}} * 100$$

The quantification was done using a two-way anti-albumin enzyme-linked immunosorbent assay (ELISA). Briefly, 96 wells plates (Costar) were coated with 100  $\mu\text{L}$  of a polyclonal anti-albumin antibody produced in goat (Sigma Aldrich, ref A1151) diluted 1:2000 in PBS by incubation overnight at 4°C. The wells were blocked with 200  $\mu\text{L}$  PBSTM solution, composed by PBS, 0.005% Tween 20 and 4% skimmed milk (Acumedia), for 1 h at RT and then washed three times with 200  $\mu\text{L}$  PBST (PBS, 0.005% Tween 20). Dilution series of the albumin-conjugated NPs samples were prepared (1 mg/mL), starting from diluting the samples 100x and then titrated 1:2 in PBSTM. 100  $\mu\text{L}$  of each dilution was subsequently added in triplicates to wells and incubated for 1 h at RT. The wells were washed as before. Alkaline phosphatase (AP)-conjugated polyclonal anti-albumin from goat (Bethyl Laboratories; A80229AP) was diluted 1:4000 in PBSTM and 100  $\mu\text{L}$  was added per well and incubated for 1 h at RT. After washing as before, visualization was performed by adding 100  $\mu\text{L}$  of AP substrate (4-nitrophenyl phosphate disodium salt hexahydrate substrate) (Sigma-Aldrich) diluted in diethanolamine buffer. The absorbance was measured at 405 nm using the sunrise spectrophotometer (TECAN).

### 5. Protein structure

#### 5.1. Determination of secondary structure

The secondary structure elements of insulin loaded and albumin conjugated PLGA-PEG NPs were assessed by Fourier Transform Infrared Spectroscopy (FTIR). The spectra analysis was performed in ABB MB3000 FTIR spectrometer from ABB (Zurich, Switzerland) equipped with a MIRacle single reflection attenuated total reflectance (ATR) accessory from PIKE Technologies (Madison, WI, U.S.A.). Samples were freeze-dried before analysis. The spectra were made with 256 scans and a 4  $\text{cm}^{-1}$  resolution in the region of 600-4000  $\text{cm}^{-1}$ , and each formulation was analyzed in triplicate. In order to obtain the insulin and albumin spectra, a double subtraction procedure, followed by a 15

points Savitsky-Golay second derivative, and a baseline correction using a 3-4 point adjustment at the amide I region ( $1710\text{-}1590\text{ cm}^{-1}$ )<sup>203</sup>. This spectral treatment was executed using the HorizonMB FTIR software from ABB (Zurich, Switzerland). Lastly, all spectra were area-normalized for comparison using Origin 8 software (OriginLab Corporation, Northampton, MA, USA).

The quantitative comparison of the similarity of the FTIR spectra between insulin-loaded NPs with that of native insulin, as well as between functionalized NPs and native albumin, were determined using the area overlap (AO) and spectral correlation coefficient (SCC) algorithms<sup>204</sup>. Both algorithms were used considering the area normalized second-derivative amide I spectra of native insulin or albumin. All the results are displayed in percentage, and the percentage is proportionally correlated with the similarity of spectra. The reference chosen was the insulin or albumin solutions because it is known that the stability of a solid protein formulation increases with the rise of similarity to the FTIR spectra in solution<sup>204</sup>.

## **5.2. Confirmation of the conjugation**

The <sup>1</sup>H NMR spectra was conducted to confirm the chemical structure of albumin and its conjugation to maleimide of NPs. The spectra were acquired at 80 °C by using a Bruker AVANCE III spectrometer (400 MHz). For these analyses, samples were freeze-dried and then dissolved in DMSO-d<sub>6</sub> (1/1 v/v) to result in 13 mg/mL. The available thiol content in HSA and HSA-conjugated NPs was also determined by Ellman's assay, as described elsewhere<sup>205</sup>.

## **6. Binding to human FcRn**

Microtiter wells were coated with a human IgG1 mutant variant (M252Y/S254T/T256E/H433K/N434F) (10 µg/mL) in 100 µL PBS pH 7.4 by incubation overnight at 4°C. The wells were blocked with 200 µL PBSTM for 1 h at RT and then washed three times with 200 µL PBST pH 5.5. Recombinant soluble human FcRn (10 µg/mL) in 100 µL PBSTM pH 5.5 was added per well and incubated for 1 h at RT, before repeating the washing step above. Dilution series of the albumin-conjugated NPs samples were prepared, starting from diluting the samples 20x in PBSTM pH 5.5, followed by 1:2 titrations. 100 µL each dilution was subsequently added in triplicates to wells and incubated for 1 h at RT. The wells were washed as before. AP-conjugated anti-albumin from goat was diluted 1:4000 in PBSTM and 100 µL was added per well and



incubated for 1 h at RT. After washing as above, visualization was done by adding 100  $\mu\text{L}$  of AP substrate (Sigma-Aldrich) diluted in diethanolamine buffer. The absorbance was measured at 405 nm after 1h using the Sunrise spectrophotometer (TECAN).

## 7. *In vitro* experiments

### 7.1. Transcytosis assay

MDCK-hFcRn were seeded at a density of  $1.2\text{-}1.4 \times 10^6$  cells per well onto Transwell<sup>®</sup> inserts ( $1.12 \text{ cm}^2$ ) with collagen coated polytetrafluoroethylene (PTFE) membranes of  $0.4 \mu\text{m}$  pore size (Corning Costar, Durham, NC, USA). Cells with a passage number from 9 to 13 were used for all experiments. Cells form a monolayer with a transepithelial electrical resistance (TEER) value of  $600\text{--}900 \Omega\cdot\text{cm}^2$  on the day after seeding. TEER was monitored using a MILLICELL-ERS-2 V-ohm meter (MILLIPORE). Prior to experiments, the monolayers were washed twice then starved for 1 h in Hank's Balanced Salt Solution (HBSS). For transport experiments at acidic pH, HBSS was buffered to pH 6.0 by addition of MES buffer (Sigma-Aldrich). Then,  $200 \mu\text{L}$  of 500 nM albumin variants or albumin-conjugated NPs were added to the apical chamber and  $500 \mu\text{L}$  of HBSS at the basolateral side. Samples were collected from the basolateral chambers at time 0 and 4 h post adding to the apical side. Results were expressed in relative transport and apparent permeability ( $P_{app}$ ), using the following formulas:

$$\text{Equation (4)} \quad \text{Relative Transport} = \frac{\text{Amount of sample}}{\text{Mean amount of control}}$$

$$\text{Equation (5)} \quad P_{app} = \frac{\Delta Q}{A \times C_0 \times \Delta t} * 100$$

where  $C_0$  is the initial concentration in the apical compartment (mg/mL),  $A$  is the surface area of the insert ( $\text{cm}^2$ ),  $\Delta t$  is the time during which the experiment occurred (seconds) and  $\Delta Q$  is the amount of compound detected in the basolateral side (mg).

### 7.2. Uptake and recycling assays

The human endothelial cell-based recycling assay (HERA) was performed as previously described <sup>71</sup>. Briefly,  $3.0 \times 10^5$  HMEC1 cells per mL (p.13-16) expressing HA-hFcRn-EGFP were seeded into 24-well plates per well (Costar) and cultured for 2 days in growth medium. The cells were washed twice and starved for 1 h in Hank's balanced salt solution (HBSS) (Life Technologies). Then, 500 nM of naked albumin and the

correspondent of NPs conjugated with 500 nM of albumin were diluted in 250  $\mu$ L HBSS (pH 7.4) and added to the cells followed by 4 h incubation. The medium was removed and the cells were washed four times with ice cold HBSS (pH 7.4), before fresh warm HBSS (pH 7.4) or growth medium without FCS and supplemented with MEM non-essential amino acids (ThermoFisher) was added. Samples were collected at 4 h or ON. The amounts of albumin variants were quantified using ELISA as described above. In parallel, total protein lysates were obtained using RIPA lysis buffer (ThermoFisher) completed with protease inhibitor tablets (Roche). The mixture was incubated with the cells on ice and a shaker for 10 min followed by centrifugation for 15 min at 10,000  $\times$  g to remove cellular debris. Quantification of the amounts of HSA variants present in the lysates was done by ELISA.

The relative recycling was calculated by following the equation:

$$\text{Equation (6)} \quad \text{Relative Recycling} = \frac{\text{Amount of sample}}{\text{Mean amount of control}}$$

The derived values for recycling and residual amount for each of the albumin variants were used to calculate the HERA score. The following formula was used:

$$\text{Equation (7)} \quad \text{Mean HERA score} = \frac{\frac{\text{Mean R sample}}{\text{Mean R control}}}{\frac{\text{Mean RA sample}}{\text{Mean RA control}}}$$

The parameter R (in ng) is recycling at a given time while RA (in ng) is the residual amount. The sample is the albumin variant naked or conjugated to NPs, while the control is the WT or WT-conjugated NPs, used to standardize results.

## 8. *Ex vivo* experiments

### 8.1. Tissue dissection and cultivation

All animal procedures were conducted in accordance with protocols approved by the MIT Committee on Animal Care in compliance with federal, state, local and institutional regulations, including the Animal Welfare Act and Public Health Service Policy. Small sections of intestinal tissue were isolated from freshly procured intact GI tracts from pigs from selected local slaughterhouses. A section of the tissue was cut out of the GI tract, dissected longitudinally and the outer muscle layer and serosa were removed. For standard transport experiments, duodenum tissue was used. The tissue was washed in a series of saline solutions under sterile conditions. The tissue was then either mounted on the porcine *ex vivo* platform or maintained in culture. For cultivation, the media advanced DMEM/F-12 (Life Technologies, 12634028) was used and supplemented with

10% fetal bovine serum (FBS) and 5% antibiotic–antimycotic solution (Thermo Fisher Scientific, 15240062). Tissue was cultured in this cell culture medium in a sealed polystyrene container that was then stored in an incubator kept at 37°C (no supplement gas was provided). A set of experiments was conducted with fixed time points as well as longer-term experiments monitoring the tissue daily, with analyses performed at varying time points.

## **8.2. Immunohistochemistry and hematoxylin and eosin staining**

Sections of the porcine GI tract were put into cassettes, fixed with 10% (v/w) formalin for 24 h at 4°C and then storage in 70% ethanol at 4°C. Paraffin sections (5-µm) on glass slides were dried at 70°C for 30 min, deparaffinized and heat induced epitope retrieve (HIER) at 97°C for 20 min in citrate buffer pH 6. These procedures were completely automated by using a ThermoFisher IHC Autostainer 360. Briefly, for immunohistochemistry (IHC), endogenous peroxidase blocking was done for 10 min followed by the protein block for 30 min. Primary antibody (1:100 anti-FCGRT, abcam, ab193148) was incubated for 1 h and the secondary antibody (1:2000 goat anti-rabbit IgG, abcam, ab205718) for 30 min. Both antibodies diluted with Tris Buffered Saline with Tween 20 (TBST) and incubated at room temperature. Finally, an incubation of 5 min with 3,3'-Diaminobenzidine (DAB) was done. For hematoxylin and eosin (H&E) staining, paraffin sections were counterstained with hematoxylin and eosin, according to standard protocols, using an automatic self-contained slide stainer (ThermoShandon Varistain Gemini). The stained cells were then mounted on a cover slide using ConsulMount (Thermo Fisher, 9990440). Representative images using Koehler illumination were obtained with an Olympus Microfire digital camera (M/N S97809) attached to an Olympus BX60 microscope.

## **8.3. RT-PCR analysis**

The FcRn expression of *ex vivo* cultured porcine-derived intestinal tissue was determined by reverse transcription polymerase chain reaction (RT–PCR) analysis and detected by agarose electrophoresis. Initially, the tissue was removed from fresh GI, frozen in liquid nitrogen and storage at -80°C. Then, total RNA from each tissue sample was extracted and purified with Quick-RNA plus (Zymo Research) followed by reverse transcription into complementary DNA using a High-Capacity cDNA reverse transcription kit (ThermoFisher Scientific). Target genes were amplified using the reported primers

(GAATTGGGCCCCGACAAT and CTGCTCACCCCTTCCACTCC)<sup>167</sup> and Platinum™ SuperFi™ DNA Polymerase (ThermoFisher Scientific, 12351010). The PCR program was optimized and consisted of an enzyme activation step (98°C, 10min), forty cycles of denaturation (98°C, 30 sec), annealing extension (62°C, 1 min) and extension (72°C, 45 sec), followed by an extension at 72°C for 10 min. The expression level of FcRn was measured with 1.5% agarose gel electrophoreses, with SYBR Safe DNA gel stain (Thermofisher, S33102) and 100 bp DNA Ladder (New England BioLab, N3231S) and detected using the Bio-Rad Image suite.

#### **8.4. Transport experiments using the *ex vivo* platform**

For assembly of the *ex vivo* platform, freshly isolated intestinal tissue from the duodenum was prepared according to the above-described tissue dissection procedure and mounted on the manufactured interface design with a generic 96-well plate (96-well plates, clear bottom, Corning), as previously described<sup>169</sup>. To the plate from the bottom, the basolateral side, it was added 100 µL of Hanks' Balanced Salt solution (HBSS) pH 7.4. The duodenum was identified as the region of the small intestine approximately 1 m that followed the stomach. Duodenum tissue was then carefully moved over the bottom magnetic plate with the apical side facing upwards. Afterwards, the top magnetic plate was mounted, and 90 µL of 189.83 µg/mL (500 nM) of albumin or albumin-conjugated to NPs was added, at the apical side. Samples were prepared at acidic pH, using HBSS buffered to pH 6.0 by addition of 2-(N-morpholino) ethanesulfonic acid (MES) buffer (Sigma Aldrich). After 4 h of incubation, samples were collected from the basolateral side, with a syringe, at the bottom magnetic plate and quantified by ELISA. All experiments, including sample incubation, were performed at room temperature. Results were expressed in relative transport and apparent permeability ( $P_{app}$ ), as described in section 7.1.

### **9. *In vivo* experiments**

#### **9.1. Induction of T1DM**

Male homozygous human FcRn Tg32 mice (The Jackson Laboratory, B6.Cg-Fcgrt<sup>tm1Dcr</sup>Tg(FCGRT)32Dcr/DcrJ)<sup>157</sup>, age 7-11 weeks and weighing between 16-25 g, were used to determine the glycemic decrease after oral administration of albumin decorated insulin-loaded NPs. Experiments were conducted in accordance with the provisions of FELASA and EU (Council Directive 86/609/EEC), after approval by local

Ethic Committee. The mice were maintained under standard laboratory conditions (12 h light/dark cycles, temperature of  $21 \pm 2^\circ\text{C}$  and relative humidity of 35% to 60%) and fed with standard pellets and water *ad libitum*. Diabetes induction was done in 12 h fasting mice by intraperitoneal injection of 150 mg/kg streptozotocin (STZ) (Sigma-Aldrich). STZ with a concentration of 20 mg/mL was freshly dissolved in citrate buffer 0.1 M at pH 4.5<sup>201, 206</sup>. STZ destroy pancreatic  $\beta$ -cells, possible leading to a massive insulin release and consequent fatal hypoglycemia. To prevent this, water supplemented with 10% sucrose was provided to animals over 48 h after STZ induction. After this period, it was substituted by tap water and glucose levels and body weight were measured daily.

## 9.2. Pharmacodynamics

One week after STZ induction, 12 h fasted animals with glucose levels above 250 mg/dL were randomly divided into 6 groups: (1) PBS, (2) 50 IU/kg of insulin-loaded NPs-NF, (3) 50 IU/kg of insulin-loaded NPs-WT, (4) 50 IU/kg of insulin-loaded NPs-KP, (5) 50 IU/kg of insulin in solution, all diluted in PBS and administered by oral gavage and (6) 2.5 IU/kg of s.c. insulin diluted in PBS. The dose was chosen based on previous studies<sup>201, 206</sup>. Blood glucose levels were measured by tail puncture at different time points (0, 0.5, 1, 2, 4, 6 and 8 h) after administration. Plasma glucose levels were plotted against time to evaluate the cumulative hypoglycemic effect (HD) over time, quantified by the area under the curve (AUC), determined using the trapezoidal method. Pharmacological availability (PA), quantified by the area above the curve (AAC), of insulin-loaded NPs and in solution were determined as the relative measure of the cumulative reduction in glucose blood levels. Both parameters were compared to 0% of decrease or 100% availability, respectively, of the control insulin administered subcutaneously at a dose of 2.5 IU/kg. PA and HD in serum glucose levels were calculated as follows<sup>201, 206</sup>:

$$\text{Equation (8)} \quad \text{PA (\%)} = \frac{\frac{\text{AAC test}}{\text{Dose test}}}{\frac{\text{AAC control}}{\text{Dose control}}} \times 100$$

$$\text{Equation (9)} \quad \text{HD (\%)} = \frac{\text{AUC (control 0-480min)} - \text{AUC (group 0-480min)}}{\text{AUC (control 0-480min)}} \times 100$$

Plasma glucose levels were determined using the Medisense Precision Xceed Kit (Abbot, range 20-500 mg/dL) and expressed as the percentage of the baseline plasma glucose level.

## **10. Statistical analysis**

Statistical analysis was performed using the GraphPad Prism Software vs. 6.0 (GraphPad Software Inc). Statistical significance of the difference between two groups was evaluated by the Student's *t*-test. Differences between groups were compared using one-way analysis of variance (ANOVA) Tukey's multiple comparisons test or Dunnett's multiple comparison test. Results are expressed as mean  $\pm$  standard deviation and geometric means with 95% confidence intervals.



## Chapter IV

---

# RESULTS AND DISCUSSION

---





This chapter was based in the following publications:

- **Azevedo C.**, Andersen J.T., Sarmiento B., Traverso G., The potential of porcine *ex vivo* platform for intestinal permeability screening of FcRn-targeted drugs, *European Journal of Pharmaceutics and Biopharmaceutics* 2021, 162: 99-104.

In this original paper, I was responsible for the design and execution of the experimental work, as well as the data analysis, their interpretation and discussion and conception and revision of the manuscript. The supervisors were responsible for reviewing and submit the manuscript. This paper was not previously included in other thesis and it is partially reproduced in this section. The integral version of the original paper was included at the end of the thesis, at **Appendix IV**.

- **Azevedo C**, Nilsen J, Grevys A, Nunes R, Andersen JT, Sarmiento B, Engineered albumin-functionalized nanoparticles for improved FcRn binding enhances oral delivery of insulin, *Journal of Controlled Release* 2020, 327: 161-173.

In this original paper, I was responsible for the design and execution of the experimental work, as well as data analysis, their interpretation and discussion and conception and revision of the manuscript. Jeannette Nilsen taught and helped me to produce engineered albumin variants. Algirdas Grevys taught me how to handle with MDCK-hFcRn and HMEC1-hFcRn cells and to perform permeability and recycling assays. Rute Nunes helped me with the *in vivo* assays. The supervisors were responsible for reviewing and submit the manuscript. This paper was not previously included in other thesis and it is partially reproduced in this section. The integral version of the original paper was included at the end of the thesis, at **Appendix IV**.



## 1. Rationale for the design of albumin decorated nanoparticles

To design biodegradable insulin-loaded PLGA-PEG NPs decorated with albumin for targeting of FcRn, a recombinant wild-type (WT) human albumin and an engineered variant with improved human FcRn binding properties were used. The engineered variant contains a single amino acid substitution in the C-terminal domain III (K573P, KP), which has been shown to extend serum half-life in human FcRn expressing mice and non-human primates<sup>207, 208</sup>. In addition, a human albumin variant engineered to abolish binding to the receptor (K500A/H464Q, KAHQ) was included<sup>207, 208</sup>. These mutations are also located in the C-terminal domain III of albumin, which harbors the principle binding site for FcRn (**Figure 10 A**).

To ensure directional attachment of the albumin variants to the NPs, an exposed and free cysteine residue within the N-terminal domain I of albumin (Cys34) (**Figure 10 A**), which is located distally from the core FcRn binding site, was explored<sup>207, 208</sup>. Maleimide (MAL) chemistry was used to promote formation of a thioether bond between Cys34 of albumin and the maleimide group of PLGA-PEG-MAL on the surface of the NP (**Figure 10 B**). As such, this approach secures directional and site-specific conjugation, as opposed to random conjugation.

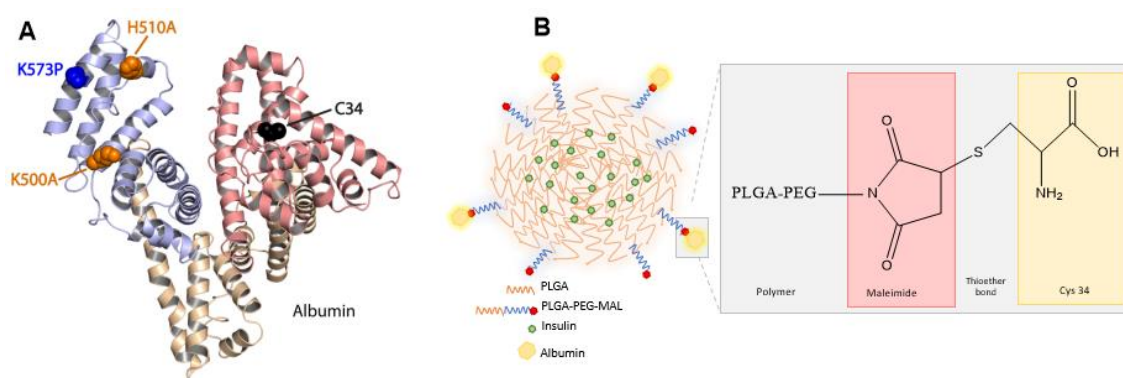


**Figure 10 | Representation of the rationale of this study: (A)** Illustration of the crystal structure of human albumin where targeted residues are shown as spheres: the free cys34 (black) in the N-terminal domain I and K500 (orange), H510 (orange) and K573 (blue) in the C-terminal domain III. The figure was made using Pymol and the crystal structure data of human albumin (PDB 1A06); **(B)** Schematic illustration of the designed NPs build up of PLGA and PLGA-PEG-MAL with encapsulated soluble recombinant insulin and recombinant human albumin on the NPs' surface. Albumin was conjugated to the NP using maleimide chemistry, which resulted in a thioether bond formed between the Cys34 of albumin and the maleimide group of PLGA-PEG-MAL.

## 2. Characterization of the produced nanoparticles

### 2.1. Physical-chemical properties of albumin-decorated PLGA-PEG NPs

To establish a factorial production strategy, a well-established solvent emulsification-evaporation method based on a w/o/w double emulsion technique was used<sup>200, 201</sup>. PLGA, PLGA-PEG-MAL and WT albumin were mixed in different ratios following determination of parameters such as size, polydispersity index (Pdl), zeta potential (ZP) and conjugation efficiency (CE). Based on previous works<sup>209, 210</sup>, and corroborated by JMP software analysis, we selected the ratio 1:0.05:0.005 of PLGA: PLGA-PEG-MAL: albumin, due to favorable CE, lowest Pdl, more negative ZP and size around 150 nm (not shown). In fact, the NPs composition is of utmost importance to surpass mucosal barriers. In the particular case of PEGylated nanoparticles, PLGA-PEG is responsible by forming a hydrophilic corona and PEG is regularly used to prevent NPs from aggregation and enzymatic degradation, contributing for their stability. PEG is the “gold standard” to promote mucus penetration, since interactions with mucins by its hydrophilic and net-neutrally charged character are reduced<sup>211, 212</sup>. It has been demonstrated that a minimal surface coverage of 5% PEG in NPs is crucial for a rapid mucus penetration<sup>213</sup>. These features were important to modulate and facilitate mucus penetration, epithelial absorption and transcytosis of NPs.

### 2.2. Albumin conjugation to NPs

To ensure that Cys34 was accessible for covalent conjugation to PLGA-PEG-MAL containing NPs, human albumin was reduced by tris(2-carboxyethyl)phosphine hydrochloride (TCEP). Albumin combined with NPs without maleimide (MAL) (**Figure 11 B**) or non-reduced albumin with PLGA-PEG-MAL NPs (**Figure 11 C**) were included as controls. To remove unconjugated albumin, NPs were washed three times with phosphate buffer (PB) using an Amicon<sup>®</sup> filter with 100 kDa cut off. Initially, the washing procedure was performed with free albumin, which confirmed that albumin passes through the filter (**Figure 11 A**). To indirectly determine the conjugation efficiency, the unbound albumin fraction was quantified using a two-way anti-human albumin ELISA. The results revealed that only 10% of the total albumin incubated with the NPs was detected in the wash solution, supporting that 90% was bound to the NPs (**Figure 11 B**). Interestingly, this was also the case in the absence of reactive MAL groups on the NPs or a reduced Cys34 of albumin, both necessary for the formation of a covalent thioether bond, which suggest that albumin also bound nonspecifically to the NPs. To reduce the

amount of nonspecifically bound albumin, the incubation time for conjugation was reduced to 1 h, however, no difference in absorption was detected (**Figure 11 B**). In this regard, it is well known that NPs absorb plasma proteins *in vivo*, including albumin, which form a protein corona<sup>214, 215</sup>. Although the presence of PEG is well documented to prevent formation of a protein corona<sup>211, 212</sup>, these results show that this did not necessarily prevent adsorption of albumin completely. The covalent bond guarantee that albumin is permanently attached to NPs, which may not happen with nonspecific bound albumin. Here, the focus is to make sure that NPs have albumin to bind FcRn and thus nonspecific bound albumin do not interfere with this.

Moreover, the size, Pdl and ZP were determined for the albumin-decorated NPs, which demonstrated similar values as that measured for the bare NPs (**Table 3**). No measurable difference in size and ZP between NPs with and without albumin may be explained by the fact that a maximum of only 0.5% of the NPs' surface was decorated with albumin.

**Table 3** | Physical-chemical properties of developed PLGA-NPs.

Loading	Albumin	Particle size ± SD (nm)	Pdl ± SD	ZP ± SD (mV)	CE ± SD (%)	AE ± SD (%)	DL ± SD (%)
Insulin	n.a.	160 ± 2	0.15 ± 0.01	-8.1 ± 0.1	n.a.		
	WT	155 ± 7	0.13 ± 0.03	-9.6 ± 0.3	89.7 ± 1.0	83.8 ± 6.5	10.9 ± 0.8
	KAHQ	157 ± 4	0.14 ± 0.02	-9.1 ± 0.2	93.5 ± 0.2		
	KP	154 ± 7	0.14 ± 0.02	-9.3 ± 0.2	98.9 ± 0.2		
Empty	n.a.	147 ± 0	0.12 ± 0.01	-8.5 ± 0.2	n.a.		
	WT	147 ± 1	0.15 ± 0.01	-10.6 ± 0.4	96.8 ± 0.1	n.a.	n.a
	KAHQ	145 ± 1	0.17 ± 0.01	-10.5 ± 0.2	98.3 ± 0.1		
	KP	144 ± 1	0.13 ± 0.01	-10.4 ± 0.3	99.3 ± 0.3		

Pdl: polydispersity index; ZP: zeta potential; CE: conjugation efficiency; AE: association efficiency; DL: drug loading; n.a.: non applicable; NF: non-functionalized; SD: standard deviation.

The presence of albumin was confirmed using elementary dispersive scanning (EDS), as sulfur was detected for free WT albumin and albumin-decorated NPs, but not for bare NPs (**Figure 11 D**). In addition, using non-invasive attenuated total reflection Fourier transform IR (ATR-FTIR) spectroscopy, the secondary structure elements of WT albumin conjugated to empty NPs were compared with that of free albumin in both qualitative (**Figure 11 E**) and quantitative manner (**Figure 11 F**). Previous measurements using

ATR-FTIR spectroscopy demonstrated that albumin consists of 55%  $\alpha$ -helix and 45% of turns, disordered and  $\beta$  structures <sup>216</sup>. The spectrum for albumin decorated NPs presents  $\beta$ -sheet at 1610-1640  $\text{cm}^{-1}$ ,  $\alpha$ -helix at 1650-1658  $\text{cm}^{-1}$  and  $\beta$ -turn at 1660-1700  $\text{cm}^{-1}$ , as described previously <sup>217</sup>. However, lyophilization or the conjugation method is likely the reason for the observed reduction in the content of  $\alpha$ -helix, a left shift and intensified  $\beta$ -sheet from 1630  $\text{cm}^{-1}$  to 1615  $\text{cm}^{-1}$  (**Figure 11 E**). Quantitatively, this resulted in 76% of area overlap (AO) and 91% of spectral correlation coefficient (SCC) (**Figure 11 F**).

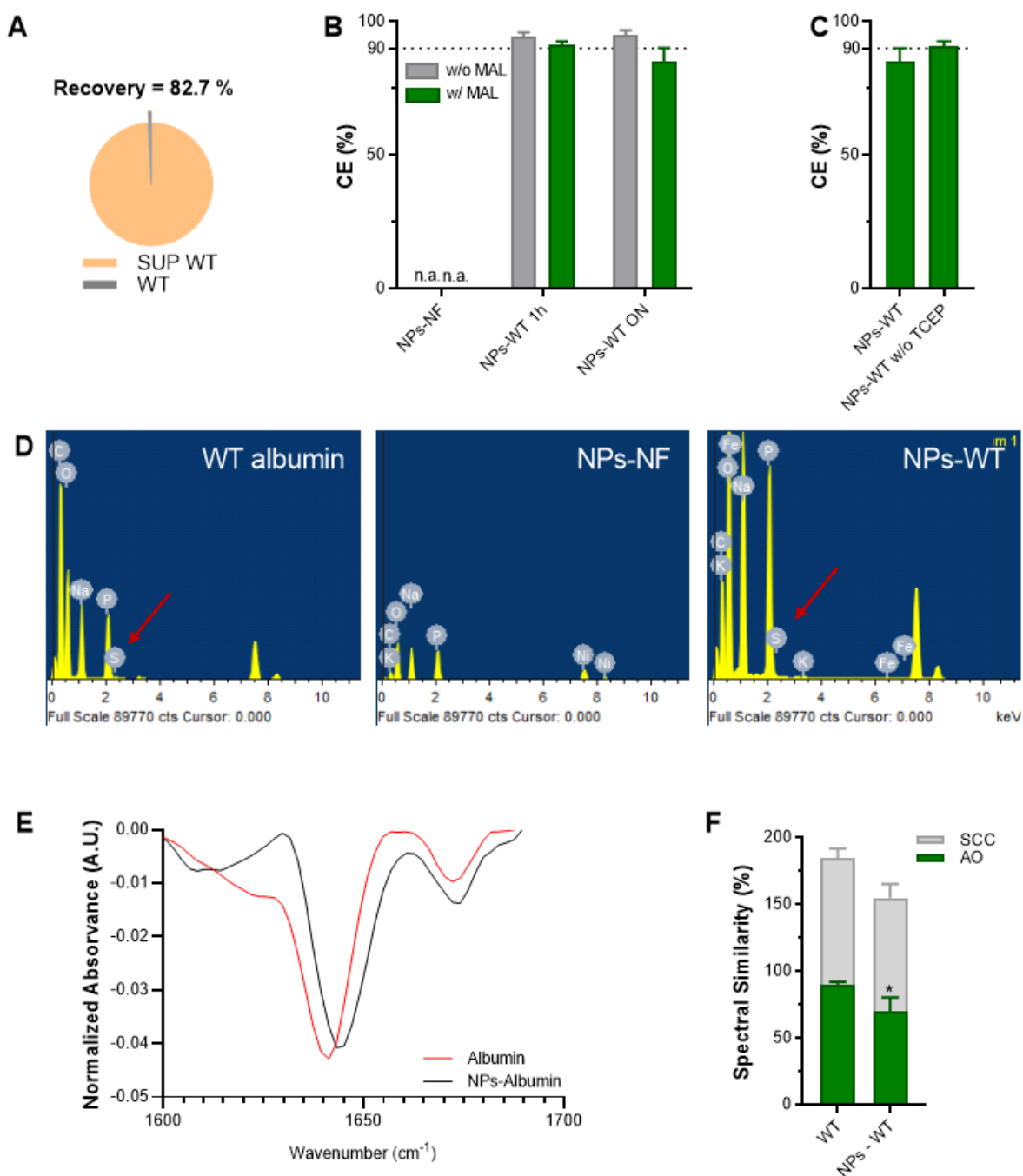


**Figure 11 | Site-specific conjugation of albumin to NPs:** (A) ELISA quantification of free WT albumin detected after the washing step with Amicon® filter of 100 KDa; (B) Conjugation efficiency (CE) with or without the presence of maleimide (MAL) after conjugation of 1 h or overnight (ON) with WT albumin; (C) Conjugation efficiency (CE) of NPs conjugated with reduced WT albumin (NP-WT) and non-reduced WT albumin (NP-WT without TCEP); (D) Elementary analysis of native albumin, non-functionalized empty NPs (NPs-NF) and WT albumin-conjugated empty NPs (NPs-WT); (E) Qualitative and (F) quantitative analysis showing the similarity of the FTIR spectra between WT albumin and NPs-WT, using the area overlap (AO) and spectral correlation coefficient (SCC) algorithms. Shown are the arithmetic means  $\pm$  SD. \*P < 0.05, comparing with native albumin by Student's t-test.

An attempt was also made, using nuclear magnetic resonance (NMR) as a complementary technique (**Appendix I**). Despite not being able to confirm the thioether binding between albumin and the polymeric NPs, it was possible to confirm the presence of albumin.

### 2.3. Functional encapsulation of insulin in NPs

NPs loaded with insulin were prepared with the optimal ratio of PLGA and PLGA-PEG-MAL using the double emulsion technique. The mean particle size of insulin-loaded NPs increased 1.2-fold compared with empty NPs (**Table 3**). Notably, this increase was measured for both albumin functionalized and bare NPs, suggesting that insulin adsorption was the reason. No significant difference in ZP was noticed between empty and insulin-encapsulated NPs (**Table 3**). Furthermore, the association efficiency (AE) and drug loading (DL) were indirectly evaluated using high performance liquid chromatography (HPLC), which revealed that insulin was successfully encapsulated with approximately 80% of AE and 10% of DL (**Table 3**).

Next, the insulin release profile was evaluated in fluids mimicking those found in the stomach and small intestine. The results showed that around 2.5% of the insulin was released in the presence of simulated gastric fluid (SGF) for 2 h, which was maintained under simulated intestinal fluid (SIF) for 4 h (**Figure 12 B**). Here, the SIF was used at pH 6, since it is the pH of duodenum, where it is supposed to occur the main absorption, due to the favorable pH for binding between albumin-conjugated NPs and FcRn<sup>218</sup>.

The initial burst release in the first 2 h followed by a sustained release is characteristic in PLGA NPs. At acidic pH, the carboxylic group is protonated, which contributes to PLGA destabilizing and disintegrating due to their pH-sensitivity. However, the insulin



released could also be some adsorbed on the NPs' surface. Either way, it is not significant, considering the 2.5% of the released profile. Besides, insulin has an isoelectric point of 5.3, meaning that above this value, insulin is negatively charged. As PLGA-PEG NPs have a negative charge, at pH lower than 5.3, there is a strong electrostatic attraction between insulin and NPs, decreasing the release rate. It is described that PLGA is strongly degraded at the alkaline and acidic conditions due to the ester hydrolysis caused by acid-base catalysis <sup>219</sup>. Thus, we expect that insulin can be sustainly released at neutral pH, as blood circulation. The results show that NPs are able to sustain low release of insulin under gastrointestinal conditions and thus, prevent the premature release of insulin, which suggest that it will be protected against degradation in the GIT. The slow release is a good omen to reduce the frequency of administrations and reduce the cost of therapy. In line with this, a previous report demonstrated that peptides were protected from low gastric pH value and enzymatic hydrolysis when encapsulated in anionic polymeric NPs <sup>220, 221</sup>. In fact, it was described the reduction in drug release from PLGA microparticles due to the surface crosslinking of PLGA microparticles <sup>222</sup>. Plus, albumin-based NPs can also protect the encapsulated drug from enzymatic degradation, due to the level of chemical crosslinking <sup>223</sup>. Albumin adsorbed to alginate/dextran sulfate (ADS)-NPs have shown a 30% of insulin released in SGF and a slow release following insulin passage to intestinal conditions. Plus, these authors claimed that chitosan and albumin coating augmented intestinal interactions between glyocalix and the NPs, which translated in enhanced intestinal permeability <sup>89</sup>. Moreover, to determine the morphology of insulin-loaded NPs decorated with WT albumin, transmission electron microscopy (TEM) was performed, which revealed a spherical shape and smooth surface (**Figure 12 A**). This feature is in line with expected morphology based on the encapsulation methodology used <sup>200, 201</sup>. The size of the NPs was calculated to be in the range of 150 nm, in agreement with the DLS analysis (**Table 3**).

To address if the double emulsion technique affected the integrity of insulin, ATR-FTIR spectroscopy was used to determine the secondary structure elements in both a qualitative (**Figure 12 C**) and a quantitative manner (**Figure 12 D**). When proteins are associated with PLGA NPs, the C=O stretching vibrations of the ester group of PLGA appear at 1750 cm<sup>-1</sup> and structural modifications can be determined following normalization of the area of the second derivative amide I spectra <sup>203</sup>. In addition, qualitatively assessment can be done by comparing the spectra or quantitatively by calculating the AO and SCC where AO indicates modifications in structure elements,

while SCC represents the changes in the band positions <sup>200</sup>. Notably, the normalized area of the second-derivative of insulin spectrum is characterized by  $\beta$ -sheets bands at 1610-1604,  $\alpha$ -helix at 1650-1658  $\text{cm}^{-1}$ , a random coil at 1640-1650  $\text{cm}^{-1}$  and a  $\beta$ -turn structure 1660-1700  $\text{cm}^{-1}$  <sup>224</sup>. The obtained spectra for insulin in solution and encapsulated in NPs were similar. However, some bands were modified, indicating alterations in secondary structure (**Figure 12 A**). This was evident from the spectrum on the insulin-loaded NPs with a shift of  $\alpha$ -helix from  $\sim 1645 \text{ cm}^{-1}$  to  $\sim 1655 \text{ cm}^{-1}$  and increased intensity, in addition to a left shift and higher intensity in  $\beta$ -turn, which is in agreement with previous work <sup>225</sup>. Moreover, the 68% of AO and 79% of SCC (**Figure 12 B**) support the visualization of the spectrum, which can be justified by the encapsulation method or by lyophilization of the samples, suggesting the necessity of adding lyoprotectants before performing ATR-FTIR spectroscopy. Notably, it has been shown that lyoprotectants stabilize the protein by protecting it from denaturation caused by pore formation on NPs <sup>201, 226</sup>. It has also been reported that lyophilization leads to protein aggregation with intermolecular  $\beta$ -sheets formation (caused by intermolecular hydrogen bonds) that increases protein–protein interactions while decreasing the  $\alpha$ -helix content and stability <sup>227</sup>. In addition, the helical structure of protein is destabilized during evaporation, since water molecules compete for the hydrogen bonds with amino and carboxyl groups of peptide bonds <sup>228</sup>. Regarding the tertiary structure, related to insulin bioactivity, we have previously analyzed it by fluorescence spectroscopy, after extracting insulin from NPs, confirming similarity with FTIR results after encapsulation <sup>201, 225</sup>.

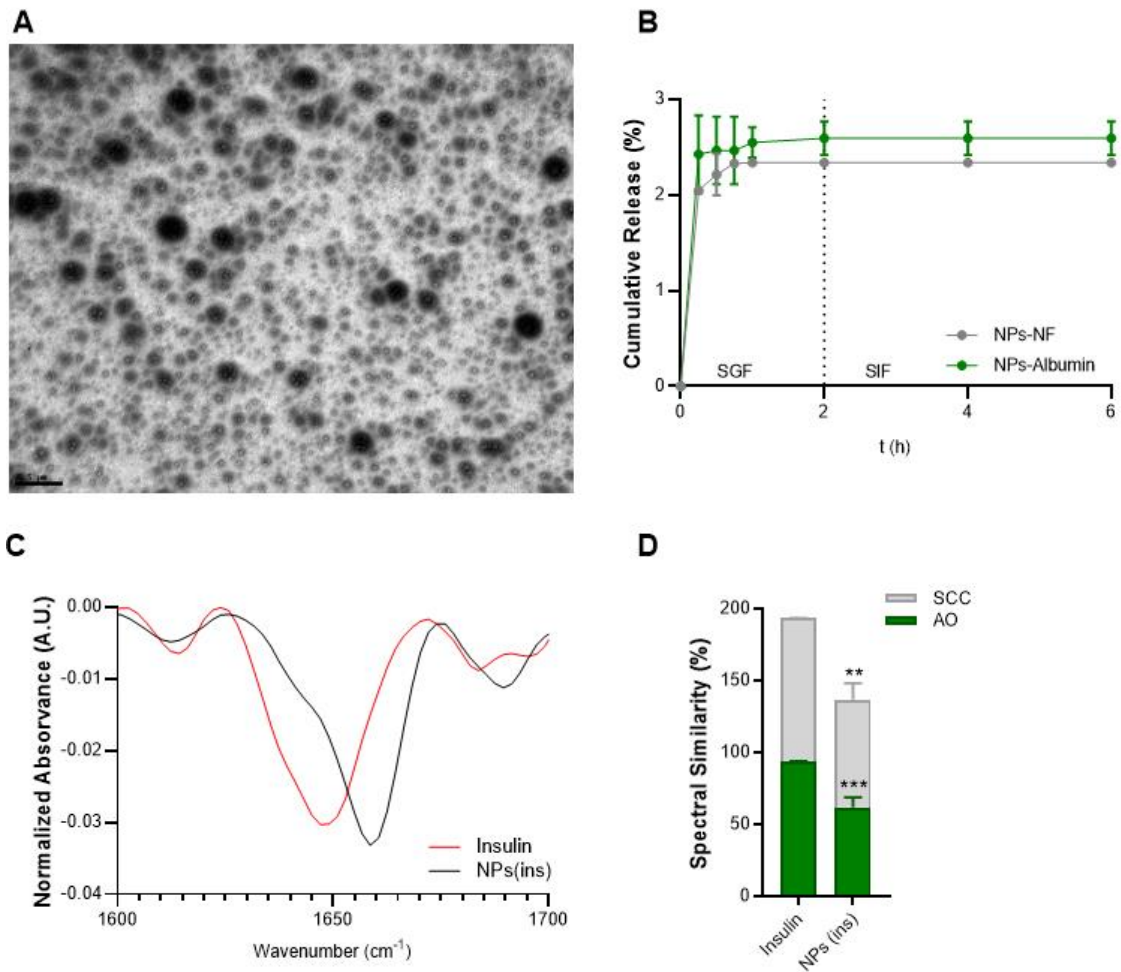


**Figure 12 | Insulin NPs characterization:** (A) Representative TEM microphotograph of WT albumin decorated PLGA-PEG NPs encapsulated with insulin, lyophilized 25000x. Scale bar: 500 nm. (B) Insulin release profile of functionalized and non-functionalized NPs under SGF (2 h) and SIF (from 2 h to 6 h). (C) The qualitative and (D) quantitative effect of NPs encapsulation on protein structure. Analysis showing area-normalized second-derivative amide I spectra of native insulin vs insulin-encapsulated NPs using the area overlap (AO) and spectral correlation coefficient (SCC) algorithms. Shown are the arithmetic means  $\pm$  SD. \*\* $P < 0.001$ , \*\*\* $P < 0.0001$  comparing with native insulin by Student's t-test.

#### 2.4. Albumin decorated NPs bind FcRn in a pH dependent manner

To address whether albumin is functional post conjugation to insulin-loaded NPs, binding to FcRn at pH 5.5 was tested by ELISA. Equal amounts of the NPs formulations or the free human albumin variants were added to wells where recombinant human FcRn had been captured on a coated engineered IgG molecule that strongly binds the receptor

(**Figure 13 A**), which were subsequently detected using a polyclonal anti-human albumin antibody. The three albumin variants bound as expected, as KAHQ did not bind while the KP variant bound more strongly than the WT (**Figure 13 B**). These results are in line with the reported in literature <sup>207, 208</sup>. Importantly, the same binding hierarchy was detected for the three NPs formulations (**Figure 13 C**). Specifically, KP decorated NPs bound more strongly to human FcRn than WT-decorated NPs, while the KAHQ-containing NPs ignored the receptor. As expected, no signal was detected for non-functionalized NPs. Thus, PLGA-PEG NPs decorated with albumin retain the ability to interact with human FcRn.

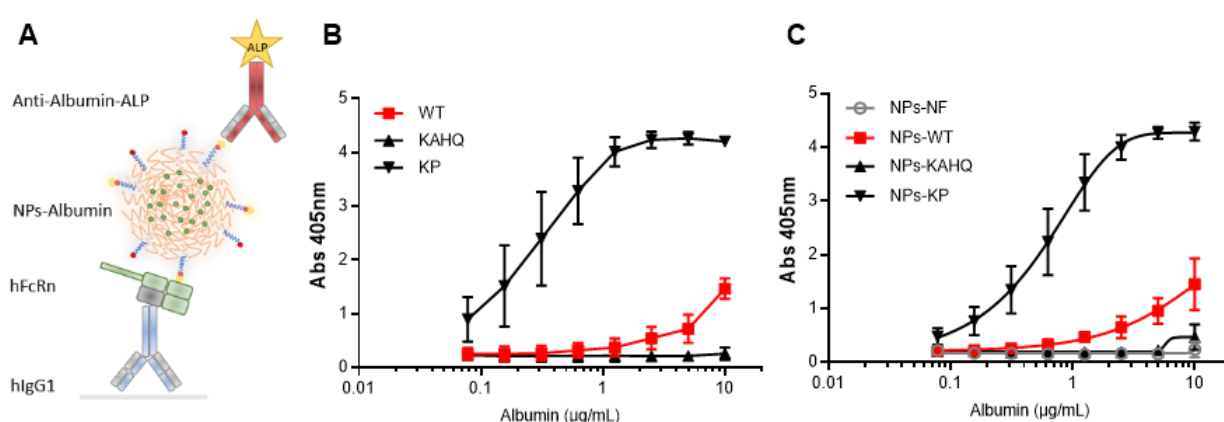


**Figure 13 | Albumin decorated NPs bind human FcRn. (A)** A schematic illustration of the ELISA set-up for measuring functional binding to human FcRn at pH 5.5. An engineered IgG1 antibody (MST/HN) was coated in wells, to which recombinant soluble human FcRn was captured, before adding naked albumin or albumin-decorated NPs. Bound albumin and albumin-decorated NPs were detected using ALP-conjugated polyclonal anti-human albumin antibodies. **(B)** Binding of naked human albumin variants (WT, KAHQ or KP) to human FcRn at pH 5.5. **(C)** Binding of NPs decorated with human albumin variants (WT, KAHQ or KP) to human FcRn at pH 5.5.

### 3. *In vitro* validation

#### 3.1. Produced NPs show enhanced *in vitro* transcytosis in epithelial cells

The finding that albumin decorated NPs bound human FcRn favorably, motivated me to investigate if this property could translate into enhanced transcellular transport. To test this, a Transwell<sup>®</sup> assay was run using a polarizing Madin-Darby Canine Kidney cell line over-expressing human FcRn (MDCK-hFcRn). To verify that the system could be adopted to study transcytosis of human albumin, equal amounts of the WT, KAHQ and

KP variants were added to the apical side of polarized MDCK-hFcRn cells followed by incubation for 4 h, before samples were collected at the basolateral side. To quantify the amounts of transported albumin, the collected samples were added to a two-way anti-albumin ELISA (**Figure 14 A**).

Next, transcytosis of albumin decorated NPs was compared using the same set-up, where equal amounts of the NPs were added to the apical side of the MDCK-hFcRn cells, followed by quantification of NPs transported to the basolateral compartment using ELISA. As expected, the non-functionalized NPs were negative, while KP-decorated NPs were 2-fold more efficiently transported than WT-decorated NPs. NPs decorated with KAHQ resulted in no or poor transport capacity (**Figure 14 B**). As expected, the percentage and apparent permeability of the free albumin were significantly higher compared to albumin-decorated NPs. Also, the engineered albumin KP demonstrated to be more efficiently transported, both free and conjugated to NPs (**Table 4**).

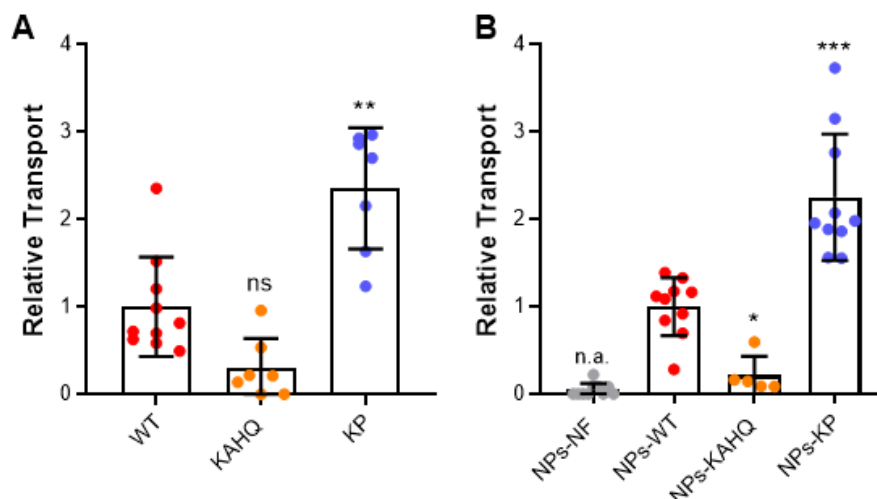


**Figure 14 | Albumin-decorated NPs showed enhanced transcytosis capacity.** Relative amounts of **(A)** naked albumin variants (WT, KAHQ and KP) and **(B)** albumin-decorated NPs detected in media collected at the basolateral side of polarized epithelial MDCK-hFcRn cells 4 h after adding the variants to the apical side in the Transwell® system (n=5-9). The amounts were quantified by two-way anti-albumin ELISA, where WT albumin or NPs decorated with WT albumin were set to 1, as a control. Shown are the arithmetic means ± SD. \*\*P<0.001, \*\*\*P<0.0001 comparing with WT or NPs-WT by one-way ANOVA Dunnett's multiple comparison test; n.a.: non applicable; ns: non-significant.

The endocytosis of NPs, mediated by FcRn rather than other receptors, was already reported by others <sup>105</sup>. Thus, decoration of NPs with human albumin that have the ability

to engage human FcRn resulted in enhanced apical to basolateral transport across polarized epithelial cells. Importantly, transport could be further enhanced by taking advantage of a human albumin variant (KP) engineered for improved pH dependent FcRn binding.

**Table 4 |** Permeability percentage and apparent permeability coefficient calculated after 4 h of incubation in MDCK-hFcRn cells.

<b>Formulation</b>	<b>Permeability <math>\pm</math> SD (%)</b>	<b><i>Papp</i> <math>\pm</math> SD (<math>\times 10^{-6}</math>)</b>
<b>WT</b>	11.4 $\pm$ 6.9	1.44 $\pm$ 0.87
<b>KAHQ</b>	5.2 $\pm$ 2.8	0.66 $\pm$ 0.36
<b>KP</b>	28.7 $\pm$ 4.9	3.63 $\pm$ 0.62
<b>NPs-NF</b>	0.31 $\pm$ 0.28	0.04 $\pm$ 0.04
<b>NPs-WT</b>	0.84 $\pm$ 0.36	0.11 $\pm$ 0.05
<b>NPs-KAHQ</b>	0.72 $\pm$ 0.57	0.09 $\pm$ 0.07
<b>NPs- KP</b>	1.86 $\pm$ 0.60	0.25 $\pm$ 0.08

Considering the NPs size (~150 nm) is relatively easy to obtain good cellular uptake outputs. As described in the literature, NPs are passively translocated across epithelium through enterocytes and specifically M cells, within Peyer's patches <sup>229</sup>. It was also reported that NPs are able to transverse the lymphatic system and by lymphatic drainage through thoracic duct reach the systemic circulation <sup>230</sup>. On top of this, receptor targeting is likely to increase the chance of absorption, since FcRn is expressed in epithelial cells <sup>231</sup>. Notably, a significant increase of insulin permeability by using chitosan-based NPs with adsorbed albumin has been shown in cell-based engineered intestinal models <sup>89</sup>.

A similar assay was performed with Caco-2 cells, using insulin-loaded NPs conjugated with WT albumin. This was done within the scope of a pioneer project, to investigate the potential of simulated hypergravity to be used in oral delivery of biopharmaceuticals (**Appendix II**).

### **3.2. Produced NPs show enhanced *in vitro* uptake and recycling in endothelial cells**

Next, it was investigated what happens to NPs after being transported through epithelial cells. There is no reported data related to FcRn-mediated recycling of NPs, thus, to clarify this, a recycling assay was performed. For this assay it was used a modified human

dermal microvascular endothelial (HMEC1) cell line, expressing human  $\beta 2$ -microglobulin and the hFcRn HC with an N-terminal HA-tag and EGFP-fused C-terminally (HMEC1-hFcRn) <sup>198</sup>. The amount of ligand, taken up after 4 h of incubation, was collected from the supernatant and cell lysis correspond to 0 h and uptake, respectively. After the ON incubation the same procedure was done to obtain the residual amount (RA) and the recycling, which were all quantified by ELISA (**Figure 15**).

As expected, the albumin variant with higher affinity to FcRn, KP, was more efficiently taken up and recycled, while KAHQ had the opposite effect, confirming the robustness of the model (**Figure 15 A and C left**). As already mentioned, the binding is pH-dependent, being favorable at acidic pH (5.0-6.5) and weaker at pH 7.4. Despite the low affinity at this pH the variants present the same behavior pattern. KP presented 2-fold and 3-fold increase of uptake and recycling, respectively, while KAHQ was similar to WT. Additionally, through the calculated amounts, it was verified that the addition of RA and recycling does not correspond to the uptake amount, which suggest some degradation (**Figure 15 B and D, left**). Notwithstanding, the obtained amounts are proportionally in line with reported data, taking into consideration the albumin concentration (1600 nM in the literature and 500 nM here) <sup>71</sup>.

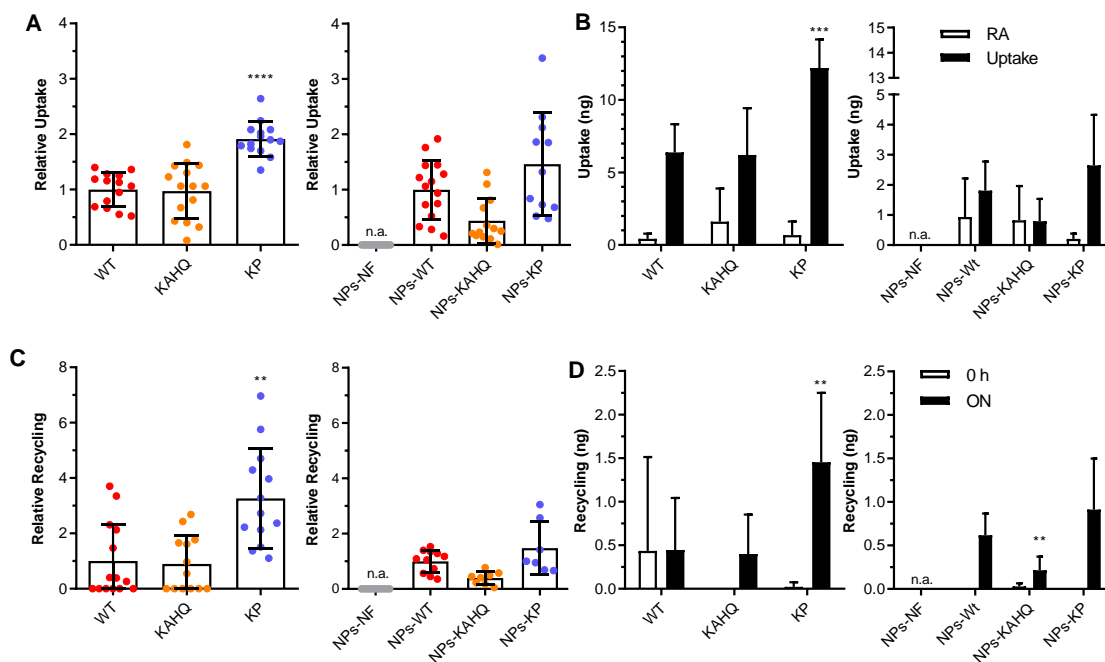


**Figure 15 | HERA screening of engineered albumin variants and albumin-conjugated NPs: (A) Relative uptake of naked albumin and albumin-conjugated NPs and (B) their correspondent amount quantified by ELISA. (C) Relative recycling of naked albumin and albumin-conjugated**

NPs and **(D)** their correspondent amount quantified by ELISA (n=9-11) in HMEC1-hFcRn cells. Shown are the arithmetic means  $\pm$  SD. \*P<0.05, \*\*P<0.005, \*\*\*P<0.0005, \*\*\*\* P< 0.0001 comparing with WT or NPs-WT, n.a.: non applicable, by one-way ANOVA Dunnett's multiple comparison test.

The results related to albumin-conjugated NPs were on the same trend as naked albumin, but with a ratio fold less pronounced between variants. Both uptake and recycling of NPs-KP were 1.5-fold higher and of NPs-KAHQ were 0.4-fold lower, compared to NPs-WT (**Figure 15 A and C, right**). This may be the behavior of endothelium cells to large sizes and possible avidity effect, which explains the reduced amount detected and some observed degradation (**Figure 15 B and D, right**).

Through these results, it was possible to calculate the mean HERA score. From **Figure 16** it was observed that KP variant had a mean HERA score of 2-fold higher compared to WT, which as mentioned has a half-life of 3 weeks. These results are line with previous reported data<sup>71</sup>. In addition, this score reflects the extended half-life of the KP variant in hFcRn transgenic mice and cynomolgus monkeys<sup>51</sup>. Interestingly, when KP variant was conjugated to NPs the score increased 6.7-fold, enhancing even more the half-life of the drug. On the other hand, KAHQ revealed to have a HERA score of 0.2 and NPs-KAHQ of 0.4. To the best of my knowledge, the recycling profiles of KAHQ and NPs, were for the first time reported here, using HERA.

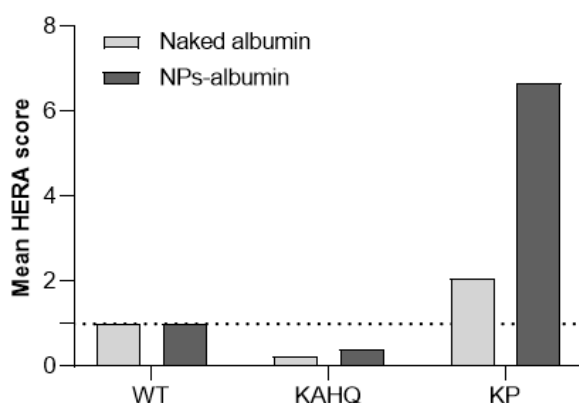


**Figure 16 | Mean HERA score for naked albumin variants or conjugated to NPs.** These were calculated from the data shown in Figure 4.2 B and D.

The endocytosis of large particles was already described in endothelial cells. Coated 100 nm polymeric nanoparticles with bovine serum albumin (BSA) showed to have an



improved NPs' internalization, via caveolae, in bovine lung microvessel endothelial cells (BLMVEC), due to the presence of albumin <sup>232</sup>. Furthermore, by using human umbilical vein endothelial cells (HUVECs), it was shown that microparticles can also be internalized. This process occurs in a few hours, involving anionic phospholipids, lactadherin and avb3 integrin <sup>233</sup>. Inclusively, it is reported that larger-sized hydrogel nanodiscs and nanorods are more efficiently internalized than their smallest counterparts <sup>234</sup>. This synergic effect can possibly explain the favorable HERA score of the produced NPs.

#### **4. Ex vivo validation**

Due to the physiological and anatomical similarities to human, the porcine has gaining importance and attention from investigators. In fact, the pig is considered a suitable model to perform PK studies of HSA, since PSA provides minimal competition for binding to FcRn <sup>160</sup>. Plus, it has been used as a potential model for transepithelial delivery of FcRn-targeted proteins <sup>166</sup>.

##### **4.1. The tissue integrity is maintained in the porcine ex vivo model**

Before studying the FcRn expression and FcRn-targeted ligands transcytosis, it was crucial to understand how the porcine GI tract is organized. Initially, it was evaluated the integrity and morphology of the GI tract from the porcine *ex vivo* model, using H&E staining. According to **Figure 17 A**, it was possible to see morphologic differences throughout intestinal sections. The porcine duodenum has a light-staining with a branched and tubular structure with Brunner's glands in its sub mucosa, which has a protective role against the acidic chyme. Ileum is highlighted by the presence of lymphatic aggregates, as Peyer's patches, with phagocytic M-cells in the sub mucosa and lamina propria regions. On the other hand, jejunum is marked by the lack of Brunner's glands and Peyer's patches. In general, the absence of villi and Paneth cells and reduction of lymph nodes aggregates distinguishes the large from the small intestine. However, crypts and goblet cells are more abundant in the colon. By contrast, esophagus and stomach have a different composition and cell types since they are not responsible for the absorption function. For instance, the mucosa of the stomach is in a columnar format and is covered with a protective layer of alkaline mucus. In its epithelium it is possible to find gastric glands, mucus neck cells to produce mucus, parietal cells to secrete acid, and chief cells to release pepsinogen. These evidences are in line with

what is described for humans <sup>235</sup>.

As shown, most of the GI tract presents mucosa, sub mucosa, muscularis externa and serosa, which is particularly exemplified by a duodenum section (**Figure 17 B**). The human intestine is described by having the same pattern and characteristics. The mucosa has an important role in absorption since it is 90% composed by enterocytes and microvilli (capillary branches as a door for the hepatic portal vein). Mucosa is divided in epithelium, lamina propria (connective tissue) and muscularis mucosae (smooth muscle). It is in epithelium where cells can proliferate, differentiate in absorptive enterocytes or secretory cells (goblet cells, enteroendocrine cells and Paneth cells) and suffer apoptosis, by the presence of proliferative crypts. Particularly, enterocytes, as polarized cells, are the ones responsible for absorbing nutrients and transport them from the apical to the basolateral side. On the other hand, M cells control the transepithelial transport of macromolecules or particles and microorganisms. Sub mucosa is characterized by being a connective tissue with lymphatic and blood vessels, ganglion and nerve cells. Finally, muscularis externa (smooth muscles) and a serosa (mesothelium) layer (**Figure 17 C**) <sup>236</sup>. However, it is reported that porcine and human intestine present some anatomical differences, as the length of small intestine and shape of the colon, as described elsewhere <sup>237</sup>.

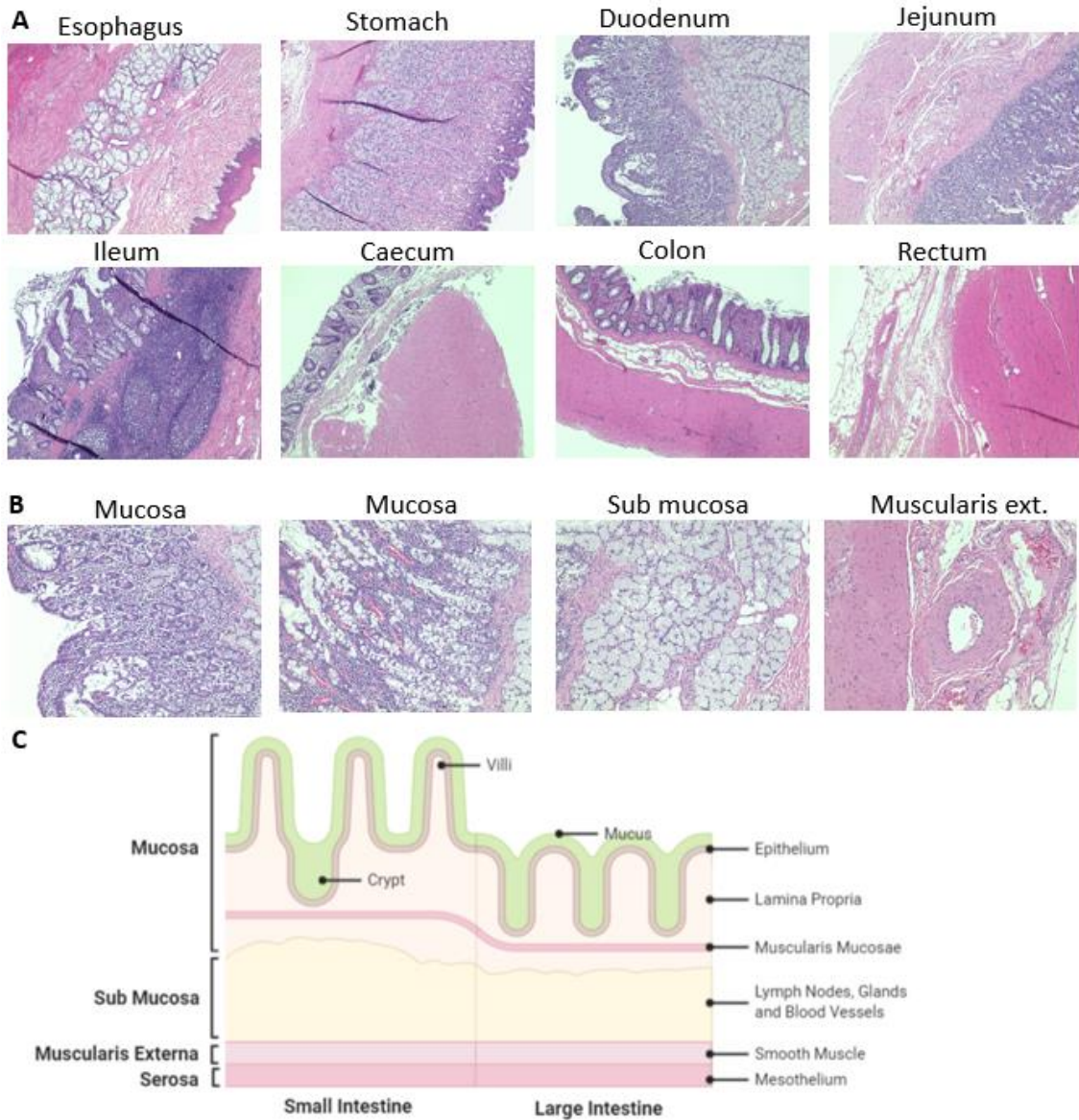


**Figure 17 | H&E stained sections of porcine GI tract. (A)** Morphologic differences between esophagus, stomach, duodenum, jejunum, ileum, caecum, colon and rectum (10X); **(B)** Identification of duodenum sections, as mucosa, sub mucosa, muscularis externa and serosa (20X); **(C)** Schematic representation of intestinal morphology and sections division (mucosa, sub mucosa and muscularis externa).

#### 4.2. FcRn is expressed across the gastrointestinal tract

After confirming the viability and morphology of the GI tract from the porcine *ex vivo* model, the FcRn expression was confirmed by RT-PCR, after collecting the tissue, extracting RNA and amplifying cDNA (**Figure 18**). As expected, the porcine receptor is broadly expressed throughout the GI tract, as previously confirmed<sup>166, 167</sup>.

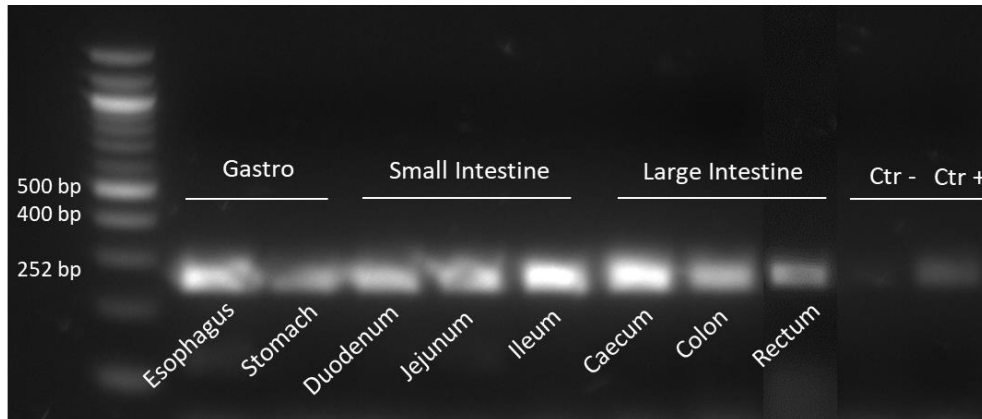


**Figure 18 | Confirmation of FcRn gene expression across GI tract.** Before performing the RT-PCR, RNA was extracted from fresh tissue of different sections of GI tract and cDNA was amplified. Results shown were performed with one tissue batch. Water and porcine blood were included as negative and positive controls, respectively. Results shown were performed with one tissue batch.

Subsequent this analysis, only stomach, duodenum and jejunum sections were considered for further studies, due to their acidic pH, having duodenum the most favorable pH for FcRn binding<sup>218, 238</sup>. As described, FcRn binds to its ligands in a pH-dependent manner. This is an important feature, since the receptor helps ligands to escape from lysosomes degradation and be successfully transcytosed to the basolateral side<sup>208, 239</sup>. Results from IHC staining showed that FcRn is expressed in stomach, duodenum and jejunum, which is consistent with the PCR results, being more intense in epithelial cells of villi, especially in duodenum (**Figure 19 A**). This evidence makes sense, since, intestinal epithelium is highly composed by enterocytes responsible for the absorption, suggesting the involvement of FcRn in the import and export of albumin and IgG at mucosal surfaces<sup>236</sup>. These results are then in line with published data<sup>166</sup>.

There are no available antibodies for porcine FcRn (pFcRn), thus antibodies for hFcRn were used, due to their similar genomic structure. According to literature, the pFcRn DNA sequence has 80% sequence identity to the corresponding human version. Both translated proteins have the single N-linked glycosylation site (NVS<sub>V</sub>) in the  $\alpha$  domain, as well as both di-leucine- and tryptophan-based endocytosis signals present in the cytoplasmic tail. At the moment, the pFcRn structure seems to not be concordant among authors, which might be explained by authors different polymorphisms<sup>166</sup>. However, key amino acid residues involved in binding to IgG and albumin are conserved. According to literature, pFcRn is also expressed in the heart, lung, kidney, intestine, muscle, brain,

endothelial cells and monocytes, and highly expressed in liver, spleen, thymus, lymphoid, being also maintained in the adult stage, similar to humans <sup>166, 167</sup>.

Studying the durability of FcRn expression of tissue in culture, it was observed that it is maintained for up, at least, 7 days, especially in duodenum (**Figure 19 B**). These results are in line with previous characterization of the *ex vivo* platform, when evaluating other receptors' expression. Authors verified that it is possible to guarantee the complex GI architecture, mucus layer and the expression of several drug transporter for 7 days, when the tissue is intact in culture <sup>169</sup>.

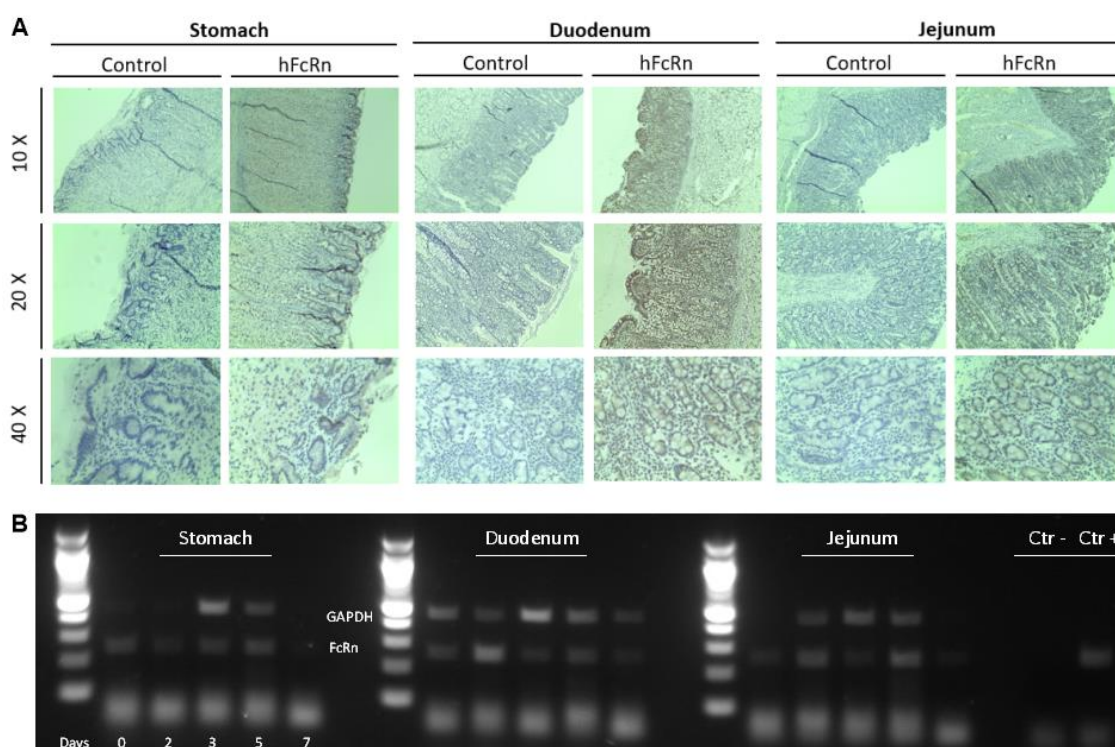


**Figure 19 | Evaluation of FcRn expression over time, of stomach, duodenum and jejunum.** (A) Evaluation of FcRn expression by IHC of fresh porcine tissue. Control samples were only treated with the secondary antibody, to check non-specific binding. **Brown** indicates the antibody signal, while **blue** is the counterstain. (B) FcRn expression after 7 days of porcine *ex vivo* incubation or freshly isolated at day zero. Before the RT-PCR, RNA was extracted from fresh tissue and cDNA was amplified. Water and porcine blood were included as negative and positive controls, respectively. Results shown were performed with one tissue batch.

### 4.3. Engineered albumin variant shows enhanced transcytosis in the porcine *ex vivo* platform

Next, the evaluation of the *ex vivo* platform, using porcine duodenum (**Figure 20 A**), for the screening of the intestinal permeability of FcRn-targeted drugs was done. For this

analysis, a porcine *ex vivo* platform, previously developed <sup>169</sup>, was used (**Figure 20 B**). Here, it was also included PSA as a control. It is reported that HSA has 2.9-fold more affinity to pFcRn than PSA, which not causes competition <sup>160</sup>.

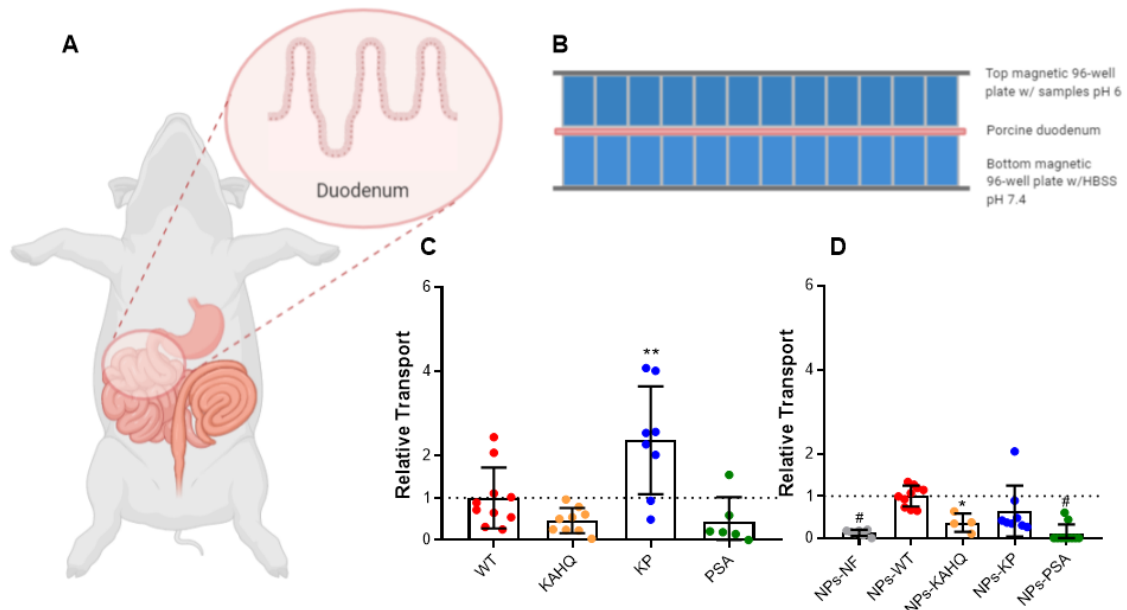


**Figure 20 | Engineered albumin showed enhanced transcytosis capacity in the porcine *ex vivo* platform.** (A) Representation showing porcine duodenum, as the tissue used to study the intestinal permeability, using the porcine *ex vivo* platform. (B) Schematic illustration of the cross-section of the interface design in a 96-well plate format. 100  $\mu$ L of HBSS pH 7.4 was added to the plate from the bottom, mimicking the basolateral side. Next, the tissue was put on the plate, facing the apical side upwards. Finally, the magnetic plate from the top was added, pressing the tissue to avoid leakage, and samples prepared in HBSS pH 6 were added. (C) Relative amounts of naked albumin variants (WT, KAHQ, KP and PSA) detected in media collected at the basolateral side, 4 h after adding the variants to the apical side in the porcine *ex vivo* platform (n=6-10); (D) Relative amounts of NPs functionalized with albumin variants (n=4-10). The amounts were quantified by two-way anti-albumin ELISA, where WT albumin or NPs-WT were set to 1, as a control. These results were obtained from 3 different pigs. Shown are the arithmetic means  $\pm$  SD. \*P < 0.05, \*\*P < 0.005, and #P < 0.0001, comparing with WT by one-way ANOVA Dunnett's multiple comparison test.

From the results from **Figure 20 C**, it was possible to verify that KP human albumin variant maintained its pattern, of being more efficiently transported compared to WT, which is translated in a ratio of 2.4-fold, being in line with *in vitro* data obtained from MDCK-hFcRn cells. Besides, these results confirmed previous reported data related with pFcRn binding affinity, which showed that  $k_d$  ( $10^{-3}$ /s) values for HSA-WT, HSA-KP

and PSA around 15, 2.6 and 53, respectively <sup>160</sup>.  $k_d$  is the constant of dissociation, meaning that higher the affinity, lower the dissociation. The albumin quantification was made by ELISA, using human albumin antibodies, which might not be the best way to quantify PSA. However, it is known that PSA is 75.1% similar to HSA <sup>160</sup>. Despite this, the results are in line with published data, since PSA was less transported by pFcRn, comparing with WT (**Table 5**). Through the  $P_{app}$  obtained values of free albumin variants, it was observed that these were 0.56-fold less transported in this *ex vivo* platform, when correlating with results previously obtained using MDCK-hFcRn *in vitro* model. After this evaluation, albumin-functionalized NPs were also tested to further study the potential of the porcine *ex vivo* platform (**Figure 20 D**). The typical pattern behavior between variants was observed, except for NPs-KP. Also, it was not expected that NPs, as larger particles, presented higher  $P_{app}$  values, compared to free albumin. Additionally, NPs-KAHQ and NPs-PSA were less transported as expected. Nevertheless, non-functionalized NPs presented some signal, which was not supposed, since they did not have HSA attached on the NPs' surface. This might be due to the presence of some interferents, possibly from the biologic fluids, contained in the tissue.

**Table 5 |** Apparent permeability coefficient calculated after 4 h of incubation in *ex vivo* porcine, based on the albumin amount quantified by ELISA. These results were obtained from 3 different pigs.

Formulation	$P_{app}$ (cm/s) $\pm$ SD ( $\times 10^{-6}$ )	Formulation	$P_{app}$ (cm/s) $\pm$ SD ( $\times 10^{-6}$ )
WT	0.83 $\pm$ 0.58	NPs-NF	0.66 $\pm$ 0.37
KAHQ	0.34 $\pm$ 0.22	NPs-WT	5.34 $\pm$ 1.44
KP	1.86 $\pm$ 1.12	NPs-KAHQ	2.66 $\pm$ 1.49
PSA	0.44 $\pm$ 0.53	NPs-KP	3.09 $\pm$ 2.95
		NPs-PSA	0.53 $\pm$ 1.14

Lately, porcine tissues have been highly used in preclinical drugs validation. Example of that is the developed InTESTine™ system, containing porcine intestine tissue, which demonstrated to have more comparable  $P_{app}$  and transepithelial electrical resistance (TEER) values, to humans, than Caco-2 and Caco-2/HT29-MTX *in vitro* models <sup>240</sup>. Also, Rani Therapeutics evaluated the PK/PD of recombinant human insulin delivered by an ingestible device, into the porcine jejunum <sup>168</sup>.

## 5. *In vivo* validation

As the *in vitro* and *ex vivo* data strongly suggested that NPs decorated site-specifically with human albumin could lead to enhanced delivery across barriers, this concept was subsequently addressed *in vivo* using the designed insulin encapsulated NPs. A state-of-the-art mouse model that is transgenic for hFcRn and knockout for mFcRn (FcRn<sup>-/-</sup> hFcRn Tg32 mice)<sup>157</sup> was chosen for this study, as conventional mice are unreliable models for evaluation of human albumin-based therapeutics due to large cross-species binding differences<sup>52, 60, 241</sup>. Specifically, HSA binds poorly to mFcRn, and as such will be competed out for binding to the murine receptor in the presence of large amounts of endogenous MSA<sup>52, 60</sup>. The hFcRn transgenic mice indeed have MSA but in this case mouse and human albumin bind equally well to the receptor<sup>52, 60</sup>.

To study the effect of albumin decorated NPs encapsulated with insulin, the transgenic mice were treated with streptozotocin (STZ) to induce diabetes. One week later, the mice were fasted for 12 h, before being divided into six groups based on their blood glucose level. After administering different formulations, pharmacodynamic parameters were evaluated over 8 h (**Figure 21 A**). This time frame was not extended, since it is not recommended starving animals for long periods. Besides, if the animal is in a starvation state it is hard to objectively discuss the results, since they could be due to the drug effect or due to organism failure. In fact, it was observed some deaths during the experiments, which were not considered for data analysis. Knowing that mice consume primarily at night, overnight fasting leads to a catabolic state, reducing 15% of body mass in lean mice<sup>242</sup>. Overnight fasting deletes liver glycogen stores, which contributes for reducing the variability in baseline blood glucose. Besides, contrary to what happens in humans, a prolonged fast in mice enhances the insulin-stimulated glucose utilization<sup>242</sup>. In this sense, it is recommended that mice used for metabolic studies, should be fasted for 14–18 h (overnight fast)<sup>243</sup>.



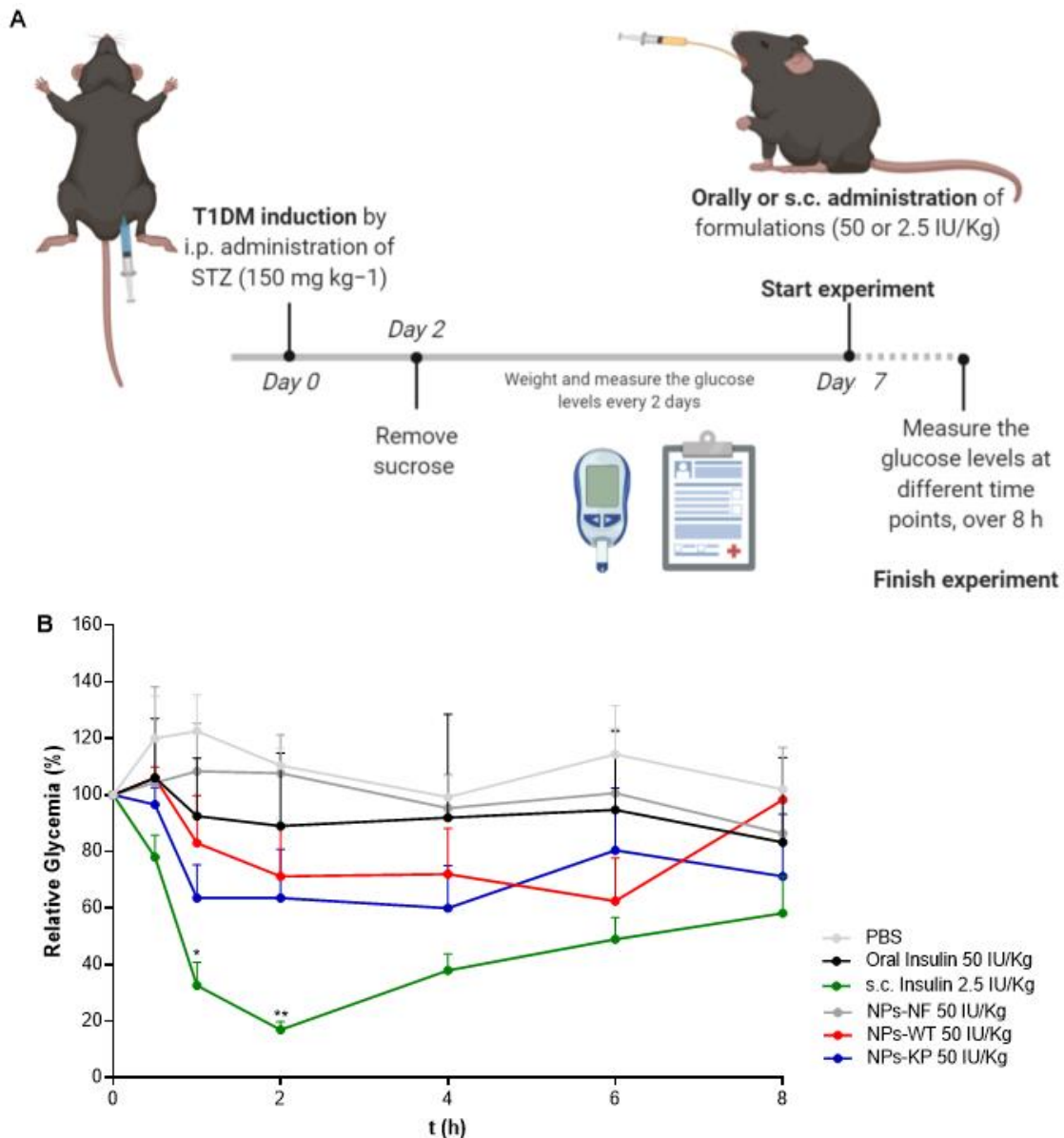


**Figure 21 | Glycemia in human FcRn expressing mice induced with diabetes. (A)** T1DM-induced Tg32 mice were i.p. administered with STZ ( $150 \text{ mg kg}^{-1}$ ) to induce diabetes. Body weight and glucose levels were followed up every 2 days, during 7 days. **(B)** At day 7, formulations were administered and plasma glucose levels were analyzed at different time points, during 8 h: PBS, oral insulin 50 IU/Kg, s.c. insulin 2.5 IU/Kg, oral insulin 50 IU/Kg loaded and non-functionalized NPs (NP-NF) and oral insulin 50 IU/Kg loaded and albumin-functionalized WT albumin and KP NPs ( $n = 3-6/$  group). Shown are the arithmetic means  $\pm$  SEM. \* $P < 0.05$ , \*\*  $P < 0.001$  comparing with oral insulin by one-way ANOVA.

The first group received free insulin via s.c. injection, which resulted in a rapid decrease of glucose within 2 h followed by an increase over the next 6 h (**Figure 21 B**). This

phenotype is in accordance with previous reports using rats <sup>6, 206</sup>. In contrast, mice treated orally with free insulin, or with bare NPs, showed no significant decrease in blood glucose (**Figure 21 B**), being most probably degraded along the way. Furthermore, the effect of oral administration of equal amounts of bare NPs, WT- or KP-decorated NPs was evaluated, which revealed that the albumin-decorated NPs had a more pronounced effect compared with free insulin and the bare NPs. In particular, the KP-decorated NPs showed the fastest glycemic decrease and maintained a decrease of around 40% between 1 h and 4 h after administration (**Table 6**). However, in this preliminary set-up, NPs containing WT and KP were not statistically different. On the other hand, it was previously reported a significant *in vivo* difference between the two naked variants <sup>207</sup>. As mentioned before, it was observed some animal deaths during the experiments, which were not considered for data analysis. In this sense, the reduced number of animals might be the reason for the non-statistical significance in *in vivo* results, which did not happen in *in vitro*.

Notably, for the control group receiving PBS, an increase in glucose level was observed within the first hour, which may be explained by stress and an adrenalin reaction to the administration. Most probably, all mice experienced this, while the effect was contradicted by the administered insulin, which should be taken into consideration when comparing pharmacological parameters. Nevertheless, functionalized NPs were more efficient in delivering encapsulated insulin to the circulation, as the orally delivered free insulin and non-functionalized NPs did not induce glycemic response.

**Table 6 |** Pharmacodynamic parameters of formulations at different time points after administration.

t (h)	Formulation	Glycemia (%)	AUC ± SD	PA ± SD (%)	HD ± SD (%)
0.5	PBS	120 ± 27	110.0 ± 13.4	7.7 ± 1.7	-23.6 ± 15.0
	Oral insulin	106 ± 32	103.0 ± 15.9	6.8 ± 2.0	-15.7 ± 17.8
	s.c insulin	78 ± 15	88.9 ± 7.5	100.0 ± 0.0	0.0 ± 0.0
	NP-NF	104 ± 41	102.2 ± 20.3	6.7 ± 2.6	-14.91 ± 22.8
	NP-WT	106 ± 6	103.0 ± 3.0	6.8 ± 0.4	-15.8 ± 3.4
	NP-KP	97 ± 9	98.4 ± 4.7	6.2 ± 0.6	-10.5 ± 5.3
1	PBS	123 ± 22	170.7 ± 25.6	21.2 ± 7.7	-46.3 ± 22.0
	Oral insulin	93 ± 32	152.6 ± 31.7	15.8 ± 9.5	-30.8 ± 27.1
	s.c insulin	33 ± 16	116.6 ± 15.1	100.0 ± 0.0	0.0 ± 0.0
	NP-NF	108 ± 22	155.4 ± 36.0	16.7 ± 10.8	-33.2 ± 30.8
	NP-WT	83 ± 25	150.2 ± 8.6	15.1 ± 2.6	-28.8 ± 7.3
	NP-KP	63 ± 22	138.4 ± 6.5	11.5 ± 2.0	-18.6 ± 5.6
2	PBS	111 ± 10	287.3 ± 41.8	-7.5 ± 3.6	-103.0 ± 29.51

	Oral insulin	89 ± 44	243.45 ± 69.6	-3.7 ± 5.95	-72.1 ± 49.2
	s.c insulin	17 ± 5	141.5 ± 23.9	100.0 ± 0.0	0.0 ± 0.0
	NP-NF	108 ± 18	263.5 ± 55.7	-5.43 ± 4.76	-86.2 ± 39.4
	NP-WT	71 ± 26	227.3 ± 33.8	-2.3 ± 2.9	-60.6 ± 23.9
	NP-KP	63 ± 33	201.8 ± 28.2	-0.2 ± 2.4	-42.6 ± 20.0
4	PBS	99 ± 12	497.8 ± 61.3	-2.4 ± 1.5	-153.2 ± 31.2
	Oral insulin	92 ± 61	424.4 ± 174.9	-0.6 ± 4.3	-116.1 ± 89.1
	s.c insulin	38 ± 10	196.4 ± 31.4	100.0 ± 0.0	0.0 ± 0.0
	NP-NF	95 ± 16	466.7 ± 88.8	-1.64 ± 2.2	-137.7 ± 45.2
	NP-WT	72 ± 24	370.5 ± 83.5	0.7 ± 2.1	-88.7 ± 42.5
	NP-KP	60 ± 25	325.2 ± 85.7	1.8 ± 2.1	-65.6 ± 43.6
6	PBS	115 ± 26	711.2 ± 91.2	-1.8 ± 1.4	-151.1 ± 32.2
	Oral insulin	95 ± 39	611.2 ± 275.2	-0.8 ± 4.3	-115.8 ± 97.2
	s.c insulin	49 ± 15	283.19 ± 51.6	100.0 ± 0.0	0.0 ± 0.0
	NP-NF	101 ± 29	662.6 ± 133.1	-1.0 ± 2.1	-134.0 ± 47.0
	NP-WT	63 ± 23	505.1 ± 130.5	1.5 ± 2.1	-78.4 ± 46.1
	NP-KP	81 ± 34	465.7 ± 144.6	2.1 ± 2.3	-64 ± 51.1
8	PBS	102 ± 18	927.8 ± 124.0	-1.6 ± 1.5	-137.8 ± 31.8
	Oral insulin	83 ± 46	789.2 ± 360.8	0.1 ± 4.4	-102.2 ± 92.5
	s.c insulin	58 ± 23	390.2 ± 88.5	100.0 ± 0.0	0.0 ± 0.0
	NP-NF	86 ± 41	849.5 ± 202.5	-0.6 ± 2.5	-117.7 ± 51.9
	NP-WT	79 ± 29	647.1 ± 182.2	1.9 ± 2.2	-65.8 ± 46.7
	NP-KP	71 ± 33	581.9 ± 212.8	2.7 ± 2.6	-49.1 ± 54.5

Protein-based drugs have been shown to have an oral bioavailability lower than 1%, when compared with injectable formulations having complete pharmacological availability (PA) <sup>244</sup>. However, a PA of 10.3% has previously been achieved using 10 IU/kg insulin loaded PLGA NPs, with a 52% drop in blood glucose levels after 10 h of administration into diabetic Wistar male rats. On the other hand, Cui *et al.* administered 20 IU/Kg insulin PLGA and PLGA-55 NPs in diabetic Wistar male rats and obtained 3.7 and 6.3%, respectively, of oral bioavailability <sup>245, 246</sup>. In addition, others preferred to administer 1.1 IU/kg of Fc-conjugated PLA-PEG-MAL NPs and elicited a prolonged hypoglycemic response in wild-type mice <sup>93</sup>. Here, 50 IU/kg KP-functionalized NPs resulted in a 37% drop in blood glucose levels after 1 h following administration (**Table 6**). After 8 h, KP-functionalized NPs presented a PA of around 3% and a hypoglycemic decrease (HD) close to zero, corresponding to the HD measured following s.c. injection of insulin (**Table 7**). The dose could be increased to have an effect like the current treatment. However, it would be preferable to have the same effect with the lowest possible dose, and was the feature tested here. All in all, the low PA might be due to the

incomplete release of insulin, which may be increased with increasing the study time.

**Table 7 |** Pharmacodynamic parameters.

	Dose (IU/Kg)	t <sub>min</sub> (h)	C <sub>min</sub> ± SD (mg/dL)	AUC 8 h	PA 8 h ± SD (%)	HD 8 h ± SD (%)
<b>PBS</b>	0	4	374.20 ± 58.64	927.8 ± 124.0	-1.6 ± 1.5	-137.8 ± 31.8
<b>Oral insulin</b>	50	8	256.75 ± 102.88	789.2 ± 360.8	0.1 ± 4.4	-102.2 ± 92.5
<b>s.c insulin</b>	2.5	2	72.50 ± 25.67	390.2 ± 88.5	100.0 ± 0.0	0.0 ± 0.0
<b>NP-NF</b>	50	8	328.00 ± 65.33	849.5 ± 202.5	-0.6 ± 2.5	-117.7 ± 51.9
<b>NP-WT</b>	50	6	290.50 ± 103.75	768.6 ± 24.7	0.4 ± 0.3	-97.0 ± 6.3
<b>NP-KP</b>	50	4	282.40 ± 137.68	581.9 ± 212.8	2.7 ± 2.6	-49.1 ± 54.5

AUC: area under the curve; PA: pharmacological availability; HD: hypoglycemic decrease; SD: standard deviation; t<sub>min</sub>: time with minimal concentration of glucose after administration of different formulations.

Taken together, the *in vivo* glycemic decrease obtained using the KP variant is a clear improvement of the therapeutic efficacy. In fact, the obtained *in vivo* results agree with *in vitro* data, supporting that albumin decorated NPs increase the effect as a result of improved FcRn-binding affinity. It is reported in the literature the use of FcRn knock out mouse, confirming the FcRn-mediated transcytosis of FcRn-targeted NPs<sup>93</sup>.

Interestingly, while the intestinal expression of FcRn in rodents has been demonstrated to be developmentally down-regulated after weaning<sup>247</sup>, this is not the case in humans or in the hFcRn expressing mice, as the transgene is expressed under the human promoter<sup>248</sup>. Thus, the transgenic mouse model mimics the tissue expression profile of human FcRn, by not being down-regulated after weaning<sup>157</sup>.

Additionally, biodistribution and pharmacokinetic preliminary studies were done, using NPs-KAHQ and an albumin triple mutant, which can give an insight of the behavior of the studied variants (**Appendix III**).



## Chapter V

---

# CONCLUSIONS AND FUTURE PERSPECTIVES

---



## 1. Conclusions

The oral delivery of antidiabetic drugs is more convenient, safe and cost-effective. Notwithstanding, biopharmaceuticals may benefit with the encapsulation in multifunctional nanomaterials. Functionalized nanomaterials are definitely the best way to reach a specific target and have reduced side effects and increased efficiency. Lately, the potential of FcRn-targeted NPs, as an attractive gateway for enhanced delivery of antidiabetic drugs across mucosal barrier, has been under investigation. Moreover, the use of engineered FcRn-targeted ligands have revealed to be a promising strategy to ameliorate the effects on binding, transport and recycling. These parameters can be crucial on modulating cell uptake, long circulation time, renal clearance, and drug stability, by surpassing extracellular barriers, select internalization via and overcome intracellular obstacles, as lysosomal degradation.

In this thesis, a FcRn-targeted nanoplatform was developed, as an advanced delivery system for the improved oral bioavailability of insulin. The developed PLGA-PEG NPs were characterized as being monodisperse with 150 nm in size and -9 mV in zeta potential, having a drug loading over 10% and around 90% of albumin conjugation efficiency. Insulin structure showed to be affected by the encapsulation method, while albumin structure was maintained after conjugation. Furthermore, the developed nanosystem revealed a prolonged and controlled release of insulin, which contributes for the reduced insulin dosing. NPs were decorated with human albumin variants, which presented different binding affinities to FcRn. Particularly, the engineered albumin variant KP, with a substitution of Lys573 by proline on DIII, showed the highest improvement on binding to hFcRn. Moreover, KP showed enhanced transcytosis in 2.5-fold across polarized MDCK-hFcRn epithelia, and 2-fold increase when conjugated to NPs, compared with WT albumin and WT albumin decorated NPs, respectively. Additionally, after being transported throughout epithelial cells, these NPs exhibited to be taken up and recycled by endothelial HMEC1-hFcRn cells, through the FcRn-recycling pathway. Again, the KP variant showed a more pronounced effect, presenting 2-fold and 3-fold increase of uptake and recycling, respectively, compared to WT albumin. After conjugation, NPs-KP maintained the marked effect, with both uptake and recycling 1.5-fold higher than NPs-WT. These results were reflected in the half-life projection, demonstrating a score of 2-fold higher for KP and 6.7-fold higher for NPs-KP, compared to WT, which has a mean half-life of 3 weeks. Through both FcRn-related biologic mechanisms, it was thus possible to show how FcRn-binding therapeutics are rescued from intracellular degradation. These advantages can play a key role in doses



management, revolutionizing the design of new materials. Furthermore, when exploring the potential of simulated hypergravity in oral delivery of biopharmaceuticals, it was shown that different hypergravity levels (2.5 g, 5.0 g and 7.5 g) did not affect the metabolic activity and cellular integrity of intestinal epithelial Caco-2 cells. Nevertheless, the expression of tight junctions and transporters of Caco-2 cells was apparently affected, which might interfere with paracellular and passive transport. However, the FcRn-mediated transport of the produced NPs revealed itself constant and not different from reference conditions. This evidence can thus open doors for the development of new strategies for oral delivery of biopharmaceuticals.

Next, to evaluate the intestinal permeability in a more reliable predictive manner, a porcine *ex vivo* model was used. The porcine has gaining importance and attention from investigators, due to its physiological and anatomical similarities. However, the potential of this platform on the screening of FcRn-targeted nanosystems was never investigated. In this sense, the FcRn expression through the GI tract, which was maintained for up 7 days, was assessed. Through the intestinal permeability assay it was shown the characteristic hierarchy of albumin variants. Expectadely, KP demonstrated to be 2.4-fold more efficiently transported, compared to WT, which is in line with *in vitro* data. The consistent results in different models, showed a robustness of the developed NPs and a correlation between models. Therefore, this porcine *ex vivo* platform revealed to be a potential model for the screening of FcRn-targeted oral drug formulations, which may have a positive and significant impact on saving time and money, during their development.

Finally, as a proof-of-concept, the ability of the developed polymeric NPs to reduce glucose levels was assessed by using hFcRn transgenic mice, to avoid cross-species differences, induced with diabetes. After oral delivery, it was observed that NPs have a controlled and prolonged effect, compared to s.c. insulin, which had only a peak effect after 2 h. In addition, encapsulated insulin showed a better effect, when comparing with oral free insulin, suggesting a drug protection. Also, funcionalized NPs were more efficient than non-functionalized NPs, due to FcRn advantageous characteristics. Particularly, NPs-KP were able to reduce glycemia up to around 40% after 1 h, which is maintained between 1 h and 4 h, and enhance pharmacologic availability. The novel concept described should pave the way for further engineering of biodegradable albumin-decorated NP formulations for tailored targeting of FcRn for enhanced intestinal delivery.

Overall, the developed nanosystem holds a tremendous promise to address the unmet

needs, as poor oral bioavailability of biopharmaceuticals and specially diabetic patient compliance. Plus, it is a versatile carrier candidate for oral delivery of biopharmaceuticals, playing a positive and significant impact in welfare of diabetic patients.

## 2. Future Perspectives

As future perspectives a panel of studies could be done, to improve the quality of this work, by clarifying some details.

Regarding the conjugation, since it was not possible to concretely demonstrate the thioether covalent bond, it would be interesting to conjugate albumin to the polymer, before producing NPs. The approach will probably facilitate the detection by p.e. NMR. Also, the potential of a recent albumin variant, E505Q/T527M/K573P (QMP), published by J.T. Andersen, could be explored. As previously mentioned, it is reported that the binding affinity of this triple mutant gains impressively more than 180-fold increase in hFcRn without affecting binding at neutral pH. Plus, QMP translated into 4-fold enhanced transcellular transport *in vitro*, compared with WT albumin <sup>87</sup>.

In general, *ex vivo* and especially *in vivo* assays need a higher number of replicates in different tissues/animals, to clarify the statistical significance of the results. Further investigation into the implication of obtained differences on the PD/PK is also required. In addition, here it was used insulin as a model drug, using diabetes as example. However, it would be interesting try to encapsulate other antidiabetic peptides, as insulin glargine, degludec, icodec or the oral i338, for the treatment of both diabetes types. To answer to some particularities of diabetes, NPs could be microencapsulated into enteric capsules, in parallel with free insulin, to ensure a fast effect (after meals, p.e.), while, NPs will assure a prolonged effect. To take advantage of the FcRn-recycling pathways and half-life extension, both free insulin and encapsulated insulin could be conjugated to simpler and smaller FcRn-targeted ligands, as FcRn binding peptides (FcBP) <sup>249, 250</sup>.

The potential of the developed technology can also be explored in diabetes-related disorders, as vasculopathy or fibrosis, or even in other diseases since FcRn is broadly expressed throughout the body, which may pave the way for using FcRn-targeting NPs for delivery to different body sites.



## Chapter VI

---

### REFERENCES

---



1. Saeedi P, Petersohn I, Salpea P, et al. Global and regional diabetes prevalence estimates for 2019 and projections for 2030 and 2045: Results from the International Diabetes Federation Diabetes Atlas, 9(th) edition. *Diabetes Res Clin Pract* 2019;157:107843.
2. Bommer C, Sagalova V, Heeseemann E, et al. Global Economic Burden of Diabetes in Adults: Projections From 2015 to 2030. *Diabetes Care* 2018;41:963-970.
3. Easa N, Alany RG, Carew M, et al. A review of non-invasive insulin delivery systems for diabetes therapy in clinical trials over the past decade. *Drug Discovery Today* 2019;24:440-451.
4. Cutfield WS, Derraik JGB, Gunn AJ, et al. Non-Compliance with Growth Hormone Treatment in Children Is Common and Impairs Linear Growth. *PLoS ONE* 2011;6:e16223.
5. Davies MJ, Gagliardino JJ, Gray LJ, et al. Real-world factors affecting adherence to insulin therapy in patients with Type 1 or Type 2 diabetes mellitus: a systematic review. *Diabetic Medicine* 2013;30:512-524.
6. Sonaje K, Lin KJ, Wey SP, et al. Biodistribution, pharmacodynamics and pharmacokinetics of insulin analogues in a rat model: Oral delivery using pH-responsive nanoparticles vs. subcutaneous injection. *Biomaterials* 2010;31:6849-58.
7. Arbit E, Kidron M. Oral Insulin Delivery in a Physiologic Context: Review. *J Diabetes Sci Technol* 2017;11:825-832.
8. Geho WB, Geho HC, Lau JR, et al. Hepatic-Directed Vesicle Insulin: A Review of Formulation Development and Preclinical Evaluation. *Journal of Diabetes Science and Technology* 2009;3:1451-1459.
9. Eldor R, Arbit E, Corcos A, et al. Glucose-Reducing Effect of the ORMD-0801 Oral Insulin Preparation in Patients with Uncontrolled Type 1 Diabetes: A Pilot Study. *PLOS ONE* 2013;8:e59524.
10. Alexander Vol, Gribova O. Methods and compositions for oral administration of insulin. In: Administration OD, ed. Volume US20100278922A1, 2014.
11. Khedkar A, Iyer H, Anand A, et al. A dose range finding study of novel oral insulin (IN-105) under fed conditions in type 2 diabetes mellitus subjects. *Diabetes Obes Metab* 2010;12:659-64.
12. Bennet D, Kim S. Polymer Nanoparticles for Smart Drug Delivery. In: Sezer AD, ed. Application of Nanotechnology in Drug Delivery: Nanotechnology and Nanomaterials, 2014:257-309.
13. Duschl A. Nanomedicine. In: Boraschi D, Penton-Rol G, eds. Immune Rebalancing - The Future of Immunosuppression: Elsevier, 2016:251-274.
14. Stewart MP, Sharei A, Ding X, et al. In vitro and ex vivo strategies for intracellular delivery. *Nature* 2016;538:183-192.
15. Banik BL, Fattahi P, Brown JL. Polymeric nanoparticles: the future of nanomedicine. *WIREs Nanomedicine and Nanobiotechnology* 2016;8:271-299.
16. Pereira C, Araújo F, Granja PL, et al. Targeting membrane transporters and receptors as a mean to optimize orally delivered biotechnological based drugs through nanoparticle delivery systems. *Current Pharmaceutical Biotechnology* 2014;15:650-658.
17. Araujo F, Shrestha N, Granja PL, et al. Antihyperglycemic potential of incretins orally delivered via nano and microsystems and subsequent glucoregulatory effects. *Current Pharmaceutical Biotechnology* 2014;15:609-19.
18. Moulari B, Beduneau A, Pellequer Y, et al. Nanoparticle targeting to inflamed tissues of gastrointestinal tract *Current Drug Delivery* 2013;10:9-17.
19. Sarmiento B, Ferreira D, Vasconcelos T. Polymer-Based Delivery Systems for Oral Delivery of Peptides and Proteins. In: Jorgensen L, Nielsen HM, eds. Delivery Technologies for Biopharmaceuticals: Peptides, Proteins, Nucleic Acids and Vaccines: John Wiley & Sons, Ltd, 2009:207-227.
20. Parodi A, Corbo C, Cevenini A, et al. Enabling cytoplasmic delivery and organelle targeting by surface modification of nanocarriers. *Nanomedicine* 2015;10:1923-1940.
21. Rekha MR, Sharma CP. Oral delivery of therapeutic protein/peptide for diabetes – Future perspectives. *International Journal of Pharmaceutics* 2013;440:48-62.
22. Soo Choi H, Liu W, Misra P, et al. Renal clearance of quantum dots. *Nat Biotech* 2007;25:1165-1170.

23. Wahajuddin, Arora S. Superparamagnetic iron oxide nanoparticles: magnetic nanoplatforms as drug carriers. *International Journal of Nanomedicine* 2012;7:3445–3471.
24. Howe SE, Lickteig DJ, Plunkett KN, et al. The Uptake of Soluble and Particulate Antigens by Epithelial Cells in the Mouse Small Intestine. *PLOS ONE* 2014;9:e86656.
25. Sun W, Hu Q, Ji W, et al. Leveraging physiology for precision drug delivery. *Physiological Reviews* 2017;97:189–225.
26. Agarwal R, Roy K. Intracellular delivery of polymeric nanocarriers: a matter of size, shape, charge, elasticity and surface composition. *Therapeutic delivery* 2013;4:705–723.
27. Blanco E, Shen H, Ferrari M. Principles of nanoparticle design for overcoming biological barriers to drug delivery. *Nature Biotechnology* 2015;9:941-951.
28. Huang H, Hernandez R, Geng J, et al. A porphyrin-PEG polymer with rapid renal clearance. *Biomaterials* 2016;76:25-32.
29. Roberts MJ, Bentley MD, Harris JM. Chemistry for peptide and protein PEGylation. *Advanced Drug Delivery Reviews* 2012;64, Supplement:116-127.
30. Schöttler S, Becker G, Winzen S, et al. Protein adsorption is required for stealth effect of poly(ethylene glycol)- and poly(phosphoester)-coated nanocarriers. *Nat Nano* 2016;11:372-377.
31. Jhaveri A, Torchilin V. Intracellular delivery of nanocarriers and targeting to subcellular organelles. *Expert Opinion on Drug Delivery* 2015;13.
32. Bera A, Jewrajka SK. Tailoring polyamide thin film composite nanofiltration membranes by polyethyleneimine and its conjugates for the enhancement of selectivity and antifouling property. *RSC Advances* 2016;6:4521-4530.
33. Noh SM, Kim W-K, Kim SJ, et al. Enhanced cellular delivery and transfection efficiency of plasmid DNA using positively charged biocompatible colloidal gold nanoparticles. *Biochimica et Biophysica Acta (BBA) - General Subjects* 2007;1770:747-752.
34. Chanthick C, Kanlaya R, Kiatbumrung R, et al. Caveolae-mediated albumin transcytosis is enhanced in dengueinfected human endothelial cells: A model of vascular leakage in dengue hemorrhagic fever. *Scientific Reports* 2016;6.
35. Alai MS, Lin WJ, Pingale SS. Application of polymeric nanoparticles and micelles in insulin oral delivery. *Journal of food and drug analysis* 2015;23:351-358.
36. Pawar VK, Meher JG, Singh Y, et al. Targeting of gastrointestinal tract for amended delivery of 3Q4 protein/peptide therapeutics: Strategies and industrial perspectives. *Journal of Controlled Release* 2014;196:168-83.
37. Xiao K, Li Y, Luo J, et al. The effect of surface charge on in vivo biodistribution of PEG-oligocholic acid based micellar nanoparticles. *Biomaterials* 2011;32:3435-3446.
38. Yoo JW, Mitragotri S. Polymer particles that switch shape in response to a stimulus. *Proc Natl Acad Sci U S A* 2010;107:11205-10.
39. Banquy X, Suarez F, Argaw A, et al. Effect of mechanical properties of hydrogel nanoparticles on macrophage cell uptake. *Soft Matter* 2009;5:3984-3991.
40. O'Reilly JR, Corrigan OI, O'Driscoll CM. The effect of mixed micellar systems, bile salt/fatty acids, on the solubility and intestinal absorption of clofazimine (B663) in the anaesthetised rat. *International Journal of Pharmaceutics* 1994;109:147-154.
41. Pabla D, Akhlaghi F, Zia H. Intestinal permeability enhancement of levothyroxine sodium by straight chain fatty acids studied in MDCK epithelial cell line. *European Journal of Pharmaceutical Sciences* 2010;40:466-472.
42. Aspenström-Fagerlund B, Sundström B, Tallkvist J, et al. Fatty acids increase paracellular absorption of aluminium across Caco-2 cell monolayers. *Chemico-Biological Interactions* 2009;181:272-278.
43. Trevino SR, Scholtz JM, Pace CN. Amino acid contribution to protein solubility: Asp, Glu, and Ser contribute more favorably than the other hydrophilic amino acids in RNase Sa. *J Mol Biol* 2007;366:449-60.
44. Li N, Huang C, Luan Y, et al. Active targeting co-delivery system based on pH-sensitive methoxy-poly (ethylene glycol)2K-poly( $\epsilon$ -caprolactone)4K-poly(glutamic acid)1K for enhanced cancer therapy. *Journal of Colloid and Interface Science* 2016;472:90-98.

45. Li X, Yu M, Fan W, et al. Orally active-targeted drug delivery systems for proteins and peptides. *Expert Opinion Drug Delivery* 2014;11:1435-1447.
46. Steinbach JM, Seo Y-E, Saltzman WM. Cell penetrating peptide-modified poly(lactic-co-glycolic acid) nanoparticles with enhanced cell internalization. *Acta Biomaterialia* 2016;30:49-61.
47. Ghuman J, Zunszain PA, Petitpas I, et al. Structural basis of the drug-binding specificity of human serum albumin. *J Mol Biol* 2005;353:38-52.
48. Tan YL, Ho HK. Navigating albumin-based nanoparticles through various drug delivery routes. *Drug Discovery Today* 2018.
49. Sand KMK, Bern M, Nilsen J, et al. Unraveling the Interaction between FcRn and Albumin: Opportunities for Design of Albumin-Based Therapeutics. *Frontiers in Immunology* 2015;5.
50. Andersen JT, Dalhus B, Cameron J, et al. Structure-based mutagenesis reveals the albumin-binding site of the neonatal Fc receptor. *Nat Commun* 2012;3:610.
51. Andersen JT, Dalhus B, Viuff D, et al. Extending Serum Half-life of Albumin by Engineering Neonatal Fc Receptor (FcRn) Binding. *Journal of Biological Chemistry* 2014;289:13492-13502.
52. Nilsen J, Bern M, Sand KMK, et al. Human and mouse albumin bind their respective neonatal Fc receptors differently. *Scientific Reports* 2018;8:14648.
53. Simister NE, Rees AR. Isolation and characterization of an Fc receptor from neonatal rat small intestine. *Eur J Immunol* 1985;15:733-8.
54. Simister NE, Mostov KE. An Fc receptor structurally related to MHC class I antigens. *Nature* 1989;337:184-7.
55. West AP, Jr., Bjorkman PJ. Crystal structure and immunoglobulin G binding properties of the human major histocompatibility complex-related Fc receptor(,). *Biochemistry* 2000;39:9698-708.
56. Burmeister WP, Huber AH, Bjorkman PJ. Crystal structure of the complex of rat neonatal Fc receptor with Fc. *Nature* 1994;372:379-83.
57. Oganessian V, Damschroder MM, Cook KE, et al. Structural insights into neonatal Fc receptor-based recycling mechanisms. *The Journal of biological chemistry* 2014;289:7812-7824.
58. Raghavan M, Bonagura VR, Morrison SL, et al. Analysis of the pH Dependence of the Neonatal Fc Receptor/Immunoglobulin G Interaction Using Antibody and Receptor Variants. *Biochemistry* 1995;34:14649-14657.
59. Stapleton NM, Andersen JT, Stemerding AM, et al. Competition for FcRn-mediated transport gives rise to short half-life of human IgG3 and offers therapeutic potential. *Nat Commun* 2011;2:599.
60. Andersen JT, Daba MB, Berntzen G, et al. Cross-species binding analyses of mouse and human neonatal Fc receptor show dramatic differences in immunoglobulin G and albumin binding. *J Biol Chem* 2010;285:4826-36.
61. Chaudhury C, Brooks CL, Carter DC, et al. Albumin binding to FcRn: distinct from the FcRn-IgG interaction. *Biochemistry* 2006;45:4983-90.
62. Sand KM, Dalhus B, Christianson GJ, et al. Dissection of the neonatal Fc receptor (FcRn)-albumin interface using mutagenesis and anti-FcRn albumin-blocking antibodies. *J Biol Chem* 2014;289:17228-39.
63. Huber AH, Kelley RF, Gastinel LN, et al. Crystallization and stoichiometry of binding of a complex between a rat intestinal Fc receptor and Fc. *J Mol Biol* 1993;230:1077-83.
64. Chaudhury C, Mehnaz S, Robinson JM, et al. The major histocompatibility complex-related Fc receptor for IgG (FcRn) binds albumin and prolongs its lifespan. *J Exp Med* 2003;197:315-22.
65. Vaughn DE, Bjorkman PJ. Structural basis of pH-dependent antibody binding by the neonatal Fc receptor. *Structure* 1998;6:63-73.
66. Schmidt MM, Townson SA, Andreucci AJ, et al. Crystal structure of an HSA/FcRn complex reveals recycling by competitive mimicry of HSA ligands at a pH-dependent hydrophobic interface. *Structure* 2013;21:1966-78.
67. Ober RJ, Martinez C, Vaccaro C, et al. Visualizing the site and dynamics of IgG salvage by the MHC class I-related receptor, FcRn. *J Immunol* 2004;172:2021-9.
68. Anderson CL, Chaudhury C, Kim J, et al. Perspective - FcRn transports albumin: relevance to immunology and medicine. *Trends Immunol* 2006;27:343-8.



69. Pyzik M, Rath T, Kuo TT, et al. Hepatic FcRn regulates albumin homeostasis and susceptibility to liver injury. *Proc Natl Acad Sci U S A* 2017;114:E2862-e2871.
70. Foss S, Grevys A, Sand KMK, et al. Enhanced FcRn-dependent transepithelial delivery of IgG by Fc-engineering and polymerization. *J Control Release* 2016;223:42-52.
71. Grevys A, Nilsen J, Sand KMK, et al. A human endothelial cell-based recycling assay for screening of FcRn targeted molecules. *Nature Communications* 2018;9:621.
72. Weflen AW, Baier N, Tang QJ, et al. Multivalent immune complexes divert FcRn to lysosomes by exclusion from recycling sorting tubules. *Mol Biol Cell* 2013;24:2398-405.
73. EMA. Levemir (insulin detemir). Available on: [https://ec.europa.eu/health/documents/community-register/2010/2010033077668/anx\\_77668\\_en.pdf](https://ec.europa.eu/health/documents/community-register/2010/2010033077668/anx_77668_en.pdf) [accessed 24/11/2020]. 2004.
74. Home P, Kurtzhals P. Insulin detemir: from concept to clinical experience. *Expert Opin Pharmacother* 2006;7:325-43.
75. Rendell M. Insulin degludec: A long-acting modern insulin analogue with a predictable pharmacokinetic/ pharmacodynamic profile. *Drugs of Today* 2013;49:387-397.
76. NovoNordisk. Tresiba®FlexTouch®100 U/mL. Available on: [https://www.novonordisk.com.br/content/dam/brazil/affiliate/www-novonordisk-br/Bulas/Profissionais/Tresiba-FlexTouch\\_bula-profissional.pdf](https://www.novonordisk.com.br/content/dam/brazil/affiliate/www-novonordisk-br/Bulas/Profissionais/Tresiba-FlexTouch_bula-profissional.pdf) [accessed on 24/11/2020]. 2016.
77. Elsadek B, Kratz F. Impact of albumin on drug delivery--new applications on the horizon. *J Control Release* 2012;157:4-28.
78. Bern M, Sand KM, Nilsen J, et al. The role of albumin receptors in regulation of albumin homeostasis: Implications for drug delivery. *J Control Release* 2015;211:144-62.
79. Wang F, Carabino JM, Vergara CM. Insulin glargine: A systematic review of a long-acting insulin analogue. *Clinical Therapeutics* 2003;25:1541-1577.
80. Rosenstock J, Bajaj HS, Janez A, et al. Once-Weekly Insulin for Type 2 Diabetes without Previous Insulin Treatment. *N Engl J Med* 2020;383:2107-2116.
81. HÖvelmann U, Brøndsted L, Kristensen NR, et al. 237-OR: Insulin Icodec: An Insulin Analog Suited for Once-Weekly Dosing in Type 2 Diabetes. *Diabetes* 2020;69.
82. Halberg IB, Lyby K, Wassermann K, et al. Efficacy and safety of oral basal insulin versus subcutaneous insulin glargine in type 2 diabetes: a randomised, double-blind, phase 2 trial. *Lancet Diabetes Endocrinol* 2019;7:179-188.
83. Hubalek F, Refsgaard HHF, Gram-Nielsen S, et al. Molecular engineering of safe and efficacious oral basal insulin. *Nat Commun* 2020;11:3746.
84. Leonard TW, Lynch J, McKenna MJ, et al. Promoting absorption of drugs in humans using medium-chain fatty acid-based solid dosage forms: GIPET. *Expert Opin Drug Deliv* 2006;3:685-92.
85. Nag OK, Delehanty JB. Active Cellular and Subcellular Targeting of Nanoparticles for Drug Delivery. *Pharmaceutics* 2019;11.
86. Mansoor S, Kondiah PPD, Choonara YE, et al. Polymer-Based Nanoparticle Strategies for Insulin Delivery. *Polymers (Basel)* 2019;11.
87. Bern M, Nilsen J, Ferrarese M, et al. An engineered human albumin enhances half-life and transmucosal delivery when fused to protein-based biologics. *Science Translational Medicine* 2020;12:eabb0580.
88. Azevedo C, Nilsen J, Grevys A, et al. Engineered albumin-functionalized nanoparticles for improved FcRn binding enhance oral delivery of insulin. *Journal of Controlled Release* 2020;327:161-173.
89. Lopes M, Derenne A, Pereira C, et al. Impact of the in vitro gastrointestinal passage of biopolymer-based nanoparticles on insulin absorption. *RSC Advances* 2016;6:20155-20165.
90. Martins JP, D'Auria R, Liu D, et al. Engineered Multifunctional Albumin-Decorated Porous Silicon Nanoparticles for FcRn Translocation of Insulin. *Small* 2018;14:e1800462.
91. Martins JP, Liu D, Fontana F, et al. Microfluidic Nanoassembly of Bioengineered Chitosan-Modified FcRn-Targeted Porous Silicon Nanoparticles @ Hypromellose Acetate Succinate for Oral Delivery of Antidiabetic Peptides. *ACS Applied Materials & Interfaces* 2018;10:44354-44367.

92. Shi Y, Sun X, Zhang L, et al. Fc-modified exenatide-loaded nanoparticles for oral delivery to improve hypoglycemic effects in mice. *Scientific Reports* 2018;8:726.
93. Pridgen EM, Alexis F, Kuo TT, et al. Transepithelial transport of Fc-targeted nanoparticles by the neonatal fc receptor for oral delivery. *Sci Transl Med* 2013;5:213ra167.
94. Nunes R, Silva C, Chaves L. 4.2 - Tissue-based in vitro and ex vivo models for intestinal permeability studies A2 - Sarmiento, Bruno. *Concepts and Models for Drug Permeability Studies: Woodhead Publishing*, 2016:203-236.
95. Braakhuis HM, Kloet SK, Kezic S, et al. Progress and future of in vitro models to study translocation of nanoparticles. *Arch Toxicol* 2015;89:1469-95.
96. Pereira C, Costa J, Sarmiento B, et al. 3.3 - Cell-based in vitro models for intestinal permeability studies. *Concepts and Models for Drug Permeability Studies: Woodhead Publishing*, 2016:57-81.
97. Lopes MA, Abraham BA, Cabral LM, et al. Intestinal absorption of insulin nanoparticles: Contribution of M cells. *Nanomedicine: Nanotechnology, Biology, and Medicine* 2014;10:1139–1151.
98. Hu M, Li X. *Oral Bioavailability: Basic Principles, Advanced Concepts, and Applications: Wiley*, 2011.
99. El-Kattan A, Varma M. Oral Absorption, Intestinal Metabolism and Human Oral Bioavailability. In: Paxton J, ed. *Topics on Drug Metabolism*. Rijeka: InTech, 2012:Ch. 1.
100. Banerjee A, Qi J, Gogoi R, et al. Role of nanoparticle size, shape and surface chemistry in oral drug delivery. *Journal of Controlled Release* 2016;238:176-185.
101. Imai S, Morishita Y, Hata T, et al. Cellular internalization, transcellular transport, and cellular effects of silver nanoparticles in polarized Caco-2 cells following apical or basolateral exposure. *Biochemical and Biophysical Research Communications* 2017;484:543-549.
102. Pindáková L, Kašpárková V, Kejlová K, et al. Behaviour of silver nanoparticles in simulated saliva and gastrointestinal fluids. *International Journal of Pharmaceutics* 2017;527:12-20.
103. Modi S, Anderson BD. Determination of drug release kinetics from nanoparticles: overcoming pitfalls of the dynamic dialysis method. *Mol Pharm* 2013;10:3076-89.
104. Kim JS, Mitchell S, Kijek P, et al. The suitability of an in situ perfusion model for permeability determinations: utility for BCS class I biowaiver requests. *Mol Pharm* 2006;3:686-94.
105. Hashem L, Swedrowska M, Vllasaliu D. Intestinal uptake and transport of albumin nanoparticles: potential for oral delivery. *Nanomedicine (Lond)* 2018;13:1255-1265.
106. Hornby PJ, Cooper PR, Kliwinski C, et al. Human and non-human primate intestinal FcRn expression and immunoglobulin G transcytosis. *Pharmaceutical research* 2014;31:908-922.
107. Gamboa JM, Leong KW. In vitro and in vivo models for the study of oral delivery of nanoparticles. *Adv Drug Deliv Rev* 2013;65:800-10.
108. McCool DJ, Marcon MA, Forstner JF, et al. The T84 human colonic adenocarcinoma cell line produces mucin in culture and releases it in response to various secretagogues. *Biochem J* 1990;267:491-500.
109. Irvine JD, Takahashi L, Lockhart K, et al. MDCK (Madin-Darby canine kidney) cells: A tool for membrane permeability screening. *J Pharm Sci* 1999;88:28-33.
110. Jin X, Luong T-L, Reese N, et al. Comparison of MDCK-MDR1 and Caco-2 cell based permeability assays for anti-malarial drug screening and drug investigations. *Journal of Pharmacological and Toxicological Methods* 2014;70:188-194.
111. Li X, Mu P, Wen J, et al. Carrier-Mediated and Energy-Dependent Uptake and Efflux of Deoxyribose in Mammalian Cells. *Scientific Reports* 2017;7:5889.
112. Khatri P, Shao J. Transport of lipid nano-droplets through MDCK epithelial cell monolayer. *Colloids and Surfaces B: Biointerfaces* 2017;153:237-243.
113. Braun A, Hämmerle S, Suda K, et al. Cell cultures as tools in biopharmacy. *European Journal of Pharmaceutical Sciences* 2000;11:S51-S60.
114. Lesuffleur T, Barbat A, Dussaulx E, et al. Growth adaptation to methotrexate of HT-29 human colon carcinoma cells is associated with their ability to differentiate into columnar absorptive and mucus-secreting cells. *Cancer Res* 1990;50.
115. Akbari A, Lavasanifar A, Wu J. Interaction of cruciferin-based nanoparticles with Caco-2 cells and Caco-2/HT29-MTX co-cultures. *Acta Biomaterialia* 2017.

116. Araujo F, Martins C, Azevedo C, et al. Chemical modification of drug molecules as strategy to reduce interactions with mucus. *Adv Drug Deliv Rev* 2017.
117. Lechanteur A, das Neves J, Sarmiento B. The role of mucus in cell-based models used to screen mucosal drug delivery. *Advanced Drug Delivery Reviews* 2017.
118. Mahler GJ, Esch MB, Glahn RP, et al. Characterization of a gastrointestinal tract microscale cell culture analog used to predict drug toxicity. *Biotechnol Bioeng* 2009;104:193-205.
119. Chen X-M, Elisia I, Kitts DD. Defining conditions for the co-culture of Caco-2 and HT29-MTX cells using Taguchi design. *Journal of Pharmacological and Toxicological Methods* 2010;61:334-342.
120. Pontier C, Pachot J, Botham R, et al. HT29-MTX and Caco-2/TC7 Monolayers as Predictive Models for Human Intestinal Absorption: Role of the Mucus Layer. *Journal of Pharmaceutical Sciences* 2001;90:1608-1619.
121. Beloqui A, Brayden DJ, Artursson P, et al. A human intestinal M-cell-like model for investigating particle, antigen and microorganism translocation. *Nat. Protocols* 2017;12:1387-1399.
122. Cabellos J, Delpivo C, Fernández-Rosas E, et al. Contribution of M-cells and other experimental variables in the translocation of TiO<sub>2</sub> nanoparticles across in vitro intestinal models. *NanoImpact* 2017;5:51-60.
123. Antunes F, Andrade F, Araújo F, et al. Establishment of a triple co-culture in vitro cell models to study intestinal absorption of peptide drugs. *European Journal of Pharmaceutics and Biopharmaceutics* 2013;83:427-435.
124. Araújo F, Sarmiento B. Towards the characterization of an in vitro triple co-culture intestine cell model for permeability studies. *International Journal of Pharmaceutics* 2013;458:128-134.
125. Lozoya-Agullo I, Araujo F, Gonzalez-Alvarez I, et al. Usefulness of Caco-2/HT29-MTX and Caco-2/HT29-MTX/Raji B Coculture Models To Predict Intestinal and Colonic Permeability Compared to Caco-2 Monoculture. *Mol Pharm* 2017;14:1264-1270.
126. Yu J, Peng S, Luo D, et al. In vitro 3D human small intestinal villous model for drug permeability determination. *Biotechnol Bioeng* 2012;109:2173-8.
127. Artursson P. Cell cultures as models for drug absorption across the intestinal mucosa. *Crit Rev Ther Drug Carrier Syst* 1991;8:305-30.
128. Hidalgo IJ. Assessing the absorption of new pharmaceuticals. *Curr Top Med Chem* 2001;1:385-401.
129. Imai M, Furusawa K, Mizutani T, et al. Three-dimensional morphogenesis of MDCK cells induced by cellular contractile forces on a viscous substrate. *Scientific Reports* 2015;5:14208.
130. Pereira C, Araujo F, Barrias CC, et al. Dissecting stromal-epithelial interactions in a 3D in vitro cellularized intestinal model for permeability studies. *Biomaterials* 2015;56:36-45.
131. Leonard F, Collnot E-M, Lehr C-M. A Three-Dimensional Coculture of Enterocytes, Monocytes and Dendritic Cells To Model Inflamed Intestinal Mucosa in Vitro. *Molecular Pharmaceutics* 2010;7:2103-2119.
132. Susewind J, Carvalho Wodarz C, Repnik U, et al. A 3D co-culture of three human cell lines to model the inflamed intestinal mucosa for safety testing of nanomaterials, 2015.
133. Sung JH, Yu J, Luo D, et al. Microscale 3-D hydrogel scaffold for biomimetic gastrointestinal (GI) tract model. *Lab Chip* 2011;11:389-92.
134. Gupta N, Liu JR, Patel B, et al. Microfluidics-based 3D cell culture models: Utility in novel drug discovery and delivery research. *Bioeng Transl Med* 2016;1:63-81.
135. Balijepalli A, Sivaramakrishnan V. Organs-on-chips: research and commercial perspectives. *Drug Discovery Today* 2017;22:397-403.
136. Kim HJ, Huh D, Hamilton G, et al. Human gut-on-a-chip inhabited by microbial flora that experiences intestinal peristalsis-like motions and flow. *Lab Chip* 2012;12:2165-74.
137. Bein A, Shin W, Jalili-Firoozinezhad S, et al. Microfluidic Organ-on-a-Chip Models of Human Intestine. *Cellular and Molecular Gastroenterology and Hepatology* 2018;5:659-668.
138. Guo Y, Li Z, Su W, et al. A Biomimetic Human Gut-on-a-Chip for Modeling Drug Metabolism in Intestine. *Artif Organs* 2018;42:1196-1205.
139. Shim KY, Lee D, Han J, et al. Microfluidic gut-on-a-chip with three-dimensional villi structure. *Biomed Microdevices* 2017;19:37.

140. Kim HJ, Ingber DE. Gut-on-a-Chip microenvironment induces human intestinal cells to undergo villus differentiation. *Integr Biol (Camb)* 2013;5:1130-40.
141. Henry OYF, Villenave R, Cronce MJ, et al. Organs-on-chips with integrated electrodes for trans-epithelial electrical resistance (TEER) measurements of human epithelial barrier function. *Lab Chip* 2017;17:2264-2271.
142. Workman MJ, Gleeson JP, Troisi EJ, et al. Enhanced Utilization of Induced Pluripotent Stem Cell-Derived Human Intestinal Organoids Using Microengineered Chips. *Cellular and Molecular Gastroenterology and Hepatology* 2017.
143. Jalili-Firoozinezhad S, Gazzaniga FS, Calamari EL, et al. A complex human gut microbiome cultured in an anaerobic intestine-on-a-chip. *Nature Biomedical Engineering* 2019.
144. Kasendra M, Tovaglieri A, Sontheimer-Phelps A, et al. Development of a primary human Small Intestine-on-a-Chip using biopsy-derived organoids. *Scientific Reports* 2018;8:2871.
145. Trietsch SJ, Naumovska E, Kurek D, et al. Membrane-free culture and real-time barrier integrity assessment of perfused intestinal epithelium tubes. *Nature Communications* 2017;8:262.
146. Huh D, Torisawa YS, Hamilton GA, et al. Microengineered physiological biomimicry: organs-on-chips. *Lab Chip* 2012;12:2156-64.
147. Maschmeyer I, Hasenberg T, Jaenicke A, et al. Chip-based human liver-intestine and liver-skin cocultures--A first step toward systemic repeated dose substance testing in vitro. *Eur J Pharm Biopharm* 2015;95:77-87.
148. Esch MB, Mahler GJ, Stokol T, et al. Body-on-a-chip simulation with gastrointestinal tract and liver tissues suggests that ingested nanoparticles have the potential to cause liver injury. *Lab on a Chip* 2014;14:3081-3092.
149. Tottey W, Denonfoux J, Jaziri F, et al. The human gut chip "HuGChip", an explorative phylogenetic microarray for determining gut microbiome diversity at family level. *PLoS One* 2013;8:e62544.
150. Bhatia SN, Ingber DE. Microfluidic organs-on-chips. *Nature Biotechnology* 2014;32:760.
151. Ingber DE. Reverse Engineering Human Pathophysiology with Organs-on-Chips. *Cell* 2016;164:1105-1109.
152. Verneti L, Gough A, Baetz N, et al. Functional Coupling of Human Microphysiology Systems: Intestine, Liver, Kidney Proximal Tubule, Blood-Brain Barrier and Skeletal Muscle. *Sci Rep* 2017;7:42296.
153. Martins JP, Kennedy PJ, Santos HA, et al. A comprehensive review of the neonatal Fc receptor and its application in drug delivery. *Pharmacology & Therapeutics* 2016;161:22-39.
154. Latvala S, Jacobsen B, Otteneder M, et al. Distribution of FcRn Across Species and Tissues. *Journal of Histochemistry and Cytochemistry* 2017;65:321-333.
155. Israel EJ, Patel VK, Taylor SF, et al. Requirement for a beta 2-microglobulin-associated Fc receptor for acquisition of maternal IgG by fetal and neonatal mice. *J Immunol* 1995;154:6246-51.
156. Junghans RP, Anderson CL. The protection receptor for IgG catabolism is the beta2-microglobulin-containing neonatal intestinal transport receptor. *Proc Natl Acad Sci U S A* 1996;93:5512-6.
157. Roopenian DC, Christianson GJ, Sproule TJ, et al. The MHC class I-like IgG receptor controls perinatal IgG transport, IgG homeostasis, and fate of IgG-Fc-coupled drugs. *J Immunol* 2003;170:3528-33.
158. Ghetie V, Hubbard JG, Kim JK, et al. Abnormally short serum half-lives of IgG in beta 2-microglobulin-deficient mice. *Eur J Immunol* 1996;26:690-6.
159. Martin M, Wu SV, Walsh J. Ontogenetic Development and Distribution of Antibody Transport and Fc Receptor mRNA Expression in Rat Intestine. *Digestive Diseases and Sciences* 1997;42:1062-1069.
160. Jason Cameron DS, Jan Terje Andersen, Inger Sandlie. *Pharmacokinetic animal model* 2018.
161. Cooper PR, Kliwinski CM, Perkinson RA, et al. The contribution of cell surface FcRn in monoclonal antibody serum uptake from the intestine in suckling rat pups. *Frontiers in pharmacology* 2014;5:225-225.
162. Zhou J, Johnson JE, Ghetie V, et al. Generation of mutated variants of the human form of the MHC class I-related receptor, FcRn, with increased affinity for mouse immunoglobulin G. *J Mol Biol* 2003;332:901-13.

163. Zhou J, Mateos F, Ober RJ, et al. Conferring the Binding Properties of the Mouse MHC Class I-related Receptor, FcRn, onto the Human Ortholog by Sequential Rounds of Site-directed Mutagenesis. *Journal of Molecular Biology* 2005;345:1071-1081.
164. Viuff D, Antunes F, Evans L, et al. Generation of a double transgenic humanized neonatal Fc receptor (FcRn)/albumin mouse to study the pharmacokinetics of albumin-linked drugs. *Journal of Controlled Release* 2016;223:22-30.
165. Andersen JT, Cameron J, Plumridge A, et al. Single-chain variable fragment albumin fusions bind the neonatal Fc receptor (FcRn) in a species-dependent manner: implications for in vivo half-life evaluation of albumin fusion therapeutics. *J Biol Chem* 2013;288:24277-85.
166. Stirling CMA, Charleston B, Takamatsu H, et al. Characterization of the porcine neonatal Fc receptor--potential use for trans-epithelial protein delivery. *Immunology* 2005;114:542-553.
167. Yang L, Chonglong W, Zhengzhu L, et al. Tissues Expression, Polymorphisms Identification of FcRn Gene and Its Relationship with Serum Classical Swine Fever Virus Antibody Level in Pigs. *Asian-Australasian journal of animal sciences* 2012;25:1089-1095.
168. Hashim M, Korupolu R, Syed B, et al. Jejunal wall delivery of insulin via an ingestible capsule in anesthetized swine-A pharmacokinetic and pharmacodynamic study. *Pharmacol Res Perspect* 2019;7:e00522.
169. von Erlach T, Saxton S, Shi Y, et al. Robotically handled whole-tissue culture system for the screening of oral drug formulations. *Nature Biomedical Engineering* 2020.
170. Fröhlich E, Roblegg E. Oral uptake of nanoparticles: human relevance and the role of in vitro systems. *Archives of Toxicology* 2016;90:2297-2314.
171. Ussing HH, Zerahn K. Active Transport of Sodium as the Source of Electric Current in the Short-circuited Isolated Frog Skin. *Acta Physiologica* 1951;23:110-127.
172. Grass GM, Sweetana SA. In vitro measurement of gastrointestinal tissue permeability using a new diffusion cell. *Pharmaceutical research* 1988;5:372-376.
173. Barthe L, Woodley J, Houin G. Gastrointestinal absorption of drugs: methods and studies. *Fundamental & clinical pharmacology* 1999;13:154-168.
174. Nunes R, atia Silva C, Chaves L. Tissue-based in vitro and ex vivo models for intestinal permeability studies. *Concepts and Models for Drug Permeability Studies: Cell and Tissue based In Vitro Culture Models* 2015:203.
175. Gitter AH, Fromm M, Schulzke J-D. Impedance analysis for the determination of epithelial and subepithelial resistance in intestinal tissues. *Journal of Biochemical and Biophysical Methods* 1998;37:35-46.
176. Lundquist P, Artursson P. Oral absorption of peptides and nanoparticles across the human intestine: Opportunities, limitations and studies in human tissues. *Advanced drug delivery reviews* 2016;106:256-276.
177. Sjöberg Å, Lutz M, Tannergren C, et al. Comprehensive study on regional human intestinal permeability and prediction of fraction absorbed of drugs using the Ussing chamber technique. *European Journal of Pharmaceutical Sciences* 2013;48:166-180.
178. Jain AS, Dhawan VV, Sarmiento B, et al. In Vitro and Ex Vivo Evaluations of Lipid Anti-Cancer Nanoformulations: Insights and Assessment of Bioavailability Enhancement. *AAPS PharmSciTech* 2016;17:553-571.
179. Alam MA, Al-Jenoobi FI, Al-mohizea AM. Everted gut sac model as a tool in pharmaceutical research: limitations and applications. *Journal of Pharmacy and Pharmacology* 2012;64:326-336.
180. Barthe L, Woodley J, Kenworthy S, et al. An improved everted gut sac as a simple and accurate technique to measure paracellular transport across the small intestine. *European journal of drug metabolism and pharmacokinetics* 1998;23:313-323.
181. Luo Z, Liu Y, Zhao B, et al. Ex vivo and in situ approaches used to study intestinal absorption. *Journal of Pharmacological and Toxicological Methods* 2013;68:208-216.
182. Ruan LP, Chen S, Yu BY, et al. Prediction of human absorption of natural compounds by the non-everted rat intestinal sac model. *European Journal of Medicinal Chemistry* 2006;41:605-610.
183. Leppert PS, Fix JA. Use of everted intestinal rings for in vitro examination of oral absorption potential. *Journal of pharmaceutical sciences* 1994;83:976-981.

184. Roopenian DC, Akilesh S. FcRn: the neonatal Fc receptor comes of age. *Nat Rev Immunol* 2007;7:715-25.
185. Tam SH, McCarthy SG, Brosnan K, et al. Correlations between pharmacokinetics of IgG antibodies in primates vs. FcRn-transgenic mice reveal a rodent model with predictive capabilities. *MAbs* 2013;5:397-405.
186. Petkova SB, Akilesh S, Sproule TJ, et al. Enhanced half-life of genetically engineered human IgG1 antibodies in a humanized FcRn mouse model: potential application in humorally mediated autoimmune disease. *Int Immunol* 2006;18:1759-69.
187. Viuff D, Antunes F, Evans L, et al. Generation of a double transgenic humanized neonatal Fc receptor (FcRn)/albumin mouse to study the pharmacokinetics of albumin-linked drugs. *J Control Release* 2016;223:22-30.
188. Low BE, Christianson GJ, Lowell E, et al. Functional humanization of immunoglobulin heavy constant gamma 1 Fc domain human FCGRT transgenic mice. *MAbs* 2020;12:1829334.
189. Roopenian DC, Christianson GJ, Proetzel G, et al. Human FcRn Transgenic Mice for Pharmacokinetic Evaluation of Therapeutic Antibodies. *Methods Mol Biol* 2016;1438:103-14.
190. Roopenian DC, Low BE, Christianson GJ, et al. Albumin-deficient mouse models for studying metabolism of human albumin and pharmacokinetics of albumin-based drugs. *MAbs* 2015;7:344-51.
191. Proetzel G, Roopenian DC. Humanized FcRn mouse models for evaluating pharmacokinetics of human IgG antibodies. *Methods* 2014;65:148-53.
192. Nilsen J, Sandlie I, Roopenian DC, et al. Animal models for evaluation of albumin-based therapeutics. *Current Opinion in Chemical Engineering* 2018;19:68-76.
193. Fan YY, Neubert H. Quantitative Analysis of Human Neonatal Fc Receptor (FcRn) Tissue Expression in Transgenic Mice by Online Peptide Immuno-Affinity LC-HRMS. *Anal Chem* 2016;88:4239-47.
194. Latvala S, Jacobsen B, Otteneder MB, et al. Distribution of FcRn Across Species and Tissues. *J Histochem Cytochem* 2017;65:321-333.
195. Aaen KH, Anthi AK, Sandlie I, et al. The neonatal Fc receptor in mucosal immune regulation. *Scand J Immunol* 2020:e13017.
196. Stein C, Kling L, Proetzel G, et al. Clinical chemistry of human FcRn transgenic mice. *Mamm Genome* 2012;23:259-69.
197. Lee CH, Kang TH, Godon O, et al. An engineered human Fc domain that behaves like a pH-toggle switch for ultra-long circulation persistence. *Nat Commun* 2019;10:5031.
198. Weflen AW, Baier N, Tang Q-J, et al. Multivalent immune complexes divert FcRn to lysosomes by exclusion from recycling sorting tubules. *Molecular biology of the cell* 2013;24:2398-2405.
199. Nilsen J, Trabjerg E, Grevys A, et al. An intact C-terminal end of albumin is required for its long half-life in humans. *Communications Biology* 2020;3:181.
200. Fonte P, Soares S, Sousa F, et al. Stability study perspective of the effect of freeze-drying using cryoprotectants on the structure of insulin loaded into PLGA nanoparticles. *Biomacromolecules* 2014;15:3753-65.
201. Fonte P, Andrade F, Azevedo C, et al. Effect of the Freezing Step in the Stability and Bioactivity of Protein-Loaded PLGA Nanoparticles Upon Lyophilization. *Pharm Res* 2016;33:2777-93.
202. Sarmiento B, Ribeiro A, Veiga F, et al. Development and validation of a rapid reversed-phase HPLC method for the determination of insulin from nanoparticulate systems. *Biomedical Chromatography* 2006;20:898-903.
203. Sousa F, Cruz A, Fonte P, et al. A new paradigm for antiangiogenic therapy through controlled release of bevacizumab from PLGA nanoparticles. *Scientific Reports* 2017;7:3736.
204. Maltesen MJ, Bjerregaard S, Hovgaard L, et al. Analysis of insulin allostery in solution and solid state with FTIR. *Journal of Pharmaceutical Sciences* 2009;98:3265-77.
205. Petersen SS, Kläning E, Ebbesen MF, et al. Neonatal Fc Receptor Binding Tolerance toward the Covalent Conjugation of Payloads to Cysteine 34 of Human Albumin Variants. *Molecular Pharmaceutics* 2016;13:677-682.
206. Sarmiento B, Ribeiro A, Veiga F, et al. Oral bioavailability of insulin contained in polysaccharide nanoparticles. *Biomacromolecules* 2007;8:3054-60.

207. Andersen JT, Dalhus B, Viuff D, et al. Extending serum half-life of albumin by engineering neonatal Fc receptor (FcRn) binding. *J Biol Chem* 2014;289:13492-502.
208. Andersen JT, Dalhus B, Cameron J, et al. Structure-based mutagenesis reveals the albumin-binding site of the neonatal Fc receptor. *Nature Communications* 2012;3:610.
209. Kennedy PJ, Perreira I, Ferreira D, et al. Impact of surfactants on the target recognition of Fab-conjugated PLGA nanoparticles. *Eur J Pharm Biopharm* 2018;127:366-370.
210. Pereira I, Sousa F, Kennedy P, et al. Carcinoembryonic antigen-targeted nanoparticles potentiate the delivery of anticancer drugs to colorectal cancer cells. *International Journal of Pharmaceutics* 2018;549:397-403.
211. Suk JS, Xu Q, Kim N, et al. PEGylation as a strategy for improving nanoparticle-based drug and gene delivery. *Adv Drug Deliv Rev* 2016;99:28-51.
212. Huckaby JT, Lai SK. PEGylation for enhancing nanoparticle diffusion in mucus. *Adv Drug Deliv Rev* 2018;124:125-139.
213. Bertrand N, Grenier P, Mahmoudi M, et al. Mechanistic understanding of in vivo protein corona formation on polymeric nanoparticles and impact on pharmacokinetics. *Nat Commun* 2017;8:777.
214. Sempf K, Arrey T, Gelperina S, et al. Adsorption of plasma proteins on uncoated PLGA nanoparticles. *European journal of pharmaceutics and biopharmaceutics : official journal of Arbeitsgemeinschaft fur Pharmazeutische Verfahrenstechnik e.V* 2013;85:53-60.
215. Sobczynski DJ, Charoenphol P, Heslinga MJ, et al. Plasma protein corona modulates the vascular wall interaction of drug carriers in a material and donor specific manner. *PLoS One* 2014;9:e107408.
216. Charbonneau D, Beauregard M, Tajmir-Riahi HA. Structural analysis of human serum albumin complexes with cationic lipids. *J Phys Chem B* 2009;113:1777-84.
217. Tang J, Luan F, Chen X. Binding analysis of glycyrrhetic acid to human serum albumin: Fluorescence spectroscopy, FTIR, and molecular modeling. *Bioorganic & Medicinal Chemistry* 2006;14:3210-3217.
218. Fallingborg J. Intraluminal pH of the human gastrointestinal tract. *Dan Med Bull* 1999;46:183-96.
219. Dinarvand R, Sepehri N, Manoochehri S, et al. Polylactide-co-glycolide nanoparticles for controlled delivery of anticancer agents. *Int J Nanomedicine* 2011;6:877-95.
220. Czuba E, Diop M, Mura C, et al. Oral insulin delivery, the challenge to increase insulin bioavailability: Influence of surface charge in nanoparticle system. *Int J Pharm* 2018;542:47-55.
221. McClements DJ. Encapsulation, protection, and delivery of bioactive proteins and peptides using nanoparticle and microparticle systems: A review. *Adv Colloid Interface Sci* 2018;253:1-22.
222. Thote AJ, Chappell JT, Kumar R, et al. Reduction in the Initial-Burst Release by Surface Crosslinking of PLGA Microparticles Containing Hydrophilic or Hydrophobic Drugs. *Drug Development and Industrial Pharmacy* 2005;31:43-57.
223. Langer K, Anhorn MG, Steinhäuser I, et al. Human serum albumin (HSA) nanoparticles: Reproducibility of preparation process and kinetics of enzymatic degradation. *International Journal of Pharmaceutics* 2008;347:109-117.
224. Fonte P, Araujo F, Seabra V, et al. Co-encapsulation of lyoprotectants improves the stability of protein-loaded PLGA nanoparticles upon lyophilization. *Int J Pharm* 2015;496:850-62.
225. Fonte P, Lino PR, Seabra V, et al. Annealing as a tool for the optimization of lyophilization and ensuring of the stability of protein-loaded PLGA nanoparticles. *Int J Pharm* 2016;503:163-73.
226. Fonte P, Soares S, Costa A, et al. Effect of cryoprotectants on the porosity and stability of insulin-loaded PLGA nanoparticles after freeze-drying. *Biomatter* 2012;2:329-39.
227. Costantino HR, Griebenow K, Mishra P, et al. Fourier-transform infrared spectroscopic investigation of protein stability in the lyophilized form. *Biochim Biophys Acta* 1995;1253:69-74.
228. Abrosimova KV, Shulenina OV, Paston SV. FTIR study of secondary structure of bovine serum albumin and ovalbumin. *Journal of Physics: Conference Series* 2016;769:012016.
229. Woitiski CB, Carvalho RA, Ribeiro AJ, et al. Strategies toward the improved oral delivery of insulin nanoparticles via gastrointestinal uptake and translocation. *BioDrugs* 2008;22:223-37.
230. Attili-Qadri S, Karra N, Nemirovski A, et al. Oral delivery system prolongs blood circulation of docetaxel nanocapsules via lymphatic absorption. *Proc Natl Acad Sci U S A* 2013;110:17498-503.

231. Goldberg M, Gomez-Orellana I. Challenges for the oral delivery of macromolecules. *Nature Reviews Drug Discovery* 2003;2:289.
232. Wang Z, Tiruppathi C, Minshall RD, et al. Size and Dynamics of Caveolae Studied Using Nanoparticles in Living Endothelial Cells. *ACS Nano* 2009;3:4110-4116.
233. Terrisse AD, Puech N, Allart S, et al. Internalization of microparticles by endothelial cells promotes platelet/endothelial cell interaction under flow. *J Thromb Haemost* 2010;8:2810-9.
234. Agarwal R, Singh V, Journey P, et al. Mammalian cells preferentially internalize hydrogel nanodiscs over nanorods and use shape-specific uptake mechanisms. *Proceedings of the National Academy of Sciences* 2013;110:17247-17252.
235. Kenhub. Histology of the lower digestive tract: want to learn more about it? Volume 2020. <https://www.kenhub.com/en/library/anatomy/histology-of-the-lower-digestive-tract>, 2020.
236. Azevedo C, Pereira I, Sarmiento B. Intestinal mucosal models to validate functionalized nanosystems In: Wiley, ed. *Characterization of Pharmaceutical Nano- and Microsystems*, 2020.
237. Gonzalez LM, Moeser AJ, Blikslager AT. Porcine models of digestive disease: the future of large animal translational research. *Translational research : the journal of laboratory and clinical medicine* 2015;166:12-27.
238. Ovesen L, Bendtsen F, Tage-Jensen U, et al. Intraluminal pH in the stomach, duodenum, and proximal jejunum in normal subjects and patients with exocrine pancreatic insufficiency. *Gastroenterology* 1986;90:958-62.
239. Roopenian DC, Akilesh S. FcRn: the neonatal Fc receptor comes of age. *Nature Reviews Immunology* 2007;7:715.
240. Westerhout J, Steeg Evd, Grossouw D, et al. A new approach to predict human intestinal absorption using porcine intestinal tissue and biorelevant matrices. *European Journal of Pharmaceutical Sciences* 2014;63:167-177.
241. Sand KM, Bern M, Nilsen J, et al. Interaction with both domain I and III of albumin is required for optimal pH-dependent binding to the neonatal Fc receptor (FcRn). *J Biol Chem* 2014;289:34583-94.
242. Ayala JE, Bracy DP, McGuinness OP, et al. Considerations in the design of hyperinsulinemic-euglycemic clamps in the conscious mouse. *Diabetes* 2006;55:390-7.
243. Ayala JE, Samuel VT, Morton GJ, et al. Standard operating procedures for describing and performing metabolic tests of glucose homeostasis in mice. *Disease models & mechanisms* 2010;3:525-534.
244. Shaji J, Patole V. Protein and Peptide drug delivery: oral approaches. *Indian J Pharm Sci* 2008;70:269-77.
245. Pan Y, Xu H, Zhao HY, et al. Study on preparation and oral efficacy of insulin-loaded poly(lactico-glycolic acid) nanoparticles. *Yao Xue Xue Bao* 2002;37:374-7.
246. Cui FD, Tao AJ, Cun DM, et al. Preparation of insulin loaded PLGA-Hp55 nanoparticles for oral delivery. *J Pharm Sci* 2007;96:421-7.
247. Martin MG, Wu SV, Walsh JH. Ontogenetic Development and Distribution of Antibody Transport and Fc Receptor mRNA Expression in Rat Intestine. *Digestive Diseases and Sciences* 1997;42:1062-1069.
248. Pyzik M, Rath T, Lencer WI, et al. FcRn: The Architect Behind the Immune and Nonimmune Functions of IgG and Albumin. *J Immunol* 2015;194:4595-603.
249. Mezo AR, McDonnell KA, Castro A, et al. Structure-activity relationships of a peptide inhibitor of the human FcRn:human IgG interaction. *Bioorg Med Chem* 2008;16:6394-405.
250. Mezo AR, McDonnell KA, Hehir CA, et al. Reduction of IgG in nonhuman primates by a peptide antagonist of the neonatal Fc receptor FcRn. *Proc Natl Acad Sci U S A* 2008;105:2337-42.





---

## APPENDIX

---



## Appendix I

---

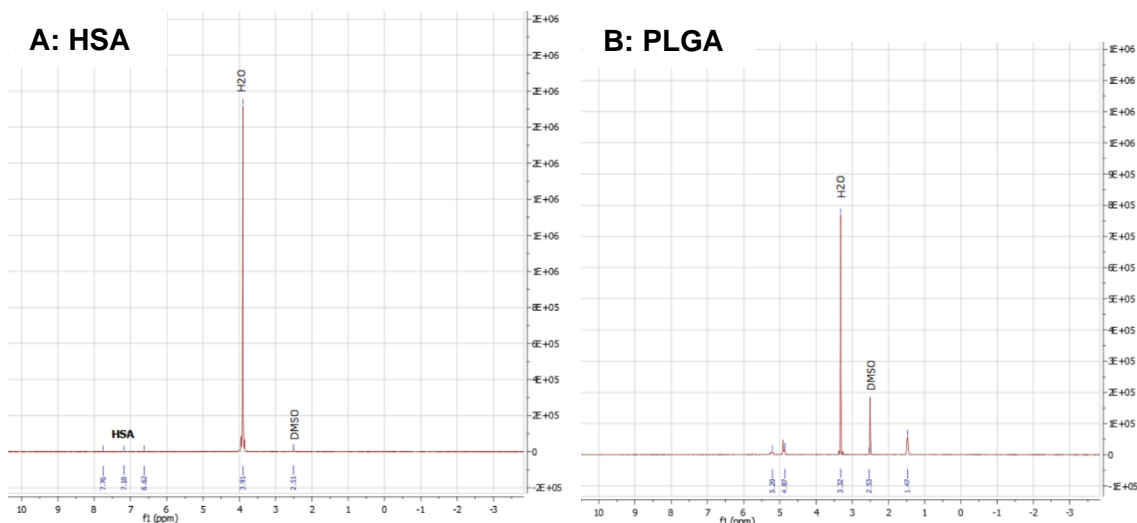
### NMR RESULTS

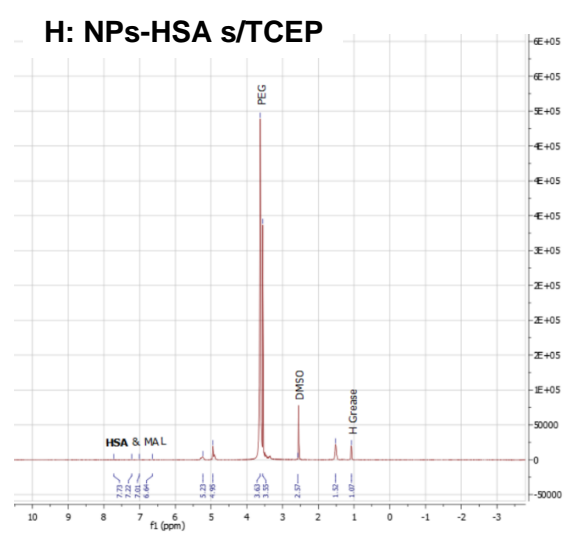
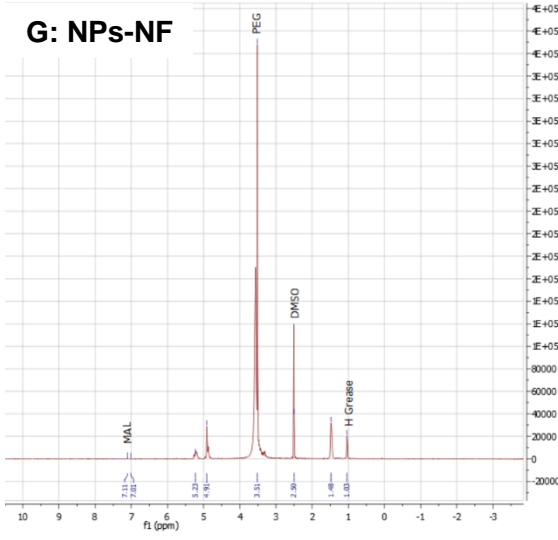
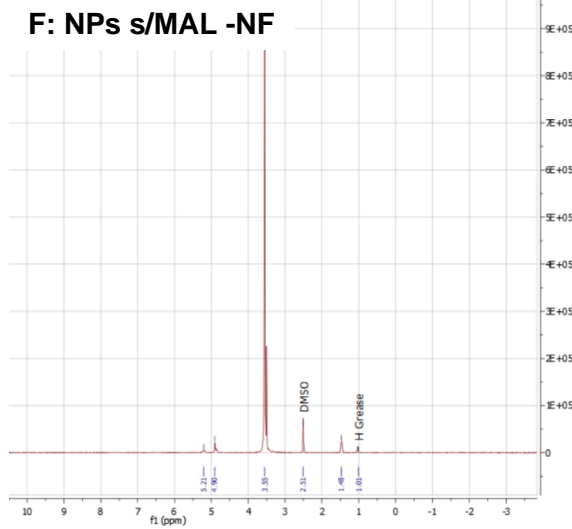
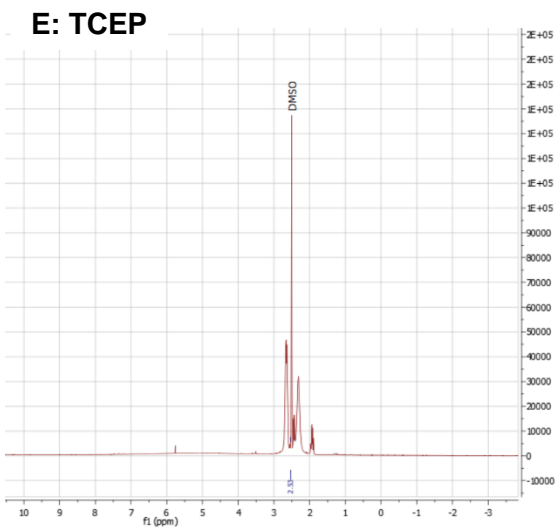
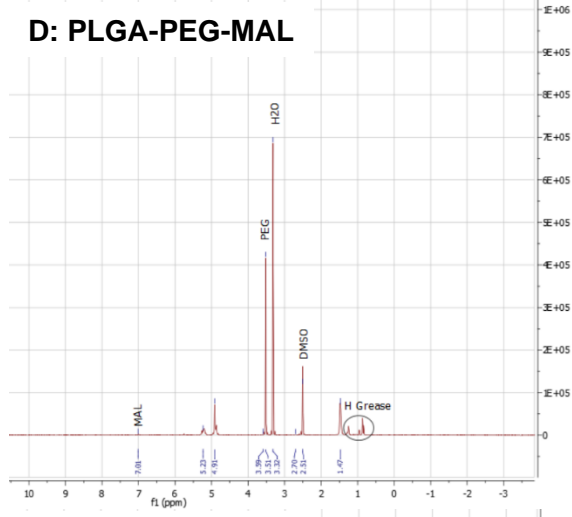
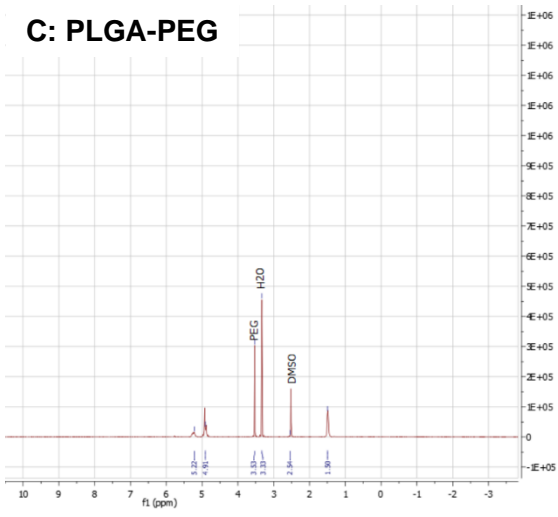
---



## Attempt to confirm the covalent thioether binding

To confirm the thioether binding, the functionalization ratio was increased for 1:1 (MAL:HSA), in order to be detected by NMR. In this way, the amount of HSA was ~5%, of the whole formulation, which is the minimum recommended amount for the detection. Through the results, it was possible to confirm some adsorption of albumin in the NPs' surface (**Figure A1**). This is evident when maleimide, necessary for the thioether bond, is not present (**Figure A1 I**) and when albumin was not reduced with TCEP, which favorably opens the albumin structure to facilitate the binding (**Figure A1 H**). In both cases, albumin was detected, suggesting adsorption. In **Figure A1 J**, where theoretically the covalent bond happens, it was not possible to verify a clear evidence due to the low concentration of the analyte. In parallel, each control, namely HSA (**Figure A1 A**), PLGA (**Figure A1 B**), PLGA-PEG (**Figure A1 C**), PLGA-PEG-MAL (**Figure A1 D**), TCEP (**Figure A1 E**), non-functionalized NPs without maleimide (**Figure A1 F**) and non-functionalized NPs (**Figure A1 G**), was runned and confirmed.





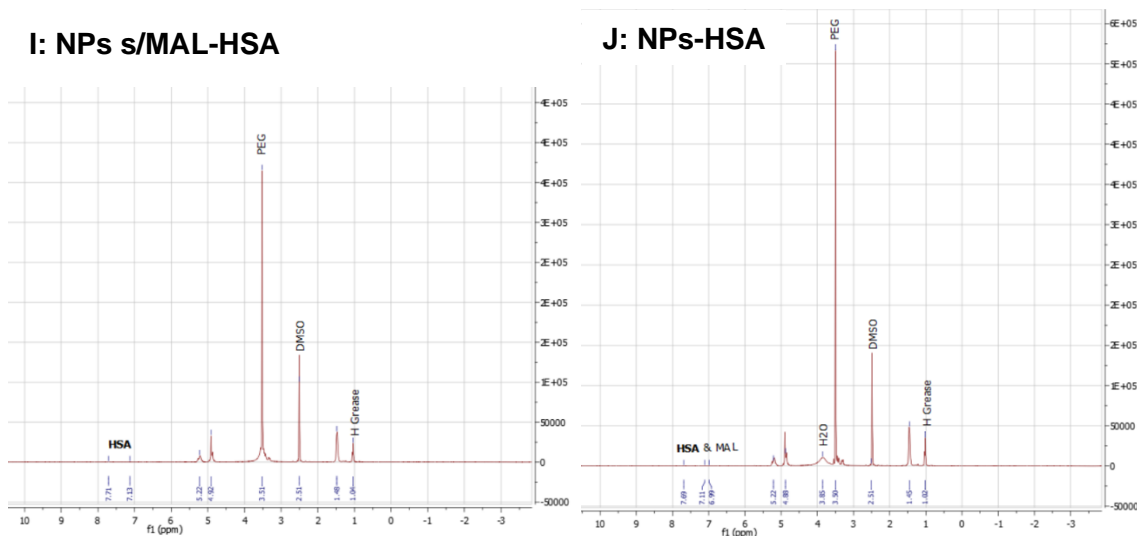


**Figure A1 | NMR analysis of all constituents from albumin-conjugated NPs loaded with insulin: (A) HSA, (B) PLGA, (C) PLGA-PEG, (D) PLGA-PEG-MAL, (E) TCEP, (F) non-functionalized NPs without maleimide, (G) non-functionalized NPs, (H) NPs functionalized with non-reduced albumin, (I) albumin-functionalized NPs without maleimide and (J) albumin-functionalized NPs.**

As a complementary assay, it was also tried the Ellman's assay. However, once again, samples were below the detection limit. When testing a standard curve of L-cysteine, it was confirmed that is not possible to detected at low concentrations (which were the working concentrations).





## Appendix II

---

### **THE EFFECT OF HYPERGRAVITY IN INTESTINAL PERMEABILITY**

---



This chapter was based in the following paper:

- **Azevedo C.\***, Almeida A.\*, Macedo M.H.\*, Pinto S.\*, Sarmiento B, van Loon J., The effect of hypergravity in intestinal permeability of nanoformulations and molecules, *European Journal of Pharmaceutics and Biopharmaceutics* 2021, 163: 38-48. (\*equal contribution)

As leader of this project, I idealized it and managed people, funding and sources. In this original paper, I actively participated in the conception and execution of the experimental work, as well as, data analyzes, their interpretation and discussion and in the writing, formatting and revision of the manuscript. These tasks were equally done by the co-authors. As leader, I had the role of validating each task at the end. The supervisors were responsible for reviewing and submit the manuscript. This paper was not previously included in other thesis and it is partially reproduced in this section. The integral version of the original paper was included at the end of the thesis, at **Appendix IV**.



## 1. Introduction

Oral administration is considered the preferred drug delivery route due to ease and patient compliance <sup>1</sup>. However, several drugs, as biopharmaceuticals, have limited bioavailability since they do not endure the harsh environment of gastrointestinal tract and poorly cross epithelial barriers <sup>2</sup>. In order to overcome the inefficient delivery, nanotechnology has been used as a promising strategy to overcome those biological barriers and to improve the intestinal absorption of drugs, which can be assessed by *in vitro* cellular models. In fact, nanosystems provide a stable biocompatible environment to encapsulate drugs, promote a controlled release and an efficient absorption <sup>2,3</sup>. These nanosystems are also responsible to improve the therapeutic efficacy, increasing the residence time and minimizing the unwanted side effects by driving drugs towards the site of action and increasing the concentration of drug in the targeted site <sup>4,5</sup>. After developing new drugs and incorporating them into nanosystems, it is important to evaluate their absorption profile in intestinal cellular models, such as the gold standard Caco-2 monoculture model <sup>6</sup>. The Caco-2 monoculture model relies on seeding Caco-2 cells in a semi-permeable support, Transwell® inserts, and culturing them to allow their differentiation into enterocyte-like cells, forming a monolayer that mimics the intestinal epithelium. Transwell® inserts membranes are very convenient to perform permeability assays, since they provide independent access to both sides of the monolayer (apical and basolateral sides). Therefore, during the permeability assays, it is possible to measure the amount of drug that was capable of crossing the cellular membrane, enabling a correlation to the absorption that will occur *in vivo*. According to the literature, mechanical forces of strain and fluid shear can stimulate CYP3A4 activity, glucose reuptake and mucus production, which is known to be absent in static Caco-2 models <sup>7</sup>. Particularly, studies indicated that barrier function, namely downregulation of occludin expression, decrease of transepithelial electrical resistance (TEER) values and increase of paracellular transport can be altered, in endothelial cells, measured after a 1-3 g hypergravity (HG) rocket launch profile exposure <sup>8</sup>, while an on-line measurements of the barrier integrity in endothelial cells exposed to 2-4 g HG showed an increase with increasing g <sup>9</sup>. However, a very limited set of studies has exploited the effect of HG on drug absorption, and none of them related with the intestinal permeability of orally delivered nanosystems. Here, it was intended to understand the impact of HG, as mechanical force, upon metabolic activity, integrity and expression of cellular components. Ultimately, it was evaluated how receptor-mediated transcytosis was affected after HG exposure, in order to find a more advantageous strategy to enhance

drug delivery. This innovative study will help researchers and pharmaceutical industries in oral drug development areas, since it may correlate more precisely the obtained results with the permeability in the human intestine.

## 2. Materials and Methods

### 2.1. Metabolic activity studies

The influence of HG on the metabolic activity of Caco-2 cells was evaluated by a resazurin and lactate dehydrogenase (LDH) assays. Caco-2 cells ( $4.0 \times 10^4$  cells per well) were seeded in 96-well plates in 200  $\mu$ L DMEM complete medium and were incubated for 24 h inside an incubator as described before. After that, medium was removed and cells were washed twice with 200  $\mu$ L of fresh pre-heated Phosphate-Buffered Saline (PBS) 1X to remove cellular debris and 200  $\mu$ L of fresh pre-heated DMEM without FBS was added to each well. Plates were then incubated for 4 h at 1.0 g, 37°C in an orbital shaker or hypergravity in LDC at 2.5 g, 5.0 g and 7.5 g at 37°C. Afterwards, the 96-well plates were centrifuged at 250 g for 10 min at RT to remove dead cells, and the supernatant was used to perform the LDH assay, while the remaining Caco-2 cells attached at the bottom of the plate were used for resazurin assay. For this, cells were washed twice with 200  $\mu$ L PBS 1X and then treated with DMEM complete medium containing 20% resazurin (0.1 mg/mL; Merck) during 2 h at 37°C, 5% CO<sub>2</sub> and 95% relative humidity, protected from light. After 2 h of incubation, the 150  $\mu$ L of each well was transferred to a black 96-well plate and the fluorescence was measured at 530/590 nm (excitation/emission wavelengths, respectively), using a plate reader (Victor Nivo™, PerkinElmer). The negative control consisted in cells incubated with 1% (v/v) of Triton X-100 in complete medium at 1.0 g and the positive control consisted in cells incubated with complete medium at 1.0 g, while shaking. A number of six replicates were performed for each group. The metabolic activity was expressed according to the following equation:

Equation (1)

$$\text{Cellular viability (\%)} = \frac{\text{Absorbance (Experimental value)} - \text{Absorbance (Positive control)}}{\text{Absorbance (Negative control)} - \text{Absorbance (Positive control)}} \times 100$$

To the 100  $\mu$ L of supernatant collected after centrifugation from the 96-well plates, 100  $\mu$ L of the reaction mixture composed by the catalyst solution and the dye solution (LDH Cytotoxicity Detection Kit, Takara Bio) were added to each well and incubated for 10 min at RT in the dark. The absorbance was measured at 492 nm and 690 nm, using a plate

reader (Victor Nivo™, PerkinElmer, Inc.). The negative control was composed by cells incubated with complete medium only at 1.0 g and the positive control was composed by cells incubated with 1% (v/v) of Triton X-100 in complete medium at 1.0 g, while shaking. A number of six replicates were performed for each group. The cellular cytotoxicity was expressed according to the following equation:

Equation (2)

$$\text{Cellular Cytotoxicity (\%)} = \frac{\text{Absorbance (Experimental value)} - \text{Absorbance (Negative control)}}{\text{Fluorescence (Positive control)} - \text{Fluorescence (Negative control)}} \times 100$$

To evaluate the effect of insulin-loaded NPs conjugated to WT albumin (Ins-NPs-Alb) upon metabolic activity of Caco-2 cells, a MTT assays was performed. In this case, Caco-2 monoculture was seeded at a density of 10 000 cells/well in 200  $\mu$ L per well and incubated for 4 hours. After that, the medium was aspirated, and the wells were washed twice with 100 mL of fresh pre-heated HBSS buffer (pH 7.4). After washing, 0.2 mL of the nanoparticle solutions corresponding to insulin amounts of 25, 50, 100 or 150  $\mu$ g/mL of insulin and the correspondent that was encapsulated in NPs were added to each well and the plates were incubated for a period of 4 and 24 h at 37°C. After the incubation period, the media was removed, and 150  $\mu$ L of 0.5 mg/mL MTT solution was added at each well, followed by incubation of the plates at 37°C during 4 h. The reaction was terminated by removal of the media and addition of 150  $\mu$ L of dimethyl sulfoxide. The levels of reduced MTT were determined by measuring the absorbance at 470 nm and 630 nm using a microtiter plate reader (Biotek-Synergy H1 Hibrid reader, using the Gen5 2.01 program). The % of MTT reduction was calculated as follows:

$$\text{Equation (3) MTT reduction (\%)} = \frac{\text{absorbance of treated cells}}{\text{absorbance of untreated cells}} \times 100$$

The final results of MTT reduction, are expressed as the percentage of the absorbance of control cells.

## 2.2. Expression of cellular components by immunocytochemistry

To understand if HG could have an impact in tight junctions (TJs) and drug transporters expression of cells, the models were subjected to the different g-levels, without any treatment. The TJ presence was assessed using claudin-1, which is an integral transmembrane protein, and zona occludens 1 (ZO-1), a peripheral TJ protein. The presence of the drug transporters peptide transporter 1 (PEPT-1) and neonatal Fc receptor (FcRn) was also evaluated. Mucin 2 (MUC2) was chosen to evaluate mucin



expression, since it is the mostly expressed mucin in the small intestine <sup>10</sup>. After 4 h of exposure to HG, samples were washed once with PBS 1X and fixed with 2% PFA for 20 min. Then, cells were washed three times with PBS 1X. To stain with different antibodies, a permeabilization step using a solution of 0.2% (v/v) Triton X-100 in PBS 1X for 5 min at RT was performed. Afterward, cells were washed thrice with PBS 1X for 5 min. A blocking step was performed using a solution containing 1.5% BSA and 5% FBS in PBS 1X for 1 h at RT. Inserts were incubated with the primary antibodies' solutions [rabbit anti-human Claudin-1 (1:200; SAB5500083-100, Sigma Aldrich) + mouse anti-human MUC2 primary antibody (1:50; ab118964, Abcam)], [rabbit anti-human ZO-1 primary antibody conjugated with Alexa Fluor 488 (1:50, SC-33725, Santa Cruz Biotechnology) + mouse anti-human PEPT1 primary antibody (1:100; ab203043, Abcam)] and [rabbit anti-human FcRn primary antibody (1:100; ab193148, Abcam) + Phalloidin (1:50; A22287, Thermo Fisher Scientific)] overnight at 4°C in a humidified chamber protected from light. Inserts were washed three times for 5 min with PBST and incubated with the secondary antibodies and DAPI to counterstain the nuclei (500 ng/mL; Sigma Aldrich). Depending on the primary antibodies used, Goat anti-Mouse Alexa Fluor 594 F(ab')<sub>2</sub> fragment of IgG (H+L) (1:500; A11020, Invitrogen), Goat anti-Rabbit Alexa Fluor 488 F(ab') fragment of IgG (H+L) (1:500; A11070, Invitrogen) and Donkey anti-Rabbit IgG H&L Alexa Fluor 594 preadsorbed (1:500; Ab150064, Abcam) were used. Secondary antibodies were added to samples for 2 h at 4°C in a humidified chamber protected from light. Cells were then washed twice with PBST and once with PBS 1X, all for 5 min. Inserts were mounted in slices using fluorescent mounting medium (Dako). Samples were left to dry protected from light and were maintained at 4°C until visualization by a spectral confocal laser scanning microscope TCS-SP5 AOBS (Leica). Since the aim was to compare the amount and localization of tight and adherens junctions between samples and also the expression of drug transporters, laser power and gain of each laser were maintained for all samples regarding each antibody.

### **2.3. Cell culture**

C2BBE1 [Caco-2 clone] (human colorectal adenocarcinoma) cells were acquired from ATCC and maintained in a complete medium consisting of Dulbecco's Modified Eagle's Medium (DMEM, ATCC) supplemented with 10% (v/v) fetal bovine serum (FBS, Biochrom) and 1% (v/v) antibiotic-antimitotic mixture (final concentration of 100 U/mL penicillin and 100 U/mL streptomycin) in 75 cm<sup>2</sup> T-flasks, inside an incubator at 37°C

and 5% CO<sub>2</sub> and 95% relative humidity. DMEM medium was changed three times per week. Caco-2 cells were used at passages 77 to 83. When confluence reached about 70% to 80%, cells were detached from the flasks by treating it with trypsin-EDTA at 37°C and transferred to another 75 cm<sup>2</sup> T-flasks or Transwell® and multiwell plates.

#### **2.4. Hypergravity exposure**

Cells were exposed to hypergravity in the Large Diameter Centrifuge (LDC) <sup>12</sup> at the TEC-MMG LIS Lab from the Technology Center (ESTEC) of the European Space Agency, ESA, in Noordwijk, The Netherlands. The LDC, with a diameter of 8 meters, allows for the application of up to 20 g. The four arms of the centrifuge hold at maximum six gondolas, plus one gondola in the center for a 1 g rotational control, if required (**Figure A2.1 A**). The gondolas of the centrifuge swing out, resulting in an acceleration vector that is always perpendicular to the samples surface. Because of this and its size, the systems avoid inertial shear forces common in smaller centrifuges <sup>13</sup>. The Transwell® multiwell plates were placed in a 37°C incubator (Thermo Scientific Heratherm IMC-18 mini incubator) that were accommodated in one of the gondolas. Since multi g-levels can be created during one run the experiment was performed during 2 rounds.

#### **2.5. Cellular integrity by hematoxylin and eosin staining**

To assess cellular integrity after exposure to different g-levels, hematoxylin and eosin (H&E) staining was performed. For this, inserts with the cells were washed once with PBS 1X for 5 min and fixed using 2% paraformaldehyde (PFA) in PBS 1X for 20 min at RT. Then, inserts were washed thrice with PBS 1X for 5 min and kept in PBS 1X at 4°C until further processing for paraffin embedding. Sections of 3 μm were obtained using an RM2255 microtome (Leica) and then stained for H&E. Briefly, sections were deparaffinized and rehydrated, stained for 3 min in Gil's Hematoxylin (Thermo Scientific), 6 min in running water, dehydrated, stained for 1 min in Eosin Y (Thermo Scientific), cleared, and mounted in Entellan (Merck). Representative images of each condition were obtained with a Light microscope Olympus DP 25 Camera Software Cell B.

#### **2.6. Intestinal permeability study**

Caco-2 cells were seeded at a density of  $1.0 \times 10^5$  cells per cm<sup>2</sup> onto 12-Transwell® cell culture inserts (surface area of 1.1 cm<sup>2</sup>, inner diameter of 12 mm and pore size of 1 μm; Millicell®) and were allowed to grow and differentiate for 21 days inside an incubator at

37°C, 5% CO<sub>2</sub> and 95% relative humidity (**Figure A2.1**). The medium was replaced every two/three days from the apical (0.5 mL) and basolateral (1.5 mL) sides. The permeability assays through the cell monolayers were performed in the apical-to-basolateral direction in Hank's Balanced Salt Solution (HBSS) buffer at 1.0 g, 37°C, in an orbital shaker and at 2.5 g, 5.0 g and 7.5 g, 37°C, in the LDC. Prior to the experiment, the cell culture medium was removed from both sides of the inserts and the monolayers were washed twice with pre-warmed HBSS. Then, the monolayers were allowed to equilibrate with 0.5 mL and 1.5 mL of HBSS in the apical and basolateral compartments, respectively, for 30 min at 37°C, 100 rpm, 1.0 g. After that, the HBSS of the apical compartment was removed and 0.5 mL of Ins-NPs-Alb (150 µg/mL insulin and 500 nM WT albumin) in HBSS with MES (pH 6) were added to the apical side. At different time-points (0.5, 1, 2, 3 and 4 h), TEER values were measured using an EVOM2 epithelial voltohmmeter equipped with a STX2 electrode (World Precision Instruments) and 200 µL of each sample was removed from the basolateral side of the inserts and replaced for the same volume of pre-warmed HBSS buffer (**Figure A2.1 B**). The amount of albumin that permeate the intestinal monolayer was quantified by enzyme linked immunosorbent assays (ELISA). The integrity of the cell monolayers was checked before and during the permeability experiment by measuring the TEER. The permeability percentage and apparent permeability coefficient (*P<sub>app</sub>*) of each formulation after 240 min of experiment were determined by the following equations:

$$\text{Equation (3)} \quad \% = \frac{\text{total mass}}{\text{theoretic mass}} \times 100$$

$$\text{Equation (4)} \quad P_{app} = \frac{dQ}{A \times C_0 \times dt} ,$$

where dQ (µg) is the total amount of compound detected in the basolateral side, A is the surface area of the insert (cm<sup>2</sup>), C<sub>0</sub> is the initial concentration in the apical side (µg/mL) and dt (s) is the time of the experiment.

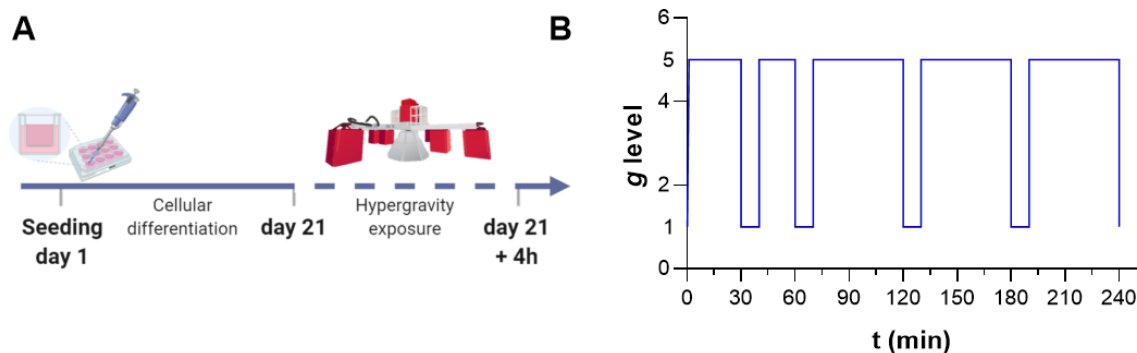


**Figure A2.1 | Experimental procedure of the intestinal permeability under different g-levels;**

**(A)** Schematic illustration of cell culture and HG exposure process: Caco-2 cells were cultured for 21 days, to allow their differentiation into enterocyte-like cells. After this, Ins-NPs-Alb were incubated for 4 h, at different g-levels; **(B)** Schematic diagram for an example of HG exposure, which entailed 10 min rest period, at different time points (0.5, 1, 2, 3 and 4 h). During this rest period at 1 g, TEER was measured and samples were removed from the basolateral side, for further quantification. This set up was performed for 2.5 g, 5.0 g and 7.5 g using the LDC and 1.0 g using an orbital-shaker, as control.

### **3. Results and Discussion**

#### **3.1. No influence of hypergravity in cellular metabolic activity**

The *in vitro* metabolic activity studies (resazurin and LDH assays) were performed using an intestinal cell line, Caco-2 clone, in order to resemble the intestinal enterocytes (representing 90% of the total intestinal epithelial cells)<sup>13, 14</sup>. To assess the effect of HG on the cellular metabolism, viability and cytotoxicity were measured after exposure to different g-levels (2.5 g, 5.0 g and 7.5 g), for 4 h inside a LDC from ESTEC-ESA. The obtained data showed similar cellular viability for nearly all the tested g-levels as compared with the shaker control (1.0 g), of approximately 100% (**Figure A2.2 A**). It was observed that at 2.5 g, cellular viability presented a statistically significant increase when compared to the control. However, in biological terms, this difference is not relevant. These outcomes were in accordance with the values obtained in the cytotoxicity assay (**Figure A2.2 B**), where no cytotoxicity was found. Despite there are no published studies reporting the influence of g-levels in the metabolism of intestinal epithelial cells, the obtained results are in line with the reported data using different cell lines. Previous studies on osteoblasts and human tendon cells demonstrated no significant influence on cellular viability after exposure to HG (5 g, 10 g, 15 g and 20 g) during 3 and 4 h, respectively<sup>15, 16</sup>. Additionally, the exposure of nasal epithelial cells to 10 g during three cycles of 20 min, with 20 min resting periods between each time, also did not cause significant loss of cellular metabolic activity<sup>17</sup>.

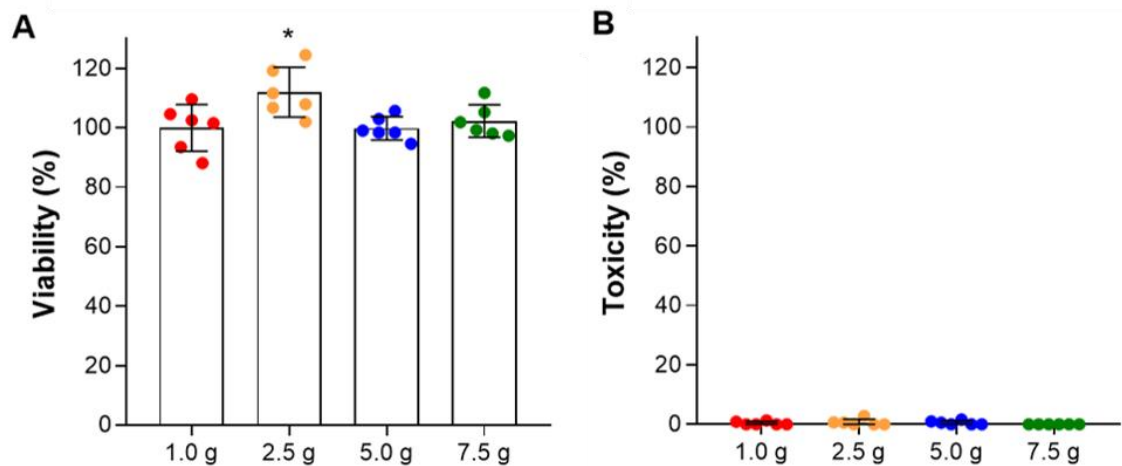


**Figure A2.2 | Evaluation of metabolic activity of Caco-2 clone cells after HG exposure. (A)** Evaluation of cellular viability through resazurin assays; **(B)** Evaluation of cellular toxicity through LDH assay. Shown are the arithmetic means  $\pm$  SD. \* $P < 0.05$  comparing with 1 g, by one-way analysis of variance (ANOVA) Dunnett's multiple comparison test.  $N = 6$ .

### 3.2. Hypergravity effect might induce a tipping point on the expression of cellular components

Before studying the effect of HG upon transport, it was crucial to understand how transporters and TJs proteins might be affected (**Figure A2.3 A**). Different TJs proteins were evaluated, namely claudin-1 and ZO-1. Claudins are integral transmembrane proteins, whereas ZO-1 is a peripheral membrane adaptor, acting as a bridge between the integral membrane TJs and the actin cytoskeleton, which is extremely important to maintain TJ formation and function<sup>18-20</sup>. Observing **Figure A2.3 B**, claudin-1 expression showed to decrease with the increase in the g-levels from reference conditions to 5.0 g and then, an increase, which can affect permeability, allowing a greater passage of compounds in higher HG conditions. In fact, claudins are the major determinant of the barrier function, defining the paracellular flux of small solutes<sup>21</sup>. Regarding ZO-1, although its role and importance is not yet clearly understood, some studies have been showing that cells with lower expression or absence of this protein present normal permeability, being more impactful in the assembly of other TJ proteins, as occludin and claudins<sup>22</sup>. Since it was not possible to observe significant changes in the expression of ZO-1 between the different g-levels, it is likely that this protein had no impact in permeability outcomes (**Figure A2.3 C**).

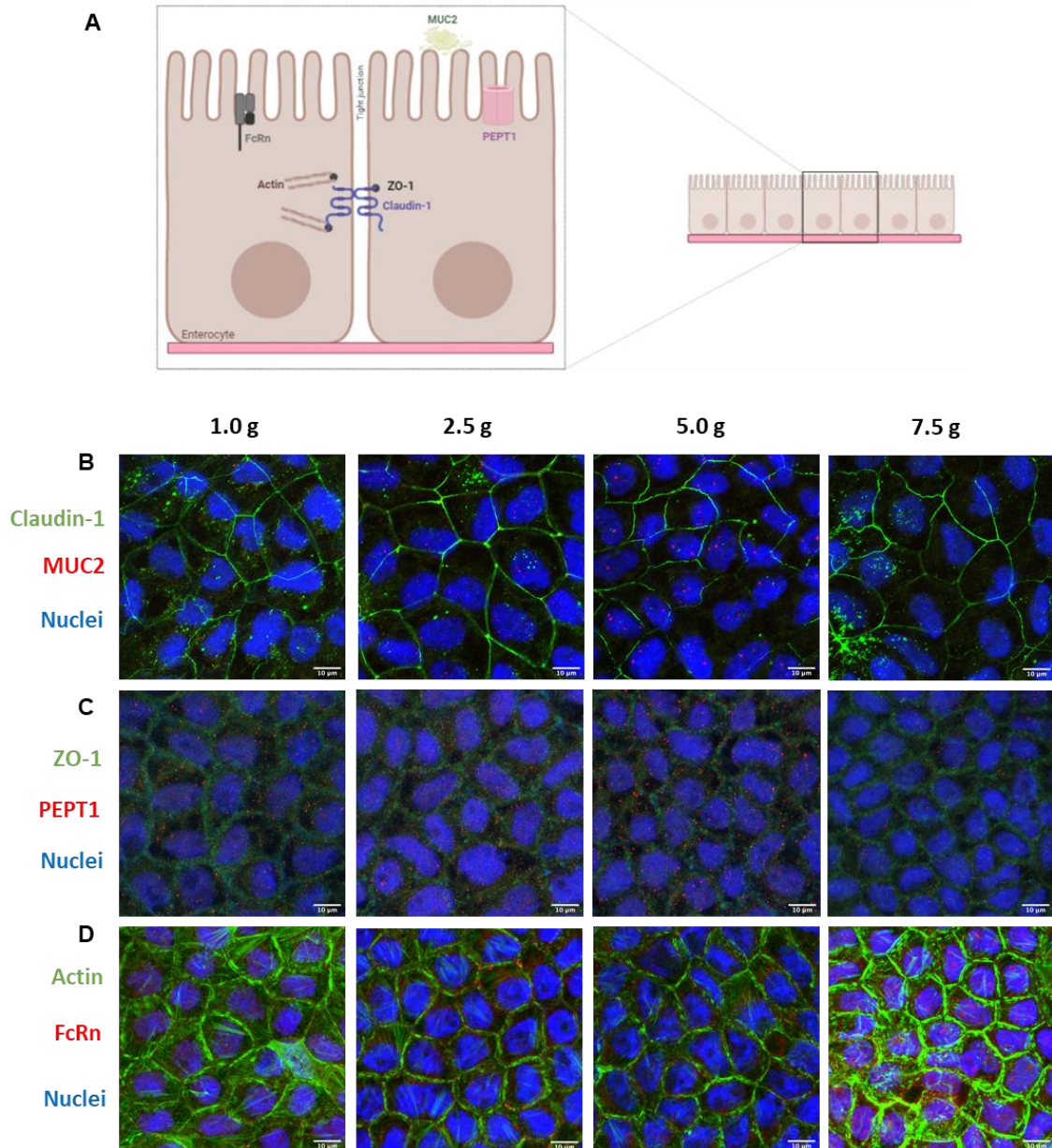


**Figure A2.3 | Assessment and comparison of cellular integrity at different g-levels. (A)** Schematic illustration of the studied cellular components involved in different transport vias. Visualization of **(B)** claudin-1 and MUC2; **(C)** ZO-1 and PEPT1, **(D)** actin and FcRn. Claudin-1, ZO-1 and actin are presented in **green**. MUC2, PEPT1 and FcRn are presented in **red**. Nuclei are **blue**.

There is no doubt that expression and assembly of TJs present a key role concerning the permeability outcomes of compounds that cross the intestinal barrier by the paracellular route. Nevertheless, when it comes to the transcellular pathway, the different drug transporters located in intestinal cells might have a wide impact on the permeability

of compounds, mostly in the ones that are substrates of these transporters. Taking into consideration that FcRn mediates the uptake of Ins-NPs-Alb, the expression of this transporter after the exposure to HG was evaluated. Despite PEPT-1 not being directly linked to the drugs tested in this study, its expression was evaluated, since this is an important uptake transporter present in intestinal cells and it is considered highly attractive as a drug target<sup>23</sup>. When looking at the expression of PEPT1 (**Figure A2.3 C**), its expression was increased from reference to 2.5 g and then a decrease was observed for the higher g-levels. When looking at the expression of FcRn, the behavior was different, where a decrease in the expression was observed from reference to 5.0 g, and a steep increase was observed at from 5.0 g to 7.5 g (**Figure A2.3 D**). In the case of actin, there was a decrease from reference to 2.5 g, a stable signal between 2.5 g and 5.0 g and then an increase at 7.5 g (**Figure A2.3 D**). MUC2 was evaluated because this is the most expressed mucin in the small intestine and it is known that mechanical forces can interfere with the production of mucus, as previously stated<sup>7,10</sup>. In this sense, it could be interesting to understand if HG might have an impact on its secretion. However, the change of MUC2 with the increase in g-levels seems to be negligible (**Figure A2.3 B**). Considering all these results, it was possible to conclude that HG affects protein expression in different ways. It is interesting to see that there seems to be a tipping point at 2.5 g or 5.0 g and proteins revert their behavior when reaching that point. For PEPT-1 this turning point occurs at 2.5 g, whether for FcRn and Claudin-1, this occurs at 5.0 g. Other interesting fact is that this change in behavior can occur in both directions, meaning protein expression can first increase and then decrease or the other way around, depending on the protein (**Figure A2.4**).

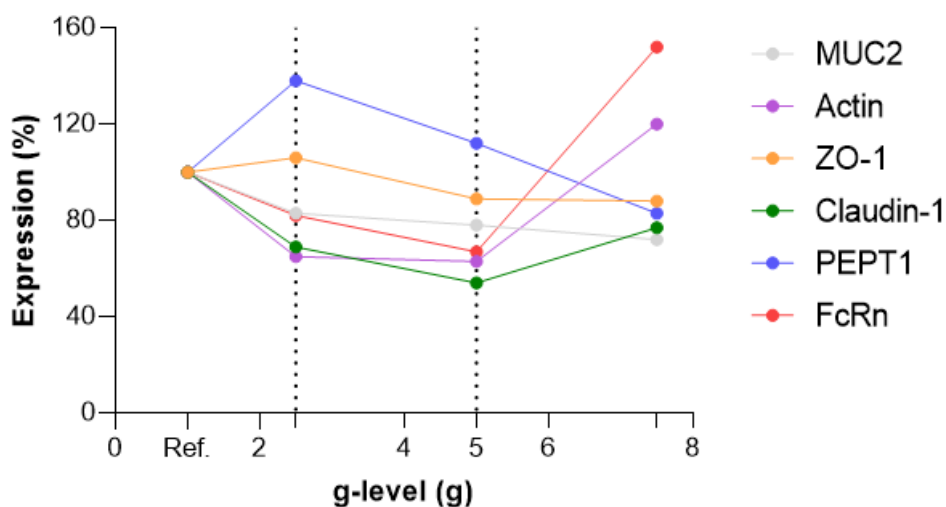


**Figure A2.4 | Overview sketch of the quantitative expression.** Analysis of the expression percentage of **(A)** transporters of influx and efflux; **(B)** components of tight junctions; **(C)** cytoskeleton and **(D)** mucus production, after exposure to different g-levels. The quantitative data are related to images presented at Figure 3. Quantification was done using ImageJ and each sample was normalized to the reference condition.

Regarding the localization of the transporters (**Figure A2.5**), FcRn it was present at the membrane and throughout the cytoplasm, which is in line with the literature, that states this transporter is located in the apical region of epithelial cells and within acidified endosomes <sup>25, 26</sup>. In the case of PEPT1, its apical localization was also confirmed <sup>27</sup>. When it comes the localization of different transporters, it was possible to conclude that HG did not have an impact in this regard, being that no differences were observed between the localization of the different proteins when comparing the different g-levels.

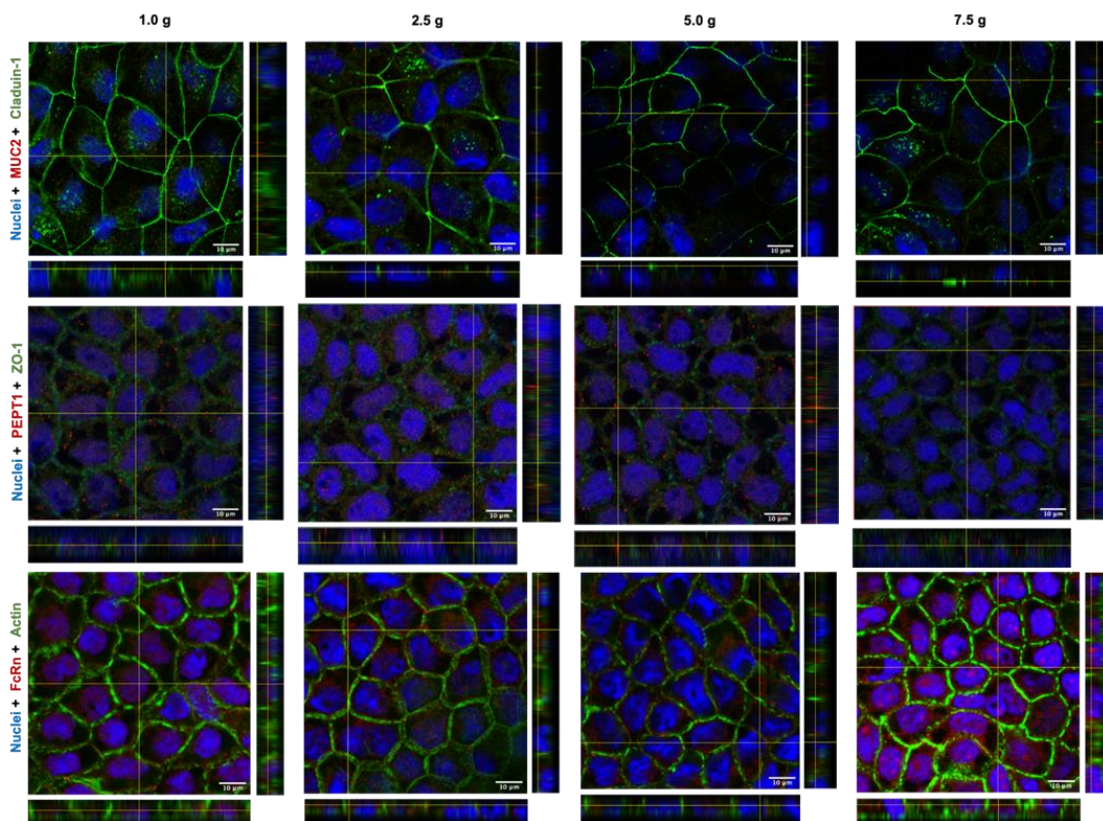


**Figure A2.5 | ORTO visualization of cellular components at different g-levels.** Claudin-1, ZO-1 and actin are presented in **green**. MUC2, PEPT1 and FcRn are presented in **red**. Nuclei are **blue**.



### 4.3. Barrier integrity is maintained after hypergravity exposure

To assess the cellular integrity and morphology after exposure to HG and samples, H&E staining was performed (**Figure A2.6**). In this assay two dyes were used, haematoxylin and eosin, that work as basic and acidic dyes, respectively. Haematoxylin was used to stain acidic structures in purple, as the nucleus containing nucleic acids. On the other hand, eosin dyes basic structures in pink, so it was used to stain cytoplasm and extracellular matrix, by containing proteins<sup>28</sup>. Taking this in mind, it was possible to verify that the cellular membrane integrity was generally maintained and attached to the Transwell® membrane. There was no significant difference of Ins-NPs-Alb to the standard conditions, demonstrating an apparent resemblance with the control group (1.0 g). Thus, the possibility of the effect be due to compounds and not due to the HG was discarded.

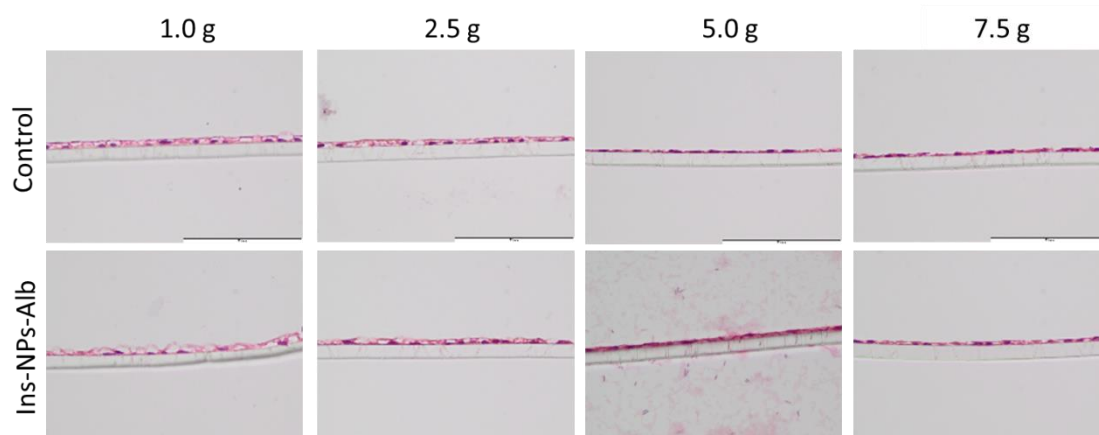


**Figure A2.6 | H&E staining to address the cellular integrity when exposing to different g-levels.** Ins-NPs-Alb were exposed to different g-levels (2.5 g, 5.0 g and 7.5 g) for 4 h. Cells with no treatment and shaking at 1.0 g were included as controls. Cytoplasm stained with **pink** and nucleus with **purple**. The Transwell® membrane is transparent and is right below the cellular monolayer. Scale bar = 100  $\mu$ m.

Actually, the safety of Ins-NPs-Alb was assessed, and the used concentrations were therefore compatible with the permeability model and quantifying method (**Figure A2.7**). However, some portions of the monolayer suffered membrane disruption and release of cytoplasm content, which could be due to handling procedure, as normally happens.

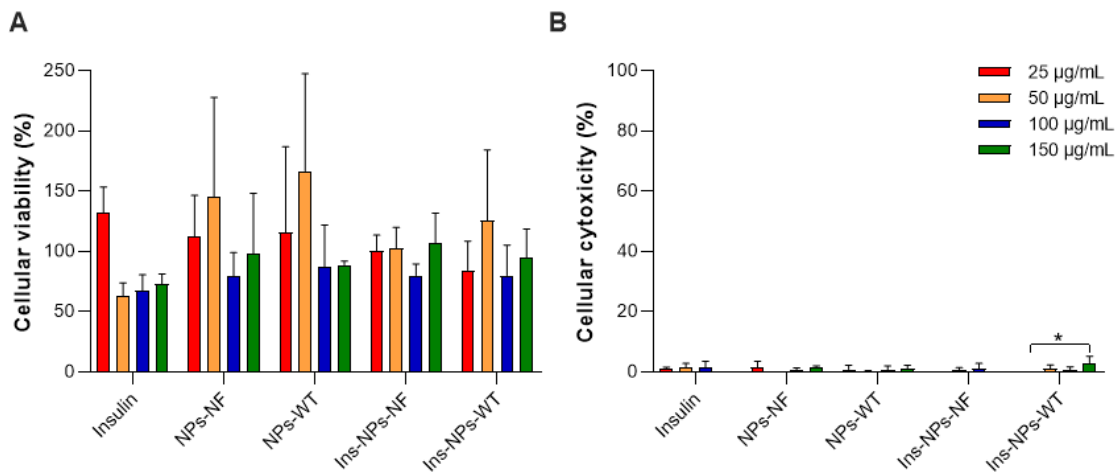


**Figure A2.7 | Evaluation of the safety of Ins-NPs-Alb in Caco-2 clone cells. (A)** Cellular viability, assessed by the MTT assays and **(B)** cellular cytotoxicity assessed by the LDH assay, of NPs loaded or not with insulin and conjugated or not with WT albumin. Free insulin was included as a control.

#### 4.4. Hypergravity interfered differently among transport mechanisms

In this study, Ins-NPs-Alb were used to evaluate the effect of HG upon receptor-mediated transcellular transport. The produced Ins-NPs-Alb were covalently conjugated to the free Cys34 of domain I of albumin. This allows NPs to be recognized by the FcRn (**Figure A2.8 A**).

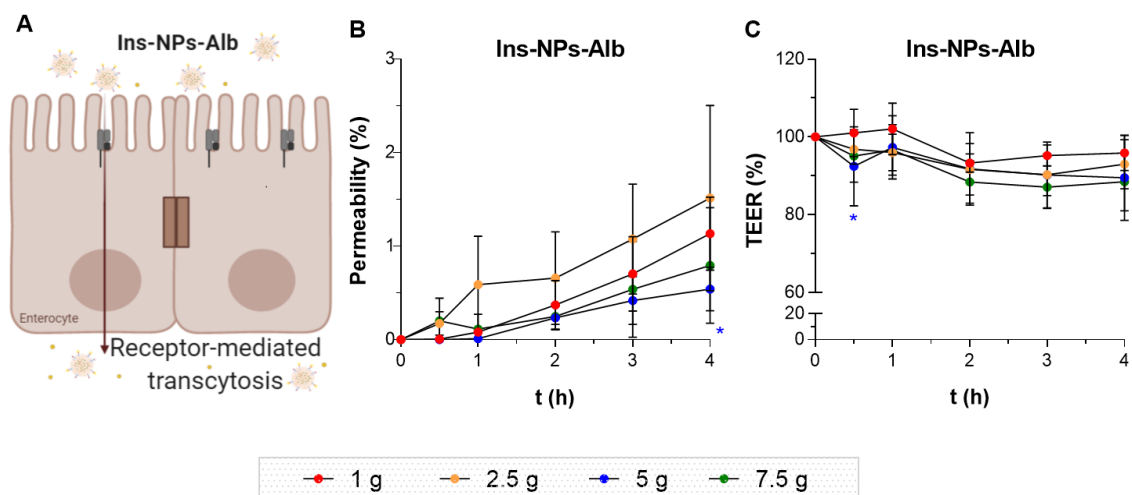


**Figure A2.8 | Intestinal permeability and respective TEER values of Ins-NPs-Alb after HG exposure. (A)** Schematic representation of FcRn-mediated transcytosis used by Ins-NPs-Alb through intestinal epithelial cells; **(B)** Permeability percentage of Ins-NPs-Alb, quantified by

ELISA, and **(C)** respective TEER values during 4 h of incubation at different g-levels. Shown are the arithmetic means  $\pm$  SD. \*P < 0.05 comparing with 1.0 g, by two-way analysis of variance (ANOVA) Dunnett's multiple comparison test. N=6 for all groups.

Reported data using the Caco-2 monolayer demonstrated that albumin transport is a saturable process, which indicates a receptor-mediated uptake. To confirm, with a competition assay, these authors showed that albumin-decorated NPs were 1.85-fold less transported when incubated with free albumin <sup>28</sup>. Here, after performing the permeability assay at different g-levels, it was shown that the transcytosis was similar to the reference, being concordant with the TEER values. Plus, it is possible to claim that the monolayer was maintained, and that NPs were not transported in a paracellular way, since the TEER values were barely reduced (**Figure A2.8 B and C**). For some reason, cells adapted better when in the presence of these NPs. Probably, the presence of insulin, albumin or biodegradable polymers can contribute to this. The confocal images suggested a switch behavior between 5.0 g and 7.5 g, since the FcRn expression decreased until 5.0 g and then increased, which might explain the significant decrease of permeability at 5.0 g after 4 h. All in all, this tendency seemed to not have biologic significance, since *Papp* ( $\pm$  SD  $\times 10^{-6}$  cm/s) values of Ins-NPs-Alb at standard conditions ( $0.36 \pm 0.12$ ) were similar to 2.5 g ( $0.48 \pm 0.31$ ), 5 g ( $0.17 \pm 0.07$ ) and 7.5 g ( $0.25 \pm 0.20$ ). As future perspectives, it would be interesting to increase the incubation time to confirm if the permeability tendency is maintained or if it has a statistical difference at some point. Taking all this into consideration, the transport mediated by FcRn suggested to not be affected by HG. This evidence adds to the basic understanding of the impact of mechanical stimuli i.e. HG, on drug transportation processes and can bring new treatment strategies for subjects exposed to different gravity environments.

#### 4. References

1. B. Sarmiento DF, T. Vasconcelos (Eds: L. Jorgensen, H. M. Nielsen), John Wiley & Sons, Ltd Polymer-based delivery systems for oral delivery of peptides and proteins, in: L. Jorgensen HMN, ed. *Delivery Technologies for Biopharmaceuticals: Peptides, Proteins, Nucleic Acids and Vaccines*: John Wiley & Sons, Ltd 2009:207.
2. Araujo F, Shrestha N, Granja PL, et al. Antihyperglycemic potential of incretins orally delivered via nano and microsystems and subsequent glucoregulatory effects. *Current Pharmaceutical Biotechnology* 2014;15:609-19.
3. Pereira C, Araújo F, Granja PL, et al. Targeting membrane transporters and receptors as a mean to optimize orally delivered biotechnological based drugs through nanoparticle delivery systems. *Current Pharmaceutical Biotechnology* 2014;15:650-658.
4. Moulari B, Beduneau A, Pellequer Y, et al. Nanoparticle targeting to inflamed tissues of gastrointestinal tract *Current Drug Delivery* 2013;10:9-17.
5. Sarmiento B, Ferreira D, Vasconcelos T. Polymer-Based Delivery Systems for Oral Delivery of Peptides and Proteins. In: Jorgensen L, Nielsen HM, eds. *Delivery Technologies for Biopharmaceuticals: Peptides, Proteins, Nucleic Acids and Vaccines*: John Wiley & Sons, Ltd, 2009:207-227.
6. Hidalgo IJ, Raub TJ, Borchardt RT. Characterization of the human colon carcinoma cell line (Caco-2) as a model system for intestinal epithelial permeability. *Gastroenterology* 1989;96:736-49.
7. Kim HJ, Ingber DE. Gut-on-a-Chip microenvironment induces human intestinal cells to undergo villus differentiation. *Integr Biol (Camb)* 2013;5:1130-40.
8. Sumanasekera WK, Sumanasekera GU, Mattingly KA, et al. Estradiol and dihydrotestosterone regulate endothelial cell barrier function after hypergravity-induced alterations in MAPK activity. *Am J Physiol Cell Physiol* 2007;293:C566-73.
9. Szulcek R, van Bezu J, Boonstra J, et al. Transient Intervals of Hyper-Gravity Enhance Endothelial Barrier Integrity: Impact of Mechanical and Gravitational Forces Measured Electrically. *PLoS One* 2015;10:e0144269.
10. Schneider H, Pelaseyed T, Svensson F, et al. Study of mucin turnover in the small intestine by in vivo labeling. *Scientific Reports* 2018;8:5760.
11. Loon JJWAv, Krausse J, Cunha H, et al. *The Large Diameter Centrifuge, LDC, for Life and Physical Sciences and Technology*, 2008.
12. van Loon JJWA, Folgering EHTE, Bouten CVC, et al. Inertial Shear Forces and the Use of Centrifuges in Gravity Research. What is the Proper Control? *Journal of Biomechanical Engineering* 2003;125:342-346.
13. Araújo F, Sarmiento B. Towards the characterization of an in vitro triple co-culture intestine cell model for permeability studies. *Int J Pharm* 2013;458:128-34.
14. Pereira C, Costa J, Sarmiento B, et al. 3.3 - Cell-based in vitro models for intestinal

- permeability studies. In: Sarmento B, ed. *Concepts and Models for Drug Permeability Studies*: Woodhead Publishing, 2016:57-81.
15. Searby ND, Steele CR, Globus RK. Influence of increased mechanical loading by hypergravity on the microtubule cytoskeleton and prostaglandin E2 release in primary osteoblasts. *Am J Physiol Cell Physiol* 2005;289:C148-58.
  16. Costa-Almeida R, Carvalho DTO, Ferreira MJS, et al. Continuous Exposure to Simulated Hypergravity-Induced Changes in Proliferation, Morphology, and Gene Expression of Human Tendon Cells. *Stem Cells Dev* 2018;27:858-869.
  17. Kim D, Kim YH, Kwon S. Enhanced nasal drug delivery efficiency by increasing mechanical loading using hypergravity. *Scientific Reports* 2018;8:168.
  18. Gonzalez-Mariscal L, Betanzos A, Nava P, et al. Tight junction proteins. *Prog Biophys Mol Biol* 2003;81:1-44.
  19. Lee B, Moon KM, Kim CY. Tight Junction in the Intestinal Epithelium: Its Association with Diseases and Regulation by Phytochemicals. *J Immunol Res* 2018;2018:2645465.
  20. Lee SH. Intestinal permeability regulation by tight junction: implication on inflammatory bowel diseases. *Intest Res* 2015;13:11-8.
  21. Gunzel D, Yu AS. Claudins and the modulation of tight junction permeability. *Physiol Rev* 2013;93:525-69.
  22. Umeda K, Matsui T, Nakayama M, et al. Establishment and characterization of cultured epithelial cells lacking expression of ZO-1. *J Biol Chem* 2004;279:44785-94.
  23. Estudante M, Morais JG, Soveral G, et al. Intestinal drug transporters: an overview. *Adv Drug Deliv Rev* 2013;65:1340-56.
  24. Ober RJ, Martinez C, Vaccaro C, et al. Visualizing the site and dynamics of IgG salvage by the MHC class I-related receptor, FcRn. *J Immunol* 2004;172:2021-9.
  25. Pyzik M, Rath T, Kuo TT, et al. Hepatic FcRn regulates albumin homeostasis and susceptibility to liver injury. *Proc Natl Acad Sci U S A* 2017;114:E2862-e2871.
  26. Shugarts S, Benet LZ. The role of transporters in the pharmacokinetics of orally administered drugs. *Pharm Res* 2009;26:2039-54.
  27. Fischer AH, Jacobson KA, Rose J, et al. Hematoxylin and eosin staining of tissue and cell sections. *CSH Protoc* 2008;2008:pdb.prot4986.
  28. Hashem L, Swedrowska M, Vilasaliu D. Intestinal uptake and transport of albumin nanoparticles: potential for oral delivery. *Nanomedicine (Lond)* 2018;13:1255-1265.

## Appendix III

---

### THE ALBUMIN TRIPLE MUTANT

---



## 1. Overview

In this section, it will be presented all data related to the albumin triple mutant. Besides the K573P mutation, the triple mutant also has T83N and N111E mutations (TNNEKP). These additional mutations confere a higher binding affinity to the receptor<sup>1</sup>. However, due to a conflict of interests, all these results were not allowed to be published yet. Despite this, these were techniques that I learned, work that I did and time that I spent.

## 2. Materials and Methods

### 2.1. Binding affinity to human FcRn

Biolayer Interferometry (BLI) was used to investigate the hFcRn affinity of engineered albumin variants comjugated to NPs. Measurements were performed on Octet RED96e system (ForteBio, Pall Life Sciences, USA). Biotinylated engineered albumin variants were conjugated to NPs and attached to the streptavidin sensor by biotin-streptavidin interactions. The Dip and Read™ High Precision Streptavidin (SAX) Biosensors were dipped in PBS (Sigma-Aldrich, USA) pH 7.4 containing 0.01% Tween® 20 (PBST) (Sigma-Aldrich, USA) before coating with biotinylated albumin-conjugated NPs in PBST pH 7.4. The sensor was then washed in PBST pH 7.4. Kinetic measurements were performed at increasing FcRn concentrations at room temperature in association buffer (25mM Na Acetate, 25mM NaH<sub>2</sub>PO<sub>4</sub>, and 150mM NaCl 0.01% Tween® 20. pH 5.5). Two baselines were made for 30 s using PBST pH 7.4 and 60 s using association buffer pH 5.5. Inicially, different NPs concentrations (0.78 µg/mL, 1.56 µg/mL, 3.10 µg/mL, 6.25 µg/mL, 12.50 µg/mL, 25.00 µg/mL and 50.00 µg/mL) were tested in order to find the desired loading curve. Kinetic measurements were performed from titrating 1 µM of FcRn. The association phase lasted for 200 s and the dissociation phase 300 sec followed by a regeneration step for 50 sec in PBST pH 7.4. Shaker speed for all measurements were 2200 rpm. All values were zero-adjusted, and the buffer reference value was subtracted. The three binding profiles were fitted to a 1:1 binding model after intercept correction using global fit.

### 2.2. Assessment of FcRn expression in Caco-2 cells

The FcRn expression in Caco-2 cells was assessed by Fluorescence-activated cell sorting (FACS) assay. Cells were detached from culture flask with versene and  $4 \times 10^6$  cells/mL were resuspended in FACS buffer (PBS with 1% BSA and 0.1% NaN<sub>3</sub>) for 30



min at 4°C. 100 µL of cells suspension was aliquot, in triplicate, into each well of a round-bottom 96-well plate. The plate was then centrifuged at 300 x g for 3 min at 4°C. After discard the supernatant, the blocked cells were resuspended in 12.5 µg/mL of mouse IgG2a antibody anti-FcRn, previously prepared in FACS buffer for 1 h at 4°C. Cells were washed three times with 100 µL of FACS buffer following centrifugation. Supernatant was discarded and cells were resuspended in goat anti-mouse Alexa 594, diluted 1:500 in FACS buffer, for 1 h at 4°C. Repeat the washing step and at the end, cells were prepared in PBS and transferred into FACS tubes.

## **2.3. In vivo studies**

### *2.3.1. Biodistribution*

#### *2.3.1.1. Production of fluorescent nanoparticles*

The synthesis of fluorescently labeled PLGA with Cyanine7.5 amine (Cy7.5; acquired from Lumiprobe, Hunt Valley, MD, USA) was conducted using click chemistry. The protocol used in this work was adapted from das Neves *et al.*<sup>2</sup>. Briefly, PLGA-COOH (0.012 mmol, 528 mg) and Cy7.5 (0.018 mmol, 14.75 mg) were combined to PLGA-Cy7.5 in DCM, in the presence of excess EDC (0.06 mmol, 11.50 mg) and NHS (0.06 mmol, 6.90 mg) under stirring for 2h. PLGA-Cy7.5 was then precipitated with 30 mL of ice-cold ethyl ether/methanol (1:1) and collected by 5min of centrifugation at 1,500 x g (Eppendorf 5810R Refrigerated Centrifuge). The polymer was re-dissolved in 1 mL of DCM and the precipitation process repeated twice as described, with 6 mL of ice-cold ethyl ether/methanol in order to remove residual EDC and NHS. Then the solution was dried under vacuum at room temperature for 48 h. The NPs production was conducted according to what was mentioned before on **Chapter III - Section 3.3.1**, including 0.02% (w/w) of PLGA-Cy7.5.

#### *2.3.1.2. Imaging*

Fresh fluorescent NPs were orally administered as previously mentioned. Whole body near infrared (NIR) imaging of animals treated with NPs-Cy7.5 was performed at pre-established time points by using an IVIS Lumina LT system (Perkin Elmer, Waltham, MA, USA) after brief anesthetization with inhalational isoflurane. Abdominal fur was removed with a hair clipper before imaging. Background signal from non-treated animals was used to establish relevant radiance signal ( $\geq 0.4 \times 10^8 \text{ p cm}^2 \text{ s}^{-1} \mu\text{W}^{-1}$ ).

Animals were sacrificed at 2 h or 8 h by isoflurane overdose followed by cervical

dislocation. Necropsy was then performed and the liver, kidneys, pancreas, heart, lungs, stomach, as well as the GIT were isolated. Tissues were placed in petri dishes and analyzed using the IVIS system. Quantification of the radiant efficiency from same sized regions including complete excised tissues was performed using Living Image<sup>®</sup> software v. 4.4 (Caliper, Hopkinton, MA, USA).

### 2.3.2. *Pharmacokinetic*

For plasmatic insulin measurements, at the time points of 0 h, 2 h, 4 h and 8 h after administration, the withdrawn blood was collected into Eppendorf tubes containing 0.5 M of EDTA (10% of the final volume) to prevent blood clotting. The samples were centrifuged at 2,000 x g for 10 min at 4°C. The supernatants were collected and stored at -80°C until further studies. Insulin quantification was done according to the manufacturer's instructions using a rat insulin ELISA kit from Mercodia (Sweden).

## 3. Results and discussion

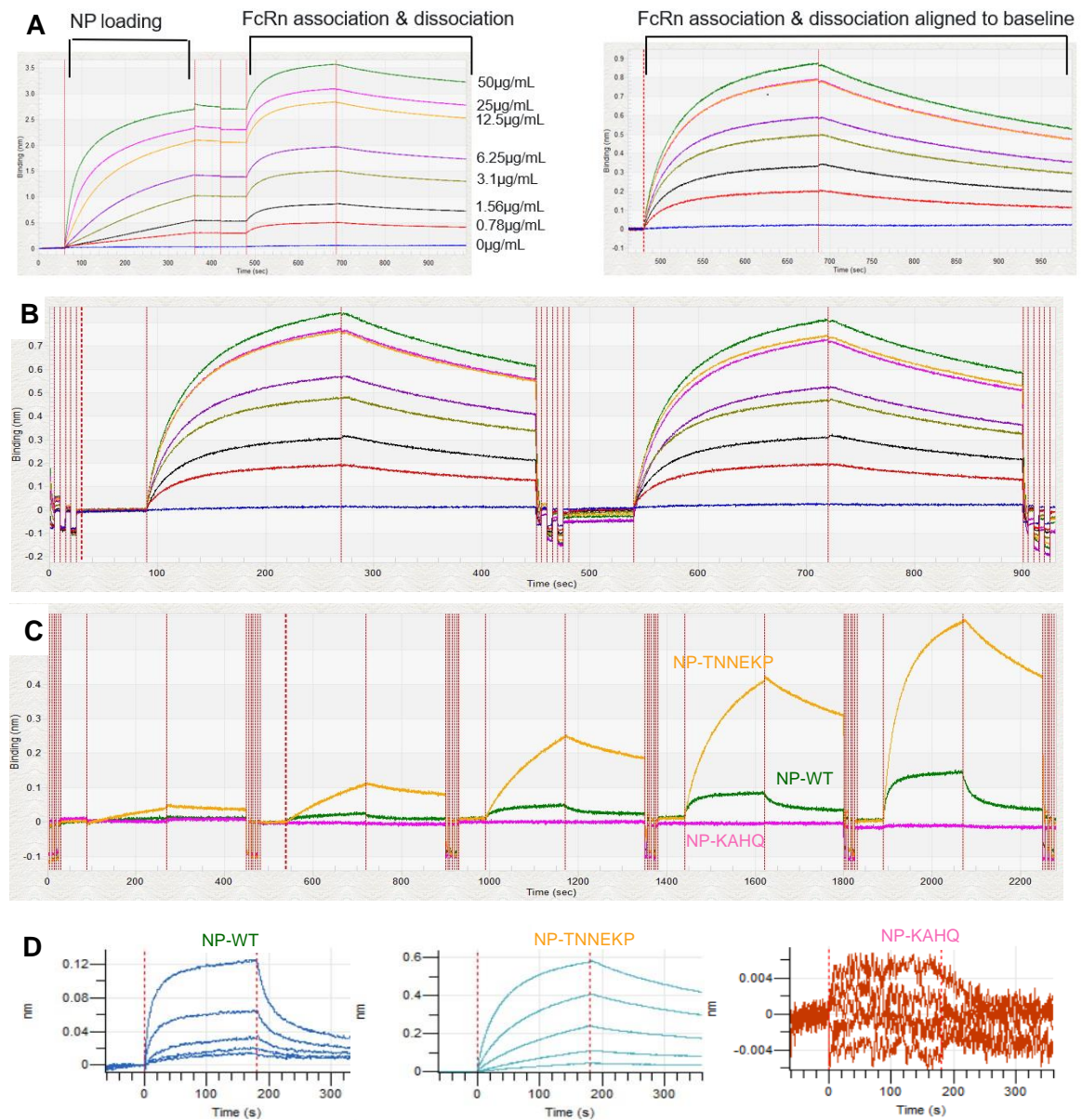
### 3.1. Physical-chemical characterization

NPs conjugated to the triple mutant were characterized physical and chemically. It was obtained NPs-TNNEKP with 153 nm in size, monodisperse, a zeta potential of -9.6 mV and a CE of 90%. These results are in line with the NPs conjugated with other albumin variants, detailed in Table 3.

### 3.2. Binding affinity to human FcRn

A preliminary assay using bio-layer interferometry (BLI) was performed to address the binding profile of albumin variants. Initially, several NPs concentrations were tested and it was selected the optimal loading concentration. At 6.25 µg/mL it was possible to observe desired loading curve characteristics, significant loading signal with fairly slow initial binding that does not go to saturation, and a high signal in the association step (**Figure A3.1 A**). After this, a regeneration test was performed to analyze the effectiveness of dissociation (**Figure A3.1 B**). Buffer at pH 7.4 was the suitable solution for regeneration. A kinetic assay was also done with NPs-KAHQ, NPs-WT and NPs-TNNEKP, as shown in **Figure A3.1 C** and their shape and intensity in **Figure A3.1 D**. Through these results it was possible to do an overlay plots comparison and see a clear difference on shapes and amplitude, between albumin variants.

A 1-1 fitting was done but in case of the triple mutant it seems that it was not the best one. However, it was possible to obtain the kinetic parameters:  $K_D = 1.19 \times 10^{-7} \text{ M}$ ,  $k_a = 1.43 \times 10^4 \text{ M}^{-1} \text{ s}^{-1}$  and  $k_d = 1.71 \times 10^{-3} \text{ s}^{-1}$ . Here, albumin was biotinylated on the free cysteine, so the conjugation was based on adsorption, meaning physical reaction. In the future, it would be worth to try to fix FcRn, through IgG, and titrate NPs, also to avoid avidity.



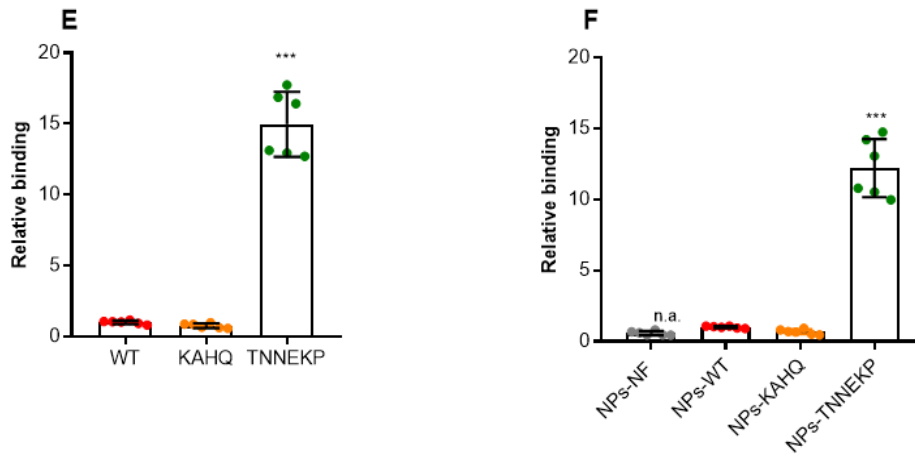


**Figure A3.1 | Analysis of protein interaction using Bio-layer interferometry (BLI): (A)** screening of NPs concentrations; **(B)** regeneration test, **(C)** kinetic test of the three formulations, against different FcRn concentrations, **(D)** differences between shape and intensity of the FcRn binding affinity with engineered albumin conjugated NPs. Relative binding of **(E)** naked human albumin variants and **(F)** NPs decorated with human albumin variants to human FcRn at pH 5.5, quantified by ELISA.

Similar to the results from **Figure 13**, the binding affinity of the triple mutant to FcRn, was evaluated using the anti-FcRn 2-way ELISA for naked human albumin variants (**Figure A3.1 E**) and for NPs decorated with human albumin variants (**Figure A3.1 F**). The results from both techniques, BLI and ELISA, were in agreement, demonstrating the high affinity of the triple mutant, compared to WT.

### 3.3. FcRn expression in Caco-2 cells

Before evaluating the permeability, it was important to understand the differences of FcRn expression between Caco-2 cells and the commonly used Caco-2 C2BBE1 clone (**Figure A3.2**).

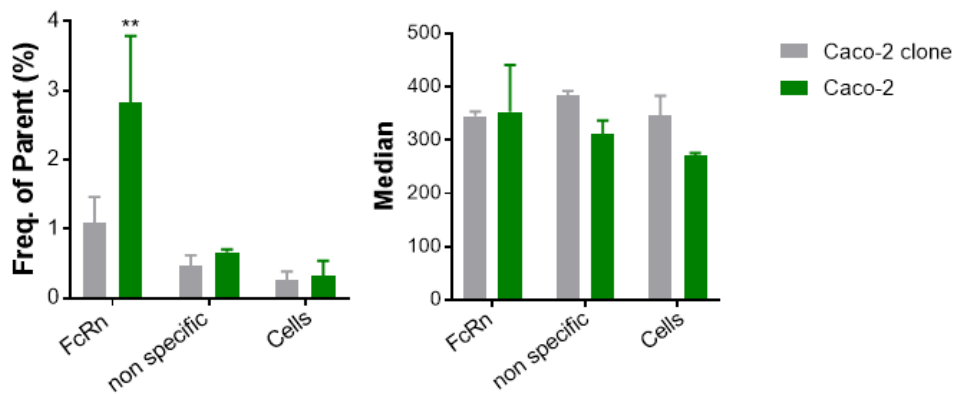


**Figure A3.2 | FcRn expression in Caco-2 cells and Caco-2 C2BBE1 clone: (A)** Frequency of parent, corresponding to the fluorescence and **(B)** median of the considered cells.

According to the results Caco-2 cells expressed more FcRn, thus this was one of the cell lines used in the permeability assay.

### 3.4. *In vitro* experiments

Similar to the results from Figures 14, the FcRn-mediated transcytosis was performed for the triple mutant before **(Figure A3.3 A)** and after conjugation to NPs **(Figure A3.3 B)**, using MDCK-hFcRn cells, with the protocol described in **Chapter III at section 7.1**.

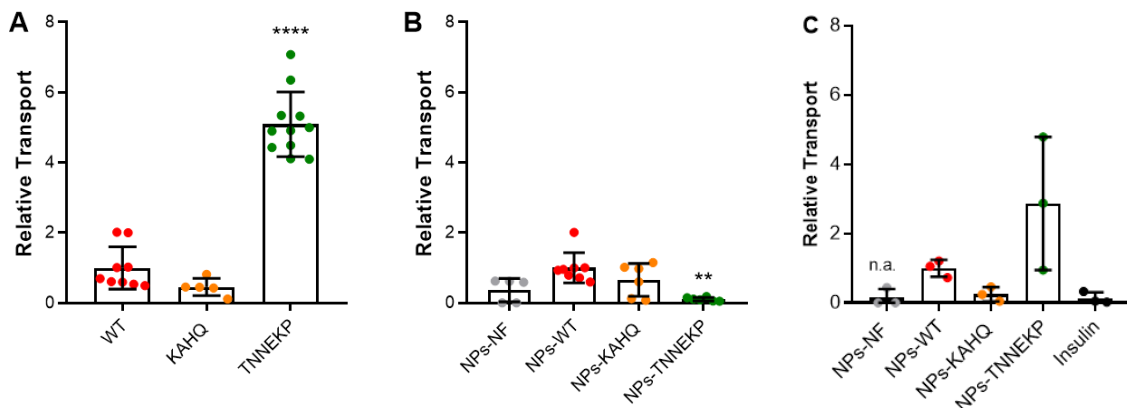


**Figure A3.3 | The relative transport of: (A)** naked albumin variants (WT, KAHQ and TNNEKP), and **(B)** albumin-decorated NPs detected in media collected at the basolateral side of MDCK-hFcRn cells 4 h after adding the variants to the apical side (n=5-9). The amounts were quantified by two-way anti-albumin ELISA. **(C)** Relative transport of albumin-decorated NPs detected in media collected at the basolateral side of polarized Caco-2 cells. The amounts were quantified by two-way anti-insulin ELISA. In both cases, WT albumin or NPs decorated with WT albumin were set to 1, as a control. Shown are the arithmetic means  $\pm$  SD. \*\*P<0.005, \*\*\*P<0.0001 comparing with WT or NPs-WT by one-way ANOVA Dunnett's multiple comparison test.

Unexpectedly, the transport behavior of the triple mutant, in MDCK-hFcRn cells was not the same after conjugation to NPs, which did not happen in Caco-2 cells (**Figure A3.3 C**). The permeability assay with Caco-2 cells was performed in reference conditions as described in **Appendix II** at **section 2.6**. Both assays were quantified by ELISA, as detailed in **Chapter III** at **section 4.5**. Additionally, the FcRn-mediated recycling was also analyzed, according to the protocol detailed at **Chapter III** at **section 7.2**, as presented in the **Figure A3.4**. Again, after conjugation to NPs, the ameliorate effect of the triple mutant was interfered, either in uptake and recycling in endothelial cells. In both experiments more replicates should be added to clarify this issue.

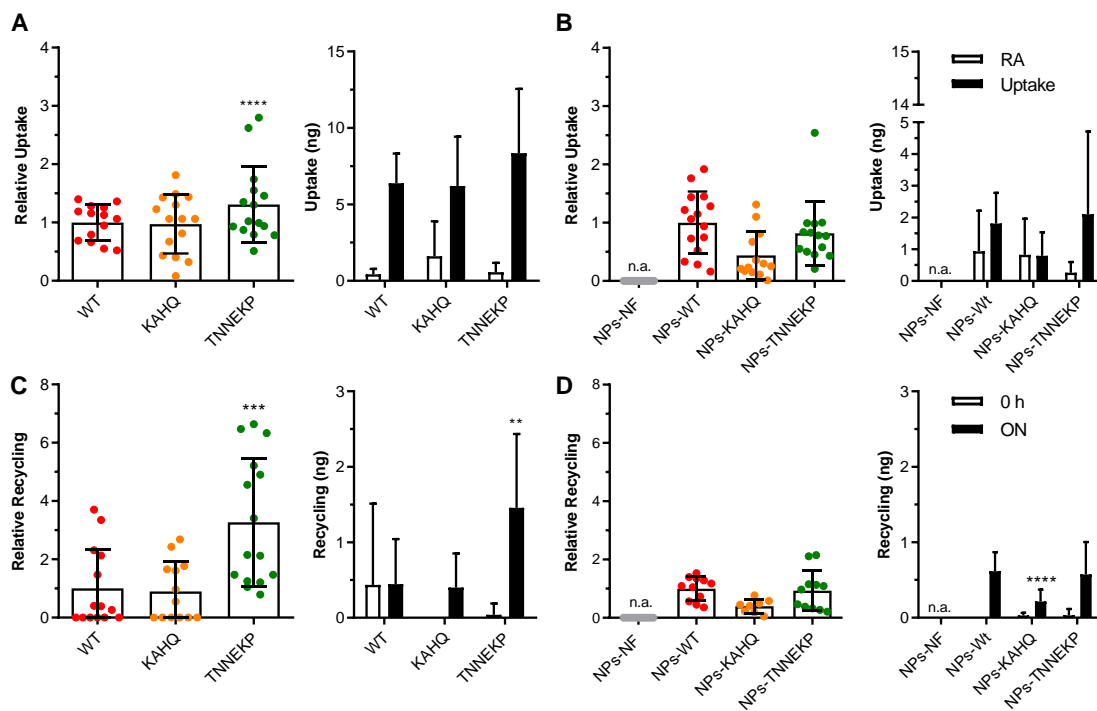


**Figure A3.4 | The relative uptake and recycling of: (A) naked albumin variants (WT, KAHQ and TNNEKP), and (B) albumin-decorated NPs, and their correspondent amount quantified by ELISA (n=9-15) in HMEC1-hFcRn cells. Shown are the arithmetic means  $\pm$  SD. \*\*\*\* $P < 0.0005$ , \*\*\*\* $P < 0.0001$  comparing with WT or NPs-WT, by one-way ANOVA Dunnett's multiple comparison test.**

### 3.5. NPs are widely maintained in the gut

As a preclinical validation, the biodistribution and PK/PD profiles of these NPs were

evaluated, using transgenic mice induced with T1DM.

To confirm if NPs reach and are retained in the gut, a biodistribution study was done using IVIS, to detect NPs-cy7.5. In fact, the obtained images (Figure A3.5 A) suggest that after 30 min, NPs are located in the gut area. However, this is only indicative, since the strength of the signal is dependent of the plan of where the NPs are. Visually, the triple mutant seems to have a higher signal, however when the fluorescence is quantified, it was verified that there is no significative difference between formulations and over time (Figure A3.5 B). The same trend was observed in GIT, after euthanizing animals at 2 h (Figure A3.5 C and D). At this point, the fluorescence was already at the colon, so in the future it would be better to desiccate earlier. According to literature, albumin formulations have a faster and deeper distribution and a slower elimination, improving the efficacy<sup>3</sup>. Also, FcRn was found to enhance tissue distribution and penetration while the targeting prevents the drugs' excretion. Thus, the delivery of albumin-conjugated NPs interferes with drug distribution and elimination through a FcRn-mediated process<sup>4</sup>.

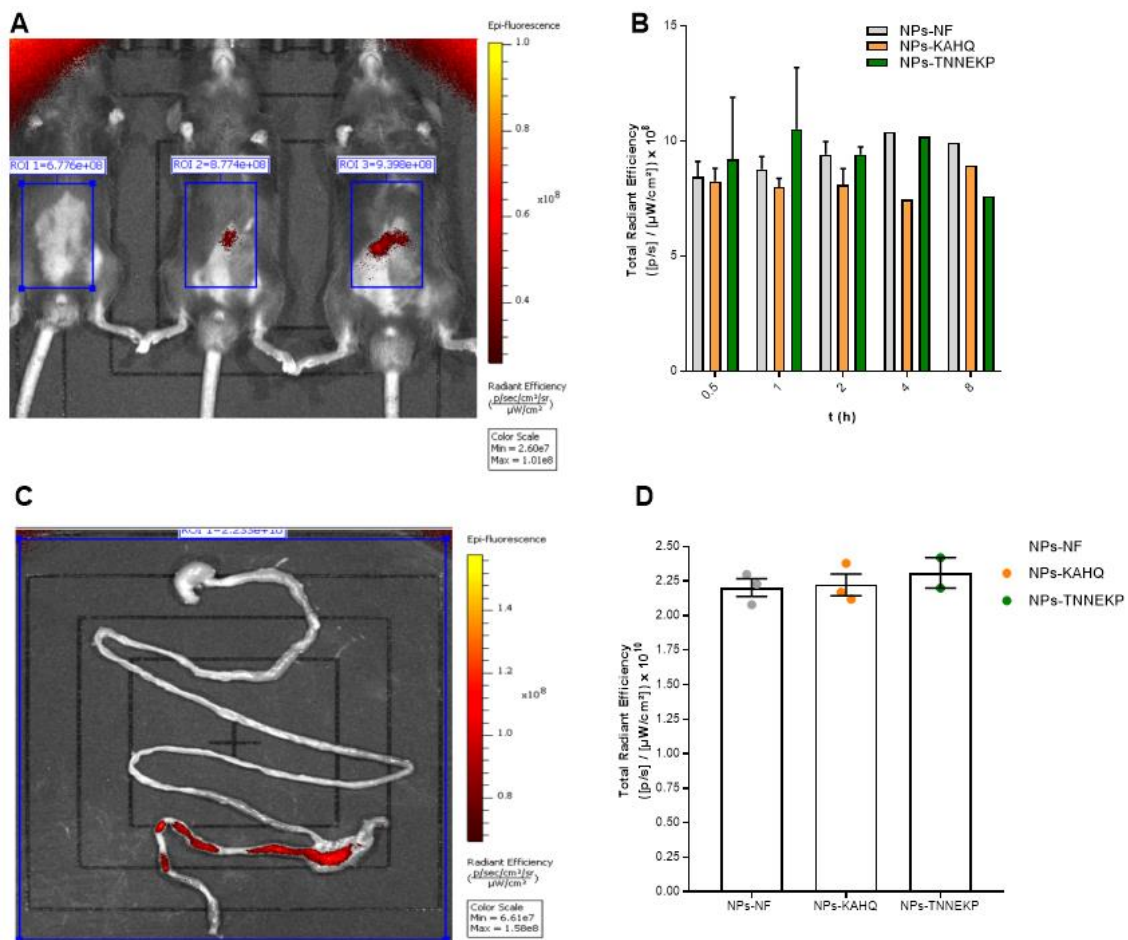
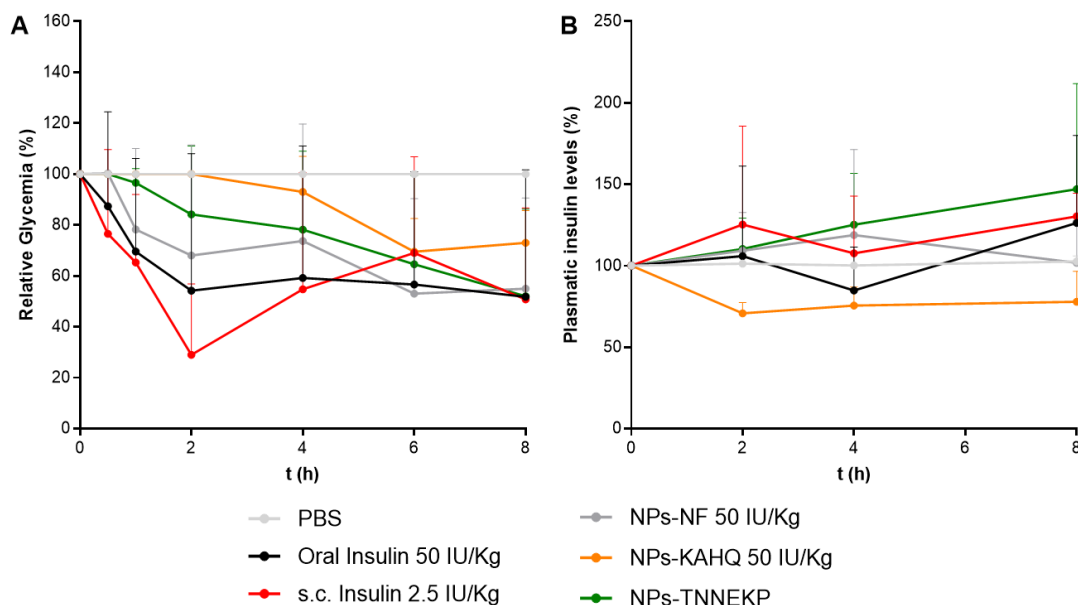


Figure A3.5 | Biodistribution *in vivo* detection. (A) Qualitative analysis of the fluorescence,

after 30 min of administration of NPs with cy7.5 and respective blanks without cy7.5; and **(B)** quantitative of the fluorescence present in mice, at different time points during 8 h. **(C)** Qualitative and **(D)** quantitative analysis of the GIT after 2 h of administration. NPs without cy7.5 were included as controls. All images were normalized by the control (same scale and ROI window).

### 3.6. The hypoglycemic effect

Also the PK/PD profiles were assessed, using hFcRn transgenic mice induced with diabetes. These animals were fasted for a shorter time (4-6 h), due to the animal well-being, which might lead to a less evidenced effect. In fact, results related to glycemia levels (**Figure A3.6 A**) are not in line with the plasmatic insulin levels (**Figure A3.6 B**). Looking to the PD profile, it seems that NPs-TNNEKP has the behavior that should be from oral insulin. Notwithstanding, the PK profile is in line with the *in vitro* results, since the triple presented higher levels. As expected, on the opposite side, it is NPs-KAHQ, oral insulin and NPs-NF, with lower insulin levels. NPs present a controlled and prolonged effect, being enhanced with the triple mutant.



**Figure A3.6 | Hypoglycemic effect of T1DM-induced mice following i.p. administration of STZ (150 mg kg<sup>-1</sup>).** **(A)** Plasma glucose levels and **(B)** Plasma insulin level following PBS, oral insulin 50 IU/Kg, s.c. insulin 2.5 IU/Kg, non-functionalized NPs (NPs-NF) and functionalized with KAHQ and TNNEKP (n = 5-6 animals).

From the obtained results it was possible to calculate the PK parameters, as presented in the following table:



**Table A3.1** | The pharmacokinetic parameters.

PK parameters	Dose (IU)	t <sub>max</sub> (h)	C <sub>max</sub> (µg/L)	AUC 8h (µIU h/mL)	Relative Bioavailability 8h (%)
PBS	0	8	2.033	707.44	4.31
Oral insulin	50	8	2.619	715.95	4.36
S.c insulin	2.5	2	3.536	821.60	100
NPs-NF	50	4	2.538	773.92	4.71
NPs-KAHQ	50	8	2.369	538.50	3.28
NPs-TNNEKP	50	8	3.015	885.12	5.39

#### 4. References

1. Delahay KAN, GB), inventor NOVOZYMES BIOPHARMA DK A/S, assignee. ALBUMIN VARIANTS. United States. 2015.
2. J. das Neves, F. Araújo, F. Andrade, J. Michiels, K.K. Ariën, G. Vanham, M. Amiji, M.F. Bahia, B. Sarmiento, In vitro and ex vivo evaluation of polymeric nanoparticles for vaginal and rectal delivery of the anti-HIV drug dapivirine, *Molecular Pharmaceutics*, 10 (2013) 2793-2807.
3. N. Chen, Y. Li, Y. Ye, M. Palmisano, R. Chopra, S. Zhou, Pharmacokinetics and pharmacodynamics of nab-paclitaxel in patients with solid tumors: disposition kinetics and pharmacology distinct from solvent-based paclitaxel, *Journal of Clinical Pharmacology*, 54 (2014), 1097.
4. F. Li, H. Yuan, H. Zhang, M. He, J. Liao, N. Chen, Y. Li, S. Zhou, M. Palmisano, A. Yu, M. Pai, D. Sun, Neonatal Fc Receptor (FcRn) Enhances Tissue Distribution and Prevents Excretion of nab-Paclitaxel, *Molecular Pharmaceutics*, 16 (2019) 2385-2393.

## Appendix IV

---

### PUBLISHED AND SUBMITTED PAPERS

---



## Prevention of diabetes-associated fibrosis: Strategies in FcRn-targeted nanosystems for oral drug delivery

*Cláudia Azevedo<sup>1,2,#</sup>, Soraia Pinto<sup>1,2,#</sup>, Sopisa Benjakul<sup>3,4,#</sup>, Jeannette Nilsen<sup>3,4</sup>, Hélder A. Santos<sup>5,6</sup>, Giovanni Traverso<sup>7,8,9</sup>, Jan Terje Andersen<sup>3,4</sup>, Bruno Sarmiento<sup>1,10,\*</sup>*

<sup>1</sup> Instituto de Investigação e Inovação em Saúde (i3S), University of Porto, Rua Alfredo Allen, 208, 4200-135 Porto, Portugal.

<sup>2</sup> Instituto de Ciências Biomédicas Abel Salazar (ICBAS), University of Porto, Rua Jorge Viterbo Ferreira, 228, 4150-180 Porto, Portugal.

<sup>3</sup> Department of Immunology, Oslo University Hospital Rikshospitalet and University of Oslo, N-0424 Oslo, Norway.

<sup>4</sup> Institute of Clinical Medicine and Department of Pharmacology, University of Oslo and Oslo University Hospital, 0372 Oslo, Norway.

<sup>5</sup> Drug Research Program, Division of Pharmaceutical Chemistry and Technology, Faculty of Pharmacy, University of Helsinki, FI-00014 Helsinki, Finland.

<sup>6</sup> Helsinki Institute of Life Science (HiLIFE), University of Helsinki, FI-00014 Helsinki, Finland.

<sup>7</sup> Department of Chemical Engineering and Koch Institute for Integrative Cancer Research, Massachusetts Institute of Technology, 02139 Cambridge, MA, USA.

<sup>8</sup> Division of Gastroenterology, Brigham and Women's Hospital, Harvard Medical School, 02115 Boston, MA, USA.

<sup>9</sup> Department of Mechanical Engineering, Massachusetts Institute of Technology, 02139 Cambridge, MA, USA.

<sup>10</sup> CESPUP, Instituto de Investigação e Formação Avançada em Ciências e Tecnologias da Saúde & Instituto Universitário de Ciências da Saúde, 4585-116 Gandra, Portugal.

# Cláudia Azevedo, Soraia Pinto and Sopisa Benjakul contributed equally.

\* Corresponding authors: [bruno.sarmiento@ineb.up.pt](mailto:bruno.sarmiento@ineb.up.pt)

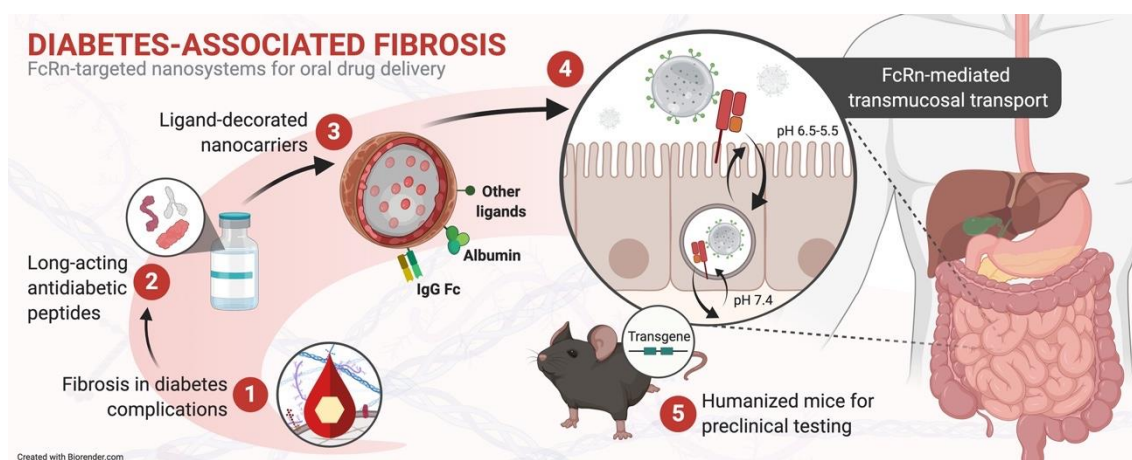
## Abstract

Diabetes *mellitus* is a chronic disease with an elevated risk of micro- and macrovascular complications, such as fibrosis. To prevent diabetes-associated fibrosis, the symptomatology of diabetes must be controlled, which is commonly done by subcutaneous injection of antidiabetic peptides. To minimize the pain and distress associated with such injections, there is an urgent need for non-invasive oral transmucosal drug delivery strategies. However, orally administered peptide-based drugs are exposed to harsh conditions in the gastrointestinal tract and poorly cross the selective intestinal epithelium. Thus, targeting of drugs to receptors expressed in epithelial cells, such as the neonatal Fc receptor (FcRn), may therefore enhance uptake and transport through mucosal barriers. This review compiles how in-depth studies of FcRn biology and engineering of receptor-binding molecules may pave the way for design of new classes of FcRn-targeted nanosystems. Tailored strategies may open new avenues for oral delivery and provide better treatment options for diabetes and, consequently, fibrosis prevention.

**Keywords:** Antidiabetic peptides, FcRn, IgG, albumin, intestinal epithelium, transcytosis, half-life, nanoparticles, active targeting, transgenic mouse model.

**Teaser:** This review provides a brief overview of FcRn biology, engineering of receptor-targeting molecules, and recent advances in FcRn-targeted nanosystems with the aim of improving drug transport across selective intestinal epithelial barriers for the treatment of diabetes *mellitus* and, consequently, prevention of fibrosis.

## Graphical abstract:



## Introduction

Diabetes *mellitus* (DM) is a chronic metabolic disease that develops when the pancreas does not produce insulin or when the body does not respond fully to insulin, leading to impaired glucose tolerance. More than 460 million people worldwide are suffering from DM, and the number of cases is predicted to rise to 700 million by 2045<sup>1,2</sup>. Chronic exposure to hyperglycemia may cause tissue injury and lead to fibrosis, which increases the risk of micro- and macrovascular complications in several organs, such as the eyes (diabetic retinopathy), kidneys (diabetic nephropathy), skin, heart, liver, lungs, nerves (neuropathy) and blood vessels (angiopathy)<sup>3,4</sup>. Fibrosis is characterized by abnormal deposition of the extracellular matrix (ECM), and there is currently no specific treatment available<sup>5</sup>. As such, there is an urgent need for strategies that could delay the progression or prevent diabetes-associated fibrosis.

Conventional treatment of DM requires subcutaneous injection of peptide-based antidiabetic drugs for glycemic control, which is considered a painful and invasive approach. The preferred route of administration is oral delivery via mucosal surfaces, due to its ease of administration and high patient compliance, without the need for syringes, needles, and trained health workers<sup>6,7</sup>. Notwithstanding, orally administered antidiabetic peptides are susceptible to the harsh environment of the gastrointestinal tract (GIT) and the selective barrier of the intestinal epithelium<sup>8,9</sup>. Hence, there is a demand for innovative strategies to overcome these limitations.

Biodegradable and biocompatible nanoparticles (NPs) have emerged as promising oral drug delivery systems that protect encapsulated drugs from acidic pH and enzymatic degradation in the GIT, as well as providing controlled release and enhanced bioavailability of drugs to target sites. However, the transport of NPs across intestinal mucosa is restricted by polarized epithelial cell layers<sup>8,10</sup>. Several recent studies support that targeting of the neonatal Fc receptor (FcRn), which is expressed by such epithelial cells and mediates bidirectional transport and recycling of immunoglobulin G (IgG) and albumin, may be used as a gateway for more efficient transcellular transport of NPs<sup>11-15</sup>. Furthermore, in light of successes in the development of engineered ligands and alternative scaffolds with improved FcRn binding and transport properties, researchers may now harvest from these advances in the design of new classes of NPs decorated with FcRn-targeted molecules, with the aim of enhancing transmucosal delivery upon oral administration. This review provides a brief overview of FcRn biology and discusses how receptor-binding molecules may be incorporated into nanosystems for improved FcRn-mediated oral delivery of antidiabetic peptides for the treatment of DM and the

prevention of fibrosis.

## 2. Diabetes-associated fibrosis

Fibrosis is one of the major complications of DM, induced by chronic hyperglycemia, which leads to excessive accumulation of ECM macromolecules and imbalance in tissue homeostasis<sup>3,5</sup>. Normally, ECM is responsible for the mechanical and structural support of cells and mediates intercellular communication. However, under cell and tissue injury, formation of ECM is dysregulated. This is a complex and multifactorial process involving increased production of advanced glycation end-products (AGEs) and growth factors, activation of protein kinase C as well the renin-angiotensin-aldosterone system (RAAS) and plasminogen and protease systems<sup>3, 16</sup>. A schematic overview of fibrosis development, due to diabetes-induced hyperglycemia, is shown in **Figure 1**.

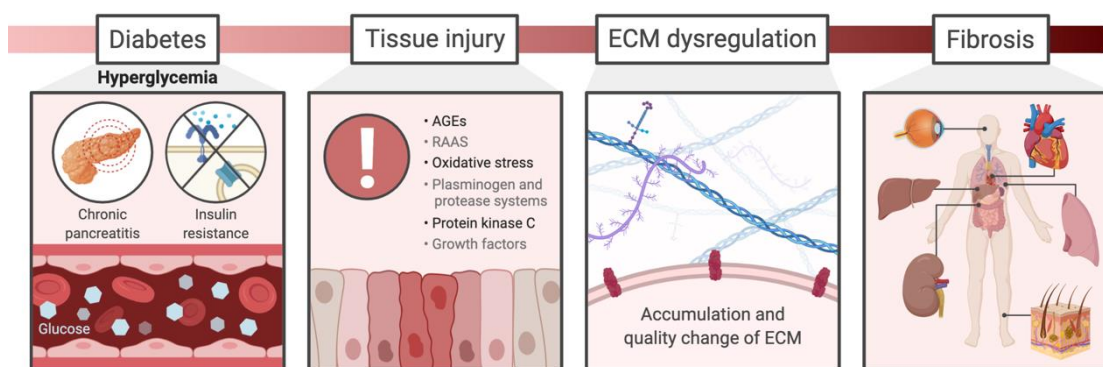


**Figure 1 | Fibrosis as a complication of diabetes.** In DM, impaired pancreatic function or insulin resistance causes blood glucose levels to rise higher than normal. Prolonged hyperglycemic condition may induce severe tissue injury by the action of AGEs, RAAS, oxidative stress, plasminogen and protease systems, protein kinase C and circulating growth factors. This leads to dysregulation of the ECM, characterized by excessive accumulation of components and alteration in ECM quality, that triggers the formation of fibrosis in several organs. The figure was created with BioRender.

AGEs are lipids or proteins that are glycated upon exposure to sugars<sup>16</sup>, which are prevalent in patients with DM. Under hyperglycemic conditions, AGEs stimulate the excess production of ECM macromolecules, which affects the ECM integrity and the profibrotic process<sup>3,5</sup>. RAAS, in which angiotensin II is considered the main effector molecule, promotes the accumulation of ECM components as well as the release of inflammatory cytokines and growth factors, such as transforming growth factor beta

(TGF- $\beta$ ), vascular endothelial growth factor, platelet-derived growth factor, and connective tissue growth factor<sup>3, 5</sup>. In addition, oxidative stress can trigger the progression of fibrosis [2]. In particular, the increase in TGF- $\beta$  stimulates the epithelial-to-mesenchymal transition, which contributes to the accumulation of ECM components, culminating in tissue fibrosis<sup>17, 18</sup>.

Interestingly, antidiabetic peptides have great potential in the treatment of fibrosis. For instance, dipeptidyl peptidase-4 (DDP-4) inhibitors, known as gliptins, and glucagon-like peptide 1 (GLP-1) agonists, have demonstrated mild antifibrotic properties in models of liver fibrosis by reducing oxidative stress<sup>19</sup>. Owing to the antidiabetic activity of gliptins, they are used for treatment of type 2 diabetes (T2DM)<sup>20</sup>. Moreover, GLP-1 analogs, such as exendin-4, liraglutide and semaglutide, are also used to treat T2DM, which have antifibrotic effects by reducing inflammation and oxidative stress<sup>21-23</sup>. As such, the encapsulation of these peptide drugs into nanosystems targeting FcRn may lead to enhanced transmucosal delivery. In addition, these drugs may be engineered for half-life extension by taking advantage of FcRn-binding molecules. Notably, FcRn is expressed by cells of the lungs, eyes and kidneys<sup>24-26</sup>, where fibrosis typically occurs.

### **3. The biology and molecular mechanisms of FcRn**

#### **3.1. Structure and binding of ligands**

FcRn is a heterodimeric glycoprotein that is structurally similar to major histocompatibility complex class I (MHC-I) molecules, consisting of a unique transmembrane heavy chain (40-46 kDa) that is non-covalently associated with the common beta-2-microglobulin ( $\beta$ 2m) light chain (12 kDa)<sup>27, 28</sup>. The heavy chain contains three extracellular domains, denoted  $\alpha$ 1,  $\alpha$ 2 and  $\alpha$ 3, where the  $\alpha$ 1 and  $\alpha$ 2 domains assemble a platform of eight antiparallel  $\beta$ -strands topped by two  $\alpha$ -helices followed by the  $\alpha$ 3 domain, which is folded up on the soluble  $\beta$ 2m<sup>29, 30</sup>.

Unlike MHC-I molecules that present antigenic peptides via their peptide binding groove to cytotoxic T cells, the corresponding binding groove of FcRn is closed<sup>29-32</sup>. Instead, FcRn has evolved to bind IgG and albumin, two structurally and functionally unrelated proteins. Both ligands bind in a pH-dependent manner, binding at acidic pH (6.5-5.0) and no binding or release at physiological pH (7.4)<sup>33-38</sup>. The strict pH-dependent mode of action is mediated by protonation of the imidazole side chains of conserved histidine residues found on both the receptor and the ligands. When the pH increases towards neutral, protonation of the histidine residues is gradually lost, and the ligands are



released from the receptor <sup>34, 36, 37, 39, 40</sup>. Importantly, FcRn binds both ligands simultaneously in a non-cooperative manner as a ternary complex (**Figure 2**) <sup>35, 38, 40</sup>.

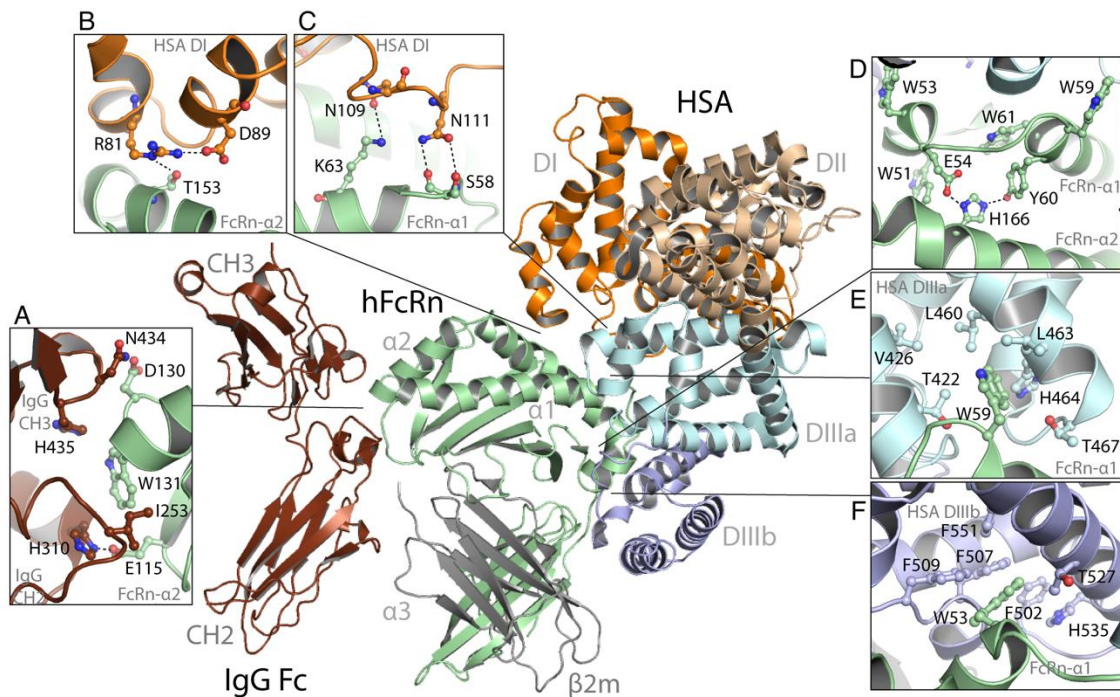


**Figure 2 | Crystallographic illustration of the ternary complex of hFcRn bound to hIgG and HSA.** The three domains of the hFcRn heavy chain (denoted  $\alpha 1$ ,  $\alpha 2$ , and  $\alpha 3$ ) are shown in green, and the  $\beta 2m$  subunit in gray. The hIgG1 Fc fragment is shown in brown. The subdomains DI, DII, DIIIa and DIIIb of HSA are colored in orange, wheat, light cyan and light blue, respectively. (**A**) Close-ups showing key amino acid residues involved in the interaction between hIgG1 (H310, I253, H435, N434) and hFcRn (E115, W131, D130). (**B** and **C**) Close-ups of the interactions between two loops in DI of albumin (loop I; R81, D89, and loop II; N109, N111) and hFcRn (T153, K63, S58). (**D**) Close-ups of the intramolecular interactions between H166 of the  $\alpha 2$  domain and E54 and Y60 of the  $\alpha 1$  domain in hFcRn, which form at acidic pH and in turn stabilize the loop containing W51, W53, W59 and W61. (**E** and **F**) Close-ups showing W59 and W53 of hFcRn inserted into hydrophobic pockets in DIIIa (T422, V426, L460, L463, H464 and T467) and DIIIb (F502, F507, F509, T527 and F551) of HSA, respectively. The figure was made using PyMol and the crystal structure data of hFcRn in complex with hIgG1 Fc and HSA (4N0U) <sup>38</sup>.

IgG (150 kDa) is the most prevalent antibody in blood, with a concentration around 12 mg/mL in mice and humans <sup>41</sup>. It is produced by B and plasma cells and protects the body from foreign substances, such as pathogens and toxins. This Y-shaped homodimeric protein contains four polypeptides that make up two fragment antigen-binding (Fab) arms, linked via a hinge to a constant N-glycosylated fragment

crystallizable (Fc) part<sup>41-43</sup>. While the Fab arms are recognizing foreign antigens, the Fc is responsible for binding to effector molecules, including FcRn<sup>41, 42</sup>. The interaction between FcRn and IgG occurs primarily at the CH2-CH3 elbow region with a stoichiometry of two FcRn molecules per monomeric IgG, where the conserved residues I253, H310 and H435 are key players<sup>30, 38, 44-49</sup>. Specifically, protonation of the histidine residue H310 at acidic pH enables interaction with E115 on the  $\alpha$ 2-domain of the human FcRn (hFcRn) heavy chain<sup>38, 49</sup>. Moreover, I253 interacts with W131 of the receptor, whereas the side chain of H435 does not make any direct contacts but have been shown to regulate a loop within the Fc, including residues 429-436, prior to binding<sup>30, 38, 49, 50</sup>. Replacement of these residues with alanine abrogates receptor binding, and results in inefficient transport and short half-life<sup>25, 45, 48, 49, 51-53</sup>. Also, the soluble  $\beta$ 2m of rat FcRn has been shown to contribute to binding of rat IgG via residue Ile1 by making van der Waals contacts with residues V309 and P307 of the Fc<sup>30, 54</sup>. In addition, increasing evidence supports the possibility for Fab regions to modulate the interaction with FcRn<sup>55-58</sup>. The key interactions between hFcRn and human IgG1 (hIgG1) Fc are given in

## Figure 2.

The other ligand, albumin (66.5 kDa), is the most prevalent blood protein, with a concentration of roughly 40 mg/mL in both mice and humans<sup>59</sup>. Its natural function is to transport a range of small insoluble cargos, including fatty acids, hormones, metal ions and waste products, for delivery to tissues and organs<sup>59</sup>. Due to its hydrophobic binding capacity and high aqueous solubility, albumin may be used as a transporter for poorly soluble drugs<sup>60</sup>. Also, it is an attractive fusion partner for protein-based drugs<sup>61</sup>. In contrast to the multi-domain structure of IgG, human serum albumin (HSA) contains a non-glycosylated single polypeptide made up of 585 amino acids, which forms a heart-shaped structure with three homologous domains (denoted DI, DII and DIII)<sup>62</sup>. These are connected via flexible loops, where each domain can be divided into two subdomains (A and B)<sup>62</sup>. While DIII contains the principle-binding site for hFcRn, DI modulates the interaction<sup>37, 38, 40, 63</sup>. Hydrophobic residues of the subdomains DIIIA and DIIIB make contacts with the hFcRn residues W59 and W53, located within a pH-sensitive  $\alpha$ 1-domain loop<sup>38, 63, 64</sup>. At acidic pH, the histidine residue at position 166 within the FcRn  $\alpha$ 2-domain (H166) is protonated and interacts with E54 and Y60 in the  $\alpha$ 1-domain loop, which stabilizes the orientation of the loop required for efficient albumin binding<sup>37, 38, 40, 63, 64</sup>. Substitution of H166 with an alanine abolishes binding to albumin<sup>36, 37, 64</sup>. In addition, other DIII residues, including histidine residues (H464, H510 and H535) and K500, are required for strong binding at acidic pH<sup>37, 38, 63</sup>. Targeting of these residues by

mutagenesis reduces receptor binding considerably, which results in short half-lives in hFcRn transgenic mice<sup>37</sup>. The contribution from DI is minor but important for optimal hFcRn binding. Notably, a recombinant form of HSA DIII binds 10-fold weaker to hFcRn than the full-length version<sup>65, 66</sup>. Structurally, the DI residues involved are N109, N111 and R81-D89 that make contacts with K63, S58, and T153 of hFcRn, respectively<sup>38, 63, 65</sup>. Close-ups of the interactions between hFcRn and HSA are given in **Figure 2**.

### 3.2. Recycling and transcytosis of ligands

IgG and HSA share a half-life of 3 weeks in humans on average<sup>67-69</sup>. This results from their molecular sizes above the renal clearance threshold and FcRn-mediated rescue from intracellular degradation<sup>35, 70-73</sup>. The astonishing role of FcRn in half-life regulation is evident in patients suffering from rare human disease hypercatabolic hypoproteinemia that have remarkably low blood amounts of both ligands, which is due to the deficient FcRn expression<sup>74, 75</sup>. In addition, mice lacking FcRn expression have about 4-fold and 2-fold lower levels of IgG and albumin than normal mice, respectively<sup>35, 71, 72</sup>. As such, FcRn is a key homeostatic regulator of IgG and albumin by transporting the ligands within and across cells via two cellular pathways, recycling and transcytosis. Both processes are regulated by strict pH-dependent binding-and-release interactions between FcRn and its ligands<sup>66, 70, 73, 76-78</sup>.

Insights into how FcRn mediates cellular recycling have been extensively studied by *in vitro* cellular transport assays combined with advanced imaging technologies, mainly with a focus on IgG<sup>70, 73, 76, 79-85</sup>. However, recent studies have also revealed knowledge about how FcRn transports both ligands simultaneously<sup>70, 78, 86</sup>. Together, the studies demonstrate that the ligands are taken up via fluid-phase pinocytosis at neutral pH, followed by entering of acidified endosomal compartments where FcRn is predominantly located. The mildly acidic pH (6.0-6.5) herein facilitates protonation of the histidine residues and engagement of the receptor. Bound ligands are then rescued from intracellular lysosomal degradation by sorting of the FcRn-ligand complexes to the cell surface, where exposure to neutral pH triggers ligand release from FcRn into the extracellular space. Proteins that do not bind the receptor will be rapidly degraded in lysosomes<sup>70, 76</sup>. Studies in mice have shown that both non-hematopoietic and hematopoietic cells are equally important for FcRn-mediated half-life regulation<sup>77, 87-93</sup>. Furthermore, FcRn can transport the ligands in both directions across polarized cellular barriers, such as the epithelial cell layers of the lungs and the intestine<sup>25, 51, 66, 77, 94-102</sup>. Regarding the polarized intestinal epithelium of the GIT, IgG and albumin are taken up

at the basolateral side via fluid-phase pinocytosis, where the pH is neutral, for subsequent delivery to acidified endosomes in which engagement of FcRn directs the transport across the cells. If the pH at the apical side is neutral, the ligands will be released. However, if the intestinal lumen milieu is mildly acidic, the ligands may remain bound to the receptor and, again, be taken up by the cells, either in a monomeric form, or as IgG-containing immune complexes. This may result in either recycling at the apical side or transcytosis through the polarized cell layers for release at the basolateral side into lamina propria. The ligands may then be transported via the lymphatic system and enter the systemic circulation via the thoracic lymph nodes, or be processed by immune cells as IgG-containing immune complexes, as recently reviewed<sup>93, 103</sup>.

FcRn-mediated transcytosis has been studied *in vitro* by the use of Transwell® assays with polarizing cell lines that either endogenously express the receptor or are manipulated to overexpress the receptor<sup>51, 66, 77, 96-98, 100, 102</sup>. In addition, transcytosis across mucosal epithelial barriers have been studied *in vivo*, either by administering the ligands systemically followed by sampling at mucosal sides<sup>95, 99, 101</sup>, or by giving them via mucosal sites in a needle-free manner followed by sampling of tissues or blood over time<sup>25, 52, 66</sup>. The principles of FcRn-mediated recycling and bidirectional transcytosis are shown in **Figure 3**.

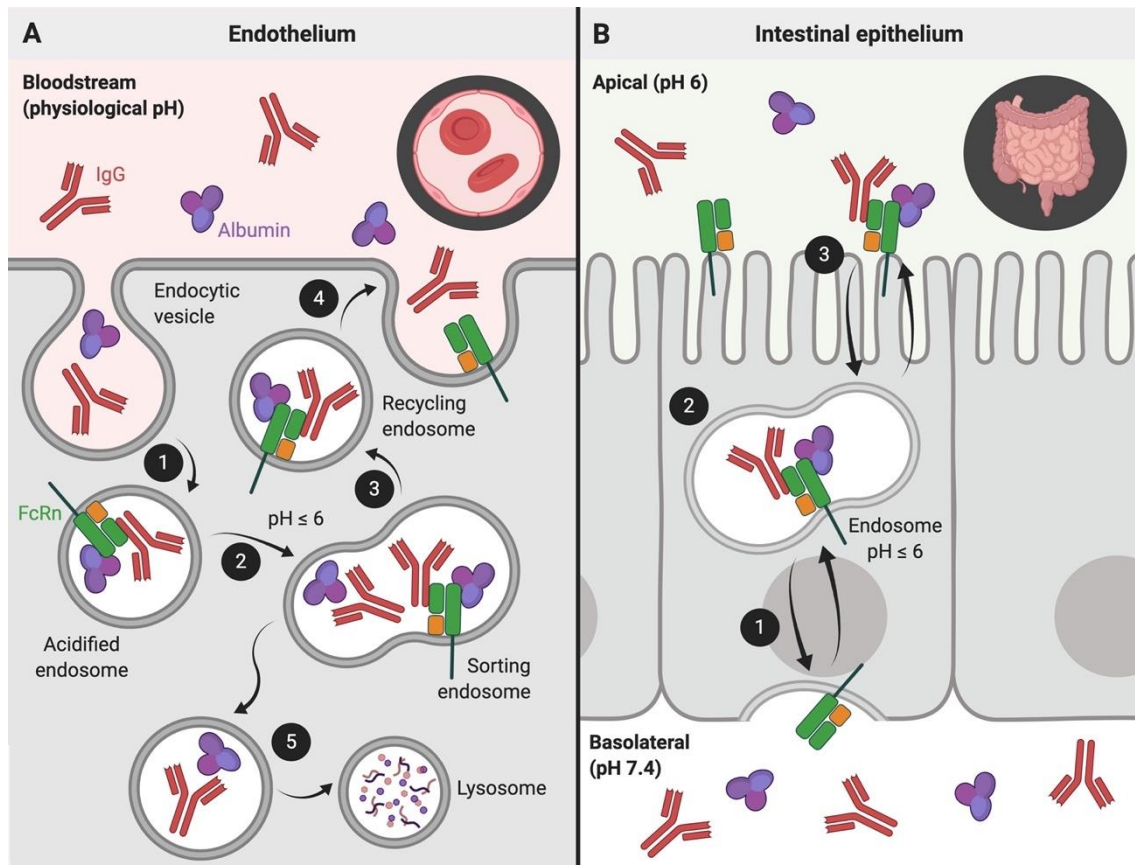


**Figure 3 | Schematic illustration of FcRn-mediated recycling and bidirectional transepithelial transport. (A) Recycling:** (1) IgG and albumin are internalized into cells expressing FcRn, such as vascular endothelial cells, via fluid-phase pinocytosis, and subsequently (2) bind FcRn located within acidic endosomes. (3) The receptor-ligand complex is then recycled back to the cell surface, (4) where the ligands are released to the systemic circulation upon exposure to the neutral pH following exocytosis. (5) Proteins that do not bind FcRn will be catabolised in lysosomal compartments. **(B) Transcytosis:** (1) In polarized epithelial cells, such as enterocytes, IgG and albumin are taken up via fluid-phase pinocytosis at the basolateral side where the pH is neutral. (2) Ligand are subsequently sorted into acidified endosomes where they bind to FcRn. (3) The receptor-ligand complex is then directed to the apical surface of the cells, where it promotes the release of ligands upon exposure to acidic pH of the intestinal mucosa. In addition, the ligands may remain bound to the receptor and be taken up by the cells again. The figure was created with BioRender.

#### 4. IgG and albumin-based drug delivery of antidiabetic peptides

About 90% of patients diagnosed with DM have T2DM, while the remaining have type 1 DM (T1DM) <sup>1</sup>. The primary aim of T2DM treatment is to maintain glycemic control by antidiabetic medication. This can be achieved by the use of GLP-1 peptide analogs that

stimulate insulin secretion by pancreatic  $\beta$  cells, or insulin analogs that promote efficient glucose disposal. However, such peptides have a very short half-life of about a few minutes, due to their small size and rapid clearance from the circulatory system via kidney filtration. Hence, efficient treatment would require regular monitoring and frequent dosing schedules <sup>1</sup>. To improve the efficacy and patient compliance of DM therapy, the natural long half-life of hIgG4 Fc and HSA may be used in drug design, which have already been explored for a range of antidiabetic peptides (**Table 1**).

The first GLP-1 analog to reach the market was liraglutide (Victoza<sup>®</sup>), which is linked to a fatty acid (palmitic acid) that binds reversibly to hydrophobic pockets of HSA <sup>104</sup>. As such, it associates non-covalently with endogenous HSA within the subcutaneous tissue and bloodstream. This strategy extends the half-life to 11-15 hours and allows for once-daily dosing <sup>104-106</sup>. Another example is the zinc-based taspoglutide, where aminoisobutyric acid is covalently linked to two positions of GLP-1. This was shown to extend the half-life up to 2-3 days in humans <sup>107, 108</sup>. However, clinical testing was halted due to severe gastrointestinal side effects and hypersensitivity reactions <sup>109</sup>. Furthermore, for the treatment of not only T2DM but also T1DM, other fatty acid-based strategies have been developed for insulin. One is insulin detemir (Levemir<sup>®</sup>) <sup>110, 111</sup> and another is insulin degludec (Tresiba<sup>®</sup>) <sup>112, 113</sup>. Both are recombinant human insulin analogs with a fatty acid linked to a lysine residue, while insulin degludec also lacks a threonine residue. They have distinct half-lives of 18-26 hours and 42 hours for insulin detemir and insulin degludec, respectively <sup>61, 110-114</sup>. An insulin analog with an activity profile close to that of insulin detemir is insulin glargine (Lantus<sup>®</sup>) with a half-life of about 24 hours <sup>115</sup>. Instead of modification of the fatty acid side chains, insulin glargine includes two additional arginine residues in the beta chain and an amino acid replacement of asparagine at position 21 with glycine. Nevertheless, these products have gained market approval for once-daily dosing. To further extend half-lives of insulin analogs, insulin icodec has been developed as a once-weekly insulin that is currently in phase I and phase III clinical trials in patients with T1DM and T2DM, respectively <sup>116, 117</sup>. As a result of three amino acid substitutions and the addition of an icosane fatty diacid to this insulin analog, it shows an extended half-life of 8 days in humans and improved stability and solubility.

Despite that these strategies secure prolonged blood persistence compared with native peptides, treatment relies on subcutaneous injections. To allow oral administration, semaglutide has been developed <sup>118</sup>. It is a modified GLP-1 where alanine and lysine residues at positions 8 and 34 have been replaced with 2-aminoisobutyric acid and

arginine, respectively, to prevent degradation by DPP-4. In addition, lysine at position 26 is engineered to contain a spacer and a fatty acid that can bind endogenous HSA upon injection. This formulation provides a half-life of about 7 days in humans<sup>119, 120</sup>. When semaglutide is co-formulated with an absorption enhancer, namely sodium N-(8-[2-hydroxybenzoyl]amino) caprylate, which neutralizes the pH of the gastric fluid and hinders enzymatic activity, it is protected from degradation in the GIT upon oral administration<sup>118</sup>. The injected version of semaglutide (Ozempic®) was clinically approved in the US and Europe in 2017-2018, while the oral formulation (Rybelsus®) was approved last year<sup>118, 121-123</sup>. The latter is the first GLP-1 receptor agonist to be approved for oral delivery. Notably, there may be room for further optimization as its oral bioavailability is limited ( $\leq 1.0\%$ )<sup>124, 125</sup>. Currently, there are no oral insulin (OI)-based drugs available for DM treatment. However, very recently, the first clinically tested once-weekly OI analog, named OI338, demonstrated efficacy near subcutaneously injected insulin glargine<sup>126</sup>, which has led to the development of long-acting OI formulations<sup>127</sup>. Commonly, a tyrosine at position 14 and a phenylalanine at position 25 are replaced by glycine and histidine, respectively, in addition of a deletion of threonine at position 30<sup>127</sup>. These amino acid modifications make OI less susceptible to degradation in the GIT upon oral administration<sup>126, 127</sup>, in combination with the use of an absorption enhancer, such as Gastro Intestinal Permeation Enhancer Tablet I (GIPET®1) based on sodium caprate<sup>128</sup>. To gain improved HSA binding, the lysine residue at position 29 of the OI is coupled to a strong albumin binding molecule (C18 fatty diacid) via a hydrophilic linker. Moreover, OI molecules can be designed for prolonged half-life by engineering for decreased insulin receptor affinity. This design resulted in OI338 with a half-life of 70 hours in T2DM patients<sup>126</sup>. In the context of FcRn, it has been demonstrated that binding of fatty acids to the hydrophobic pockets of HSA is in fact negatively affecting receptor binding, in which the effect depends on the length of the fatty acid<sup>63</sup>. As such, half-life extension upon conjugation to fatty acids will have limitations. Regarding oral delivery, this means that fatty acid-based strategies may not benefit from albumin binding to FcRn expressed at epithelial cell barriers. This is a highly interesting topic that should be addressed in future studies.

An alternative strategy to non-covalent association with HSA is site-specific conjugation. One example is conjugation of the GLP-1 receptor agonist exendin-4<sup>129-131</sup>. Notably, exendin-4 increases insulin secretion in a glucose-dependent manner at the same time as it stimulates  $\beta$ -cell proliferation and restores sensitivity to glucose<sup>132</sup>. When injected in the absence of HSA, it has a half-life below 1 hour<sup>132, 133</sup>, however, when linked to

HSA (CJC-1134-PC), it has been shown to gain a half-life of about 8 days in a clinical phase II trial<sup>105, 130, 134</sup>. This allows for once-a-week dosing. Specifically, exendin-4 is linked to HSA via the PC-DAC<sup>™</sup> technology that utilizes maleimide (MAL) chemistry for stable conjugation to the thiol group of a free cysteine residue (C34) in DI<sup>106, 133</sup>. The same technology has been used for conjugation of insulin (PC-DAC<sup>™</sup>:Insulin), which is under preclinical development, where it has demonstrated 30 times longer half-life compared with native insulin in rats<sup>135</sup>. Importantly, C34 is distant from the hFcRn interaction site in HSA DI<sup>63, 136</sup>. However, it has been demonstrated that conjugation to C34 may compromise pH-dependent FcRn binding<sup>137-139</sup>. How pronounced this effect could be will depend on the biophysical properties of the conjugated drug and, as such, needs to be addressed in a case-to-case scenario. Notably, the loss of receptor binding may be restored by taking advantage of engineered HSA variants with improved hFcRn binding, as will be discussed in **Section 6**. Another alternative strategy is to genetically fuse the peptide of interest to the N- or C-terminal end of HSA. In the context of DM, a di-peptide of GLP-1 has been fused to wild-type (WT) HSA (albiglutide)<sup>140-142</sup>, a product known as Tanzeum<sup>®</sup> in the US and Eperzan<sup>®</sup> in Europe, which was recently withdrawn from the market due to economic reasons. Nevertheless, the design gave rise to a half-life of 5 days in humans, allowing for weekly subcutaneous injection<sup>140-142</sup>. This fusion was based on the addition of the di-peptide to the N-terminal of HSA, which leaves the C-terminal end free. Interestingly, the last leucine residue of the C-terminal end of HSA may be enzymatically cleaved in blood, which has been demonstrated to reduce hFcRn binding and lead to a short half-life in mice and humans<sup>143</sup>. Hence, this biological phenomenon should be considered when designing HSA fusions. A way to compensate for loss of receptor binding is to take advantage of engineered HSA variants with improved receptor affinity, as recently demonstrated<sup>143</sup>.

The last example is the use of hIgG Fc fusion technology, where an GLP-1 receptor agonist, again engineered to be resistant to enzymatic degradation, is fused to an IgG4 Fc fragment via a short linker (dulaglutide, Trulicity<sup>®</sup>)<sup>144, 145</sup>. IgG4 is likely to be chosen instead of IgG1 due to safety concerns, as IgG4 Fc is less potent in induction of effector functions<sup>42</sup>, without altering the ability to engage hFcRn. Dulaglutide has a half-life of nearly 5 days in humans, and the product is approved for once-weekly subcutaneous administration<sup>144, 145</sup>.

Hitherto, only one of these strategies has been approved for oral delivery. However, in principle, all the antidiabetic peptide strategies may be combined with nanosystems tailored for oral administration to achieve more efficient delivery across the selective



mucosal barriers. Although, this will require a sophisticated design that allows the nanosystems to be taken up and delivered to the circulatory system more efficiently than what has been demonstrated to date. This may be achieved by harvesting from recent knowledge about FcRn biology and advances in the engineering of receptor-targeting molecules with favorable binding and transport properties. Such molecules may be directly fused to the peptides, but they may also be used to decorate nanosystems, as will be discussed below.

**Table 1 | IgG Fc and albumin as platform for half-life extension of antidiabetic peptides in clinic.**

Analog	Name	Ligand	Drug type	Clinical status	$t_{1/2}$	ROA	Company	Reference
GLP-1 (T2DM)	Victoza®	HSA	Liraglutide	Marketed	11-15 h	SC	Novo Nordisk	104, 105
	Rybelsus®	HSA	Semaglutide	Marketed	6-7 d	Oral	Novo Nordisk	118, 122, 123
	Ozempic®	HSA	Semaglutide	Marketed	7 d	SC	Novo Nordisk	121
	Trulicity®	IgG4 Fc	Dulaglutide	Marketed	4.7-5 d	SC	Eli Lilly and Company	144, 145
	CJC-1134	HSA	Exendin-4	Phase II	8 d	SC	ConjuChem	129, 130, 133
	R1538	HSA	Taspoglutide	Halted phase III	2-3 d	SC	Roche/Ipsen	107-109
	Tanzeum® / Eperzan®	HSA	Albiglutide	Withdrawn	5-8 d	SC	GlaxoSmithKline	140-142
Insulin (T1DM, T2DM)	Lantus®	HSA	Insulin glargine	Marketed	24 h	SC	Sanofi	115
	Levemir®	HSA	Insulin detemir	Marketed	18-26 h	SC	Novo Nordisk	110, 111
	Tresiba®	HSA	Insulin degludec	Marketed	42 h	SC	Novo Nordisk	112, 113
	LAI-287	HSA	Insulin icodect	Phase I/III	> 8 d	SC	Novo Nordisk	116, 117
	OI-338	HSA	Insulin-338	Phase II	70 h	Oral	Novo Nordisk	126, 127
	PC-DAC™	HSA	Insulin	Preclinical	5-15 h	SC	ConjuChem	135

$t_{1/2}$ : half-life; ROA: route of administration; SC: subcutaneous administration.

## 5. Ligand engineering for improved FcRn binding

The therapeutic efficacy of many protein-based drug candidates is hampered by their short half-life, and those that have reached the market require frequent administration, which is a burden for the patients. As hIgG and HSA have a naturally long half-life, they are extensively used in therapy, either as full-length hIgG antibodies, or as Fc or HSA fused to therapeutic peptides or proteins of interest<sup>61, 146, 147</sup>.

The in-depth knowledge gained from dissecting of the relationship between FcRn and its ligands at molecular and cellular level has been used in the design of hIgG and HSA variants with improved hFcRn binding and transport properties<sup>41, 61, 66, 147-149</sup>. One motivation for this is the clinical approval rate of monoclonal hIgG antibodies and HSA fusions used to treat a range of different diseases. In fact, hIgG antibodies are the fastest growing class of protein-based drugs with more than 100 products on the market, and impressively over 800 antibodies under clinical testing<sup>150, 151</sup>. One example is orelizumab (TRX4), a hIgG1 antibody targeting CD3 to suppress pathogenic T cells, which is used to treat T1DM caused by antigen-specific T cells that infiltrate pancreatic beta cells and lead to loss of insulin secretion<sup>152</sup>. While many of the early developed antibodies are based on WT hIgG1, next-generation of monoclonal antibodies will be engineered for either lack or improved effector functions, including optimal hFcRn-mediated transport properties<sup>149</sup>. In addition, recent research has also resulted in engineering of HSA variants with improved half-life<sup>63, 66, 153</sup>. Moreover, several alternative scaffolds with FcRn-binding properties have been reported<sup>154-158</sup>, but a major challenge for such engineering is fine-tuning of strict pH-dependent receptor binding in order to gain favorable recycling and transcytosis capacity. Improvements in FcRn engagement and transport may result in more favorable pharmacokinetic profiles, and consequently less frequent administration and higher patient compliance.

### 5.1. IgG Fc-engineering

Scrutinizing the FcRn-IgG interaction has led to the development of Fc-engineered variants where amino acid substitutions within the CH2 and CH3 domains have been modified to gain improved pH-dependent binding to hFcRn (**Table 2**). Importantly, a prerequisite for successful engineering is to augment receptor binding at acidic pH while, at the same time, avoiding increase in receptor affinity at neutral pH<sup>41, 148, 159, 160</sup>. The first proof-of-concept was given in 1997 by isolation of mouse IgG1 (mIgG1) Fc fragments by phage display that gave 3.5-fold improved binding towards mouse FcRn (mFcRn), which resulted in about 1.6-fold extended half-life in conventional mice<sup>161</sup>. This was followed by a generation of hIgG Fc-engineered variants with increased affinity for hFcRn, which provided a several fold extended half-life in mice, non-human primates and humans. One example is the YTE triple mutant (M252Y/S254T/T256E) with 10-fold improved binding at pH 6.0, which resulted in about 3.5-fold extended half-life in non-human primates and humans<sup>148, 162, 163</sup>. Another well-studied hIgG1 variant, harboring two amino acid substitutions within the CH<sub>3</sub> domains (M428L/N434S: LS variant), with 11-fold increased

binding to hFcRn at acidic pH, and negligible binding at neutral pH, gave more than 3-fold extended half-life in hFcRn transgenic mice and non-human primates <sup>164</sup>. Importantly, such engineering has shown to improve therapeutic efficacy in mouse tumor models when combined with antibodies targeting tumor antigens <sup>164</sup>. In addition, extended half-life improves antibody-based prophylaxis, as shown in non-human primates upon viral challenge <sup>165, 166</sup>. Clinical data on the use of the LS substitutions have revealed that the antibody can reach a half-life of over 100 days compared to 20 days for the WT counterpart <sup>167, 168</sup>. A range of additional hIgG Fc-engineered variants have been reported with increased persistence over the WT antibody when tested in hFcRn transgenic mice or non-human primates <sup>159, 160, 169-176</sup>, but these do not reach the same half-life values as that of YTE and LS. However, a few recent examples are of interest. In one report, three double mutant variants (M252Y/T256D (YD), T256D/T307Q (DQ) and T256D/T307W (DW)) with enhanced pH-dependent binding to hFcRn resulted in similar extended half-lives in hFcRn expressing mice and non-human primates as that of LS used for benchmarking <sup>177</sup>. Another recent Fc-engineered variant with three Fc substitutions (L309D/Q311H/N434S (DHS)) showed a half-life of 2 to 3-fold beyond that of the clinical stage YTE and LS variants in hFcRn expressing mice [89-91, 95]. This is interesting as it has only 5-fold improved affinity to hFcRn at acidic pH with no detectable binding at pH 7.4 <sup>178</sup>. The authors speculate that this may be explained by complete lack of binding at neutral pH, which warrants further studies on how binding throughout the pH gradient is regulating FcRn-mediated transport within and across cells. These Fc-engineered variants may be used as fusion partners for therapeutic proteins, such as antidiabetic peptides, to achieve extended half-life and improved bioavailability. Preclinically examples are the combination of Fc-containing YTE or LS variants fused to cytotoxic T lymphocyte-associated protein 4, where both Fc fusion products yielded more than 2-fold extended half-life in non-human primates <sup>179, 180</sup>. In addition, studies on transcytosis have demonstrated that Fc-engineering can enhance delivery across polarized cells, as shown for hIgG1 antibodies containing LS or YTE substitutions that were transported almost twice as efficiently across human epithelial cells *in vitro* as the WT counterpart [43]. Interestingly, the capacity to be transported in an hFcRn-dependent manner could be further enhanced when the Fc-engineered antibodies were administered as multivalent immune complexes <sup>51</sup>. As such, FcRn-directed transepithelial transport may be enhanced by Fc engineering for improved pH-dependent receptor binding combined with increased avidity, factors that should inspire the design of nanosystems aiming for enhanced mucosal delivery.

## 5.2. HSA-engineering

IgG antibodies and Fc fusions have the ability to engage effector molecules, such as the complement factor C1q and the classical Fcγ receptors, and as such induce a range of effector functions, like antibody-mediated cellular cytotoxicity or complement dependent cytotoxicity<sup>42, 151</sup>. Although these immune responses are therapeutically attractive, they may also cause undesirable negative side effects<sup>151, 181</sup>. To avoid the latter, a solution may be to use the effector-negative HSA as a fusion partner. As the C-terminal DIII of HSA contains the principal binding sites for hFcRn<sup>37, 38, 40, 63, 182</sup>, engineering for improved binding has so far focused on this domain (**Table 2**). Among the first examples to be published was a single amino acid substitution introduced in the last α-helix (K573P (KP)), which gave a 12-fold stronger binding to hFcRn at acidic pH with negligible binding at neutral pH<sup>153</sup>. This resulted in about 1.5-fold extended half-life in hFcRn transgenic mice and non-human primates compared with WT HSA<sup>153</sup>. This variant has been shown to be transported up to 2.5 times more efficiently across polarized epithelial cell lines<sup>15, 66</sup>. Similarly, another single amino acid substitution (V547A (VA)) showed 13-fold stronger binding to hFcRn at acidic pH, and 1.5-fold longer half-life in hFcRn transgenic mice<sup>63</sup>. However, in an unrelated study, VA gave comparable improved binding to hFcRn as that of KP, but was transcytosed less well across polarized human epithelial cells<sup>66</sup>. Very recently, a triple mutant variant (E505Q/T527M/K573P (QMP)) was reported with impressively more than 180-fold increased hFcRn binding affinity without affecting binding at neutral pH<sup>66</sup>. QMP translated into 4-fold enhanced transcellular transport *in vitro*, and upon intranasal delivery, 2-fold more of the engineered variant reached the blood compared with WT HSA. Importantly, following intravenous injection, QMP gained 2-fold longer half-life in hFcRn transgenic mice in the presence of strong competition with endogenous albumin<sup>66</sup>. The QMP variant has been benchmarked toward a panel of engineered HSA variants and shown to display more favorable binding and transport properties<sup>66</sup>. As such, QMP should be an attractive fusion partner for antidiabetic peptides to achieve prolonged half-life upon subcutaneous or mucosal delivery. The encouraging data on enhanced delivery across polarized lung epithelial barriers should inspire research exploring if QMP can be used for oral drug delivery to facilitate more efficient uptake and delivery across the selective intestinal epithelial barriers of the GIT.

**Table 2** | Examples of engineered human IgG and HSA variants with improved pH-dependent hFcRn binding. Fold compared with WT hIgG or WT HSA.

Ligand	Variant	Mutation	Increase in hFcRn binding at pH 6	Increase in transcytosis	Increase in half-life	Reference
IgG	YTE	M252Y/S254T/T256E	10-fold	1.6-fold	3.5-fold (humans), 3.7-fold (NHP)	148, 162, 163
	LS	M428L/N434S	11-fold	1.9-fold	3.2-fold (NHP)	164
	QL	T250Q/M428L	29-fold	-	2.5-fold (NHP)	171
	YD	M252Y/T256D	6.8-fold	-	1.5-fold (hFcRn Tg mice)	177
	DQ	T256D/T307Q	7-fold	-	2.1-fold (hFcRn Tg mice)	177
	DW	T256D/T307W	9.8-fold	-	1.7-fold (hFcRn Tg mice)	177
	DHS	L309D/Q311H/N434S	5-fold	-	5.9-fold (hFcRn Tg mice)	178
Albumin	VA	V547A	13.2-fold	-	1.5-fold (hFcRn Tg mice)	63
	KP	K573P	12-fold	1.5-fold	1.4-fold (hFcRn Tg mice), 1.6-fold (NHP)	66, 153
	QMP	E505Q/T527M/K573P	180-fold	4-fold	2-fold (hFcRn Tg mice)	66

NHP: non-human primates; Tg mice: transgenic mice.

### 5.3. Alternative engineered FcRn-binding scaffolds

#### 5.3.1. FcRn-binding peptides

Besides engineering of hIgG Fc and HSA, alternative scaffolds with FcRn-binding properties have been developed. One example is the selection of FcRn-binding peptides (FcRnBPs) by phage display technology that bind in the micromolar affinity range at both acidic and neutral pH, and with only minor differences in binding under both conditions (**Table 3**)<sup>154, 155</sup>. As such, these peptides are not directly attractive for half-life extension. However, a 26-amino acid peptide (SYN1436), which blocks the IgG binding site of FcRn, has been shown to lower the systemic levels of endogenous IgG in mice and non-human primates by up to 80%, but this required the peptide to be dimeric<sup>154, 155</sup>. Conjugation of polyethylene glycol (PEG) chains to the dimeric peptide affected the binding of FcRn to different degrees<sup>183</sup>. Still, the most optimal PEG-peptide conjugate could accelerate the catabolism of hIgG when administered to hFcRn transgenic mice<sup>183</sup>. Notably, a range of on-going clinical trials are evaluating FcRn-targeting molecules for blockage of the IgG site, as a strategy to lower the levels of pathogenic IgG in autoimmune diseases, as reviewed<sup>184-186</sup>. Inspired by the work on SYN1436,

Sokolosky and colleagues made an engineered version by introducing a single point substitution (Y14H) to make it binds more pH-dependently to the receptor<sup>187</sup>. When fused to a model fusion partner, it bound hFcRn without affecting the biological function of the fusion partner. Notably, the fusion protein bound hFcRn more strongly at acidic pH than at neutral pH, and still better at neutral pH than hIgG1. Further, one of the fusion proteins was shown to be transcytosed 14-fold more efficiently than the non-fused counterpart across hFcRn-expressing polarized cell monolayers, but not to the same extent as that to hIgG1<sup>187, 188</sup>. The ability of the fused FcRnBPs to extend the half-life or deliver the fusion partner across mucosal barriers *in vivo* was not addressed in this study. However, in another study, Y14H-containing FcRnBPs were used to build a panel of antibody Fab fusions where linear and cyclic versions of the peptides that were fused to the light chain or heavy chain of the Fab at either the N- or C-terminal end, or both, via a glycine-serine-linker<sup>188</sup>. Screening for hFcRn binding followed by transcytosis experiments, showed that the fusion proteins had varying degree of receptor binding activity and ability to be transported across polarized human cells. In addition, determination of the half-life in non-human primates revealed that a fusion with four linear FcRnBPs fused to the N- and C-terminal ends of both light and heavy chains gave the greatest systemic exposure<sup>188</sup>. While the half-life of a Fab fragment was measured to be only about 3-5 hours due to its molecular weight below the renal clearance threshold, the fused FcRnBPs could extend the half-life to 67 hours, which is far from that of IgG and albumin with a half-life of about 5 days in non-human primates<sup>153, 162</sup>. In spite of this, the study pinpoints the importance of avidity for efficient receptor engagement and transport.

### 5.3.2. Engineered protein domains

Protein domains (16kDa) with FcRn-binding properties have been generated by combining the CH2 domain of an IgG1 Fc (m01s) with the grafting of a stretch of five amino acids derived from the CH3 domain, containing the key FcRn interaction residues H433 and H435 (**Table 3**)<sup>157</sup>. Although this fusion bound hFcRn, further engineering was done by the use of phage display to select mutant versions with increased and strict pH-dependent binding to the receptor. One such variant (2C10) showed the capacity to be transcytosed across polarized cells in a *Transwell*® system but did not perform as well as the hIgG1 Fc fragment. When tested in non-human primates, the half-life was measured to be 40-44 hours, more than 3-fold longer than that of m01s<sup>157</sup>. While this example shows that protein domains with a size below the renal clearance threshold

combined with FcRn-binding properties can be rescued from degradation *in vivo*, the gain in half-life was modest compared with full-length hIgG. In another phage display approach, single chain variable fragments (scFv) were selected towards hFcRn, which yielded candidates (FnAb-8 and FnAb-12) with nanomolar affinity at acidic pH (**Table 3**)<sup>158</sup>. These scFv bound 10 to 100-fold more strongly to hFcRn than hIgG, and with no or slightly weak binding observed at neutral pH. While FnAb-8 showed overlapping binding with that of IgG, FnAb-12 apparently strengthened IgG binding to the receptor. Further, fusion of FnAb-8 and FnAb-12 to GLP-1 resulted in maintained pH-dependent hFcRn binding as well as binding to the GLP-1 receptor. When FnAb-8 was studied in non-human primates, it revealed a half-life of 100-200 hours, which was about 2-fold longer than that measured for 2C10. Curiously, while the GLP-1 analog exenatide reduced blood glucose concentrations for 2 hours in WT mice, engineered scFvs fused to GLP-1 prolonged this effect for up to 8 hours, despite not having the ability to engage mFcRn<sup>158</sup>. The last example is phage display selection of affibody molecules. This scaffold is a three-helix bundle based on a domain (6 kDa) derived from IgG-binding Protein A from *Staphylococcus aureus*<sup>189</sup>. The identified FcRn binders ( $Z_{FcRn\_2}$ ,  $Z_{FcRn\_4}$  and  $Z_{FcRn\_16}$ ) (**Table 3**) were shown to bind in a pH-dependent manner not only to hFcRn but also mFcRn, where binding was mediated by the presence of two histidine residues that gave 20 to 43-fold stronger binding than that of hIgG<sup>156</sup>. Fusion of the affibody molecules to an albumin-binding domain (ABD), which will hijack albumin *in vivo*, resulted in a half-life of 91-73 hours, 1.6 to 2.7-fold longer than that of a control protein when injected in mice expressing mFcRn<sup>156</sup>. Notably, ABD interacts with albumin across species without affecting FcRn binding<sup>190</sup>. Lastly, when ABD-fused  $Z_{FcRn\_2}$ , which bound less pH-dependent, was tested for its ability to out-compete IgG binding to the receptor, a reduction of up to 40% in IgG levels were measured in mice<sup>191</sup>.

**Table 3 | Engineered FcRn binding peptides and domains.**

Ligand	Name	Sequence <sup>a</sup>	$K_d$ at pH 6.0 (nM)	$K_d$ at pH 7.4 (nM)	Reference
FcRnBP	SYN722	QRFCTGHFGGLYPCNGP	5,700*	45,000*	154, 155
	SYN723	GGGCVTGHFGGIYCNYQ	5,200*	35,000*	
	SYN724	KIICSPGHFGGMYCQ GK	22,000*	78,000*	
	SYN725	PSYCIEGHIDGIYCFNA	8,800*	76,000*	
	SYN726	NSFCRGRPGHFGGCYLF	9,400*	93,000*	
	SYN746	Ac-NH-[QRFCTGHFGGLYPCNGP]-CONH <sub>2</sub>	5,100*	30,000*	

	SYN1327	Ac-NH-[RF-Pen-TGHFG-Sar-NMeLeu-YP <sup>C</sup> ]-CONH <sub>2</sub>	31 ± 4*	170 ± 20*	
	SYN1436	Dimer of -[RF-Pen-TGHFG-Sar-NMeLeu-YP <sup>C</sup> ]-CONH <sub>2</sub>	< 0.5*	< 0.8*	
<b>Protein domain</b>	m01s	-	Low*	Low*	
	a2b	(m01s)-RCPRWMRTPHNHYT	2,200*	Negligible*	157
	2C10	(m01s)-FGNCAYLRPHNHYT	1,100*	Low*	
<b>scFv</b>	FnAb-8	-	4.32*	Negligible*	158
	FnAb-12	-	43.2*	Low*	
<b>Affibody</b>	Z <sub>FcRn_2</sub>	VDAKYAKEQDAAAHEIRWLPNLTFDQRVAFIH KLADDPSQSSELLSEAKKLND <sup>S</sup> QAPK	12 <sup>#</sup>	> 500 <sup>#</sup>	
	Z <sub>FcRn_4</sub>	VDAKYAKEFESAAAHEIRWLPNLTYDQRVAFIHK LSDDPSQSSELLSEAKKLND <sup>S</sup> QAPK	50 <sup>#</sup>	> 1,000 <sup>#</sup>	156
	Z <sub>FcRn_16</sub>	VDAKYAKEWMRAAHEIRWLPNLTFDQRVAFIH KLEDDPSQSSELLSEAKKLND <sup>S</sup> QAPK	14 <sup>#</sup>	> 500 <sup>#</sup>	

(a) Single-letter amino acid codes are used except for Pen, l-penicillamine; NMeLeu, l-N-methylleucine; Sar, sarcosine. Amino acids colored in orange are connected by a disulfide bridge. Binding affinity ( $K_d$ ) was determined by (\*) surface plasmon resonance and (#) biosensor analysis.

## 6. The importance of considering cross-species FcRn differences for preclinical evaluation

Non-human primates are considered the most suitable animal model for preclinical testing of hlgG- and HSA-based drugs, but economic and ethical reasons exclude it from routine screening of drug candidates and exploration of proof-of-concepts<sup>192</sup>. On the other hand, mouse models are more suitable for initial preclinical assessment due to their convenience, cost-effectiveness and genetic background. However, the examples given in this review on engineered hlgG Fc and HSA variants were all evaluated in mice transgenic for hFcRn prior to testing in non-human primates. The reason for this is that there are large cross-species ligand binding differences between the mouse and human form of FcRn that must be taken into consideration to obtain reliable preclinical *in vivo* data.

### 6.1. Biology of FcRn and its ligand in mice and humans

FcRn is expressed in almost all cell types and tissues of the body, with a few exceptions, as described<sup>193, 194</sup>. Regarding its role in IgG transcytosis, FcRn has been shown to mediate the delivery of endogenous IgG from the mother to the fetus via transplacental transport during the third trimester of pregnancy<sup>195, 196</sup>. This secures passive immunity



of the newborn at a critical time of life. In mice, such transport occurs via the placenta, but mostly via intestinal uptake of neonatal mice during the suckling period, when large amounts of IgG are taken up from the mother's milk via pH-dependent FcRn-directed transcytosis<sup>197</sup>. Interestingly, while the intestinal tissue expression of FcRn in humans are maintained throughout life, it is developmentally downregulated in conventional mice<sup>87, 198</sup>. For this reason, caution should be taken when addressing FcRn-targeting approaches and, due to this, it has been suggested that such studies should be performed no later than 6-16 weeks after weaning in mice expressing mFcRn<sup>199</sup>. Notably, mFcRn is expressed in high levels in duodenum and jejunum during neonatal life<sup>198, 200, 201</sup>. In humans, the receptor is expressed in different sections of the human intestine, including the colon and ileum, but somewhat less in jejunum and duodenum<sup>102, 193, 199, 202</sup>. Although the FcRn expression of intestinal tissues is down-regulated in mice, it persists throughout life in other tissues and, as such, regulates IgG and albumin half-life and biodistribution.

Despite the fact that the mouse and human forms of the FcRn heavy chain share nearly 70% similarity in the amino acid composition, and that the key interacting residues responsible for pH-dependent binding are conserved<sup>29, 203</sup>, there are distinct variations that give rise to large differences in cross-species binding. Specifically, this results in no or very poor binding of mIgG to the human receptor, while hIgG binds more strongly to the mouse receptor than to the human form<sup>204, 205</sup>. As such, hIgG Fc-engineering for improved binding to hFcRn does not translate into extended half-life in conventional mice, but rather shorter half-life than the WT counterpart, as engineering for more favorable pH-dependent binding is not preserved<sup>70, 206</sup>. This is the case for all hIgG Fc-engineered variants reported to date, which means that they cannot be used in mouse models expressing mFcRn. In contrast to hIgG, HSA binds very poorly to mFcRn, with more than 20-fold weaker binding than mouse serum albumin (MSA), whereas MSA binds slightly stronger than HSA to hFcRn<sup>37, 192, 204, 207, 208</sup>. Thus, HSA injected into conventional mice is out-competed for binding to mFcRn in the presence of high amounts of natural endogenous MSA, produced continuously by the liver. This means that HSA is not rescued from intracellular degradation in mice expressing mFcRn, as illustrated by the fact that WT HSA has nearly identical half-life as HSA engineered for considerably reduced binding to hFcRn<sup>153</sup>. Therefore, studies conducted under such conditions do not take into consideration the contribution of FcRn and, as such, this preclinical setting is non-physiological. The molecular explanations for the large cross-species differences have been described in depth elsewhere<sup>73, 153, 192, 207, 209, 210</sup>.

## 6.2. Human FcRn transgenic mouse models

To solve this preclinical challenge, several genetically engineered mouse strains have been developed where the mFcRn heavy chain has been replaced with the human counterpart, either under the control of the mouse or human promoter elements<sup>35, 72, 175, 208, 211-215</sup>. These strains are the current gold standards for the evaluation of hFcRn-targeting strategies addressing pharmacokinetics, pharmacodynamics and delivery across selective mucosal barriers prior to studies in non-human primates. The most commonly used hFcRn-expressing strains are generated from conventional C57BL/6J mice, named Tg32 and Tg276 (**Figure 4 A**), which are extensively used to assess the half-life of hIgG and HSA variants<sup>35, 72, 175, 212, 214, 215</sup>. Both strains have substituted the mouse heavy chain with that of the human form, which can pair non-covalently with the endogenous mouse  $\beta 2m$ <sup>35, 72, 175, 214, 215</sup>. A distinct difference between these strains is that the Tg32 mice express the heavy chain under the control of its human regulatory elements<sup>72, 175, 212, 214, 215</sup>, while the expression in Tg276 mice is regulated by a constitutive CAG promoter, a human cytomegalovirus enhancer fused to chicken  $\beta$ -actin/rabbit  $\beta$ -globin hybrid<sup>35, 175</sup>. This results in a much more widespread expression profile of hFcRn in Tg276, whereas the FcRn expression profile in Tg32 mice has been mapped to be similar to that in humans<sup>193, 216</sup>. There is also a modified version of Tg32 that expresses human  $\beta 2m$ , but no difference in half-life of the ligands has been reported that can be related to whether the mice carry a mouse or human form of  $\beta 2m$ <sup>214</sup>. In general, the half-life of IgG is shorter in Tg276 homozygous mice relative to the Tg32 strain, and longer in the Tg32 hemizygous than the homozygous strain<sup>214</sup>. Since the expression profile of the Tg32 strains resembles more closely to that of humans, studies of FcRn in mucosal immunity and receptor targeting for delivery across the epithelial barriers have been mainly studied in these mice, as recently reviewed<sup>93</sup>. Therefore, the Tg32 strains should be used for studies addressing the mucosal delivery of FcRn-targeted molecules or nanosystems.

In humans, injected hIgG and HSA variants as well as fusions will compete for binding to FcRn in the presence of high concentrations of IgG (10 mg/mL) and albumin (40 mg/mL), produced by the plasma cells and liver, respectively. This is in stark contrast to what has been found in mice kept under pathogen-free housing, where the concentrations of endogenous mIgG are low (roughly 1.0-0.2 mg/mL) compared to those found in nature, while the concentrations of MSA are high due to constitutive production by the liver (20-50 mg/mL)<sup>35, 217</sup>. These conditions must be taken into consideration in

the preclinical evaluation of FcRn-targeted strategies, since the outcome can be greatly affected by a lack of competition for receptor binding, as in the case of the IgG binding site, which is in contrast to strong competition for the albumin-binding site. To address how competition for the IgG binding site of FcRn affects targeting approaches, mice may be pre-loaded with excess amounts of hIgG prior to administration, which has been shown to modulate the half-life of injected IgG variants<sup>175, 211, 218</sup>. Interestingly, a modified version of the Tg32 strain was recently reported that is engineered to produce hIgG1 Fc combined with mIgG Fab arms, which is rescued by hFcRn (**Figure 4 B**)<sup>211</sup>. The levels of endogenous chimeric mouse-human IgG1 were shown to be greatly increased upon immunization, which modulated the half-life of injected hIgG. Thus, this Tg32-hFc mouse model may be attractive for studies addressing competition for the IgG binding sites. A similar mouse model that also expresses the human classical Fcγ receptors have been reported<sup>219</sup>.

Regarding studies of HSA-based strategies, a version of Tg32 that lacks expression of MSA has been developed<sup>213</sup>. This model allows studies in the absence of competition, but also in the presence HSA following preloading (**Figure 4 C**). An alternative to this is a mouse strain, named Albumus<sup>TM</sup>, that has been genetically modified to express both hFcRn and HSA<sup>208</sup>. However, the expression of the heavy chain of hFcRn is here not under control of the human promoter (**Figure 4 D**). Despite this, studies of engineered HSA variants in Tg32 with competition and in the double transgenic mouse model have revealed similar half-lives<sup>153, 208, 215</sup>. Due to differences in the construction of these strain, they may vary regarding the expression of the receptor in different mucosal tissues, which has not yet been studied in detail. Importantly, it has recently been shown that competition for the albumin-binding site strongly affects the half-life of injected HSA<sup>66, 213</sup>. While the half-life in Tg32 mice lacking expression of albumin was measured to be around 3 weeks for injected WT HSA, it was only a few days in the presence of competition<sup>66, 213</sup>. This demonstrates that the competitive pressure is high for the albumin-binding site of FcRn. As such, only minor alterations to the binding kinetics of WT HSA fusions may affect their half-life. To compensate for this, HSA engineered for improved hFcRn binding may be used. When QMP HSA variant was compared with WT HSA in Tg32 mice lacking albumin, it only showed a 1.2-fold longer half-life, whereas a 2-fold difference was measured in presence of competition<sup>66</sup>. The same effect of competition was observed when the HSA variants were administered intranasally, followed by homing to the lungs and uptake into the bloodstream<sup>66</sup>. Moreover, when QMP was fused to an antibody fragment, more than 4-fold the amount of WT fusion was

detected in the blood for 24 hours following intranasal administration, which corresponded to around 10% of the dose given <sup>66</sup>. Importantly, uptake and transport across the mucosal lung barriers were much more efficient for HSA than for hIgG <sup>66</sup>. As such, QMP should be an attractive fusion partner for more favorable pharmacokinetics and transepithelial delivery.

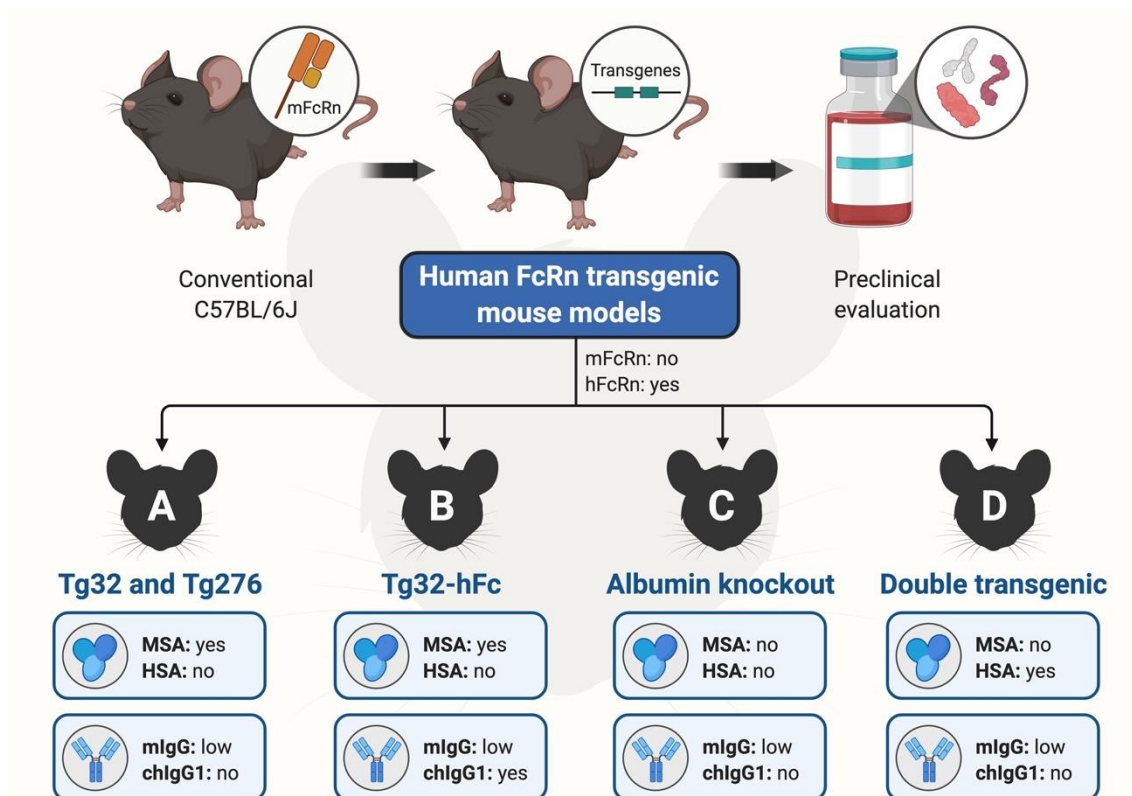


**Figure 4 | Human FcRn transgenic mouse models for evaluation of IgG and albumin-based therapeutics.** Conventional C57BL/6J mice have been used to generate humanized mouse strains that are transgenic for hFcRn. While (A) the Tg32 and Tg276 strains express mIgG, (B) the Tg32-hFc strain expresses chimeric hIgG1 (chIgG1). In comparison to these mouse strains, (C) Tg32 albumin knockout mice do not express MSA, while (D) the double transgenic mouse model (Albumus™) have both hFcRn and HSA. The figure was created with BioRender.

## 7. FcRn-targeted nanosystems for oral delivery of antidiabetic peptides

An attractive strategy for enhancing oral delivery of antidiabetic peptides is to encapsulate them into NPs <sup>7, 220-222</sup>. This will improve protection against harsh conditions in the GIT, which may enhance uptake and transport across the selective barriers <sup>8, 9</sup>. While several reports have shown promising results, oral delivery of NPs is still limited by low bioavailability. Thus, there is a need to make a quantum leap in how nanosystems

are designed to make oral delivery far more efficient. One way to achieve this may be to combine the biotechnological advances of NP design with strategies to target FcRn at mucosal surfaces<sup>11-15</sup>. This may allow active transport across the polarized intestinal epithelium for delivery to the systemic circulation<sup>11, 12, 15</sup>. The NP design must then be done in a way that favors FcRn engagement and transcellular transport, parameters that are not yet fully defined. However, while NPs can be decorated with FcRn-targeting molecules, the encapsulated peptides may also be engineered for efficient FcRn-mediated recycling, as discussed in **Section 4**, which can improve half-life and bioavailability upon release from the NPs. Next, a brief overview of parameters that are relevant to be considered in the context of NP design and FcRn-targeting will be discussed.

### 7.1. Design of targeting nanosystems

The stability and characteristics of nanosystems, including their size, charge, shape, material and coating are parameters that dictate their internalization and transport properties (**Figure 5**), as extensively reviewed<sup>7, 8, 223-226</sup>. However, for the NPs to be targeted to FcRn, they must be engineered to display receptor-targeting molecules on their surface in such a manner that will allow for efficient binding-and-release and stability throughout the endosomal pH gradient. Relevant parameters to be considered are how the pH-dependent binding kinetics of the FcRn-binding molecules affect the ability of the NPs to be transported, and in this context, how the number and density of the targeting molecules and, as such, avidity and flexibility are affecting the outcome<sup>227</sup>. Decoration of NPs with FcRn-targeting molecules could be achieved in a non-covalent manner by adsorption, but preferably covalently to secure stability<sup>228</sup>. To ensure the latter, conjugation should be irreversible and site-specific to fix the orientation of the molecules in such a way that guarantees availability and functional display. One strategy is to use MAL-thiol or carbodiimide chemistry for site-specific conjugation. Regarding the MAL-thiol reaction, it requires coupling of sulfhydryl reactive MAL on the surface of NPs to thiol groups present on hIgG or HSA, which will result in irreversible thioether bonds<sup>229</sup>. As hIgG or the constant Fc does not contain any free cysteine residues, functional groups using primary amine reactive reagents or crosslinkers must be used<sup>11, 12</sup>. However, when it comes to HSA, C34 in DI is an attractive site for conjugation<sup>15</sup>. On the other hand, carbodiimide crosslinking can be achieved using 1-ethyl-3-(3-dimethylaminopropyl)-carbodiimide/N-hydroxysuccinimide (EDC/NHS) reaction to form an amide bond between the carboxylic groups of hIgG Fc or HSA and the functionalized aminated NPs

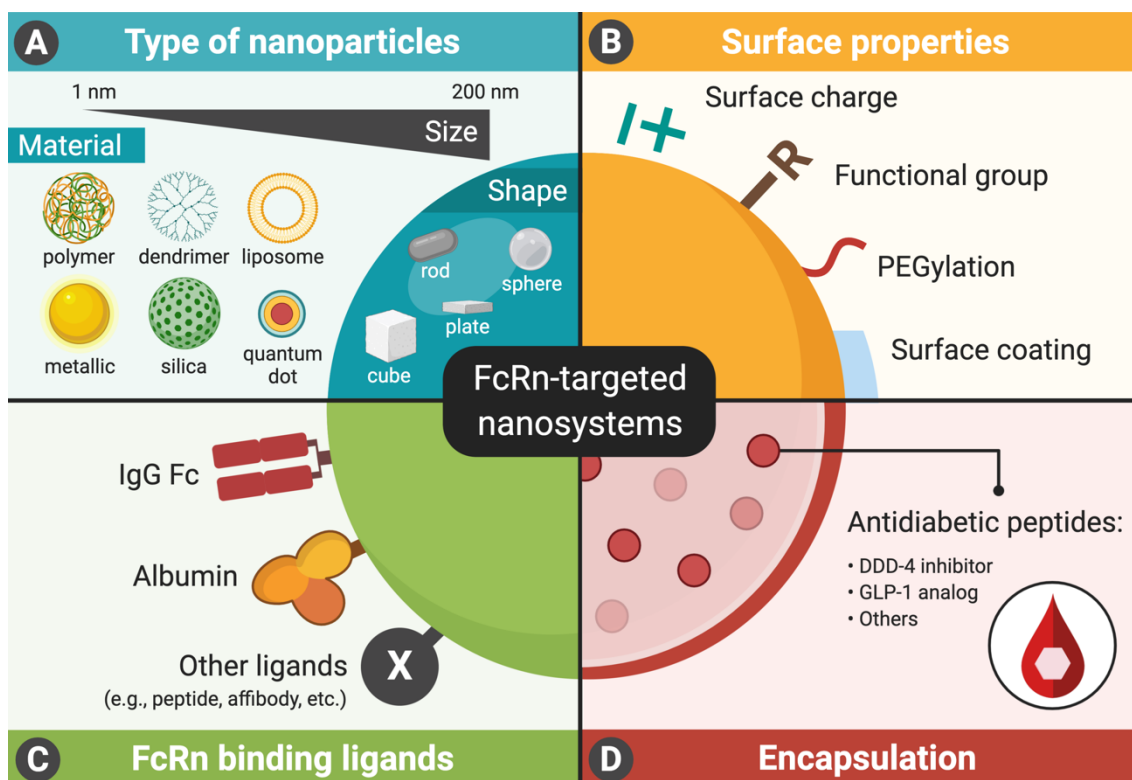


**Figure 5 | Design of FcRn-targeted nanosystems for oral delivery of antidiabetic peptides.**

The physicochemical characteristics of engineered NPs can be tailored by altering **(A)** the particle size, shape and composition as well as **(B)** their surface properties. To ensure efficient transport of the NPs across selective polarized epithelial barriers that express FcRn, the surface of NPs may be decorated with **(C)** receptor-binding molecules engineered for improved binding and transport properties, such as IgG Fc and albumin. Such nanosystems may be used in the treatment of DM and prevention of fibrosis by **(D)** encapsulating antidiabetic peptides or fusion proteins, in the internal core of the NPs, allowing for drug protection and controlled release upon oral administration. The figure was created with BioRender.

## 7.2. IgG Fc- decorated nanosystems

The first FcRn-targeted nanosystems were developed using the Fc fragment of hIgG antibodies as a targeting moiety<sup>11-13</sup>. Several of these studies focused on the use of polymeric NPs as a scaffold for drug encapsulation<sup>11, 12, 232</sup>. A major advantage of such polymeric NPs is their biocompatibility and biodegradability, which are desirable features to avoid potential toxicity of a range of inorganic classes of NPs when considering translation of developed nanosystems into a clinical setting<sup>225, 226</sup>. An example of this is polymer-based nanosystems of poly(lactic acid) (PLA), in which thiolated hIgG Fc was

covalently conjugated to the MAL-functionalized NPs, with an average hydrodynamic diameter of about 55 nm, via MAL-thiol reaction <sup>11</sup>. The conjugation of Fc resulted in a slight increase in the particle size and showed a maintained monodispersity of the NPs before and after coupling. Since IgG antibodies generally carry a weakly negative charge under physiological conditions <sup>233</sup>, the surface charge of the Fc-decorated NPs (Fc-NPs) became slightly more negatively charged when coupled to the Fc fragments. Interestingly, Fc-NPs gave a 2-fold rise in transcytosis *in vitro* compared with non-targeted NPs across a polarized epithelial cell line that endogenously expresses hFcRn, while transport was reduced in the presence of free IgG Fc competing for receptor binding, suggesting that the increase in uptake and transcytosis was FcRn-dependent <sup>11</sup>. In conventional WT BALB/c mice, which express mFcRn throughout the small intestine and colon, Fc-targeting of FcRn enhanced *in vivo* biodistribution of the NPs in several organs, as well as the absorption efficiency by 11.5-fold following oral administration. Importantly, insulin-loaded Fc-NPs showed prolonged hypoglycemic responses in fasted mice when administered orally at a clinically relevant insulin dose compared with non-targeted NPs and to injected insulin, while free OI solution did not generate a glucose response. This effect was not observed in mice lacking FcRn expression, which may indicate FcRn-induced transcytosis of Fc-NPs in the GIT and, as such, the release of insulin from the NP matrix in blood circulation. While these studies were done in WT mice, further studies on molecules engineered for improved hFcRn should be performed in mice transgenic for the human receptor <sup>212, 215</sup>.

A similar strategy has been explored to improve oral efficacy of exenatide, a GLP-1 receptor agonist for T2DM treatment, in which the peptides were loaded into poly(lactic-co-glycolic acid) (PLGA) NPs using the same coupling chemistry as PLA-based nanosystems <sup>12</sup>. The particle size of native PLGA NPs was about 109 nm, which was larger than that of the PLA NPs <sup>11</sup>. The difference in hydrodynamic diameters observed can be explained by the methods used to synthesize NPs and the chemical composition of NP formulations. Similar increase in particle size and surface charge of human Fc-decorated PLGA NPs as that of PLA NPs was observed. In this study, relative to non-targeted nanosystems, Fc-NPs showed to be more efficiently taken up and transcytosed in a polarized epithelial cell line expressing endogenous hFcRn <sup>12</sup>. Notably, it would be of importance to compare to what degree the particle size may affect the internalization of NPs <sup>234, 235</sup>. On the other hand, a mouse model of human TD2M (db/db) was used to study the hypoglycemic response of the peptide-loaded NPs. Upon oral administration, the Fc-NPs showed a higher reduction in blood glucose levels and particle retention in

the GIT compared with non-decorated NPs<sup>12</sup>. Furthermore, FcRn-targeting of Fc-decorated nanosystems exhibited a prolonged hypoglycemic response relative to injected exenatide, although the reduction effect of the injection solution was shown to be more efficient in the first few hours following subcutaneous injection.

In addition to polymer-based NPs, nanosystems may be designed with inorganic components having unique electrical, magnetic and optical properties<sup>225, 226</sup>. Such inorganic NPs allow for fine-tuning of the size, structure and geometry for enhanced performance that may benefit oral delivery across epithelial barriers of the tailored-made nanosystems. Nevertheless, due to the toxicity and solubility limitations of such NPs, the use of inorganic materials in humans must be carefully examined<sup>236, 237</sup>. An example of inorganic nanosystems explored for oral delivery of antidiabetic peptides is undecylenic acid-coated silicon NPs (SiNPs) that were loaded with GLP-1<sup>13</sup>. In contrast to the examples of polymeric NP formulations given<sup>11, 12</sup>, SiNPs were functionalized with amine-modified Fc via EDC/NHS reaction. The NPs were then treated with mucoadhesive chitosan and eventually entrapped into a pH-responsive polymeric matrix of hypromellose acetate succinate (HPMC) to improve drug adsorption at mucosal sites and prevent premature release of encapsulated drugs under strong acidic conditions in the GIT<sup>13</sup>. The Fc-NPs showed enhanced transcytosis *in vitro* in polarized epithelial cell lines expressing hFcRn compared with non-targeted NPs, which resulted in higher amounts of GLP-1 released from the NP matrix at the basolateral side of *Transwell*® system<sup>13</sup>.

Overall, these findings have demonstrated that decoration with hIgG Fc fragments may enable the oral delivery of peptide-loaded NPs across epithelial barriers for delivery to the systemic circulation<sup>11-13</sup>. However, in addition to the lack of use of hFcRn expressing mouse models, pH-dependent binding affinity and functional avidity for the receptor of the Fc ligands decorating the surface NPs have yet to be examined to ensure optimal receptor-mediated binding and transepithelial transport of nanosystems. Furthermore, the mechanisms of action of the FcRn-targeted NPs should be studied in detail.

### **7.3. Albumin- decorated nanosystems**

Although IgG Fc have been explored as FcRn-targeting moieties, their use is impeded due to the need for chemical modification for conjugation. As such, HSA may be used for decoration of NPs owing to low immunogenicity and ease of production<sup>238, 239</sup>. Furthermore, it was very recently shown that HSA is transported more efficiently than hIgG across mucosal lung barriers *in vivo* in hFcRn transgenic mice<sup>66</sup>. On this basis, HSA



may be an attractive targeting molecule for favorable FcRn-mediated transepithelial delivery of nanosystems for oral administration of antidiabetic peptides <sup>14, 15, 232</sup>.

An example of nanosystems that have been combined with albumin is polymeric alginate-dextran sulfate-based (ADS) NPs with an average hydrodynamic diameter of 233 nm, that were coated with chitosan <sup>232</sup>. In contrast to synthetic PLA and PLGA, the polymers alginate, dextran and chitosan used to synthesize NPs are natural product-derived compounds that provide nanosystems with mucoadhesive characteristics <sup>239</sup>. In this study, bovine serum albumin (BSA) was non-specifically adsorbed onto the surface of ADS NPs <sup>232</sup>, in contrary to site-directed chemical coupling of Fc-decorated NPs <sup>11-13</sup>. In an *in vitro* model of polarized epithelial cells expressing hFcRn combined with mucus-producing goblet cells, BSA-decorated NPs loaded with insulin showed an improved permeability profile of the peptides compared to free insulin <sup>232</sup>. However, cautious should be taken when interpreting the result since the binding kinetics of BSA for hFcRn is not identical to that of HSA <sup>35</sup>. Aside from that, strategies for surface modification of NPs and pH-dependent functionality of ligands are two other important parameters to address.

An attempt was made to decorate the surface of HPMC-treated undecylenic acid-coated SiNPs with HSA via EDC/NHS reaction <sup>14</sup>. The chemical surface modification of NPs with HSA showed an increase in particle size from 162 nm to 238 nm after conjugation, with high monodispersity. Interestingly, HSA-conjugated NPs (HSA-NPs) exhibited improved cytocompatibility in human epithelial cell lines relative to non-conjugated NPs, which suggests that decorating nanosystems with biocompatible compounds, such as HSA, may reduce the toxicity of inorganic nanomaterials. Furthermore, the presence of HSA on the NP surface demonstrated enhanced cellular uptake and internalization of nanosystems *in vitro* with the aid of hFcRn expressed on the cell surface <sup>14</sup>. Done in this fashion, HSA-NPs encapsulating insulin showed enhanced transport of loaded peptides across polarized epithelial cell monolayers in an *in vitro* transcytosis assays. The data also suggested an improvement in the transepithelial delivery of encapsulated antidiabetic peptides when comparing HSA-NPs with IgG Fc-NPs <sup>13</sup>, which encourages research on the use of engineered HSA variants tailored for improved FcRn binding and transport properties as targeting ligands, as discussed in **Section 5** <sup>66</sup>.

Recently, the KP variant of HSA, which shows a 12-fold improved hFcRn binding compared to WT HSA <sup>153</sup>, has been explored in an NP formulation of polymeric PLGA with an average hydrodynamic diameter of about 150 nm <sup>15</sup>. In this study, the surface of PLGA NPs was functionalized with HSA through MAL-thiol conjugation chemistry, in

which no or slight increase in particle size was observed as a result of protein coupling. Most importantly, the pH-dependent binding characteristics for hFcRn of HSA-NPs were in line with reported studies for free/uncoupled HSA<sup>66, 153</sup>. Compared to WT-decorated NPs, KP-decorated NPs showed enhanced binding to hFcRn at mildly acidic pH (5.5), while receptor binding was not observed for NPs decorated with an engineered HSA variant that does not bind hFcRn<sup>15</sup>. Similar results were demonstrated in an *in vitro* transcytosis assays, where KP-decorated NPs were transported 2-fold more efficiently than WT-decorated NPs across polarized epithelial cells expressing hFcRn<sup>15</sup>. Intriguingly, when studying the effect of HSA functionalization on the hypoglycemic response of insulin-loaded PLGA NPs in T1DM-induced mice transgenic for hFcRn, KP-decorated NPs showed the most efficient glycemic reduction following oral administration compared with other HSA-NPs and to OI solution.

Altogether, engineered HSA shows promise in the next-generation design of FcRn-targeted nanosystems for oral delivery of antidiabetic peptides. The ultimate aim now will be to tailor-design such strategies for further improvement in receptor engagement and transport properties to favor efficient transepithelial transport of NPs across the GIT upon oral administration. The QMP HSA variant, should be an attractive FcRn targeting partner for decoration of NPs to achieve not only enhanced mucosal delivery but also prolonged half-life of fused peptides<sup>66</sup>.

## **8. Conclusions**

Nanosystems for encapsulation of drugs have the potential to make a significant impact on the treatment of many diseases, including diabetes and fibrosis. While a number of NP-based strategies have entered clinical trials or have been approved for use, they can only be administered by parenteral delivery methods. An alternative and preferable approach would be oral administration, but this remains a challenge because uptake and delivery across selective epithelial barriers is very limited. Furthermore, frequent administration is often required. As such, design of nanosystems tailored for oral administration is preferable due to patient convenience and compliance. In this review, we have highlighted how in-depth insights into the biology of FcRn may be used to engineer NPs decorated with receptor-binding molecules with the aim to overcome the highly inefficient uptake at the intestinal epithelial barriers. If this major challenge is solved, it will allow for more cost-effective self-administered methods. In addition, the encapsulated drugs, such as antidiabetic peptides, may also be engineered for extended

half-life and increased bioavailability by taking advantage of pH-dependent FcRn engagement. For preclinical testing of such strategies, considerable cross-species FcRn binding differences must be taken into account to secure reliable results from mouse model systems.

### **Conflict of interest**

The authors declare no conflict of interest.

### **Acknowledgements**

This paper was financed by Portuguese funds through FCT - Fundação para a Ciência e a Tecnologia/Ministério da Ciência, Tecnologia e Ensino Superior in the framework of the project "Institute for Research and Innovation in Health Sciences" UID/BIM/04293/2019. Cláudia Azevedo (SFRH/BD/117598/2016) and Soraia Pinto (SFRH/BD/144719/2019) would like to thank to Fundação para a Ciência e a Tecnologia (FCT), Portugal for financial support. S.B., J.N. and J.T.A. were supported by the Research Council of Norway (Grant no. 274993; 287927), and J.T.A. by the South-Eastern Norway Regional Health Authority (Grant no. 2018052; 2019084).

## References

1. Zheng Y, Ley SH, Hu FB. Global aetiology and epidemiology of type 2 diabetes mellitus and its complications. *Nature Reviews Endocrinology* 2018;14:88-98.
2. WHO. Classification of diabetes mellitus 2019. Volume 2020, 2019.
3. Basson R, Bayat A. Chapter 7 - Fibrosis and diabetes: Chronic hyperglycemia triggers organ-specific fibrotic mechanisms. In: Bagchi D, Das A, Roy S, eds. *Wound Healing, Tissue Repair, and Regeneration in Diabetes: Academic Press*, 2020:121-147.
4. Fowler MJ. Microvascular and Macrovascular Complications of Diabetes. *Clinical Diabetes* 2008;26:77-82.
5. Ban CR, Twigg SM. Fibrosis in diabetes complications: pathogenic mechanisms and circulating and urinary markers. *Vascular health and risk management* 2008;4:575-596.
6. Sosnik A, das Neves J, Sarmiento B. Mucoadhesive polymers in the design of nano-drug delivery systems for administration by non-parenteral routes: A review. *Progress in Polymer Science* 2014;39:2030-2075.
7. Thwala LN, Pr eat V, Csaba NS. Emerging delivery platforms for mucosal administration of biopharmaceuticals: a critical update on nasal, pulmonary and oral routes. *Expert Opin Drug Deliv* 2017;14:23-36.
8. Ara ujo F, das Neves J, Martins JP, et al. Functionalized materials for multistage platforms in the oral delivery of biopharmaceuticals. *Progress in Materials Science* 2017;89:306-344.
9. Goldberg M, Gomez-Orellana I. Challenges for the oral delivery of macromolecules. *Nat Rev Drug Discov* 2003;2:289-95.
10. Patra JK, Das G, Fraceto LF, et al. Nano based drug delivery systems: recent developments and future prospects. *J Nanobiotechnology* 2018;16:71.
11. Pridgen EM, Alexis F, Kuo TT, et al. Transepithelial transport of Fc-targeted nanoparticles by the neonatal fc receptor for oral delivery. *Sci Transl Med* 2013;5:213ra167.
12. Shi Y, Sun X, Zhang L, et al. Fc-modified exenatide-loaded nanoparticles for oral delivery to improve hypoglycemic effects in mice. *Scientific Reports* 2018;8:726.
13. Martins JP, Liu D, Fontana F, et al. Microfluidic Nanoassembly of Bioengineered Chitosan-Modified FcRn-Targeted Porous Silicon Nanoparticles @ Hypromellose Acetate Succinate for Oral Delivery of Antidiabetic Peptides. *ACS Applied Materials & Interfaces* 2018;10:44354-44367.
14. Martins JP, D'Auria R, Liu D, et al. Engineered Multifunctional Albumin-Decorated Porous Silicon Nanoparticles for FcRn Translocation of Insulin. *Small* 2018;14:e1800462.
15. Azevedo C, Nilsen J, Grevys A, et al. Engineered albumin-functionalized nanoparticles for improved FcRn binding enhance oral delivery of insulin. *Journal of Controlled Release* 2020;327:161-173.

16. Goldin A, Beckman JA, Schmidt AM, et al. Advanced glycation end products: sparking the development of diabetic vascular injury. *Circulation* 2006;114:597-605.
17. Lamouille S, Xu J, Derynck R. Molecular mechanisms of epithelial-mesenchymal transition. *Nat Rev Mol Cell Biol* 2014;15:178-96.
18. Yu MA, Shin KS, Kim JH, et al. HGF and BMP-7 ameliorate high glucose-induced epithelial-to-mesenchymal transition of peritoneal mesothelium. *J Am Soc Nephrol* 2009;20:567-81.
19. Zeisberg M, Zeisberg EM. Evidence for antifibrotic incretin-independent effects of the DPP-4 inhibitor linagliptin. *Kidney Int* 2015;88:429-31.
20. Wang X, Hausding M, Weng SY, et al. Gliptins Suppress Inflammatory Macrophage Activation to Mitigate Inflammation, Fibrosis, Oxidative Stress, and Vascular Dysfunction in Models of Nonalcoholic Steatohepatitis and Liver Fibrosis. *Antioxid Redox Signal* 2018;28:87-109.
21. Jensterle M, Janez A, Fliers E, et al. The role of glucagon-like peptide-1 in reproduction: from physiology to therapeutic perspective. *Hum Reprod Update* 2019;25:504-517.
22. de Mesquita FC, Guixé-Muntet S, Fernández-Iglesias A, et al. Liraglutide improves liver microvascular dysfunction in cirrhosis: Evidence from translational studies. *Scientific Reports* 2017;7:3255.
23. Seghieri M, Christensen AS, Andersen A, et al. Future Perspectives on GLP-1 Receptor Agonists and GLP-1/glucagon Receptor Co-agonists in the Treatment of NAFLD. *Frontiers in Endocrinology* 2018;9.
24. Haymann JP, Levraud JP, Bouet S, et al. Characterization and localization of the neonatal Fc receptor in adult human kidney. *J Am Soc Nephrol* 2000;11:632-9.
25. Spiekermann GM, Finn PW, Ward ES, et al. Receptor-mediated immunoglobulin G transport across mucosal barriers in adult life: functional expression of FcRn in the mammalian lung. *J Exp Med* 2002;196:303-10.
26. Akilesh S, Huber TB, Wu H, et al. Podocytes use FcRn to clear IgG from the glomerular basement membrane. *Proc Natl Acad Sci U S A* 2008;105:967-72.
27. Simister NE, Rees AR. Isolation and characterization of an Fc receptor from neonatal rat small intestine. *Eur J Immunol* 1985;15:733-8.
28. Simister NE, Mostov KE. An Fc receptor structurally related to MHC class I antigens. *Nature* 1989;337:184-7.
29. West AP, Jr., Bjorkman PJ. Crystal structure and immunoglobulin G binding properties of the human major histocompatibility complex-related Fc receptor(,). *Biochemistry* 2000;39:9698-708.
30. Burmeister WP, Huber AH, Bjorkman PJ. Crystal structure of the complex of rat neonatal Fc receptor with Fc. *Nature* 1994;372:379-83.

31. Bjorkman PJ, Saper MA, Samraoui B, et al. The foreign antigen binding site and T cell recognition regions of class I histocompatibility antigens. *Nature* 1987;329:512-8.
32. Burmeister WP, Gastinel LN, Simister NE, et al. Crystal structure at 2.2 Å resolution of the MHC-related neonatal Fc receptor. *Nature* 1994;372:336-43.
33. Raghavan M, Bonagura VR, Morrison SL, et al. Analysis of the pH Dependence of the Neonatal Fc Receptor/Immunoglobulin G Interaction Using Antibody and Receptor Variants. *Biochemistry* 1995;34:14649-14657.
34. Vaughn DE, Bjorkman PJ. Structural basis of pH-dependent antibody binding by the neonatal Fc receptor. *Structure* 1998;6:63-73.
35. Chaudhury C, Mehnaz S, Robinson JM, et al. The major histocompatibility complex-related Fc receptor for IgG (FcRn) binds albumin and prolongs its lifespan. *J Exp Med* 2003;197:315-22.
36. Andersen JT, Dee Qian J, Sandlie I. The conserved histidine 166 residue of the human neonatal Fc receptor heavy chain is critical for the pH-dependent binding to albumin. *Eur J Immunol* 2006;36:3044-51.
37. Andersen JT, Dalhus B, Cameron J, et al. Structure-based mutagenesis reveals the albumin-binding site of the neonatal Fc receptor. *Nat Commun* 2012;3:610.
38. Oganessian V, Damschroder MM, Cook KE, et al. Structural insights into neonatal Fc receptor-based recycling mechanisms. *J Biol Chem* 2014;289:7812-24.
39. Raghavan M, Bonagura VR, Morrison SL, et al. Analysis of the pH dependence of the neonatal Fc receptor/immunoglobulin G interaction using antibody and receptor variants. *Biochemistry* 1995;34:14649-57.
40. Chaudhury C, Brooks CL, Carter DC, et al. Albumin binding to FcRn: distinct from the FcRn-IgG interaction. *Biochemistry* 2006;45:4983-90.
41. Roopenian DC, Akilesh S. FcRn: the neonatal Fc receptor comes of age. *Nature Reviews Immunology* 2007;7:715.
42. de Taeye SW, Rispens T, Vidarsson G. The Ligands for Human IgG and Their Effector Functions. *Antibodies (Basel)* 2019;8.
43. Saphire EO, Parren PW, Pantophlet R, et al. Crystal structure of a neutralizing human IGG against HIV-1: a template for vaccine design. *Science* 2001;293:1155-9.
44. Kim JK, Tsen MF, Ghetie V, et al. Localization of the site of the murine IgG1 molecule that is involved in binding to the murine intestinal Fc receptor. *Eur J Immunol* 1994;24:2429-34.
45. Kim JK, Tsen MF, Ghetie V, et al. Identifying amino acid residues that influence plasma clearance of murine IgG1 fragments by site-directed mutagenesis. *Eur J Immunol* 1994;24:542-8.

46. Raghavan M, Chen MY, Gastinel LN, et al. Investigation of the interaction between the class I MHC-related Fc receptor and its immunoglobulin G ligand. *Immunity* 1994;1:303-315.
47. Medesan C, Matesoi D, Radu C, et al. Delineation of the amino acid residues involved in transcytosis and catabolism of mouse IgG1. *The Journal of Immunology* 1997;158:2211-2217.
48. Kim JK, Firan M, Radu CG, et al. Mapping the site on human IgG for binding of the MHC class I-related receptor, FcRn. *Eur J Immunol* 1999;29:2819-25.
49. Martin WL, West AP, Gan L, et al. Crystal Structure at 2.8 Å of an FcRn/Heterodimeric Fc Complex. *Molecular Cell* 2001;7:867-877.
50. Walters BT, Jensen PF, Larraillet V, et al. Conformational Destabilization of Immunoglobulin G Increases the Low pH Binding Affinity with the Neonatal Fc Receptor. *J Biol Chem* 2016;291:1817-25.
51. Foss S, Grevys A, Sand KMK, et al. Enhanced FcRn-dependent transepithelial delivery of IgG by Fc-engineering and polymerization. *J Control Release* 2016;223:42-52.
52. Bitonti AJ, Dumont JA, Low SC, et al. Pulmonary delivery of an erythropoietin Fc fusion protein in non-human primates through an immunoglobulin transport pathway. *Proc Natl Acad Sci U S A* 2004;101:9763-8.
53. Medesan C, Matesoi D, Radu C, et al. Delineation of the amino acid residues involved in transcytosis and catabolism of mouse IgG1. *J Immunol* 1997;158:2211-7.
54. Vaughn DE, Milburn CM, Penny DM, et al. Identification of critical IgG binding epitopes on the neonatal Fc receptor. *J Mol Biol* 1997;274:597-607.
55. Piche-Nicholas NM, Avery LB, King AC, et al. Changes in complementarity-determining regions significantly alter IgG binding to the neonatal Fc receptor (FcRn) and pharmacokinetics. *mAbs* 2018;10:81-94.
56. Wang W, Lu P, Fang Y, et al. Monoclonal antibodies with identical Fc sequences can bind to FcRn differentially with pharmacokinetic consequences. *Drug Metab Dispos* 2011;39:1469-77.
57. Schoch A, Kettenberger H, Mundigl O, et al. Charge-mediated influence of the antibody variable domain on FcRn-dependent pharmacokinetics. *Proc Natl Acad Sci U S A* 2015;112:5997-6002.
58. Jensen PF, Larraillet V, Schlothauer T, et al. Investigating the interaction between the neonatal Fc receptor and monoclonal antibody variants by hydrogen/deuterium exchange mass spectrometry. *Mol Cell Proteomics* 2015;14:148-61.
59. Theodore Peters J. *All About Albumin: Biochemistry, Genetics, and Medical Applications*, 1995.
60. Ghuman J, Zunszain PA, Petitpas I, et al. Structural basis of the drug-binding specificity of human serum albumin. *J Mol Biol* 2005;353:38-52.

61. Bern M, Sand KM, Nilsen J, et al. The role of albumin receptors in regulation of albumin homeostasis: Implications for drug delivery. *J Control Release* 2015;211:144-62.
62. Curry S, Mandelkow H, Brick P, et al. Crystal structure of human serum albumin complexed with fatty acid reveals an asymmetric distribution of binding sites. *Nat Struct Biol* 1998;5:827-35.
63. Schmidt MM, Townson SA, Andreucci AJ, et al. Crystal structure of an HSA/FcRn complex reveals recycling by competitive mimicry of HSA ligands at a pH-dependent hydrophobic interface. *Structure* 2013;21:1966-78.
64. Sand KM, Dalhus B, Christianson GJ, et al. Dissection of the neonatal Fc receptor (FcRn)-albumin interface using mutagenesis and anti-FcRn albumin-blocking antibodies. *J Biol Chem* 2014;289:17228-39.
65. Sand KM, Bern M, Nilsen J, et al. Interaction with both domain I and III of albumin is required for optimal pH-dependent binding to the neonatal Fc receptor (FcRn). *J Biol Chem* 2014;289:34583-94.
66. Bern M, Nilsen J, Ferrarese M, et al. An engineered human albumin enhances half-life and transmucosal delivery when fused to protein-based biologics. *Science Translational Medicine* 2020;12:eabb0580.
67. Peters T, Jr. Serum albumin. *Adv Protein Chem* 1985;37:161-245.
68. Spiegelberg HL, Fishkin BG. The catabolism of human G immunoglobulins of different heavy chain subclasses. 3. The catabolism of heavy chain disease proteins and of Fc fragments of myeloma proteins. *Clinical and experimental immunology* 1972;10:599-607.
69. Waldmann TA, Strober W. Metabolism of immunoglobulins. *Prog Allergy* 1969;13:1-110.
70. Grevys A, Nilsen J, Sand KMK, et al. A human endothelial cell-based recycling assay for screening of FcRn targeted molecules. *Nature Communications* 2018;9:621.
71. Israel EJ, Wilsker DF, Hayes KC, et al. Increased clearance of IgG in mice that lack beta 2-microglobulin: possible protective role of FcRn. *Immunology* 1996;89:573-8.
72. Roopenian DC, Christianson GJ, Sproule TJ, et al. The MHC class I-like IgG receptor controls perinatal IgG transport, IgG homeostasis, and fate of IgG-Fc-coupled drugs. *J Immunol* 2003;170:3528-33.
73. Ward ES, Ober RJ. Chapter 4: Multitasking by exploitation of intracellular transport functions the many faces of FcRn. *Adv Immunol* 2009;103:77-115.
74. Wani MA, Haynes LD, Kim J, et al. Familial hypercatabolic hypoproteinemia caused by deficiency of the neonatal Fc receptor, FcRn, due to a mutant beta2-microglobulin gene. *Proc Natl Acad Sci U S A* 2006;103:5084-9.
75. Waldmann TA, Terry WD. Familial hypercatabolic hypoproteinemia. A disorder of endogenous catabolism of albumin and immunoglobulin. *J Clin Invest* 1990;86:2093-8.
76. Ober RJ, Martinez C, Vaccaro C, et al. Visualizing the site and dynamics of IgG salvage by the MHC class I-related receptor, FcRn. *J Immunol* 2004;172:2021-9.



77. Pyzik M, Rath T, Kuo TT, et al. Hepatic FcRn regulates albumin homeostasis and susceptibility to liver injury. *Proc Natl Acad Sci U S A* 2017;114:E2862-e2871.
78. Schmidt EGW, Hvam ML, Antunes F, et al. Direct demonstration of a neonatal Fc receptor (FcRn)-driven endosomal sorting pathway for cellular recycling of albumin. *J Biol Chem* 2017;292:13312-13322.
79. Gan Z, Ram S, Ober RJ, et al. Using multifocal plane microscopy to reveal novel trafficking processes in the recycling pathway. *J Cell Sci* 2013;126:1176-88.
80. Gan Z, Ram S, Vaccaro C, et al. Analyses of the recycling receptor, FcRn, in live cells reveal novel pathways for lysosomal delivery. *Traffic* 2009;10:600-14.
81. Ober RJ, Martinez C, Lai X, et al. Exocytosis of IgG as mediated by the receptor, FcRn: an analysis at the single-molecule level. *Proc Natl Acad Sci U S A* 2004;101:11076-81.
82. Prabhat P, Gan Z, Chao J, et al. Elucidation of intracellular recycling pathways leading to exocytosis of the Fc receptor, FcRn, by using multifocal plane microscopy. *Proc Natl Acad Sci U S A* 2007;104:5889-94.
83. Ward ES, Martinez C, Vaccaro C, et al. From sorting endosomes to exocytosis: association of Rab4 and Rab11 GTPases with the Fc receptor, FcRn, during recycling. *Mol Biol Cell* 2005;16:2028-38.
84. Ward ES, Zhou J, Ghetie V, et al. Evidence to support the cellular mechanism involved in serum IgG homeostasis in humans. *Int Immunol* 2003;15:187-95.
85. Weflen AW, Baier N, Tang QJ, et al. Multivalent immune complexes divert FcRn to lysosomes by exclusion from recycling sorting tubules. *Mol Biol Cell* 2013;24:2398-405.
86. Chia J, Louber J, Glauser I, et al. Half-life-extended recombinant coagulation factor IX-albumin fusion protein is recycled via the FcRn-mediated pathway. *J Biol Chem* 2018;293:6363-6373.
87. Akilesh S, Christianson GJ, Roopenian DC, et al. Neonatal FcR expression in bone marrow-derived cells functions to protect serum IgG from catabolism. *J Immunol* 2007;179:4580-8.
88. Montoyo HP, Vaccaro C, Hafner M, et al. Conditional deletion of the MHC class I-related receptor FcRn reveals the sites of IgG homeostasis in mice. *Proc Natl Acad Sci U S A* 2009;106:2788-93.
89. Sarav M, Wang Y, Hack BK, et al. Renal FcRn reclaims albumin but facilitates elimination of IgG. *J Am Soc Nephrol* 2009;20:1941-52.
90. Kobayashi K, Qiao SW, Yoshida M, et al. An FcRn-dependent role for anti-flagellin immunoglobulin G in pathogenesis of colitis in mice. *Gastroenterology* 2009;137:1746-56 e1.
91. Tenten V, Menzel S, Kunter U, et al. Albumin is recycled from the primary urine by tubular transcytosis. *J Am Soc Nephrol* 2013;24:1966-80.

92. Challa DK, Wang X, Montoyo HP, et al. Neonatal Fc receptor expression in macrophages is indispensable for IgG homeostasis. *MAbs* 2019;11:848-860.
93. Aaen KH, Anthi AK, Sandlie I, et al. The neonatal Fc receptor in mucosal immune regulation. *Scand J Immunol* 2020:e13017.
94. Kuo TT, Baker K, Yoshida M, et al. Neonatal Fc Receptor: From Immunity to Therapeutics. *Journal of Clinical Immunology* 2010;30:777-789.
95. Yoshida M, Claypool SM, Wagner JS, et al. Human neonatal Fc receptor mediates transport of IgG into luminal secretions for delivery of antigens to mucosal dendritic cells. *Immunity* 2004;20:769-83.
96. Dickinson BL, Badizadegan K, Wu Z, et al. Bidirectional FcRn-dependent IgG transport in a polarized human intestinal epithelial cell line. *J Clin Invest* 1999;104:903-11.
97. McCarthy KM, Yoong Y, Simister NE. Bidirectional transcytosis of IgG by the rat neonatal Fc receptor expressed in a rat kidney cell line: a system to study protein transport across epithelia. *J Cell Sci* 2000;113 ( Pt 7):1277-85.
98. Claypool SM, Dickinson BL, Yoshida M, et al. Functional reconstitution of human FcRn in Madin-Darby canine kidney cells requires co-expressed human beta 2-microglobulin. *J Biol Chem* 2002;277:28038-50.
99. Yoshida M, Kobayashi K, Kuo TT, et al. Neonatal Fc receptor for IgG regulates mucosal immune responses to luminal bacteria. *J Clin Invest* 2006;116:2142-2151.
100. Tzaban S, Massol RH, Yen E, et al. The recycling and transcytotic pathways for IgG transport by FcRn are distinct and display an inherent polarity. *J Cell Biol* 2009;185:673-84.
101. Li Z, Palaniyandi S, Zeng R, et al. Transfer of IgG in the female genital tract by MHC class I-related neonatal Fc receptor (FcRn) confers protective immunity to vaginal infection. *Proc Natl Acad Sci U S A* 2011;108:4388-93.
102. Hornby PJ, Cooper PR, Kliwinski C, et al. Human and non-human primate intestinal FcRn expression and immunoglobulin G transcytosis. *Pharm Res* 2014;31:908-22.
103. Rath T, Kuo TT, Baker K, et al. The immunologic functions of the neonatal Fc receptor for IgG. *J Clin Immunol* 2013;33 Suppl 1:S9-17.
104. Drucker DJ, Dritselis A, Kirkpatrick P. Liraglutide. *Nat Rev Drug Discov* 2010;9:267-8.
105. Elsadek B, Kratz F. Impact of albumin on drug delivery — New applications on the horizon. *Journal of Controlled Release* 2012;157:4-28.
106. Alavi SE, Cabot PJ, Moyle PM. Glucagon-Like Peptide-1 Receptor Agonists and Strategies To Improve Their Efficiency. *Molecular Pharmaceutics* 2019;16:2278-2295.
107. Sebokova E, Christ AD, Wang H, et al. Taspoglutide, an analog of human glucagon-like Peptide-1 with enhanced stability and in vivo potency. *Endocrinology* 2010;151:2474-82.

108. Kapitza C, Heise T, Birman P, et al. Pharmacokinetic and pharmacodynamic properties of tasoglutide, a once-weekly, human GLP-1 analogue, after single-dose administration in patients with Type 2 diabetes. *Diabet Med* 2009;26:1156-64.
109. Rosenstock J, Balas B, Charbonnel B, et al. The fate of tasoglutide, a weekly GLP-1 receptor agonist, versus twice-daily exenatide for type 2 diabetes: the T-emerge 2 trial. *Diabetes Care* 2013;36:498-504.
110. EMA. Levemir (insulin detemir). Available on: [https://ec.europa.eu/health/documents/community-register/2010/2010033077668/anx\\_77668\\_en.pdf](https://ec.europa.eu/health/documents/community-register/2010/2010033077668/anx_77668_en.pdf) [accessed 24/11/2020]. 2004.
111. Home P, Kurtzhals P. Insulin detemir: from concept to clinical experience. *Expert Opin Pharmacother* 2006;7:325-43.
112. Rendell M. Insulin degludec: A long-acting modern insulin analogue with a predictable pharmacokinetic/ pharmacodynamic profile. *Drugs of Today* 2013;49:387-397.
113. NovoNordisk. Tresiba®FlexTouch®100 U/mL. Available on: [https://www.novonordisk.com.br/content/dam/brazil/affiliate/www-novonordisk-br/Bulas/Profissionais/Tresiba-FlexTouch\\_bula-profissional.pdf](https://www.novonordisk.com.br/content/dam/brazil/affiliate/www-novonordisk-br/Bulas/Profissionais/Tresiba-FlexTouch_bula-profissional.pdf) [accessed on 24/11/2020]. 2016.
114. Elsadek B, Kratz F. Impact of albumin on drug delivery--new applications on the horizon. *J Control Release* 2012;157:4-28.
115. Wang F, Carabino JM, Vergara CM. Insulin glargine: A systematic review of a long-acting insulin analogue. *Clinical Therapeutics* 2003;25:1541-1577.
116. Rosenstock J, Bajaj HS, Janez A, et al. Once-Weekly Insulin for Type 2 Diabetes without Previous Insulin Treatment. *N Engl J Med* 2020;383:2107-2116.
117. Hövelmann U, Brøndsted L, Kristensen NR, et al. 237-OR: Insulin Icodec: An Insulin Analog Suited for Once-Weekly Dosing in Type 2 Diabetes. *Diabetes* 2020;69.
118. Anderson SL, Beutel TR, Trujillo JM. Oral semaglutide in type 2 diabetes. *J Diabetes Complications* 2020;34:107520.
119. Baekdal TA, Thomsen M, Kupcova V, et al. Pharmacokinetics, Safety, and Tolerability of Oral Semaglutide in Subjects With Hepatic Impairment. *J Clin Pharmacol* 2018;58:1314-1323.
120. Granhall C, Sondergaard FL, Thomsen M, et al. Pharmacokinetics, Safety and Tolerability of Oral Semaglutide in Subjects with Renal Impairment. *Clin Pharmacokinet* 2018;57:1571-1580.
121. Dhillon S. Semaglutide: First Global Approval. *Drugs* 2018;78:275-284.
122. Blakely KK, Weaver K. Semaglutide Is a New Once-Daily Oral Medication to Treat Type 2 Diabetes. *Nurs Womens Health* 2020;24:370-376.
123. Semanya AM, Wilson SA. Oral Semaglutide (Rybelsus) for the Treatment of Type 2 Diabetes Mellitus. *Am Fam Physician* 2020;102:627-628.

124. Husain M, Birkenfeld AL, Donsmark M, et al. Oral Semaglutide and Cardiovascular Outcomes in Patients with Type 2 Diabetes. *N Engl J Med* 2019;381:841-851.
125. Mosenzon O, Miller EM, Warren ML. Oral semaglutide in patients with type 2 diabetes and cardiovascular disease, renal impairment, or other comorbidities, and in older patients. *Postgrad Med* 2020;132:37-47.
126. Halberg IB, Lyby K, Wassermann K, et al. Efficacy and safety of oral basal insulin versus subcutaneous insulin glargine in type 2 diabetes: a randomised, double-blind, phase 2 trial. *Lancet Diabetes Endocrinol* 2019;7:179-188.
127. Hubalek F, Refsgaard HHF, Gram-Nielsen S, et al. Molecular engineering of safe and efficacious oral basal insulin. *Nat Commun* 2020;11:3746.
128. Leonard TW, Lynch J, McKenna MJ, et al. Promoting absorption of drugs in humans using medium-chain fatty acid-based solid dosage forms: GIPET. *Expert Opin Drug Deliv* 2006;3:685-92.
129. Leger R, Thibaudeau K, Robitaille M, et al. Identification of CJC-1131-albumin bioconjugate as a stable and bioactive GLP-1(7-36) analog. *Bioorg Med Chem Lett* 2004;14:4395-8.
130. Baggio LL, Huang Q, Cao X, et al. An albumin-exendin-4 conjugate engages central and peripheral circuits regulating murine energy and glucose homeostasis. *Gastroenterology* 2008;134:1137-47.
131. Kim JG, Baggio LL, Bridon DP, et al. Development and characterization of a glucagon-like peptide 1-albumin conjugate: the ability to activate the glucagon-like peptide 1 receptor in vivo. *Diabetes* 2003;52:751-9.
132. Fan R, Kang Z, He L, et al. Exendin-4 improves blood glucose control in both young and aging normal non-diabetic mice, possible contribution of beta cell independent effects. *PLoS One* 2011;6:e20443.
133. Giannoukakis N. CJC-1131. *ConjuChem. Curr Opin Investig Drugs* 2003;4:1245-9.
134. Pilati D, Howard KA. Albumin-based drug designs for pharmacokinetic modulation. *Expert Opin Drug Metab Toxicol* 2020;16:783-795.
135. *ConjuChem. PC-DAC™: Insulin, 2020.*
136. Oganessian V, Damschroder MM, Cook KE, et al. Structural insights into neonatal Fc receptor-based recycling mechanisms. *The Journal of biological chemistry* 2014;289:7812-7824.
137. Bukrinski JT, Sonderby P, Antunes F, et al. Glucagon-like Peptide 1 Conjugated to Recombinant Human Serum Albumin Variants with Modified Neonatal Fc Receptor Binding Properties. Impact on Molecular Structure and Half-Life. *Biochemistry* 2017;56:4860-4870.

138. Schmokel J, Voldum A, Tsakiridou G, et al. Site-selective conjugation of an anticoagulant aptamer to recombinant albumins and maintenance of neonatal Fc receptor binding. *Nanotechnology* 2017;28:204004.
139. Petersen SS, Klaning E, Ebbesen MF, et al. Neonatal Fc Receptor Binding Tolerance toward the Covalent Conjugation of Payloads to Cysteine 34 of Human Albumin Variants. *Mol Pharm* 2016;13:677-82.
140. Rendell MS. Albiglutide: a unique GLP-1 receptor agonist. *Expert Opin Biol Ther* 2016;16:1557-1569.
141. Poole RM, Nowlan ML. Albiglutide: first global approval. *Drugs* 2014;74:929-38.
142. Baggio LL, Huang Q, Brown TJ, et al. A recombinant human glucagon-like peptide (GLP)-1-albumin protein (albugon) mimics peptidergic activation of GLP-1 receptor-dependent pathways coupled with satiety, gastrointestinal motility, and glucose homeostasis. *Diabetes* 2004;53:2492-500.
143. Nilsen J, Trabjerg E, Grevys A, et al. An intact C-terminal end of albumin is required for its long half-life in humans. *Commun Biol* 2020;3:181.
144. Jimenez-Solem E, Rasmussen MH, Christensen M, et al. Dulaglutide, a long-acting GLP-1 analog fused with an Fc antibody fragment for the potential treatment of type 2 diabetes. *Curr Opin Mol Ther* 2010;12:790-7.
145. Sanford M. Dulaglutide: first global approval. *Drugs* 2014;74:2097-103.
146. Lu RM, Hwang YC, Liu IJ, et al. Development of therapeutic antibodies for the treatment of diseases. *J Biomed Sci* 2020;27:1.
147. Rath T, Baker K, Dumont JA, et al. Fc-fusion proteins and FcRn: structural insights for longer-lasting and more effective therapeutics. *Crit Rev Biotechnol* 2015;35:235-54.
148. Acqua WFD, Woods RM, Ward ES, et al. Increasing the Affinity of a Human IgG1 for the Neonatal Fc Receptor: Biological Consequences. *The Journal of Immunology* 2002;169:5171.
149. Ward ES, Ober RJ. Targeting FcRn to Generate Antibody-Based Therapeutics. *Trends Pharmacol Sci* 2018;39:892-904.
150. Lu R-M, Hwang Y-C, Liu IJ, et al. Development of therapeutic antibodies for the treatment of diseases. *Journal of Biomedical Science* 2020;27:1.
151. Carter PJ, Lazar GA. Next generation antibody drugs: pursuit of the 'high-hanging fruit'. *Nat Rev Drug Discov* 2018;17:197-223.
152. Keymeulen B, van Maurik A, Inman D, et al. A randomised, single-blind, placebo-controlled, dose-finding safety and tolerability study of the anti-CD3 monoclonal antibody oteelixumab in new-onset type 1 diabetes. *Diabetologia* 2021;64:313-324.
153. Andersen JT, Dalhus B, Viuff D, et al. Extending Serum Half-life of Albumin by Engineering Neonatal Fc Receptor (FcRn) Binding. *Journal of Biological Chemistry* 2014;289:13492-13502.

154. Mezo AR, McDonnell KA, Castro A, et al. Structure-activity relationships of a peptide inhibitor of the human FcRn:human IgG interaction. *Bioorg Med Chem* 2008;16:6394-405.
155. Mezo AR, McDonnell KA, Hehir CA, et al. Reduction of IgG in nonhuman primates by a peptide antagonist of the neonatal Fc receptor FcRn. *Proc Natl Acad Sci U S A* 2008;105:2337-42.
156. Seijsing J, Lindborg M, Höidén-Guthenberg I, et al. An engineered affibody molecule with pH-dependent binding to FcRn mediates extended circulatory half-life of a fusion protein. *Proc Natl Acad Sci U S A* 2014;111:17110-5.
157. Ying T, Wang Y, Feng Y, et al. Engineered antibody domains with significantly increased transcytosis and half-life in macaques mediated by FcRn. *MAbs* 2015;7:922-30.
158. Qiu Y, Lv W, Xu M, et al. Single chain antibody fragments with pH dependent binding to FcRn enabled prolonged circulation of therapeutic peptide in vivo. *J Control Release* 2016;229:37-47.
159. Borrok MJ, Wu Y, Beyaz N, et al. pH-dependent binding engineering reveals an FcRn affinity threshold that governs IgG recycling. *J Biol Chem* 2015;290:4282-90.
160. Yeung YA, Leabman MK, Marvin JS, et al. Engineering human IgG1 affinity to human neonatal Fc receptor: impact of affinity improvement on pharmacokinetics in primates. *J Immunol* 2009;182:7663-71.
161. Ghetie V, Popov S, Borvak J, et al. Increasing the serum persistence of an IgG fragment by random mutagenesis. *Nat Biotechnol* 1997;15:637-40.
162. Dall'Acqua WF, Kiener PA, Wu H. Properties of human IgG1s engineered for enhanced binding to the neonatal Fc receptor (FcRn). *J Biol Chem* 2006;281:23514-24.
163. Robbie GJ, Criste R, Dall'acqua WF, et al. A novel investigational Fc-modified humanized monoclonal antibody, motavizumab-YTE, has an extended half-life in healthy adults. *Antimicrob Agents Chemother* 2013;57:6147-53.
164. Zalevsky J, Chamberlain AK, Horton HM, et al. Enhanced antibody half-life improves in vivo activity. *Nature Biotechnology* 2010;28:157-159.
165. Gautam R, Nishimura Y, Pegu A, et al. A single injection of anti-HIV-1 antibodies protects against repeated SHIV challenges. *Nature* 2016;533:105-109.
166. Ko SY, Pegu A, Rudicell RS, et al. Enhanced neonatal Fc receptor function improves protection against primate SHIV infection. *Nature* 2014;514:642-5.
167. Gaudinski MR, Coates EE, Houser KV, et al. Safety and pharmacokinetics of the Fc-modified HIV-1 human monoclonal antibody VRC01LS: A Phase 1 open-label clinical trial in healthy adults. *PLoS Med* 2018;15:e1002493.
168. Gaudinski MR, Houser KV, Doria-Rose NA, et al. Safety and pharmacokinetics of broadly neutralising human monoclonal antibody VRC07-523LS in healthy adults: a phase 1 dose-escalation clinical trial. *Lancet HIV* 2019;6:e667-e679.

169. Deng R, Loyet KM, Lien S, et al. Pharmacokinetics of Humanized Monoclonal Anti-Tumor Necrosis Factor- $\alpha$  Antibody and Its Neonatal Fc Receptor Variants in Mice and Cynomolgus Monkeys. *Drug Metabolism and Disposition* 2010;38:600-605.
170. Borrok MJ, Mody N, Lu X, et al. An "Fc-Silenced" IgG1 Format With Extended Half-Life Designed for Improved Stability. *J Pharm Sci* 2017;106:1008-1017.
171. Hinton PR, Xiong JM, Johlfs MG, et al. An Engineered Human IgG1 Antibody with Longer Serum Half-Life. *The Journal of Immunology* 2006;176:346.
172. Datta-Mannan A, Chow CK, Dickinson C, et al. FcRn affinity-pharmacokinetic relationship of five human IgG4 antibodies engineered for improved in vitro FcRn binding properties in cynomolgus monkeys. *Drug Metab Dispos* 2012;40:1545-55.
173. Hinton PR, Johlfs MG, Xiong JM, et al. Engineered human IgG antibodies with longer serum half-lives in primates. *J Biol Chem* 2004;279:6213-6.
174. Monnet C, Jorieux S, Souyris N, et al. Combined glyco- and protein-Fc engineering simultaneously enhance cytotoxicity and half-life of a therapeutic antibody. *MAbs* 2014;6:422-36.
175. Petkova SB, Akilesh S, Sproule TJ, et al. Enhanced half-life of genetically engineered human IgG1 antibodies in a humanized FcRn mouse model: potential application in humorally mediated autoimmune disease. *Int Immunol* 2006;18:1759-69.
176. Van de Walle I, Silence K, Budding K, et al. ARGX-117, a therapeutic complement inhibiting antibody targeting C2. *J Allergy Clin Immunol* 2020.
177. Mackness BC, Jaworski JA, Boudanova E, et al. Antibody Fc engineering for enhanced neonatal Fc receptor binding and prolonged circulation half-life. *MAbs* 2019;11:1276-1288.
178. Lee C-H, Kang TH, Godon O, et al. An engineered human Fc domain that behaves like a pH-toggle switch for ultra-long circulation persistence. *Nature Communications* 2019;10:5031.
179. Bennett MJ, Chu SY, Leung I, et al. Immune suppression in cynomolgus monkeys by XPro9523: an improved CTLA4-Ig fusion with enhanced binding to CD80, CD86 and neonatal Fc receptor FcRn. *MAbs* 2013;5:384-96.
180. Douthwaite J, Moisan J, Privezentzev C, et al. Correction: A CD80-Biased CTLA4-Ig Fusion Protein with Superior In Vivo Efficacy by Simultaneous Engineering of Affinity, Selectivity, Stability, and FcRn Binding. *J Immunol* 2017;199:1943.
181. Lagasse HAD, Hengel H, Golding B, et al. Fc-Fusion Drugs Have Fc $\gamma$ R/C1q Binding and Signaling Properties That May Affect Their Immunogenicity. *AAPS J* 2019;21:62.
182. Andersen JT, Daba MB, Sandlie I. FcRn binding properties of an abnormal truncated analbuminemic albumin variant. *Clin Biochem* 2010;43:367-72.

183. Mezo AR, Low SC, Hoehn T, et al. PEGylation enhances the therapeutic potential of peptide antagonists of the neonatal Fc receptor, FcRn. *Bioorg Med Chem Lett* 2011;21:6332-5.
184. Peter HH, Ochs HD, Cunningham-Rundles C, et al. Targeting FcRn for immunomodulation: Benefits, risks, and practical considerations. *J Allergy Clin Immunol* 2020;146:479-491 e5.
185. Zuercher AW, Spirig R, Baz Morelli A, et al. Next-generation Fc receptor-targeting biologics for autoimmune diseases. *Autoimmun Rev* 2019;18:102366.
186. Gable KL, Guptill JT. Antagonism of the Neonatal Fc Receptor as an Emerging Treatment for Myasthenia Gravis. *Front Immunol* 2019;10:3052.
187. Sockolosky JT, Tiffany MR, Szoka FC. Engineering neonatal Fc receptor-mediated recycling and transcytosis in recombinant proteins by short terminal peptide extensions. *Proc Natl Acad Sci U S A* 2012;109:16095-100.
188. Datta-Mannan A, Boyles J, Huang L, et al. Engineered FcRn Binding Fusion Peptides Significantly Enhance the Half-Life of a Fab Domain in Cynomolgus Monkeys. *Biotechnol J* 2019;14:e1800007.
189. Nygren PA. Alternative binding proteins: affibody binding proteins developed from a small three-helix bundle scaffold. *FEBS J* 2008;275:2668-76.
190. Andersen JT, Pehrson R, Tolmachev V, et al. Extending half-life by indirect targeting of the neonatal Fc receptor (FcRn) using a minimal albumin binding domain. *J Biol Chem* 2011;286:5234-41.
191. Seijsing J, Yu S, Frejd FY, et al. In vivo depletion of serum IgG by an affibody molecule binding the neonatal Fc receptor. *Sci Rep* 2018;8:5141.
192. Nilsen J, Bern M, Sand KMK, et al. Human and mouse albumin bind their respective neonatal Fc receptors differently. *Sci Rep* 2018;8:14648.
193. Latvala S, Jacobsen B, Otteneder MB, et al. Distribution of FcRn Across Species and Tissues. *J Histochem Cytochem* 2017;65:321-333.
194. Martins JP, Kennedy PJ, Santos HA, et al. A comprehensive review of the neonatal Fc receptor and its application in drug delivery. *Pharmacol Ther* 2016;161:22-39.
195. Firan M, Bawdon R, Radu C, et al. The MHC class I-related receptor, FcRn, plays an essential role in the maternofetal transfer of gamma-globulin in humans. *Int Immunol* 2001;13:993-1002.
196. Roy S, Nanovskaya T, Patrikeeva S, et al. M281, an anti-FcRn antibody, inhibits IgG transfer in a human ex vivo placental perfusion model. *Am J Obstet Gynecol* 2019;220:498 e1-498 e9.
197. Israel EJ, Patel VK, Taylor SF, et al. Requirement for a beta 2-microglobulin-associated Fc receptor for acquisition of maternal IgG by fetal and neonatal mice. *J Immunol* 1995;154:6246-51.



198. Martin MG, Wu SV, Walsh JH. Ontogenetic development and distribution of antibody transport and Fc receptor mRNA expression in rat intestine. *Dig Dis Sci* 1997;42:1062-9.
199. Israel EJ, Taylor S, Wu Z, et al. Expression of the neonatal Fc receptor, FcRn, on human intestinal epithelial cells. *Immunology* 1997;92:69-74.
200. Cooper PR, Kliwinski CM, Perkinson RA, et al. The contribution of cell surface FcRn in monoclonal antibody serum uptake from the intestine in suckling rat pups. *Front Pharmacol* 2014;5:225.
201. Kliwinski C, Cooper PR, Perkinson R, et al. Contribution of FcRn binding to intestinal uptake of IgG in suckling rat pups and human FcRn-transgenic mice. *Am J Physiol Gastrointest Liver Physiol* 2013;304:G262-70.
202. Shah U, Dickinson BL, Blumberg RS, et al. Distribution of the IgG Fc receptor, FcRn, in the human fetal intestine. *Pediatr Res* 2003;53:295-301.
203. Story CM, Mikulska JE, Simister NE. A major histocompatibility complex class I-like Fc receptor cloned from human placenta: possible role in transfer of immunoglobulin G from mother to fetus. *J Exp Med* 1994;180:2377-81.
204. Andersen JT, Daba MB, Berntzen G, et al. Cross-species binding analyses of mouse and human neonatal Fc receptor show dramatic differences in immunoglobulin G and albumin binding. *J Biol Chem* 2010;285:4826-36.
205. Ober RJ, Radu CG, Ghetie V, et al. Differences in promiscuity for antibody-FcRn interactions across species: implications for therapeutic antibodies. *Int Immunol* 2001;13:1551-9.
206. Vaccaro C, Bawdon R, Wanjie S, et al. Divergent activities of an engineered antibody in murine and human systems have implications for therapeutic antibodies. *Proc Natl Acad Sci U S A* 2006;103:18709-14.
207. Andersen JT, Cameron J, Plumridge A, et al. Single-chain variable fragment albumin fusions bind the neonatal Fc receptor (FcRn) in a species-dependent manner: implications for in vivo half-life evaluation of albumin fusion therapeutics. *J Biol Chem* 2013;288:24277-85.
208. Viuff D, Antunes F, Evans L, et al. Generation of a double transgenic humanized neonatal Fc receptor (FcRn)/albumin mouse to study the pharmacokinetics of albumin-linked drugs. *J Control Release* 2016;223:22-30.
209. Zhou J, Johnson JE, Ghetie V, et al. Generation of Mutated Variants of the Human Form of the MHC Class I-related Receptor, FcRn, with Increased Affinity for Mouse Immunoglobulin G. *Journal of Molecular Biology* 2003;332:901-913.
210. Zhou J, Mateos F, Ober RJ, et al. Conferring the binding properties of the mouse MHC class I-related receptor, FcRn, onto the human ortholog by sequential rounds of site-directed mutagenesis. *J Mol Biol* 2005;345:1071-81.

211. Low BE, Christianson GJ, Lowell E, et al. Functional humanization of immunoglobulin heavy constant gamma 1 Fc domain human FCGRT transgenic mice. *MAbs* 2020;12:1829334.
212. Roopenian DC, Christianson GJ, Proetzel G, et al. Human FcRn Transgenic Mice for Pharmacokinetic Evaluation of Therapeutic Antibodies. *Methods Mol Biol* 2016;1438:103-14.
213. Roopenian DC, Low BE, Christianson GJ, et al. Albumin-deficient mouse models for studying metabolism of human albumin and pharmacokinetics of albumin-based drugs. *MAbs* 2015;7:344-51.
214. Proetzel G, Roopenian DC. Humanized FcRn mouse models for evaluating pharmacokinetics of human IgG antibodies. *Methods* 2014;65:148-53.
215. Nilsen J, Sandlie I, Roopenian DC, et al. Animal models for evaluation of albumin-based therapeutics. *Current Opinion in Chemical Engineering* 2018;19:68-76.
216. Fan YY, Neubert H. Quantitative Analysis of Human Neonatal Fc Receptor (FcRn) Tissue Expression in Transgenic Mice by Online Peptide Immuno-Affinity LC-HRMS. *Anal Chem* 2016;88:4239-47.
217. Stein C, Kling L, Proetzel G, et al. Clinical chemistry of human FcRn transgenic mice. *Mamm Genome* 2012;23:259-69.
218. Tam SH, McCarthy SG, Brosnan K, et al. Correlations between pharmacokinetics of IgG antibodies in primates vs. FcRn-transgenic mice reveal a rodent model with predictive capabilities. *MAbs* 2013;5:397-405.
219. Lee CH, Kang TH, Godon O, et al. An engineered human Fc domain that behaves like a pH-toggle switch for ultra-long circulation persistence. *Nat Commun* 2019;10:5031.
220. Shrestha N, Araujo F, Shahbazi MA, et al. Oral hypoglycaemic effect of GLP-1 and DPP4 inhibitor based nanocomposites in a diabetic animal model. *J Control Release* 2016;232:113-9.
221. Zhang Z, Shan H, Chen L, et al. Synthesis of pH-responsive starch nanoparticles grafted poly (l-glutamic acid) for insulin controlled release. *European Polymer Journal* 2013;49:2082-2091.
222. Cui M, Wu W, Hovgaard L, et al. Liposomes containing cholesterol analogues of botanical origin as drug delivery systems to enhance the oral absorption of insulin. *Int J Pharm* 2015;489:277-84.
223. Azevedo C, Macedo MH, Sarmiento B. Strategies for the enhanced intracellular delivery of nanomaterials. *Drug Discovery Today* 2017.
224. Xu Q, Ensign LM, Boylan NJ, et al. Impact of Surface Polyethylene Glycol (PEG) Density on Biodegradable Nanoparticle Transport in Mucus ex Vivo and Distribution in Vivo. *ACS Nano* 2015;9:9217-27.

225. Mitchell MJ, Billingsley MM, Haley RM, et al. Engineering precision nanoparticles for drug delivery. *Nat Rev Drug Discov* 2020.
226. Khan I, Saeed K, Khan I. Nanoparticles: Properties, applications and toxicities. *Arabian Journal of Chemistry* 2019;12:908-931.
227. Oliveira JP, Prado AR, Keijok WJ, et al. Impact of conjugation strategies for targeting of antibodies in gold nanoparticles for ultrasensitive detection of 17beta-estradiol. *Sci Rep* 2019;9:13859.
228. Werengowska-Ciećwierz K, Wiśniewski M, Terzyk AP, et al. The Chemistry of Bioconjugation in Nanoparticles-Based Drug Delivery System. *Advances in Condensed Matter Physics* 2015;2015:1-27.
229. Ravasco J, Faustino H, Trindade A, et al. Bioconjugation with Maleimides: A Useful Tool for Chemical Biology. *Chemistry* 2019;25:43-59.
230. Bartczak D, Kanaras AG. Preparation of Peptide-Functionalized Gold Nanoparticles Using One Pot EDC/Sulfo-NHS Coupling. *Langmuir* 2011;27:10119-10123.
231. Keleştemur S, Altunbek M, Culha M. Influence of EDC/NHS coupling chemistry on stability and cytotoxicity of ZnO nanoparticles modified with proteins. *Applied Surface Science* 2017;403:455-463.
232. Lopes M, Derenne A, Pereira C, et al. Impact of the in vitro gastrointestinal passage of biopolymer-based nanoparticles on insulin absorption. *RSC Advances* 2016;6:20155-20165.
233. Bremer MGE, Duval J, Norde W, et al. Electrostatic interactions between immunoglobulin (IgG) molecules and a charged sorbent. *Colloids and Surfaces A: Physicochemical and Engineering Aspects* 2004;250:29-42.
234. Awaad A, Nakamura M, Ishimura K. Imaging of size-dependent uptake and identification of novel pathways in mouse Peyer's patches using fluorescent organosilica particles. *Nanomedicine* 2012;8:627-36.
235. Desai MP, Labhsetwar V, Amidon GL, et al. Gastrointestinal uptake of biodegradable microparticles: effect of particle size. *Pharm Res* 1996;13:1838-45.
236. Arias LS, Pessan JP, Vieira APM, et al. Iron Oxide Nanoparticles for Biomedical Applications: A Perspective on Synthesis, Drugs, Antimicrobial Activity, and Toxicity. *Antibiotics (Basel)* 2018;7.
237. Manshian BB, Jimenez J, Himmelreich U, et al. Personalized medicine and follow-up of therapeutic delivery through exploitation of quantum dot toxicity. *Biomaterials* 2017;127:1-12.
238. Nag OK, Delehanty JB. Active Cellular and Subcellular Targeting of Nanoparticles for Drug Delivery. *Pharmaceutics* 2019;11.
239. Mansoor S, Kondiah PPD, Choonara YE, et al. Polymer-Based Nanoparticle Strategies for Insulin Delivery. *Polymers (Basel)* 2019;11.

## Strategies for enhanced intracellular delivery of nanomaterials

*Cláudia Azevedo<sup>1,2</sup>, Maria Helena Macedo<sup>1</sup>, Bruno Sarmiento<sup>\*,1,3</sup>*

<sup>1</sup> i3S – Instituto de Investigação e Inovação em Saúde, Universidade do Porto, Rua Alfredo Allen, 208, 4200-135 Porto, Portugal

<sup>2</sup> Instituto de Ciências Biomédicas Abel Salazar, Universidade do Porto, Porto, Portugal

<sup>3</sup> CESPU, Instituto de Investigação e Formação Avançada em Ciências e Tecnologias da Saúde & Instituto Universitário de Ciências da Saúde, Gandra, Portugal

\*Corresponding author:

Tel: +351 22 040 8800

E-mail: [bruno.sarmiento@ineb.up.pt](mailto:bruno.sarmiento@ineb.up.pt)

**Abstract**

Intracellular delivery of nanomaterials and drugs has been attracting aggregate interest, mostly due to their effect and important functions in several organelles. Targeting specific organelles can in fact treat or decrease symptoms of diabetes, cancer, infectious and autoimmune diseases. Tuning biological and chemical properties allows creating functionalized nanomaterials with enhanced intracellular uptake, ability to escape to premature lysosomes degradation and reach a specific target. The overall aim of this review is to update recent advances of intracellular delivery events and report mechanisms that may help reach the target efficiently.

**Keywords:** Nanomaterials; Intracellular delivery; Drugs; Intracellular targets; Endosomal escape

**Teaser:** This review updates recent advances of intracellular delivery events and report mechanisms that may help reach the target efficiently, in order to create smarter drugs that reach the target with the original bioavailability.

## 1. Introduction

The developments in nanomedicine drug delivery have opened up new perspectives to design and synthesize efficient nanocarriers and multifunctional nanomaterials. At the beginning, the production was focused on biocompatibility and toxicity. The second-generation of nanomaterials aimed for having an optimized surface, to give more stability, stealth, and targeting capabilities. The most recent model support the “smart nanomedicine” idea, improving targeting mechanisms and theranostic abilities <sup>1</sup>. This nanotechnological advance became very important since it allows drugs to cross physiological barriers to reach target sites, safely and sustainably <sup>2</sup>. In fact, nanomaterials provide a stable biocompatible environment to encapsulate drugs, promote a controlled release and an efficient absorption <sup>3,4</sup>. It is also noted that they improve the therapeutic effects duration and minimize unwanted effects by driving drugs toward the site of action and increasing the concentration of a drug in the area of pathology in a specific way <sup>5,6</sup>. Depending on the accumulation of the delivery system in the tissue, cell or in a specific subcellular compartment of interest, targeting approaches can be primary, secondary or tertiary, respectively <sup>7</sup>. This nanotechnologic advance became very important since it allows drugs to cross physiological barriers to reach target sites, safely and sustainably <sup>2</sup>.

Now more than ever, the subcellular targeting is more important for an efficient and specific treatment, making also known specific barriers that must be overcome. The importance of organelle targeting increases when drugs efficiently treat or decrease symptoms of several diseases like cancer, Alzheimer, diabetes, infectious and autoimmune diseases <sup>8</sup>. Specifically, intracellular environment possesses important compounds, responsible for cell growth, proliferation, differentiation, and death that can be promising targets. Therefore, target sites can be distributed by cytoplasm, nucleus, mitochondria, endoplasmic reticulum and Golgi complex <sup>9</sup>. However, there are also factors that can lead to drug degradation or nonspecific distribution, endosomes and lysosomes with low pH and rich in enzymes <sup>10,11</sup>. So a strategy to overcome this problem is the modulation of nanomaterials size, charge and surface composition, in order to dictate the internalization pathway, escape lysosomes and interact with the target organelle <sup>12</sup>. Indeed, the potential of nanomaterials to overcome the barriers have led to the development of platforms capable of improving their bioavailability <sup>13</sup>.

In short, it is crucial taking into consideration pathways of nanomaterials uptake and understanding intracellular mechanisms in order to create smarter drugs that reach the target with the original bioavailability <sup>14</sup>. In this sense, this review attempts to focus on

every step until reaching the target, in order to identify all the challenges that must be surpassed. Facing the presented challenges, it will be described the recent research advancements related with intracellular delivery approaches. So, it begins with the preferred intracellular transport process and the influence of certain nanomaterials characteristics. Then unmodified nanomaterials are addressed as well as functionalized nanomaterials and their mechanisms of molecular recognition, as an advantage. Next, it will be focused the intracellular transport, along with their obstacles, and the most important target organelles. This overview will contribute to a more efficient design, guaranteeing a better nanomaterials uptake.

## **2. Physical and chemical barriers**

There are three fundamental steps, during nanomaterials production for drug delivery that must be taken into account: (1) nanomaterials must be able to surpass the harsh conditions of gastrointestinal tract GIT; (2) once internalized, they must reach the target; and (3) guarantee that pharmacokinetics is maintained.

Nanomaterials can be administrated by ocular, buccal, sublingual, oral, intravenous, intramuscular, subcutaneous, transdermal, pulmonary/nasal or vaginal/rectal routes, being the oral the most convenient <sup>15</sup>. However, for orally delivering they pass through: oral cavity - coated by proteins, mucosal compounds and bacterial flora; stomach - attacked by acid bath; intestine - contacting with the alkaline environment, being subjected to the activity of different digestive enzymes, the presence of a mucus layer (glycoprotein mucin) and tight junctions; blood - if nanomaterials are absorbed, they pass through endothelial cells, reach the blood and then can be taken up by a monocyte; and target - after travel through endosomal and lysosomal environments, nanomaterials could arrive in the cytoplasm where they may find their intended drug target <sup>16</sup>. Normally, in intracellular drug delivery, target sites can be distributed by cytoplasm, nucleus, mitochondria and lysosomes <sup>9</sup>.

It is already known that the harsh conditions from GIT are the main barrier, specially contributing for drug degradation, due to enzymes such as proteolytic enzymes in lysosomes, brush-border peptidases in the villi, and pancreatic proteases in the duodenal region; and bacterial flora from the complex hydrogel containing mucin, known as mucus of intestine. Also, epithelial cells contribute as a physiological barrier, since they are bond by tight junctions. Nanomaterials can also suffer physicochemical modifications

originated by low pH, high temperature, reactions with surrounding molecules, besides nanoparticle weight and charge which also influence poor absorption and degradation. The second main barrier is the intestinal epithelium which is responsible for the control of drugs passage. Its surface area, which is 99% covered by enterocytes and consequently by microvilli, has an important impact on absorption<sup>17</sup>. Morphologically, intestinal crypts are constituted by absorptive enterocytes and secretory cells (goblet cells, enteroendocrine cells and Paneth cells). Away from intestinal crypts there are isolated lymphoid follicles, Peyer's patches, which contain specialized M cells<sup>3,18</sup>.

So, it is mandatory that nanomaterials surpass the mononuclear phagocyte system, avoid nonspecific distribution, drug resistance, escape to endosomes and reach the target with the original bioavailability<sup>19</sup>. As is described in literature by Blanco *et al*, the mononuclear phagocyte system can be surpassed by modulating certain characteristics of nanomaterials, the nonspecific distribution can be resolved with functionalization or adding biomimetic surfaces, the drug efflux pumps and consequent drug resistance can be avoided with CD44 targeting and drugs can escape endosomes by disrupting their membrane<sup>11</sup>. All these issues will be more deeply addressed over the whole manuscript.

### **3. Cellular internalization**

After administration via different routes and reaching the target cell, the nanomaterials internalization gathers a set of processes, such as pre-absorption, uptake, translocation and reaching the final target<sup>3,20</sup>. On the first phase, nanomaterials activate the transport into the cell. After ligands have recognized their receptors, in case of that, nanomaterials enter the cell.

#### **3.1. Transport mechanisms**

According to literature there are several possible pathways for nanomaterials internalization. However, this review will only address paracellular pathway and endocytosis which can be through or not a receptor, since they are the most used pathways to non-functionalized and functionalized nanomaterials,

Nanomaterials with a particular nature, size or absence of receptors frequently preferred the paracellular route as internalization pathway. So, nanomaterials can be transported through two juxtaposed cells where there are aquaporin and also tight junctions. Aquaporins are proteins that facilitate water transport across the luminal space to the basolateral membrane<sup>21</sup>, while tight junctions are responsible to maintain structural integrity. Tight junctions (TJ) are gaps between cells with occludin and claudin-2 proteins, which



thanks to their permeability nature dictates the paracellular transport <sup>22</sup>. The presence of TJ and low surface area limit the transport of nanomaterials, since they cannot pass through the intestinal barrier through this via. So, TJ must be reversibly opened by chemically modifying nanomaterials using permeation enhancers such as chitosan, polyacrylate, and thiolated polymers (anionic and cationic polymers) <sup>23</sup>. Hence, the paracellular pathway occurs to one side of the cell and mainly transports hydrophilic drugs thanks to the diffusion through these channels and its deficiency? in proteolytic activity <sup>3, 6</sup>. A recent study exemplified this situation, using a cationic cyclodextrin-polyethylenimine 2k conjugate complexed with anionic mRNA encoding HIV gp120. With this approach it is possible to open tight junctions and enhance the paracellular transport <sup>24</sup>.

For instance, thiolated polymers, known as thiomers, are hydrophilic polymers and currently conjugated with hydrophilic macromolecules for a better uptake. Thiomers have the ability to mimic the mechanism of secreted mucus glycoproteins, covalently binding through disulphide bonds with cysteine from mucus, enhancing mucoadhesion and inhibit enzyme action <sup>25</sup>. This allows thiomers to stay concentrated at absorption membrane, through the protection of thiol groups and the inhibition of efflux, which can be beneficial for certain treatments <sup>26</sup>. Briefly, thiomers can reduce oxidized glutathione (GSSG) to GSH, at the same time that thiol groups are oxidized to disulfide bonds, attaching to the mucosa glycoproteins <sup>27</sup>. Then, GSH can bind to cysteine active site of protein tyrosine phosphatase (PTP) via disulfide bond, preventing PTP action of removing phosphate group from tyrosine residues. Consequently, the tyrosine phosphorylation permits the opening of tight junctions, improving permeation properties and facilitating the diffusion <sup>28</sup>. An early study shows protein tyrosine phosphatase inhibition, with sodium orthovanadate, which leads to tyrosine phosphorylation at tight junctions and inducing permeability in bovine corneal epithelial cells <sup>29</sup>. In fact, TJ are responsible for hydrophilic nanomaterials uptake throughout paracellular route and their association with thiomers increases increases the apparent permeability (Papp)<sup>30, 31</sup>.

On the other hand, functionalized and some of the non-functionalized nanomaterials are typically endocytosed. Endocytosis involves engulfment in membrane invaginations and formation of intracellular vesicles <sup>9, 11</sup>. Actually, this pathway represents the classic mechanism of nanomaterials uptake, which can be divided into five types. Even when the nanomaterial is already inside the cell, drugs can be pumped out through drug efflux pumps, creating drug resistance <sup>32</sup>.

Phagocytosis is a receptor-mediated process, where large particles are engulfed by the cellular membrane. It is limited to macrophages, dendritic cells and M cells <sup>33, 34</sup>. On the

other hand, pinocytosis is the uptake of fluids and solutes and can be sub-classified as macropinocytosis, clathrin- and caveolae-mediated uptake, and clathrin- and caveolae-independent uptake. In macropinocytosis, a large volume of fluid with nanomaterials is engulfed. It is an active and actin-dependent process, which means that this mechanism needs actin to grow and cholesterol to membrane projection<sup>33,35</sup>. It is also non-specific receptor mediated and so, does not need a specific binding between ligand-receptor, or a specific cellular type. Requires, however, a cellular stimulation to initiate the process<sup>36</sup>. Clathrin-mediated endocytosis is a receptor-mediated uptake mechanism, under the control of dynamin. Briefly, dynamin is a GTPase protein which leads to division of clathrin pits from membrane, so small vesicles (60-200 nm) are formed coated by clathrin. After internalization, clathrin is removed by auxilin and hsc 70 and vesicles are fused with Rab5 early endosomes<sup>33,37</sup>. This mechanism is seen as a housekeeping, to degrade and maintain the homeostasis and is usually taken by low density lipoprotein, transferrin and ligand-receptor complexes<sup>36</sup>. In transport studies, pharmacological inhibitors are used to analyze the topology of endocytosis<sup>38,39</sup>. Particularly, Steinbach and co-workers used chlorpromazine - specific for clathrin, nystatin - specific for caveolin and LY294002 that is specific for macropinocytosis. In analysis, they verified that clathrin-mediated endocytosis was the predominant mechanism of nanoparticles internalization<sup>39</sup>. Actually, several studies verify that clathrin-mediated endocytosis is the main used via<sup>37,40</sup>. Yet, when nanomaterials are decorated with certain ligands, such as folic acid and cholesterol, caveolin-mediated endocytosis is the used mechanism<sup>11</sup>. Albumin, because of its negative charge, is an example demonstrated by Chanthick and colleagues<sup>41</sup>. Concisely, small caveolae-coated vesicles (50–80 nm), also under the control of dynamin, are formed through flask shaped invaginations in a non-specific uptake process. Therefore, caveolin is an integral membrane protein responsible for the formation of caveolae and consequently the formation of invaginations through caveolin-1 expression. Its morphology and functions are different depending on the cell type. During the internalization, they are endocytosed together with vesicles. Caveolae is similar to lipid rafts, since it is also composed by cholesterol and sphingolipids, being also associated with glycosylphosphatidylinositol (GPI) and several kinases. Contrasting with clathrin, caveolae mediated needs a signal to start the process. Basically, endocytosis begins with tyrosine phosphorylation of the protein associated, which leads to depolymerization and enlistment of actin<sup>36</sup>. This via of endocytosis leads to the escape from the endolysosomes and to direct exocytosis of drug carriers, which is interesting and call attention of several investigators<sup>33,35</sup>. Finally, clathrin and caveolin independent

transport occurs via non-specific endocytosis, not needing a receptor and also characterized as dynamin in- and dependent pathway<sup>3,36</sup>. In this case, EIPA is normally used as transport inhibitor<sup>42</sup>.

A recent and very promising advance biomanufacturing for intracellular delivery of nanomaterials is microfluidics, a membrane disruption method. Microfluidics is a technology that improves the quality of the delivery system and establishes a relationship between structure-function of nanomaterials, presenting also as advantages the uniform-sized emulsion droplet and the understanding of the intracellular delivery barriers. However, it is not clear yet if it is possible to scale-up<sup>43</sup>. The microfluidic device allows passing single cells, through parallel channels, into a thin constriction. This approach allows creating transient pores in the plasmatic membrane, which enhance the intracellular delivery via mechanoporation<sup>44</sup>. Authors already demonstrated its efficiency in intracellular delivery of NPs loaded with dexamethasone, and also studied the effect of NPs design in stem cells fate<sup>45</sup>. Others choose this strategy to prevent the rapid clearance and consequent loss of microbubbles, stable producing them, with flow-focusing microfluidic devices, in real time and near to the therapeutic site<sup>46</sup>.

### **3.2. Nanomaterials characteristics and their influence**

Internalization and intracellular transport mechanisms are affected by nanomaterials properties (**Figure 1**). Different characteristics (size, charge, shape, elasticity) contribute to a different interaction between the nanomaterial and the cell membrane, causing altered signaling events and activation of different pathways of adhesion and internalization. Thus, the desired result, for more effective and distinctly targeted delivery, can be obtained controlling these parameters, which are important to attain the target and specific activity at a predetermined rate and time<sup>1,15</sup>.

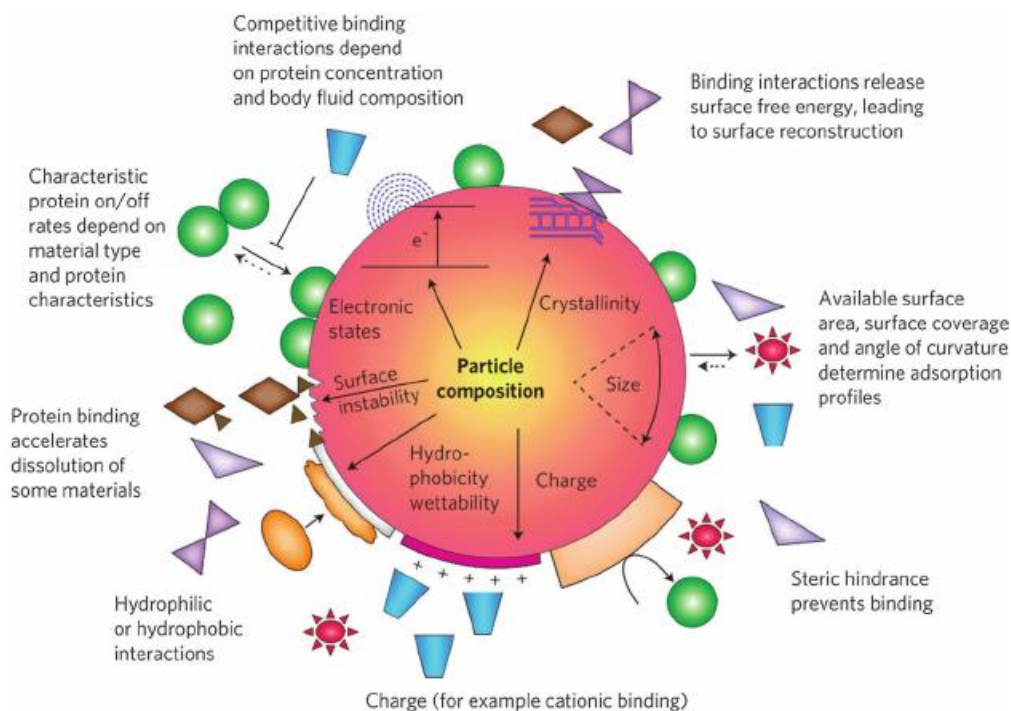


**Figure 1 | Effects of protein corona surrounding a nanoparticle.** The corona constitutes a primary nanobio-interface that determines the fate of the nanoparticle and can cause deleterious effects on the interactive proteins. Pre-existing or initial material characteristics contribute to the formation of the corona in a biological environment. Characteristic protein attachment/detachment rates, competitive binding interactions, steric hindrance by detergents and adsorbed polymers, and the protein profile of the body fluid lead to dynamic changes in the corona. The corona can change when particles move from one biological compartment to another. Figure reprinted with permission from <sup>47</sup>.

### Size

Size is the priority parameter because it determines the endocytosis pathway and also states which cells uptake the particle. Particles smaller than 10 nm are mainly removed by renal clearance <sup>48</sup>. Particles, when orally administered, with a size between 10-100 nm have higher cellular uptake efficiency, since they are taken up in Peyer's patches, and then absorbed into systemic circulation, avoiding rapid renal clearance. On the other hand, larger particles are removed by mononuclear phagocyte system (MPS), and those within 200–300 nm cannot even pass, being concentrated in the spleen <sup>49, 50</sup>. In internalization, larger particles (>1µm) enter the cell by macropinocytosis; with 120 nm by clathrin-dependent pathway; those with 50–100 nm by caveolae-dependent pathway and finally smaller particles (<50 nm) can be internalized through clathrin- and caveolae-independent pathway. So the internalized nanomaterials are intimately connected with

the size of vacuole formed <sup>20</sup>.

A penetration enhancer can be added to the macromolecules with high molecular weight, such as dimethyl palmitoyl ammonio propanesulfonate (PPS), a zwitterionic surfactant. According to microscopy studies, PPS allows macromolecules to diffuse through paracellular and transcellular pathway, improving 45-fold of their bioavailability <sup>51</sup>. Also, polyacrylate, chitosan <sup>52</sup>, phytic acid <sup>53</sup> and self-assembling lipid-like peptides <sup>54</sup> work as enhancers, as well as thiomers and lectins <sup>55</sup>. These enhancers have the ability to reversibly open tight junctions, increasing the paracellular transport of macromolecular drugs. This is due to the down-regulation of occludin and claudin, TJ proteins, besides the synergism of reductive effects of  $\text{Ca}^{2+}$  <sup>56, 57</sup>. On the last case, the cations bind with more affinity to the polyacrylate derivatives, causing an inhibition of lumen enzymes (p.e. trypsin). Thus the complex polyacrylate- $\text{Ca}^{2+}$  trigger the TJ opening <sup>58, 59</sup>. It was also demonstrated that cyclodextrin improves the macromolecular absorption by the pulmonary delivery <sup>60</sup>. Finally, an alternative strategy is the use of palmitoyl glycol chitosan hydrogels <sup>61</sup> or the development of liposomes with enhancers to delivery hydrophilic macromolecules <sup>62</sup>.

#### *Surface composition*

Nanomaterials surface is also an important aspect, since its composition is in contact with the cell, which can be affected by hydrophobicity or hydrophilicity. So, this parameter determines the cellular internalization and intracellular transport and influences the circulation time and nanocarrier association with cells and their recognition. Hydrophobic particles can be delivered to immune cells and penetrate into the bilayer membrane, being easily internalized <sup>11, 34</sup>. Normally, polymers are added to nanomaterials to turn their surface more inert, hydrophilic, avoid immune clearance and increase the blood circulation time. PEGylation is a strategy to make nanomaterials invisible to macrophages or phagocytes and to prolong half-life <sup>63</sup>. In this case, ethylene glycol (PEG) chains are covalently conjugated added to nanomaterials, conferring a hydrophilic nature <sup>64</sup>. According to Schottler S. et al., PEG can capture water molecules and form a natural barrier around the nanomaterial hindering proteins from adsorption, usually known as the “stealth” effect <sup>65</sup>.

Other strategy is to use biomimetic surfaces, where the nanomaterials surface is modified with natural membrane coating to avoid phagocytic clearance, prolong drug circulation and improve their biocompatibility. In this case, markers as CD47 <sup>66</sup> or even from leukocytes are attached to the surface to camouflage nanomaterials, being

recognized as 'self' <sup>67</sup>.

### *Charge*

Also surface charge can be manipulated. For example, intestinal cell membrane is negatively charged, as plasmatic membrane, due to phospholipids, so positively charged nanomaterials interact more strongly, enhancing internalization <sup>9</sup>. A typical example is polyethyleneimine (PEI), which is commonly used to permeate membranes and let nanomaterials enter <sup>68</sup>. In terms of transport, positively charged particles utilize clathrin and macropinocytosis <sup>69</sup> while negatively charged particles tend to utilize caveolae mediated pathway <sup>23, 41</sup>. Neutral or slightly negatively charged particles are considered the best for long circulation, since they are not susceptible to MPS. On the other hand, charges highly positive or negative are taken up by macrophages <sup>17, 23, 70</sup>.

### *Shape*

Shape can also dictate the path of the particle and, inclusively, can change over time or after receiving external stimuli for long circulation and surpass barriers. It is an important factor in flow margination, avoidance of immune system and tissue accumulation. Spherical particles are better internalized by macrophages, while asymmetrical nanomaterials are more advantageous for sensing, self-assembly, tissue engineering, immunoengineering, therapeutic and diagnostic delivery <sup>1, 34</sup>. So, one of the strategies, as mentioned before, is to create elliptical particles to escape macrophages and then, after a stimuli, change to a sphere form for a better internalization <sup>20, 71</sup>.

### *Elasticity and solubility*

Finally, increasing elasticity also increases blood residence time and avoids clearance by immune system. Soft nanomaterials use macropinocytosis while harder ones are internalized through clathrin-dependent mechanisms <sup>34, 72</sup>.

It is also popular chemically modify nanomaterials to change the fluidity and/or solubility of mucus, regarding orally administration. According to literature it is possible to add fatty acids or to substitute amino acids to obtain an increased solubility. The fatty acids addition is proportional to the increased solubility, which may increase 16-fold with linoleic acid <sup>73</sup>. A similar effect was also observed with capric acid, lauric acid and oleic acid. These fatty acids increase the hydrophilic transport and reduce the transepithelial electrical resistance, which indicates the opening of TJ <sup>74</sup>. In fact, the paracellular transport has been related, in several papers, with the transport of poorly absorbed

drugs. It was even studied the relation of that event with fatty acids and their effects on increased absorption of mannitol, a paracellular marker, and on morphology changes of TJ<sup>75</sup>. The amino acid substitution is demonstrated by a group of scientists that introduced 20 amino acids in ribonuclease (RNase) Sa at position 76, confirming that asparagine, glutamine and threonine have more significantly for protein solubility<sup>76</sup>.

In short, it is clear that these characteristics (**Table 1**) influence the uptake, renal clearance, drug stability, circulation time, and make nanomaterials release the drug or even change properties by internal (pH, redox, temperature, enzymes) and external stimuli (ultrasound, magnetic, light, electrical)<sup>9, 15</sup>. Stimuli-responsive nanocarriers, already reviewed elsewhere<sup>77</sup>, are definitely a smart approach for intracellular drug delivery. Recently, authors inclusively created porous silica nanocarriers sensitive to three stimuli (protease/redox/pH) for drug delivery<sup>78</sup>.

Blanco E and co-workers summarized the main effects of nanoparticle size, shape and surface charge among different organs including the lungs, liver, spleen and kidneys<sup>11</sup>. Besides the importance of intracellular delivery/targeting, the drug or nanomaterials is equally significant as well. So, it is crucial imaging and analyze the nanomaterials in intracellular organs. Nowadays, that is possible using methods like magnetic resonance, ultrasound, fluorescence PET, phosphorescence, X-ray, optical coherence tomography, photoacoustic and Raman, fluorescence and photoacoustic. On the other hand intracellular delivering can be sensed by electrochemistry or electrophysiology methods, reviewed elsewhere<sup>79, 80</sup>.

In fact, the characteristics manipulation helps non- and functionalized nanomaterials to reach the target. These two types of nanomaterials will be discussed on the following section.

**Table 1 |** Synthesis of the influence of nanomaterials characteristics on cellular uptake and internalization pathway and their strategies

Characteristic	Cellular uptake	Internalization pathway	Strategy
<b>Size</b>	<10 nm	Renal clearance	Add a penetration enhancer (PPS, polyacrylate, chitosan, phytic acid, self-assembling lipid-like peptides, thiomers and lectins) to
	10-10 nm	Peyer's patches	
	100-200 nm	Removed by MPS	
	200-300 nm	Spleen	
			<b>&lt;50 nm:</b> clathrin- and caveolae-independent <b>50-100 nm:</b> caveolae-dependent <b>120 nm:</b> clathrin-dependent Macropinocytosis

				macromolecules to open TJ
<b>Surface composition</b>	Hydrophobic	Immune cells	---	Avoid phagocytic clearance, prolong drug circulation and improve their biocompatibility: -Add hydrophilic polymers (PEGylation) -Biomimetic surfaces (CD47, leukocytes)
<b>Charge</b>	Positive	Highly positive: taken up by macrophages	Clathrin and macropinocytosis	
	Neutral	The best for long circulation -Highly negative: taken up by macrophages	---	Positively charged nanomaterials interact more strongly with the negatively intestinal cell membrane
	Negative	- Slightly negative: the best for long circulation	Caveolae mediated	
<b>Shape</b>	Spherical	Macrophages	---	Elliptical particles to escape macrophages and after a stimuli change to a sphere form for a better internalization
	Asymmetrical	---	---	
<b>Elasticity and Solubility</b>	Soft	Avoid immune system	Macropinocytosis	-Add fatty acids
	Harder	---	Clathrin-dependent mechanisms	-Substitute amino acids

#### 4. Non-functionalized nanomaterials

Non-functionalized nanomaterials are less specific carriers, since they do not have a specific target, limiting their functionality besides being less stable. However, these carriers can, in fact, delivery drug to or into cells, as is the case of nanocrystals, nanoparticles and macromolecules. They can be taken up by M-cells or enterocytes of intestinal epithelium or even by phagocytes<sup>81</sup>. Usually, non-functionalized nanomaterials are used as negative control of functionalized nanomaterials.

##### 4.1. Nanocrystals

Nanocrystals are solid particles formed by a set of atoms that can be structured with an aspect ratio of 10-100. Cellulose nanocrystals (CNCs), in particular, are elongated and rigid, being obtained by the acidic hydrolysis of cellulose<sup>82</sup>. Nanocrystals have the ability



to be loaded with high amounts of drug, which makes them an efficient option to obtain pharmacologic effects <sup>81</sup>. CNCs with polyethylenimine (PEI) were already developed to delivery siRNA to gene silencing. The formulation allowed the siRNA protection and, furthermore, PEI facilitated the delivery into tumor cells, as an anti-tumor strategy, through endosomal escape via “proton sponge effect” <sup>83</sup>. In another study, it was evaluated the effect of unmodified CNCs and its cationic derivatives in mitochondria stress. The authors verified that these compounds induce reactive oxygen species (ROS) production and immune response <sup>82</sup>. The benefic effect of non-functionalized cellulose nanocrystals was also demonstrated by adding them to  $\beta$ -lactoglobulin to prolong the stability at low pH <sup>84</sup>. Also the surface pH influences the affinity, agglomeration and aggregation of nanomaterials. According to some results, surface pH affects phagocytosis and cellular homeostasis, being TF-2 able to trigger inflammatory responses at acid pH while TF-1, with a basic pH, suppress the release of cytokines <sup>85</sup>. In terms of cellular internalization, it is described that nanocrystals enter cells through passive diffusion <sup>86</sup> or even by endocytosis <sup>87, 88</sup>.

#### 4.2. Nanoparticles

Nanoparticles (NPs) (1-1000 nm) are nontoxic, safe and carriers that can be divided into inorganic (porous nanoparticles, silica nanoparticles, carbon nanotubes, gold nanoparticles, quantum dots and iron oxide nanoparticles) and organic (liposomes, drug-polymer conjugates, micelles, polymeric nanoparticles, dendrimers and protein-polymer conjugates) <sup>89</sup> (Figure 2).

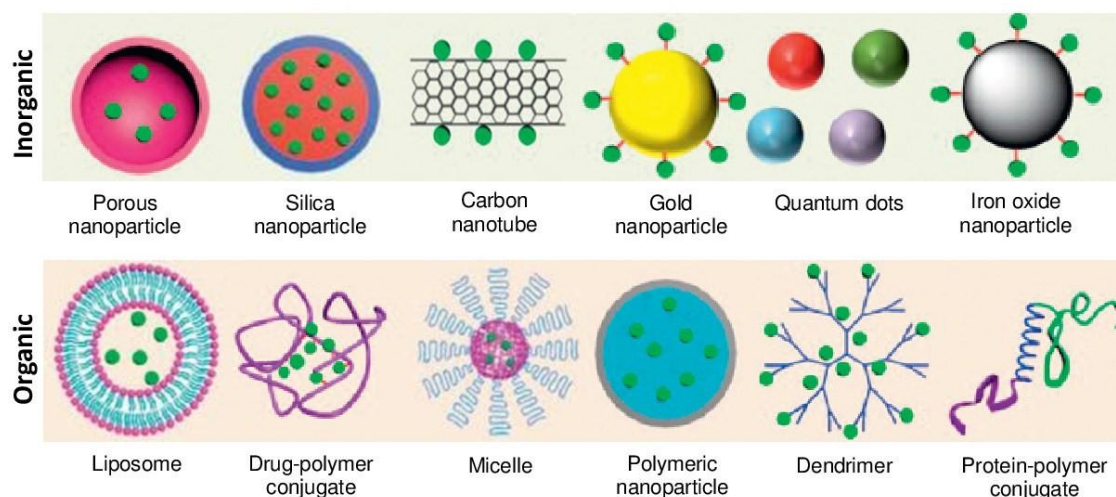


**Figure 2 | Examples of inorganic and organic nanoparticles used in medicine.** Figures reprinted with permission from <sup>89</sup> and adapted.

For instance, porous NPs have properties as high loading capacity, chemical and physical robustness, low toxicity and easy and cheap production. They can be divided into mesoporous silica nanoparticles (MSNs) and porous silicon nanoparticles (PSiNP)<sup>90,91</sup>. In both types it is possible to avoid the prior release of drugs, controlling the binding affinity with cargos. Gatekeepers (e.g., gold NPs) can be attached on the pore outlets through covalent bonds which can be broken by an externally applied stimulus (light, magnetic fields, ultrasounds or temperature) or by an internal stimulus inherent to the treated pathology (ex. acid or basic environments and presence of enzymes) [13]. For instance, silica encapsulated solid lipid (SESL) particles were developed for cinnarizine (CIN) delivery. This was to overcome the limited oral absorption of weak basic drugs, due to their pH dependency in intestinal conditions<sup>92</sup>. Another example of inorganic NPs is quantum dots (QD) that can be rapidly taken up by macrophages, showing the ability to move around cytoplasm and target the nucleus histones through nuclear pore complexes<sup>93</sup>. In this case, despite the small size (2-10 nm), this ability is certainly due to the associated charge. QD are also theranostic, showing great potential to promote drug delivery into cells<sup>94</sup>. The intracellular drug delivery was already demonstrated with non-functionalized gold nanoparticles (AuNPs). Authors verified that unmodified AuNPs, i.e. without surface modification, can interact with pancreatic tumor cells and being located in cytoplasm<sup>95</sup>.

As mentioned before, playing with charge and surface characteristics of NPs can maximize internalization and intracellular transport. Actually, cationic liposomes effects were already studied<sup>96</sup> being a frequent choice for gene delivery<sup>97</sup>. A recent study associated T-Rp3 protein with cationic liposomes to improve the efficiency of plasmid DNA (pDNA) delivery in nucleus of mammalian cells<sup>98</sup>. Liposomes, as one of the main non-viral vector, can be produced for pDNA delivery into cells through macropinocytosis<sup>99</sup>. Liposomes are composed by 3-4 nm of lamellar phospholipid bilayers, with a hydrophilic center, a hydrophobic part of the membrane and amphiphilic molecules. It is known that administered liposomes are taken up by monocytes and macrophages, which is an advantage if the aim is to modulate the immunity<sup>16, 100</sup>. However, they occasionally induce complement activation which can lead to hypersensitivity reactions<sup>101</sup>.

Polymeric nanoparticles are solid colloidal particles where the drug is entrapped, encapsulated or absorbed in biocompatible polymeric materials, to improve drug absorption across biological membranes<sup>102</sup>. Polymeric materials can be biodegradable (such as poly(lactide) (PLA), poly(lactide-co-glycolide) copolymers (PLGA), poly ( $\epsilon$ -caprolactone) (PCL) and poly(amino acids)), non-biodegradable (such as poly(methyl

methacrylate) (PMMA), polyacrylamide, polystyrene, and polyacrylates) or natural (such as chitosan, dextran, heparin, alginate, gelatin, and albumin) <sup>1</sup>. Polymeric NPs are widely used for drug delivery in several cells, including macrophages <sup>103, 104</sup>, being also able to reach some organelles like mitochondria and nucleus <sup>105</sup>. They seem to be a promising strategy applied in inflammatory bowel diseases <sup>106</sup>, diabetes <sup>107</sup>, cancer <sup>108, 109</sup> and ophthalmologic purpose <sup>110</sup>.

In case of drug-polymer conjugate, polymeric nanoparticles are conjugated with drugs. The conjugation can be by a direct covalent linkage or by noncovalent interactions. Normally, the two components are connected by a stable or cleavable linker, especially if drug have to reach the conjugate intracellular target <sup>111</sup>. A recent study of Liang *et al.* is a clear example of a stable polymer-drug conjugate for an enhanced anticancer effect in colon cancer. Basically, these investigators have chemical conjugated the amine group of Gemcitabine (GEM; 2',2'difluorodeoxycytidine) with the PLA carboxylic acid group of methoxy poly(ethylene glycol)-poly(lactic acid) (mPEG-PLA) polymer block. PEG avoids the protein absorption and the body's defense system, while the hydrophobic PLA gives biocompatibility, biodegradability, and a non-toxic nature <sup>112</sup>.

Micelles are one more example of organic NPs, which are composed of amphiphilic copolymers (15-80 nm) usually formed by self-assembly in a liquid <sup>101</sup>. They are constituted by a hydrophilic shell, which prevents interactions with the solvent and make the loaded micelles thereby stable in aqueous solution, and a hydrophobic core that can hold therapeutic drug molecules <sup>100</sup>. Micelles have also attracted interest for drug administration owing to their high stability and solubilization capacity due to their hydrophilic shell, controlled drug release, and low toxicity. A recent study proposes a micelle formulation composed by PLGA-PEG-PLGA to prevent cancer metastasis. The authors showed that a derivative of ursolic acid act as an anti-cancer agent, inducing apoptosis by targeting nucleus and mitochondria <sup>105</sup>.

### **4.3. Macromolecules**

Despite their size, macromolecules can also diffuse across membranes. Prove of that is the study where it is shown, through diffusion coefficient, the transport of macromolecules in skin layers <sup>113</sup>. On the other hand, their delivery can also be achieved with an external stimulus. For instance, a controlled release can be achieved using a NIR-light irradiation in AuNPs which are associated with macromolecules and light-responsive microcapsules, causing heating and capsules disruption <sup>114</sup>. Furthermore, there are other ways to delivery macromolecules, such as by mechanoporation, where

pores are formed to allow the access <sup>115</sup>. A common strategy is the conjugation of macromolecules to mucoadhesive polymers, such as chitosan, to open the tight junctions, which facilitates the paracellular transport <sup>116</sup>.

The mechanisms of non-functionalized nanomaterials internalization are not yet well established, so more investigation is needed. Indeed, reports within this topic are scarce due to the limitations of non-functionalization, being almost mandatory an improvement in this sense. Thus, functionalization is fundamental in several biomedical applications, guaranteeing more specificity.

## 5. Functionalized nanomaterials

Functionalized nanomaterials are directed to a specific target, improving their effect and minimizing unwanted effects by driving drugs towards the exact site of action. Inclusive, the upgrading of their ADME (absorption, distribution, metabolism, and excretion), enhance the therapeutic efficiency <sup>16, 20</sup>.

Active targeting of nanomaterials is commonly referred when drugs reach the right target through the site-specific targeting. This means that there is an interaction between the targeting ligands on nanocarriers and the receptors on cell membranes. The recognition performed during the interaction is specific, promoting particles internalization <sup>117, 118</sup>. So, modifying nanomaterials surface with certain ligands is an option to improve cell uptake and endosomal escape <sup>39</sup>. **Table 2** resumes some receptors mentioned in recent studies, such as CD31, integrin  $\beta$ 3 and transferrin <sup>119</sup>, TLR2, TLR3 and TLR9 <sup>120</sup>,  $\alpha$ v $\beta$ 3 integrin <sup>121</sup>, transferrin <sup>122</sup>, EGFR <sup>123</sup>, CD44 <sup>124</sup>, IGFR <sup>125</sup>, FcRn <sup>126</sup>, CD163 <sup>127</sup>, biotin <sup>128</sup>, folate <sup>129</sup> and vitamin B12 <sup>130</sup>.

Cell penetrating peptides (CPPs) are a group of peptides (10-30 a.a.) with the ability to promote the molecular transport and are important to enhance the intracellular uptake. CPPs can be conjugated via covalent binding to protein drugs and it is believed that endocytosis is involved on their translocation. Since they are typically positively charged, CPPs easily have electrostatic interactions with negatively charged cells, such as glycosaminoglycans (GAGs) and sialic acids, at the beginning of translocation <sup>131</sup>. Authors already developed a CPP-adaptor fusion protein, TAT-calmodulin (TAT-CaM), which leads to an efficient intracellular delivery and endosomal escape. In this case there is a reversible and high affinity noncovalent binding that delivery cargo into cytoplasm of eukaryotic cells <sup>132</sup>. Others simply used analogs of the CPP transportan10 conjugated

with nanoparticles to transport siRNA. This group of scientists concluded that the pH change may lead to a more efficient delivery, being the positive charges responsible for the complex stability. <sup>133</sup>

Other approach is the drug conjugation with lectins, which have a nonimmunological origin, facilitating the interaction with cells and then drugs diffusion. Lectins have the ability of binding specifically and noncovalently to proteins and lipids, which because of glycosylation they have glycans <sup>134</sup>. Glycans work as receptor-like structures allowing lectins to bind directly to epithelial cells, known as cytoadhesion. And, this situation can trigger transcytosis of larger molecules <sup>135</sup>. In a study conducted in the past, it was found that 15 of 32 analysed lectins (for instance, ECL-erythrina cristagalli lectin, LEL-lycopersicon esculentum lectin and WGA- wheat germ agglutinin) bound to the apical membranes of airway epithelium and were taken up by endocytosis <sup>136</sup>. In fact, WGA was analyzed and showed to have cytoadhesive and cytoinvasive properties, which facilitates the transport of molecules with high molecular weight. This lectin binds to N-acetyl-glucosamine and sialic acid and improves binding and uptake of proteins drugs <sup>137, 138</sup>.

Thus, the best strategy is to look in the target tissue/cell for the principal receptor or if there are any overexpressed. Nanomaterials are functionalized using certain targeting ligands (antibodies, peptides) on the surface, which will fit in the specific receptor. Inclusive, some investigators are apologists of using dual ligands to get a synergetic effect <sup>139</sup>. Polysaccharide-nanosystems association as well as sialyl Lewis<sup>x</sup>, hyaluronic acid, heparin, dextran, fucoidan, chitosan and cyclodextrin are examples described in literature which contribute to local drug delivery, stealthness, enhanced affinity and stabilization against aggregation <sup>140</sup>.

**Table 2 |** Examples of used receptor and ligands in intracellular drug delivery.

Receptor	Drug	Nanocarrier	Material / Ligand	Disease	Size	Zeta potential	Ref
CD31, integrin β3, transferrin	DOX, DIR or DID	Liposomes	SSL,RGD-SSL, 7PEP-SSL	Sarcoma	100 nm	-3.7 to -1.7 mV	119
TLR2, TLR3, TLR9	MALP-2, poly(I:C), ODN	Polymeric NPs	PLGA, Eudragit FS30D	Genitorectal viral infection	10 μm	---	120
αβ3 integrin	c(RGDyC) or CTX	Nanochains	Dextran, IONPs	Glioma	100 nm	---	121
Transferrin	Cyclosporine A	Polymeric NPs	PLGA, xanthanoid gambogic acid,	---	100 nm	---	122

EGFR	PTX, parthenolide	Micelles	PEG2000-DSPE, vitamin E-TPGS	Lung Cancer	15 nm	-34 mV	123
CD44	SLM, PTX	Polymeric NPs	PLGA, HA	Breast Cancer	150 nm	50 mV	124
IGFR	Insulin-sodium oleate complex	Polymeric NPs	PLGA, Eudragit FS30D	Diabetes	213 nm	-32.6 mV	125
FcRn	Insulin	Polymeric NPs	PLA-PEG, IgG	Diabetes	63 nm	-5.6 mV	126
CD163	Calcein	Liposomes	PEG	Inflammatory and malignant processes	46 nm	---	127
Biotin	QUE and DOX	Polymeric NPs	PEG-PCL	Breast Cancer	105.8 nm	-9.56 mV	128
Folate	Nucleic acids	Polymeric NPs	aminoglycoside-derived	Breast and Bladder cancer	<200 nm	-4 mV	129
VB12	Insulin	Polymeric NPs	Dextran	Diabetes	192 nm	---	130

**Abbreviations** DOX: doxorubicin acid, SSL: sterically-stabilized liposomes, RGD-SSL: RGD functionalized SSL, 7PEP-SSL: 7PEP functionalized SSL, TLR: Toll-like receptors, MALP-2: macrophage-activating lipoprotein, poly(I:C): polyinosine-polycytidylic acid, ODN: CpG oligodeoxynucleotides, c(RGDyC): cyclic pentapeptide, CTX: chlorotoxin, IONPs: iron oxide nanoparticles, EGFR: epidermal growth factor receptor, PEG2000-DSPE: 1,2-distearoyl-sn-glycero-3-phosphoethanolamine-N-[amino(polyethylene glycol)-2000, vitamin E-TPGS: vitamin E D-alpha tocopheryl polyethyleneglycol succinate, SLM: Salinomycin, PTX: paclitaxel, HA: Hyaluronic acid, IGFR: insulin-like growth factor, FcRn: Neonatal Fc receptor, QUE: Quercetin, PEG-PCL: poly(ethylene glycol)-b-poly( $\epsilon$ -caprolactone).

## 6. Intracellular transport of nanoparticles

Once inside the cell, nanomaterials have three options: be captured by endosomes and consequently degraded by lysosomes; escape into cytoplasm or be recycled<sup>39</sup>. Obviously, nanomaterials must escape in order to reach the intended intracellular target. Endosomal escape is then a critical point for intracellular delivery of drugs<sup>9</sup>.

### 6.1. Endocytic route and how to escape it

Nanomaterials are trafficked into endosomes, then under normal conditions, they are transported via the endolysosomal route. Early endosomes with pH 6 mature to late endosomes with pH 5, which can then fuse with lysosomes which contain certain digestive enzymes (**Figure 3**)<sup>9,12</sup>. In addition, endosomal traffick and maturation can be contoured by peptide association, pH manipulation or dispersing drugs into cytosol<sup>141, 142</sup>. Endosome lysis, transport of dissociated products, fusion of nanomaterials with the limiting membrane are also described strategies to exit endosomes<sup>19</sup>. In fact, the main methods, described in literature, to escape endosomes are proton-sponge effect, nanoparticle-endosome membrane fusion, pore formation and membrane disruption.

Specifically, the proton-sponge effect causes acidification, through translocation of protons into the endosomes, causing osmosis, lysis and release of content. Polyamine-based polymers present a pKa around 5-7 that leads to the increased ions influx by inflow of water and consequently endosomal membrane rupture. The most representative polymer is polyethylenimine (PEI) <sup>20, 36</sup>. In nanoparticle-endosome membrane fusion, fusogenic lipids are incorporated in the carriers. Fusogenic lipids are essentially constituted by alanine, glycine, as well as certain hydrophobic residues. For instance 1,2-dioleoyl-sn-glycero-3-phosphoethanolamine (DOPE) is acidresponsive, so the acid pH drives to glutamate and aspartate protonation, resulting in a new hexagonal conformational. This means that the reposition facilitates the insertion of fusogenic lipids between juxtaposed membranes and destroys the lipid packing <sup>20, 36</sup>. In pore formation, after peptides binding in  $\alpha$ -helical structure, they are obliquely inserted into the hydrophobic core of endosomal membrane, which stabilizes the transmembrane pore, and then oriented by their hydrophilic part. On the other hand, that does not happen in membrane disruption process. In this case, peptides bind to the hydrophilic part of phospholipids; suffer a reorientation of the hydrophobic residues, gaining an amphipathic  $\alpha$ -helical structure, which allows peptides to cover the membrane like a carpet; and then there is a disintegration by micellization of membrane <sup>36</sup>.

As a practical example, Berguig and colleagues created antibody-peptide drug conjugates to suppress tumor growth and prolong half-life with low-dose cytotoxicity. The polymer was constituted with two blocks: the first one to improve pharmacokinetics and the second to allow endosomal escape, containing a pH-responsive composition. With the second block they were able to form the micelle at physiological pH and disrupt the membrane at endosomal pH, promoting endosomal escape and intracellular delivery of the first block <sup>143</sup>. Recently the hydrophobic amino acid R groups in viral escape from endosomes were also used <sup>144</sup>;  $\text{Ca}^{2+}$ -siRNA nanocomplexes, where electrostatic interactions lead to siRNA release into the cytoplasm <sup>145</sup>; and TMab4 variant with 3-fold improved endosomal escape through membrane pores <sup>142</sup>. An interesting study about disulfide-bonded dimer of TAT (dfTAT), found at cytosol and nucleus, shows that it is essential to cell penetration but also to membrane leakage. In this study, Erazo-Oliveras and co-workers demonstrated that dfTAT interacting with bis(monoacylglycero)phosphate (BMP), present in late endosomes, mediates the endosomal leakage <sup>111</sup>.

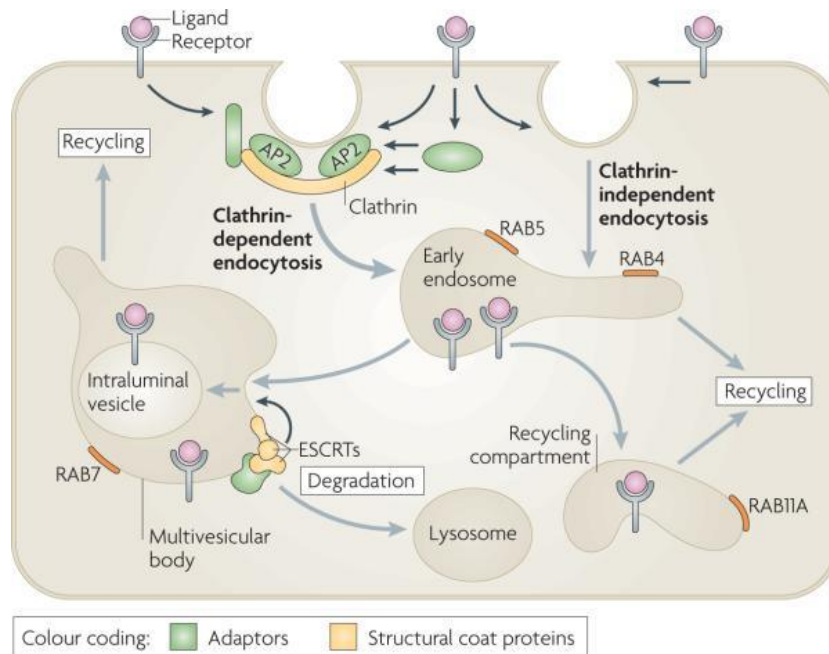


**Figure 3 | Pathways of receptor endocytosis.** Endocytosis involves the capture of transmembrane proteins and their extracellular ligands into cytoplasmic vesicles that are pinched off from the plasma membrane (see the figure). The best-studied pathway of receptor internalization is mediated by clathrin-coated pits. These are small areas of the plasma membrane that are covered from the cytoplasmic surface with clathrin triskelions, which consist of three clathrin heavy chains and three clathrin light chains assembled into the polyhedral clathrin lattice. Receptors are recruited to clathrin-coated pits by directly interacting with the clathrin coat adaptor complex AP2 or by binding to other adaptor proteins, which in turn interacts with the clathrin heavy chain and/or AP2. Clathrin-coated pits invaginate inwards with the help of several accessory proteins and pinch off to form a clathrin-coated vesicle in a process that requires the GTPase dynamin. Several clathrin-independent pathways of endocytosis also exist, although the precise mechanisms and structural components involved in these pathways are not well understood. Endocytic vesicles derived from both clathrin-dependent and clathrin-independent endocytosis fuse with early endosomes. Endosomal trafficking is controlled by several Rab proteins — small GTP-binding proteins of the Ras superfamily. Each GTP-bound Rab protein resides in a particular type of endosome and functions by recruiting specific effector proteins. Following their internalization into early RAB5-containing endosomes, receptors can rapidly recycle back to the plasma membrane by a RAB4-dependent mechanism, traffic to the recycling compartment that contains RAB11A or remain in endosomes, which mature into multivesicular bodies (MVBs) and late endosomes. MVBs are defined by the presence of intraluminal vesicles (ILVs) that are formed in a process of inward membrane invagination involving ESCRT (endosomal sorting complex required for transport) complexes. Early-to-late endosome maturation involves the acquisition of RAB7 and the removal of endosomal components that are capable of, and necessary for, recycling. In the MVBs, cargo destined for degradation is incorporated into ILVs. Fusion of late



endosomes and MVBs with lysosomes carrying proteolytic enzymes results in cargo degradation. Figure reprinted with permission from <sup>146</sup>.

## 6.2. Non-endocytic route as an alternative

When nanomaterials escape endosomes, they escape into cytoplasm or through the endoplasmic reticulum (ER) or Golgi complex. The first via is not recommended in transcellular transport, since most drugs must go to blood circulation to have pharmacological functions <sup>143</sup>. Despite the difficulty to exit cells from the basolateral side, nanomaterials also face, in cytoplasm, degradation factors, such as enzymes <sup>10</sup>.

Those nanomaterials who have an intracellular destiny prefer ER and Golgi routes or as it is also known, the retrograde trafficking pathway. This route is responsible for recycling several molecules, like receptors, which are targeted from Golgi complex <sup>147</sup>. Besides, ER and Golgi complexes are important for the secretory and endocytic pathways, and are also an option to escape the acidic lysosomal environment <sup>12</sup>. Yu and colleagues found a cycle between ER and plasmatic membrane (PM), and then from PM to ER throughout Golgi complex. This trafficking was basically mediated by a retromer-mediated endocytic recycling in Golgi pathway <sup>148</sup>. As described in literature, the binding to the class A receptor allows the internalization by caveolae-mediated endocytosis or lipid raft-mediated pathway <sup>11</sup>. In early endosomes, the nanocarrier content is delivered into ER, Golgi complex, mitochondria or even outside the cells <sup>149</sup>. Actually, syntaxin-6 (present in *trans*-Golgi network-TGN and early endosomes) plays an important role in retrograde trafficking, due to its tyrosine-based sorting motif that regulates post-Golgi transport and the delivery of certain components, such as caveolin-1, into the membrane. The inhibition of syntaxin-6, proportionally decreases the caveolae-mediated endocytosis. Hence, and due to the composition of caveolae, the transport of lipidic classes depends on syntaxin-6 <sup>150</sup>. For instance, syntaxin-6 also interferes with retrograde trafficking of mannose 6-phosphate receptors (in pancreatic  $\beta$ -cells) and insulin-responsive membrane proteins (in endocrine cells) to lysosome and TGN and to insulin-responsive compartment, respectively. Du Y and collaborators demonstrated the movement of epidermal growth factor receptor (EGFR) to Golgi complex via microtubule-dependent movement and the fusion with it through syntaxin-6. They also verified that the translocation is necessary for a future fusion with the nucleus, which becomes a route to travel from the cell surface to the Golgi complex or even the nucleus <sup>151</sup>. So, this ability would be preferred for nucleus-targeted delivery than diffusing throughout the cytoplasm <sup>20</sup>.

### 6.3. Preferred intracellular targets

The final step is the most important of the process. It is crucial to ensure that delivered drugs get to their site of action with the initial pharmacodynamics and bioavailability<sup>9</sup>.

The delivered drug can target several intracellular components, like is shown in **Figure 4**, but normally the main target organelles are the nucleus, mitochondria, cytoplasm, ER and Golgi complex<sup>10, 152</sup>.

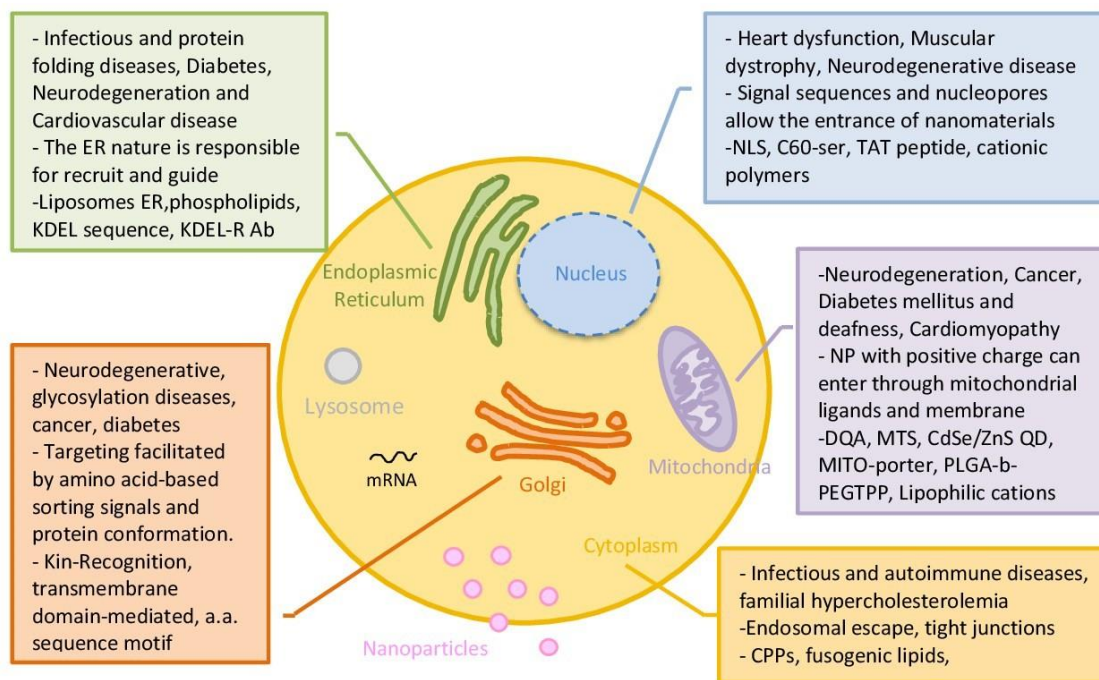


**Figure 4| Illustration of possible intracellular sites of action of delivered drug.** The main target organelles present consequent diseases, crucial characteristics for internalization and transport and the more used nanomaterials.

#### *Nucleus*

The nucleus is organized in a double-layered lipidic envelope with nuclear pore complexes (NPCs) (size~10 nm) that regulate the ins and outs of molecules and an underlying nuclear lamina. In practice, molecules with a size higher than 9 nm and a molecular weight higher than 40 KDa cannot diffuse passively through the pores. Large molecules need carriers to actively pass through the membrane, such as nuclear localization sequences (NLS). NLS present SV40 sequences containing basic residues (Pro-Lys-Lys-Lys-Arg-Lys-Val) that are recognized by importins, a class of karyopherin- $\beta$  proteins responsible for nuclear import<sup>153, 154</sup>. This organelle controls DNA transcription, reproduction, metabolism and cell cycle and important functions as

electron transport, ATP synthesis, ROS generation, genetic programming and cellular signaling regulation may also be affected. According to literature, it is possible to use nanomaterials smaller than nucleus pores, apply a positive charge to the nuclear membrane, interact with nuclear signals or even try molecules with high affinity for DNA, like C60-ser, TAT peptide <sup>7</sup>. Being the most important organelle, it has a crucial role in the treatment of heart diseases, dystrophy, neurodegenerative diseases, cancer and infection, where occurred gene mutation. A strategy to overcome nuclear membrane is to use positive charge in nanomaterials surface, as mentioned before <sup>10, 20</sup>. Induce permeabilization or even use nanomaterials coated with certain molecules that are recognized by nuclear receptors present in cytoplasm, like dexamethasone which is identified by glucocorticoid receptors, may be a way to interfere with DNA transcription and genetic programming <sup>154</sup>. Actually, there are various systems for gene delivery, which is the most common way for nucleus targeting <sup>155</sup>. For instance, micelles with two synergetic anti-cancer drugs co-encapsulated into hyaluronic acid-vitamin E succinate were already produced. The nanoformulation was internalized via caveolae-mediated endocytosis and accumulated in the nucleus. Then cell apoptosis was confirmed and reverse multidrug resistance via CD44 targeting <sup>156</sup>. Some scientists also created PLGA nanoparticles coated with AS1411 aptamer (Apt) and loaded them with superparamagnetic iron oxide nanoparticles (SPIONs) with DOX. The secret, in this case, is Apt that targets to nucleolin. Nucleolin proteins are present in the nucleus and have an important role in angiogenesis and cell proliferation and adhesion. This fact is very useful in cancer, especially when it is associated with DOX, a DNA intercalating agent <sup>157</sup>. Izeddin *et al.* developed a technique to track protein molecules in the nucleus and determine transcription factors (TFs) dynamics. They found that c-Myc and P-TEFb are a global and local explorer of the nucleus, respectively. As the authors say, the control of TFs influence gene regulation, proteins reaction and function in the nucleus, which may be an advantage <sup>158</sup>. Another interesting approach is NPs of PEG-benzoic imine-oligo-L-lysine/iridium (III) metallodrug complex with pH-activated size reduction. Meaning, at pH 7 they are large and protected by PEG shell. But at acid pH of endosomes, NPs stay smaller due to the dissociation and PEG detachment. After this, smaller NPs present oligo-L-lysine that works as a nuclear localization, favoring translocation into the nucleus <sup>159</sup>.

### *Mitochondria*

This organelle is characterized by an external membrane, intermembrane space, an

internal membrane (rich in protein) and the mitochondrial matrix with its own DNA. It is responsible for cellular homeostasis, so it is a good target to interfere with oxidative phosphorylation, apoptosis and production of ROS, intracellular signaling and metabolism. In this way, it makes sense that mitochondria contributes to obesity, Alzheimer, neurodegeneration, cancer, diabetes mellitus and cardiomyopathy, since when polymorphisms or mutation occurs in mitochondrial DNA, it means deficient energy production. Following this, lipophilicity and positive charge are requirements for mitochondrial targeting. As it is also known, the internal negative membrane potential of this organelle is a possible target for positive charged particles <sup>7</sup>. Mitochondriotropic molecules are an approach to get an accumulation inside the cell, insofar as they are amphiphilic. These molecules have the ability to escape to endosomes and deliver their cargo into the mitochondria <sup>10</sup>. Nanoformulations can be guided by mitochondrial processing proteinases (MPP) which process mitochondrial targeting sequences (MTSs) <sup>160</sup>. It is already described that DQA, MTS, CdSe/ZnS QD, MITO-porter, PLGA-b-PEGTPP, lipophilic cations are potential approaches <sup>7</sup>. As an example, a recent study tried mitochondria targeting using hyaluronic acid (HA) protective shell encapsulated with gold nanostar (AuNs) and an anticarcinogenic DOX, in cancer cells. They verified that the formulation is internalized via CD44 receptor. Coated to AuNs was triphenylphosphine modified  $\alpha$ -helical pro-apoptotic peptide (TPP-KLA) that has as function to localize mitochondria, interrupt its membranes, induce dysfunction and a consequent apoptosis <sup>161</sup>. On the other hand, it was also proposed to produce folate-coated chitosan nanoparticles loaded ursolic acid as anti-breast cancer drug. It was confirmed that these NPs were internalized through a folate-receptor mediated endocytotic pathway. After destroying the permeability of lysosomal membrane, NPs were localized into mitochondria. This allowed to overproduce reactive oxygen species (ROS), destroy the mitochondrial membrane potential and consequently the irreversible apoptosis of cancer cells <sup>162</sup>. In fact, there are several polymeric conjugations, especially for cancer. Also, chitosan is used to reach mitochondria, conjugated with mitochondria-targeting ligand triphenylphosphine (TPP) to delivery ionidamine and siRNA and trigger the mitochondrial apoptosis pathway <sup>163</sup>. In short, the best way to target mitochondria and the metabolic pathway is coating nanomaterials with mitochondrial targeting signals/peptides conjugated with pro-apoptotic drugs.

### *Endoplasmic reticulum*

ER is organized in membrane structures, called “cisternae” and intermembrane space.

It is in this organelle that protein folding and lipid biosynthesis occur. It is also responsible for controlling drug detoxification, apoptosis, immune responses and signaling pathways. Besides, it is where peptides are loaded to the major histocompatibility complex (MHC) class I and antigens are delivered, being basically a presentation site<sup>10</sup>. Protein transport is mediated by KDEL sequence that works as a localization signal, which is recognized by its receptor (KDEL-R), expressed in ER. Once again, it is a good organelle for pharmaceutical target, being biomimetic models a possible approach. Another method for ER targeting is the use of localization signals or antibodies against ER receptors that lead to ER stress, protein misfolding and aggregation, calcium homeostasis disturbance and exposure to free radicals<sup>7</sup>. Associated to ER dysfunctions are infectious and protein folding diseases, diabetes, neurodegeneration and cardiovascular diseases<sup>152</sup>. Murugan and colleagues developed mesoporous silica nanoparticle pores loaded with topotecan and coated with poly (acrylic acid)-Chitosan conjugated with quercetin. This approach allowed a cell death from structural changes in organelles like ER, nucleus and mitochondria in breast cancer cells<sup>164</sup>. In diabetes it was explored the possibility to imaging  $O_2^{\cdot-}$  using two photon fluorescent probes termed ER-BZT and treat it with metformin. As mentioned before, the production of ROS leads to ER stress and disease formation<sup>165</sup>. It was found that the natural compound jaceosidin contributes to sarco-endoplasmic reticulum  $Ca^{2+}$ -ATPase 2b (SERCA2b) upregulation, decreasing ER stress<sup>166</sup>. Finally, liposomes ER, phospholipids, KDEL sequence and KDEL-R antibodies are approaches already reviewed<sup>7</sup>.

### *Golgi complex*

Only 4% of intracellular delivery of nanomaterials target this organelle, which is composed by a system of tubular membranes oriented by *cis* or *trans* direction<sup>152</sup>. The main function of the Golgi complex is N- or O-glycosylation, transport and sorting proteins, in addition to its influence in lipid biosynthesis<sup>167</sup>. The *trans*-Golgi network (TGN) is found in the middle of endocytic and exocytic pathways, playing an important role in straighten out lipids and proteins. It is normally associated with ER, since different cargos are transported from there to *cis*-Golgi network and then to TNG, where cargos are sorted and forwarded to their destinations<sup>168</sup>. In fact, Matsuto and colleagues demonstrated that BICD2 allows Rab6A binding to Golgi complex. They also showed that Rab6A and BICD2 are responsible for the fusion between Golgi tubule and ER, in retrograde trafficking<sup>169</sup>. Logically, some dysfunctions contributes to Alzheimer, cancer, neurodegenerative diseases and diabetes<sup>152</sup>. In 2011, a group of scientists discovered

a Golgi Complex-Targeting Signal in a coronavirus responsible for severe acute respiratory syndrome. They showed that in the cytoplasmic tail there is a motif, beta-hairpin structural, that controls Golgi complex localization <sup>170</sup>. This could be a way to improve targeting of Golgi complex. Moreover, Banfield described several mechanisms of protein retention in the Golgi complex, like Kin-Recognition, transmembrane domain-mediated and amino acid sequence motifs <sup>167</sup>.

### *Cytoplasm*

Cytoplasm is the intracellular space, where several organelles meet, and can be a target or a way to reach specific organelles. On the last case, drugs are diffused and have random interactions with organelles. For instance, siRNA acts in the cytoplasm and nanomaterials that have a high metabolic stability <sup>171</sup>. Also SH3 and SH2 of SLAP can be delivered into cytoplasm to inhibit T cell receptor, which can be favourable for autoimmune diseases treatment <sup>172</sup>. Typically, this organelle is targeted when infectious and autoimmune diseases and familial hypercholesterolemia occurs <sup>8</sup>. Nowadays, there are a gathering of approaches that allow the delivery of nanomaterials into cytoplasm, between the cell penetrating peptides (CPPs) <sup>173</sup> and cationic nanomaterials <sup>174</sup>. Besides, liposomes with fusogenic properties <sup>175</sup> or pH sensitive as drug carriers <sup>176</sup> have been studied, since they have the ability to destabilize endosomal membranes and release drugs into the cytoplasm <sup>9</sup>. Authors suggest polyampholyte nanoparticles and freeze concentration in order to deliver proteins into cytoplasm <sup>172</sup>. Others choose to apply a faded electric treatment-induced for siRNA delivering <sup>177</sup>, use connectosomes to diffuse through tight junctions <sup>178</sup> or even bubble liposomes and ultrasound <sup>179</sup>. Throughout literature it is also possible to find that the use of enzyme-sensitive linkers or redox responsive are responsible for degradation <sup>7</sup>.

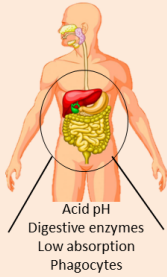
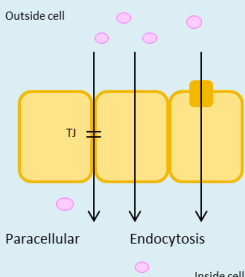

Currently, all these nanomaterials parameters are highly considered by pharmaceutical industry to ensure delivery to the systemic circulation, ideally through the oral route <sup>180</sup>. Proof of the scientific effort is the currently 43 approved drugs, recently reviewed by Weissig et al., as nanopharmaceuticals <sup>181</sup>. Particularly for intracellular applications, Feraheme™ (Ferumoxytol) was approved in 2009 by FDA to treat the iron deficiency anemia in adults with chronic kidney disease. This nanopharmaceutical is composed by superparamagnetic iron oxide nanoparticles coated with dextran, and basically, the iron is released inside macrophages and consequently into intracellular storage iron pool or is transferred to plasma transferrin. In 2014 was approved Plegridy® (Biogen), a polymer-

protein conjugate (PEGylated IFN beta-1a) with improved stability of protein due to PEGylation, for multiple sclerosis. This drug binds to the type I interferon receptor on the surface of cells and causes intracellular events which leads to the regulation of interferon-responsive gene expression. Also in 2015, Onivyde<sup>®</sup> (Merrimack), liposomal Irinotecan, was approved by FDA. This drug is useful for pancreatic cancer, since increases the intracellular uptake of irinotecan and low the systemic toxicity arising from side-effects (<https://www.fda.gov/>).

## 7. Conclusion

Functionalized nanomaterials are definitely the best way to reach a specific target and have reduced side effects and increased efficiency. However, there are several parameters that must be taken into account, such as size, charge, composition and shape, since they are correlated with cell uptake, long circulation times, renal clearance and drug stability. All the details count to face extracellular barriers, select internalization via and overcome intracellular obstacles. The final step is characterized by endosomal escape, organelle location and membrane translocation. Some drugs demand to be delivered in an organelle, which increases the challenge. It is evident that organelle dysfunction is the origin of several diseases, so one of the strategies is to target a set of organelles to reach the expected therapeutic effect.

As future perspectives, it is crucial to conjugate several best characteristics in order to have an ideal nanoformulation with multifunctions. Like is synthesized in **Figure 5**, the ideal is to have the positive surface charge and the ligands affinity to improve endocytosis, the retrograde pathway to avoid the lysosomal degradation or to escape to endosomes. Finally, a biomimetic strategy may be a way to improve intracellular transport and/or exocytosis. Nevertheless, it is not clear yet and need a better understanding about the mechanisms underlying the intracellular transport and the nanomaterials integrity during and after drug releasing. To conclude, this review presented an overview of intracellular barriers that nanoformulations have to surpass and enhanced mechanism to reach the target.

Physical and Chemicals	Portals of entry	Endosomal Escape	Transport and Targeting
 <p>Acid pH Digestive enzymes Low absorption Phagocytes</p>	 <p>Outside cell</p> <p>TJ</p> <p>Paracellular</p> <p>Endocytosis</p> <p>Inside cell</p>		
<ul style="list-style-type: none"> <li>-Biomimetic surfaces</li> <li>-Playing with nanomaterials characteristics</li> <li>-Functionalization</li> </ul>	<ul style="list-style-type: none"> <li>-Cationic coatings to reversibly open TJ</li> <li>-Microfluidics</li> <li>-Stimuli-responsive</li> <li>-Negative coatings for a caveolae-mediated pathway</li> </ul>	<ul style="list-style-type: none"> <li>-Membrane disruption</li> <li>-Dissociated products</li> <li>-NPS-entosome membrane fusion (fusogenic lipids)</li> <li>-Proton-sponge effect (PEI)</li> <li>-Pore formation</li> <li>-pH responsive</li> <li>-Non-endocytic pathway (caveolae-mediated pathway)</li> <li>-CPP, dTAT, TMab4</li> </ul>	<ul style="list-style-type: none"> <li>-Nucleus: apply positive charge, nuclear signals (dexamethasone), molecules with high affinity to DNA (TAT, C60-ser)</li> <li>-Mitochondria: lipophilicity, positive charge, MPP, TPP,</li> <li>-ER: localization signals (KDEL sequence)</li> <li>-Golgi: golgi complex targeting signal</li> <li>-Cytoplasm: CPP</li> </ul>

**Figure 5 | Resume of the challenges and strategies addressed, for an enhanced intracellular delivery of nanomaterials.**

### Conflict of interest

The authors declare no conflict of interest.

### Acknowledgments

This work was also financed by FEDER - Fundo Europeu de Desenvolvimento Regional funds through the COMPETE 2020 - Operational Programme for Competitiveness and Internationalisation (POCI), Portugal 2020, and by Portuguese funds through FCT - Fundação para a Ciência e a Tecnologia/ Ministério da Ciência, Tecnologia e Inovação in the framework of the projects "Institute for Research and Innovation in Health Sciences" (POCI-01-0145-FEDER-007274). Cláudia Azevedo would like to thank to Fundação para a Ciência e a Tecnologia (FCT), Portugal for financial support (SFRH/BD/117598/2016).



## References

1. Banik BL, Fattahi P, Brown JL. Polymeric nanoparticles: the future of nanomedicine. *WIREs Nanomedicine and Nanobiotechnology* 2016;8:271–299.
2. Rekha MR, Sharma CP. Oral delivery of therapeutic protein/peptide for diabetes – Future perspectives. *International Journal of Pharmaceutics* 2013;440:48-62.
3. Pereira C, Araújo F, Granja PL, et al. Targeting membrane transporters and receptors as a mean to optimize orally delivered biotechnological based drugs through nanoparticle delivery systems. *Current Pharmaceutical Biotechnology* 2014;15:650-658.
4. Araujo F, Shrestha N, Granja PL, et al. Antihyperglycemic potential of incretins orally delivered via nano and microsystems and subsequent glucoregulatory effects. *Current Pharmaceutical Biotechnology* 2014;15:609-19.
5. Moulari B, Beduneau A, Pellequer Y, et al. Nanoparticle targeting to inflamed tissues of gastrointestinal tract *Current Drug Delivery* 2013;10:9-17.
6. Sarmiento B, Ferreira D, Vasconcelos T. Polymer-Based Delivery Systems for Oral Delivery of Peptides and Proteins. In: Jorgensen L, Nielsen HM, eds. *Delivery Technologies for Biopharmaceuticals: Peptides, Proteins, Nucleic Acids and Vaccines*: John Wiley & Sons, Ltd, 2009:207-227.
7. Parodi A, Corbo C, Cevenini A, et al. Enabling cytoplasmic delivery and organelle targeting by surface modification of nanocarriers. *Nanomedicine* 2015;10:1923–1940.
8. Sakhrani NM, Padh H. Organelle targeting: third level of drug targeting. *Drug Des Devel Ther* 2013;7:585-99.
9. Jhaveri A, Torchilin V. Intracellular delivery of nanocarriers and targeting to subcellular organelles. *Expert Opinion on Drug Delivery* 2015;13.
10. Ma X, Gong N, Zhong L, et al. Future of nanotherapeutics: Targeting the cellular sub-organelles. *Biomaterials* 2016;97:10-21.
11. Blanco E, Shen H, Ferrari M. Principles of nanoparticle design for overcoming biological barriers to drug delivery. *Nature Biotechnology* 2015;9:941-951.
12. Fan W, Xia D, Zhu Q, et al. Intracellular transport of nanocarriers across the intestinal epithelium. *Drug Discovery Today* 2016;21:856-863.
13. Lopes M, Shrestha N, Correia A, et al. Dual chitosan/albumin-coated alginate/dextran sulfate nanoparticles for enhanced oral delivery of insulin. *Journal of Controlled Release* 2016;232:29–41.
14. Mann SK, Czuba E, Selby LI, et al. Quantifying Nanoparticle Internalization Using a High Throughput Internalization Assay. *Pharmaceutical Research* 2016;33:2421-2432.
15. Bennet D, Kim S. Polymer Nanoparticles for Smart Drug Delivery. In: Sezer AD, ed. *Application of Nanotechnology in Drug Delivery: Nanotechnology and Nanomaterials*, 2014:257-309.

16. Duschl A. Nanomedicine. In: Boraschi D, Penton-Rol G, eds. *Immune Rebalancing - The Future of Immunosuppression*: Elsevier, 2016:251-274.
17. Pawar VK, Meher JG, Singh Y, et al. Targeting of gastrointestinal tract for amended delivery of 3Q4 protein/peptide therapeutics: Strategies and industrial perspectives. *Journal of Controlled Release* 2014;196:168-83.
18. Lopes MA, Abraham BA, Cabral LM, et al. Intestinal absorption of insulin nanoparticles: Contribution of M cells. *Nanomedicine: Nanotechnology, Biology, and Medicine* 2014;10:1139–1151.
19. Stewart MP, Sharei A, Ding X, et al. In vitro and ex vivo strategies for intracellular delivery. *Nature* 2016;538:183-192.
20. Sun W, Hu Q, Ji W, et al. Leveraging physiology for precision drug delivery. *Physiological Reviews* 2017;97:189–225.
21. Agarwal SK, Gupta A. Aquaporins: The renal water channels. *Indian J Nephrol* 2008;18:95-100.
22. DiMarco RL, Hunt DR, Dewi RE, et al. Improvement of paracellular transport in the Caco-2 drug screening model using protein-engineered substrates. *Biomaterials* 2017;129:152-162.
23. Alai MS, Lin WJ, Pingale SS. Application of polymeric nanoparticles and micelles in insulin oral delivery. *Journal of food and drug analysis* 2015;23:351-358.
24. Li M, Zhao M, Fu Y, et al. Enhanced intranasal delivery of mRNA vaccine by overcoming the nasal epithelial barrier via intra- and paracellular pathways. *Journal of Controlled Release* 2016;228:9-19.
25. Bernkop-Schnürch A. *Oral Delivery of Macromolecular Drugs: Barriers, Strategies and Future Trends*: Springer New York, 2009.
26. Rahmat D, Sakloetsakun D, Shahnaz G, et al. HEC-cysteamine conjugates: Influence of degree of thiolation on efflux pump inhibitory and permeation enhancing properties. *International Journal of Pharmaceutics* 2012;422:40-46.
27. Clausen AE, Kast CE, Bernkop-Schnürch A. The Role of Glutathione in the Permeation Enhancing Effect of Thiolated Polymers. *Pharmaceutical Research* 2002;19:602-608.
28. Bernkop-Schnürch A. Thiomers: A new generation of mucoadhesive polymers. *Advanced Drug Delivery Reviews* 2005;57:1569-1582.
29. Chen Y-M, Tu IH, Hu F-R, et al. The role of protein tyrosine phosphorylation in the cell–cell junctions and intercellular permeability of post-confluent bovine corneal epithelial cells. *Taiwan Journal of Ophthalmology* 2013;3:37-41.
30. Palazzo C, Trapani G, Ponchel G, et al. Mucoadhesive properties of low molecular weight chitosan- or glycol chitosan- and corresponding thiomers-coated poly(isobutylcyanoacrylate) core-shell nanoparticles. *European Journal of Pharmaceutics and Biopharmaceutics* 2017;117:315-323.

31. Mahmood A, Bonengel S, Laffleur F, et al. An in-vitro exploration of permeation enhancement by novel polysulfonate thiomers. *International Journal of Pharmaceutics* 2015;496:304-313.
32. Dartier J, Lemaitre E, Chourpa I, et al. ATP-dependent activity and mitochondrial localization of drug efflux pumps in doxorubicin-resistant breast cancer cells. *Biochimica et Biophysica Acta (BBA) - General Subjects* 2017;1861:1075-1084.
33. Fonte P, Araújo F, Silva C, et al. Polymer-based nanoparticles for oral insulin delivery: Revisited approaches. *Biotechnology Advances* 2015;33:1342–1354.
34. Agarwal R, Roy K. Intracellular delivery of polymeric nanocarriers: a matter of size, shape, charge, elasticity and surface composition. *Therapeutic delivery* 2013;4:705–723.
35. Woitiski CB, Carvalho RA, Ribeiro AJ, et al. Strategies Toward the Improved Oral Delivery of Insulin Nanoparticles via Gastrointestinal Uptake and Translocation. *Biodrugs* 2008;22:223-237.
36. Mundra V, Mahato RI. Design of nanocarriers for efficient cellular uptake and endosomal release of small molecule and nucleic acid drugs: learning from virus. *Frontiers of Chemical Science and Engineering* 2014;8:387–404.
37. Forte M, Iachetta G, Tussellino M, et al. Polystyrene nanoparticles internalization in human gastric adenocarcinoma cells. *Toxicology in Vitro* 2016;31:126-136.
38. Iversen T-G, Skotland T, Sandvig K. Endocytosis and intracellular transport of nanoparticles: Present knowledge and need for future studies. *Nano Today* 2011;6:176—185.
39. Steinbach JM, Seo Y-E, Saltzman WM. Cell penetrating peptide-modified poly(lactic-co-glycolic acid) nanoparticles with enhanced cell internalization. *Acta Biomaterialia* 2016;30:49-61.
40. Surassmo S, Saengkrit N, Ruktanonchai UR, et al. Surface modification of PLGA nanoparticles by carbopol to enhance mucoadhesion and cell internalization. *Colloids and Surfaces B: Biointerfaces* 2015;130:229-236.
41. Chanthick C, Kanlaya R, Kiatbumrung R, et al. Caveolae-mediated albumin transcytosis is enhanced in dengue-infected human endothelial cells: A model of vascular leakage in dengue hemorrhagic fever. *Scientific Reports* 2016;6.
42. Forte M, Iachetta G, Tussellino M, et al. Polystyrene nanoparticles internalization in human gastric adenocarcinoma cells. *Toxicology in Vitro* 2016;31:126-136.
43. Chan HF, Ma S, Leong KW. Can microfluidics address biomanufacturing challenges in drug/gene/cell therapies? *Regen Biomater* 2016;3:87-98.
44. Szeto GL, Van Egeren D, Worku H, et al. Microfluidic squeezing for intracellular antigen loading in polyclonal B-cells as cellular vaccines. *2015;5:10276.*

45. Hasani-Sadrabadi MM, Pour Hajrezaei S, Hojjati Emami S, et al. Enhanced osteogenic differentiation of stem cells via microfluidics synthesized nanoparticles. *Nanomedicine: Nanotechnology, Biology and Medicine* 2015;11:1809-1819.
46. Dixon AJ, Dhanaliwala AH, Chen JL, et al. Enhanced Intracellular Delivery of a Model Drug Using Microbubbles Produced by a Microfluidic Device. *Ultrasound in Medicine & Biology* 2013;39:1267-1276.
47. Nel AE, Madler L, Velegol D, et al. Understanding biophysicochemical interactions at the nano-bio interface. *Nat Mater* 2009;8:543-557.
48. Soo Choi H, Liu W, Misra P, et al. Renal clearance of quantum dots. *Nat Biotech* 2007;25:1165-1170.
49. Wahajuddin, Arora S. Superparamagnetic iron oxide nanoparticles: magnetic nanoplatforms as drug carriers. *International Journal of Nanomedicine* 2012;7:3445–3471.
50. Howe SE, Lickteig DJ, Plunkett KN, et al. The Uptake of Soluble and Particulate Antigens by Epithelial Cells in the Mouse Small Intestine. *PLOS ONE* 2014;9:e86656.
51. Gupta V, Hwang BH, Doshi N, et al. A permeation enhancer for increasing transport of therapeutic macromolecules across the intestine. *Journal of Controlled Release* 2013;172:541-549.
52. Wang J, Kong M, Zhou Z, et al. Mechanism of surface charge triggered intestinal epithelial tight junction opening upon chitosan nanoparticles for insulin oral delivery. *Carbohydrate Polymers* 2017;157:596-602.
53. Fu Q, Wang H, Xia M, et al. The effect of phytic acid on tight junctions in the human intestinal Caco-2 cell line and its mechanism. *European Journal of Pharmaceutical Sciences* 2015;80:1-8.
54. Karavasili C, Spanakis M, Papagiannopoulou D, et al. Bioactive Self-Assembling Lipid-Like Peptides as Permeation Enhancers for Oral Drug Delivery. *Journal of Pharmaceutical Sciences* 2015;104:2304-2311.
55. Dünnhaupt S, Barthelmes J, Köllner S, et al. Thiolated nanocarriers for oral delivery of hydrophilic macromolecular drugs. *Carbohydrate Polymers* 2015;117:577-584.
56. Yeh T-H, Hsu L-W, Tseng MT, et al. Mechanism and consequence of chitosan-mediated reversible epithelial tight junction opening. *Biomaterials* 2011;32:6164-6173.
57. Chi Y, Zhang X, zhang Z, et al. Connexin43 hemichannels contributes to the disassembly of cell junctions through modulation of intracellular oxidative status. *Redox Biology* 2016;9:198-209.
58. Lueßen HL, Rentel CO, Kotzé AF, et al. Mucoadhesive polymers in peroral peptide drug delivery. IV. Polycarbophil and chitosan are potent enhancers of peptide transport across intestinal mucosae in vitro. *Journal of Controlled Release* 1997;45:15-23.

59. Borchard G, Lueßen HL, de Boer AG, et al. The potential of mucoadhesive polymers in enhancing intestinal peptide drug absorption. III: Effects of chitosan-glutamate and carbomer on epithelial tight junctions in vitro. *Journal of Controlled Release* 1996;39:131-138.
60. Zhang H, Huang X, Sun Y, et al. Improvement of pulmonary absorption of poorly absorbable macromolecules by hydroxypropyl- $\beta$ -cyclodextrin grafted polyethylenimine (HP- $\beta$ -CD-PEI) in rats. *International Journal of Pharmaceutics* 2015;489:294-303.
61. Martin L, Wilson CG, Koosha F, et al. The release of model macromolecules may be controlled by the hydrophobicity of palmitoyl glycol chitosan hydrogels. *Journal of Controlled Release* 2002;80:87-100.
62. Parmentier J, Hartmann FJ, Fricker G. In vitro evaluation of liposomes containing bio-enhancers for the oral delivery of macromolecules. *European Journal of Pharmaceutics and Biopharmaceutics* 2010;76:394-403.
63. Huang H, Hernandez R, Geng J, et al. A porphyrin-PEG polymer with rapid renal clearance. *Biomaterials* 2016;76:25-32.
64. Roberts MJ, Bentley MD, Harris JM. Chemistry for peptide and protein PEGylation. *Advanced Drug Delivery Reviews* 2012;64, Supplement:116-127.
65. Schöttler S, Becker G, Winzen S, et al. Protein adsorption is required for stealth effect of poly(ethylene glycol)- and poly(phosphoester)-coated nanocarriers. *Nat Nano* 2016;11:372-377.
66. Qie Y, Yuan H, von Roemeling CA, et al. Surface modification of nanoparticles enables selective evasion of phagocytic clearance by distinct macrophage phenotypes. *Scientific Reports* 2016;6:26269.
67. Evangelopoulos M, Parodi A, Martinez JO, et al. Cell source determines the immunological impact of biomimetic nanoparticles. *Biomaterials* 2016;82:168-177.
68. Bera A, Jewrajka SK. Tailoring polyamide thin film composite nanofiltration membranes by polyethyleneimine and its conjugates for the enhancement of selectivity and antifouling property. *RSC Advances* 2016;6:4521-4530.
69. Noh SM, Kim W-K, Kim SJ, et al. Enhanced cellular delivery and transfection efficiency of plasmid DNA using positively charged biocompatible colloidal gold nanoparticles. *Biochimica et Biophysica Acta (BBA) - General Subjects* 2007;1770:747-752.
70. Xiao K, Li Y, Luo J, et al. The effect of surface charge on in vivo biodistribution of PEG-oligocholeic acid based micellar nanoparticles. *Biomaterials* 2011;32:3435-3446.
71. Yoo JW, Mitragotri S. Polymer particles that switch shape in response to a stimulus. *Proc Natl Acad Sci U S A* 2010;107:11205-10.
72. Banquy X, Suarez F, Argaw A, et al. Effect of mechanical properties of hydrogel nanoparticles on macrophage cell uptake. *Soft Matter* 2009;5:3984-3991.

73. O'Reilly JR, Corrigan OI, O'Driscoll CM. The effect of mixed micellar systems, bile salt/fatty acids, on the solubility and intestinal absorption of clofazimine (B663) in the anaesthetised rat. *International Journal of Pharmaceutics* 1994;109:147-154.
74. Pabla D, Akhlaghi F, Zia H. Intestinal permeability enhancement of levothyroxine sodium by straight chain fatty acids studied in MDCK epithelial cell line. *European Journal of Pharmaceutical Sciences* 2010;40:466-472.
75. Aspenström-Fagerlund B, Sundström B, Tallkvist J, et al. Fatty acids increase paracellular absorption of aluminium across Caco-2 cell monolayers. *Chemico-Biological Interactions* 2009;181:272-278.
76. Trevino SR, Scholtz JM, Pace CN. Amino acid contribution to protein solubility: Asp, Glu, and Ser contribute more favorably than the other hydrophilic amino acids in RNase Sa. *J Mol Biol* 2007;366:449-60.
77. Mura S, Nicolas J, Couvreur P. Stimuli-responsive nanocarriers for drug delivery. *Nat Mater* 2013;12:991-1003.
78. Qiu L, Zhao Y, Li B, et al. Triple-stimuli (protease/redox/pH) sensitive porous silica nanocarriers for drug delivery. *Sensors and Actuators B: Chemical* 2017;240:1066-1074.
79. Park S-m, Aalipour A, Vermesh O, et al. Towards clinically translatable in vivo nanodiagnostics. *Nature Reviews Materials* 2017;2:17014.
80. Wang D, Zhao X, Gu Z. Advanced optoelectronic nanodevices and nanomaterials for sensing inside single living cell. *Optics Communications* 2017;395:3-15.
81. Müller RH, Gohla S, Keck CM. State of the art of nanocrystals – Special features, production, nanotoxicology aspects and intracellular delivery. *European Journal of Pharmaceutics and Biopharmaceutics* 2011;78:1-9.
82. Sunasee R, Araoye E, Pyram D, et al. Cellulose nanocrystal cationic derivative induces NLRP3 inflammasome-dependent IL-1 $\beta$  secretion associated with mitochondrial ROS production. *Biochemistry and Biophysics Reports* 2015;4:1-9.
83. Ndong Ntoutoume GMA, Grassot V, Brégier F, et al. PEI-cellulose nanocrystal hybrids as efficient siRNA delivery agents—Synthesis, physicochemical characterization and in vitro evaluation. *Carbohydrate Polymers* 2017;164:258-267.
84. Scheuble N, Geue T, Windhab EJ, et al. Tailored Interfacial Rheology for Gastric Stable Adsorption Layers. *Biomacromolecules* 2014;15:3139-3145.
85. Boonrungsiman S, Suchaoin W, Chetprayoon P, et al. Shape and surface properties of titanate nanomaterials influence differential cellular uptake behavior and biological responses in THP-1 cells. *Biochemistry and Biophysics Reports* 2017;9:203-210.
86. Junyaprasert VB, Morakul B. Nanocrystals for enhancement of oral bioavailability of poorly water-soluble drugs. *Asian Journal of Pharmaceutical Sciences* 2015;10:13-23.

87. Li J, Qiu J, Guo W, et al. Cellular internalization of LiNbO<sub>3</sub> nanocrystals for second harmonic imaging and the effects on stem cell differentiation. *Nanoscale* 2016;8:7416-7422.
88. Murugan K, Choonara YE, Kumar P, et al. Cellular internalisation kinetics and cytotoxic properties of statistically designed and optimised neo-geometric copper nanocrystals. *Materials Science and Engineering: C* 2017;78:376-388.
89. Tang L, Cheng J. Nonporous silica nanoparticles for nanomedicine application. *Nano Today* 2013;8:290—312.
90. Baeza A, Ruiz-Molina D, Vallet-Regí M. Recent advances in porous nanoparticles for drug delivery in antitumoral applications: inorganic nanoparticles and nanoscale metal-organic frameworks. *Expert Opinion on Drug Delivery* 2016:1-14.
91. Santos HA, Mäkilä E, Airaksinen AJ, et al. Porous silicon nanoparticles for nanomedicine: preparation and biomedical applications. *Nanomedicine* 2014;9:535–554.
92. Yasmin R, Rao S, Bremmell K, et al. Synergistic role of solid lipid and porous silica in improving the oral delivery of weakly basic poorly water soluble drugs. *European Journal of Pharmaceutical Sciences* 2017;96:508-514.
93. Nabiev I, Mitchell S, Davies A, et al. Nonfunctionalized Nanocrystals Can Exploit a Cell's Active Transport Machinery Delivering Them to Specific Nuclear and Cytoplasmic Compartments. *Nano Letters* 2007;7:3452-3461.
94. Volkov Y. Quantum dots in nanomedicine: recent trends, advances and unresolved issues. *Biochemical and Biophysical Research Communications* 2015;468:419-427.
95. Sobhan MA, Sreenivasan VKA, Withford MJ, et al. Non-specific internalization of laser ablated pure gold nanoparticles in pancreatic tumor cell. *Colloids and Surfaces B: Biointerfaces* 2012;92:190-195.
96. Li Y, Wang J, Gao Y, et al. Relationships between Liposome Properties, Cell Membrane Binding, Intracellular Processing, and Intracellular Bioavailability. *Aaps j* 2011;13:585-97.
97. Ran R, Liu Y, Gao H, et al. Enhanced gene delivery efficiency of cationic liposomes coated with PEGylated hyaluronic acid for anti P-glycoprotein siRNA: A potential candidate for overcoming multi-drug resistance. *International Journal of Pharmaceutics* 2014;477:590-600.
98. Alves RF, Favaro MTP, Balbino TA, et al. Recombinant protein-based nanocarriers and their association with cationic liposomes: Characterization and in vitro evaluation. *Colloids and Surfaces A: Physicochemical and Engineering Aspects* 2017;513:1-10.
99. Kim BK, Seu YB, Bae YU, et al. Efficient delivery of plasmid DNA using cholesterol-based cationic lipids containing polyamines and ether linkages. *Int J Mol Sci* 2014;15:7293-312.
100. Wang Y, Chen L. Quantum dots, lighting up the research and development of nanomedicine. *Nanomedicine: Nanotechnology, Biology, and Medicine* 2011;7:385–402.

101. KB K, H N, PE K, et al. In vivo toxicity of cationic micelles and liposomes. *Nanomedicine* 2015;11:467-477.
102. Desai PP, Date AA, Patravale VB. Overcoming poor oral bioavailability using nanoparticle formulations – opportunities and limitations. *Drug Discovery Today: Technologies* 2012;9: e87–e95.
103. Lee SY, Cho H-J. Dopamine-conjugated poly(lactic-co-glycolic acid) nanoparticles for protein delivery to macrophages. *Journal of Colloid and Interface Science* 2017;490:391-400.
104. Vene E, Barouti G, Jarnouen K, et al. Opsonisation of nanoparticles prepared from poly( $\beta$ -hydroxybutyrate) and poly(trimethylene carbonate)-b-poly(malic acid) amphiphilic diblock copolymers: Impact on the in vitro cell uptake by primary human macrophages and HepaRG hepatoma cells. *International Journal of Pharmaceutics* 2016;513:438-452.
105. Chen X, Chen J, Li B, et al. PLGA-PEG-PLGA triblock copolymeric micelles as oral drug delivery system: In vitro drug release and in vivo pharmacokinetics assessment. *Journal of Colloid and Interface Science* 2017;490:542–552.
106. Lee S, Kimb Y-C, Parkc J-H. Zein-alginate based oral drug delivery systems: Protection and release of therapeutic proteins. *International Journal of Pharmaceutics* 2016;515:300–306.
107. Lin Y-H, Chen C-T, Liang H-F, et al. Novel nanoparticles for oral insulin delivery via the paracellular pathway. *Nanotechnology* 2007;18:1-11.
108. Quinteros DA, Ferreira LM, Schaffazick SR, et al. Novel Polymeric Nanoparticles Intended for Ophthalmic Administration of Acetazolamide. *Journal of Pharmaceutical Sciences* 2016;105:3183-3190.
109. Lv Y, Hao L, Hu W, et al. Novel multifunctional pH-sensitive nanoparticles loaded into microbubbles as drug delivery vehicles for enhanced tumor targeting. *Scientific Reports* 2016;6.
110. Yousry C, Elkheshen SA, El-laithy HM, et al. Studying the influence of formulation and process variables on Vancomycin-loaded polymeric nanoparticles as potential carrier for enhanced ophthalmic delivery. *European Journal of Pharmaceutical Sciences* 2017;100:142-154.
111. Erazo-Oliveras A, Najjar K, Truong D, et al. The Late Endosome and Its Lipid BMP Act as Gateways for Efficient Cytosolic Access of the Delivery Agent dTAT and Its Macromolecular Cargos. *Cell Chemical Biology* 2016;23:1-10.
112. Lianga T-J, Zhoub Z-M, Caoc Y-Q, et al. Gemcitabine-based polymer-drug conjugate for enhanced anticancer effect in colon cancer. *International Journal of Pharmaceutics* 2016;513:564–571.



113. Römgens AM, Bader DL, Bouwstra JA, et al. Diffusion profile of macromolecules within and between human skin layers for (trans)dermal drug delivery. *Journal of the Mechanical Behavior of Biomedical Materials* 2015;50:215-222.
114. Carregal-Romero S, Ochs M, Rivera-Gil P, et al. NIR-light triggered delivery of macromolecules into the cytosol. *Journal of Controlled Release* 2012;159:120-127.
115. Matsumoto D, Yamagishi A, Saito M, et al. Mechanoporation of living cells for delivery of macromolecules using nanoneedle array. *Journal of Bioscience and Bioengineering* 2016;122:748-752.
116. Sheng J, He H, Han L, et al. Enhancing Insulin Oral Absorption by Using Mucoadhesive Nanoparticles Loaded with LMWP-linked Insulin Conjugates. *Journal of Controlled Release* 2016;233:181- 190.
117. Li N, Huang C, Luan Y, et al. Active targeting co-delivery system based on pH-sensitive methoxy-poly (ethylene glycol)2K-poly(e-caprolactone)4K-poly(glutamic acid)1K for enhanced cancer therapy. *Journal of Colloid and Interface Science* 2016;472:90-98.
118. Li X, Yu M, Fan W, et al. Orally active-targeted drug delivery systems for proteins and peptides. *Expert Opinion Drug Delivery* 2014;11:1435-1447.
119. Wang D, Fu J, Shi Y, et al. The modulation of tumor vessel permeability by thalidomide and its impacts on different types of targeted drug delivery systems in a sarcoma mouse model. *Journal of Controlled Release* 2016;238:186–196.
120. Zhu Q, Talton J, Zhang G, et al. Large intestine–targeted, nanoparticle-releasing oral vaccine to control genitoretal viral infection. *Nature Medicine* 2012;18:1291-1297.
121. Zhang Y, Huang Z, Wu Z, et al. Functionalized magnetic nanochains with enhanced MR imaging: a novel nanosystem for targeting and inhibition of early glioma. *Colloids Surf B Biointerfaces* 2016;140:437-445.
122. Saini P, Ganugula R, Arora M, et al. The Next Generation Noncompetitive Active Polyester Nanosystems for Transferrin Receptor-mediated Peroral Transport Utilizing Gambogic Acid as a Ligand. *Scientific Reports* 2016;6.
123. Gill KK, Kamal MM, Kaddoumi A, et al. EGFR targeted delivery of paclitaxel and parthenolide co-loaded in PEG-Phospholipid micelles enhance cytotoxicity and cellular uptake in non-small cell lung cancer cells. *Journal of Drug Delivery Science and Technology* 2016;36:150-155.
124. Muntimadugua E, Kumarb R, Saladic S, et al. CD44 targeted chemotherapy for co-eradication of breast cancer stem cells and cancer cells using polymeric nanoparticles of salinomycin and paclitaxel. *Colloids and Surfaces B: Biointerfaces* 2016;143:532-546.
125. Sun S, Liang N, Yamamoto H, et al. pH-sensitive poly(lactide-co-glycolide) nanoparticle composite microcapsules for oral delivery of insulin. *International Journal of Nanomedicine* 2015;10:3489–3498.

126. Pridgen EM, Alexis F, Kuo TT, et al. Transepithelial Transport of Fc -Targeted Nanoparticles by the Neonatal Fc Receptor for Oral Delivery. *Science Translational Medicine* 2013;5:213ra167.
127. Etzerodt A, Maniecki MB, Graversen JH, et al. Efficient intracellular drug-targeting of macrophages using stealth liposomes directed to the hemoglobin scavenger receptor CD163. *Journal of Controlled Release* 2012;160:72-80.
128. Lv L, Liu C, Chen C, et al. Quercetin and doxorubicin co-encapsulated biotin receptor-targeting nanoparticles for minimizing drug resistance in breast cancer. *Oncotarget* 2016;7:32184-99.
129. Godeshala S, Nitiyanandan R, Thompson B, et al. Folate receptor-targeted aminoglycoside-derived polymers for transgene expression in cancer cells. *Bioengineering & Translational Medicine* 2016;1:220-231.
130. Chalasani KB, Russell-Jones GJ, Jain AK, et al. Effective oral delivery of insulin in animal models using vitamin B12-coated dextran nanoparticles. *J Control Release* 2007;122:141-50.
131. Kristensen M, Birch D, Mørck Nielsen H. Applications and Challenges for Use of Cell-Penetrating Peptides as Delivery Vectors for Peptide and Protein Cargos. *Int J Mol Sci* 2016;17.
132. Salerno JC, Ngwa VM, Nowak SJ, et al. Novel cell penetrating peptide-adaptors effect intracellular delivery and endosomal escape of protein cargos. *Journal of Cell Science* 2016.
133. Pärnaste L, Arukuusk P, Langel K, et al. The Formation of Nanoparticles between Small Interfering RNA and Amphipathic Cell-Penetrating Peptides. *Molecular Therapy - Nucleic Acids* 2017;7:1-10.
134. Gavrovic-Jankulovic M, Prodanovic R. Drug Delivery: Plant Lectins as Bioadhesive Drug Delivery Systems. *Journal of Biomaterials and Nanobiotechnology* 2011;2:614-621.
135. Lehr C-M. Lectin-mediated drug delivery:: The second generation of bioadhesives. *Journal of Controlled Release* 2000;65:19-29.
136. Yi SM, Harson RE, Zabner J, et al. Lectin binding and endocytosis at the apical surface of human airway epithelia. *Gene Ther* 2001;8:1826-32.
137. Gabor F, Schwarzbauer A, Wirth M. Lectin-mediated drug delivery: binding and uptake of BSA-WGA conjugates using the Caco-2 model. *International Journal of Pharmaceutics* 2002;237:227-239.
138. Wirth M, Gerhardt K, Wurm C, et al. Lectin-mediated drug delivery: influence of mucin on cytoadhesion of plant lectins in vitro. *J Control Release* 2002;79:183-91.
139. Bayyurt B, Tincer G, Almacioglu K, et al. Encapsulation of two different TLR ligands into liposomes confer protective immunity and prevent tumor development *Journal of Controlled Release* 2017:in press.

140. Silva AKA, Letourneur D, Chauvierre C. Polysaccharide Nanosystems for Future Progress in Cardiovascular Pathologies. *Theranostic* 2014;4:579-591.
141. Torchilin V. Intracellular delivery of protein and peptide therapeutics. *Drug Discovery Today: Technologies* 2008;5:95-103.
142. Kim J-S, Choi D-K, Shin J-Y, et al. Endosomal acidic pH-induced conformational changes of a cytosol-penetrating antibody mediate endosomal escape. *Journal of Controlled Release* 2016;235:165-175.
143. Berguig GY, Convertine AJ, Frayo S, et al. Intracellular Delivery System for Antibody–Peptide Drug Conjugates. *Molecular Therapy* 2015;23:907–917.
144. Lönn P, Kacsinta AD, Cui X-S, et al. Enhancing Endosomal Escape for Intracellular Delivery of Macromolecular Biologic Therapeutics. *Scientific Reports* 2016;6:32301.
145. Goldshtein M, Forti E, Ruvinov E, et al. Mechanisms of cellular uptake and endosomal escape of calcium-siRNA nanocomplexes. *International Journal of Pharmaceutics* 2016;515:46-56.
146. Sorkin A, Zastrow Mv. Endocytosis and signalling: intertwining molecular networks. *Nature Reviews | Molecular Cell Biology* 2009;10:609-622.
147. Carney DW, Nelson CDS, Ferris BD, et al. Structural optimization of a retrograde trafficking inhibitor that protects cells from infections by human polyoma- and papillomaviruses. *Bioorganic & Medicinal Chemistry* 2014;22:4836–4847.
148. Yu J, Chia J, Canning CA, et al. WLS Retrograde Transport to the Endoplasmic Reticulum during Wnt Secretion. *Developmental Cell* 2014;29:277-291.
149. Kou L, Sun J, Zhai Y, et al. The endocytosis and intracellular fate of nanomedicines: Implication for rational design. *Asian Journal of Pharmaceutical Sciences* 2013;8:1-10.
150. Jung J-J, Inamdar SM, Tiwari A, et al. Regulation of intracellular membrane trafficking and cell dynamics by syntaxin-6. *Bioscience Reports* 2012;32:383–391.
151. Du Y, Shen J, Hsu J, et al. Syntaxin 6-mediated Golgi translocation plays an important role in nuclear functions of EGFR through microtubule-dependent trafficking. *Oncogene* 2014;33:756–770.
152. Maity AR, Stepensky D. Delivery of drugs to intracellular organelles using drug delivery systems: Analysis of research trends and targeting efficiencies. *International Journal of Pharmaceutics* 2015;496:268–274.
153. Sun Q, Chen X, Zhou Q, et al. Inhibiting cancer cell hallmark features through nuclear export inhibition. *Signal Transduction and Targeted Therapy* 2016;1.
154. Tammam SN, Azzazy HME, Lamprecht A. How successful is nuclear targeting by nanocarriers? *Journal of Controlled Release* 2016;229:140-153.
155. Chen K, Guo L, Zhang J, et al. A gene delivery system containing nuclear localization signal: Increased nucleus import and transfection efficiency with the assistance of RanGAP1. *Acta Biomaterialia* 2017;48:215-226.

156. Ma W, Guo Q, Li Y, et al. Co-assembly of doxorubicin and curcumin targeted micelles for synergistic delivery and improving anti-tumor efficacy. *European Journal of Pharmaceutics and Biopharmaceutics* 2017;112:209-223.
157. Mosafer J, Abnous K, Tafaghodi M, et al. In vitro and in vivo evaluation of anti-nucleolin-targeted magnetic PLGA nanoparticles loaded with doxorubicin as a theranostic agent for enhanced targeted cancer imaging and therapy. *European Journal of Pharmaceutics and Biopharmaceutics* 2017;113:60-74.
158. Izeddin I, Récamier V, Bosanac L, et al. Single-molecule tracking in live cells reveals distinct target-search strategies of transcription factors in the nucleus. *Elife* 2014;3.
159. Fan Y, Li C, Li F, et al. pH-activated size reduction of large compound nanoparticles for in vivo nucleus-targeted drug delivery. *Biomaterials* 2016;85:30-39.
160. Marcus D, Lichtenstein M, Cohen N, et al. Heterologous mitochondrial targeting sequences can deliver functional proteins into mitochondria. *The International Journal of Biochemistry & Cell Biology* 2016;81:48-56.
161. Chen S, Lei Q, Qiu W-X, et al. Mitochondria-targeting "Nanoheater" for enhanced photothermal/ chemo-therapy. *Biomaterials* 2017;17:92-104.
162. Jin H, Pi J, Yang F, et al. Folate-Chitosan Nanoparticles Loaded with Ursolic Acid Confer Anti-Breast Cancer Activities in vitro and in vivo. *Scientific Reports* 2016;6.
163. Zhang B-F, Xing L, Cui P-F, et al. Mitochondria apoptosis pathway synergistically activated by hierarchical targeted nanoparticles co-delivering siRNA and Isoniazid. *Biomaterials* 2015;61:178-189.
164. Murugan C, Rayappan K, Thangam R, et al. Combinatorial nanocarrier based drug delivery approach for amalgamation of anti-tumor agents in breast cancer cells: an improved nanomedicine strategies. *Scientific Reports* 2016;6.
165. Xiao H, Liu X, Wu C, et al. A new endoplasmic reticulum-targeted two-photon fluorescent probe for imaging of superoxide anion in diabetic mice. *Biosensors and Bioelectronics* 2017;91:449-455.
166. Ouyang Z, Li W, Meng Q, et al. A natural compound jaceosidin ameliorates endoplasmic reticulum stress and insulin resistance via upregulation of SERCA2b. *Biomedicine & Pharmacotherapy* 2017;89:1286-1296.
167. Banfield DK. Mechanisms of Protein Retention in the Golgi. *Cold Spring Harbor Perspectives in Biology* 2011;3:a005264.
168. Matteis MAD, Luini A. Exiting the Golgi complex. *Nature Reviews | Molecular Cell Biology* 2008;9:273-284.
169. Matsuto M, Kano F, MasayukiMurata. Reconstitution of the targeting of Rab6A to the Golgi apparatus in semi-intact HeLa cells: A role of BICD2 in stabilizing Rab6A on Golgi membranes and a concerted role of Rab6A/BICD2 interactions in Golgi-to-ER retrograde transport. *Biochimica et Biophysica Acta* 2015;1853:2592-2609.

170. Cohen JR, Lin LD, Machamer CE. Identification of a Golgi Complex-Targeting Signal in the Cytoplasmic Tail of the Severe Acute Respiratory Syndrome Coronavirus Envelope Protein. *Journal of Virology* 2011;85:5794–5803.
171. Tanaka K, Kanazawa T, Horiuchi S, et al. Cytoplasm-responsive nanocarriers conjugated with a functional cell-penetrating peptide for systemic siRNA delivery. *International Journal of Pharmaceutics* 2013;455:40-47.
172. Kim J-H, Moon J-S, Yu J, et al. Intracellular cytoplasm-specific delivery of SH3 and SH2 domains of SLAP inhibits TcR-mediated signaling. *Biochemical and Biophysical Research Communications* 2015;460:603-608.
173. Zou X, Rajendran M, Magda D, et al. Cytoplasmic delivery and selective, multicomponent labeling with oligoarginine-linked protein tags. *Bioconjug Chem* 2015;26:460-5.
174. Kozielski KL, Tzeng SY, Hurtado De Mendoza BA, et al. Bioreducible Cationic Polymer-Based Nanoparticles for Efficient and Environmentally Triggered Cytoplasmic siRNA Delivery to Primary Human Brain Cancer Cells. *ACS Nano* 2014;8:3232-41.
175. Atif SM, Hasan I, Ahmad N, et al. Fusogenic potential of sperm membrane lipids: Nature's wisdom to accomplish targeted gene delivery. *FEBS Letters* 2006;580:2183-2190.
176. Kim SK, Foote MB, Huang L. Targeted delivery of EV peptide to tumor cell cytoplasm using lipid coated calcium carbonate nanoparticles. *Cancer Letters* 2013;334:311-318.
177. Hasan M, Nishimoto A, Ohgita T, et al. Faint electric treatment-induced rapid and efficient delivery of extraneous hydrophilic molecules into the cytoplasm. *Journal of Controlled Release* 2016;228:20-25.
178. Gadok AK, Busch DJ, Ferrati S, et al. Connectosomes for Direct Molecular Delivery to the Cellular Cytoplasm. *Journal of the American Chemical Society* 2016;138:12833-12840.
179. Negishi Y, Endo Y, Fukuyama T, et al. Delivery of siRNA into the cytoplasm by liposomal bubbles and ultrasound. *Journal of Controlled Release* 2008;132:124-130.
180. Rajendran L, Knölker H-J, Simons K. Subcellular targeting strategies for drug design and delivery. *Nature Reviews | Drug Discovery* 2010;9:29-42.
181. Weissig V, Pettinger TK, Murdock N. Nanopharmaceuticals (part 1): products on the market. *International Journal of Nanomedicine* 2014;9:4357–4373.

## Engineered albumin-functionalized nanoparticles for improved FcRn binding enhance oral delivery of insulin

*Cláudia Azevedo<sup>1,2,3</sup>, Jeannette Nilsen<sup>4,5</sup>, Algirdas Grevys<sup>4,5</sup>, Rute Nunes<sup>1,2</sup>, Jan Terje Andersen<sup>4,5</sup>, Bruno Sarmiento<sup>1, 2,6</sup>\**

<sup>1</sup> Instituto de Investigação e Inovação em Saúde (i3S), University of Porto, Rua Alfredo Allen, 208, 4200-135, Porto, Portugal;

<sup>2</sup> Instituto de Engenharia Biomédica (INEB), University of Porto, Rua Alfredo Allen, 208 4200-135, Porto, Portugal;

<sup>3</sup> Instituto Ciências Biomédicas Abel Salazar (ICBAS), University of Porto, Rua Jorge Viterbo 228, 4150-180, Porto, Portugal;

<sup>4</sup> Department of Immunology, Centre for Immune Regulation (CIR), Oslo University Hospital Rikshospitalet and University of Oslo, N-0424 Oslo, Norway;

<sup>5</sup> Department of Pharmacology, Institute of Clinical Medicine, University of Oslo and Oslo University Hospital, N-0424 Oslo, Norway

<sup>6</sup> CESPUP, Instituto de Investigação e Formação Avançada em Ciências e Tecnologias da Saúde & Instituto Universitário de Ciências da Saúde, 4585-116, Gandra, Portugal

\* Corresponding Author: Tel: +351 22 040 8800; E-mail: [bruno.sarmiento@ineb.up.pt](mailto:bruno.sarmiento@ineb.up.pt)

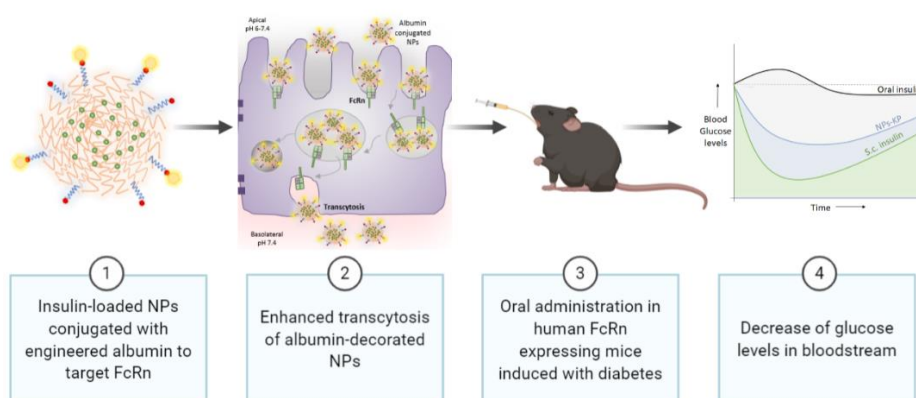
## Abstract

Oral delivery of biopharmaceuticals, as insulin, is hampered by rapid degradation and inefficient absorption in the gastrointestinal tract (GIT). To solve this, a new class of biodegradable poly(lactic-co-glycolic)-poly(ethylene glycol) (PLGA-PEG) mucodiffusive nanoparticles (NPs) was designed. Specifically, these were decorated with site-specific conjugated human albumin, engineered for improved pH dependent binding to the neonatal Fc receptor (FcRn), which naturally mediates transport of albumin across the intestinal epithelium. The designed NPs of monodisperse 150 nm in size were 10% loaded with insulin and their surface was successfully functionalized with human albumin. Importantly, the engineered albumin-functionalized NPs bound human FcRn favorably in a pH dependent manner and showed enhanced transport across polarized cell layers. When orally administered to human FcRn expressing mice induced with diabetes, a reduction of glycemia was measured as a function of receptor targeting, with up to around 40% reduction after 1 hour post-delivery. Thus, biodegradable PLGA-PEG NPs decorated with human albumin for improved FcRn-dependent transport offer a novel attractive strategy for delivery of encapsulated biopharmaceuticals across intestinal barriers.

**Keywords:** Engineered albumin variants; FcRn binding; glycemic decrease; intestinal permeability; PLGA-PEG nanoparticles; type 1 *diabetes mellitus*.

**Teaser:** This study intends to analyze the potential of engineered albumin variants conjugated to mucodiffusive NPs, for enhanced intestinal permeability through the binding to FcRn.

## Graphical abstract



## 1. Introduction

Diabetes *mellitus* is a metabolic and chronic disease and according to the latest data, around 463 million people were living with diabetes worldwide by 2019, and this number will rise up to 700 million by 2045 if current trends were maintained [1]. In addition, it is estimated that the full global costs of diabetes in adults will increase from U.S. \$1.3 trillion in 2015 to \$2.1 trillion by 2030 [2]. Specifically, type 1 diabetes *mellitus* (T1DM) is caused by an autoimmune reaction, characterized by the attack of the immune system to the pancreatic insulin-producing beta cells. Commonly a childhood-onset disease, requires daily injections of recombinant insulin, which is invasive and painful and suffer from poor patient compliance, which contributes to a leading cause of mortality and morbidity [3]. To secure patients' convenience and compliance, oral administration is the preferred route for drug delivery [4, 5]. However, biopharmaceuticals do not endure the harsh environment of the gastrointestinal tract (GIT) and uptake and transport across mucosal epithelial barriers is inefficient [6, 7]. Thus, there is a need for strategies that protect biopharmaceuticals from degradation and secure efficient delivery across the GIT.

One possible solution is the use of biodegradable nanoparticles (NPs) that can promote local absorption and controlled release of biopharmaceuticals [6, 7]. In fact, it has been demonstrated that NPs encapsulated with biopharmaceuticals improve the duration of the therapeutic effect, decrease side effects and increase the drug concentration at the site of action [5, 8]. However, delivery across the selective polarized intestinal cell layer is still poor [9]. Novel strategies that can enhance the delivery of NPs across epithelial barriers in an efficient and cost-effective manner are therefore desired.

In this paper, the design of biodegradable poly(lactic-co-glycolic)-poly(ethylene glycol) (PLGA-PEG) NPs decorated with human albumin variants, recently developed by us, with distinct ability to interact with the human form of neonatal Fc receptor (FcRn), is described [10]. The rationale is based on targeting of albumin to FcRn, which is expressed by polarized intestinal epithelial cells, where it mediates bidirectional transcytosis of its ligands [11, 12]. FcRn does not only bind albumin but also IgG in a non-cooperative manner to distal binding sites and in a pH dependent manner [13, 14]. The receptor binds its ligands at acidic pH (6.5-5.0) and not at neutral pH, which is crucial for the transcytosis process [13, 14] (**Figure 1A**). Interestingly, PEG-PLGA and PLA-PEG-MAL NPs functionalized with human Fc fragments have been shown to transport encapsulated exenatide and insulin, respectively, across intestinal barriers [15, 16]. However, a drawback with using the Fc fragment of IgG is its ability to bind other Fc receptors, which could affect the biodistribution of the functionalized NPs or possibly lead to an immune



reaction. The scenario is more complicated when NPs are not functionalized. In this case, they have to (1) be taken up by fluid-phase pinocytosis, instead by receptor-mediated, before being excreted; (2) they are not sensitive to pH and so are poorly taken up and transcytosed or do not escape to endosomes, being later degraded; (3) finally, they do not take advantage of the recycling pathway and consequent extended half-life. In our study, it was hypothesized that functionalization of NPs with engineered human albumin would result in higher affinity to FcRn, more efficient transport across the intestinal barriers and enhanced delivery of NPs encapsulated with biopharmaceuticals via FcRn-mediated transcytosis (**Figure 1B**), compared to wild-type (WT) albumin.

Albumin constitutes more than 60% of the total protein in the blood, where it functions as a transporter of various endogenous molecules, such as fatty acids, thyroxine and bilirubin [10]. In addition, many small chemical drugs bind to albumin once administered. The fact that it is nontoxic, nonimmunogenic and biodegradable makes it a desirable carrier of drugs. Indeed, the use of albumin to improve the efficacy of biotherapeutics and chemical drugs is continuously growing. Albumin is also exploited in the context of NPs for drug delivery. Abraxane<sup>®</sup> was the first human albumin-based NP to enter the market when it was approved for treatment of breast cancer in 2005. It consists of albumin molecules enclosing a hydrophobic core with the lipophilic anticancer drug, paclitaxel. Importantly, Abraxane<sup>®</sup> is injected, more quickly effective and able to be administered with higher doses while causing less toxicity and side effects compared to other formulations of paclitaxel [17]. In recent years, increased interest has been given to design albumin-NPs for oral delivery, but none of these strategies have so far reached the clinic. However, these studies have shown *in vitro* that albumin-NPs have higher epithelial transport capacity [18, 19]. To the best of our knowledge, none of the strategies have aimed for decoration of biodegradable NPs with engineered human albumin with a particular focus on favorable pH dependent binding to FcRn for enhanced transepithelial transport capacity, applicable for diabetes or oral route.

Thus, in this study, the aim was to design insulin-loaded PLGA-PEG NPs decorated with engineered human albumin for altered FcRn binding and transport properties. The results demonstrated favorable receptor binding and enhanced transcellular transport of NPs decorated with albumin engineered for improved FcRn binding, which further translated into enhanced glycemic control upon oral administration into diabetic human FcRn transgenic mice.

## **2. Experimental section**

### **2.1. Cell culture**

HEK293E (human embryonic kidney) cells were acquired from ATCC (Manassas, VA, USA) and maintained in RDMI 1640 (Sigma-Aldrich) with 10% heat-inactivated fetal calf serum (FCS) (Sigma-Aldrich). A MDCK (Madin-Darby Canine Kidney) cell line overexpressing human FcRn (MDCK-hFcRn) was generated by Drs. Alex Haas and Jens Fischer (Roche Pharma Research and Early Development, pRED, Roche Innovation Center Munich, Germany) and maintained until passage 20. MDCK-hFcRn cells were cultured in DMEM (Gibco) with 15% fetal calf serum (FCS) and 200 µg/mL of G418 (Sigma-Aldrich). The expression level of FcRn- Enhanced Green Fluorescent Protein (EGFP) was stably maintained by G418 and regularly checked by ThermoFisher cell counter Countess II equipped with EVOS Light Cubes for GFP detection, being always above 80%. The culture medium was supplied with 25 µg/mL streptomycin and 25 U/mL penicillin (BioWhittaker), and the cells were incubated at 37°C in a humidified 5% CO<sub>2</sub>, 95% air incubator. All the cells were passaged twice per week.

### **2.2. Protein production**

WT albumin and engineered albumin variants, namely K500A/K510Q (KAHQ) and K573P (KP), were produced by following the procedures previously described, using HEK293E cells [20]. Purification of albumin variants was performed using a Capture select albumin affinity column (GE Healthcare) and followed by gel filtration with a Superdex 200 increased column (GE Healthcare) connected to an Avant25 instrument (GE Healthcare). Human IgG1-MST/HN and recombinant soluble human FcRn were produced as previously described [21].

### **2.3. PLGA-PEG NPs production**

#### *2.3.1. Insulin encapsulation*

Engineered albumin-conjugated and insulin encapsulated poly(lactic-co-glycolic)-poly(ethylene glycol) (PLGA-PEG) NPs were prepared through a modified solvent emulsification-evaporation method based on a w/o/w double emulsion technique [22, 23]. Briefly, 100 mg of polymer, in which 95% was PLGA (PURASORB® PDLG 5004A, in a 50/50 molar ratio of DL-lactide and Glycolide, kindly provided by Corbion) and 5% PLGA-PEG-MAL (Akina, PolyScitech, Ref AI110), was overnight dissolved in 2 mL of ethyl acetate. Then, 0.2 mL of 75 mg/mL insulin solution (Sigma-Aldrich) in 0.1 M of HCl was added to the polymeric solution and homogenized using a Bioblock vibracell 75186

sonicator (Fischer Bioblock Scientific), for 1 min with 70% of amplitude. This primary emulsion (w/o) was poured into 8 mL of 2% (w/v) Pluronic F-127 (Sigma) aqueous solution and homogenized for 1 min using the same equipment, forming the second emulsion (w/o/w). To this, it was added 15 mL of 2% Pluronic F-127 and the organic solvent was then removed by evaporation during 3 h under magnetic stirring (300 rpm). The NPs were washed twice with 0.25 mL of ultrapure water by centrifugation using Amicon® filters of 100 KDa (Millipore Corporation, Bedford, MA, USA) at 1000 x g for 40 min, and redispersed in 0.1 M phosphate buffer (Na<sub>2</sub>HPO<sub>4</sub>, NaH<sub>2</sub>PO<sub>4</sub>) at pH 6.

### *2.3.2. Albumin conjugation*

The amount of albumin was set to the molar ratio 1:0.1 of PLGA-PEG-MAL:Albumin. For each albumin variant, 500 µL of NPs (20 mg/mL) were transferred to an eppendorf Amicon® filter of 100 KDa and centrifuged at 10,000 x g for 5 min at 4°C. The supernatant was discarded, and NPs were resuspended in 250 µL of 0.1 M phosphate buffer. Thereafter, it was added 250 µL of 5.71 µM of albumin-TCEP solution. Each variant was diluted and incubated with 5.71 µM tris(2-carboxyethyl)phosphine hydrochloride (TCEP) for 1 h at room temperature (RT), in order to have a 5.71 µM of albumin-TCEP solution. The reaction was incubated overnight at 4°C. The following day, samples were washed three times with 0.1 M Phosphate Buffer at pH 7 by centrifugation using Amicon® filters of 100 KDa at 10,000 x g for 5 min at 4°C. The same procedure was followed to unloaded PLGA-PEG NPs.

## **2.5. Physical-chemical characterization**

### *2.5.1. Particle size and zeta potential analysis*

Three µL of NPs were characterized for hydrodynamic diameter, polydispersity index (Pdl) and zeta potential (ZP) upon dispersion in 10 mM sodium chloride by dynamic light scattering (DLS) and laser Doppler electrophoresis (LDE) using a Zetasizer Nano ZS (Malvern Instruments, Malvern, UK).

### *2.5.2. Insulin release*

Insulin-loaded NPs (1 mL) were dispersed in 10 mL of pH 1.2 buffer (50 mM KCl) to simulate the gastric fluid (SGF) and incubated at 37 °C under magnetic stirring at 100 rpm. After 2h, the 10 mL suspension was ultracentrifuged at 14,000 x g for 20 min to remove SGF and the NPs were then resuspended with 10 mL of pH 6.0 buffer (50 mM KH<sub>2</sub>PO<sub>4</sub>, 15 mM NaOH) to simulate the intestinal fluid (SIF) and incubated at 37°C under

magnetic stirring at 100 rpm. Aliquots of 0.2 mL were taken at predetermined time points (15, 30, 45, 60, 120, 180, 240, 360 and 480 min) and the samples were replaced with a respective pre-heated fresh buffer, keeping the volume constant. With the purpose to calculate the released insulin, each aliquot was ultracentrifuged, and the supernatant was used for HPLC analysis in order to quantify the insulin released from the NPs over time. Samples were run in triplicate.

### 2.3.3. Morphological characterization and elementary analysis

The morphology of NPs was measured by transmission electron microscopy (TEM) and the elementary analysis by elementary dispersive scanning (EDS). The samples were placed on a grid and observed in a JEOL JEM-1400 electron microscope (JEOL Ltd, Tokyo, Japan). During the preparation, samples were mounted onto metal stubs and vacuum-coated with a layer of gold/palladium.

### 2.3.4. Albumin conjugation efficiency

The conjugation efficiency (CE) of albumin was determined using the following formula:

$$\text{Equation (1)} \quad \text{CE (\%)} = \frac{\text{total amount of albumin} - \text{free albumin in supernatant}}{\text{total amount of albumin}} * 100$$

The quantification was done using a two-way anti-albumin enzyme-linked immunosorbent assay (ELISA). Briefly, 96 wells plates (Costar) were coated with 100  $\mu\text{L}$  of a polyclonal anti-albumin antibody produced in goat (Sigma Aldrich, ref A1151) diluted 1:2000 in PBS by incubation overnight at 4°C. The wells were blocked with 200  $\mu\text{L}$  PBSTM solution, composed by PBS, 0.005% Tween 20 and 4% skimmed milk (Acumedia), for 1 h at RT and then washed three times with 200  $\mu\text{L}$  PBST (PBS, 0.005% Tween 20). Dilution series of the albumin-conjugated NPs samples were prepared (1 mg/mL), starting from diluting the samples 100x and then titrated 1:2 in PBSTM. 100  $\mu\text{L}$  of each dilution was subsequently added in triplicates to wells and incubated for 1 h at RT. The wells were washed as before. Alkaline phosphatase (AP)-conjugated polyclonal anti-albumin from goat (Bethyl Laboratories, Inc.; A80229AP) was diluted 1:4000 in PBSTM and 100  $\mu\text{L}$  was added per well and incubated for 1 h at RT. After washing as before, visualization was performed by adding 100  $\mu\text{L}$  of AP substrate (4-nitrophenyl phosphate disodium salt hexahydrate substrate) (Sigma-Aldrich) diluted in

diethanolamine buffer. The absorbance was measured at 405 nm using the sunrise spectrophotometer (TECAN).

### 2.3.5. Insulin association efficiency and drug loading

The association efficiency (AE) and drug loading (DL) were determined using the following formulas:

$$\text{Equation (2)} \quad \text{AE (\%)} = \frac{\text{total amount of insulin-free insulin in supernatant}}{\text{total amount of insulin}} * 100$$

$$\text{Equation (3)} \quad \text{DL (\%)} = \frac{\text{total amount of insulin-free insulin in supernatant}}{\text{total amount of NPs}} * 100$$

The free insulin in supernatant was isolated during the first washing step by centrifugation with Amicon® filters at 1000 x g for 40 min at 4 °C. The insulin that did not associate to NPs and remained in the aqueous phase was then collected and quantified by a high-performance liquid chromatography (HPLC) method previously validated [24]. Briefly, insulin quantification was performed using a Merck-Hitachi LaChrom HPLC instrument (Merck, Whitehouse Station, NJ, U.S.A.) equipped with a XTerra RP 18 column, 5 µm particle size, 4.6 mm internal diameter, ×250 mm length from Waters (Milford, MA, U.S.A.), and a LiChrospher 100 RP-18, 5 µm particle size guard column (Merk, Whitehouse Station, NJ, U.S.A.). Samples were run in triplicate.

## 2.6. Protein structure

### 2.6.1. Determination of secondary structure

The secondary structure elements of insulin loaded and albumin conjugated PLGA-PEG NPs were assessed by Fourier Transform Infrared Spectroscopy (FTIR). The spectra analysis was performed in ABB MB3000 FTIR spectrometer from ABB (Zurich, Switzerland) equipped with a MIRacle single reflection attenuated total reflectance (ATR) accessory from PIKE Technologies (Madison, WI, U.S.A.). Samples were freeze-dried before analysis. The spectra were made with 256 scans and a 4 cm<sup>-1</sup> resolution in the region of 600-4000 cm<sup>-1</sup>, and each formulation was analyzed in triplicate. In order to obtain the insulin and albumin spectra, a double subtraction procedure, followed by a 15 points Savitsky-Golay second derivative, and a baseline correction using a 3-4 point adjustment at the amide I region (1710-1590 cm<sup>-1</sup>) [25]. This spectral treatment was executed using the HorizonMB FTIR software from ABB (Zurich, Switzerland). Lastly, all spectra were area-normalized for comparison using Origin 8 software (OriginLab Corporation, Northampton, MA, USA).

### 2.6.2. Spectral similarity analysis

The quantitative comparison of the similarity of the FTIR spectra between insulin-loaded NPs with that of native insulin, as well as between functionalized NPs and native albumin, were determined using the area overlap (AO) and spectral correlation coefficient (SCC) algorithms [26]. Both algorithms were used considering the area normalized second-derivative amide I spectra of native insulin or albumin. All the results are displayed in percentage, and the percentage is proportionally correlated with the similarity of spectra. The reference chosen was the insulin or albumin solutions because it is known that the stability of a solid protein formulation increases with the rise of similarity to the FTIR spectra in solution [26].

## 2.7. Binding to human FcRn

Microtiter wells were coated with a human IgG1 mutant variant (M252Y/S254T/T256E/H433K/N434F) (10 µg/mL) in 100 µL PBS pH 7.4 by incubation overnight at 4°C. The wells were blocked with 200 µL PBSTM for 1 h at RT and then washed three times with 200 µL PBST pH 5.5. Recombinant soluble human FcRn (10 µg/mL) in 100 µL PBSTM pH 5.5 was added per well and incubated for 1 h at RT, before repeating the washing step above. Dilution series of the albumin-conjugated NPs samples were prepared, starting from diluting the samples 20x in PBSTM pH 5.5, followed by 1:2 titrations. 100 µL each dilution was subsequently added in triplicates to wells and incubated for 1 h at RT. The wells were washed as before. AP-conjugated anti-albumin from goat was diluted 1:4000 in PBSTM and 100 µL was added per well and incubated for 1 h at RT. After washing as above, visualization was done by adding 100 µL of AP substrate (Sigma-Aldrich) diluted in diethanolamine buffer. The absorbance was measured at 405 nm after 1h using the Sunrise spectrophotometer (TECAN).

## 2.8. Transcytosis assay

MDCK-hFcRn were seeded at a density of  $1.2\text{-}1.4 \times 10^6$  cells per well onto Transwell® inserts (1.12 cm<sup>2</sup>) with collagen coated polytetrafluoroethylene (PTFE) membranes of 0.4 µm pore size (Corning Costar, Durham, NC, USA). Cells with a passage number from 9 to 13 were used for all experiments. Cells form a monolayer with a transepithelial electrical resistance (TEER) value of 6000–900 Ω·cm<sup>2</sup> on the day after seeding. TEER was monitored using a MILLICELL-ERS-2 V-ohm meter (MILLIPORE). Prior to experiments, the monolayers were washed twice then starved for 1 h in Hank's Balanced

Salt Solution (HBSS). For transport experiments at acidic pH, HBSS was buffered to pH 6.0 by addition of MES buffer (Sigma-Aldrich). Then, 200  $\mu$ L of 500 nM albumin variants or albumin-conjugated NPs were added to the apical chamber and 500  $\mu$ L of HBSS at the basolateral side. Samples were collected from the basolateral chambers at time 0 and 4 h post adding to the apical side. Results were expressed in relative transport and apparent permeability ( $P_{app}$ ), using the following formulas:

$$\text{Equation (4)} \quad \text{Relative Transport} = \frac{\text{Amount of sample}}{\text{Mean amount of control}}$$

$$\text{Equation (5)} \quad P_{app} = \frac{\Delta Q}{A \times C_0 \times \Delta t} * 100$$

where  $C_0$  is the initial concentration in the apical compartment (mg/mL),  $A$  is the surface area of the insert ( $\text{cm}^2$ ),  $\Delta t$  is the time during which the experiment occurred (seconds) and  $\Delta Q$  is the amount of compound detected in the basolateral side (mg).

## 2.9. *In vivo* experiment

### 2.9.1. Induction of T1DM

Male homozygous human FcRn Tg32 mice (The Jackson Laboratory, B6.Cg-Fcgrt<sup>tm1Dcr</sup>Tg(FCGRT)32Dcr/DcrJ) [27], age 7-11 weeks and weighing between 16-25 g, were used to determine the glycemic decrease after oral administration of albumin decorated insulin-loaded NPs. Experiments were conducted in accordance with the provisions of FELASA and EU (Council Directive 86/609/EEC), after approval by local Ethic Committee. The mice were maintained under standard laboratory conditions (12 h light/dark cycles, temperature of  $21 \pm 2^\circ\text{C}$  and relative humidity of 35% to 60%) and fed with standard pellets and water added libitum. Diabetes induction was done in 12 h fasting mice by intraperitoneal injection of 150 mg/kg streptozotocin (STZ) (Sigma-Aldrich). STZ with a concentration of 20 mg/mL was freshly dissolved in citrate buffer 0.1 M at pH 4.5 [23, 28]. STZ destroy pancreatic  $\beta$ -cells, possible leading to a massive insulin release and consequent fatal hypoglycemia. To prevent this, water supplemented with 10% sucrose was provided to animals over 48 h after STZ induction. After this period, it was substituted by tap water and glucose levels and body weight were measured daily.

### 2.9.2. Pharmacodynamics

One week after STZ induction, 12 h fasted animals with glucose levels above 250 mg/dL were randomly divided into 6 groups: (1) PBS, (2) 50 IU/kg of insulin-loaded NPs-NF, (3) 50 IU/kg of insulin-loaded NPs-WT, (4) 50 IU/kg of insulin-loaded NPs-KP, (5) 50

IU/kg of insulin in solution, all diluted in PBS and administered by oral gavage and (6) 2.5 IU/Kg of sub-cutaneous (s.c.) insulin diluted in PBS. The dose was chosen based on previous studies [23, 28]. Blood glucose levels were measured by tail puncture at different time points (0, 0.5, 1, 2, 4, 6 and 8 h) after administration. Plasma glucose levels were plotted against time to evaluate the cumulative hypoglycemic effect (HD) over time, quantified by the area under the curve (AUC), determined using the trapezoidal method. Pharmacological availability (PA), quantified by the area above the curve (AAC), of insulin-loaded NPs and in solution were determined as the relative measure of the cumulative reduction in glucose blood levels. Both parameters were compared to 0% of decrease or 100% availability, respectively, of the control insulin administered subcutaneously at a dose of 2.5 IU/kg. PA and HD in serum glucose levels were calculated as follows [23, 28]:

$$\text{Equation (6)} \quad \text{PA (\%)} = \frac{\frac{\text{AAC test}}{\text{Dose test}}}{\frac{\text{AAC control}}{\text{Dose control}}} \times 100$$

$$\text{Equation (7)} \quad \text{HD (\%)} = \frac{\text{AUC (control 0-480min)} - \text{AUC (group 0-480min)}}{\text{AUC (control 0-480min)}} \times 100$$

Plasma glucose levels were determined using the Medisense Precision Xceed Kit (Abbot, range 20-500 mg/dL) and expressed as the percentage of the baseline plasma glucose level.

## 2.10. Statistical analysis

Statistical analysis was performed using the GraphPad Prism Software vs. 6.0 (GraphPad Software Inc). Statistical significance of the difference between two groups was evaluated by the Student's *t*-test. Differences between groups were compared using one-way analysis of variance (ANOVA) Tukey's multiple comparisons test or Dunnett's multiple comparison test. Results are expressed as mean  $\pm$  standard deviation and geometric means with 95% confidence intervals.

## 3. Results and Discussion

### 3.1. Rationale for design of albumin decorated NPs

To design biodegradable insulin-loaded PLGA-PEG NPs decorated with albumin for targeting of FcRn, a recombinant wild-type (WT) human albumin and an engineered variant with improved human FcRn binding properties were used. The engineered variant



contains a single amino acid substitution in the C-terminal domain III (K573P, KP), which has been shown to extend serum half-life in human FcRn expressing mice and non-human primates [14, 29]. In addition, a human albumin variant engineered to abolish binding to the receptor (K500A/H464Q, KAHQ) was included [14, 29]. These mutations are also located in the C-terminal domain III of albumin, which harbors the principle binding site for FcRn (**Figure 1C**).

To ensure directional attachment of the albumin variants to the NPs, an exposed and free cysteine residue within the N-terminal domain I of albumin (Cys34) (**Figure 1C**), which is located distally from the core FcRn binding site, was explored [14, 29]. Maleimide (MAL) chemistry was used to promote formation of a thioether bond between Cys34 of albumin and the maleimide group of PLGA-PEG-MAL on the surface of the NP (**Figure 1D**). As such, this approach secures directional and site-specific conjugation, as opposed to random conjugation.

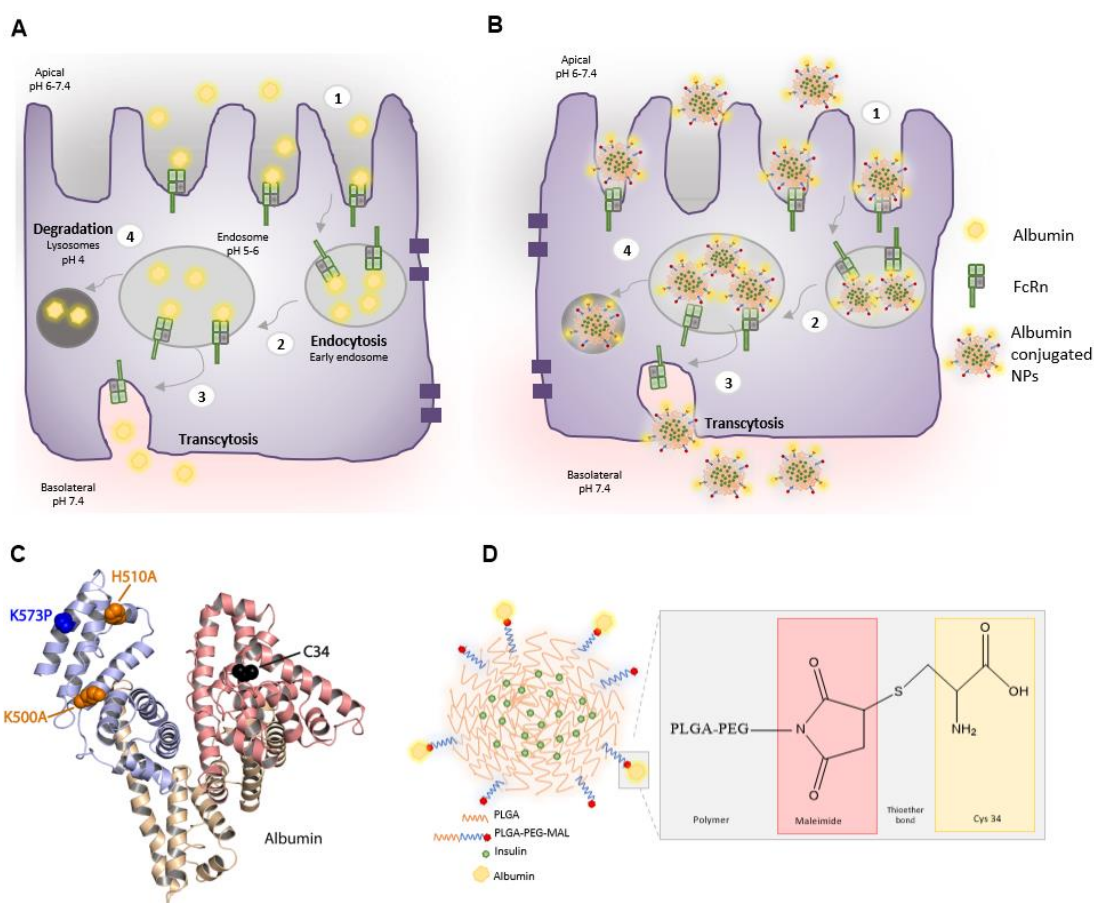


**Figure 1 | Representation of the rationale of this study:** (A) A schematic illustration of the pH dependent FcRn-mediated transcytosis in polarized intestinal epithelial cells: (1) Albumin may be taken up by fluid-phase pinocytosis or by receptor-mediated uptake, as the slightly acidic pH at

intestinal mucosal sites (apical side) promotes binding of albumin to FcRn at or near the luminal/apical cell surface; (2) Albumin enters endosomes and (3) albumin bound to FcRn is transported to the basolateral side of the cell, where fusion with the basolateral cell membrane and exposure to the neutral pH of the extravascular space result in dissociation and release of albumin. (4) Molecules that do not bind FcRn may be destined for intracellular degradation in the lysosomes. **(B)** A schematic illustration of transcellular transport of FcRn-targeted NPs. The proposed model is based on the FcRn-mediated transport mechanism shown in A. (1) NPs decorated with albumin is actively taken up at the apical side of intestinal epithelial cells, (2) enter in the endosomes and (3) are transported to the basolateral side in an FcRn-dependent manner. (4) Non-functionalized NPs that do not have the ability to engage FcRn are poorly taken up and transcytosed, or destined for lysosomal degradation. **(C)** Illustration of the crystal structure of human albumin where targeted residues are shown as spheres: the free cys34 (black) in the N-terminal domain I and K500 (orange), H510 (orange) and K573 (blue) in the C-terminal domain III. The figure was made using Pymol and the crystal structure data of human albumin (PDB 1AO6); **(D)** Schematic illustration of the designed NPs build up of PLGA and PLGA-PEG-MAL with encapsulated soluble recombinant insulin and recombinant human albumin on the NPs' surface. Albumin was conjugated to the NP using maleimide chemistry, which resulted in a thioether bond formed between the Cys34 of albumin and the maleimide group of PLGA-PEG-MAL.

### 3.2. Physical-chemical properties of albumin-decorated PLGA-PEG NPs

To establish a factorial production strategy, a well-established solvent emulsification-evaporation method based on a w/o/w double emulsion technique was used [22, 23]. PLGA, PLGA-PEG-MAL and WT albumin were mixed in different ratios following determination of parameters such as size, polydispersity index (Pdl), zeta potential (ZP) and conjugation efficiency (CE). Based on our previous works [30, 31], and corroborated by JMP software analysis, we selected the ratio 1:0.05:0.005 of PLGA: PLGA-PEG-MAL: albumin, due to favorable CE, lowest Pdl, more negative ZP and size around 150 nm (not shown). In fact, the NPs composition is of utmost importance to surpass mucosal barriers. In the particular case of PEGylated nanoparticles, PLGA-PEG is responsible by forming a hydrophilic corona and PEG is regularly used to prevent NPs from aggregation and enzymatic degradation, contributing for their stability. PEG is the “gold standard” to promote mucus penetration, since interactions with mucins by its hydrophilic and net-neutrally charged character are reduced [32, 33]. It has been demonstrated that a minimal surface coverage of 5% PEG in NPs is crucial for a rapid mucus penetration

[34]. These features were important to modulate and facilitate mucus penetration, epithelial absorption and transcytosis of NPs.

### 3.3. Albumin conjugation to NPs

To ensure that Cys34 was accessible for covalent conjugation to PLGA-PEG-MAL containing NPs, human albumin was reduced by tris(2-carboxyethyl)phosphine hydrochloride (TCEP). Albumin combined with NPs without maleimide (MAL) (**Figure 2B**) or non-reduced albumin with PLGA-PEG-MAL NPs (**Figure 2C**) were included as controls. To remove unconjugated albumin, NPs were washed three times with phosphate buffer (PB) using an Amicon® filter with 100 kDa cut off. Initially, the washing procedure was performed with free albumin, which confirmed that albumin passes through the filter (**Figure 2A**). To indirectly determine the conjugation efficiency, the unbound albumin fraction was quantified using a two-way anti-human albumin ELISA. The results revealed that only 10% of the total albumin incubated with the NPs was detected in the wash solution, supporting that 90% was bound to the NPs (**Figure 2B**). Interestingly, this was also the case in the absence of reactive MAL groups on the NPs or a reduced Cys34 of albumin, both necessary for the formation of a covalent thioether bond, which suggest that albumin also bound nonspecifically to the NPs. To reduce the amount of nonspecifically bound albumin, the incubation time for conjugation was reduced to 1 h, however, no difference in absorption was detected (**Figure 2B**). In this regard, it is well known that NPs absorb plasma proteins *in vivo*, including albumin, which form a protein corona [35, 36]. Although the presence of PEG is well documented to prevent formation of a protein corona [32, 33], our results show that this did not necessarily prevent adsorption of albumin completely. The covalent bond guarantee that albumin is permanently attached to NPs, which may not happen with nonspecific bound albumin. Here, the focus is to make sure that NPs have albumin to bind FcRn and thus nonspecific bound albumin do not interfere with this.

Moreover, the size, Pdl and ZP were determined for the albumin-decorated NPs, which demonstrated similar values as that measured for the bare NPs (**Table 1**). No measurable difference in size and ZP between NPs with and without albumin may be explained by the fact that a maximum of only 0.5% of the NPs' surface was decorated with albumin.

**Table 1** | Physical-chemical properties of developed PLGA-NPs.

Loading	Albumin	Particle size ± SD (nm)	Pdl ± SD	ZP ± SD (mV)	CE ± SD (%)	AE ± SD (%)	DL ± SD (%)
Insulin	n.a.	160 ± 2	0.15 ± 0.01	-8.1 ± 0.1	n.a.		
	WT	155 ± 7	0.13 ± 0.03	-9.6 ± 0.3	89.7 ± 1.0	83.8 ± 6.5	10.9 ± 0.8
	KAHQ	157 ± 4	0.14 ± 0.02	-9.1 ± 0.2	93.5 ± 0.2		
	KP	154 ± 7	0.14 ± 0.02	-9.3 ± 0.2	98.9 ± 0.2		
Empty	n.a.	147 ± 0	0.12 ± 0.01	-8.5 ± 0.2	n.a.		
	WT	147 ± 1	0.15 ± 0.01	-10.6 ± 0.4	96.8 ± 0.1	n.a.	n.a
	KAHQ	145 ± 1	0.17 ± 0.01	-10.5 ± 0.2	98.3 ± 0.1		
	KP	144 ± 1	0.13 ± 0.01	-10.4 ± 0.3	99.3 ± 0.3		

Pdl: polydispersity index; ZP: zeta potential; CE: conjugation efficiency; AE: association efficiency; DL: drug loading; n.a.: non applicable; NF: non-functionalized; SD: standard deviation.

The presence of albumin was confirmed using elementary dispersive scanning (EDS), as sulfur was detected for free WT albumin and albumin-decorated NPs, but not for bare NPs (**Figure 2D**). In addition, using non-invasive attenuated total reflection Fourier transform IR (ATR-FTIR) spectroscopy, the secondary structure elements of WT albumin conjugated to empty NPs were compared with that of free albumin in both qualitative (**Figure 2E**) and quantitative manner (**Figure 2F**). Previous measurements using ATR-FTIR spectroscopy demonstrated that albumin consists of 55%  $\alpha$ -helix and 45% of turns, disordered and  $\beta$  structures [37]. The spectrum for albumin decorated NPs presents  $\beta$ -sheet at 1610-1640  $\text{cm}^{-1}$ ,  $\alpha$ -helix at 1650-1658  $\text{cm}^{-1}$  and  $\beta$ -turn at 1660-1700  $\text{cm}^{-1}$ , as described previously [38]. However, lyophilization or the conjugation method is likely the reason for the observed reduction in the content of  $\alpha$ -helix, a left shift and intensified  $\beta$ -sheet from 1630  $\text{cm}^{-1}$  to 1615  $\text{cm}^{-1}$  (**Figure 2E**). Quantitatively, this resulted in 76% of area overlap (AO) and 91% of spectral correlation coefficient (SCC) (**Figure 2F**).

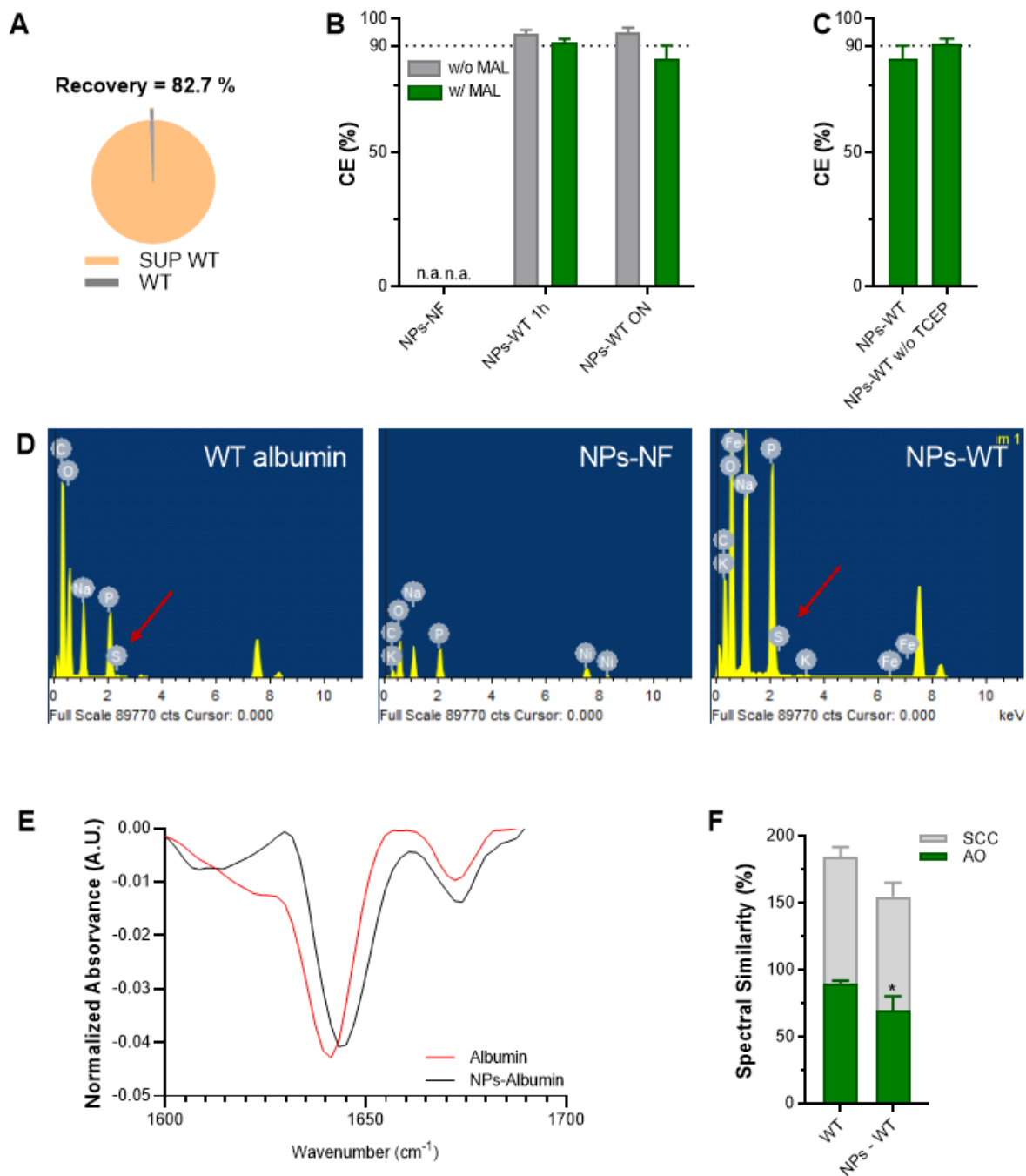


**Figure 2 | Site-specific conjugation of albumin to NPs:** (A) ELISA quantification of free WT albumin detected after the washing step with Amicon® filter of 100 KDa; (B) Conjugation efficiency (CE) with or without the presence of maleimide (MAL) after conjugation of 1 h or overnight (ON) with WT albumin; (C) Conjugation efficiency (CE) of NPs conjugated with reduced WT albumin (NP-WT) and non-reduced WT albumin (NP-WT without TCEP); (D) Elementary analysis of native albumin, non-functionalized empty NPs (NPs-NF) and WT albumin-conjugated empty NPs (NPs-WT); (E) Qualitative and (F) quantitative analysis showing the similarity of the FTIR spectra between WT albumin and NPs-WT, using the area overlap (AO) and spectral correlation

coefficient (SCC) algorithms. Shown are the arithmetic means  $\pm$  SD. \*P < 0.05, comparing with native albumin by Student's t-test.

### 3.4. Functional encapsulation of insulin in NPs

NPs loaded with insulin were prepared with the optimal ratio of PLGA and PLGA-PEG-MAL using the double emulsion technique. The mean particle size of insulin-loaded NPs increased 1.2-fold compared with empty NPs (**Table 1**). Notably, this increase was measured for both albumin functionalized and bare NPs, suggesting that insulin adsorption was the reason. No significant difference in ZP was noticed between empty and insulin-encapsulated NPs (**Table 1**). Furthermore, the association efficiency (AE) and drug loading (DL) were indirectly evaluated using high performance liquid chromatography (HPLC), which revealed that insulin was successfully encapsulated with approximately 80% of AE and 10% of DL (**Table 1**).

Next, the insulin release profile was evaluated in fluids mimicking those found in the stomach and small intestine. The results showed that around 2.5% of the insulin was released in the presence of simulated gastric fluid (SGF) for 2 h, which was maintained under simulated intestinal fluid (SIF) for 4 h (**Figure 3B**). Here, the SIF was used at pH 6, since it is the pH of duodenum, where it is supposed to occur the main absorption, due to the favorable pH for binding between albumin-conjugated NPs and FcRn [39].

The initial burst release in the first 2 h followed by a sustained release is characteristic in PLGA NPs. At acidic pH, the carboxylic group is protonated, which contributes to PLGA destabilizing and disintegrating due to their pH-sensitivity. However, the insulin released could also be some adsorbed on the NPs' surface. Either way, it is not significant, considering the 2.5% of the released profile. Besides, insulin has an isoelectric point of 5.3, meaning that above this value, insulin is negatively charged. As PLGA-PEG NPs have a negative charge, at pH lower than 5.3, there is a strong electrostatic attraction between insulin and NPs, decreasing the release rate. It is described that PLGA is strongly degraded at the alkaline and acidic conditions due to the ester hydrolysis caused by acid-base catalysis [40]. Thus, we expect that insulin can be sustainly released at neutral pH, as blood circulation. The results show that NPs are able to sustain low release of insulin under gastrointestinal conditions and thus, prevent the premature release of insulin, which suggest that it will be protected against degradation in the GIT. The slow release is a good omen to reduce the frequency of administrations and reduce the cost of therapy. In line with this, a previous report

demonstrated that peptides were protected from low gastric pH value and enzymatic hydrolysis when encapsulated in anionic polymeric NPs [41, 42]. In fact, it was described the reduction in drug release from PLGA microparticles due to the surface crosslinking of PLGA microparticles [43]. Plus, albumin-based NPs can also protect the encapsulated drug from enzymatic degradation, due to the level of chemical crosslinking [44]. Albumin adsorbed to alginate/dextran sulfate (ADS)-NPs have shown a 30% of insulin released in SGF and a slow release following insulin passage to intestinal conditions. Plus, these authors claimed that chitosan and albumin coating augmented intestinal interactions between glycocalix and the NPs, which translated in enhanced intestinal permeability [45]. Moreover, to determine the morphology of insulin-loaded NPs decorated with WT albumin, transmission electron microscopy (TEM) was performed, which revealed a spherical shape and smooth surface (**Figure 3A**). This feature is in line with expected morphology based on the encapsulation methodology used [22, 23]. The size of the NPs was calculated to be in the range of 150 nm, in agreement with the DLS analysis (**Table 1**).

To address if the double emulsion technique affected the integrity of insulin, ATR-FTIR spectroscopy was used to determine the secondary structure elements in both a qualitative (**Figure 3C**) and a quantitative manner (**Figure 3D**). When proteins are associated with PLGA NPs, the C=O stretching vibrations of the ester group of PLGA appear at  $1750\text{ cm}^{-1}$  and structural modifications can be determined following normalization of the area of the second derivative amide I spectra [25]. In addition, qualitatively assessment can be done by comparing the spectra or quantitatively by calculating the AO and SCC where AO indicates modifications in structure elements, while SCC represents the changes in the band positions [22]. Notably, the normalized area of the second-derivative of insulin spectrum is characterized by  $\beta$ -sheets bands at  $1610\text{-}1604$ ,  $\alpha$ -helix at  $1650\text{-}1658\text{ cm}^{-1}$ , a random coil at  $1640\text{-}1650\text{ cm}^{-1}$  and a  $\beta$ -turn structure  $1660\text{-}1700\text{ cm}^{-1}$  [46]. The obtained spectra for insulin in solution and encapsulated in NPs were similar. However, some bands were modified, indicating alterations in secondary structure (**Figure 3A**). This was evident from the spectrum on the insulin-loaded NPs with a shift of  $\alpha$ -helix from  $\sim 1645\text{ cm}^{-1}$  to  $\sim 1655\text{ cm}^{-1}$  and increased intensity, in addition to a left shift and higher intensity in  $\beta$ -turn, which is in agreement with previous work [47]. Moreover, the 68% of AO and 79% of SCC (**Figure 3B**) support the visualization of the spectrum, which can be justified by the encapsulation method or by lyophilization of the samples, suggesting the necessity of adding lyoprotectants before performing ATR-FTIR spectroscopy. Notably, it has been shown

that lyoprotectants stabilize the protein by protecting it from denaturation caused by pore formation on NPs [23, 48]. It has also been reported that lyophilization leads to protein aggregation with intermolecular  $\beta$ -sheets formation (caused by intermolecular hydrogen bonds) that increases protein–protein interactions while decreasing the  $\alpha$ -helix content and stability [49]. In addition, the helical structure of protein is destabilized during evaporation, since water molecules compete for the hydrogen bonds with amino and carboxyl groups of peptide bonds [50]. Regarding the tertiary structure, related to insulin bioactivity, we have previously analyzed it by fluorescence spectroscopy, after extracting insulin from NPs, confirming similarity with FTIR results after encapsulation [23, 47].

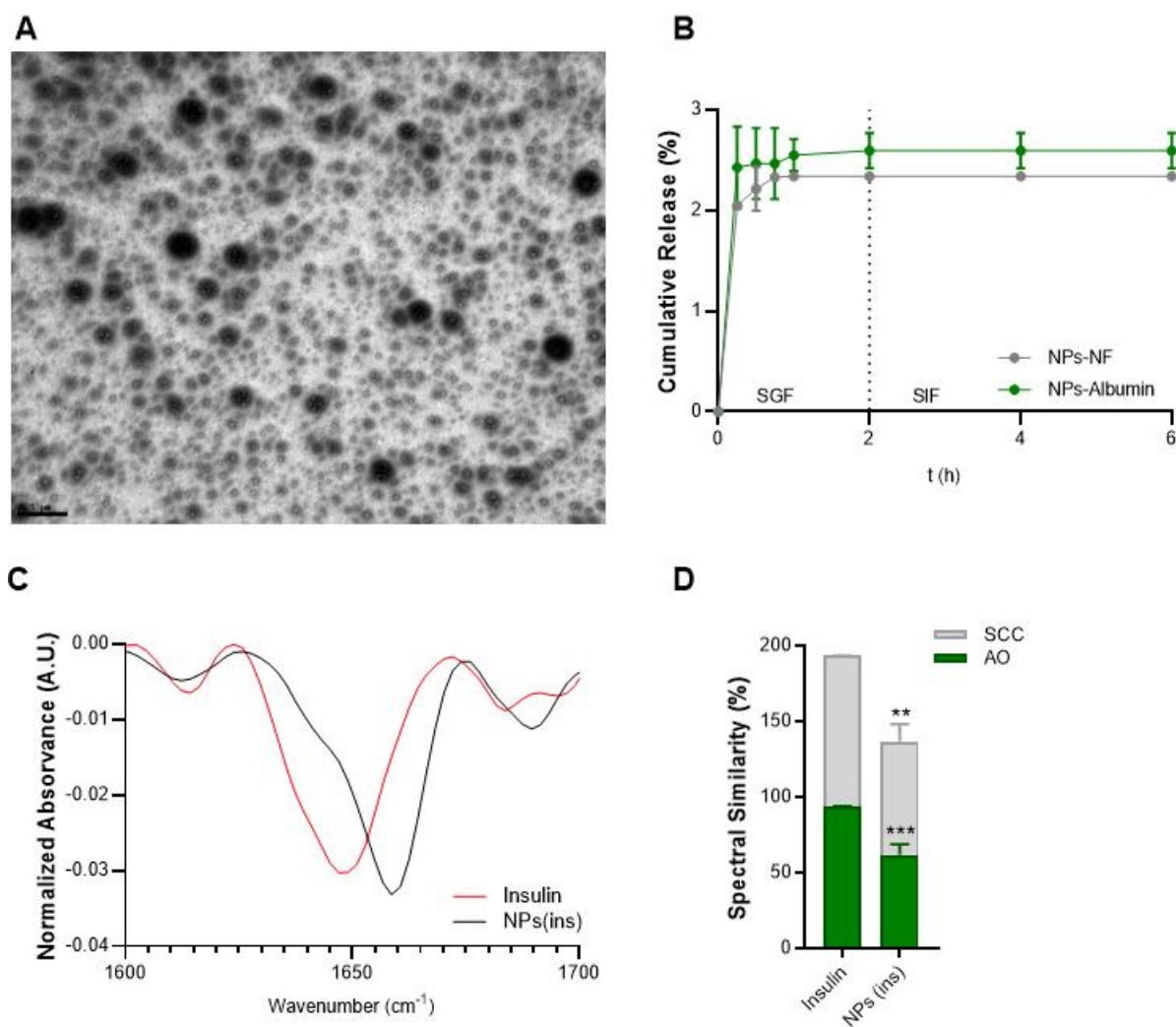


**Figure 3 | Insulin NPs characterization:** (A) Representative TEM microphotograph of WT albumin decorated PLGA-PEG NPs encapsulated with insulin, lyophilized 25000x. Scale bar: 500 nm. (B) Insulin release profile of functionalized and non-functionalized NPs under SGF (2 h) and SIF (from 2 h to 6 h). (C) The qualitative and (D) quantitative effect of NPs encapsulation on protein structure. Analysis showing area-normalized second-derivative amide I spectra of native



insulin vs insulin-encapsulated NPs using the area overlap (AO) and spectral correlation coefficient (SCC) algorithms. Shown are the arithmetic means  $\pm$  SD. \*\* $P < 0.001$ , \*\*\* $P < 0.0001$  comparing with native insulin by Student's t-test.

### 3.5. Albumin decorated NPs bind FcRn in a pH dependent manner

To address whether albumin is functional post conjugation to insulin-loaded NPs, binding to FcRn at pH 5.5 was tested by ELISA. Equal amounts of the NPs formulations or the free human albumin variants were added to wells where recombinant human FcRn had been captured on a coated engineered IgG molecule that strongly binds the receptor (**Figure 4A**), which were subsequently detected using a polyclonal anti-human albumin antibody. The three albumin variants bound as expected, as KAHQ did not bind while the KP variant bound more strongly than the WT (**Figure 4B**). These results are in line with the reported in literature [14, 29]. Importantly, the same binding hierarchy was detected for the three NPs formulations (**Figure 4C**). Specifically, KP decorated NPs bound more strongly to human FcRn than WT-decorated NPs, while the KAHQ-containing NPs ignored the receptor. As expected, no signal was detected for non-functionalized NPs. Thus, PLGA-PEG NPs decorated with albumin retain the ability to interact with human FcRn.

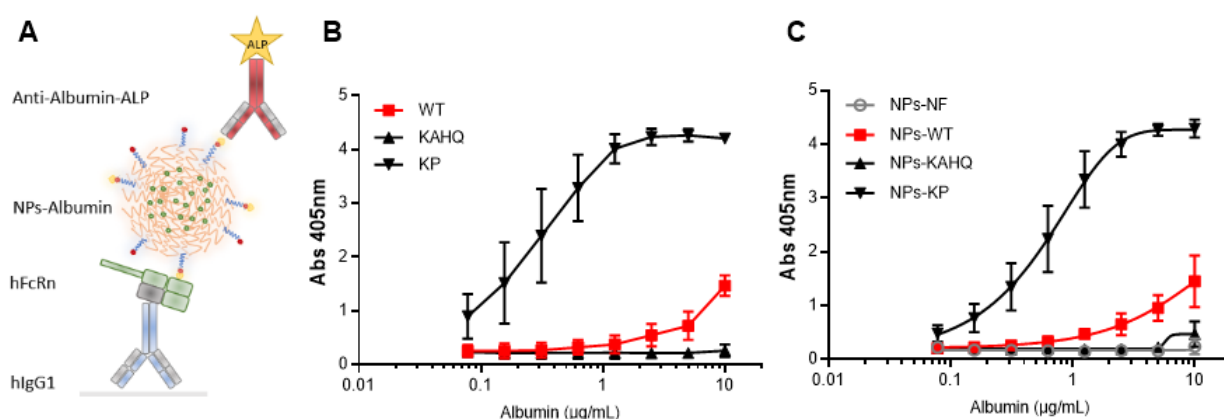


**Figure 4 | Albumin decorated NPs bind human FcRn.** (A) A schematic illustration of the ELISA set-up for measuring functional binding to human FcRn at pH 5.5. An engineered IgG1 antibody (MST/HN) was coated in wells, to which recombinant soluble human FcRn was captured, before adding naked albumin or albumin-decorated NPs. Bound albumin and albumin-decorated NPs were detected using ALP-conjugated polyclonal anti-human albumin antibodies. (B) Binding of naked human albumin variants (WT, KAHQ or KP) to human FcRn at pH 5.5. (C) Binding of NPs decorated with human albumin variants (WT, KAHQ or KP) to human FcRn at pH 5.5.

### 3.6. Engineered albumin decorated NPs show enhanced *in vitro* transcytosis

The finding that albumin decorated NPs bound human FcRn favorably, motivated us to investigate if this property could translate into enhanced transcellular transport. To test this, a Transwell® assay was run using a polarizing Madin-Darby Canine Kidney cell line over-expressing human FcRn (MDCK-hFcRn). To verify that the system could be adopted to study transcytosis of human albumin, equal amounts of the WT, KAHQ and KP variants were added to the apical side of polarized MDCK-hFcRn cells followed by incubation for 4 h, before samples were collected at the basolateral side. To quantify the amounts of transported albumin, the collected samples were added to a two-way anti-albumin ELISA (**Figure 5A**).

Next, transcytosis of albumin decorated NPs was compared using the same set-up, where equal amounts of the NPs were added to the apical side of the MDCK-hFcRn cells, followed by quantification of NPs transported to the basolateral compartment using ELISA. As expected, the non-functionalized NPs were negative, while KP-decorated NPs were 2-fold more efficiently transported than WT-decorated NPs. NPs decorated with KAHQ resulted in no or poor transport capacity (**Figure 5 B**). As expected, the percentage and apparent permeability of the free albumin were significantly higher compared to albumin-decorated NPs. Also, the engineered albumin KP demonstrated to be more efficiently transported, both free and conjugated to NPs (**Table S1 of Supplementary Information**).

The endocytosis of NPs, mediated by FcRn rather than other receptors, was already reported by others [18]. It was verified that albumin transport through Caco-2 monolayer is a saturable process, above 40 µg/mL, indicating a receptor-mediated uptake. Plus, a competition assay was performed by incubating 40 µg/mL of WT albumin with NPs-WT and the authors verified that NPs were 1.85-fold less transcytosed. When incubating with the excess of albumin, as blocking agent for FcRn transcytosis, the NPs' transport reduces significantly, indicating that the enhanced transport of albumin-conjugated NPs is FcRn-mediated [18].

Thus, decoration of NPs with human albumin that have the ability to engage human FcRn resulted in enhanced apical to basolateral transport across polarized epithelial cells. Importantly, transport could be further enhanced by taking advantage of a human albumin variant (KP) engineered for improved pH dependent FcRn binding.

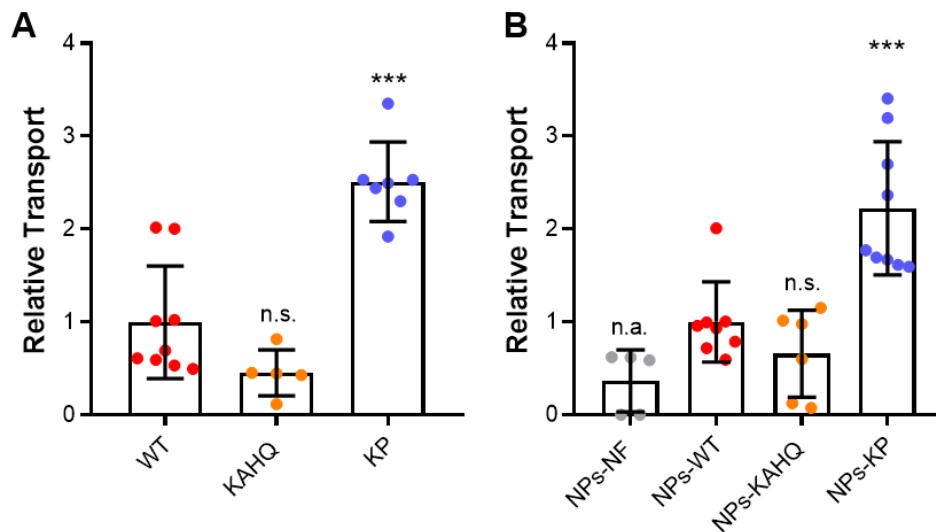


**Figure 5 | Albumin-decorated NPs showed enhanced transcytosis capacity.** Relative amounts of **(A)** naked albumin variants (WT, KAHQ and KP) and **(B)** albumin-decorated NPs detected in media collected at the basolateral side of polarized epithelial MDCK-hFcRn cells 4 h after adding the variants to the apical side in the Transwell® system (n=5-9). The amounts were quantified by two-way anti-albumin ELISA, where WT albumin or NPs decorated with WT albumin were set to 1, as a control. Shown are the arithmetic means  $\pm$  SD. \*\*\* $P < 0.0001$  comparing with WT or NPs-WT by Student's t-test; n.a.: non applicable; ns: non-significant.

Considering the NPs size (~150 nm) is relatively easy to obtain good cellular uptake outputs. As described in the literature, NPs are passively translocated across epithelium through enterocytes and specifically M cells, within Peyer's patches [51]. It was also reported that NPs are able to transverse the lymphatic system and by lymphatic drainage through thoracic duct reach the systemic circulation [52]. On top of this, receptor targeting is likely to increase the chance of absorption, since FcRn is expressed in epithelial cells [53]. Notably, a significant increase of insulin permeability by using chitosan-based NPs with adsorbed albumin has been shown in cell-based engineered intestinal models [45].

### 3.7. Albumin-conjugated NPs enhance glycemia reduction

As the *in vitro* transcytosis data strongly suggested that NPs decorated site-specifically with human albumin could lead to enhanced delivery across barriers, this concept was subsequently addressed *in vivo* using the designed insulin encapsulated NPs. A state-

of-the-art mouse model that is transgenic for human FcRn and knockout for mouse FcRn (FcRn<sup>-/-</sup> hFcRn Tg32 mice) [27] was chosen for this study, as conventional mice are unreliable models for evaluation of human albumin-based therapeutics due to large cross-species binding differences [54-56]. Specifically, human albumin binds poorly to mouse FcRn, and as such will be competed out for binding to the receptor in the presence of large amounts of endogenous mouse albumin [54, 56]. The human FcRn transgenic mice indeed have mouse albumin but in this case mouse and human albumin bind equally well to the receptor [54, 56].

To study the effect of albumin decorated NPs encapsulated with insulin, the transgenic mice were treated with streptozotocin (STZ) to induce diabetes. One week later, the mice were fasted for 12 h, before being divided into six groups based on their blood glucose level. After administering different formulations, pharmacodynamic parameters were evaluated over 8 h (**Figure 6 A**). This time frame was not extended, since it is not recommended starving animals for long periods. Besides, if the animal is in a starvation state it is hard to objectively discuss the results, since they could be due to the drug effect or due to organism failure. In fact, it was observed some deaths during the experiments, which were not considered for data analysis. Knowing that mice consume primarily at night, overnight fasting leads to a catabolic state, reducing 15% of body mass in lean mice [57]. Overnight fasting deletes liver glycogen stores, which contributes for reducing the variability in baseline blood glucose. Besides, contrary to what happens in humans, a prolonged fast in mice enhances the insulin-stimulated glucose utilization [57]. In this sense, it is recommended that mice used for metabolic studies, should be fasted for 14–18 h (overnight fast) [58].

The first group received free insulin via subcutaneous (s.c.) injection, which resulted in a rapid decrease of glucose within 2 h followed by an increase over the next 6 h (**Figure 6 B**). This phenotype is in accordance with previous reports using rats [28, 59]. In contrast, mice treated orally with free insulin, or with bare NPs, showed no significant decrease in blood glucose (**Figure 6 B**), being most probably degraded along the way. Furthermore, the effect of oral administration of equal amounts of bare NPs, WT- or KP-decorated NPs was evaluated, which revealed that the albumin-decorated NPs had a more pronounced effect compared with free insulin and the bare NPs. In particular, the KP-decorated NPs showed the fastest glycemic decrease and maintained a decrease of around 40% between 1 h and 4 h after administration (**Table S2 of Supplementary Information**). However, in this preliminary set-up, NPs containing WT and KP were not statistically different. On the other hand, it was previously reported a significant *in vivo*

difference between the two naked variants [29]. As mentioned before, it was observed some animal deaths during the experiments, which were not considered for data analysis. In this sense, the reduced number of animals might be the reason for the non-statistical significance in *in vivo* results, which did not happen in *in vitro*.

Notably, for the control group receiving PBS, an increase in glucose level was observed within the first hour, which may be explained by stress and an adrenalin reaction to the administration. Most probably, all mice experienced this, while the effect was contradicted by the administered insulin, which should be taken into consideration when comparing pharmacological parameters. Nevertheless, functionalized NPs were more efficient in delivering encapsulated insulin to the circulation, as the orally delivered free insulin and non-functionalized NPs did not induce glycemic response.

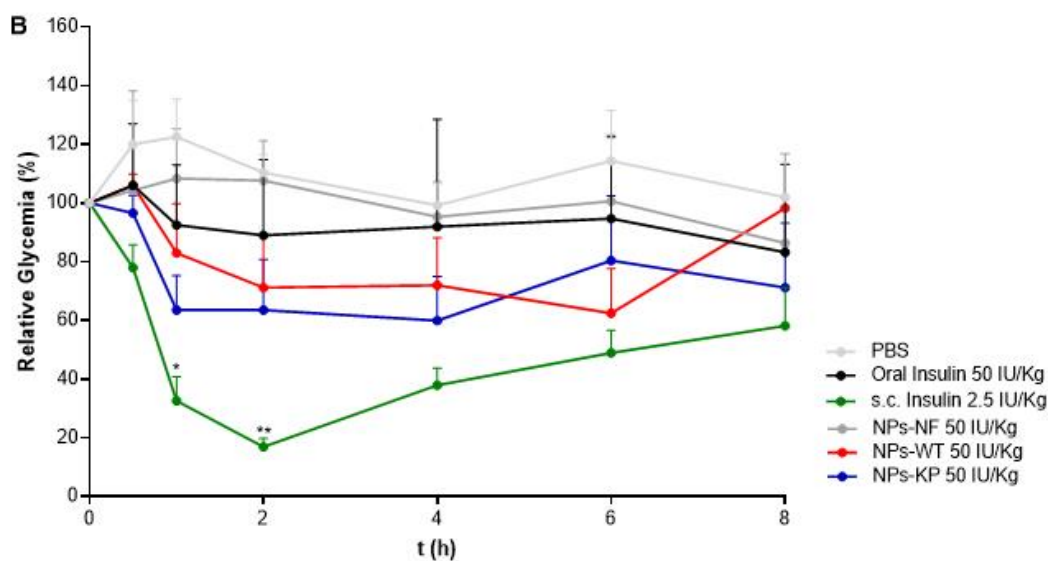
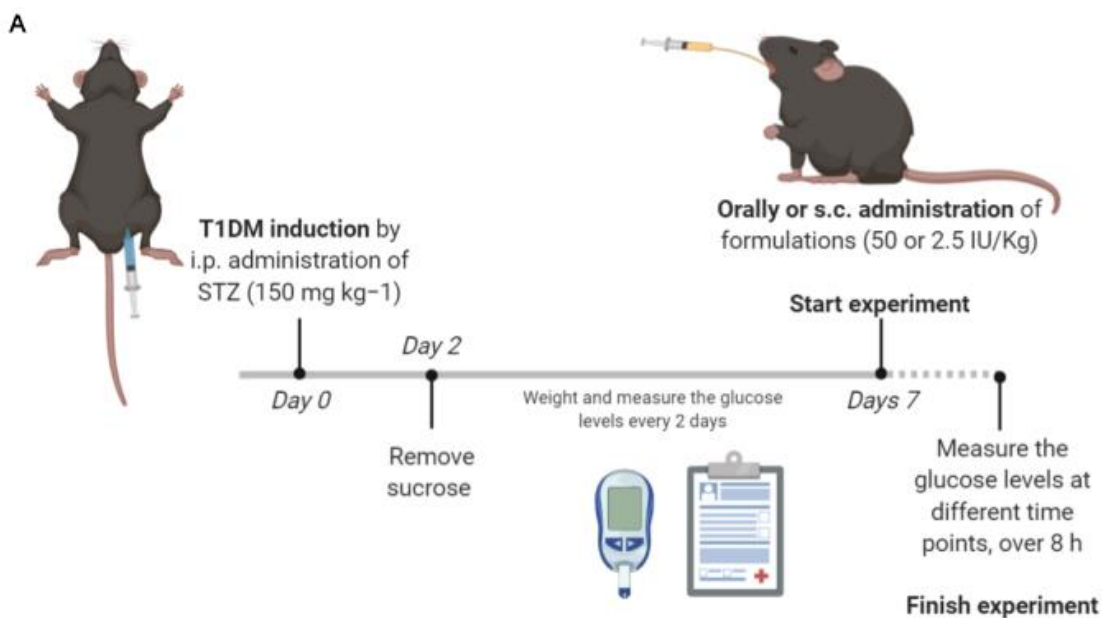


**Figure 6 | Glycemia in human FcRn expressing mice induced with diabetes. (A)** T1DM-induced Tg32 mice were i.p. administered with STZ (150 mg kg<sup>-1</sup>) to induce diabetes. Body weight and glucose levels were followed up every 2 days, during 7 days. **(B)** At day 7, formulations were administered and plasma glucose levels were analyzed at different time points, during 8 h: PBS, oral insulin 50 IU/Kg, s.c. insulin 2.5 IU/Kg, oral insulin 50 IU/Kg loaded and non-functionalized NPs (NP-NF) and oral insulin 50 IU/Kg loaded and albumin-functionalized WT albumin and KP NPs (n = 3-6/ group). Shown are the arithmetic means ± SEM. \*P<0.05, \*\* P< 0.001 comparing with oral insulin by one-way ANOVA.

Protein-based drugs have been shown to have an oral bioavailability lower than 1%, when compared with injectable formulations having complete pharmacological availability (PA) [60]. However, a PA of 10.3% has previously been achieved using 10 IU/kg insulin loaded PLGA NPs, with a 52% drop in blood glucose levels after 10 h of administration into diabetic Wistar male rats. On the other hand, Cui *et al.* administered 20 IU/Kg insulin PLGA and PLGA-55 NPs in diabetic Wistar male rats and obtained 3.7 and 6.3%, respectively, of oral bioavailability [61, 62]. In addition, others preferred to administer 1.1 IU/kg of Fc-conjugated PLA-PEG-MAL NPs and elicited a prolonged hypoglycemic response in wild-type mice [15]. Here, 50 IU/kg KP-functionalized NPs resulted in a 37% drop in blood glucose levels after 1 h following administration (**Table S2 of Supplementary Information**). After 8 h, KP-functionalized NPs presented a PA of around 3% and a hypoglycemic decrease (HD) close to zero, corresponding to the HD measured following s.c. injection of insulin (**Table 2**). The dose could be increased to have an effect like the current treatment. However, it would be preferable to have the same effect with the lowest possible dose, and that is what was tested here. All in all, the low PA might be due to the incomplete release of insulin, which may be increased with increasing the study time.

**Table 2 | Pharmacodynamic parameters**

	Dose (IU/Kg)	t <sub>min</sub> (h)	C <sub>min</sub> ± SD (mg/dL)	AUC 8 h	PA 8 h ± SD (%)	HD 8 h ± SD (%)
<b>PBS</b>	0	4	374.20 ± 58.64	927.8 ± 124.0	-1.6 ± 1.5	-137.8 ± 31.8
<b>Oral insulin</b>	50	8	256.75 ± 102.88	789.2 ± 360.8	0.1 ± 4.4	-102.2 ± 92.5
<b>s.c insulin</b>	2.5	2	72.50 ± 25.67	390.2 ± 88.5	100.0 ± 0.0	0.0 ± 0.0
<b>NP-NF</b>	50	8	328.00 ± 65.33	849.5 ± 202.5	-0.6 ± 2.5	-117.7 ± 51.9
<b>NP-WT</b>	50	6	290.50 ± 103.75	768.6 ± 24.7	0.4 ± 0.3	-97.0 ± 6.3
<b>NP-KP</b>	50	4	282.40 ± 137.68	581.9 ± 212.8	2.7 ± 2.6	-49.1 ± 54.5

AUC: area under the curve; PA: pharmacological availability; HD: hypoglycemic decrease; SD: standard deviation;  $t_{\min}$ : time with minimal concentration of glucose after administration of different formulations.

Taken together, the *in vivo* glycemic decrease obtained using the KP variant is a clear improvement of the therapeutic efficacy. In fact, the obtained *in vivo* results agree with *in vitro* data, supporting that albumin decorated NPs increase the effect as a result of improved FcRn-binding affinity. It is reported in the literature the use of FcRn knock out mouse, confirming the FcRn-mediated transcytosis of FcRn-targeted NPs [15].

Interestingly, while the intestinal expression of FcRn in rodents has been demonstrated to be developmentally down-regulated after weaning [63], this is not the case in humans or in the human FcRn expressing mice, as the transgene is expressed under the human promoter [64]. Thus, the transgenic mouse model mimics the tissue expression profile of human FcRn, by not being down-regulated after weaning [27]. On the other hand, it has been shown that the hFcRn transgenic mice have higher levels of FcRn expression in the liver, lung, small intestine and heart, compared to Swiss Webster mice as well as the human tissues [65]. Further investigation into the implication of these differences on the PD/PK is required. In addition, human FcRn is globally expressed in many cells and tissues including immune cells, vascular endothelial cells, epidermal keratinocytes, the blood-brain-barrier, retina-blood barrier, lungs, kidneys, liver, genital tissues, mammary glands as well as the placenta [10], which may pave the way for using FcRn-targeting NPs for delivery to different body sites.

Either way, further studies are needed with higher number of animals to clarify the statistical significance of the results as well as biodistribution and pharmacokinetic studies. In addition, as previously mentioned, here it was used insulin as a model drug, using diabetes as example. For this specific example, more studies should be considered to address all the particularities of diabetes or even try to encapsulate as insulin glargine, for the treatment of both diabetes types.

#### **4. Conclusions**

In this work, we report on a novel class of monodisperse 150 nm PLGA-PEG NPs, with a drug loading over 10% and around 90% of conjugation efficiency. These NPs were decorated with an engineered human albumin variant with improved human FcRn binding, which enhanced transcytosis in 2-fold across polarized epithelia compared with

WT albumin decorated NPs. When tested for oral delivery in human FcRn transgenic mice, induced with diabetes, such NPs were able to reduce glycemia up to around 40% after 1 h and enhance pharmacologic availability. The novel concept described should pave the way for further engineering of biodegradable albumin-decorated NP formulations for tailored targeting of FcRn for enhanced intestinal delivery.

### **Author Contributions**

C.A., J.N, J.T.A. and B.S. designed research; C.A., J.N., A.G. and R.N. performed research; C.A., J.N., A.G. and R.N. analyzed data; C.A, J.T.A. and B.S. wrote the paper.

### **Conflict of Interest**

J.T.A. is a co-inventor of pending patent applications related to albumin variants.

### **Acknowledgement**

This project is a result of the project NORTE-01-0145-FEDER-000012, supported by Norte Portugal Regional Operational Programme (NORTE 2020), under the PORTUGAL 2020 Partnership Agreement, through the European Regional Development Fund (ERDF). This work was also financed by FEDER - Fundo Europeu de Desenvolvimento Regional funds through the COMPETE 2020 - Operacional Programme for Competitiveness and Internationalisation (POCI), Portugal 2020, and by Portuguese funds through FCT - Fundação para a Ciência e a Tecnologia/ Ministério da Ciência, Tecnologia e Ensino Superior in the framework of the project "Institute for Research and Innovation in Health Sciences" (UID/BIM/04293/2019). Cláudia Azevedo would like to thank to Fundação para a Ciência e a Tecnologia (FCT), Portugal for financial support (SFRH/BD/117598/2016). The authors acknowledge the support of Abbot Laboratório, Lda for the glucose strips as well as Flávia Sousa for JMP software guidance and the following i3S Scientific Platforms: Biointerfaces and Nanotechnology (FCT - UID/BIM/04293/2019), Histology and Electron Microscopy (PPBI-POCI-01-0145-FEDER-022122) and Animal Facility. The authors thank Tore-Geir Iversen for assistance with the Malvern Zetasizer Nano ZS instrument. This work was supported by the Research Council of Norway (Grant no. 274993).



## References

- [1] P. Saeedi, I. Petersohn, P. Salpea, B. Malanda, S. Karuranga, N. Unwin, S. Colagiuri, L. Guariguata, A.A. Motala, K. Ogurtsova, J.E. Shaw, D. Bright, R. Williams, Global and regional diabetes prevalence estimates for 2019 and projections for 2030 and 2045: Results from the International Diabetes Federation Diabetes Atlas, 9(th) edition, *Diabetes Research and Clinical Practice*, 157 (2019) 107843.
- [2] C. Bommer, V. Sagalova, E. Heesemann, J. Manne-Goehler, R. Atun, T. Barnighausen, J. Davies, S. Vollmer, Global Economic Burden of Diabetes in Adults: Projections From 2015 to 2030, *Diabetes Care*, 41 (2018) 963-970.
- [3] M.J. Davies, J.J. Gagliardino, L.J. Gray, K. Khunti, V. Mohan, R. Hughes, Real-world factors affecting adherence to insulin therapy in patients with Type 1 or Type 2 diabetes mellitus: a systematic review, *Diabetic medicine: a Journal of the British Diabetic Association*, 30 (2013) 512-524.
- [4] P. Fonte, F. Araujo, C. Silva, C. Pereira, S. Reis, H.A. Santos, B. Sarmento, Polymer-based nanoparticles for oral insulin delivery: Revisited approaches, *Biotechnology Advances*, 33 (2015) 1342-1354.
- [5] B. Sarmento, D. Ferreira, T. Vasconcelos Polymer-based delivery systems for oral delivery of peptides and proteins, in *Delivery Technologies for Biopharmaceuticals: Peptides, Proteins, Nucleic Acids and Vaccines*, (Eds: L. Jorgensen, H. M. Nielsen) John Wiley & Sons Ltd (2009) pp. 207.
- [6] F. Araujo, N. Shrestha, M.A. Shahbazi, P. Fonte, E.M. Makila, J.J. Salonen, J.T. Hirvonen, P.L. Granja, H.A. Santos, B. Sarmento, The impact of nanoparticles on the mucosal translocation and transport of GLP-1 across the intestinal epithelium, *Biomaterials*, 35 (2014) 9199-9207.
- [7] C. Pereira, F. Araujo, P.L. Granja, H.A. Santos, B. Sarmento, Targeting membrane transporters and receptors as a mean to optimize orally delivered biotechnological based drugs through nanoparticle delivery systems, *Current Pharmaceutical Biotechnology*, 15 (2014) 650-658.
- [8] B. Moulari, A. Beduneau, Y. Pellequer, A. Lamprecht, Nanoparticle Targeting to Inflamed Tissues of the Gastrointestinal Tract, *Current Drug Delivery*, 10 (2013) 9-17.
- [9] M.R. Rekha, C.P. Sharma, Oral delivery of therapeutic protein/peptide for diabetes-future perspectives, *International Journal of Pharmaceutics*, 440 (2013) 48-62.
- [10] K.M.K. Sand, M. Bern, J. Nilsen, H.T. Noordzij, I. Sandlie, J.T. Andersen, Unraveling the Interaction between FcRn and Albumin: Opportunities for Design of Albumin-Based Therapeutics, *Frontiers in Immunology*, 5 (2015).
- [11] P.J. Hornby, P.R. Cooper, C. Kliwinski, E. Ragwan, J.R. Mabus, B. Harman, S. Thompson, A.L. Kauffman, Z. Yan, S.H. Tam, H. Dorai, G.D. Powers, J. Giles-Komar, Human and non-human

primate intestinal FcRn expression and immunoglobulin G transcytosis, *Pharmaceutical Research*, 31 (2014) 908-922.

[12] B.L. Dickinson, K. Badizadegan, Z. Wu, J.C. Ahouse, X. Zhu, N.E. Simister, R.S. Blumberg, W.I. Lencer, Bidirectional FcRn-dependent IgG transport in a polarized human intestinal epithelial cell line, *The Journal of Clinical Investigation*, 104 (1999) 903-911.

[13] D.C. Roopenian, S. Akilesh, FcRn: the neonatal Fc receptor comes of age, *Nature Reviews Immunology*, 7 (2007) 715.

[14] J.T. Andersen, B. Dalhus, J. Cameron, M.B. Daba, A. Plumridge, L. Evans, S.O. Brennan, K.S. Gunnarsen, M. Bjørås, D. Sleep, I. Sandlie, Structure-based mutagenesis reveals the albumin-binding site of the neonatal Fc receptor, *Nature Communications*, 3 (2012) 610.

[15] E.M. Pridgen, F. Alexis, T.T. Kuo, E. Levy-Nissenbaum, R. Karnik, R.S. Blumberg, R. Langer, O.C. Farokhzad, Transepithelial transport of Fc-targeted nanoparticles by the neonatal fc receptor for oral delivery, *Science Translational Medicine*, 5 (2013) 213ra167.

[16] Y. Shi, X. Sun, L. Zhang, K. Sun, K. Li, Y. Li, Q. Zhang, Fc-modified exenatide-loaded nanoparticles for oral delivery to improve hypoglycemic effects in mice, *Scientific Reports*, 8 (2018) 726.

[17] A. Moreno-Aspitia, E.A. Perez, North Central Cancer Treatment Group N0531: Phase II Trial of Weekly Albumin-Bound Paclitaxel (ABI-007; Abraxane®) in Combination with Gemcitabine in Patients with Metastatic Breast Cancer, *Clinical Breast Cancer*, 6 (2005) 361-364.

[18] L. Hashem, M. Swedrowska, D. Vllasaliu, Intestinal uptake and transport of albumin nanoparticles: potential for oral delivery, *Nanomedicine*, 13 (2018) 1255-1265.

[19] J.P. Martins, R. D'Auria, D. Liu, F. Fontana, M.P.A. Ferreira, A. Correia, M. Kemell, K. Moslova, E. Makila, J. Salonen, L. Casettari, J. Hirvonen, B. Sarmiento, H.A. Santos, Engineered Multifunctional Albumin-Decorated Porous Silicon Nanoparticles for FcRn Translocation of Insulin, *Small*, 14 (2018) e1800462.

[20] J. Nilsen, E. Trabjerg, A. Grevys, C. Azevedo, S.O. Brennan, M. Stensland, J. Wilson, K.M.K. Sand, M. Bern, B. Dalhus, D.C. Roopenian, I. Sandlie, K.D. Rand, J.T. Andersen, An intact C-terminal end of albumin is required for its long half-life in humans, *Communications Biology*, 3 (2020) 181.

[21] A. Grevys, J. Nilsen, K.M.K. Sand, M.B. Daba, I. Øynebråten, M. Bern, M.B. McAdam, S. Foss, T. Schlothauer, T.E. Michaelsen, G.J. Christianson, D.C. Roopenian, R.S. Blumberg, I. Sandlie, J.T. Andersen, A human endothelial cell-based recycling assay for screening of FcRn targeted molecules, *Nature Communications*, 9 (2018) 621.

[22] P. Fonte, S. Soares, F. Sousa, A. Costa, V. Seabra, S. Reis, B. Sarmiento, Stability study perspective of the effect of freeze-drying using cryoprotectants on the structure of insulin loaded into PLGA nanoparticles, *Biomacromolecules*, 15 (2014) 3753-3765.

- [23] P. Fonte, F. Andrade, C. Azevedo, J. Pinto, V. Seabra, M. van de Weert, S. Reis, B. Sarmento, Effect of the Freezing Step in the Stability and Bioactivity of Protein-Loaded PLGA Nanoparticles Upon Lyophilization, *Pharmaceutical Research*, 33 (2016) 2777-2793.
- [24] B. Sarmento, A. Ribeiro, F. Veiga, D. Ferreira, Development and validation of a rapid reversed-phase HPLC method for the determination of insulin from nanoparticulate systems, *Biomedical Chromatography*, 20 (2006) 898-903.
- [25] F. Sousa, A. Cruz, P. Fonte, I.M. Pinto, M.T. Neves-Petersen, B. Sarmento, A new paradigm for antiangiogenic therapy through controlled release of bevacizumab from PLGA nanoparticles, *Scientific Reports*, 7 (2017) 3736.
- [26] M.J. Maltesen, S. Bjerregaard, L. Hovgaard, S. Havelund, M. van de Weert, Analysis of insulin allostery in solution and solid state with FTIR, *Journal of Pharmaceutical Sciences*, 98 (2009) 3265-3277.
- [27] D.C. Roopenian, G.J. Christianson, T.J. Sproule, A.C. Brown, S. Akilesh, N. Jung, S. Petkova, L. Avanesian, E.Y. Choi, D.J. Shaffer, P.A. Eden, C.L. Anderson, The MHC class I-like IgG receptor controls perinatal IgG transport, IgG homeostasis, and fate of IgG-Fc-coupled drugs, *Journal of Immunology*, 170 (2003) 3528-3533.
- [28] B. Sarmento, A. Ribeiro, F. Veiga, D. Ferreira, R. Neufeld, Oral bioavailability of insulin contained in polysaccharide nanoparticles, *Biomacromolecules*, 8 (2007) 3054-3060.
- [29] J.T. Andersen, B. Dalhus, D. Viuff, B.T. Ravn, K.S. Gunnarsen, A. Plumridge, K. Bunting, F. Antunes, R. Williamson, S. Athwal, E. Allan, L. Evans, M. Bjoras, S. Kjaerulff, D. Sleep, I. Sandlie, J. Cameron, Extending serum half-life of albumin by engineering neonatal Fc receptor (FcRn) binding, *The Journal of Biological Chemistry*, 289 (2014) 13492-13502.
- [30] P.J. Kennedy, I. Perreira, D. Ferreira, M. Nestor, C. Oliveira, P.L. Granja, B. Sarmento, Impact of surfactants on the target recognition of Fab-conjugated PLGA nanoparticles, *European Journal of Pharmaceutics and Biopharmaceutics*, 127 (2018) 366-370.
- [31] I. Pereira, F. Sousa, P. Kennedy, B. Sarmento, Carcinoembryonic antigen-targeted nanoparticles potentiate the delivery of anticancer drugs to colorectal cancer cells, *International Journal of Pharmaceutics*, 549 (2018) 397-403.
- [32] J.S. Suk, Q. Xu, N. Kim, J. Hanes, L.M. Ensign, PEGylation as a strategy for improving nanoparticle-based drug and gene delivery, *Advanced drug delivery reviews*, 99 (2016) 28-51.
- [33] J.T. Huckaby, S.K. Lai, PEGylation for enhancing nanoparticle diffusion in mucus, *Advanced Drug Delivery Reviews*, 124 (2018) 125-139.
- [34] N. Bertrand, P. Grenier, M. Mahmoudi, E.M. Lima, E.A. Appel, F. Dormont, J.M. Lim, R. Karnik, R. Langer, O.C. Farokhzad, Mechanistic understanding of in vivo protein corona formation on polymeric nanoparticles and impact on pharmacokinetics, *Nature Communications*, 8 (2017) 777.

- [35] K. Sempf, T. Arrey, S. Gelperina, T. Schorge, B. Meyer, M. Karas, J. Kreuter, Adsorption of plasma proteins on uncoated PLGA nanoparticles, *European Journal of Pharmaceutics and Biopharmaceutics*, 85 (2013) 53-60.
- [36] D.J. Sobczynski, P. Charoenphol, M.J. Heslinga, P.J. Onyskiw, K. Namdee, A.J. Thompson, O. Eniola-Adefeso, Plasma protein corona modulates the vascular wall interaction of drug carriers in a material and donor specific manner, *PloS one*, 9 (2014) e107408.
- [37] D. Charbonneau, M. Beauregard, H.A. Tajmir-Riahi, Structural analysis of human serum albumin complexes with cationic lipids, *The Journal of Physical Chemistry*, 113 (2009) 1777-1784.
- [38] J. Tang, F. Luan, X. Chen, Binding analysis of glycyrrhetic acid to human serum albumin: Fluorescence spectroscopy, FTIR, and molecular modeling, *Bioorganic & Medicinal Chemistry*, 14 (2006) 3210-3217.
- [39] J. Fallingborg, Intraluminal pH of the human gastrointestinal tract, *Danish Medical Bulletin*, 46 (1999) 183-196.
- [40] R. Dinarvand, N. Sepehri, S. Manoochehri, H. Rouhani, F. Atyabi, Poly(lactide-co-glycolide) nanoparticles for controlled delivery of anticancer agents, *International Journal of Nanomedicine*, 6 (2011) 877-895.
- [41] E. Czuba, M. Diop, C. Mura, A. Schaschkow, A. Langlois, W. Bietiger, R. Neidl, A. Virciglio, N. Auberval, D. Julien-David, E. Maillard, Y. Frere, E. Marchioni, M. Pinget, S. Sigrist, Oral insulin delivery, the challenge to increase insulin bioavailability: Influence of surface charge in nanoparticle system, *International Journal of Pharmaceutics*, 542 (2018) 47-55.
- [42] D.J. McClements, Encapsulation, protection, and delivery of bioactive proteins and peptides using nanoparticle and microparticle systems: A review, *Advances in Colloid and Interface Science*, 253 (2018) 1-22.
- [43] A.J. Thote, J.T. Chappell, R. Kumar, R.B. Gupta, Reduction in the Initial-Burst Release by Surface Crosslinking of PLGA Microparticles Containing Hydrophilic or Hydrophobic Drugs, *Drug Development and Industrial Pharmacy*, 31 (2005) 43-57.
- [44] K. Langer, M.G. Anhorn, I. Steinhauser, S. Dreis, D. Celebi, N. Schrickel, S. Faust, V. Vogel, Human serum albumin (HSA) nanoparticles: Reproducibility of preparation process and kinetics of enzymatic degradation, *International Journal of Pharmaceutics*, 347 (2008) 109-117.
- [45] M. Lopes, A. Derenne, C. Pereira, F. Veiga, R. Seica, B. Sarmento, A. Ribeiro, Impact of the in vitro gastrointestinal passage of biopolymer-based nanoparticles on insulin absorption, *RSC Advances*, 6 (2016) 20155-20165.
- [46] P. Fonte, F. Araujo, V. Seabra, S. Reis, M. van de Weert, B. Sarmento, Co-encapsulation of lyoprotectants improves the stability of protein-loaded PLGA nanoparticles upon lyophilization, *International Journal of Pharmaceutics*, 496 (2015) 850-862.
- [47] P. Fonte, P.R. Lino, V. Seabra, A.J. Almeida, S. Reis, B. Sarmento, Annealing as a tool for the optimization of lyophilization and ensuring of the stability of protein-loaded PLGA nanoparticles, *International Journal of Pharmaceutics*, 503 (2016) 163-173.

- [48] P. Fonte, S. Soares, A. Costa, J.C. Andrade, V. Seabra, S. Reis, B. Sarmiento, Effect of cryoprotectants on the porosity and stability of insulin-loaded PLGA nanoparticles after freeze-drying, *Biomatter*, 2 (2012) 329-339.
- [49] H.R. Costantino, K. Griebenow, P. Mishra, R. Langer, A.M. Klibanov, Fourier-transform infrared spectroscopic investigation of protein stability in the lyophilized form, *Biochimica et Biophysica Acta*, 1253 (1995) 69-74.
- [50] K.V. Abrosimova, O.V. Shulenina, S.V. Paston, FTIR study of secondary structure of bovine serum albumin and ovalbumin, *Journal of Physics: Conference Series*, 769 (2016) 012016.
- [51] C.B. Woitiski, R.A. Carvalho, A.J. Ribeiro, R.J. Neufeld, F. Veiga, Strategies toward the improved oral delivery of insulin nanoparticles via gastrointestinal uptake and translocation, *BioDrugs: Clinical Immunotherapeutics, Biopharmaceuticals and Gene Therapy*, 22 (2008) 223-237.
- [52] S. Attili-Qadri, N. Karra, A. Nemirovski, O. Schwob, Y. Talmon, T. Nassar, S. Benita, Oral delivery system prolongs blood circulation of docetaxel nanocapsules via lymphatic absorption, *Proceedings of the National Academy of Sciences of the United States of America*, 110 (2013) 17498-17503.
- [53] M. Goldberg, I. Gomez-Orellana, Challenges for the oral delivery of macromolecules, *Nature Reviews Drug Discovery*, 2 (2003) 289.
- [54] J. Nilsen, M. Bern, K.M.K. Sand, A. Grevys, B. Dalhus, I. Sandlie, J.T. Andersen, Human and mouse albumin bind their respective neonatal Fc receptors differently, *Scientific Reports*, 8 (2018) 14648.
- [55] K.M. Sand, M. Bern, J. Nilsen, B. Dalhus, K.S. Gunnarsen, J. Cameron, A. Grevys, K. Bunting, I. Sandlie, J.T. Andersen, Interaction with both domain I and III of albumin is required for optimal pH-dependent binding to the neonatal Fc receptor (FcRn), *The Journal of Biological Chemistry*, 289 (2014) 34583-34594.
- [56] J.T. Andersen, M.B. Daba, G. Berntzen, T.E. Michaelsen, I. Sandlie, Cross-species binding analyses of mouse and human neonatal Fc receptor show dramatic differences in immunoglobulin G and albumin binding, *The Journal of Biological Chemistry*, 285 (2010) 4826-4836.
- [57] J.E. Ayala, D.P. Bracy, O.P. McGuinness, D.H. Wasserman, Considerations in the design of hyperinsulinemic-euglycemic clamps in the conscious mouse, *Diabetes*, 55 (2006) 390-397.
- [58] J.E. Ayala, V.T. Samuel, G.J. Morton, S. Obici, C.M. Croniger, G.I. Shulman, D.H. Wasserman, O.P. McGuinness, N.I.H.M.M.P.C. Consortium, Standard operating procedures for describing and performing metabolic tests of glucose homeostasis in mice, *Disease Models & Mechanisms*, 3 (2010) 525-534.
- [59] K. Sonaje, K.J. Lin, S.P. Wey, C.K. Lin, T.H. Yeh, H.N. Nguyen, C.W. Hsu, T.C. Yen, J.H. Juang, H.W. Sung, Biodistribution, pharmacodynamics and pharmacokinetics of insulin analogues in a rat model: Oral delivery using pH-responsive nanoparticles vs. subcutaneous injection, *Biomaterials*, 31 (2010) 6849-6858.

- [60] J. Shaji, V. Patole, Protein and Peptide drug delivery: oral approaches, *Indian journal of Pharmaceutical Sciences*, 70 (2008) 269-277.
- [61] Y. Pan, H. Xu, H.Y. Zhao, G. Wei, J.M. Zheng, Study on preparation and oral efficacy of insulin-loaded poly(lactic-co-glycolic acid) nanoparticles, *Acta Pharmaceutica Sinica*, 37 (2002) 374-377.
- [62] F.D. Cui, A.J. Tao, D.M. Cun, L.Q. Zhang, K. Shi, Preparation of insulin loaded PLGA-Hp55 nanoparticles for oral delivery, *Journal of Pharmaceutical Sciences*, 96 (2007) 421-427.
- [63] M.G. Martin, S.V. Wu, J.H. Walsh, Ontogenetic Development and Distribution of Antibody Transport and Fc Receptor mRNA Expression in Rat Intestine, *Digestive Diseases and Sciences*, 42 (1997) 1062-1069.
- [64] M. Pyzik, T. Rath, W.I. Lencer, K. Baker, R.S. Blumberg, FcRn: The Architect Behind the Immune and Nonimmune Functions of IgG and Albumin, *Journal of Immunology*, 194 (2015) 4595-4603.
- [65] T. Li, J.P. Balthasar, FcRn Expression in Wildtype Mice, Transgenic Mice, and in Human Tissues, *Biomolecules*, 8 (2018).

## Supplementary material

---

### Engineered albumin-functionalized nanoparticles for improved FcRn binding enhance oral delivery of insulin

*Cláudia Azevedo, Jeannette Nilsen, Algirdas Grevys, Rute Nunes, Jan Terje Andersen, Bruno Sarmiento*

**Table S1** | Permeability percentage and apparent permeability coefficient calculated after 4 h of incubation in MDCK-hFcRn cells.

Formulation	Permeability $\pm$ SD (%)	$P_{app} \pm$ SD ( $\times 10^{-6}$ )
WT	11.44 $\pm$ 6.92	1.44 $\pm$ 0.87
KAHQ	5.20 $\pm$ 2.83	0.66 $\pm$ 0.36
KP	28.73 $\pm$ 4.90	3.63 $\pm$ 0.62
NPs-NF	0.31 $\pm$ 0.28	0.04 $\pm$ 0.04
NPs-WT	0.84 $\pm$ 0.36	0.11 $\pm$ 0.05
NPs-KAHQ	0.72 $\pm$ 0.57	0.09 $\pm$ 0.07
NPs- KP	1.86 $\pm$ 0.60	0.25 $\pm$ 0.08

**Table S2** | Pharmacodynamic parameters of formulations at different time points after administration.

t (h)	Formulation	Glycemia (%)	AUC ± SD	PA ± SD (%)	HD ± SD (%)
0.5	PBS	120 ± 27	110.0 ± 13.4	7.7 ± 1.7	-23.6 ± 15.0
	Oral insulin	106 ± 32	103.0 ± 15.9	6.8 ± 2.0	-15.7 ± 17.8
	s.c insulin	78 ± 15	88.9 ± 7.5	100.0 ± 0.0	0.0 ± 0.0
	NP-NF	104 ± 41	102.2 ± 20.3	6.7 ± 2.6	-14.91 ± 22.8
	NP-WT	106 ± 6	103.0 ± 3.0	6.8 ± 0.4	-15.8 ± 3.4
	NP-KP	97 ± 9	98.4 ± 4.7	6.2 ± 0.6	-10.5 ± 5.3
1	PBS	123 ± 22	170.7 ± 25.6	21.2 ± 7.7	-46.3 ± 22.0
	Oral insulin	93 ± 32	152.6 ± 31.7	15.8 ± 9.5	-30.8 ± 27.1
	s.c insulin	33 ± 16	116.6 ± 15.1	100.0 ± 0.0	0.0 ± 0.0
	NP-NF	108 ± 22	155.4 ± 36.0	16.7 ± 10.8	-33.2 ± 30.8
	NP-WT	83 ± 25	150.2 ± 8.6	15.1 ± 2.6	-28.8 ± 7.3
	NP-KP	63 ± 22	138.4 ± 6.5	11.5 ± 2.0	-18.6 ± 5.6
2	PBS	111 ± 10	287.3 ± 41.8	-7.5 ± 3.6	-103.0 ± 29.51
	Oral insulin	89 ± 44	243.45 ± 69.6	-3.7 ± 5.95	-72.1 ± 49.2
	s.c insulin	17 ± 5	141.5 ± 23.9	100.0 ± 0.0	0.0 ± 0.0
	NP-NF	108 ± 18	263.5 ± 55.7	-5.43 ± 4.76	-86.2 ± 39.4
	NP-WT	71 ± 26	227.3 ± 33.8	-2.3 ± 2.9	-60.6 ± 23.9
	NP-KP	63 ± 33	201.8 ± 28.2	-0.2 ± 2.4	-42.6 ± 20.0
4	PBS	99 ± 12	497.8 ± 61.3	-2.4 ± 1.5	-153.2 ± 31.2
	Oral insulin	92 ± 61	424.4 ± 174.9	-0.6 ± 4.3	-116.1 ± 89.1
	s.c insulin	38 ± 10	196.4 ± 31.4	100.0 ± 0.0	0.0 ± 0.0
	NP-NF	95 ± 16	466.7 ± 88.8	-1.64 ± 2.2	-137.7 ± 45.2
	NP-WT	72 ± 24	370.5 ± 83.5	0.7 ± 2.1	-88.7 ± 42.5
	NP-KP	60 ± 25	325.2 ± 85.7	1.8 ± 2.1	-65.6 ± 43.6
6	PBS	115 ± 26	711.2 ± 91.2	-1.8 ± 1.4	-151.1 ± 32.2
	Oral insulin	95 ± 39	611.2 ± 275.2	-0.8 ± 4.3	-115.8 ± 97.2
	s.c insulin	49 ± 15	283.19 ± 51.6	100.0 ± 0.0	0.0 ± 0.0
	NP-NF	101 ± 29	662.6 ± 133.1	-1.0 ± 2.1	-134.0 ± 47.0
	NP-WT	63 ± 23	505.1 ± 130.5	1.5 ± 2.1	-78.4 ± 46.1
	NP-KP	81 ± 34	465.7 ± 144.6	2.1 ± 2.3	-64 ± 51.1
8	PBS	102 ± 18	927.8 ± 124.0	-1.6 ± 1.5	-137.8 ± 31.8
	Oral insulin	83 ± 46	789.2 ± 360.8	0.1 ± 4.4	-102.2 ± 92.5
	s.c insulin	58 ± 23	390.2 ± 88.5	100.0 ± 0.0	0.0 ± 0.0
	NP-NF	86 ± 41	849.5 ± 202.5	-0.6 ± 2.5	-117.7 ± 51.9
	NP-WT	79 ± 29	647.1 ± 182.2	1.9 ± 2.2	-65.8 ± 46.7
	NP-KP	71 ± 33	581.9 ± 212.8	2.7 ± 2.6	-49.1 ± 54.5





## The potential of porcine ex vivo platform for intestinal permeability screening of FcRn-targeted drugs

*Cláudia Azevedo<sup>1,2,3</sup>, Jan Terje Andersen<sup>4,5</sup>, Bruno Sarmiento<sup>1,2,6</sup>, Giovanni Traverso<sup>7,8,9\*</sup>*

<sup>1</sup> Instituto de Investigação e Inovação em Saúde (i3S), University of Porto, Porto, Portugal;

<sup>2</sup> Instituto de Engenharia Biomédica (INEB), University of Porto, Porto, Portugal;

<sup>3</sup> Instituto Ciências Biomédicas Abel Salazar (ICBAS), University of Porto, Porto, Portugal;

<sup>4</sup> Department of Immunology, Centre for Immune Regulation (CIR), Oslo University Hospital Rikshospitalet and University of Oslo, Oslo, Norway.

<sup>5</sup> Institute of Clinical Medicine and Department of Pharmacology, University of Oslo and Oslo University Hospital, Oslo, Norway.

<sup>6</sup> CESPU, Instituto de Investigação e Formação Avançada em Ciências e Tecnologias da Saúde & Instituto Universitário de Ciências da Saúde, Gandra, Portugal

<sup>7</sup> Department of Chemical Engineering and Koch Institute for Integrative Cancer Research, Massachusetts Institute of Technology, Cambridge, MA, USA.

<sup>8</sup> Division of Gastroenterology, Brigham and Women's Hospital, Harvard Medical School, Boston, MA, USA

<sup>9</sup> Department of Mechanical Engineering, Massachusetts Institute of Technology, Cambridge, MA, USA.

\* Corresponding Author: Tel: (617) 417-8061; E-mail: [cgt20@mit.edu](mailto:cgt20@mit.edu)

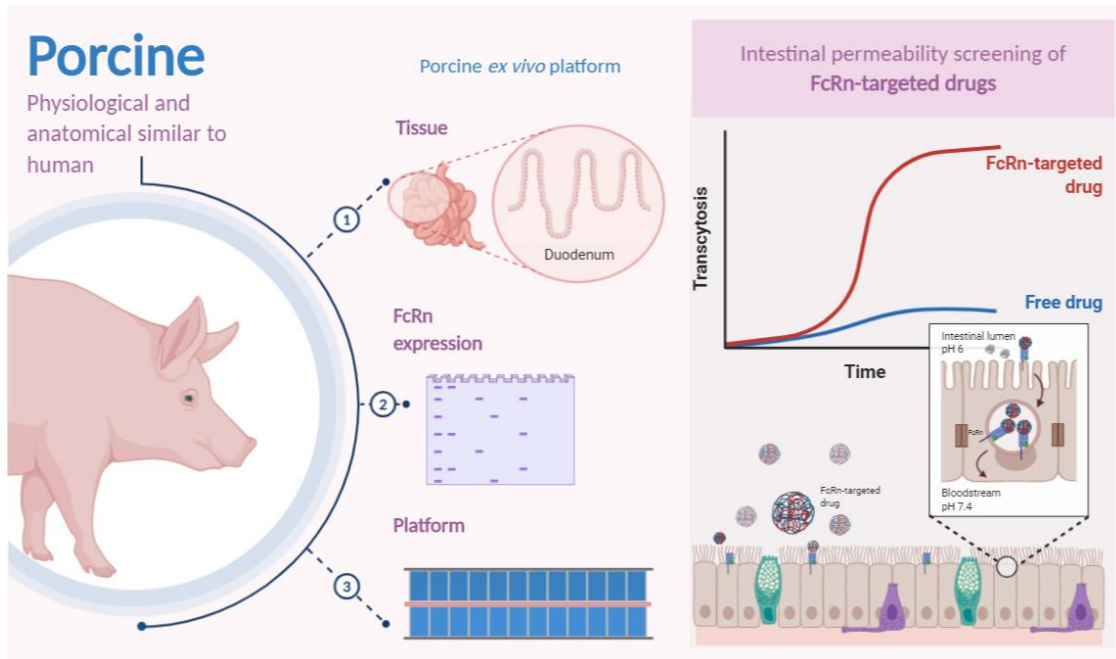
**Abstract**

Conventionally, the intestinal permeability of drugs is evaluated using cell monolayers models that lack morphological, physiological and architectural features, as well as, realistic FcRn expression. In addition, is time-consuming, expensive and un-ethical to use mice for large scale-screening of FcRn-targeted candidates. It is then critical to use suitable models, for preclinical validation, that mimic the human intestine as the porcine *ex vivo* model, due to its physiological and anatomical similarities. This study intended to analyze the FcRn-potential in intestinal permeability analysis, using a porcine *ex vivo* platform, able to analyze 96 samples at the same time. Besides, it allows the screening of FcRn-targeting for transmucosal delivery, taken into consideration (cross-species) receptor-ligand binding kinetics. After analyzing the porcine morphology tissue, the FcRn expression across the gastrointestinal tract was verified. Studying the stomach, duodenum and jejunum it was demonstrated that FcRn-expression is maintained for up 7 days. When evaluating the duodenum permeability of free engineered human albumin variants, it was shown that KP is more efficiently transported. Taking this, the porcine *ex vivo* platform revealed to be a potential model for the screening of FcRn-targeted oral drug formulations.

**Keywords:** Engineered human albumin variants; FcRn expression; FcRn-mediated transcytosis; Polymeric and mucodiffusive nanoparticles; Screening of FcR-targeted drugs

**Teaser:** This study intended to analyze the FcRn-potential in intestinal permeability analysis, using the porcine *ex vivo* platform.

## Graphical abstract



## 1. Introduction

After the development of new pharmaceutical and nutritional products, for oral administration, there is the need of understanding their permeability in the small intestine before proceeding to further studies. Obviously, a suitable model with reliable prediction is crucial and of high interest to reach the desired effect in humans. Nowadays, Caco-2 cell line, derived from human colorectal adenocarcinoma, is the gold-standard model to validate the intestinal permeability of oral drugs. However, it is known that this model presents some drawbacks by lacking morphological and physiological features, not mimicking a human intestine, as different levels of drug transporters and metabolizing enzymes, besides forming a monolayer with tighter tight junctions and affecting transport via [1]. These differences are reflected in the correlation of drug permeability data with humans, which is around 0.3 [2]. Besides Caco-2 cells, also human colon carcinoma cell line (T84) and human colorectal adenocarcinoma cell line (HT29) express neonatal Fc receptor (FcRn). Meanwhile, it was developed a modified Madin-Darby canine kidney (MDCK) cell line, to overexpress human FcRn (hFcRn), MDCK-hFcRn [3]. Despite MDCK cell line be accepted for intestinal permeability and has a faster culture time, it was demonstrated differences comparing with Caco-2 cells, as heterogeneity, metabolic properties and transport as reasons of variability [4]. In addition, the level of expression is higher compared to human intestinal cell models [3]. This shows that current models, widely used, are not able to provide accurate and reliable results because they do not represent all the intestinal cells types, neither the intestinal layers that are responsible for the absorption process. The use of these models can then lead to erroneous results in a first stage of drug development, which can lead to waste of time and money in following phases of drug validation. In this sense, *ex vivo* models can be an alternative by mimicking the biology, architecture and mechanics of the human intestine. A suitable model for preclinical validation will then reduce *in vivo* testing, which is time-consuming, expensive and un-ethical to use mice for large scale-screening of FcRn-targeted candidates. Particularly, due to the physiological and anatomical similarities to human, the porcine has gaining importance and attention from investigators. In fact, these similarities are reflected in the correlation of 0.9 of the *ex vivo* porcine model with drug permeability data in humans [2]. In addition, the pig is considered a suitable model to perform pharmacokinetic (PK) studies of human serum albumin (HSA), since porcine serum albumin (PSA) provides minimal competition for binding to FcRn [5]. Plus, it has been used as a potential model for transepithelial delivery of FcRn-targeted proteins [6].

In short, this work intends to evaluate an *ex vivo* platform, using porcine tissue, for screening the intestinal permeability of FcRn-targeted drugs, taken into consideration (cross-species) receptor-ligand binding kinetics.

## **2. Experimental section**

### **2.1. Tissue dissection and cultivation**

All animal procedures were conducted in accordance with protocols approved by the Massachusetts Institute of Technology Committee on Animal Care in compliance with federal, state, local and institutional regulations, including the Animal Welfare Act and Public Health Service Policy. Small sections of intestinal tissue were isolated from freshly procured intact GI tracts from pigs from selected local slaughterhouses. A section of the tissue was cut out of the GI tract, dissected longitudinally and the outer muscle layer and serosa were removed. For standard transport experiments, duodenum tissue was used. The tissue was washed in a series of saline solutions under sterile conditions. The tissue was then either mounted on the porcine *ex vivo* platform or maintained in culture. For cultivation, the media advanced DMEM/F-12 (Life Technologies, Ref.: 12634028) was used and supplemented with 10% fetal bovine serum (FBS) and 5% antibiotic–antimycotic solution (Thermo Fisher Scientific, Ref.:15240062). Tissue was cultured in this serum-free cell culture medium in a sealed polystyrene container that was then stored in an incubator kept at 37°C (no supplement gas was provided). A set of experiments was conducted with fixed time points as well as longer-term experiments monitoring the tissue daily, with analyses performed at varying time points.

### **2.2. Immunohistochemistry**

Sections of the porcine gastrointestinal (GI) tract were put into cassettes, fixed with 10% (v/w) formalin for 24 h at 4°C and then storage in 70% ethanol at 4°C. Paraffin sections (5-µm) on glass slides were dried at 70°C for 30 min, deparaffinized and heat induced epitope retrieve (HIER) at 97°C for 20 min in citrate buffer pH 6. These procedures were completely automated by using a ThermoFisher IHC Autostainer 360. Briefly, for immunohistochemistry (IHC), endogenous peroxidase blocking was done for 10 min followed by the protein block for 30 min. Primary antibody (1:100 anti-FCGRT, abcam ref.: ab193148) was incubated for 1 h and the secondary antibody (1:2000 goat anti-rabbit IgG, abcam, ab205718) for 30 min. Both antibodies diluted with Tris Buffered Saline with Tween 20 (TBST) and incubated at room temperature. Finally, an incubation

of 5 min with 3,3'-Diaminobenzidine (DAB) was done. The stained cells were then mounted on a cover slide using ConsulMount (Thermo Fisher, 9990440). Representative images using Koehler illumination were obtained with an Olympus Microfire digital camera (M/N S97809) attached to an Olympus BX60 microscope.

### **2.3. RT-PCR analysis**

The FcRn expression of *ex vivo* cultured porcine-derived intestinal tissue was determined by reverse transcription polymerase chain reaction (RT-PCR) analysis and detected by agarose electrophoresis. Initially, the tissue was removed from fresh GI, frozen in liquid nitrogen and storage at -80°C. Then, total RNA from each tissue sample was extracted and purified with Quick-RNA plus (Zymo Research) followed by reverse transcription into complementary DNA using a High-Capacity cDNA reverse transcription kit (ThermoFisher Scientific). Target genes were amplified using the reported primers (GAATTGGGCCCCGACAAT and CTGCTCACCCCTTCCACTCC) [7] and Platinum™ SuperFi™ DNA Polymerase (ThermoFisher Scientific ref.: 12351010). The PCR program was optimized and consisted of an enzyme activation step (98°C, 10min), forty cycles of denaturation (98°C, 30 sec), annealing extension (62°C, 1 min), extension (72°C, 45 sec), followed by an extension at 72°C for 10 min. The expression level of FcRn was measured with 1.5% agarose gel electrophoreses, with SYBR Safe DNA gel stain (Thermofisher, S33102) and 100 bp DNA Ladder (New England BioLab, N3231S) and detected using the Bio-Rad Image suite.

### **2.4. PLGA-PEG NPs production**

Engineered albumin-conjugated and insulin encapsulated poly(lactic-co-glycolic)-poly(ethylene glycol) (PLGA-PEG) nanoparticles (NPs) were produced by following the procedures previously described [8]. Briefly, NPs were produced through a modified solvent emulsification-evaporation method based on a w/o/w double emulsion technique. It was used 100 mg of polymer, in which 95% was PLGA (PURASORB® PDLG 5004A, in a 50/50 molar ratio of DL-lactide and Glycolide, kindly provided by Corbion) and 5% PLGA-PEG-MAL (Akina, PolyScitech). To load the NPs, 75 mg/mL insulin solution (Sigma Aldrich) in 0.1 M of HCl was added to the polymeric solution. Finally, the conjugation was done through the covalent thioether bond between Cys34 from DI of albumin and the maleimide group of PLGA-PEG-MAL on the surface of the NP, in a molar ratio 1:0.1 of PLGA-PEG-MAL:Albumin [8]. Wild type (WT) albumin and engineered albumin variants, namely K500A/K510Q (KAHQ) and K573P (KP), were

kindly provided by Jan Terje Andersen from Oslo University Hospital. PSA was obtained from Sigma Aldrich.

## 2.5. Transport experiments using the ex vivo platform

For assembly of the *ex vivo* platform, freshly isolated intestinal tissue from the duodenum was prepared according to the above-described tissue dissection procedure and mounted on the manufactured interface design with a generic 96-well plate (96-well plates, clear bottom, Corning), as previously described [2]. To the plate from the bottom, the basolateral side, it was added 100  $\mu\text{L}$  of Hanks' Balanced Salt solution (HBSS) pH 7.4. The duodenum was identified as the region of the small intestine approximately 1 m after the stomach. Duodenum tissue was then carefully moved over the bottom magnetic plate with the apical side facing upwards. Afterwards, the top magnetic plate was mounted, and 90  $\mu\text{L}$  of 189.83  $\mu\text{g}/\text{mL}$  samples was added, at the apical side. Samples were prepared at acidic pH, using HBSS buffered to pH 6.0 by addition of MES buffer (Sigma Aldrich). After 4 h of incubation, samples were collected from the basolateral side, with a syringe, at the bottom magnetic plate and quantified by ELISA. All experiments, including sample incubation, were performed at room temperature. Results were expressed in relative transport and apparent permeability ( $P_{app}$ ), using the following formulas:

$$\text{Equation (1)} \quad \text{Relative Transport} = \frac{\text{Amount of sample}}{\text{Mean amount of control}}$$

$$\text{Equation (2)} \quad P_{app} = \frac{\Delta Q}{A \times C_0 \times \Delta t} * 100$$

where  $C_0$  is the initial concentration in the apical compartment (mg/mL),  $A$  is the surface area of the insert ( $\text{cm}^2$ ),  $\Delta t$  is the time during which the experiment occurred (seconds) and  $\Delta Q$  is the amount of compound detected in the basolateral side (mg).

## 2.6. Albumin quantification

The quantification was done using a two-way anti-albumin enzyme-linked immunosorbent assay (ELISA). Briefly, 96 wells plates (Costar) were coated with 100  $\mu\text{L}$  of a polyclonal anti-albumin antibody produced in goat (Sigma Aldrich, A1151) diluted 1:2000 in PBS by incubation overnight at  $4^\circ\text{C}$ . The wells were blocked with 200  $\mu\text{L}$  PBSTM solution, composed by PBS, 0.005% Tween 20 and 4% skimmed milk (Acumedia), for 1 h at room temperature (RT) and then washed three times with 200  $\mu\text{L}$  PBST (PBS, 0.005% Tween 20). Samples were titrated 1:2 in PBSTM, and 100  $\mu\text{L}$  of



each dilution was subsequently added in triplicates to wells and incubated for 1 h at RT. The wells were washed as before. Alkaline phosphatase (AP)-conjugated polyclonal anti-albumin from goat (Bethyl Laboratories, A80229AP) was diluted 1:4000 in PBSTM and 100  $\mu$ L was added per well and incubated for 1 h at RT. After washing as before, visualization was performed by adding 100  $\mu$ L of AP substrate (4-nitrophenyl phosphate disodium salt hexahydrate substrate) (Sigma-Aldrich) diluted in diethanolamine buffer. The absorbance was measured at 405 nm using the sunrise spectrophotometer (TECAN).

### **2.7. Statistical analysis**

Statistical analysis was performed using the GraphPad Prism Software vs. 6.0 (GraphPad Software Inc). Statistical significance of the difference between two groups was evaluated by the Student's t-test. Differences between groups were compared using one-way analysis of variance (ANOVA) Dunnett's multiple comparison test. Results are expressed as mean  $\pm$  standard deviation and geometric means with 95% confidence intervals. The level of significance was set at probabilities of \*P < 0.05, \*\*P < 0.005, and #P < 0.0001.

## **3. Results and discussion**

### **3.1. FcRn expression across GI tract**

Initially, the viability and morphology of the GI tract from the porcine *ex vivo* model, was evaluated by hematoxylin and eosin (H&E) staining, to assure the maintenance of tissue integrity (**Figure S1**). After this, FcRn expression was confirmed by RT-PCR, after collecting the tissue, extract RNA and amplify cDNA (**Figure 1**). As expected, the porcine receptor is broadly expressed throughout the GI tract, as previously confirmed [6, 7].

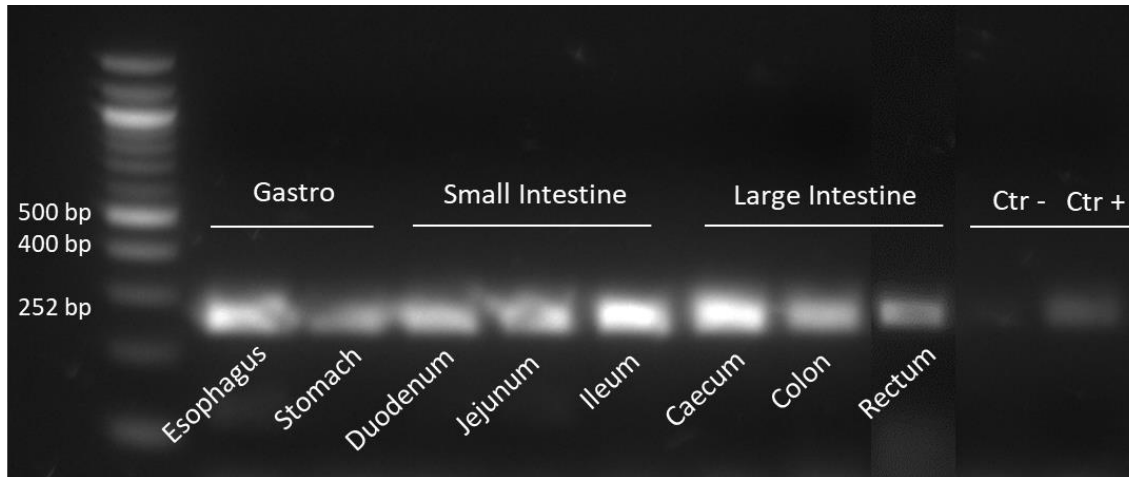


**Figure 1 | Confirmation of FcRn gene expression across GI tract.** (A) Schematic illustration of the studied porcine organs; (B) Relative band intensity quantified through the results from C, using ImageJ; (C) Before performing the RT-PCR, RNA was extracted from fresh tissue of different sections of GI tract and cDNA was amplified. Results shown were performed with one tissue batch.

Subsequently this analysis, only stomach, duodenum and jejunum sections were considered for further studies, due to their acidic pH, having duodenum the most favorable pH for FcRn binding [9, 10]. As described, FcRn binds to its ligands in a pH-dependent manner. Briefly, the receptor binds its ligands at acidic pH (6.5-5.0) and releases them upon neutral pH. This is an important feature, since the receptor helps ligands to escape from lysosomes degradation and be successfully transcytosed to the basolateral side [11, 12]. Results from IHC staining showed that FcRn is expressed in stomach, duodenum and jejunum, which is consistent with the PCR results, being more intense in epithelial cells of villi, especially in duodenum (**Figure 2 A**). This evidence makes sense, since, intestinal epithelium is highly composed by enterocytes responsible for the absorption, suggesting the involvement of FcRn in the import and export of albumin and IgG at mucosal surfaces [13]. These results are then in line with published data [6].

Since there are no available antibodies for porcine FcRn (pFcRn), hFcRn was used due to its similar genomic structure. According to literature, pFcRn gene revealed to be 80% identical to the corresponding human. Both genes have the single N-linked glycosylation site (NVSV) in the  $\alpha$  domain, as well as both di-leucine- and tryptophan-based endocytosis signals present in the cytoplasmic tail. At the moment, authors seem to not

agree about specific amino acid differences in FcRn structure between human and porcine species, which represent different polymorphisms [6]. However, it is known that the porcine receptor has a type 1 membrane protein with an N-terminal signal peptide and a single transmembrane domain. According to literature, pFcRn is also expressed in the heart, lung, kidney, intestine, muscle, brain, endothelial cells and monocytes, and highly expressed in liver, spleen, thymus, lymphoid, being also maintained in the adult stage, similar to humans [6, 7].

Studying the durability of FcRn expression of tissue in culture, it was observed that it is maintained for up, at least, 7 days in duodenum (**Figure 2 B**). These results are in line with previous characterization of the *ex vivo* platform, when evaluating other receptors' expression. Authors verified that it is possible to guarantee the complex GI architecture, mucus layer and the expression of several drug transporter for 7 days, when the tissue is intact in culture [2].

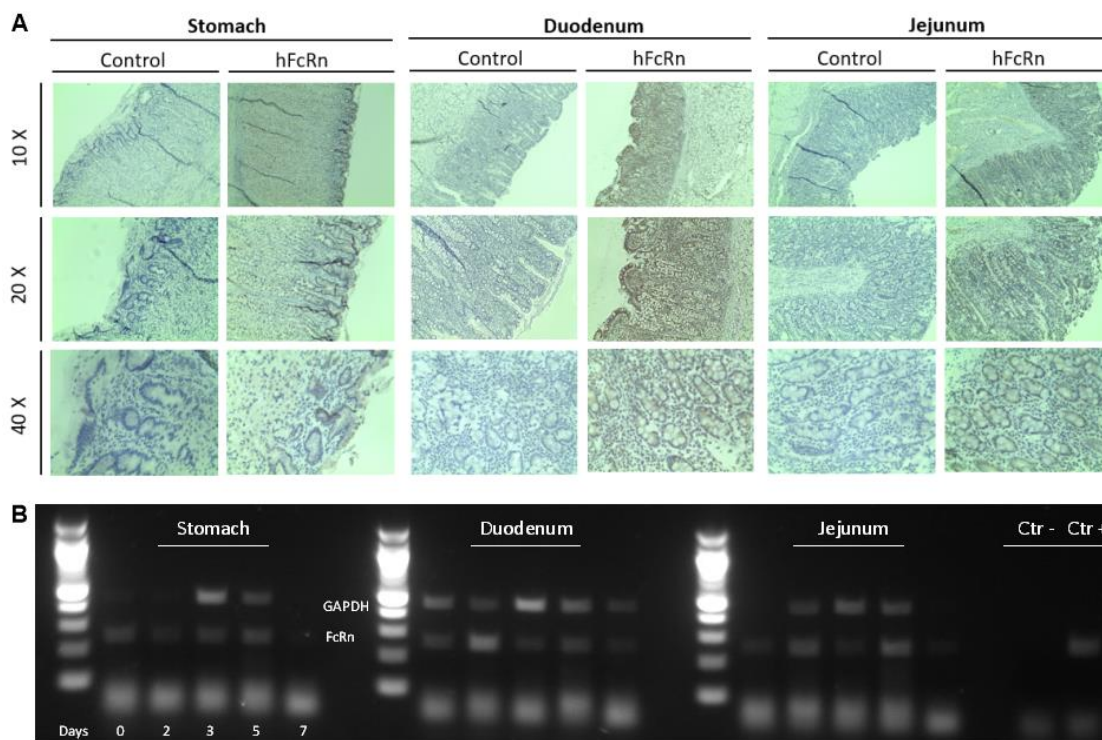


**Figure 2 | Evaluation of FcRn expression over time, of stomach, duodenum and jejunum.**

**(A)** Evaluation of FcRn expression by IHC of fresh porcine tissue. Control samples were only treated with the secondary antibody, to check non-specific binding. Brown indicates the antibody signal, while blue is the counterstain. **(B)** FcRn expression after 7 days of porcine *ex vivo* incubation or freshly isolated at day zero. Before the RT-PCR, RNA was extracted from fresh tissue and cDNA was amplified. Water and porcine blood were included as negative and positive controls, respectively. Results shown were performed with one tissue batch.

### 3.2. Transcytosis of engineered albumin variants using porcine *ex vivo* platform

Next, the evaluation of the *ex vivo* platform, using porcine duodenum (**Figure 3 A**), for the screening of the intestinal permeability of FcRn-targeted drugs was done. For this analysis, a porcine *ex vivo* platform, previously developed [2], was used (**Figure 3 B**). Plus, engineered human albumin variants with different affinities, depending on their mutation, to FcRn were used, in order to evaluate their transcytosis profile. K573P (KP) has a single a.a. substitution in the C-terminal domain III, which extends serum half-life in hFcRn expressing mice and non-human primates [12, 14]. In contrast, K500A/H464Q (KAHQ) variant is used since abolishes binding to the receptor [12, 14]. These mutations are in the C-terminal domain III of albumin, the FcRn binding site, conferring different binding affinities to the receptor. The transcytosis of these variants was previously tested by us in MDCK-hFcRn cell line. In this previous study, it was demonstrated that KP was 2.5-fold more efficiently transported than WT. Meanwhile, when conjugated to polymeric nanoparticles (NPs), NPs-KP demonstrated a transport of 2-fold higher than NPs-WT [8]. Here, for permeability studies, it was also included PSA as a control. It is reported that HSA has 2.9-fold more affinity to pFcRn than PSA, which not causes competition [5].

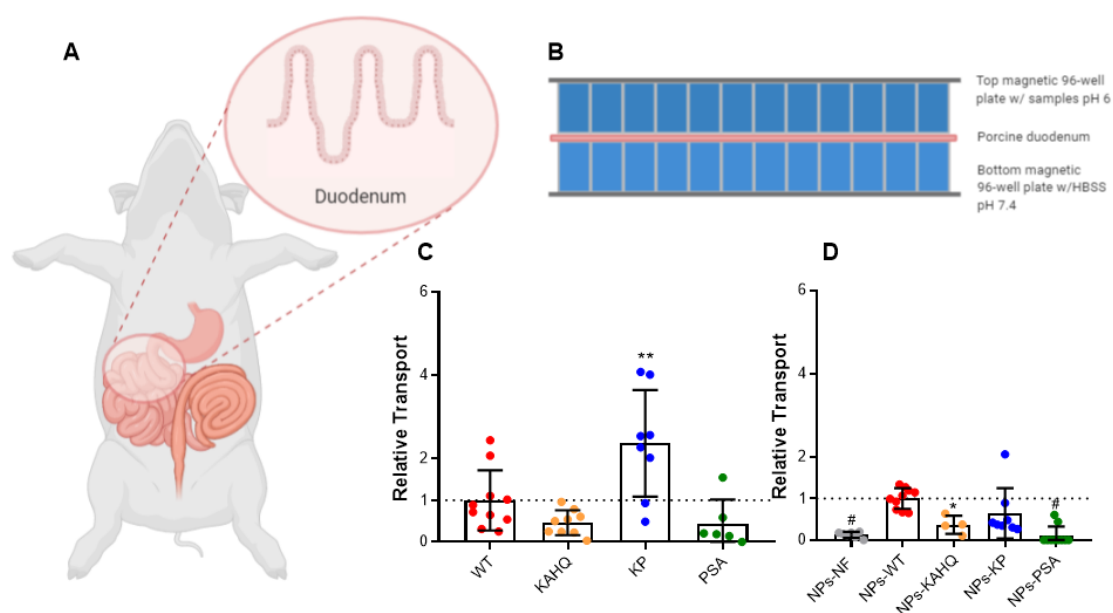


**Figure 3 | Engineered albumin showed enhanced transcytosis capacity in the porcine *ex vivo* platform. (A)** Representation showing porcine duodenum, as the tissue used to study the intestinal permeability, using the porcine *ex vivo* platform. **(B)** Schematic illustration of the cross-section of the interface design in a 96-well plate format. 100  $\mu$ L of HBSS pH 7.4 was added to the plate from the bottom, mimicking the basolateral side. Next, the tissue was put on the plate, facing

the apical side upwards. Finally, the magnetic plate from the top was added, pressing the tissue to avoid leakage, and samples prepared in HBSS pH 6 were added. **(C)** Relative amounts of naked albumin variants (WT, KAHQ, KP and PSA) detected in media collected at the basolateral side, 4 h after adding the variants to the apical side in the porcine *ex vivo* platform (n=6-10); **(D)** Relative amounts of NPs functionalized with albumin variants (n=4-10). The amounts were quantified by two-way anti-albumin ELISA, where WT albumin was set to 1, as a control. These results were obtained from 3 different pigs. Shown are the arithmetic means  $\pm$  SD. \*P < 0.05, \*\*P < 0.005, and #P < 0.0001, comparing with WT by one-way ANOVA Dunnett's multiple comparison test.

From the results from **Figure 3 C**, it is possible to verify that KP human albumin variant maintains its pattern, of being more efficiently transported compared to WT, which is translated in a ratio of 2.4-fold. These results confirm previous reported data related with pFcRn binding affinity, which showed that  $k_d$  ( $10^{-3}/s$ ) values for HSA-WT, HSA-KP and PSA are around 15, 2.6 and 53, respectively [5].  $k_d$  is the constant of dissociation, meaning that higher the affinity, lower the dissociation. The albumin quantification was made by ELISA, using human albumin antibodies, which might not be the best way to quantify PSA. However, it is known that PSA is 75.1% similar to HSA [5]. Despite this, the results are in line with publish data, since PSA was less transported ( $P_{app} = 0.44 \pm 0.53 \times 10^{-6}$ ) by pFcRn, compared with WT (**Table 1**). Through the  $P_{app}$  obtained values of free albumin variants, it was observed that these were 0.56-fold less transported in this *ex vivo* platform, when correlating with results previously published using MDCK-hFcRn *in vitro* model [8].

After this evaluation, albumin-functionalized NPs were also tested to further study the potential of the porcine *ex vivo* platform (**Figure 3 D**). The produced NPs were previously characterized, by being a monodisperse solution and having 150 nm in size, zeta potential around -9 mV and 10% loaded with insulin [8]. The typical pattern behavior between variants was observed, except for NPs-KP. Also, it was not expected that NPs, as larger particles, presented higher  $P_{app}$  values, compared to free albumin. Additionally, NPs-KAHQ and NPs-PSA were less transported as expected. Nevertheless, non-functionalized NPs presented some signal, which is not supposed to since they do not have HSA attached on the NPs' surface. This might be due to the presence of some possible interferents from the biologic fluids contained on the tissue.

Taking this into consideration, as future perspectives, it would be better to increase the number of replicates, to validate the experiment and obtain comparable *Papp* values.

**Table 1** | Apparent permeability coefficient calculated after 4 h of incubation in *ex vivo* porcine, based on the albumin amount quantified by ELISA. These results were obtained from 3 different pigs.

Formulation	<i>Papp</i> ± SD (x10 <sup>-6</sup> cm/s)	Formulation	<i>Papp</i> ± SD (x10 <sup>-6</sup> cm/s)
		<b>NPs-NF</b>	0.66 ± 0.37
<b>WT</b>	0.83 ± 0.58	<b>NPs-WT</b>	5.34 ± 1.44
<b>KAHQ</b>	0.34 ± 0.22	<b>NPs-KAHQ</b>	2.66 ± 1.49
<b>KP</b>	1.86 ± 1.12	<b>NPs- KP</b>	3.09 ± 2.95
<b>PSA</b>	0.44 ± 0.53	<b>NPs-PSA</b>	0.53 ± 1.14

Lately, porcine tissues have been highly used in preclinical drugs validation. Example of that is the developed InTESTine™ system, containing porcine intestine tissue, which demonstrated to have more comparable *Papp* and transepithelial electrical resistance (TEER) values, to humans, than Caco-2 and Caco-2/HT29-MTX *in vitro* models [15]. Also, Rani Therapeutics evaluated the PK/ pharmacodynamic (PD) of recombinant human insulin delivered by an ingestible device, into the porcine jejunum [16]. However, none of these evaluate the potential of FcRn evaluation in a platform, where 96 samples can be analyzed at the same time. Here, the results look promising and the *ex vivo* platform might be a promising tool for screening of intestinal permeability of FcRn-targeted drugs.

#### 4. Conclusions

A suitable model with reliable prediction of intestinal permeability of oral drugs is crucial and of high interest to reach the desired effect in humans. The porcine has gaining importance and attention from investigators, due to its physiological and anatomical similarities. Using a porcine *ex vivo* platform, previously developed, it was possible to study the potential for evaluation of FcRn-targeting for transmucosal delivery, taken into consideration (cross-species) receptor-ligand binding kinetics. In this study it was demonstrated that the porcine *ex vivo* platform revealed to be a potential model for the screening of FcRn-targeted oral drug formulations, since the FcRn expression was confirmed through the GI tract, which was maintained for up 7 days. Also, as a validation,

through an intestinal permeability assay it was shown the characteristic pattern of engineered human albumin variants. Therefore, this platform may have a positive and significant impact on the development of preclinical FcRn-targeted drugs, saving some time and money of the research by providing more reliable data.

### **Declaration of Competing Interest**

G.T is a co-inventor of pending patent applications related to porcine *ex vivo* platform.  
J.T.A. is a co-inventor of pending patent applications related to albumin variants.

### **Acknowledgements**

This work was financed by Portuguese funds through FCT - Fundação para a Ciência e a Tecnologia/ Ministério da Ciência, Tecnologia e Ensino Superior in the framework of the project "Institute for Research and Innovation in Health Sciences" UID/BIM/04293/2019. Cláudia Azevedo would like to thank to Fundação para a Ciência e a Tecnologia (FCT, SFRH/BD/117598/2016), Portugal for financial support, as well as recognition gave by Fulbright (PS00293218) and a grant from Fundação Luso Americana para o Desenvolvimento (FLAD, Proj. 137/2019). The authors acknowledge the support of Carneiro&Salgueirinho for some porcine tissue. This work was also supported by the Koch Institute Support (core) Grant P30-CA14051 from the National Cancer Institute. We thank the Hope Babette Tang Histology Facility at the Koch Institute at MIT for the histology work and consultation.

### **Author Contributions**

C.A., G.T and B.S. designed research; C.A. performed research; C.A. analyzed data; C.A, G.T., J.T.A. and B.S. wrote the paper.

## References

- [1] A. Almeida, C. Azevedo, M.H. Macedo, B. Sarmiento, 3D intestinal models towards a more realistic permeability screening, in: Elsevier (Ed.) *Nanotechnology for Oral Drug Delivery*, 2020.
- [2] T. von Erlach, S. Saxton, Y. Shi, D. Minahan, D. Reker, F. Javid, Y.-A.L. Lee, C. Schoellhammer, T. Esfandiary, C. Cleveland, L. Booth, J. Lin, H. Levy, S. Blackburn, A. Hayward, R. Langer, G. Traverso, Robotically handled whole-tissue culture system for the screening of oral drug formulations, *Nature Biomedical Engineering*, (2020).
- [3] B.L. Dickinson, K. Badizadegan, Z. Wu, J.C. Ahouse, X. Zhu, N.E. Simister, R.S. Blumberg, W.I. Lencer, Bidirectional FcRn-dependent IgG transport in a polarized human intestinal epithelial cell line, *The Journal of clinical investigation*, 104 (1999) 903-911.
- [4] D.A. Volpe, Variability in Caco-2 and MDCK Cell-Based Intestinal Permeability Assays, *Journal of pharmaceutical sciences*, 97 (2008) 712-725.
- [5] D.S. Jason Cameron, Jan Terje Andersen, Inger Sandlie, *Pharmacokinetic animal model in*, 2018.
- [6] C.M.A. Stirling, B. Charleston, H. Takamatsu, S. Claypool, W. Lencer, R.S. Blumberg, T.E. Wileman, Characterization of the porcine neonatal Fc receptor--potential use for trans-epithelial protein delivery, *Immunology*, 114 (2005) 542-553.
- [7] L. Yang, W. Chonglong, L. Zhengzhu, X. Jingen, F. Weixuan, W. Wenwen, D. Xiangdong, L. Jianfeng, Z. Qin, Tissues Expression, Polymorphisms Identification of FcRn Gene and Its Relationship with Serum Classical Swine Fever Virus Antibody Level in Pigs, *Asian-Australas J Anim Sci*, 25 (2012) 1089-1095.
- [8] C. Azevedo, J. Nilsen, A. Grevys, R. Nunes, J.T. Andersen, B. Sarmiento, Engineered albumin-functionalized nanoparticles for improved FcRn binding enhances oral delivery of insulin, *Journal of Controlled Release*, 327 (2020) 161-173.
- [9] J. Fallingborg, Intraluminal pH of the human gastrointestinal tract, *Danish medical bulletin*, 46 (1999) 183-196.
- [10] L. Ovesen, F. Bendtsen, U. Tage-Jensen, N.T. Pedersen, B.R. Gram, S.J. Rune, Intraluminal pH in the stomach, duodenum, and proximal jejunum in normal subjects and patients with exocrine pancreatic insufficiency, *Gastroenterology*, 90 (1986) 958-962.
- [11] D.C. Roopenian, S. Akilesh, FcRn: the neonatal Fc receptor comes of age, *Nature Reviews Immunology*, 7 (2007) 715.
- [12] J.T. Andersen, B. Dalhus, J. Cameron, M.B. Daba, A. Plumridge, L. Evans, S.O. Brennan, K.S. Gunnarsen, M. Bjørås, D. Sleep, I. Sandlie, Structure-based mutagenesis reveals the albumin-binding site of the neonatal Fc receptor, *Nature Communications*, 3 (2012) 610.
- [13] C. Azevedo, I. Pereira, B. Sarmiento, Intestinal mucosal models to validate functionalized nanosystems in: Wiley (Ed.) *Characterization of Pharmaceutical Nano- and Microsystems*, 2020.
- [14] J.T. Andersen, B. Dalhus, D. Viuff, B.T. Ravn, K.S. Gunnarsen, A. Plumridge, K. Bunting, F. Antunes, R. Williamson, S. Athwal, E. Allan, L. Evans, M. Bjaras, S. Kjaerulff, D. Sleep, I. Sandlie,



J. Cameron, Extending serum half-life of albumin by engineering neonatal Fc receptor (FcRn) binding, *The Journal of biological chemistry*, 289 (2014) 13492-13502.

[15] J. Westerhout, E.v.d. Steeg, D. Grossouw, E.E. Zeijdner, C.A.M. Krul, M. Verwei, H.M. Wortelboer, A new approach to predict human intestinal absorption using porcine intestinal tissue and biorelevant matrices, *European Journal of Pharmaceutical Sciences*, 63 (2014) 167-177.

[16] M. Hashim, R. Korupolu, B. Syed, K. Horlen, S. Beraki, P. Karamchedu, A.K. Dhalla, R. Ruffy, M. Imran, Jejunal wall delivery of insulin via an ingestible capsule in anesthetized swine-A pharmacokinetic and pharmacodynamic study, *Pharmacology research & perspectives*, 7 (2019) e00522.

[17] Kenhub, Histology of the lower digestive tract: want to learn more about it?, in, <https://www.kenhub.com/en/library/anatomy/histology-of-the-lower-digestive-tract>, 2020.

[18] L.M. Gonzalez, A.J. Moeser, A.T. Bliklager, Porcine models of digestive disease: the future of large animal translational research, *Transl Res*, 166 (2015) 12-27.

## Supplementary material

---

### The potential of porcine *ex vivo* platform for intestinal permeability screening of FcRn-targeted drugs

Cláudia Azevedo, Jan Terje Andersen, Bruno Sarmento, Giovanni Traverso

#### 1. Material and Methods

##### 1.1. Hematoxylin and Eosin staining procedure

Sections of the porcine gastrointestinal (GI) tract were put into cassettes, fixed with 10% (v/w) formalin for 24 h at 4°C and then storage in 70% ethanol at 4°C. Paraffin sections (5- $\mu$ m) on glass slides were dried at 70°C for 30 min, deparaffinized and heat induced epitope retrieve (HIER) at 97°C for 20 min in citrate buffer pH 6. These procedures were completely automated by using a ThermoFisher IHC Autostainer 360. Briefly, for hematoxylin and eosin (H&E) staining, paraffin sections were counterstained with hematoxylin and eosin, according to standard protocols, using an automatic self-contained slide stainer (ThermoShandon Varistain Gemini). The stained cells were then mounted on a cover slide using ConsulMount (Thermo Fisher, #9990440). Representative images using Koehler illumination were obtained with an Olympus Microfire digital camera (M/N S97809) attached to an Olympus BX60 microscope.

#### 2. Results

##### 2.1. Tissue integrity of the porcine *ex vivo* model

Before studying the FcRn expression and albumin transcytosis, it was crucial to understand how the porcine GI tract is organized. Initially, it was evaluated the viability and morphology of the GI tract from the porcine *ex vivo* model, using H&E staining. According to **Figure S1 A** it is possible to see morphologic differences throughout intestinal sections. The porcine duodenum has a light-staining with a branched and tubular structure with Brunner's glands in its sub mucosa, which has a protective role against the acidic chyme. Ileum is highlighted by the presence of lymphatic aggregates, as Peyer's patches, with phagocytic M-cells in the sub mucosa and lamina propria regions. On the other hand, jejunum is marked by the lack of Brunner's glands and Peyer's patches. In general, the absence of villi and Paneth cells and reduction of lymph nodes aggregates distinguishes the large from the small intestine. However, crypts and

goblet cells are more abundant in the colon. By contrast, esophagus and stomach have a different composition and cell types, since they are not responsible for the absorption function. For instance, the mucosa of the stomach is in a columnar format and is covered with a protective layer of alkaline mucus. In its epithelium it is possible to find gastric glands, mucus neck cells to produce mucus, parietal cells to secrete acid, and chief cells to release pepsinogen. These evidences are in line with what is described for humans [17].

As it is shown, most of the GI tract presents mucosa, sub mucosa, muscularis externa and serosa, which is particularly exemplified by a duodenum section (**Figure S1 B**). The human intestine is described by having the same pattern and characteristics. The mucosa has an importance role in absorption, since it is 90% composed by enterocytes and microvilli (capillary branches as a door for the hepatic portal vein). Mucosa is divided in epithelium, lamina propria (connective tissue), muscularis mucosae (smooth muscle) and serosa (mesothelium). It is in epithelium where cells can proliferate, differentiate in absorptive enterocytes or mucus secretory cells (goblet cells, enteroendocrine cells and Paneth cells) and be apoptosed, by the presence of proliferative crypts. Particularly, enterocytes, as polarized cells, are the ones responsible for absorbing nutrients and transcytose them from the apical to the basolateral side. On the other hand, M cells control the transepithelial transport of macromolecules or particles and microorganisms. Sub mucosa is characterized by being a connective tissue with lymphatic and blood vessels, ganglion and nerve cells. Finally, muscularis externa (smooth muscles) and a serosa layer (**Figure S1 C**) [13].

However, it is reported that porcine and human intestine present some anatomical differences, as the length of small intestine and shape of the colon, as described elsewhere [18].

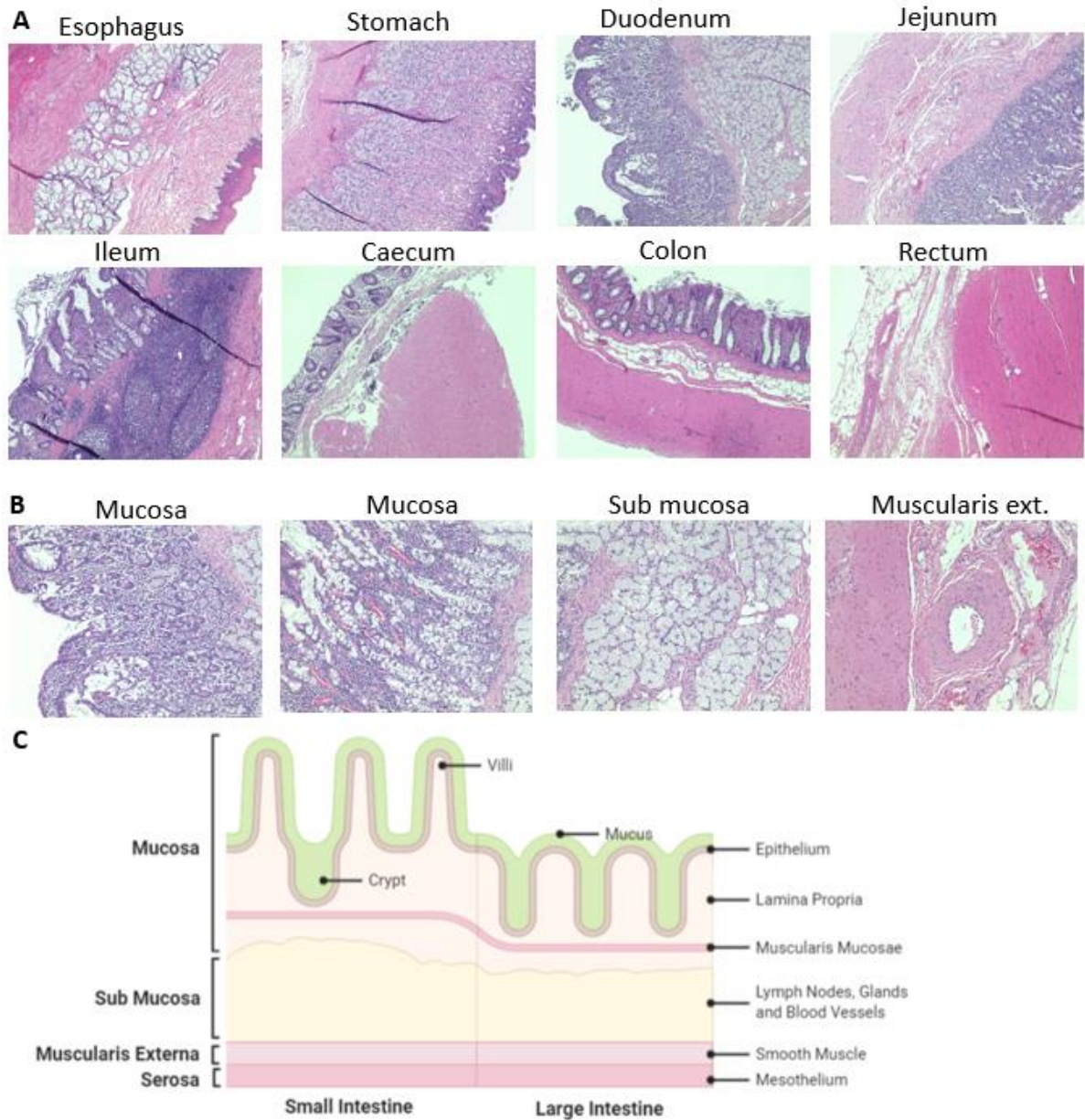


**Figure S1 | H&E stained sections of porcine GI tract. (A)** Morphologic differences between esophagus, stomach, duodenum, jejunum, ileum, caecum, colon and rectum. **(B)** Identification of duodenum sections, as mucosa, sub mucosa, muscularis externa and serosa. Experiment was performed once. **(C)** Schematic representation of intestinal morphology and sections division (mucosa, sub mucosa and muscularis externa).



## The effect of hypergravity on intestinal permeability of nanoformulations and molecules

*Cláudia Azevedo<sup>1,2,3,\*</sup>, Maria Helena Macedo<sup>1,2,3,\*</sup>, Andreia Almeida<sup>1,2,3,\*</sup>, Soraia Pinto<sup>1,2,3,\*</sup>, Jack J. W. A. van Loon<sup>4,5</sup>, Bruno Sarmiento<sup>1,2,6,#</sup>*

<sup>1</sup> INEB - Instituto de Engenharia Biomédica, Universidade do Porto, Porto, Portugal

<sup>2</sup> i3S – Instituto de Investigação e Inovação em Saúde, Universidade do Porto, Porto, Portugal

<sup>3</sup> Instituto de Ciências Biomédicas Abel Salazar, Universidade do Porto, Porto, Portugal

<sup>4</sup> Department of Oral and Maxillofacial Surgery/Oral Pathology, Amsterdam Movement Sciences & Amsterdam Bone Center (ABC), Amsterdam University Medical Center Location VUmc, Amsterdam, The Netherlands

<sup>5</sup> European Space Agency (ESA), Technology Center (ESTEC), TEC-MMG LIS lab, Noordwijk, The Netherlands

<sup>6</sup> CESPU, Instituto de Investigação e Formação Avançada em Ciências e Tecnologias da Saúde, Gandra, Portugal

\*Equal contribution

#Corresponding author: Tel +351 226074949, [bruno.sarmiento@ineb.up.pt](mailto:bruno.sarmiento@ineb.up.pt)

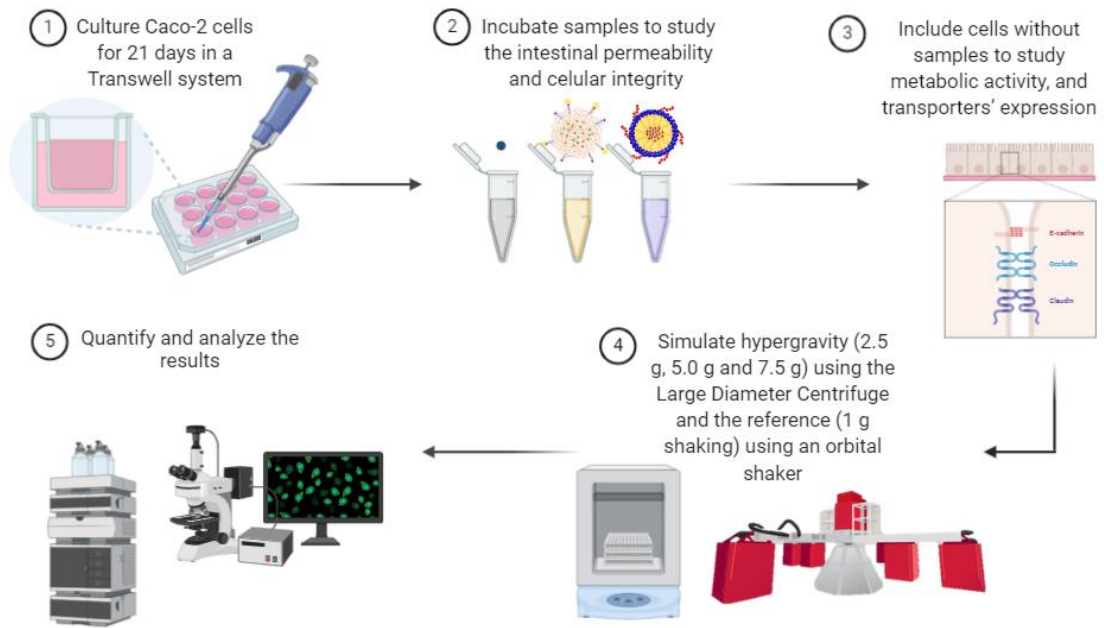
## **Abstract**

The oral administration of drugs remains a challenge due to rapid enzymatic degradation and minimal absorption in the gastrointestinal tract. According to the literature, mechanical forces, namely hypergravity can interfere with cellular integrity and drug absorption, and there is no study describing its influence in the intestinal permeability. In this study, the effect of hypergravity on intestinal Caco-2 cells and its influence in the intestinal permeability of different nanoformulations and molecules was studied using the large diameter centrifuge from the European Space Research and Technology Centre of the European Space Agency. It was shown that the cellular metabolic activity and integrity was maintained after exposure to different gravity levels. Expression of important drug transporters and tight junctions' proteins was evaluated and, interestingly, most proteins demonstrated a switch of behavior in their expression. Furthermore, paracellular transport of FITC-Dextran showed to significantly increase with hypergravity, which agrees with the decrease of transepithelial electrical resistance and the increase of claudin-2 at higher g-levels. The diffusion of camptothecin released from polymeric micelles revealed a significant decrease, which agrees with the increased expression of the P-gp observed with the increase in g-levels, responsible for pumping this drug out. The neonatal Fc receptor-mediated transport of albumin-functionalized nanoparticles loaded with insulin showed no significant changes when increasing the gravity levels. A good correlation of cellular permeability studies in hypergravity is important when developing new therapeutic nanoformulations. Thus, this study supports the potential of simulated hypergravity to be used in oral delivery of nanoformulations and molecules.

**Keywords:** Caco-2 model; intestinal absorption; large diameter centrifuge; nanoparticles; polymeric micelles.

**Teaser:** The current study shows that hypergravity influence the expression of certain drug transporters and tight junctions' proteins as well as the intestinal permeability of nanoformulations and molecules.

## Graphical abstract





## 1. Introduction

Oral administration is considered the preferred drug delivery route due to ease and patient compliance <sup>1</sup>. However, several drugs have limited bioavailability since they do not endure the harsh environment of gastrointestinal tract and poorly cross epithelial barriers <sup>2</sup>. In order to overcome the inefficient delivery, nanotechnology has been used as a promising strategy to overcome those biological barriers and to improve the intestinal absorption of drugs, which can be assessed by *in vitro* cellular models. In fact, nanosystems provide a stable biocompatible environment to encapsulate drugs, promote a controlled release and an efficient absorption <sup>2, 3</sup>. These nanosystems are also responsible to improve the therapeutic efficacy, increasing the residence time and minimizing the unwanted side effects by driving drugs towards the site of action and increasing the concentration of drug in the targeted site <sup>1, 4</sup>. After developing new drugs and incorporating them into nanosystems, it is important to evaluate their absorption profile in intestinal cellular models, such as the gold standard Caco-2 monoculture model <sup>5</sup>. The Caco-2 monoculture model relies on seeding Caco-2 cells in a semi-permeable support, Transwell<sup>®</sup> inserts, and culturing them to allow their differentiation into enterocyte-like cells, forming a monolayer that mimics the intestinal epithelium. Transwell<sup>®</sup> inserts membranes are very convenient to perform permeability assays, since they provide independent access to both sides of the monolayer (apical and basolateral sides). Therefore, during the permeability assays, it is possible to measure the amount of drug that was capable of crossing the cellular membrane, enabling a correlation to the absorption that will occur *in vivo*. According to the literature, mechanical forces of strain and fluid shear can stimulate CYP3A4 activity, glucose reuptake and mucus production, which is known to be absent in static Caco-2 models <sup>6</sup>. Particularly, studies indicated that barrier function, namely downregulation of occludin expression, decrease of transepithelial electrical resistance (TEER) values and increase of paracellular transport can be altered, in endothelial cells, measured after a 1-3 g hypergravity (HG) rocket launch profile exposure <sup>7</sup>, while an on-line measurements of the barrier integrity in endothelial cells exposed to 2-4 g HG showed an increase with increasing gravity levels (g-levels) <sup>8</sup>. However, a very limited set of studies has exploited the effect of HG on drug absorption, and none of them related with the intestinal permeability of orally delivered drugs. Here, it was intended to understand the impact of HG, as mechanical force, upon metabolic activity, integrity and expression of cellular components. Ultimately, it was evaluated how different transport vias, such as paracellular, diffusion and receptor-mediated were affected after HG exposure, in order to find a more advantageous

strategy to enhance drug delivery. This innovative study will help researchers and pharmaceutical industries in oral drug development areas, since it may correlate more precisely the obtained results with the permeability in the human intestine.

## **2. Experimental section**

### **2.1. Production of polymeric nanoformulations**

Wild-type (WT) albumin-conjugated and insulin encapsulated poly(lactic-co-glycolic)-poly(ethylene glycol) (PLGA-PEG) nanoparticles (NPs) and chitosan-based micelles were produced following the procedures previously described<sup>9-11</sup>. Throughout the manuscript, they will be referred as Ins-NPs-Alb and CPT-micelles, respectively. The safety of both formulations was assessed and the full description of the methods and results obtained can be found in **supplementary materials** (section 1).

### **2.2. Hypergravity exposure**

Cells, which culture is detailed in **supplementary material** (section 2), were exposed to HG in the large diameter centrifuge (LDC)<sup>12</sup> at the TEC-MMG LIS Lab from the European Space Research and Technology Centre (ESTEC) of the European Space Agency (ESA) in Noordwijk, Netherlands. The LDC, with a diameter of 8 meters, allows for the application of up to 20 g. The four arms of the centrifuge hold at maximum six gondolas, plus one gondola in the center for a 1.0 g rotational control, if required (**Figure 1 A**). The gondolas of the centrifuge swing out, resulting in an acceleration vector that is always perpendicular to the samples surface. Because of this and its size, the systems avoid inertial shear forces common in smaller centrifuges<sup>13</sup>. The Transwell® multiwell plates were placed in a 37 °C incubator (Thermo Scientific Heratherm IMC-18 mini incubator) that were accommodated in one of the gondolas. Since multi g-levels can be created during one run the experiment was performed during 2 rounds.

### **2.3. Metabolic activity studies**

The influence of HG on the metabolic activity of Caco-2 cells was evaluated by resazurin and lactate dehydrogenase (LDH) assays. The full description of both methods can be found in **supplementary materials** (section 3).

#### **2.4. Tight junctions and drug transporters' expression by immunocytochemistry**

To understand if HG could have an impact in tight junctions (TJs) and drug transporters expression of cells, the models were subjected to different g-levels, without any treatment.

The TJ presence was assessed using claudin-1, claudin-2 and occludin, which are integral transmembrane proteins, and zona occludens-1 (ZO-1), a peripheral TJ protein. The cytoskeleton was addressed by evaluating actin. Drug transporters P-glycoprotein (P-gp), peptide transporter 1 (PEPT-1), multidrug resistance protein 2 (MRP2) and neonatal Fc receptor (FcRn) were also evaluated. Mucin 2 (MUC2) was chosen to evaluate mucin expression, since it is the mostly expressed mucin in the small intestine<sup>14</sup>. Samples were prepared as previously described<sup>15</sup>, and detailed in the **supplementary material** (section 4).

#### **2.5. Cellular integrity by hematoxylin and eosin staining**

To assess cellular integrity after exposure to different g-levels, hematoxylin and eosin (H&E) staining was performed. Inserts with cells were washed once with PBS 1X for 5 min and fixed using 2% PFA in PBS 1X for 20 min at RT. Then, inserts were washed thrice with PBS 1X for 5 min and kept in PBS 1X at 4 °C until further processing for paraffin embedding. Sections of 3 mm were obtained using an RM2255 microtome (Leica) and then stained for H&E, as described elsewhere<sup>15</sup>.

#### **2.6. Intestinal permeability study**

Caco-2 cells were seeded at a density of  $1.0 \times 10^5$  cells per  $\text{cm}^2$  onto 12-Transwell® cell culture inserts (surface area of  $1.1 \text{ cm}^2$ , inner diameter of 12 mm and pore size of  $1 \mu\text{m}$ ; Millicell) and were allowed to grow and differentiate for 21 days inside an incubator as previously described (**Figure 1 A**). The medium was replaced every two/three days from the apical (0.5 mL) and basolateral (1.5 mL) sides. The permeability assays through the cell monolayers were performed in the apical-to-basolateral direction in Hank's balanced salt solution (HBSS) buffer at reference conditions (1.0 g shaking)<sup>16</sup>, 37 °C, in an orbital shaker and at 2.5 g, 5.0 g and 7.5 g, 37 °C, in the LDC. Prior to the experiment, the cell culture medium was removed from both sides of the inserts and the monolayers were washed twice with pre-warmed HBSS. Then, the monolayers were allowed to equilibrate with 0.5 mL and 1.5 mL of HBSS in the apical and basolateral compartments, respectively, for 30 min at 37 °C, 100 rpm (Stuart S150 Orbital Incubator), at reference

conditions. Then, the HBSS of the apical compartment was removed and 0.5 mL of CPT-micelles (0.1 µg/mL CPT) in ddH<sub>2</sub>O (pH 6) or fluorescein isothiocyanate–dextran (FITC-Dextran) 4 kDa (200 µg/mL; Sigma Aldrich) in HBSS (pH 7.4) or 0.5 mL of Ins-NPs-Alb (150 µg/mL insulin and 500 nM WT albumin) in HBSS with MES (pH 6) were added to the apical side. At different time-points (0.5, 1, 2, 3 and 4 h), TEER was measured using an EVOM2 epithelial volttohmmeter equipped with a STX2 electrode (World Precision Instruments, Inc.) and 200 µL of each sample was removed from the basolateral side of the inserts and replaced for the same volume of pre-warmed HBSS buffer (**Figure 1 B**). The amount of albumin was quantified by enzyme linked immunosorbent assays (ELISA), as detailed elsewhere <sup>9</sup>. The permeated CPT was quantified by high-performance liquid chromatography (HPLC), as previously described <sup>17</sup>. Lastly, FITC-Dextran was measured by fluorescence at an excitation/emission wavelengths of 490/520 nm, respectively, using a plate reader (Victor Nivo™ PerkinElmer, Inc.). The integrity of the cell monolayers was checked before and during the permeability experiment by measuring the TEER. The permeability percentage and the apparent permeability coefficient (*P<sub>app</sub>*) of each formulation after 240 min of experiment were determined by the following equations:

$$\text{Equation (1) } \text{Drug permeability (\%)} = \frac{\text{total mass}}{\text{theoretic mass}} \times 100$$

$$\text{Equation (2) } P_{app} = \frac{dQ}{A \times C_0 \times dt} ,$$

where dQ (µg) is the total amount of compound in the basolateral side, A is the surface area of the insert (cm<sup>2</sup>), C<sub>0</sub> is the initial concentration in the apical side (µg/mL) and dt (s) is the time of the experiment.

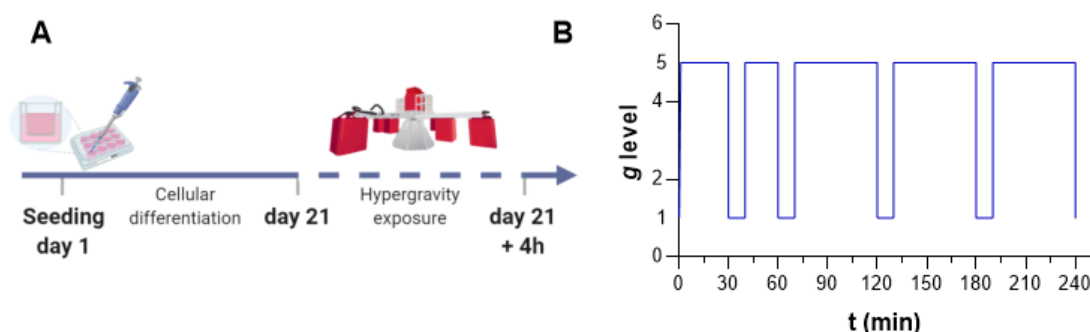


**Figure 1 | Experimental procedure of the intestinal permeability under different gravity levels (g-levels).** (A) Schematic illustration of cell culture and HG exposure process: Caco-2 cells

were cultured for 21 days, to allow their differentiation into enterocyte-like cells. After this, FITC-dextran, Ins-NPs-Alb and CPT-micelles were incubated for 4 h, at different g-levels; **(B)** Schematic diagram for an example of HG exposure, which entailed 10 min rest period at different time points (0.5, 1, 2, 3 and 4 h). During this rest period at 1.0 g, TEER was measured and samples were removed from the basolateral side, for further quantification. This set up was performed for 2.5 g, 5.0 g and 7.5 g using the LDC and for the reference using an orbital-shaker, as control.

## 2.7. Statistical analysis

Statistical analysis was performed using the GraphPad Prism Software vs. 6.0 (GraphPad Software Inc). Statistical significance of the difference between two groups was evaluated by the Student's *t*-test. Differences between groups were compared using one-way or two-way analysis of variance (ANOVA) Dunnett's multiple comparison test. Results are expressed as mean  $\pm$  standard deviation and geometric means with 95% confidence intervals. The level of significance was set at probabilities of \**P* < 0.05, \*\**P* < 0.001, and #*P* < 0.0001. N=6 for all data points.

All authors had access to the study data and reviewed and approved the final manuscript.

## 3. Results and Discussion

### 3.1. No influence of hypergravity in cellular metabolic activity

The *in vitro* metabolic activity studies (resazurin and LDH assays) were performed using an intestinal cell line, Caco-2 clone, in order to resemble the intestinal enterocytes (representing 90% of the total intestinal epithelial cells)<sup>18, 19</sup>. To assess the effect of HG on the cellular metabolism, viability and cytotoxicity were measured after exposure to different g-levels (2.5 g, 5.0 g and 7.5 g), for 4 h inside a LDC from ESTEC-ESA and compared to reference control. The obtained data showed similar cellular viability for nearly all the tested g-levels as compared with the reference conditions, of approximately 100% (**Figure 2 A**). It was observed that at 2.5 g, cellular viability presented a statistically significant increase when compared to the reference. However, in biological terms, this difference is not relevant. These outcomes were in accordance with the values obtained in the cytotoxicity assay (**Figure 2 B**), where no cytotoxicity was found. Despite there are no published studies reporting the influence of g-levels in the metabolism of intestinal epithelial cells, the obtained results are in line with the reported data using different cell lines. Previous studies on osteoblasts and human tendon cells demonstrated no significant influence on cellular viability after exposure to HG (5 g, 10 g, 15 g and 20 g)

during 3 and 4 h, respectively <sup>20, 21</sup>. Additionally, the exposure of nasal epithelial cells to 10 g during three cycles of 20 min, with 20 min resting periods between each time, also did not cause significant loss of cellular metabolic activity <sup>22</sup>.

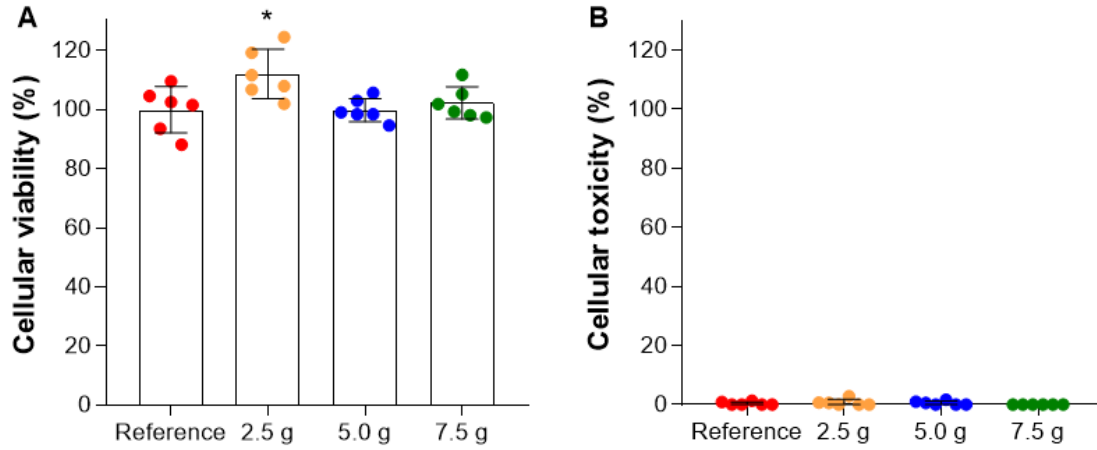


**Figure 2 | Evaluation of metabolic activity of Caco-2 cells after HG exposure. (A)** Evaluation of cellular viability through resazurin assay; **(B)** Evaluation of cellular toxicity through LDH assay. Shown are the arithmetic means  $\pm$  SD. \*P<0.05 comparing with the reference, by one-way analysis of variance (ANOVA) Dunnett's multiple comparison test. N=6.

### 3.2. Hypergravity might induce a tipping point on the expression of cellular components

Before studying the effect of HG upon transport, it was crucial to understand how transporters and TJs proteins might be affected (**Figure 3 A**).

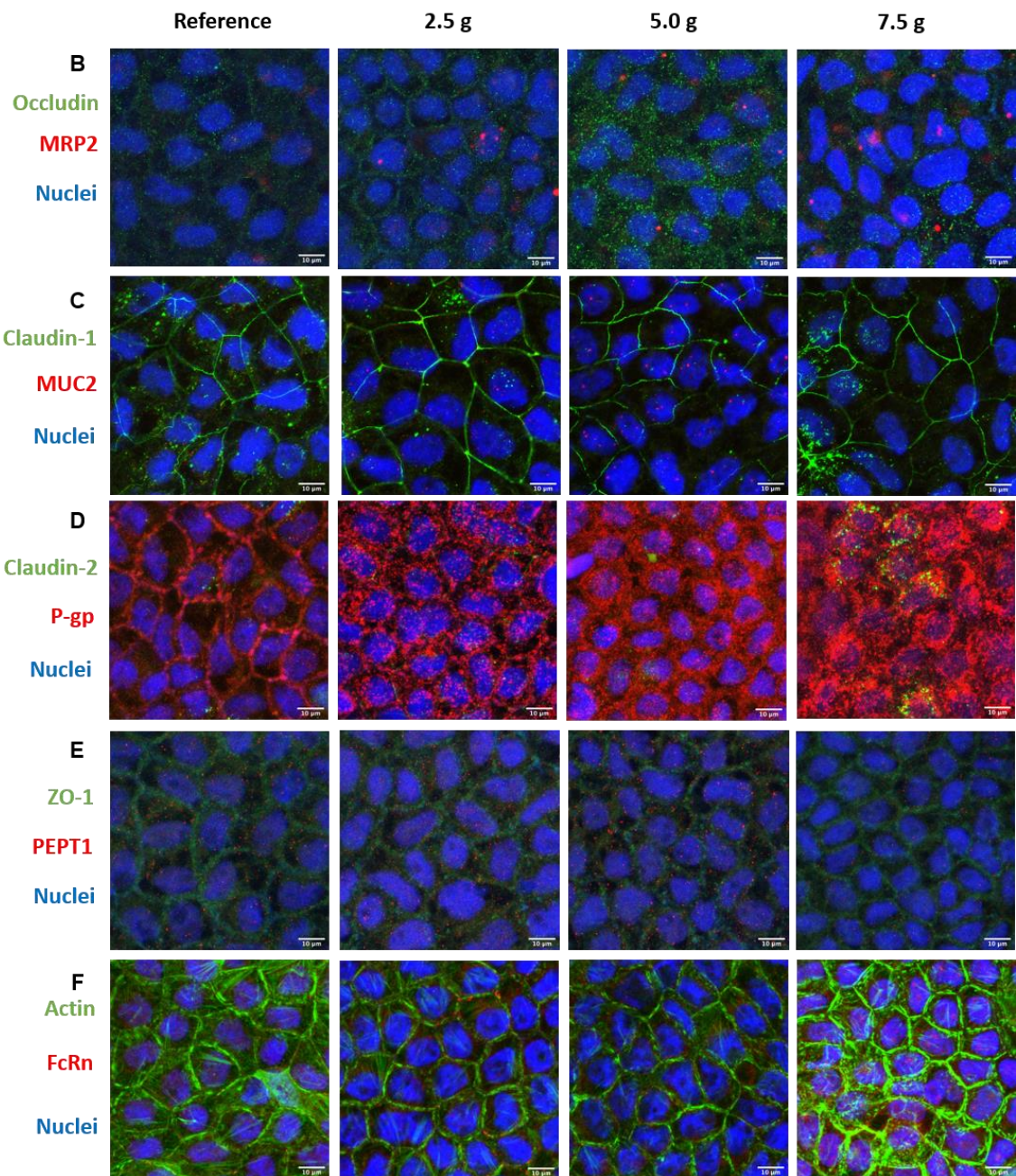
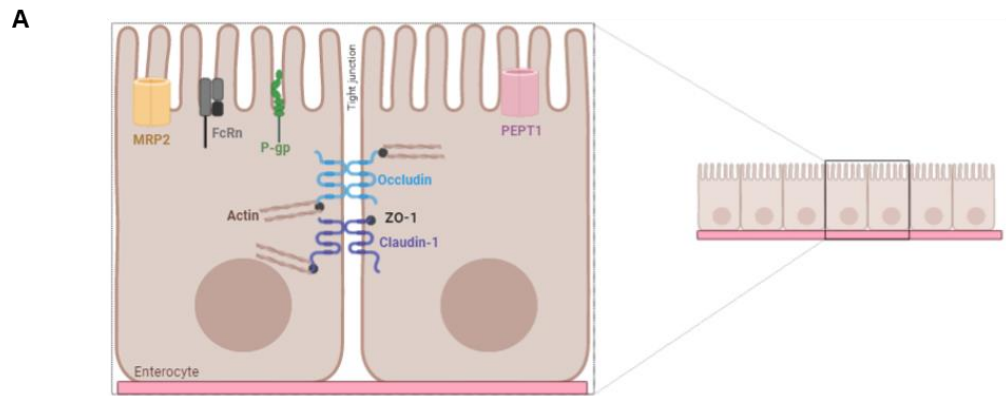


**Figure 3 | Assessment and comparison of cellular integrity at different g-levels. (A)** Schematic illustration of the studied cellular components involved in different transport vias. Visualization of nuclei and **(B)** occludin and MRP2; **(C)** claudin-1 and MUC2; **(D)** claudin-2 and P-gp; **(E)** ZO-1 and PEPT1, **(F)** actin and FcRn. Occludin, claudin-1, claudin-2, ZO-1 and actin are presented in **green**. MRP2, MUC2, P-gp, PEPT1 and FcRn are presented in **red**. Nuclei are presented in **blue**.

Different TJs proteins were evaluated, namely occludin, claudin-1, claudin-2 and ZO-1. Occludin and claudins are integral transmembrane proteins, whereas ZO-1 is a peripheral membrane adaptor, acting as a bridge between the integral membrane TJs and the actin cytoskeleton, which is extremely important to maintain TJ formation and function<sup>23-25</sup>. Occludin is normally highly expressed at cell-cell contact sites, being essential to the assembly and maintenance of TJs and, when this protein is under expressed, it can lead to an increase in the paracellular permeability of macromolecules<sup>24,26</sup>. Observing **Figures 3 B** and **4 B**, this protein showed increased expression with the increase of the g-levels from reference conditions to 5.0 g, but a decrease was observed afterwards. Because of the lack of a trend, it was hard to conclude if this could have an impact in the permeability outcomes. When looking at claudin-1 (**Figures 3 C** and **4 B**), its expression follows the opposite trend observed with occludin, with the decrease of the g-levels from reference conditions to 5.0 g and then, an increase. As for occludin, this change in behavior makes it hard to predict if it will have an impact in permeability. Claudins are the major determinant of the barrier function, defining the paracellular flux of small solutes<sup>27</sup>. There are two types of claudins: sealing and pore forming. Claudin-1 is a member of the sealing family, which means that if this protein is decreased, it results in a leakier barrier. On the other hand, claudin-2 belongs to the class of pore-forming claudins and an increase in these type of TJs means the selectivity for paracellular permeability is reduced<sup>27</sup>. In the specific case of claudin-2, it is capable of forming pores that are permeable to small cations and water, being size selective<sup>28,29</sup>. When looking at the expression of claudin-2 (**Figures 3 D** and **4 B** and **Figure S4** from supplementary materials), a decrease in its expression occurred from reference to 2.5 g, and then an increase was observed for the higher g-levels. Since claudin-2 is a pore forming TJ, these results may indicate an increase in permeability with the increase in g-force from 5.0 g to 7.5 g. Regarding ZO-1, although its role and importance is not yet clearly understood, some studies have been showing that cells with lower expression or absence of this protein present normal permeability, being more impactful in the



assembly of other TJ proteins, as occludin and claudins<sup>30</sup>. Since it was not possible to observe major changes in the expression of ZO-1 between the different g-levels, it is likely that this protein had no impact in permeability outcomes (**Figures 3 E** and **4 B**).

There is no doubt that expression and assembly of TJs present a key role concerning the permeability outcomes of compounds that cross the intestinal barrier by the paracellular route. Nevertheless, when it comes to the transcellular pathway, the different drug transporters located in intestinal cells might have a wide impact on the permeability of compounds, mostly in the ones that are substrates of these transporters. Taking into consideration that CPT can suffer efflux by P-gp and MRP2<sup>31</sup> and that FcRn mediates the uptake of Ins-NPs-Alb<sup>9</sup>, the expression of these transporters after the exposure to HG was evaluated. Despite PEPT-1 not being directly linked to the drugs tested in this study, its expression was evaluated, since this is an important uptake transporter present in intestinal cells and it is considered highly attractive as a drug target<sup>32</sup>. When looking at the expression of PEPT1 (**Figures 3 E** and **4 A** and **Figure S5** from supplementary material), its expression was increased from reference to 2.5 g and then a decrease was observed for the higher g-levels. When looking at the expression of FcRn, the behavior was different, where a decrease in the expression was observed from reference to 5.0 g, and a steep increase was observed at from 5.0 g to 7.5 g (**Figures 3 F** and **4 A** and **Figure S6** from supplementary material). Looking at the efflux pump MRP2, a slight increase was observed with the increase in g-levels, but doesn't seem to be noteworthy and, therefore, most likely not capable of affecting permeability outcomes (**Figures 3 B** and **4 A** and **Figure S3**). P-gp, the other efflux pump presents the same behavior, but much more pronounced (**Figures 3 D** and **4 A** and **Figure S4** from supplementary materials). In this case, this great increase from lower to higher g-levels can potentially lead to a greater efflux of drugs that are substrates of P-gp, such as CPT, which could translate in a decrease in the transport of these compounds through the intestinal barrier. In the case of actin, there was a decrease from reference to 2.5 g, a stable signal between 2.5 g and 5.0 g and then an increase at 7.5 g (**Figures 3 F** and **4 C** and **Figure S6** from supplementary material).

MUC2 was evaluated because this is the most expressed mucin in the small intestine and it is known that mechanical forces can interfere with the production of mucus, as previously stated<sup>6,14</sup>. In this sense, it could be interesting to understand if HG might have an impact on its secretion. However, the change of MUC2 with the increase in g-levels seems to be negligible (**Figures 3 C** and **4 D** and **Figure S3** from supplementary materials). Considering all these results, it is possible to conclude that HG affects protein

expression in different ways. In some cases, like for the efflux pumps, a trend is observed, where protein expression increases with the increase in g-levels. However, it is interesting to see that for most proteins, this trend could not be observed. In fact, there seems to be a tipping point at 2.5 g or 5.0 g and proteins revert their behavior when reaching that point. For PEPT-1 and Claudin-2 this turning point occurs at 2.5 g, whether for FcRn, Occludin and Claudin-1, this occurs at 5.0 g. Other interesting fact is that this change in behavior can occur in both directions, meaning protein expression can first increase and then decrease or the other way around, depending on the protein.

Regarding the localization of the transporters (**Figure S7** of supplementary materials), it was possible to observe that MRP2 was located at the apical side of the cells, confirming what is described in the literature<sup>33, 34</sup>. P-gp is also known to be localized at the apical side of enterocytes, a perfect location to mediate the efflux of undesired compounds, like toxins, into the organism, but also to limit the entrance of drugs<sup>35</sup>. In this study, it was possible to confirm the apical localization of P-gp, although its presence was not only at the apical side, but extended into the basolateral part of the cells. When it comes to FcRn, it was present at the membrane and throughout the cytoplasm, which is in line with the literature, that states this transporter is located in the apical region of epithelial cells and within acidified endosomes<sup>36, 37</sup>. In the case of PEPT1, its apical localization was also confirmed<sup>38</sup>. When it comes the localization of different transporters, it was possible to conclude that HG did not have an impact in this regard, being that no differences were observed between the localization of the different proteins, when comparing the different g-levels.

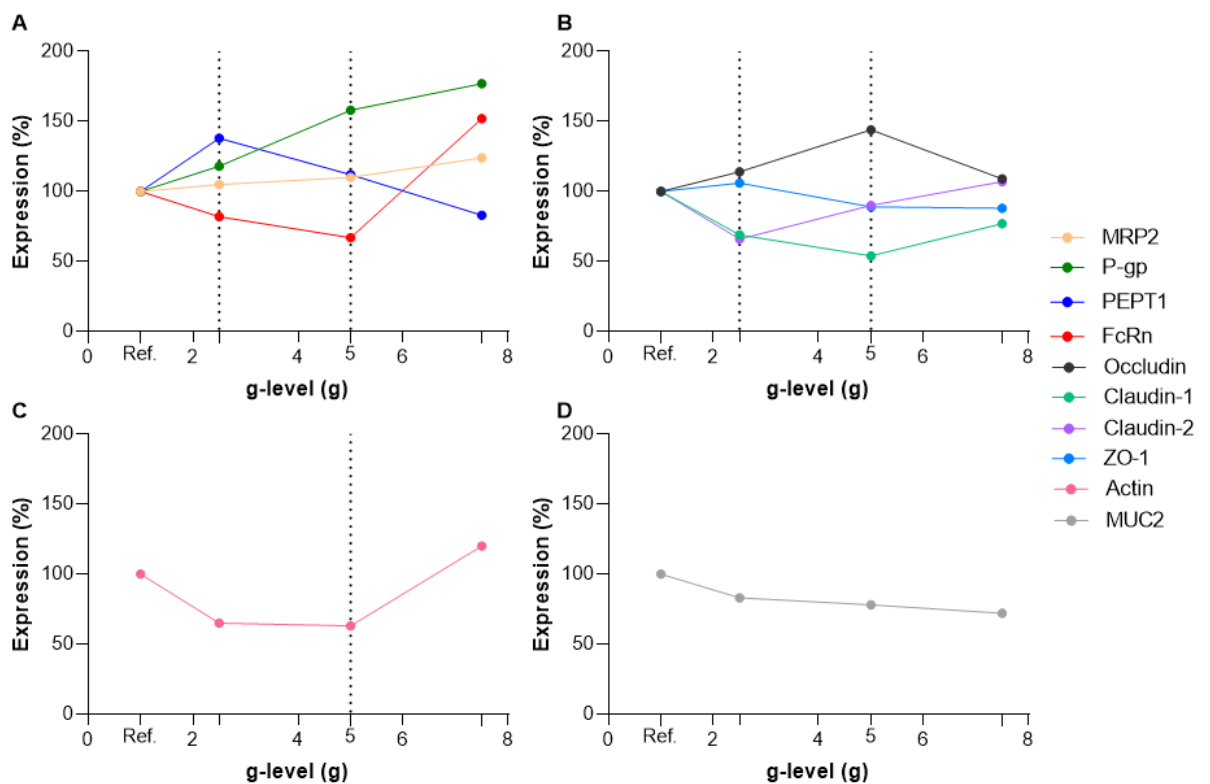


**Figure 4 | Overview sketch of the quantitative expression.** Analysis of the expression percentage of **(A)** transporters of influx and efflux; **(B)** components of tight junctions; **(C)** cytoskeleton and **(D)** mucus production, after exposure to different g-levels. The quantitative data are related to images presented at Figure 3. Quantification was done using ImageJ and each sample was normalized to the reference condition.

### 3.3. Barrier integrity is maintained after exposure to hypergravity

To assess the cellular integrity and morphology after exposure to HG, H&E staining was performed for each condition and nanoformulation/molecule (**Figure 5**). In this assay two dyes were used, hematoxylin and eosin, that work as basic and acidic dyes, respectively. Hematoxylin was used to stain acidic structures in purple, as the nucleus containing nucleic acids. On the other hand, eosin dyes basic structures in pink, so it was used to stain cytoplasm and extracellular matrix, by containing proteins<sup>39</sup>. Taking this in mind, it was possible to verify that the cellular membrane integrity was generally maintained and attached to the Transwell® membrane. Regarding the different compounds that were incubated, there was no significant difference between them, demonstrating an apparent resemblance with the reference group. Thus, the possibility of the effect be due to

compounds and not due to the HG was discarded. Actually, the safety of CPT-micelles and Ins-NPs-Alb was assessed, and the used concentrations are therefore compatible with the permeability model and quantifying methods (**Figure S1** from supplementary material). However, some portions of the monolayer suffered membrane disruption and release of cytoplasm content, which could be due to handling procedure, as normally happens.

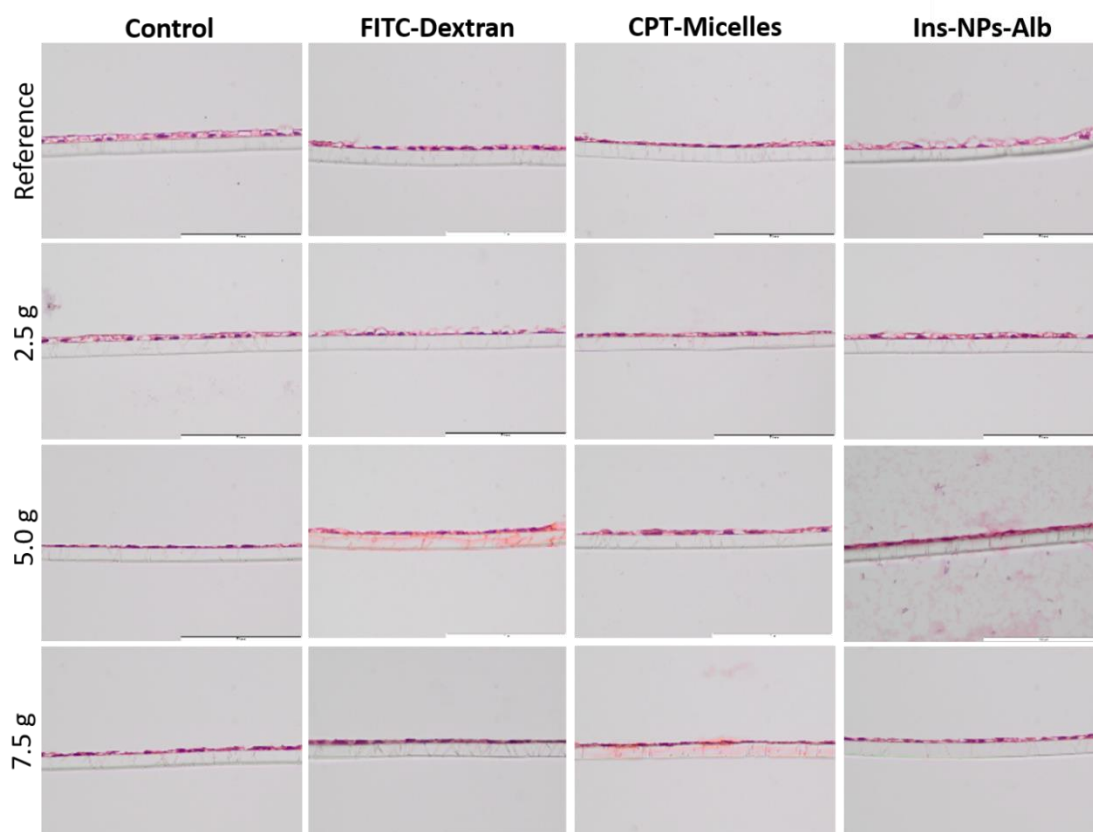


**Figure 5 | H&E staining to address the cellular integrity when cells were exposed to different compounds and g-levels.** Dextran, CPT-micelles and Ins-NPs-Alb were exposed to different g-levels (2.5 g, 5.0 g and 7.5 g) for 4 h. Cells without samples and the reference (shaking at 1.0 g) were included as controls. Cytoplasm stained with **pink** and nucleus with **purple**. The Transwell® membrane is transparent and is right below the cellular monolayer. Scale bar = 100  $\mu\text{m}$ .

### 3.4. Hypergravity interfered differently among transport mechanisms

In this study, FITC-Dextran, CPT-micelles and Ins-NPs-Alb were used to evaluate the effect of HG upon paracellular, passive and transcellular transport (**Figure 6**). The different g-levels were compared to 1.0 g shaking reference, based on the permeability protocol established in our lab <sup>10, 15, 40-44</sup>.

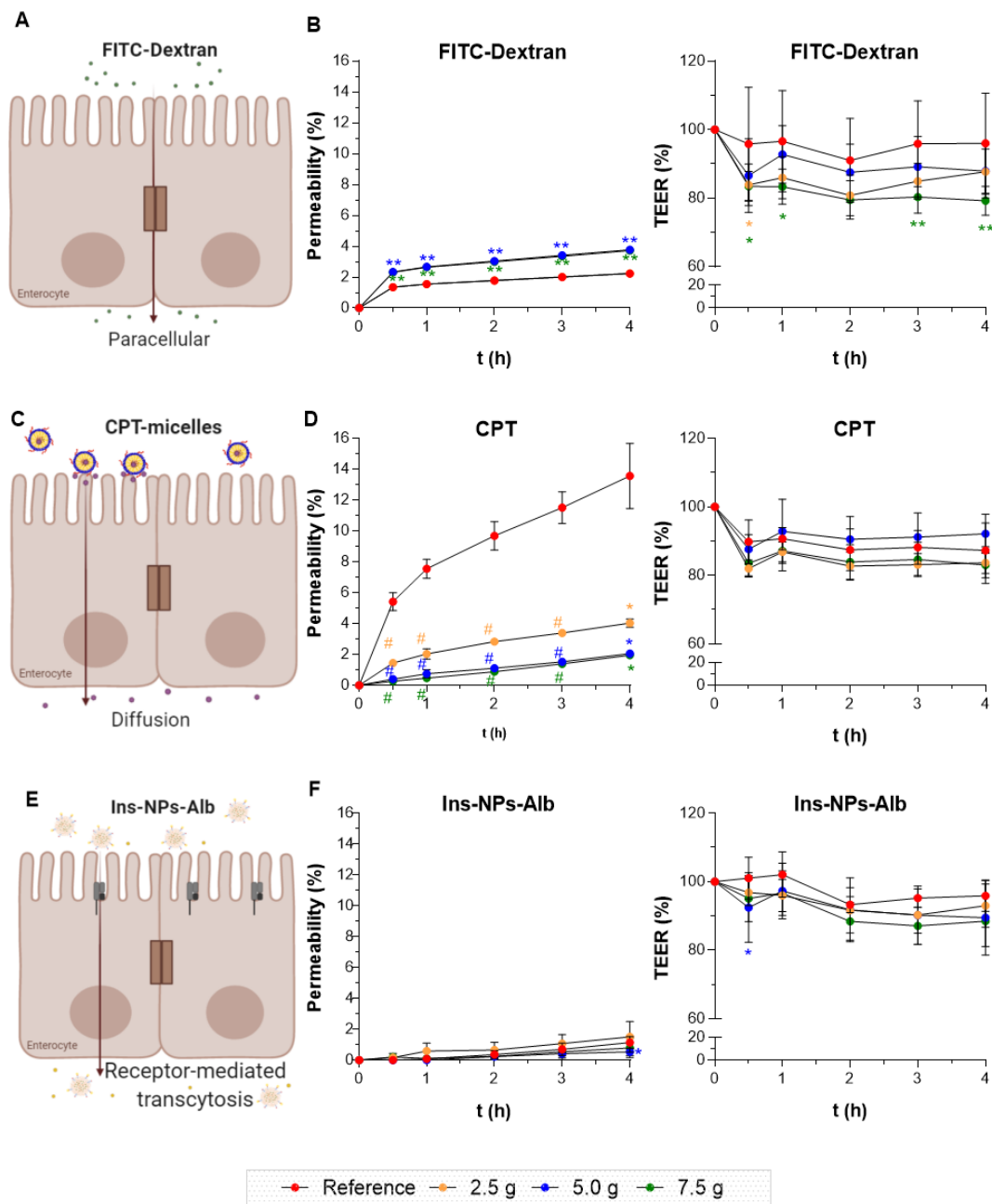


**Figure 6 | Intestinal permeability and respective TEER values of compounds with different pathways of internalization. (A)** Schematic representation of the paracellular via used by FITC-Dextran; **(B)** Permeability percentage of FITC-Dextran quantified by fluorescence and respective TEER values; **(C)** Schematic representation of the CPT transport; **(D)** Permeability percentage of CPT from the micelles, quantified by HPLC, and respective TEER values; **(E)** Schematic representation of FcRn-mediated transcytosis used by Ins-NPs-Alb through intestinal epithelial cells; **(F)** Permeability percentage of Ins-NPs-Alb, quantified by ELISA, and respective TEER values during 4 h of incubation at different g-levels. Shown are the arithmetic means  $\pm$  SD. \*P <

0.05, \*\*P < 0.001, and #P < 0.0001 comparing with the reference, by two-way analysis of variance (ANOVA) Dunnett's multiple comparison test). N=6 for all groups.

FITC-Dextran, a hydrophilic compound that is known to cross the intestinal epithelium by the paracellular route (**Figure 6 A**), with a molecular weight of 4 kDa, was used to measure the paracellular permeability and the possible impact of the different g-levels<sup>15, 45</sup>. When it comes to TEER values, it was observed that there was a significant decrease when cells were subjected to a force of 7.5 g (**Figure 6 B**). Nevertheless, the TEER values were still high, having a decrease of around 20%, comparing to the initial value. When it comes to the other g-levels tested, only other significant decrease was observed for 2.5 g at 30 min, but the models were then able to recover and increase the TEER, getting close to the initial values. Looking at the permeability, FITC-Dextran showed significantly higher permeability at 5.0 and 7.5 g (**Figure 6 B**). At the reference and 2.5 g, permeability values were around 2%, translating in a *Papp* value of around  $0.7 \times 10^6$  cm/s. On the other hand, in the case of 5.0 and 7.5 g, permeability increased to around 4%, which means *Papp* values were about  $1.1 \times 10^6$  cm/s, as demonstrated in **Table 1**. When comparing the results obtained by the TEER values, the immunostaining performed on the models and the permeability outcomes, it is possible to correlate the results. In fact, as stated in **Section 3.2** expression of claudin-2 was enhanced for the higher g-levels. These evidences could be translated in an increase in the permeability of paracellular compounds, as FITC-Dextran. Besides, TEER values are associated with the expression of TJs and a decrease in TEER can be associated with an under expression of sealing TJs, or an overexpression of pore-forming TJs, like of claudin-2<sup>46, 47</sup>, which was observed here. Nevertheless, it is important to state that although the increase in permeability had a statistical significance, in biological terms an increase from 2% to 4% is very low, suggesting that only a small fraction of the compound was able to pass, even at higher g-levels, and therefore, the barrier integrity was largely maintained. As already mentioned, the effect of HG in intestinal permeability was not reported in the literature, making it impossible to perform comparisons. Nevertheless, FITC-Dextran with a molecular weight of 4 kDa was used to test the permeability of the nasal route under 10 g HG<sup>22</sup>. These authors observed that TEER significantly decreased and permeability was enhanced by 16%. The observed decrease in TEER values correlate with the results presented here and the increase in permeability too. In the case of the mentioned study, the increase was even higher, which could be derived from the

fact that the applied force was greater or simply because other cell types were used that reacted in a different way. There are other studies that address permeability in the intestine and in the lung, but under the effect of microgravity and, in both studies, microgravity induces an increase in the permeability of FITC-Dextran <sup>48, 49</sup>. However, since applied forces are different, a direct comparison with the present study cannot be established.

Polymeric micelles based on chitosan were carefully thought out to improve the solubility and the bioavailability of CPT. Thus, the micellar system has a pegylated surface to improve the mucodiffusion and the micelle core is constituted by strong fatty acids, which maintain the drug encapsulated due to established hydrophobic interactions. These micelles were around 150 nm, had a positive superficial charge and an association efficiency of around 80% <sup>11</sup>. CPT is a substrate of some of the ABC (ATP-binding cassette) transporters, namely P-gp and MRP2 <sup>31</sup>, which leads to resistance when it comes to absorption of this drug in the small intestine. Looking for the permeability data, it was possible to observe a pattern where the intestinal permeability decreased as the g-level increased (**Figure 6 D**). It was a very interesting fact since at reference conditions the CPT permeability, around 14%, achieved a *Papp* of  $4.28 \times 10^{-6}$  cm/s and, as the g-levels increased, the CPT intestinal permeability decreased, reaching a *Papp* of  $0.62 \times 10^{-6}$  cm/s for the 7.5 g (**Table 1**). The increase P-gp expression with the increase of g-levels may have contributed for this outcome (**Figures 3 B** and **4 A**). Although the micellar system can protect the drug, with such a significant increase of the efflux pumps, it is expected that the permeability will not increase or be maintained but decrease since the opposite path is much higher. At the same time, the TEER values were monitored at all different g-levels and were recorded steadily without significant decreases (**Figure 6 D**), which was in line with no intestinal permeability increasing. In this sense, we can verify that the permeability of drugs mediated by efflux pumps, such as the case of CPT, tend to decrease their permeability with increasing HG. In any case, it is worth mentioning that the shear forces that are acting on the reference at 1.0 g, because it is at shaking conditions, can also have an impact on the permeability outcomes. In this case, the decrease in permeability may not only be related with the increase in g-levels, but it is possible that the absence of shear forces in HG conditions lead to lower permeability results.

Finally, the produced Ins-NPs-Alb were previously characterized, by being a monodisperse solution of 150 nm in size, zeta potential around -9 mV and 10% loaded with insulin <sup>9</sup>. These NPs were composed by PLGA-PEG, which confer biodegradable

and mucodiffusive characteristics. In addition, through the MAL group, NPs were covalently conjugated to the free Cys34 of domain I of albumin. This allows NPs to be recognized by the FcRn (**Figure 6 E**). FcRn is a key player in intestinal transcellular transport and half-life extension of albumin and IgG (endogenous ligands), by escaping to lysosomal degradation. FcRn binds to its ligands at acidic pH (5.0-6.5) and releases them upon physiological pH<sup>50</sup>. Reported data using the Caco-2 monolayer demonstrated that albumin transport is a saturable process, which indicates a receptor-mediated uptake. To confirm, with a competition assay, these authors showed that albumin-decorated NPs were 1.85-fold less transported when incubated with free albumin<sup>51</sup>. Here, after performing the permeability assay at different g-levels, it was shown that the transcytosis was similar to the reference, being concordant with the TEER values. Plus, it is possible to claim that the monolayer was maintained, and that NPs were not transported in a paracellular way, since the TEER values were barely reduced (**Figure 6 F**). For some reason, cells adapted better when in the presence of these NPs. Probably, the presence of insulin, albumin or biodegradable polymers can contribute to this. The confocal images suggested a switch behavior between 5.0 g and 7.5 g, since the FcRn expression decreased until 5.0 g and then increased, which might explain the significant decrease of permeability at 5.0 g after 4 h. All in all, this tendency seemed to not have biologic significance, since *Papp* values were similar to the reference (**Table 1**). As future perspectives, it would be interesting to increase the incubation time to confirm if the permeability tendency is maintained or if it has a statistical difference at some point. Taking all this into consideration, the transport mediated by FcRn suggested to not be affected by HG. This evidence adds to our basic understanding of the impact of mechanical stimuli i.e. HG, on drug transportation processes and can bring new treatment strategies for subjects exposed to different gravity environments such as astronauts and pilots.

**Table 1** | Apparent permeability coefficients calculated after 4 h of incubation in Caco-2 cells.

<i>Papp</i> ± SD (x 10 <sup>-6</sup> cm/s)	Reference	2.5 g	5.0 g	7.5 g
<b>FITC-Dextran</b>	0.70 ± 0.07	0.71 ± 0.02	1.14 ± 0.04	1.18 ± 0.05
<b>CPT</b>	4.28 ± 0.66	1.27 ± 0.09	0.65 ± 0.06	0.62 ± 0.05
<b>Ins-NPs-Alb</b>	0.36 ± 0.12	0.48 ± 0.31	0.17 ± 0.07	0.25 ± 0.20



#### **4. Conclusions**

In this study, the effect of different HG levels (2.5 g, 5.0 g and 7.5 g) in the intestinal transport of nanoformulations and molecules for oral delivery, as well as the influence of HG in the expression of TJs and drug transporters were evaluated. According to our results, the exposure to HG did not affect the metabolic activity and integrity of intestinal epithelial cells. Notwithstanding, the expression of TJs and transporters of Caco-2 cells, as well as the intestinal transport of molecules and nanoformulations by paracellular, passive and transcellular pathways were affected by the exposure to different g-levels. Regarding the paracellular transport, FITC-Dextran increased with the increase of g-levels. This can be also related with the increase of claudin-2 expression for higher g-levels. On the other side, the passive transport of CPT from micelles by diffusion decreased with the augment of g-levels, which is in line with the general increase of P-gp expression, responsible for CPT efflux. Lastly, the receptor-mediated transport of Ins-NPs-Alb by FcRn was maintained after exposure to HG. This pioneer study was important to understand biologic mechanisms and can be crucial when developing new formulations for oral delivery.

#### **Acknowledgements**

This project was supported by the Spin Your Thesis! 2020 programme, organized by European Space Agency (ESA) Education Office. Additional funding included FCT - Fundação para a Ciência e a Tecnologia/ Ministério da Ciência, Tecnologia e Ensino Superior in the framework of the project “Institute for Research and Innovation in Health Sciences” (UID/BIM/04293/2019). The authors are thankful for the ESA professional Education Office, Nigel Savage, Emmanuelle Aubert and Alan Dowson for all the support before, during and after the campaign. Cláudia Azevedo (SFRH/BD/117598/2016), Maria Helena Macedo (SFRH/BD/131587/2017), Andreia Almeida (SFRH/BD/118721/2016) and Soraia Pinto (SFRH/BD/144719/2019) would like to thank to Fundação para a Ciência e a Tecnologia (FCT), Portugal for financial support. The authors acknowledge the support of the following i3S Scientific Platforms: Biointerfaces and Nanotechnology (FCT - UID/BIM/04293/2019), Bioimaging [member of the national infrastructure PPBI – Portuguese Platform of Bioimaging (PPBI-POCI-01-0145-FEDER-022122)] and Histology and Electron Microscopy (PPBI-POCI-01-0145-FEDER-022122). The authors also are very thankful to Alamelu Sundaresan and Vivel Mann (Texas Southern University, USA) for been mentors of this project and for giving useful discussion and suggestions. Lastly, the authors would like to thank Merck for kindly

providing material for the campaign as well as for financially supporting the project, and Thais Rizzi of Perkin-Elmer for giving technical support with Victor Nivo equipment.

### **Conflict of Interest**

All the authors declare no conflict of interest.

### **Author Contributions**

C.A., H.M., A.A., S.P. and J.W.A.L designed research; C.A., H.M., A.A. and S.P. performed research; C.A., H.M., A.A., S.P. and J.W.A.L. analyzed data; C.A., H.M., A.A., S.P. and B.S. wrote the paper.

## References

1. Sarmiento B, Ferreira D, Vasconcelos T. Polymer-based delivery systems for oral delivery of peptides and proteins. In: Jorgensen L, Nielsen HM, eds. *Delivery Technologies for Biopharmaceuticals: Peptides, Proteins, Nucleic Acids and Vaccines*: John Wiley & Sons, Ltd, 2009:207-227.
2. Araújo F, Shrestha N, Granja PL, et al. Antihyperglycemic potential of incretins orally delivered via nano and microsystems and subsequent glucoregulatory effects. *Curr Pharm Biotechnol* 2014;15:609-619.
3. Pereira C, Araújo F, Granja PL, et al. Targeting membrane transporters and receptors as a mean to optimize orally delivered biotechnological based drugs through nanoparticle delivery systems. *Curr Pharm Biotechnol* 2014;15:650-658.
4. Moulari B, Beduneau A, Pellequer Y, et al. Nanoparticle targeting to inflamed tissues of gastrointestinal tract. *Curr Drug Deliv* 2013;10:9-17.
5. Hidalgo IJ, Raub TJ, Borchardt RT. Characterization of the human colon carcinoma cell line (Caco-2) as a model system for intestinal epithelial permeability. *Gastroenterology* 1989;96:736-749.
6. Kim HJ, Ingber DE. Gut-on-a-Chip microenvironment induces human intestinal cells to undergo villus differentiation. *Integr Biol* 2013;5:1130-1140.
7. Sumanasekera WK, Sumanasekera GU, Mattingly KA, et al. Estradiol and dihydrotestosterone regulate endothelial cell barrier function after hypergravity-induced alterations in MAPK activity. *Am J Physiol Cell Physiol* 2007;293:566-573.
8. Szulcek R, van Bezu J, Boonstra J, et al. Transient intervals of hyper-gravity enhance endothelial barrier integrity: Impact of mechanical and gravitational forces measured electrically. *PLoS One* 2015;10:e0144269.
9. Azevedo C, Nilsen J, Grevys A, et al. Engineered albumin-functionalized nanoparticles for improved FcRn binding enhances oral delivery of insulin. *J Control Release* 2020;327:161-173.
10. Almeida A, Silva D, Gonçalves V, et al. Synthesis and characterization of chitosan-grafted-polycaprolactone micelles for modulate intestinal paclitaxel delivery. *Drug Deliv Transl Res* 2018;8:387-397.
11. Almeida A, Araújo M, Novoa-Carballal R, et al. Novel amphiphilic chitosan micelles as carriers for hydrophobic anticancer drugs. *Mat Sci Eng C* 2020;112:110920.
12. Loon JJWAv, Krausse J, Cunha H, et al. The large diameter centrifuge, LDC, for life and physical sciences and technology. 2008.
13. van Loon JJWA, Folgering EHTE, Bouten CVC, et al. Inertial shear forces and the use of centrifuges in gravity research. What is the proper control? *J Biomech Eng* 2003;125:342-346.

14. Schneider H, Pelaseyed T, Svensson F, et al. Study of mucin turnover in the small intestine by *in vivo* labeling. *Sci Rep* 2018;8:5760.
15. Macedo MH, Martinez E, Barrias C, et al. Development of an improved 3D *in vitro* intestinal model to perform permeability studies of paracellular compounds. *Front Bioeng Biotechnol* 2020;8.
16. Hubatsch I, Ragnarsson EGE, Artursson P. Determination of drug permeability and prediction of drug absorption in Caco-2 monolayers. *Nat Protoc* 2007;2:2111-2119.
17. Martins SM, Wendling T, Gonçalves VM, et al. Development and validation of a simple reversed-phase HPLC method for the determination of camptothecin in animal organs following administration in solid lipid nanoparticles. *J Chromatogr B* 2012;880:100-107.
18. Araújo F, Sarmiento B. Towards the characterization of an *in vitro* triple co-culture intestine cell model for permeability studies. *Int J Pharmaceut* 2013;458:128-34.
19. Pereira C, Costa J, Sarmiento B, et al. 3.3 - Cell-based *in vitro* models for intestinal permeability studies. In: Sarmiento B, ed. *Concepts and Models for Drug Permeability Studies*: Woodhead Publishing, 2016:57-81.
20. Searby ND, Steele CR, Globus RK. Influence of increased mechanical loading by hypergravity on the microtubule cytoskeleton and prostaglandin E2 release in primary osteoblasts. *Am J Physiol Cell Physiol* 2005;289:148-158.
21. Costa-Almeida R, Carvalho DTO, Ferreira MJS, et al. Continuous exposure to simulated hypergravity-induced changes in proliferation, morphology, and gene expression of human tendon cells. *Stem Cells Dev* 2018;27:858-869.
22. Kim D, Kim YH, Kwon S. Enhanced nasal drug delivery efficiency by increasing mechanical loading using hypergravity. *Sci Rep* 2018;8:168.
23. Gonzalez-Mariscal L, Betanzos A, Nava P, et al. Tight junction proteins. *Prog Biophys Mol Biol* 2003;81:1-44.
24. **Lee B, Moon KM**, Kim CY. Tight junction in the intestinal epithelium: Its association with diseases and regulation by phytochemicals. *J Immunol Res* 2018;2018:2645465.
25. Lee SH. Intestinal permeability regulation by tight junction: implication on inflammatory bowel diseases. *Intest Res* 2015;13:11-8.
26. **Al-Sadi R, Khatib K**, Guo S, et al. Occludin regulates macromolecule flux across the intestinal epithelial tight junction barrier. *Am J Physiol Gastroint Liver Physiol* 2011;300:1054-1064.
27. Gunzel D, Yu AS. Claudins and the modulation of tight junction permeability. *Physiol Rev* 2013;93:525-569.
28. Van Itallie CM, Fanning AS, Anderson JM. Reversal of charge selectivity in cation or anion-selective epithelial lines by expression of different claudins. *Am J Physiol Renal Physiol* 2003;285:1078-1084.

29. Rosenthal R, Milatz S, Krug SM, et al. Claudin-2, a component of the tight junction, forms a paracellular water channel. *J Cell Sci* 2010;123:1913-1921.
30. Umeda K, Matsui T, Nakayama M, et al. Establishment and characterization of cultured epithelial cells lacking expression of ZO-1. *J Biol Chem* 2004;279:44785-44794.
31. Lalloo AK, Luo FR, Guo A, et al. Membrane transport of camptothecin: facilitation by human P-glycoprotein (ABCB1) and multidrug resistance protein 2 (ABCC2). *BMC Med* 2004;2:16.
32. Estudante M, Morais JG, Soveral G, et al. Intestinal drug transporters: An overview. *Adv Drug Deliv Rev* 2013;65:1340-1356.
33. Liu YH, Di YM, Zhou ZW, et al. Multidrug resistance-associated proteins and implications in drug development. *Clin Exp Pharmacol Physiol* 2010;37:115-120.
34. Yu XQ, Xue CC, Wang G, et al. Multidrug resistance associated proteins as determining factors of pharmacokinetics and pharmacodynamics of drugs. *Curr Drug Metab* 2007;8:787-802.
35. Hediger MA, Romero MF, Peng JB, et al. The ABCs of solute carriers: physiological, pathological and therapeutic implications of human membrane transport proteinsIntroduction. *Pflugers Arch* 2004;447:465-468.
36. Ober RJ, Martinez C, Vaccaro C, et al. Visualizing the site and dynamics of IgG salvage by the MHC class I-related receptor, FcRn. *J Immunol* 2004;172:2021-2029.
37. Pyzik M, Rath T, Kuo TT, et al. Hepatic FcRn regulates albumin homeostasis and susceptibility to liver injury. *Proc Natl Acad Sci USA* 2017;114:2862-2871.
38. Shugarts S, Benet LZ. The role of transporters in the pharmacokinetics of orally administered drugs. *Pharm Res* 2009;26:2039-2054.
39. Fischer AH, Jacobson KA, Rose J, et al. Hematoxylin and eosin staining of tissue and cell sections. *CSH Protoc* 2008;4986.
40. Silva DS, Almeida A, Prezotti FG, et al. Self-aggregates of 3, 6-O, O'-dimyristoylchitosan derivative are effective in enhancing the solubility and intestinal permeability of camptothecin. *Carbohydr Polym* 2017;177:178-186.
41. Silva DS, Almeida A, Prezotti F, et al. Synthesis and characterization of 3, 6-O, O'-dimyristoyl chitosan micelles for oral delivery of paclitaxel. *Colloids Surf B Biointerfaces* 2017;152:220-228.
42. Silva DS, M dos Santos D, Almeida A, et al. N-(2-hydroxy)-propyl-3-trimethylammonium, o-mysristoyl chitosan enhances the solubility and intestinal permeability of anticancer curcumin. *Pharmaceutics* 2018;10:245.
43. Sgorla D, Lechanteur A, Almeida A, et al. Development and characterization of lipid-polymeric nanoparticles for oral insulin delivery. *Expert Opin Drug Deliv* 2018;15:213-222.

44. Heep G, Almeida A, Marcano R, et al. Zein-casein-lysine multicomposite nanoparticles are effective in modulate the intestinal permeability of ferulic acid. *Int J Biol Macromol* 2019;138:244-251.
45. Woting A, Blaut M. Small intestinal permeability and gut-transit time determined with low and high molecular weight fluorescein isothiocyanate-dextrans in C3H mice. *Nutrients* 2018;10:685.
46. Li N, Wang D, Sui Z, et al. Development of an improved three-dimensional *in vitro* intestinal mucosa model for drug absorption evaluation. *Tissue Eng Part C Methods* 2013;19:708-719.
47. Yi B, Shim KY, Ha SK, et al. Three-dimensional *in vitro* gut model on a villi-shaped collagen scaffold. *Biochip J* 2017;11:219-232.
48. Alvarez R, Stork CA, Sayoc-Becerra A, et al. A Simulated microgravity environment causes a sustained defect in epithelial barrier function. *Sci Rep* 2019;9:17531.
49. dos Santos MA, Bosquillon C, Russomano T, et al. Modelling the effects of microgravity on the permeability of air interface respiratory epithelial cell layers. *Adv Space Res* 2010;46:712-718.
50. Roopenian DC, Akilesh S. FcRn: the neonatal Fc receptor comes of age. *Nat Rev Immunol* 2007;7:715.
51. Hashem L, Swedrowska M, Vllasaliu D. Intestinal uptake and transport of albumin nanoparticles: potential for oral delivery. *Nanomedicine* 2018;13:1255-1265.

## Supplementary Material

---

### The effect of hypergravity in intestinal permeability of nanoformulations and molecules

*Cláudia Azevedo, Maria Helena Macedo, Andreia Almeida, Soraia Pinto, Jack J. W. A. van Loon, Bruno Sarmento*

#### Section 1 | Safety of CPT-micelles and Ins-NPs-Alb

Caco-2 monoculture was seeded at a density of 10 000 cells/well in 200 µL per well and incubated during 4 hours. After that, the medium was aspirated and the wells were washed twice with 100 µL of fresh pre-heated HBSS buffer (pH 7.4). After washing, 200 µL of the nanoparticle solutions corresponding to insulin amounts of 25, 50, 100 or 150 µg/mL and 200 µL of the micelles solutions corresponding to CPT amounts of 0.78, 1.56, 3.12 and 6.25 µg/mL were added to each well and the plates were incubated for a period of 4 and 24 h at 37°C. After the incubation period, the media was removed, and 150 µL of 0.5 mg/mL MTT solution was added at each well, followed by incubation of the plates at 37°C during 4 h. The reaction was terminated by removal of the media and addition of 150 µL of DMSO. The levels of reduced MTT were determined by measuring the absorbance at 470 nm and 630 nm using a microtiter plate reader (Biotek-Synergy H1 Hibrid reader, using the Gen5 2.01 program). The % of MTT reduction was calculated as follows:

$$\text{Equation (3) } MTT \text{ reduction (\%)} = \frac{\text{absorbance of treated cells}}{\text{absorbance of untreated cells}} \times 100$$

The final results of MTT reduction, are expressed as the percentage of the absorbance of control cells.

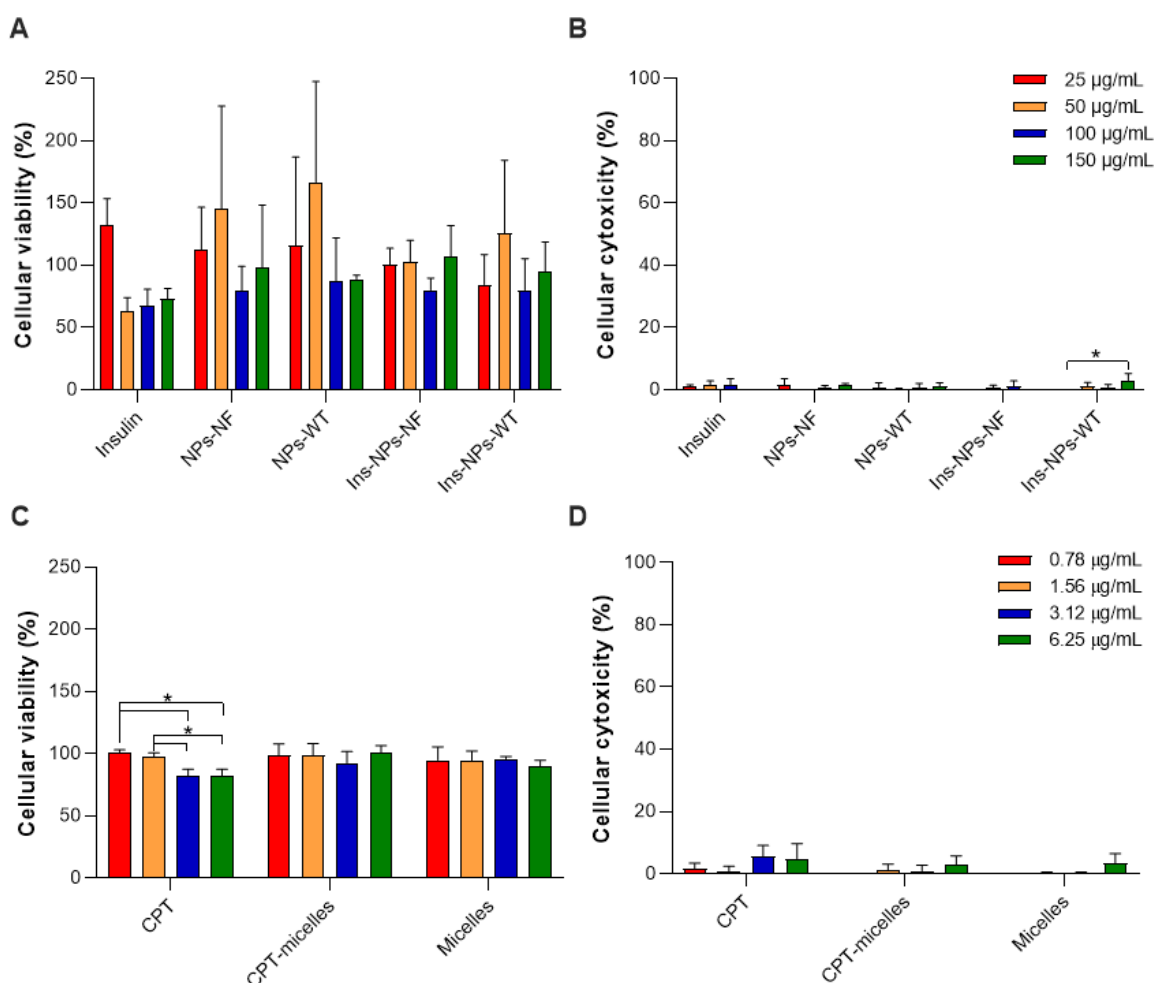


**Figure S1 | Evaluation of the safety of nanosystems. (A)** Cellular viability, assessed by the MTT assays and **(B)** cellular cytotoxicity assessed by the LDH assay, of NPs loaded or not with insulin and conjugated or not with WT albumin. Free insulin was included as a control. **(C)** Cellular viability, assessed by the MTT assays and **(D)** cellular cytotoxicity assessed by the LDH assay, of micelles loaded with CPT or not. CPT was included as control. Shown are the arithmetic means  $\pm$  SD. \* $P < 0.05$ , comparing with the control, by two-way analysis of variance (ANOVA) Tukey's multiple comparison test).  $N=4$  for all groups.

## Section 2 | Cell culture

C2BBe1 [Caco-2 clone] (human colorectal adenocarcinoma) cells were acquired from ATCC and maintained in a complete medium consisting of Dulbecco's Modified Eagle's Medium (DMEM, ATCC) supplemented with 10% (v/v) fetal bovine serum (FBS, Biochrom) and 1% (v/v) antibiotic-antimitotic mixture (final concentration of 100 U/mL penicillin and 100 U/mL streptomycin) in 75 cm<sup>2</sup> T-flasks, inside an incubator at 37 °C and 5% CO<sub>2</sub> and 95% relative humidity. DMEM medium was changed three times per



week. Caco-2 cells were used at passages 77 to 83. When confluence reached about 70% to 80%, cells were detached from the flasks by treating it with trypsin-ethylenediaminetetraacetic acid (EDTA) at 37 °C and transferred to another 75 cm<sup>2</sup> T-flasks or Transwell® and multiwell plates.

### Section 3 | Metabolic activity studies

Caco-2 cells ( $4.0 \times 10^4$  cells per well) were seeded in 96-well plates in 200  $\mu$ L of DMEM complete medium and were incubated for 24 h. Then, medium was removed, and cells were washed twice with 200  $\mu$ L of fresh pre-heated phosphate-buffered saline (PBS, 1X) to remove cellular debris and 200  $\mu$ L of fresh pre-heated DMEM without FBS was added to each well. Plates were then incubated for 4 h at 37 °C in an orbital shaker (Stuart S150 Orbital Incubator at 100 rpm) for the reference condition (1.0 g shaking), while plates at HG were placed in the LDC at 2.5 g, 5.0 g and 7.5 g at 37 °C. Afterwards, the 96-well plates were centrifuged at 250 g for 10 min at RT to remove dead cells, and the supernatant was used to perform the LDH assay, while the remaining Caco-2 cells attached at the bottom of the plate were used for resazurin assay. For this, cells were washed twice with 200  $\mu$ L PBS 1X and then treated with DMEM complete medium containing 20% resazurin (0.1 mg/mL; Merck) during 2 h at 37 °C, 5% CO<sub>2</sub> and 95% relative humidity, protected from light. After 2 h of incubation, 150  $\mu$ L of each well was transferred to a black 96-well plate and the fluorescence was measured at 530/590 nm (excitation/emission wavelengths, respectively), using a plate reader (Victor Nivo™, PerkinElmer, Inc.). The negative control consisted in cells incubated with 1% (v/v) of Triton X-100 in complete medium and the positive control consisted in cells incubated with complete medium, both at reference conditions. A number of six replicates were performed for each group. The metabolic activity was expressed according to the following equation:

$$\text{Equation (1) } \textit{Cellular viability (\%)} = \frac{\textit{Fluorescence (Experimental value)} - \textit{Fluorescence (Positive control)}}{\textit{Fluorescence (Negative control)} - \textit{Fluorescence (Positive control)}} \times 100$$

To the 100  $\mu$ L of supernatant collected after centrifugation from 96-well plates, 100  $\mu$ L of the reaction mixture composed by the catalyst solution and the dye solution (LDH Cytotoxicity Detection Kit, Takara Bio) were added to each well and incubated for 10 min at RT in the dark. The absorbance was measured at 492 nm and 690 nm, using a plate

reader (Victor Nivo™, PerkinElmer, Inc.). The negative control was composed by cells incubated with complete medium only and the positive control was composed by cells incubated with 1% (v/v) of Triton X-100 in complete medium, both at reference conditions. A number of six replicates were performed for each group. The cellular cytotoxicity was expressed according to the following equation:

$$\text{Equation (2) Cellular cytotoxicity (\%)} = \frac{\text{Absorbance (Experimental value)} - \text{Absorbance (Negative control)}}{\text{Absorbance (Positive control)} - \text{Absorbance (Negative control)}} \times 100$$

#### **Section 4 | Tight junction and drug transporters' expression by immunocytochemistry**

After 4 h of exposure to HG, samples were washed once with PBS 1X and fixed with 2% paraformaldehyde (PFA) for 20 min. Then, cells were washed three times with PBS 1X. To stain with different antibodies, a permeabilization step using a solution of 0.2% (v/v) Triton X-100 in PBS 1X for 5 min at RT was performed. Afterward, cells were washed thrice with PBS 1X for 5 min. A blocking step was performed using a solution containing 1.5% bovine serum albumin (BSA) and 5% FBS in PBS 1X for 1 h at RT. Inserts were incubated with the primary antibodies' solutions [rabbit anti-human occludin primary antibody (1:100; 701161, ThermoFisher Scientific) + mouse anti-human MRP2 primary antibody (1:100; MA1-26536, Invitrogen)], [rabbit anti-human P-gp primary antibody (1:250; PA5-61300, ThermoFisher Scientific)], [rabbit anti-human Claudin-1 (1:200; SAB5500083-100, Sigma Aldrich) + mouse anti-human MUC2 primary antibody (1:50; ab118964, Abcam)], [rabbit anti-human ZO-1 primary antibody conjugated with Alexa Fluor 488 (1:50, SC-33725, Santa Cruz Biotechnology) + mouse anti-human PEPT1 primary antibody (1:100; ab203043, Abcam)] and [rabbit anti-human FcRn primary antibody (1:100; ab193148, Abcam) + Phalloidin (1:50; A22287, Thermo Fisher Scientific)] overnight at 4 °C in a humidified chamber protected from light. Inserts were washed three times for 5 min with PBST, composed by PBS 1X and 0.05% Tween® 20, and incubated with the secondary antibodies and 4', 6-diamidino-2-phenylindole (DAPI) to counterstain the nuclei (500 ng/mL; Sigma Aldrich). Depending on the primary antibodies used, Goat anti-Mouse Alexa Fluor 594 F(ab')<sub>2</sub> fragment of immunoglobulin G (IgG) (H+L) (1:500; A11020, Invitrogen), Goat anti-Rabbit Alexa Fluor 488 F(ab')<sub>2</sub> fragment of IgG (H+L) (1:500; A11070, Invitrogen) and Donkey anti-Rabbit IgG H&L Alexa Fluor 594 pre-adsorbed (1:500; Ab150064, Abcam) were used. Secondary

antibodies were added to samples for 2 h at 4 °C in a humidified chamber protected from light. Cells were then washed twice with PBST and once with PBS 1X, all for 5 min. Inserts were mounted in slices using fluorescent mounting medium (Dako). Samples were left to dry protected from light and were maintained at 4 °C until visualization by a spectral confocal laser scanning microscope TCS-SP5 AOBS (Leica). Since the aim was to compare the amount and localization of tight and adherens junctions between samples and also the expression of drug transporters, laser power and gain of each laser were maintained for all samples regarding each antibody. The signal expression was quantified using the ImageJ and samples were normalized according the following expression:

$$\text{Equation (4) } \textit{Expression} (\%) = \frac{\textit{Samples in HG}}{\textit{Reference condition}} \times 100$$

## Section 5 | Hypergravity effect on the expression of junctional proteins and drug transporters

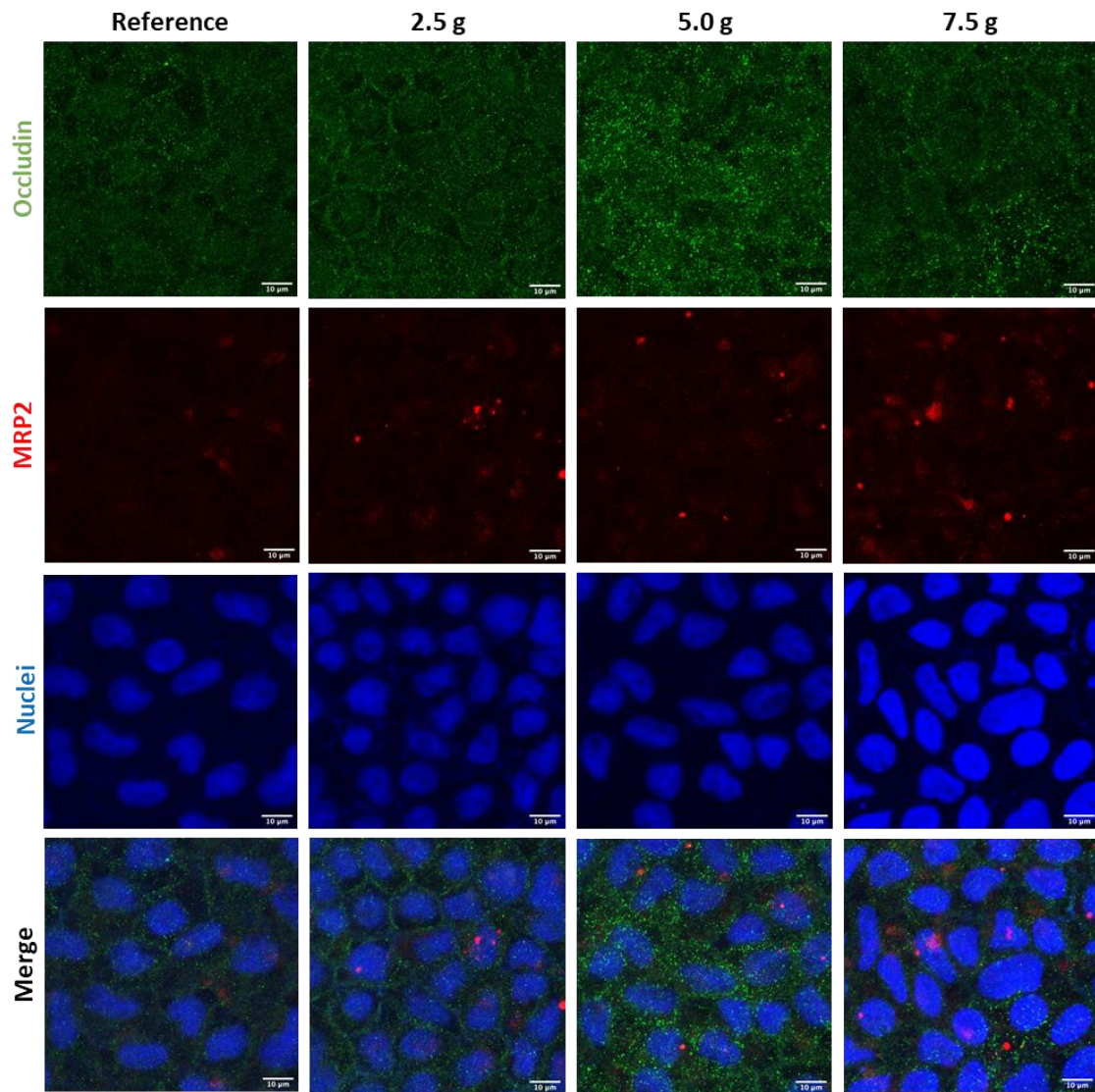


Figure S2 | Visualization of occludin and MRP2 at different g-levels. Occludin is presented in **green**, MRP2 in **red** and nuclei in **blue**.

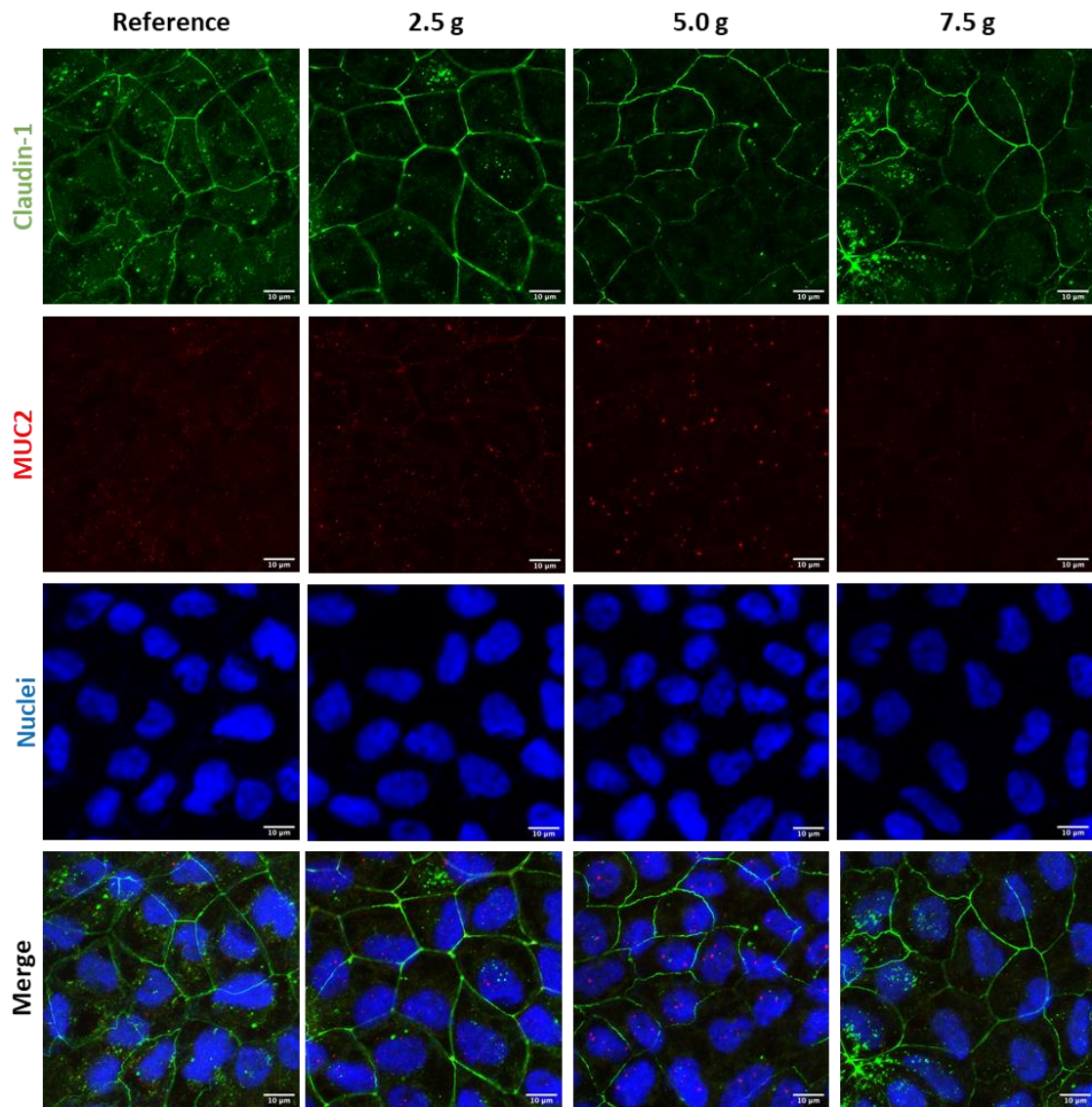
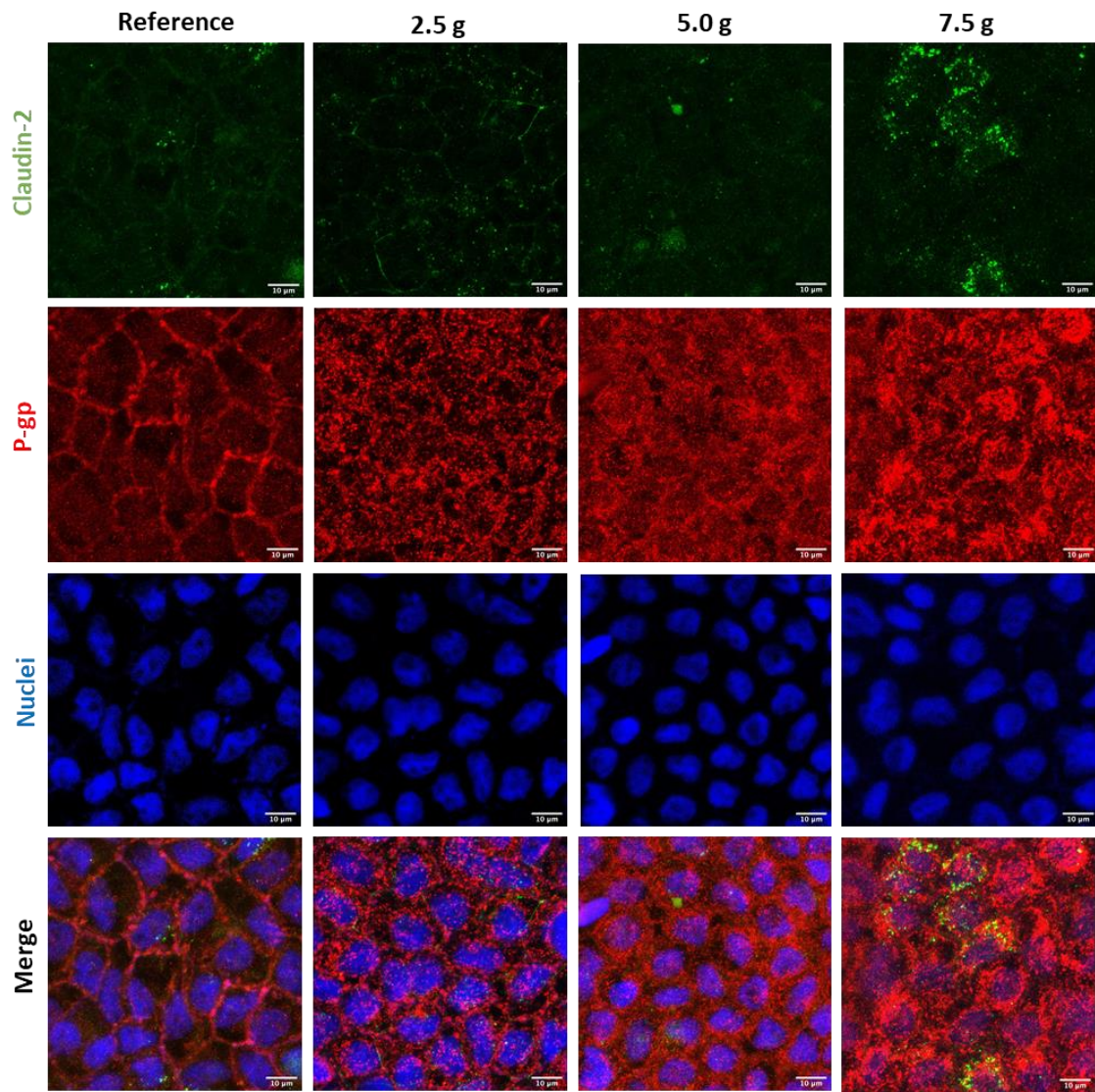
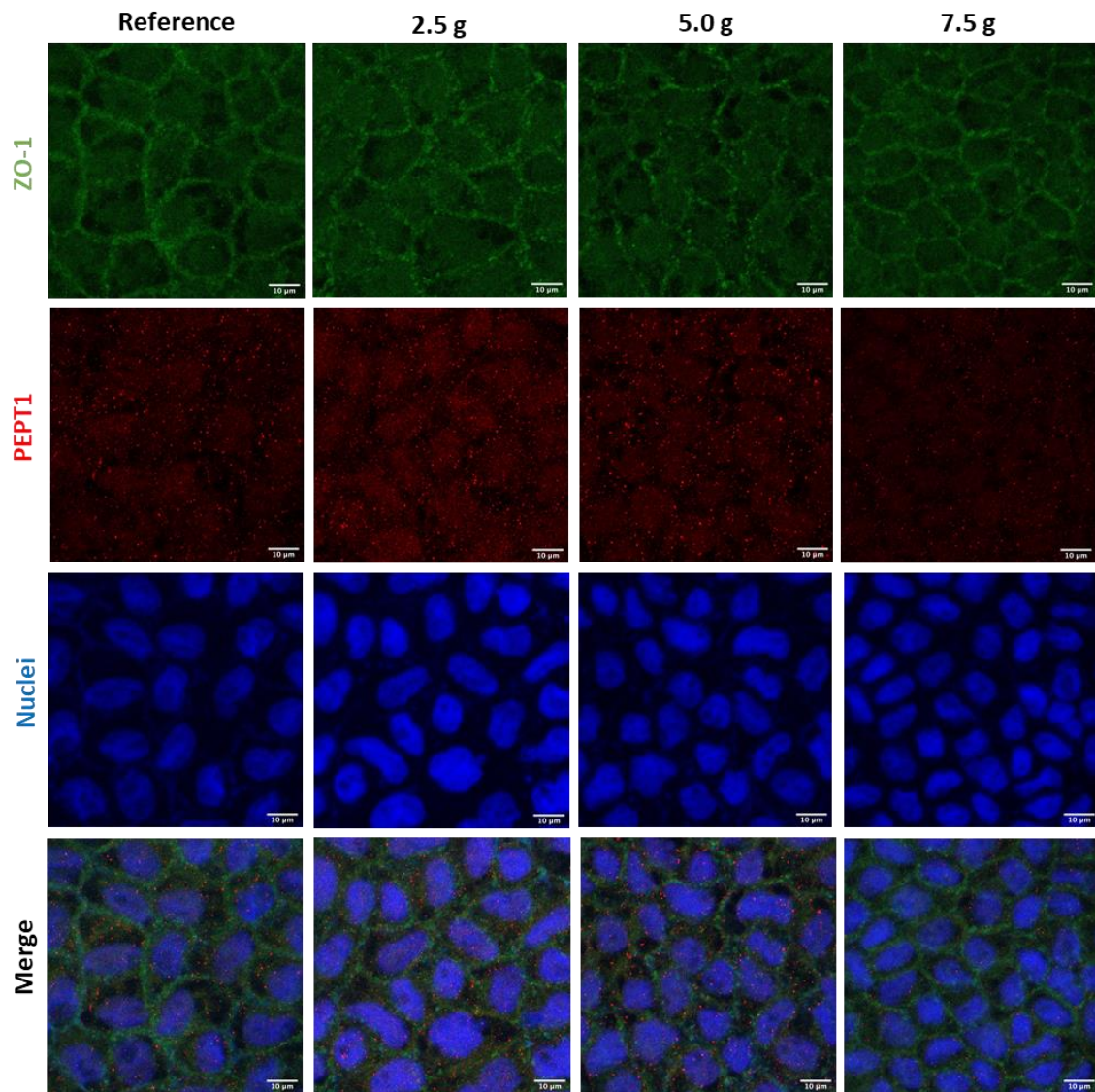


Figure S3 | Visualization of claudin-1 and MUC2 at different g-levels. Claudin-1 is presented in **green**, MUC2 in **red** and nuclei in **blue**.



**Figure S4 | Visualization of claudin-2 and P-gp at different g-levels.** Claudin-2 is presented in **green**, P-gp in **red** and nuclei in **blue**.



**Figure S5 | Visualization of ZO-1 and PEPT1 at different g-levels. ZO-1 is presented in green, PEPT1 in red and nuclei in blue.**

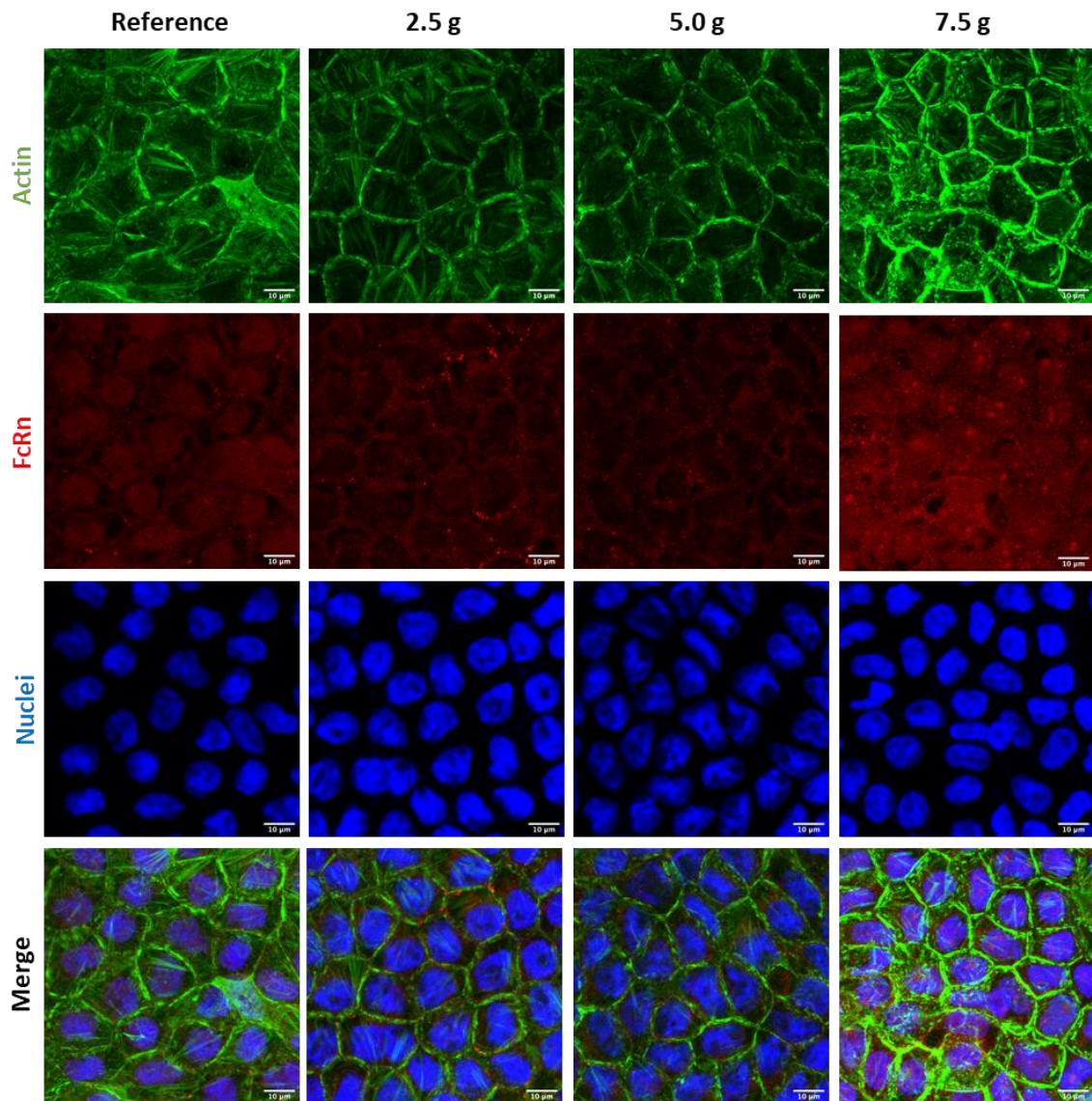


**Figure S6 | Visualization of actin and FcRn at different g-levels.** Actin is presented in **green**, FcRn in **red** and nuclei in **blue**.



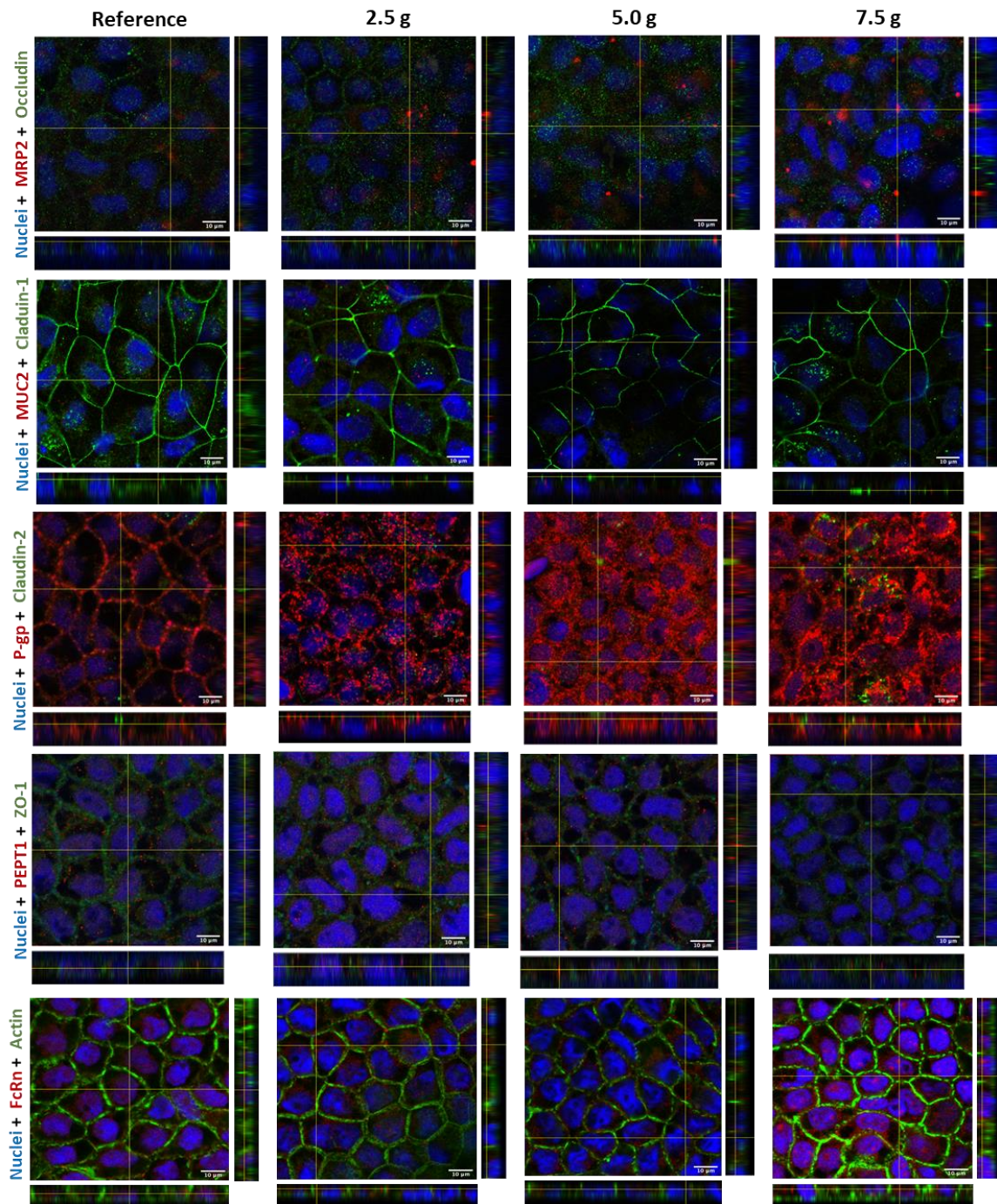


**Figure S7 | ORTO visualization of cellular components at different g-levels.** Occludin, claudin-1, claudin-2, ZO-1 and actin are presented in **green**. MRP2, MUC2, P-gp, PEPT1 and FcRn are presented in **red**. Nuclei are **blue**.

## BIBLIOGRAPHIC NOTE

---

Cláudia Azevedo was born on July 26, 1990 in Trofa, Porto, Portugal. She obtained her Bachelor in Science degree in Bioscience (2011) from Escola Superior de Biotecnologia da Universidade Católica do Porto (ESB-UCP), Porto, Portugal. Further, she obtained her Master in Science degree in Molecular Oncology, granted by Instituto de Ciências Biomédicas de Abel Salazar (ICBAS), Porto, Portugal. Since 2017, she has been developing her PhD thesis in Biomedical Sciences, PhD program from ICBAS, at Instituto de Investigação e Inovação em Saúde (I3S) / Instituto de Engenharia Biomédica (INEB), Porto, Portugal. Her research mainly focused on functionalized polymeric nanoparticles for oral drug delivery. Her current interest is also focused in controlling delivery of drugs across biological barriers, oral delivery of macromolecules, new materials for nanoparticle drug delivery systems and *in vivo/in vitro* correlation of drug absorption using cell-based co-culture models. She obtained several skills in the development and characterization of nanosystems and proteins, as well as in performing molecular and chemical techniques. She has also a broad training in cell culture techniques and cell-based assays, as well as conducting *ex vivo* and *in vivo* experiments in porcine tissues and mice models, respectively. Her research work resulted in 3 peer-reviewed original articles (two published and two submitted for publication), 4 review articles (three published and one submitted for publication), and 2 book chapters. Also, she actively collaborated in other projects that resulted in peer reviewed publications.

During her doctorate she was also able to ameliorate her skills in innovation, strategy, technology transfer and entrepreneurship, by participating in a startup acceleration program with a business idea, to create a service to screen the intestinal permeability of drugs, using *in vitro* models developed in the group. Additionally, she was always involved in activities inside and outside the institute, as organizer (PhDay, Pint of Science) or volunteer (performing diagnostic and serologic tests for COVID19, monitor in primary schools, logistic of MIT European Career Fair). She also demonstrated proactivity and networking by establishing collaborations with Massachusetts Institute of Technology (MIT) and European Space Agency (ESA), diffusing the work of the group and the institute through the world. Also, Cláudia showed initiative in attending some courses related with biomolecular interactions and clinical trials. Fruit of all these skills, was the recognition gave by Fulbright, a grant by FLAD, a prize of “Norte Empreendedor” by Associação Empresarial de Portugal (AEP), an ITC conference grant by Cost and a prize of the video competition by Controlled Release Society (CRS).

